BEHAVIOR OF CONCENTRATED COLLOIDAL SUSPENSIONS

BY

STOKESIAN DYNAMICS SIMULATION

Thesis by

Thanh Ngoc Phung

In Partial Fulfillment of the Requirements

for the Degree of

Doctor of Philosophy

California Institute of Technology

Pasadena, California

1993

(Defended on November 10, 1992)

To my god parents and my parents,

To my brothers and my sisters,

To Le-Hang and Mike Phung.

ACKNOWLEDGMENTS

I have been very fortunate to have met many special people and friends who have contributed to my education and learning. Without them, my success would not have been possible and they all deserve my heartfelt thanks.

First of all, I must thank my research advisor, John F. Brady. He is a very special teacher who has taught me the science of fluid mechanics, programming, and writing. His constant support, when I struggled with my studies or otherwise, considerable interest, when I made some breakthroughs in research, and challenge for more advanced studies have undoubtedly elevated my potential and introduced more opportunities to my career. Most important of all, John has made my years at Caltech very enjoyable and filled with good memories. For these things, I am extremely grateful.

I have also benefitted from working with Dr. Georges Bossis of Laboratoire de Physique de la Matière Condesèe, Universitè de Nice, France, who, along with J. F. Brady, invented and pioneered the use of the Stokesian dynamics simulation method for modeling the particulate flow. In addition to teaching me the methods for analyzing the microstructure and helping me to obtain the accuracy in Stokesian dynamics codes, Georges has taught me a great deal and provided me with the computing codes for the structure factors. I am very proud to have him on my thesis committee and acknowledge his support and interest in my research. I would also like to express my appreciation to Dr. Zeng-Gang Wang for allowing me to use his IBM RiSC/6000 530H computer for my research. Dr. Julie Kornfield is thanked for her interest in my studies. Mr. Suresha Guptha has been a teacher and nice friend. With expertise in computers and electronics, Suresha has made

my managing job for group computers a very educational and valuable experience. For these indispensable assistances, thank you. I would like to acknowledge two National Science Foundation summer scholarships from the San Diego Super Computers and the friendly technical staff from whom I have studied and gained the knowledge of fast computing.

I have been very fortunate to have many special friends and teachers in Hung Nguyen, Thu Pham, Truong Nguyen, Julia Lester, John and Tammy Bauer, Ivan Claeys, Roger Bonnecaze, Willem Boersma, Jeff Morris, Phil Lovalenti and Prabhu Nott. Special thanks to Jeff Morris who is truly a great friend and has helped to proofread part of my thesis. I would like to thank Mrs. Patricia Houseworth for her assistance. Her office has always provided a welcome short break from my studies, a place where I can chat, laugh, and relax. Finally, many special thanks to my highschool friends: Daniel and Trang Trinh, Quang Tran and his family, and Van Trang, who have been great friends throughout these memorable years.

ABSTRACT

The Stokesian dynamics simulation method is applied to study the behavior of concentrated suspensions of hydrodynamically interacting colloidal particles in a shear flow. The aim of this study is the prediction of suspension macroscopic properties from the microstructure - the temporal and spatial distribution of suspended particles. The macroscopic properties includes the shear viscosity, normal stress differences, short- and long-time self-diffusivities. Suspension macroscopic properties and the microstructure are modeled as functions of two parameters: particle volume fraction, ϕ, and the Péclet number, Pe, which measures the relative importance of the imposed shear and Brownian forces. Stokesian dynamics accurately accounts for both the hydrodynamic and Brownian forces of a colloidal dispersion. The method, which is very general and computationally efficient, imposes no restriction on the particle displacements and allows simulation of flowing suspension with particle volume fractions from infinite dilution to dense packing and a continuous range of the Péclet number from pure Brownian motion ($Pe \rightarrow 0$) to pure hydrodynamics ($Pe \rightarrow \infty$).

The method is first employed for the pure Brownian suspensions (Pe=0) at a volume fraction ϕ=0.45. The accuracy of Stokesian dynamics is demonstrated by an excellent comparison of the radial pair-distribution function obtained from dynamic simulation which captures the same isotropic hard-sphere distribution computed by the random Monte-Carlo method. The simulation method is then applied to study the dynamics of sheared SCC, BCC, and FCC periodic lattices of non-colloidal spheres ($Pe \rightarrow \infty$) with particle volume fraction ranging from dilution to maximum close packing. Results of the

resistivity and the shear viscosity of sheared periodic lattices are successfully determined as a function of the volume fraction.

The Stokesian dynamics simulation method is finally applied to the dynamic simulation of unbounded concentrated suspensions of force- and torque-free colloidal particles. The particle volume fractions are varied from 0.316 to 0.6 and the Péclet numbers are ranged from the strong Brownian limit (Pe=0.01) to the hydrodynamic dominated regime (Pe=10^5). Comparisons of simulation results for the steady shear viscosities, self-diffusivities, and the structure factors with experiments are remarkably good. For the first time, the flow of particles are probed with detail to illustrate the shearing deformation to suspension microstructure. This information provides a physical understanding of the fundamental mechanisms causing interesting shear thinning and shear thickening behavior and its important relation to the shear-induced microstructure. The simulation results reveal three distinct behaviors of hard-sphere suspensions in the regions of strong Brownian motion, balance of Brownian and hydrodynamic interactions, and hydrodynamic domination.

In the region of strong Brownian motion with small Péclet numbers ($Pe < 1$), the suspension shear thins due to a decrease of Brownian contribution to particle stress. The isotropic microstructure is slightly deformed, but the particles are very well dispersed. More importantly, simulation results do not reveal ordered microstructure in the shear thinning region. For the special plateau region with $Pe \simeq 10$, the suspension no longer shear thins and the shear viscosity is minimized. The balance of hydrodynamic and Brownian forces induce a strongly ordered flowing suspension with hexagonally packed

strings of particles flowing with the bulk flow. The string formation is due to the Brownian forces which act as short-range springlike repulsive and random forces to counter the shearing deformation to the suspension by the imposed shear; the string formation does not relate to the shear thinning. In the region of hydrodynamic domination ($Pe > 10^2$), the suspension shear thickens due to formation of large, elongated clusters of particles. In this region, the hydrodynamics contribute all particle stress as the direct Brownian contribution has essentially vanished, but weak Brownian forces are seen to perturb and induce a local anisotropic microstructure. The complete relation of the steady shear viscosity to particle volume fraction and the Péclet number for concentrated hard-sphere suspensions is also given.

TABLE OF CONTENTS

Chapter I

INTRODUCTION

The two goals of this thesis are to study the behavior of colloidal dispersions and to develop very general, fast Stokesian dynamics simulation programs which can be used for modeling a wide variety of particulate flows. The first goal centralizes on the prediction of macroscopic equilibrium and transport properties of concentrated colloidal suspensions from their microstructural mechanics. While applications of Stokesian dynamics for studying of suspension macroscopic properties have appeared in the past (Brady and Bossis (1988), Brady (1990), Bonnecaze and Brady (1992)), here we shall focus on the "rheological" behavior, which includes the shear viscosity and normal stress differences, short- and long-time self-diffusion coefficients. The microstructural mechanics governing suspensions include hydrodynamic forces, stochastic forces which give rise to Brownian motion, internal and external forces acting on particles, as well as their temporal and spatial distribution which is commonly referred to as the suspension microstructure. In flowing, nonequilibrium suspensions, the suspension microstructure is not given but must be determined as part of the solution; it determines and is determined by the macroscopic flow behavior. The second goal concerns the science of programming and the development of accurate, fast and general Stokesian dynamics codes.

Particles suspended or dispersed in a fluid medium are very common in nature and in many engineering fields, e.g., the mixing and spray application of emulsion polymers and latexes, dispersions of pigments in coating and paint industries, flows of coal slurries, polymer processing, and the manufacture of ceramics and composite materials. For dispersions of submicronsized particles, there is a large body of literature and technical reports on the non-Newtonian rheological behavior of these multiphase materials (Rutgers (1962), Krieger (1972), Jeffrey and Acrivos (1976), Gadala-Maria (1979), Pätzold

(1980), Hoffman (1972, 1974 and 1982), Krieger and Choi (1986), Barne (1989), van der Werff and de Kruif (1989), Boersma *et al.* (1990), Ericksson *et al.* (1990), Ferrini *et al.* (1990)). The general observations for dense suspensions can be summarized as follows: As the shear rate increases, it is observed that at first the shear viscosity decreases, i.e., the suspension shear thins. At higher shear rates, the shear viscosity goes to a minimum and then may increase to a much higher value if the suspension is shear thickening or dilatant. (In contrast to dilatancy, in some suspensions the shear viscosity is observed to increase with shear time at a constant shear rate, and this time-dependent shear thickening is usually referred to as rheopexy.) As the particle volume fraction increases, these rheological responses are intensified. In addition to shear thinning and shear thickening, discontinuing in shear viscosity, normal stress differences, and yield stresses have also been reported. While these experimental findings are not new and have been known for a long time, there is still no clear physical understanding and explanation for these nonideal rheological response of flowing suspensions. This is partly because in many experiments the characterization for both the chemistry and transport mechanisms operating in the suspensions is often difficult and incomplete. Therefore, it is impossible to link the influence of specific colloidal forces and macroscopic properties.

Predicting the rheological behavior of concentrated suspensions is a difficult and challenging theoretical problem. Theories must be able to address the physics of many-body hydrodynamic interactions and the important near-field lubrication forces in dense suspensions. Also, exact knowledge of particle forces and stresses for a particular configuration is insufficient to determine the rheology. A large number of different configurations sampled by particles is needed for the statistical average of suspension macroscopic

properties. These configurations are themselves the results of the interplay between the imposed shear flow and the internal hydrodynamic, interparticle and Brownian forces. The microstructure of a flowing suspension is a dynamic entity which cannot be set a priori but must be determined as part of the problem. Stokesian dynamics is capable of addressing these aspects.

Molecular-dynamics-like computer simulations are a promising tool for studying concentrated colloidal suspensions. Simulation, together with experiments, can provide the physical understanding which is necessary for theoretical development. Among the simulation methods, Stokesian dynamics is an excellent choice because it is capable of treating dense flowing suspensions and the computational algorithm is efficient. The method is very general, allows simulation of flowing suspension with particle volume fractions, ϕ, from infinite dilution to dense packing and a continuous range of the Péclet number, Pe. The Péclet number measures the relative importance of shear and Brownian forces.

We shall study the rheology of concentrated suspensions of hydrodynamically interacting colloidal particles in a simple shear flow by Stokesian dynamics simulation. The simulation accurately accounts for both the hydrodynamic and Brownian forces of a colloidal dispersion. From the time evolution of particle configurations, we can determine the microstructure and its relation to the bulk properties. Furthermore, the simulations can provide detailed results to test theories and constitutive models, as well as other simulation methods. Our success in developing efficient and accurate Stokesian dynamics computer programs allows a detailed study of dense hard-sphere suspensions. The majority of our simulations are in three dimensions. Dynamic simulations with a large

number of particles (N=123 and 126), which were once prohibitively costly to run on a Supercomputer such as the Cray Y-MP are now routinely simulated on IBM RiSC/6000 workstations. At the present level of efficiency and cost effectiveness, Stokesian dynamics is considered not only a research but also a valuable production tool for the study of more complex physical models. Bossis and Brady (1987, 1989) developed and pioneered the application of Stokesian dynamics to study the rheology and self-diffusivities of hard-sphere suspensions in simple shear flow. Their results for the steady shear viscosities compare favorably with experiments and more importantly they were able to explain the rheological behavior of dense suspensions from the shear-induced microstructures. The simulations were restricted to a monolayer of 25 particles with particle areal fraction ϕ_A= 0.452 which is comparable to ϕ=0.301 in three dimensions. We follow their success and study more dense suspensions with emphasis on 3D simulations. The 3D simulations provide more details of the microstructure and we can compare them directly with experiment. For the shear viscosity, both 3D and monolayer simulations at comparable areal and volume fraction ($\phi \approx 3/2\phi_A$) give similar results, indicating the correct physics in monolayer simulations; our results strongly reinforce this point.

The hard-sphere suspension is a well-characterized model and has been extensively used in statistical mechanics. A hard-sphere fluid is one which the interparticle potential is zero except if the particles come in contact where the potential is infinite. The only parameter in the equilibrium hard-sphere fluid is the particle volume fraction, ϕ. The hard-sphere model is fundamental and simple, yet it has a phase transition at high particle volume fraction. Under equilibrium conditions, the existence of a freezing phase transition of hard spheres has been observed and studied both by experiments (Pusey and van

Megen (1986, 1987) and simulation method (Hoover and Ree (1968), Kose and Hachisu (1974)). At freezing, colloidal fluid and colloidal crystals coexist and the particle volume fractions were found to be $\phi_F = 0.494 \pm 0.002$ for the fluid phase and $\phi_M = 0.545 \pm 0.002$ for the crystalline phase. At even higher volume fractions, the computer simulations of Woodcock (1981) identify a glass transition with $\phi_G \approx 0.58$. Pusey and van Megen have reported a detailed study for colloidal hard spheres using the PMMA/decalin/CS2 system, where PMMA stands for polymethyl methacrylate particles and CS2 denotes carbon disulfide solvent. They were able to determine the remarkable phase diagram for the hard-sphere model. A great challenge and motivation for engineers and scientists is to predict the rheological behavior of not just the equilibrium Brownian suspensions but also the more practical flowing hard spheres. This is indeed the central theme of this research work, which focuses on the understanding of the behavior of dense colloidal dispersions in shear flow. The choice of a hard-sphere model allows direct comparisons of our results for the rheology and the dynamics of shear-induced microstructures with that from experiments. We can study the specific influence of hydrodynamic and Brownian forces on suspension macroscopic properties. The simple model has only two parameters ϕ and Pe, the Péclet number, and this thesis is devoted to understanding the rheological behavior as a function of these two parameters.

The outline of this thesis is the following: In chapter II, we present Stokesian dynamics, a molecular-dynamics-like simulation method for colloidal dispersions and define the method to determine macroscopic properties: the shear viscosity and normal stress differences, and the short- and long-time self-diffusion coefficients. A computing flowchart of Stokesian dynamics is provided in chapter III to show how the process of dynamic

simulation proceeds. In addition, the sampling method for simulation results and its statistics are illustrated with samples obtained by Stokesian dynamics.

In chapter IV, we illustrate the correctness and accuracy of Stokesian dynamics by comparing simulation results of the angularly averaged pair-distribution function $g(r)$ for the purely Brownian limit (Pe=0) with that for a system of hard spheres at identical volume fraction ϕ=0.45 obtained by a Monte-Carlo calculation. In addition, we present dynamic simulations for the resistivity and rheology of spatially periodic arrays of non-colloidal spheres in shear flow from the dilute limit up to maximum packing. Simple cubic (SCC), face-centered cubic (FCC) and body-centered cubic (BCC) lattices are sheared at $Pe \rightarrow \infty$.

Chapter V is an introduction to the main topic of the thesis: sheared hard-sphere suspensions as a function of ϕ and Pe. In our simulations, ϕ is varied from 0.316 to as high as 0.6; this range of volume fraction spans from the colloidal fluid phase to the fluid-crystalline phase and the glass transition. Different numbers of particles are studied for a three dimensional model (N = 27, 28, 63, 64, 81, 123 and 126) and for a monolayer (N = 25, 80 and 120). The Péclet number ranges from the strong Brownian limit, $Pe \approx 0.01$, to the pure hydrodynamic limit, $Pe \rightarrow \infty$. In our study, hard-sphere suspensions are grouped into three systems: the moderately dense suspensions with ϕ ranging from 0.316 to 0.419, a very complete study at ϕ=0.45 and the very dense suspensions with ϕ varying from 0.47 to 0.6.

Hard-sphere suspensions at ϕ=0.45 are presented in chapter VI, followed by the moderately dense suspensions in chapter VII and the very dense suspensions in chapter

VIII. Chapters VI to VIII have three main sections: the rheology, the shear-induced microstructure and the self-diffusivities. The final results of the complete dense hard-sphere suspensions are summarized in chapter IX. Comparison of our simulation results with theories and other simulation methods are presented in this chapter. Suspension temperatures, which are computed from the mean square of particle fluctuation velocities and the time-correlation function for the particle velocities are also included in chapter IX.

The simulation results for the steady shear viscosity show the shear thinning and shear thickening region and compare very well with experiments. We successfully determine the relation of shear viscosity as a function of Pe and ϕ and examine the shear thinning and shear thickening mechanisms in detail. As Pe increases, the microstructure changes from an isotropic structure at rest to a slightly deformed structure in the strong Brownian limit ($Pe \rightarrow 0$) and the suspension shear thins. In the region of balance of the hydrodynamic and Brownian forces ($Pe \approx 10$), the shear viscosity remains relatively unchanged and is minimum and the flowing suspension is strongly ordered with distinct hexagonally packed particles flowing as strings along the flow direction. In the limit of hydrodynamic domination ($Pe > 10^2$), strong shear rates destroy the ordered structures; the string phase melts. Particles formed large, elongated clusters in this region of large Péclet number and the suspension shear thickens. Comparison of our structure factors $S(\mathbf{k})$ and light scattering or small angle neutron scattering (SANS) results are good. We also investigate the relaxation time of a string-ordered microstructure when the imposed shear is terminated and the suspension returns to the equilibrium structure at a rest state.

The results of self-diffusivities also show a clear transition from a strong Brownian motion limit ($Pe < 1$) to a hydrodynamic dominated regime ($Pe > 10$) with a remarkable change in short- and long-time self-diffusion coefficients. By examining the rheology, the shear-induced microstructures and the self-diffusivities, we are able to provide our interpretation of the connection between the microstructures and the shear thinning and shear thickening phenomena.

We present our most recent simulation results for the sedimentation of Brownian particles in concentrated suspensions in chapter X. While the sedimentation of non-Brownian particles ($Pe \rightarrow \infty$) have been examined by experiments (Mirza and Richardson (1979), Acrivos and Herbolzheimer (1979), Herbolzheimer and Acrivos (1981)), simulations (Ansell and Dickinson (1986), Lester (1987), Ladd (1988, 1990, 1992)) and theories (Batchelor (1972, 1982), Batchelor and Wen (1982), Kock and Brady (1985, 1987), Kock and Shaqfeh (1989, 1991)), the sedimentation of colloidal particles have not been investigated. For particles with uniform density which is greater than the fluid, we discover an ordered structure of settling particles similar to that of sheared suspension. The ordering is seen for ϕ=0.419 and $Pe \approx 10$, where Pe measures the relative importance of of sedimentation and Brownian forces. For bi-dense particles (particles with two different densities dispersed in a less dense fluid) at the same ϕ and Pe, the ordered structure is destroyed.

Details of the calculation and numerical optimizations for Brownian motion and Brownian stress are presented in appendix A. Appendix B shows complete details on the procedure of starting and executing a simulation. In appendix C, we present and

discuss the speed and timing of Stokesian dynamics on both the workstations and the super computer Cray Y-MP. We shall present our implementation techniques to avoid the poor scalability and significantly increase the speed of a workstation with high-speed computing CPU but relatively small memory CACHE like the IBM RiSC models. The central computing tasks of most numerical methods will be the operations of matrix-matrix and matrix-vector, and the Stokesian dynamics simulation method is a good example. Here in this section, we present the numerical algorithms of blocking and rolling a matrix and a vector to speed-up the computations. We successfully obtain an average speed from 20 to 40 MFLOPS (millions floating operations per second) on the the IBM RiSC/6000 530 model, which is designed and rated at 10 MFLOPS for LINPACK with matrix of dimension (100×100). With fast vectorization of the Ewald summation and inversion for the mobility tensor, the average speed of our simulation programs with N=123 (matrix size of 1353×1353) on the Cray Y-MP is marked at 230 MFLOPS, a speed up of nearly 10-fold compared to older versions of Stokesian dynamics and about 76.0 % of the rated speed per CPU on the Cray Y-MP.

Chapter II

THE STOKESIAN DYNAMICS SIMULATION METHOD

II.1 Stokesian Dynamics Simulation of Colloidal Suspensions

In this section, we will present the Stokesian dynamics method with an emphasis on the formulation and the actual procedure used in carrying out the simulations. For a more complete derivation of Stokesian dynamics, please see Brady and Bossis (1985, 1988) and Bossis and Brady (1984, 1987,1989). The dynamic simulation starts with the N-body Langevin equation for the particle motion:

$$\mathbf{m} \cdot \frac{d\mathbf{U}}{dt} = \mathbf{F}^{H} + \mathbf{F}^{B} + \mathbf{F}^{P} \quad . \tag{2.1}$$

Equation (2.1) simply states the mass $\times$ acceleration equals the sum of the forces. Here, $\mathbf{m}$ is the generalized mass/moment of inertia matrix of dimension $(6N \times 6N)$, where N is the number of particles, $\mathbf{U}$ is the particle translational/rotational velocity vector of dimension $(6N)$ and the force/torque vectors of dimension $(6N)$ on the right hand side of (2.1) describe three different types of forces. $\mathbf{F}^{H}$ is the hydrodynamic forces exerted on particles due to their motion relative to fluid. The stochastic force $\mathbf{F}^{B}$ gives rise to Brownian motion, the force which tends to restore the equilibrium structure from any deformation. $\mathbf{F}^{P}$ is the deterministic non-hydrodynamic forces, which may be of many forms, for example: London-van der waals dispersion, screened electrostatic, Derjaguin-Landau-Verwey-Overbeek (DVLO), etc. Furthermore, $\mathbf{F}^{P}$ may be repulsive or attractive, short-ranged or long-ranged, interparticle (pairwise or many-body) or external. Our intention here is not to characterize $\mathbf{F}^{P}$, but to focus on the effects of each specific force in (2.1) on the rheological behavior of colloidal dispersions. The classification of the interparticle/external force $\mathbf{F}^{P}$ belongs to the field of Colloidal Sciences (van de Ven

(1989), Russel, Saville and Scholwalter (1989)).

The Langevin equation can be viewed as a coarse grain model of suspensions, a model which treats the suspending fluid as a continuum and gives rise to the hydrodynamic drag forces, $\mathbf{F}^H$, and the random thermal forces, $\mathbf{F}^B$. For N rigid particles suspended in an incompressible Newtonian fluid of viscosity η and density ρ, the motion of the fluid is governed by the Navier-Stokes equations. When the motion on particle scale is such that the particle Reynolds number, Re, is small ($Re = \rho a^2 \dot{\gamma}/\eta \ll 1$, with a the characteristic particle size and $\dot{\gamma}$ the shear rate), the inertial terms can be neglected and we solve the simpler inertialess Stokes equation. For suspensions of spheres with $a \simeq 1\mu m$, in water, under a shear rate of $\dot{\gamma} \simeq 1 sec^{-1}$, we have $Re \approx O(10^{-5})$ while the Péclet number, $Pe \approx O(10^2)$. Here $Pe \equiv \dot{\gamma} a^2/D_o = 6\pi\eta a^3 \dot{\gamma}/kT$ is the ratio of the shear and Brownian forces. Neglecting inertia, equation (2.1) becomes:

$$\mathbf{0} = \mathbf{F}^H + \mathbf{F}^B + \mathbf{F}^P \quad . \tag{2.2}$$

Equation (2.2) states that any deformation to the microstructure by the the shear and/or by the interparticle/external forces is balanced by the Brownian motion which restores the structure to an isotropic random state.

For Stokes' flow, the hydrodynamic force $\mathbf{F}^H$ exerted on the particles in suspension undergoing a bulk linear flow is:

$$\mathbf{F}^H = - \mathbf{R}_{FU} \cdot (\mathbf{U} - \mathbf{U}^\infty) + \mathbf{R}_{FE} : \mathbf{E}^\infty \quad . \tag{2.3}$$

Here, $\mathbf{U}^{\infty}$ is the imposed flow at infinity evaluated at the particle center $\mathbf{x}_\alpha$, $\mathbf{E}^{\infty}$ is the symmetric part of the velocity gradient tensor and is constant in space, although it may be an arbitrary function of time, for example in an oscillatory flow. The resistance tensors $\mathbf{R}_{FU}(\mathbf{x})$ of dimension $(6N\times6N)$ and $\mathbf{R}_{FE}(\mathbf{x})$ of dimension $(6N\times5N)$ depend only on the instantaneous particle configuration and the particle shapes and sizes. They are purely geometric quantities and independent of the flow field. $\mathbf{R}_{FU}(\mathbf{x})$ is the coupling between the hydrodynamic force/torque on the particles and their motion relative to the fluid. $\mathbf{R}_{FE}(\mathbf{x})$ is the coupling between the hydrodynamic force/torque on the particles and their motion due to an imposed shear flow. The vector $\mathbf{x}$ of dimension $(6N)$ represents the generalized configuration vector specifying the location and orientation of all N particles. The inverse of the resistance tensor $\mathbf{R}_{FU}$ is known as the mobility matrix $\mathbf{M}$ $(=\mathbf{R}_{FU}^{-1})$ and is the central element describing the hydrodynamic interactions among N particles. Stokesian dynamics, with its hydrodynamic origin, offers an accurate and efficient method for computing these hydrodynamic tensors.

The stochastic or Brownian force $\mathbf{F}^{B}$ arises from the thermal fluctuations in the fluid and is characterized by

$$\langle \mathbf{F}^{B} \rangle = 0 \quad , \tag{2.4.a}$$

$$\langle \mathbf{F}^{B}(0)\mathbf{F}^{B}(t) \rangle = 2kT\,\mathbf{R}_{FU}\delta(t) \quad . \tag{2.4.b}$$

In (2.4) the angle brackets denote an ensemble average, k is Boltzmann's constant, T is the absolute temperature and $\delta(t)$ is the delta function. The amplitude of the correlation between the Brownian forces at time 0 and at time t results from the fluctuation-

dissipation theorem for the N-body system.

The evolution equation for the particles is obtained by integrating the stochastic differential equation (2.2) over a time step Δt that is large compared with the Brownian relaxation time τ (τ=$m/6\pi\eta a$, where m is the mass of a particle), and small compared with the time over which the configuration changes. A second integration in time produces the evolution equation for the particle positions with an error of $O(\Delta t^2)$:

$$\Delta \mathbf{x} = \{ \mathbf{U}^{\infty} + \mathbf{R}_{FU}^{-1} \cdot [\mathbf{R}_{FE} : \mathbf{E}^{\infty} + \mathbf{F}^{P}] \} \Delta t + kT \nabla \cdot \mathbf{R}_{FU}^{-1} \Delta t + \mathbf{X}(\Delta t) \quad . \tag{2.5}$$

Here $\Delta \mathbf{x}$ is the change in particle position during the time step Δt and $\mathbf{X}(\Delta t)$ is a random displacement due to Brownian motion that has zero mean and its corvariance given by the inverse of the resistance $\mathbf{R}_{FU}$ tensor.

$$\langle \mathbf{X} \rangle = 0 \quad , \tag{2.6.a}$$

$$\langle \mathbf{X}(\Delta t)\, \mathbf{X}(\Delta t) \rangle = 2kT\, \mathbf{R}_{FU}^{-1} \delta(t) \quad . \tag{2.6.b}$$

As seen in (2.5), there are three main contributions to the motion of a particle, each resulting from the basic forces in equation (2.2). There is a deterministic contribution due to the hydrodynamic shear forces: $[\mathbf{U}^{\infty} + \mathbf{R}_{FU}^{-1} \cdot \mathbf{R}_{FE} : \mathbf{E}^{\infty}] \Delta t$, a deterministic contribution from the interparticle/external forces: $[\mathbf{R}_{FU}^{-1} \cdot \mathbf{F}^{P}] \Delta t$ and finally the contribution from the Brownian forces are included in the last two terms: the first is a deterministic displacement from the configurational-space divergence of the N-particle diffusivity $[kT \nabla \cdot \mathbf{R}_{FU}^{-1}] \Delta t$, and the second is a random step $\mathbf{X}(\Delta t)$ whose properties are such that the fluctuation-dissipation theorem is satisfied.

Nondimensionalizing $\mathbf{x}$ by the characteristic particle size a; the time by the diffusive time scale a^2/D_o, where D_o is the diffusion coefficient of a particle at infinite dilution and from the Stokes-Einstein relation is given by $D_o=kT/6\pi\eta a$; the shear force by $6\pi\eta a^2\dot{\gamma}$, where $\dot{\gamma}=|\mathbf{E}^{\infty}|$ is the magnitude of the shear rate; the interparticle/external forces by their magnitude $|\mathbf{F}^P|$; the hydrodynamic resistance tensors $\mathbf{R}_{FU}$ by $6\pi\eta a$ and $\mathbf{R}_{FE}$ by $6\pi\eta a^2$, the evolution equation (2.5) and (2.6) become:

$$\Delta\mathbf{x} = Pe\ \{\ \mathbf{U}^{\infty} + \mathbf{R}_{FU}^{-1}\cdot\ [\mathbf{R}_{FE}:\mathbf{E}^{\infty} + \dot{\gamma}^{*-1}\ \mathbf{F}^P]\ \}\Delta t + \ \nabla\cdot\mathbf{R}_{FU}^{-1}\ \Delta t + \mathbf{X}(\Delta t)\ , \qquad (2.7)$$

$$\langle\ \mathbf{X}\ \rangle = 0\ , \qquad (2.8.a)$$

$$\langle\ \mathbf{X}(\Delta t)\ \mathbf{X}(\Delta t)\ \rangle = 2\ \mathbf{R}_{FU}^{-1}\ \Delta t\ . \qquad (2.8.b)$$

Here, the Péclet number, $Pe \equiv \dot{\gamma}a^2/D_o=6\pi\eta a^3\dot{\gamma}/kT$, measures the relative importance of the shear and Brownian forces. The Péclet number can also be considered as the ratio of two time scales, the time for the Brownian motion to restore the equilibrium state over the time which the shearing motion deforms the suspension. The nondimensional shear rate $\dot{\gamma}^* \equiv 6\pi\eta a^2\dot{\gamma}/|\mathbf{F}^P|$ is defined as the ratio of the shear and interparticle/external forces. As shown here, Pe is scaled with a^3 and $\dot{\gamma}$. For submicronsized particles and even particles with $a \approx O(10^{-3}m)$ and $\dot{\gamma} \approx O(10^2 sec^{-1})$, Pe is large but not infinite and Brownian motion always plays a role. As we shall illustrate in chapter VI, the minute amount of Brownian motion is sufficient to destroy large clusters of particles, which reduces the shear viscosity and contributes to the diffusive behavior in the dense suspensions. In contrast, when $Pe \rightarrow \infty$ the large clusters persist resulting in very high viscosities.

If Brownian motion is less important than the shear force ($Pe > 1$), it is appropriate to scale time by the convective time given by the shear rate $\dot{\gamma}^{-1}$ rather than the diffusive time a^2/D_o. Equation (2.5) then becomes:

$$\Delta \mathbf{x} = \{ \mathbf{U}^{\infty} + \mathbf{R}_{FU}^{-1} \cdot [\mathbf{R}_{FE} : \mathbf{E}^{\infty} + \dot{\gamma}^{*-1} \mathbf{F}^{P}] \} \Delta t + \frac{1}{Pe} (\nabla \cdot \mathbf{R}_{FU}^{-1} \Delta t + \mathbf{X}(\Delta t)) \ . \qquad (2.9)$$

The evolution equation (2.7) is applied for $Pe \leq 1$ and equation (2.9) is used when $Pe \geq 1$ with $Pe = 1$ being the special case when both equations work equally well. Either equation, which are an exact description for N particles, show quite clearly that the behavior of the suspension depends on the dimensionless parameters: Pe, $\dot{\gamma}^*$ and ϕ. These equations are the central part of the dynamic simulation. Given an initial configuration of N particles at time $t = 0$, we simply integrate (2.7) or (2.9) in time to follow the dynamic evolution of the suspension microstructure and compute suspension macroscopic properties at each time step. One sees the fundamental role of the hydrodynamic interactions, as the resistance tensors $\mathbf{R}_{FU}$ (or its invert the mobility matrix $\mathbf{M}$) and $\mathbf{R}_{FE}$, along with interparticle/external forces completely specifies the dynamics. We next turn our attention to the hydrodynamic interactions.

II.2 Hydrodynamic Interactions

As seen in the evolution equation (2.7), Stokesian dynamics places no restriction of particle volume fraction ϕ, the Péclet number, or any specific configuration for the particles. There are no restriction on how particles should move in a flow. The method is very robust and allows simulation over the entire range of particle volume fraction

ϕ, from dilution up to maximum packing, and continuous values of Pe, passing the two limits: pure Brownian motion $Pe \rightarrow 0$ and pure hydrodynamic $Pe \rightarrow \infty$.

The resistance tensors $\mathbf{R}_{FU}$ and $\mathbf{R}_{FE}$ are part of the grand resistance tensor $\mathcal{R}$, which relates the force/torque ($\mathbf{F}$) and stresslet ($\mathbf{S}$) exerted by the fluid on the particles to the particle velocities and the rate of strain:

$$\begin{pmatrix} \mathbf{F} \\ \mathbf{S} \end{pmatrix} = - \mathcal{R} \begin{pmatrix} \mathbf{U} - \mathbf{U}^{\infty} \\ -\mathbf{E}^{\infty} \end{pmatrix} , \tag{2.10}$$

where the "grand resistance"tensor $\mathcal{R}$ is defined in the resistance formulation as:

$$\mathcal{R} = \begin{pmatrix} \mathbf{R}_{FU} & \mathbf{R}_{FE} \\ \mathbf{R}_{SU} & \mathbf{R}_{SE} \end{pmatrix} . \tag{2.11}$$

The invert of $\mathcal{R}$, "the grand tensor" $\mathcal{M}$, is expressed in the mobility formulation as:

$$\begin{pmatrix} \mathbf{U} - \mathbf{U}^{\infty} \\ -\mathbf{E}^{\infty} \end{pmatrix} = - \begin{pmatrix} \mathbf{M}_{UF} & \mathbf{M}_{EF} \\ \mathbf{M}_{US} & \mathbf{M}_{ES} \end{pmatrix} \cdot \begin{pmatrix} \mathbf{F} \\ \mathbf{S} \end{pmatrix} . \tag{2.12}$$

For two spherical particles, $\mathcal{R}$ and $\mathcal{M}$ are known exactly for all sphere-sphere separations. For N particles, solving full N-body problem requires some approximations. The details of the methodology can be found in Brady and Bossis and Bossis and Brady. Here, we briefly summarize the procedure for obtaining $\mathcal{M}$. Stokesian dynamics exploits the fact that the many-body hydrodynamic interactions are most easily computed in the mobility formulation, while the near-field lubrication interactions are more conveniently incorporated into the resistance formulation.

Starting with the integral solution for Stokes' flow for N rigid spheres, with the aid of Faxén laws for particle velocities, we form $\mathcal{M}$ by expanding the force density on the surface of each particle in a series of moments. The zeroth moment is the total force $\mathbf{F}$. The first moment has two parts: the anti-symmetric part is the total torque $\mathbf{L}$ and the symmetric part is the particle stresslet $\mathbf{S}$. Brady *et al.* (1988) truncate higher moments since their contributions are marginally necessary compared to the increased computational costs. Only the induced mean-field quadrupole term for the coupling between the particle translational velocities and forces is needed to be added to improve the accuracy of the method. Thus we represent each particle by its first few multipoles. While $\mathcal{M}$ is pairwise additive, Durlofsky *et al.* (1987) have shown that inverting it solves the many-body problem at the level of forces, torques and stresslets. $\mathcal{M}$ still lacks the important lubrication interactions which can be reproduced only when all of the multipole moments are included. Lubrication forces are essentially two-body interactions, as they give the singular force required to push two particles together at constant relative velocity. The nature of this singularity is completely determined by the interactions between the two particles, thus they can be combined in pairwise fashion in the grand resistance tensor. The final version of $\mathcal{R}$ that includes the far-field many-body interaction $\mathcal{M}^{-1}$ and the near-field lubrications $\mathcal{R}_{lub}$ is:

$$\mathcal{R} = \mathcal{M}^{-1} + \mathcal{R}_{lub} \quad . \tag{2.13}$$

Both $\mathcal{M}$ and $\mathcal{R}$ are symmetric and positive definite. For unbounded suspension, the long range $\mathbf{M}_{UF} \approx (\frac{1}{r})$ nature of the hydrodynamic interactions must be properly handled and this can be done with the method of O'Brien (1979) to evaluate the effect of the infinite

suspension and "renormalize" the interactions. Thus we can investigate the "thermodynamic limit", $N \to \infty$, $V \to \infty$, with n = N/V fixed. We can then form a unit cell with N particles and apply periodic boundary condition to eliminate the boundary effects as is commonly done in molecular dynamics. With the use of periodic boundary condition, O'Brien's method renormalizes all divergent and conditionally convergent interactions. We then apply the Ewald summation technique to accelerate the convergence of the interactions of the lattice sums. The Ewald-summed mobility tensor is denoted by $\mathcal{M}^*$. Once all mobility matrices $\mathbf{M}_{UF}$, $\mathbf{M}_{US}$, $\mathbf{M}_{EF}$ and $\mathbf{M}_{ES}$ are computed, $\mathcal{M}^*$ is formed and inverted. The resistance tensor $\mathcal{R}$ including lubrication is partitioned according to equation (2.12) and used in the evolution equation (2.7). The resistance tensors are also needed for the calculation of suspension macroscopic properties and described next. It should be noted that Stokesian dynamics is well capable of treating particulate flows with boundaries; for example, the pressure driven flow between parallel plates (Brady (1991)).

II.3 Suspension Macroscopic Properties

II.3.1 Suspension Rheology

The suspension bulk stress $\langle \sum \rangle$ provides information of the rheology and can be directly computed by Stokesian dynamics. Batchelor (1970, 1977) derived the following formula for calculating the average stress in a homogeneous suspension:

$$\langle \sum \rangle = I.T. + 2\eta\langle \mathbf{E} \rangle + \frac{N}{V} \sum_{\alpha=1}^{N} \mathbf{S}_\alpha - \frac{N}{V} \sum_{\alpha=1}^{N} \mathbf{r}_\alpha \mathbf{F}_\alpha \ . \tag{2.14}$$

Here $\langle\Sigma\rangle$ and $\langle\mathbf{E}\rangle$ are the macroscopic averages of the stress and the rate of strain tensors, respectively. *I.T.* stands for the isotropic part of the stress or pressure which is of no importance for homogeneous suspensions. The stresslet $\mathbf{S}_\alpha$ exerted by the fluid on the rigid particle α located at the position $\mathbf{r}_\alpha$, is the symmetric and traceless part of the first moment of the force distribution integrated over the particle surface A_α:

$$\mathbf{S}_\alpha = \frac{1}{2}\int_{A_\alpha}\left[\left((\mathbf{r}-\mathbf{r}_\alpha)\,\sigma + \sigma\,(\mathbf{r}-\mathbf{r}_\alpha)\right)\cdot\mathbf{n} - \frac{2}{3}\,\mathbf{I}\,\left((\mathbf{r}-\mathbf{r}_\alpha)\cdot\sigma\cdot\mathbf{n}\right)\right] dA \ . \tag{2.15}$$

Here $\mathbf{n}$ is the unit normal vector pointing into the fluid and σ is the stress tensor in the fluid:

$$\sigma = -p\,\mathbf{I} + 2\,\eta\,[\,\nabla\mathbf{u} + (\nabla\mathbf{u})^{\dagger}\,] \ , \tag{2.16}$$

with p is the local fluid pressure and $\nabla\mathbf{u}$ the local fluid velocity gradient. The † symbol denotes the transpose operation.

The linearity of the governing Stokes' equations allows us to write:

$$\begin{pmatrix}\mathbf{F}\\ \mathbf{S}\end{pmatrix} = -\begin{pmatrix}\mathbf{R}_{FU} & \mathbf{R}_{FE}\\ \mathbf{R}_{SU} & \mathbf{R}_{SE}\end{pmatrix}\cdot\begin{pmatrix}\mathbf{U}-\mathbf{U}^{\infty}\\ -\mathbf{E}^{\infty}\end{pmatrix} + \begin{pmatrix}\mathbf{F}^{P}\\ -\mathbf{r}\mathbf{F}^{P}\end{pmatrix}, \tag{2.17}$$

where $\mathbf{r}$ is the particle-particle separation vector and the stresslets $\mathbf{S}$ of the N particles are:

$$\mathbf{S} = -\,\mathbf{R}_{SU}\cdot(\mathbf{U}\text{-}\mathbf{U}^{\infty}) + \mathbf{R}_{SE}:\,\mathbf{E}^{\infty} - \mathbf{r}\mathbf{F}^{P} \ . \tag{2.18}$$

The column vector for the particle stresslet $\mathbf{S}$ is of dimension $5N$; each particle has five independent stresslets due to the symmetric and traceless properties given by Stokes' flow. Equation (2.18) still does not give the complete $\langle\sum\rangle$ because the contribution from Brownian motions has not yet been included. The complete set of stresslets can be obtained by following the derivation of Bossis and Brady (1989):

$$\mathbf{S} = \mathbf{S}^H + \mathbf{S}^P + \mathbf{S}^B \quad , \tag{2.19}$$

$$\mathbf{S}^H = - (\mathbf{R}_{SU}\ \mathbf{R}_{FU}^{-1}\ \mathbf{R}_{FE} - \mathbf{R}_{SE}) : \mathbf{E}^{\infty} \quad , \tag{2.20.a}$$

$$\mathbf{S}^P = - (\mathbf{rI} + \mathbf{R}_{SU}\ \mathbf{R}_{FU}^{-1})\ \mathbf{F}^P \quad , \tag{2.20.b}$$

$$\mathbf{S}^B = - kT\ \nabla\cdot(\mathbf{R}_{SU}\cdot\mathbf{R}_{FU}^{-1}) \quad . \tag{2.20.c}$$

In (2.20), $\mathbf{S}^H$ is the hydrodynamic, $\mathbf{S}^P$ is the interparticle/external force and $\mathbf{S}^B$ is the Brownian contribution to the bulk stress $\mathbf{S}$, respectively.

For simple shear flow, the relative viscosity of the suspension is defined by the ratio of the xy component of the bulk stress $\langle\sum_{xy}\rangle$ to the xy component of the rate of strain $\langle\mathbf{E}_{xy}\rangle$, with $\langle\mathbf{u}_x\rangle=\dot{\gamma}y$. In the dimensionless form, the relative viscosity becomes:

$$\eta_r = \frac{\langle\sum_{xy}\rangle}{2\eta\langle\mathbf{E}_{xy}^{\infty}\rangle} = 1 + \eta_r^H + \eta_r^P + \eta_r^B \quad , \tag{2.21}$$

with

$$\eta_r^H = \frac{9}{2}\,\phi\,\frac{1}{N}\,\overline{\sum_{\alpha=1}^{N}\,(\mathbf{S}_{\alpha}^H)_{xy}} \quad , \tag{2.22.a}$$

$$\eta_r^P = -\frac{9}{2}\phi\frac{1}{\dot{\gamma}^*}\frac{1}{N}\overline{\sum_{\alpha=1}^{N}(\mathbf{r}_\alpha\mathbf{F}_\alpha)_{xy}}\ , \tag{2.22.b}$$

$$\eta_r^B = -\frac{9}{2}\phi\frac{1}{Pe}\frac{1}{N}\overline{\sum_{\alpha=1}^{N}[\nabla_\alpha(\mathbf{R}_{FU}^{-1}\cdot\mathbf{R}_{FE})]_{xy}}\ . \tag{2.22.c}$$

We have nondimensionalized $\mathbf{R}_{SU}$ with $6\pi\eta a^2$ and $\mathbf{R}_{SE}$ with $6\pi\eta a^3$. $\mathbf{R}_{SU}$ is of dimension $(5N\times 6N)$ and $\mathbf{R}_{SE}$ if of dimension $(5N\times 5N)$. The over bar is to imply a time average over the course of the dynamic simulation.

Here we observe the same fundamental importance of the parameters - the particle volume fraction ϕ and the Péclet number, Pe - on the rheology, as well as on the microstructure through the evolution equation. Each contribution to the relative viscosity in (2.21) can be understood as follows: First particles, which are rigid and finite in size, cannot deform as the pointwise fluid in a shear flow. Therefore, the fluid must spend extra energy to overcome the resistance of the particles due to the local deformation by the fluid and η_r^H measures the extra work due to the presence of particles. η_r^P can be viewed the elastic stress which acts as a spring-like restoring force associated with the suspension with particles having an interparticle/external force $\mathbf{F}^P$. Finally any departure from the equilibrium isotropic structure either by the shear force and/or by the non-hydrodynamic force is balanced by the stochastic Brownian motion. The energy which the suspension uses to restore the equilibrium structure from any deformation is reflected in the term η_r^B.

In addition to relative viscosity, Stokesian dynamics simulation gives the normal stress differences χ_1 and χ_2; together they form the complete set of rheological function

for colloidal suspensions. The definitions of χ_1 and χ_2 are:

$$\dot{\gamma}\,\chi_1 \equiv -\langle \Sigma_{xx} - \Sigma_{yy} \rangle \ , \tag{2.23}$$

$$\dot{\gamma}\,\chi_2 \equiv -\langle \Sigma_{yy} - \Sigma_{zz} \rangle \ . \tag{2.24}$$

In appendix A, we provide the details for the numerical operations of $\nabla\cdot\mathbf{R}_{FU}^{-1}$ which is important for Brownian motion, and $\nabla\cdot(\mathbf{R}_{SU}\cdot\mathbf{R}_{FU}^{-1})$ which is used to compute the Brownian stress $\mathbf{S}^B$. The development of the Brownian contribution to the particle displacement and to particle stresses was a join effort with our colleague Bauer (1992).

II.3.2 Self-Diffusivities

Self-diffusion is the very basic properties of colloidal suspensions. The short-time self-diffusion coefficient D_o^s conveys the information on the local structure and the instantaneous mobility of the suspended particles. The long-time self-diffusivity, D_∞^s, conveys information on the dynamics of the suspension on much longer time scales which allow the particles to move far from their starting points, deform the local structure and exchange places with their neighbors. Light scattering techniques can be used to measure both these self-diffusion coefficients and the information can be linked to the particle size, shape and also the interparticle forces (Berne and Pecora (1976), Eckstein and Shapiro (1977), Leighton and Acrivos (1987), Laun (1992)). Theories have been developed to predict the self-diffusion coefficients and its dependency on the particle volume fraction ϕ, but they can only treat the equilibrium structure ($Pe \rightarrow 0$) for the short-time self-diffusivities, or are limited to dilute suspensions. There are still open questions on the behavior of D_o^s and D_∞^s both theoretically and experimentally. It is

of our interest to provide simulation results, and hopefully an understanding of the self-diffusivities of colloidal dispersions. Stokesian dynamics can compute both D_o^* and D_∞^* and their dependence on ϕ and Pe.

The short-time self-diffusion coefficient D_o^* is given by instantaneous averages over all configurations and over all identical particles:

$$D_o^* = \frac{1}{N} \langle tr\ D \rangle \quad . \tag{2.25}$$

Here tr stands for the trace of the diagonal elements of the diffusion tensor D related to the resistance resistance matrix by the Stokes-Einstein relation:

$$D \equiv kT\, \mathbf{R}_{FU}^{-1} \quad . \tag{2.26}$$

It should be noted that D_o^* is only true diffusivity in the limit of $Pe \rightarrow 0$, but it does measure the local average mobility of a particle irrespective of the Péclet number and will be used as such. The long-time self-diffusivities D_∞^*, which measures the ability of a particle moving far from its initial placement, is defined as:

$$D_\infty^* \equiv \lim_{t\rightarrow\infty} \frac{1}{2N} \frac{d}{dt} \langle (\mathbf{x} - \langle \mathbf{x} \rangle)^2 \rangle \quad . \tag{2.27}$$

Both self-diffusion coefficients are accessible by light scattering techniques in tracer diffusion experiments; the long-wavelength limit obtains D_o^*, while the short-wavelength limit gives D_∞^* (Rallison and Hinch (1986), van Megen, Underwood and Snook (1986)).

In chapter III, we explain the details of the dynamic simulation process and the

sampling statistics of simulation results. A computing flowchart of Stokesian dynamics is presented to show step-by-step the computing aspect of Stokesian dynamics method.

Chapter III

THE DYNAMIC SIMULATION PROCESS

AND

THE SAMPLING STATISTIC OF SIMULATION RESULTS

III.1 The Dynamic Simulation Process

III.1.1 The Computer Unit Cell Model

Figure 3.1 illustrates a computer model for Stokesian dynamics simulations. A simple cubic unit cell is employed containing N suspended particles. The length of the cubic cell H relates to the volume fraction ϕ by:

$$H = \left(\frac{4}{3}\frac{\pi a^3 N}{\phi}\right)^{\frac{1}{3}} . \tag{3.1}$$

The particle Reynolds number, Re, is assumed to be small, i.e., $Re = \rho a^2 \dot{\gamma}/\eta \ll 1$, where $\dot{\gamma}$ is the shear rate. Particles are rigid spheres. Periodic boundary condition is applied to model an unbounded colloidal dispersion. The simple cubic cell is also used in the Ewald summation to form the grand mobility tensor $\mathcal{M}^*$.

Figure 3.1 also shows the orthogonal reference coordinates with a simple shear flow in the x-axis, the velocity gradient in the y-axis and the vorticity in the z-axis. This reference coordinate system is used throughout the thesis. By changing the Péclet number, we can model the shear flow with different shear rates. Particle volume fraction ϕ is also varied.

III.1.2 Flowchart of Stokesian Dynamics

Figure 3.2 presents a computing flowchart of the Stokesian dynamics simulation method and gives important information on the process of a dynamic simulation. The dynamic simulation proceeds according to the following steps:

Step 1: An initial placement of N particles is selected. It can be from a random selection using the Monte-Carlo method, or a periodic lattice, or any particular configuration obtained for example from another simulation for the purpose of testing the influence of initial particle configurations on suspension macroscopic properties. It should be clear that the Stokesian dynamics method is capable of simulating any particular particle configuration, static or dynamic.

Step 2: The grand mobility tensor $\mathcal{M}^*$ is computed using The Ewald summation technique with periodic boundary condition an unbounded suspension. $\mathcal{M}^*$ is then inverted using the Cholesky inversion method for a symmetric, positive definite matrix. It is important to note here that to save computing time we do not need to form and invert $\mathcal{M}^*$ at every time step since changes in $\mathcal{M}^*$ will be small provided that particles do not move a length comparable to their characteristic size a. In the simulation, we form and invert $\mathcal{M}^*$ once every time unit of $t \approx 0.1$, which is typically every 100 time steps (Δt=10^{-3}), and during this time particles in a simple shear flow move a distance less than one particle radius. Comparisons for simulations with $\mathcal{M}^*$ and $\mathcal{M}^{*-1}$ computed at every time step and with $\mathcal{M}^*$ and $\mathcal{M}^{*-1}$ formed once every $t \approx 0.1$ show very small and negligible differences in macroscopic properties. The near-field lubrication is computed at every time step and then added to $\mathcal{M}^{*-1}$ to form the grand resistance tensor $\mathcal{R}$.

Step 3: From the partition of $\mathcal{R}$, $\mathbf{R}_{FU}$ is obtained and inverted using the same Cholesky method. During the inversion of $\mathbf{R}_{FU}$, we save $\mathbf{A}^{-1} \equiv \sqrt{\mathbf{R}_{FU}^{-1}}$ for the random step $\mathbf{X}(\Delta t)$.

Step 4: Using $\mathbf{R}_{FU}^{-1}$, the particle velocities $\mathbf{U}$ are computed according to:

$$\mathbf{U} = \mathbf{U}^{\infty} + \mathbf{R}_{FU}^{-1} \cdot [\, \mathbf{R}_{FE} : \mathbf{E}^{\infty} + \mathbf{F}^{P} \,] \ . \tag{3.2}$$

If there is the interparticle/external force $\mathbf{F}^{P}$ then it is straight forward to compute it from the specified input form.

Step 5: The Brownian motion term $\nabla \cdot \mathbf{R}_{FU}^{-1}$ is computed. Appendix A shows the numerical optimization and step-by-step computation for this Brownian contribution to the particle positions and particle stresslets.

Step 6: New particle trajectories are computed from particle velocities $\mathbf{U}$ and from Brownian motion. The 4^{th} order Adam-Basthforth integrating scheme is employed to update new particle positions from $\mathbf{U}$ of step 4. To complete particle motion, the two contributions from Brownian motion: $\nabla \cdot \mathbf{R}_{FU}^{-1}\ \Delta t$ from step 5 and $\mathbf{X}(\Delta t)$ from step 3 are added to particle displacements. The Euler integration scheme is used for both Brownian motion terms.

Step 7: $\mathbf{S}^{H}$ and $\mathbf{S}^{P}$ are computed according to equations (2.20.a) and (2.20.b), respectively. $\mathbf{S}^{H}$ is the hydrodynamic contribution to particle stresslets and $\mathbf{S}^{P}$ is the stress resulting from the interparticle/external force acted on the particle.

Step 8: Brownian stresses, $\mathbf{S}^{B}$, are computed (see appendix A). Together with $\mathbf{S}^{H}$ and $\mathbf{S}^{P}$ in step 7, we have the complete set of contributions to the bulk stress $\langle \Sigma \rangle$ to determine the rheology.

Step 9: The final step of the simulation process is designated for computing the number-averaged mean and statistics of suspension bulk properties: shear viscosity from $\langle \Sigma \rangle$,

short-time self-diffusion coefficients defined in equation (2.26) with $\mathbf{R}_{FU}^{-1}$ is saved from step 3. Output results for final analysis are saved at the desired frequency.

The dynamic simulation returns to step 2 until the final time t_{final} is reached and the execution is terminated. As presented here, Stokesian dynamics requires an $O(\mathcal{N}^3)$ operations mainly from the inversion of $\mathcal{M}^*$ and $\mathbf{R}_{FU}$. $\mathcal{N}$ is the size of the grand mobility tensor $\mathcal{M}^*$. We do not invert $\mathcal{M}^*$ of dimension $(11N\times11N)$ at every time step, resulting in a substantial saving in computer time. $\mathbf{R}_{FU}$ with smaller dimension $(6N\times6N)$ needs to be inverted at every time step. Once $\mathbf{R}_{FU}^{-1}$ is obtained, we have the full benefit of determining Brownian contribution to particle motion and to particle stresslets in addition to just solving for $\mathbf{U}$ from equation (3.2). It is important to note that we do not need to assemble the operation $\nabla\mathbf{R}_{FU}^{lub}$, $\nabla\mathcal{M}^*$ and $\nabla\mathbf{R}_{SU}^{lub}$ into matrices. These operations are analytically computed in pairwise fashion, multiplied to the proper right-hand side matrix and then summed for all pairs of particles (see appendix A). This technique saves a significant amount of computer memory and enables simulations to be run on workstations. Had we formed all of these matrices, then their sizes would be $(11N\times11N\times3)$ for $\nabla\mathcal{M}$, $(6N\times5N\times3)$ for $\nabla\mathbf{R}_{FU}^{lub}$ and $(5N\times5N\times3)$ for $\nabla\mathbf{R}_{SU}^{lub}$. For simulation with 123 particles, the matrix with a size of $(11N\times11N\times3)$ will need $\approx$ 20 Megabytes in double precision and it is a substantial block of CPU memory on a workstation. The following section emphasizes on the sampling method of simulation results.

III.2 Data Collection and The Sampling Statistics

In this section, we present our method of collecting simulation output, computing the results and statistical variation.

III.2.1 Data Collection

Computer simulations have been run on a Sun SPARC 4/360, several IBM RiSC/6000 workstation models 530, 530H, 560 and a Stardent Vistra 800. In addition, The Cray Y-MP at San Diego Super Computer was also used with vectorized codes for large system sizes (N=123). All numerical calculations are in double precision. The majority of our simulations were run on IBM RiSC/6000 workstation models 530 and 560.

The dynamic simulations starts with the selection of important parameters: ϕ, N (by setting ϕ and N, the length of the simple cubic cell H is fixed), Pe and an initial particle configuration. In general, simulation run times range from dimensionless time of 60 to 400, with 100 being the average. The run time is dimensionless, as it is scaled with either the convective time from the shear flow, $\dot{\gamma}^{-1}$ for $Pe \geq 1$ or with diffusive time, a^2/D_o for $Pe \leq 1$. The time step, Δt_{set}, ranges from 10^{-5} to 10^{-3}. A time step of 10^{-4} or smaller is needed for the simulations with very small or with large Pe and large ϕ to avoid severe particle overlapping. The average number of steps for each run, NSTEPS, is 100,000 for Δt=10^{-3} and a run time of 100. For $Pe < 1$, longer runs with time of 200 to 400 are required for the suspension macroscopic properties to have sufficient time at steady state to form the averages. The first 5,000 to 10,000 time steps are discarded before we compute any macroscopic properties.

The complete set of suspension rheology: shear viscosity η_r and normal stress differences χ_1 and χ_2 are averaged for all N particles and saved at each time step. The contribution to the bulk stress from each particle is saved less frequently than the number-averaged stress; it is collected at every unit time $t \approx 0.1$. After the simulation is complete,

instantaneous particle-averaged data is used to compute the time-averaged η_r, χ_1 and χ_2. To improve the statistic of these time-averaged values, we sample data over a number of different time intervals for the entire simulation and then compute the final mean and standard deviation. Each time interval has the same length of time, which we call t_{diff}, sufficient for the macroscopic properties to equilibrate. It is important to note here that there are two types of fluctuation statistics associated with macroscopic properties. The first type describes the time fluctuation of instantaneous values about the mean during the course of a simulation. The second type is the fluctuation of the means which are computed from different samples and/or different time intervals when the sample is taken. While we are able to compute both of these two statistics, it is the second type of statistic which is more important and relevant to our studies. It shows the certainty of the reproducibility for macroscopic properties obtained from the simulations. In the next section, we illustrate with samples from simulations to show the process of computing these various means and statistics.

Data for particle locations and orientations are saved at times $t \approx 0.05$ to 0.1. The long-time self-diffusion coefficients which are defined in (2.27) are computed by following the particle in time and in space. The suspension microstructure is determined from particle positions. We compute the angularly averaged pair-distribution function $g(r)$ and the structure factor $S(k)$ which is the Fourier transform of $g(r)$. Our aim is the determination of the relative arrangement among N particles under the influence of the shear flow, the hydrodynamic interactions and interparticle/external particle forces and its link to the suspension macroscopic properties.

Particle translational/rotational velocities are saved at every time unit $t \approx 0.1$. We compute the mean square of the particle velocity fluctuations and define the suspension temperature according to $\langle \mathbf{U}'\mathbf{U}' \rangle$ and $\langle \mathbf{\Omega}'\mathbf{\Omega}' \rangle$ with the prime denoting the fluctuation and Ω denoting the particle rotational velocities. The time-correlation for particle velocities are computed and they can be related to the long-time self-diffusion coefficients as another consistency check for equation (2.27).

In addition, from $\mathbf{R}_{FU}^{-1}$ the short-time self-diffusion coefficients are computed according to equation (2.25). Both the translational and rotational self-diffusion coefficients are saved every unit time $t \approx 0.05$.

III.2.2 The Sampling Statistics

As we proceed through this thesis, tables of results and statistics for suspension macroscopic properties are presented, and we need to specify and explain our method of computing the mean and the standard deviation for suspension macroscopic properties. The method of averaging for a macroscopic property is best illustrated by the following mathematical relation:

$$\langle \mathbf{W} \rangle \equiv \frac{1}{P} \sum_{j=1}^{P} \left[\overline{\left(\frac{1}{N} \sum_{i=1}^{N} \mathbf{W}_i \right)} \right] . \tag{3.3}$$

In (3.3) $\mathbf{W}_i$ denotes a macroscopic quantity of which we compute for each particle at every time step and $\langle \mathbf{W} \rangle$ is the mean value which we seek. $\mathbf{W}_i$ is first averaged over all N particles at every time step. It is then averaged again with running time during the simulation as indicated with the over bar. This gives the time-traced mean of $\mathbf{W}_i$,

$\overline{\mathbf{W}}$. From a number P of different initial samples, the final mean, $\langle \mathbf{W} \rangle$ and its statistics can be computed. We have to determine the number of samples, P so that the statistics are good and P is relatively small. For every case of study for the suspensions (with a particular set of parameters N, Pe, ϕ, $\mathbf{F}^P$, etc...), we then have to simulate with P samples before a suspension macroscopic property can be determined with certainty. As predicted, the demand of computer time for a *complete* study of the fundamental hard-sphere suspensions model will be undoubtedly large and possibly beyond the reach of our present computing power.

Of course this is an ideal method to obtain the most accurate results. Our simulation results with different initial samples show that we may not need to have a number of P runs for each case. We may substitute the P samples by a number of different time intervals of equal length of time t_{diff} and average a macroscopic property over these intervals. t_{diff} is chosen to be sufficient for a macroscopic property to equilibrate and converge to a steady value. With this substitution, we can modify the relation given by (3.3) to:

$$\langle \mathbf{W} \rangle \equiv \frac{1}{K} \sum_{k=1}^{K} [\overline{(\frac{1}{N} \sum_{i=1}^{N} \mathbf{W}_i)}] , \tag{3.4}$$

where the sum over index $k=1,K$ indicates an average over K time intervals.

We shall show that this substitution is rather good and gives accurate macroscopic results by examining two sets of figures. The set of figures 3.3.a-f is for suspensions with ϕ=0.316, and the set of figures 3.4.a-k is for suspensions with ϕ=0.51. These are the

simulation results of a hard-sphere suspension model with no interparticle/external force ($\mathbf{F}^P = 0$) and the particles are neutrally buoyant and rigid spheres. We shall focus on the variation of macroscopic properties with different initial samples and will discuss the relevant importance of their values in later chapters. The macroscopic properties which we present in these figures are the shear viscosity η_r, the normal stress differences χ_1 and χ_2 and the short-time translational and rotational self-diffusion coefficient D_o^* and D_r^*. Initial particle configurations are randomly chosen by the Monte-Carlo method.

Figures 3.3.a-c show the plot of time-averaged shear viscosity η_r versus shear time for two initial samples of 27 particles at volume fraction ϕ=0.316 and Pe=0.1, 1.0 and 10^5, respectively. The convergence of η_r for two different particle configurations, denoted on these plots as run #1 ($\Box$) and run #2 ($\triangle$), is seen to be very good for all three Pe cases and the difference in the final value of η_r for two runs is small. As shown in Fig.3.3.a, the simulation for Pe=0.1 requires a longer run time for η_r to reach a steady value. There is a difference of about 1 unit in value of η_r for run #1 and run #2 for time $t < 130$. The two curves then converge to the same steady value for $t \approx 150$. For Pe=1.0 and 10^5, η_r for two runs converges much sooner after time $t \approx 50$ and this is clearly seen in Figures 3.3.b and 3.3.c. Among these Pe values, only in the case Pe=0.1 do we observe some fluctuations in the shear viscosity which is expected from a Brownian dominated suspension.

Figures 3.3.d-e show the plot of time-averaged normal stress differences, χ_1 and χ_2 versus shear time for Pe=0.1. There is approximately one unit difference in χ_1 for two samples. The convergence of χ_2 for two both runs is very good and the uncertainty is

smaller than that of χ_1.

Figures 3.3.f-g show the plot of time-averaged self-diffusion coefficients D_o^* and D_r^* against shear time for Pe=0.1. Both figures give excellent convergence of both D_o^* and D_r^* for two samples and the difference in these values is very small.

As illustrated from the set of figures 3.3.a-f, the convergence of macroscopic properties is good. There is a noticeably small fluctuation in steady state values sampled from different particle configurations for Brownian dominated suspensions ($Pe \leq 1$). The next set of figures 3.4.a-k is for a more dense suspension with ϕ=0.51 and shows the fluctuation of η_r with time during the course of a simulation and the fluctuation of η_r for several initial samples of 27 particles.

Figures 3.4.a-c present the plots of both the instantaneous (solid curve) and the time-averaged ($\triangle$) η_r versus shear time for suspensions at ϕ=0.51 and Pe=0.1, 1.0 and 10^5, respectively. Figure 3.4.a for the run with Pe=0.1 shows large and rapid fluctuations in η_r for the entire shear time. The fluctuation is seen to be symmetric about the time-averaged mean value ($\triangle$). The time-averaged η_r converges steadily to a value of $\approx$ 35 after a shear time of $t \approx 60$. Figures 3.4.b for Pe=1.0 illustrates a similar behavior of η_r. The fluctuations of η_r with shear time are smaller in magnitude but as frequent as we observed in Fig.3.4.a. Good convergence of the time-averaged η_r to a value of $\approx$ 15 is seen from this plot. Figure 3.4.c shows the relation of η_r versus shear time for Pe=10^5. Sharp peaks with large increases in the value of η_r are seen in this plot, but the spikes occur less frequently than the fluctuations observed for the runs with Pe=0.1 and 1.0. After a shear time of $t \approx 20$, the suspension equilibrates and the

sharp spikes are now three or four times smaller in magnitude and occur less frequently. The time-averaged η_r converges to a value of ≈ 50 after a shear time of $t \approx 50$. We see two behaviors of the shear viscosity η_r for dense suspensions: Figures 3.4.a-b show the general behavior of η_r with large, symmetric and rapid fluctuations for Brownian dominated suspensions ($Pe \leq 1$), and Fig.3.4.c shows the behavior of the shear viscosity in hydrodynamic dominated suspensions (Pe=10^5); occasionally there are intense spikes as large clusters of particles are formed and broken. For both cases, the fluctuation of η_r in time about a time-averaged steady value is large. Next we will examine the certainty of obtaining the final values for macroscopic properties of dense suspensions from several initial samples.

Figures 3.4.d-f show the plots of time-averaged shear viscosity η_r versus shear time with different initial particle configurations for ϕ=0.51 and Pe=0.1, 1.0 and 10^5, respectively. Figure 3.4.d illustrates a small fluctuation of the steady state η_r for three different sample runs for Pe=0.1 and the uncertainty is ≈ 3 units in value of η_r with the mean $\eta_r \approx 35$. Sample run #3 (○) is taken from the run #1 (□) but at a different time interval of t_{diff}= 100 at 20 time units apart. The small difference in η_r obtained from sample #1 and sample #3 is about 9% and is within the uncertainty of the simulation. The fluctuations for Pe=1.0 and Pe=10^5, which is shown in Figures 3.4.e and 3.4.f, are small for two sample runs.

The plots of both time-averaged χ_1 and χ_2 versus shear time for small Pe cases Pe=0.1 and Pe=1.0 are presented in Figures 3.4.g and 3.4.h, respectively. The convergence of χ_1 and χ_2 for two sample runs is seen to be excellent. The same good accuracy is seen

from the plots of D_o^* and D_r^*, which are shown in Figures 3.4.i and 3.4.j.

It is evident from these two sets of figures that the suspensions macroscopic properties will equilibrate with sufficient run time independent of initial particle configurations. Their convergence is remarkably good and the uncertainty is small. It requires a longer run time for simulation with small Pe ($Pe < 1$) and for $Pe > 1$, the convergence is much faster and the run time is $t \approx 40$. In our simulations, we allow the run time to be two or three times longer than the time which suspension macroscopic properties require to come to a steady-state value. The long run time can be divided into equal time intervals. Samples of data can be obtained from these time intervals and results are computed using the relation defined in equation (3.4). This is our method of reporting results and it is the method which gives good certainty and confidence for our simulation results.

As we show in the next chapter that only when the Brownian motion is computed with great accuracy then will the hard-sphere microstructure given by a dynamic simulation for the pure Brownian case ($Pe \to 0$) be identical to that from a random structure calculated by the Metropolis Monte-Carlo method (Chae, Ree and Ree (1969)). Stokesian dynamics with its hydrodynamic origins, offers an efficient and accurate method to compute $\mathcal{M}^*$ and $\mathcal{R}$ which play the important role in dynamic simulations. More importantly, the simulation is capable of treating a continuous range of the Péclet number and particle volume fraction and it places no restriction on the particle positions. In this aspect, Stokesian dynamics is not only a very powerful method but possibly the only one which can deliver computing efficiency. In chapter IV, we present our simulation results for a pure Brownian hard-sphere model (Pe=0) and for the periodic arrays of spheres.

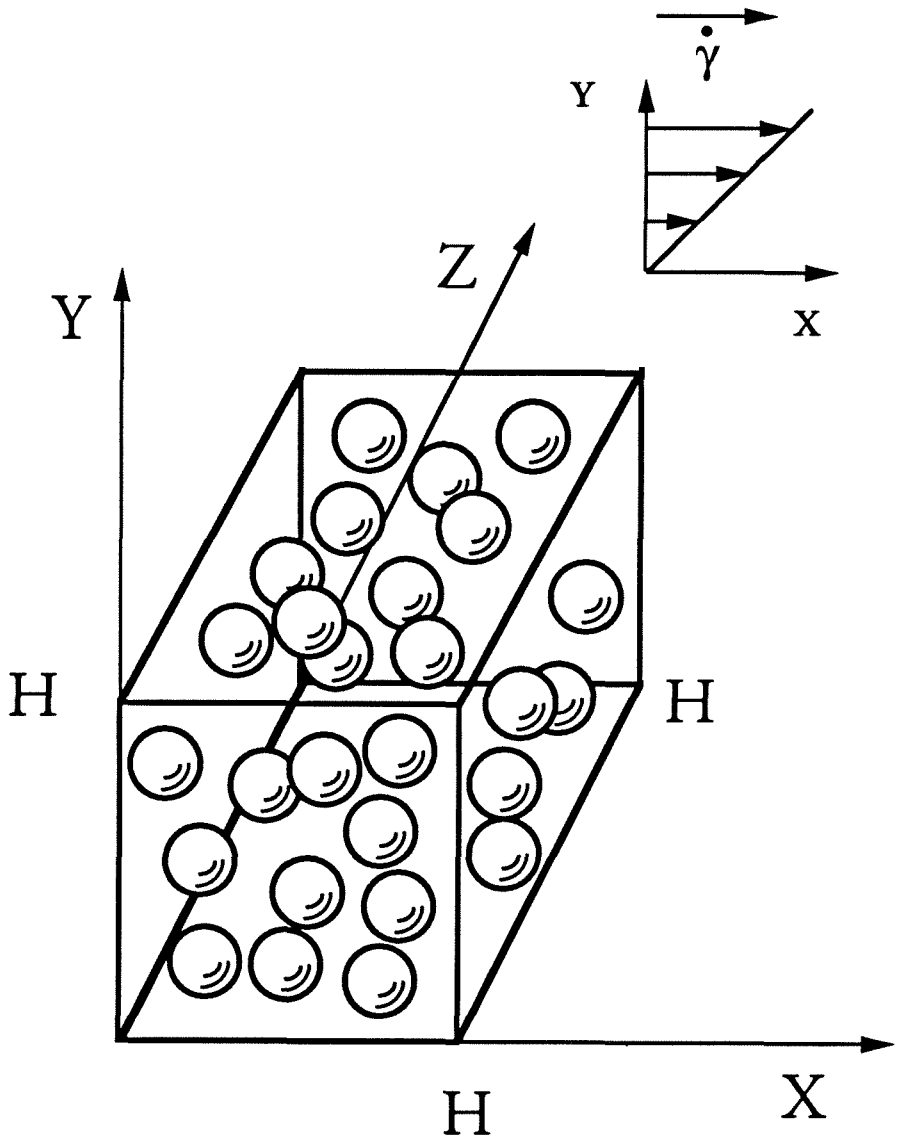

Figure 3.1: The simple cubic unit cell model for the dynamic simulations. There are N particles in the unit cell with length H. The reference orthogonal coordinate system is shown with a simple shear flow in the x-axis, velocity gradient in the y-axis, and vorticity in the z-axis. $\dot{\gamma}$ is the shear rate.

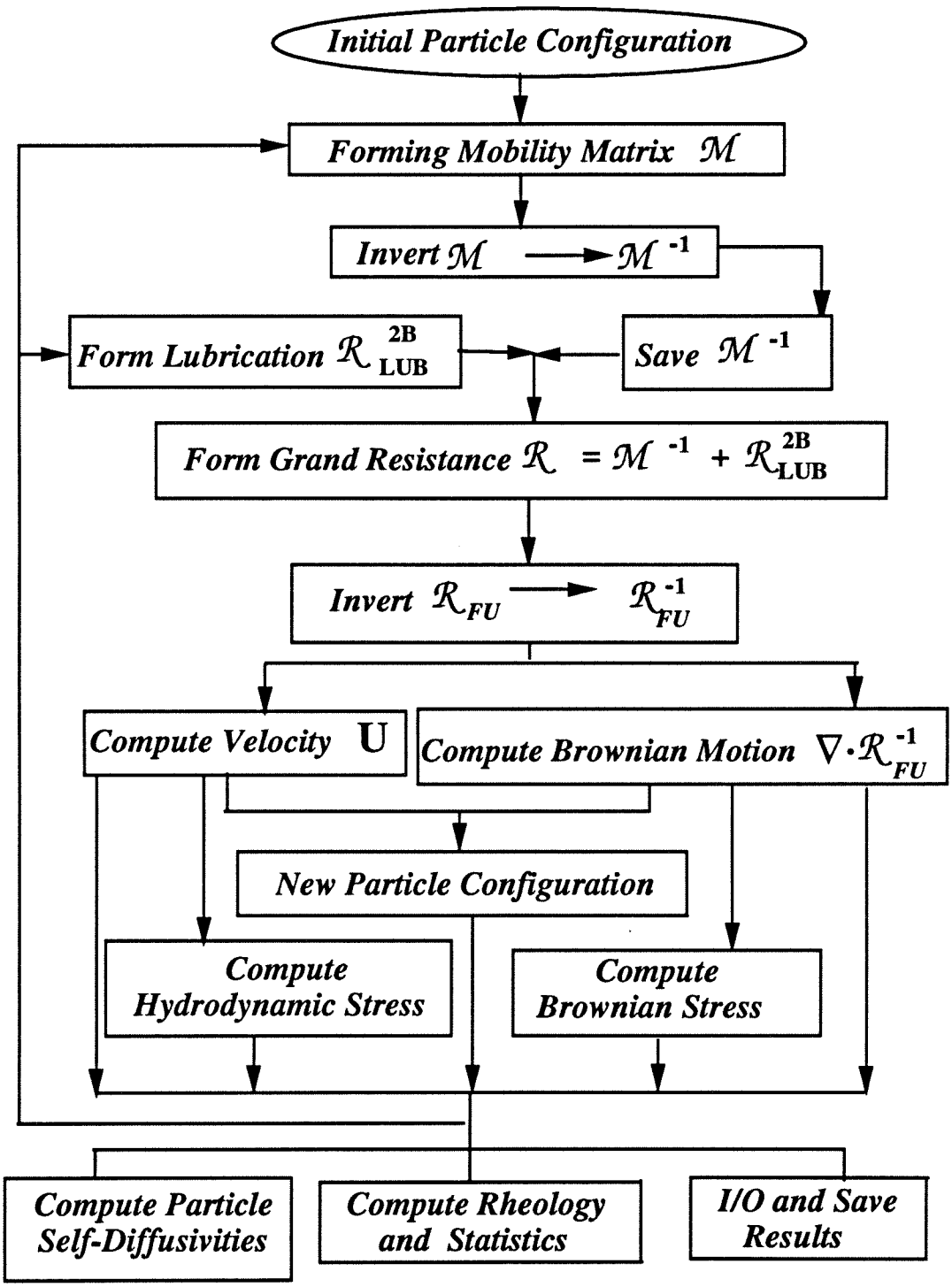

Figure 3.2: The computing flowchart of Stokesian dynamics simulation method

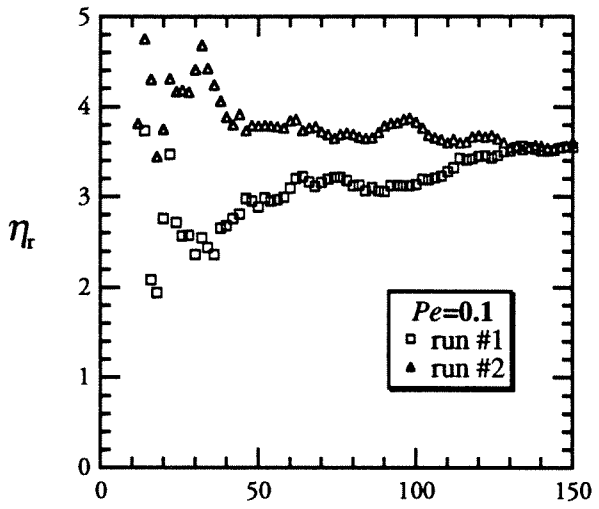

Figure 3.3.a

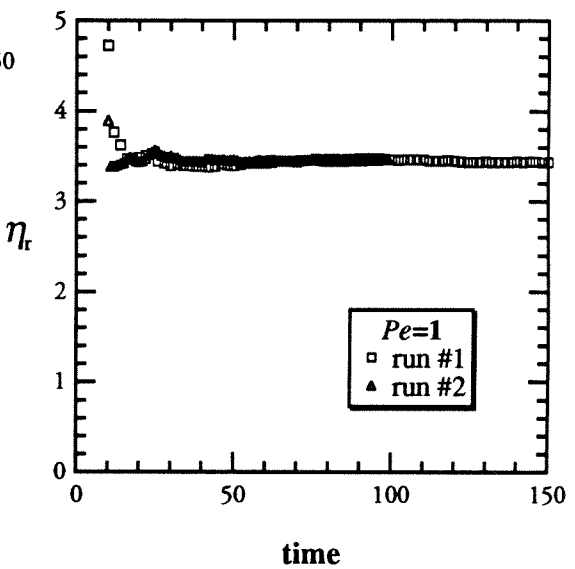

Figure 3.3.b

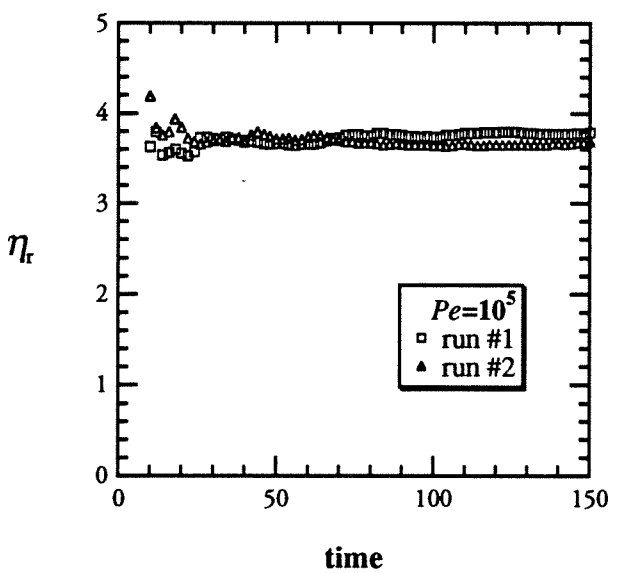

Figure 3.3.c

Figure 3.3.a-c: Plots of time-averaged shear viscosity η_r versus shear time for Pe=0.1, 1 and 10^5 and two initial random samples of 27 particles at volume fraction ϕ=0.316. These plots show good convergence of η_r for different initial particle configurations. For Pe=0.1, it requires a relative long shearing time (time≈120) to obtain a steady value for the shear viscosity.

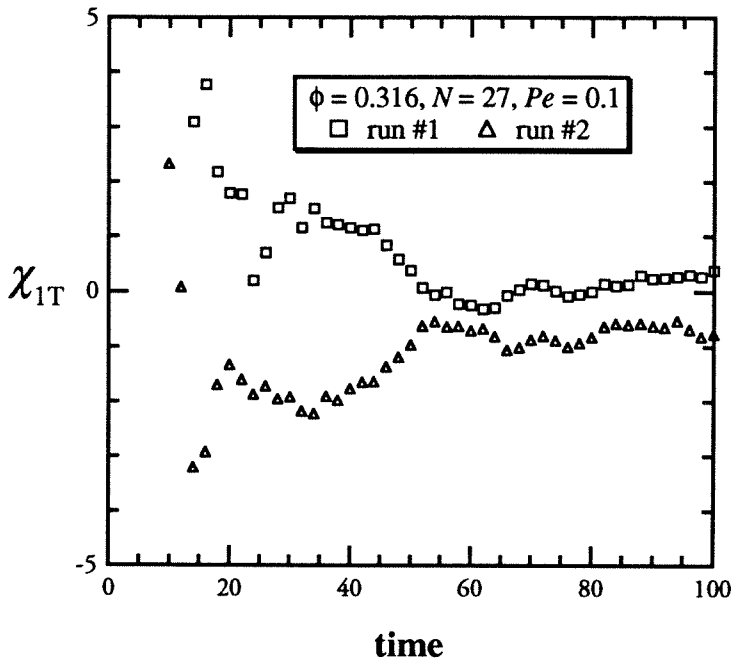

Figure 3.3.d: Plot of time-averaged first normal stress difference χ_{1T} versus shear time.

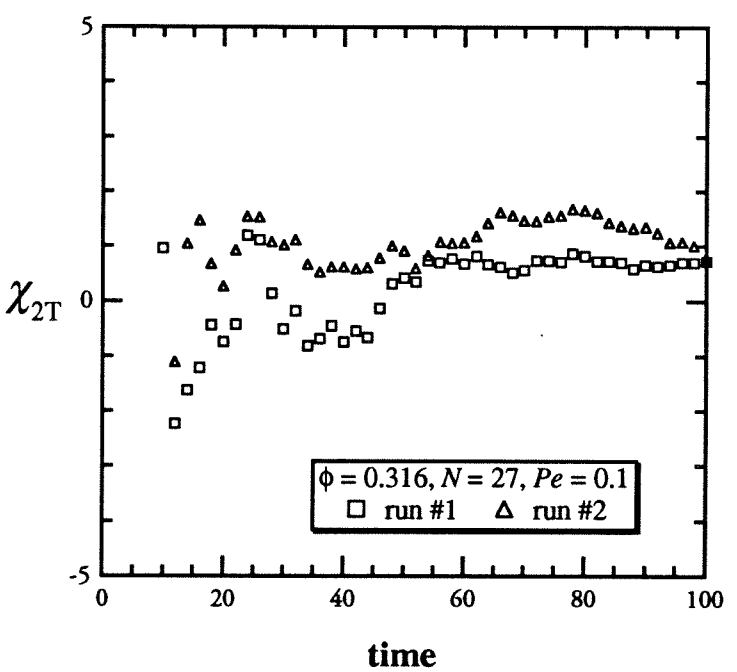

Figure 3.3.e: Plot of time-averaged second normal stress difference χ_{2T} versus shear time.

Figure 3.3.d-e: Plot of the time-averaged first and second normal stress differences χ_{1T} and χ_{2T} versus shear time for two initial random samples of 27 particles at Pe=0.1 and ϕ=0.316. Both normal stress differences converge to within a small uncertainty for different particle configurations.

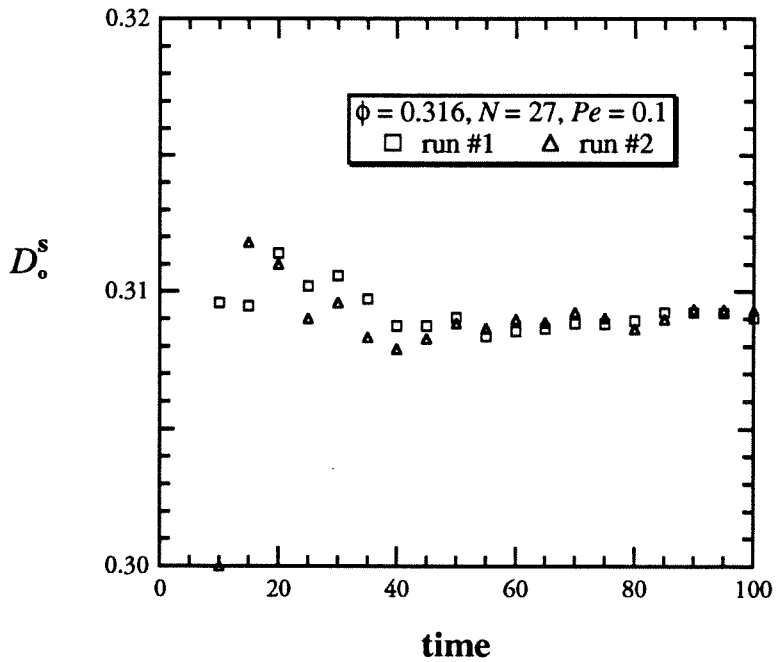

Figure 3.3.f : Plot of the short-time translational self-diffusion coefficient versus shear time.

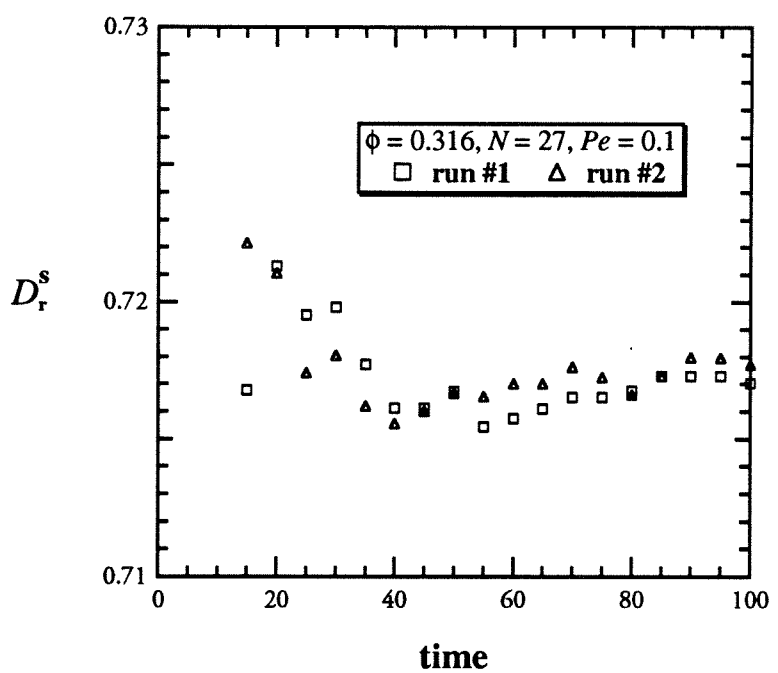

Figure 3.3.g : Plot of the short-time rotational self-diffusion coefficient versus shear time.

Figure 3.3.f-g: Plot of the steady short-time translational and rotational self-diffusion coefficients versus shear time for two initial random samples of 27 particles at a volume fraction ϕ=0.316 and *Pe*=0.1. The convergence of both self-diffusion coefficients with different initial particle configurations is excellent.

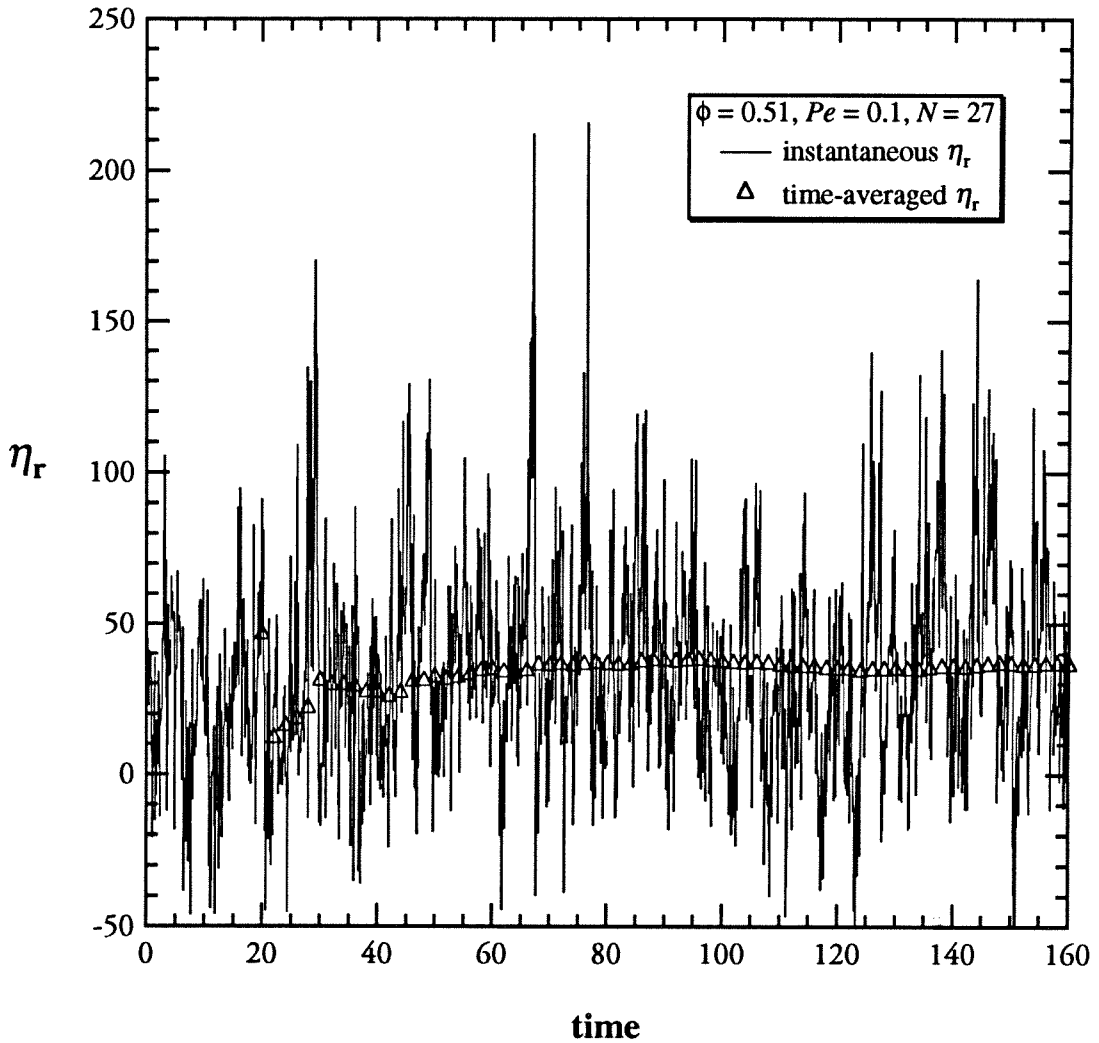

Figure 3.4.a: The instantaneous (solid curve) and (Δ) steady shear viscosity for hard-sphere suspensions at a volume fraction ϕ=0.51, *Pe*=0.1 and 27 particles. It is seen from the figure that there are large and rapid fluctuations of η_r with the entire shear history. The fluctuations are symmetric about the steady shear viscosity. After a shear time of t≈160, the steady shear viscosity equilibrates steadily to a value of 35.

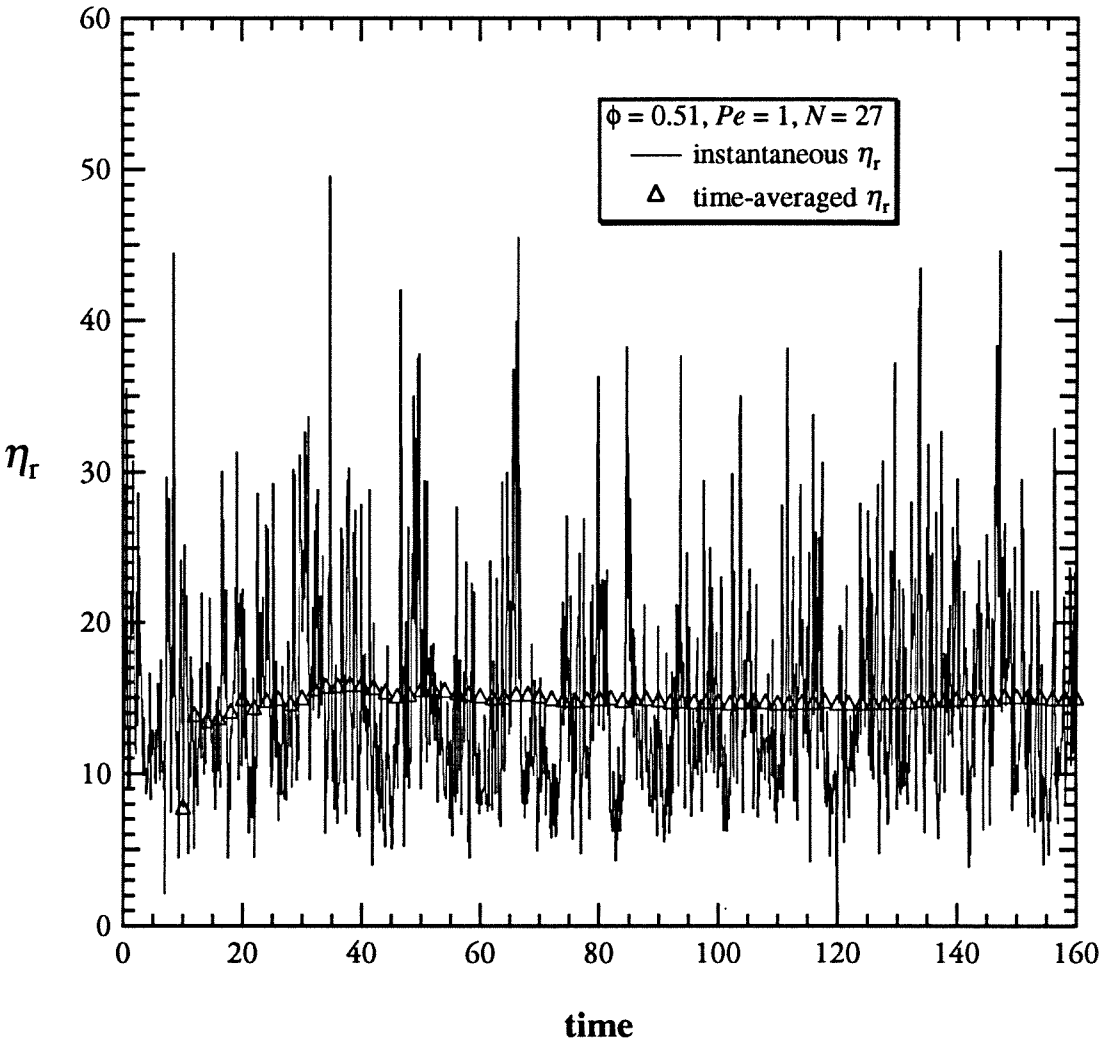

Figure 3.4.b: The instantaneous (solid curve) and (Δ) steady shear viscosity for hard-sphere suspensions at a volume fraction ϕ=0.51, Pe=1 and 27 particles. It is seen from the figure that there are large and rapid fluctuations of η_r over the entire shear history. The fluctuations are symmetric about the steady shear viscosity. After a shear time of t≈160, the steady shear viscosity equilibrates steadily to a value of 15. Compared to the fluctuations in Fig.3.4.a for Pe=0.1, the fluctuations in this figure are about five-times smaller.

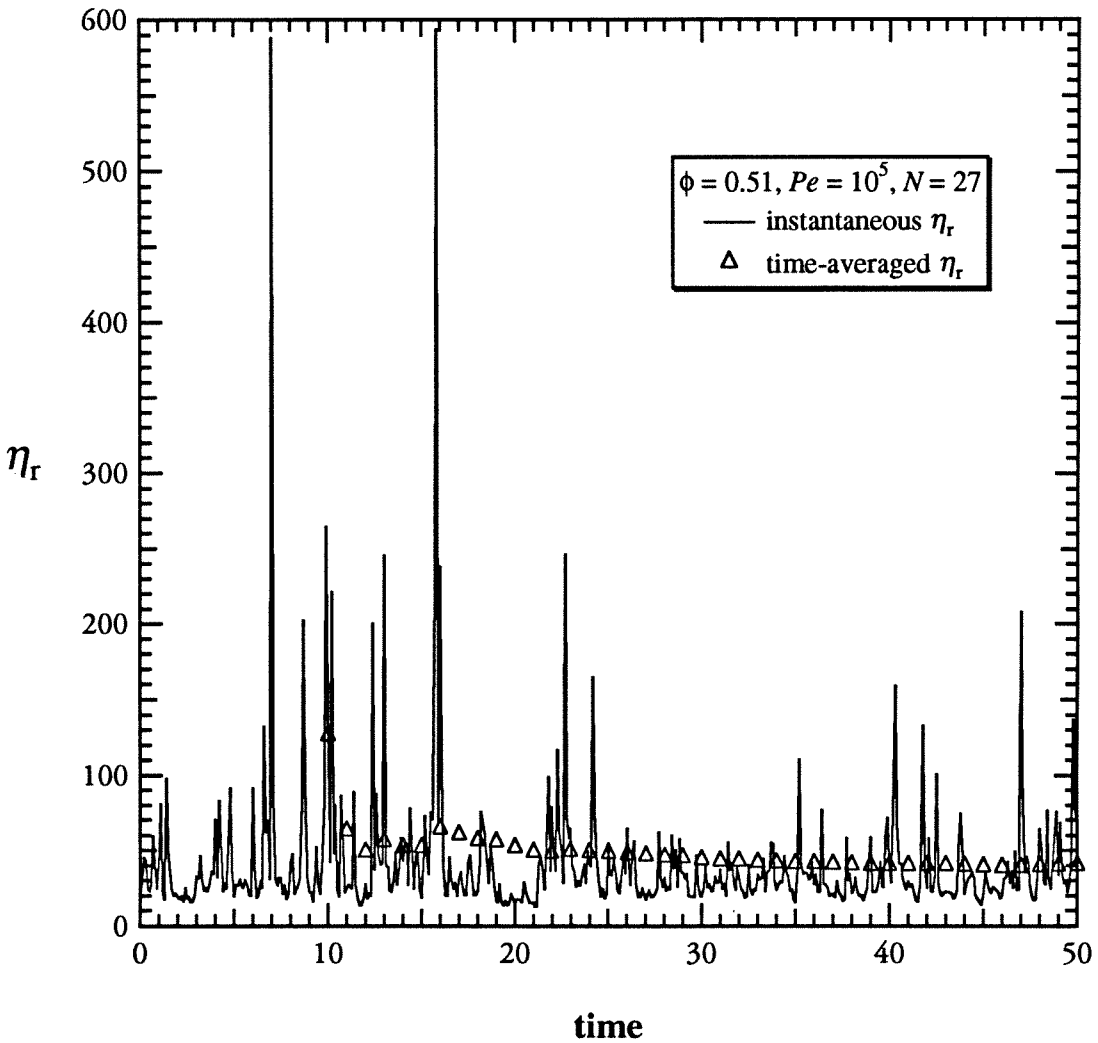

Figure 3.4.c: The (solid curve) instantaneous and (Δ) steady shear viscosity for hard-sphere suspensions at a volume fraction ϕ=0.51, Pe=10^5 and 27 particles. The figure shows very sharp and intense peaks with large increase in the shear viscosity. The sudden changes in the shear viscosity are attributed to the formation and breaking of large clusters of particles. These changes in the shear viscosity occur much less frequently than the rapid fluctuations which are seen for suspensions with strong Brownian motion (Pe=0.1 and 1) shown in Figures 3.4.a and 3.4.b. Good convergence for the steady shear viscosity is seen from the figure after a shear time of 40.

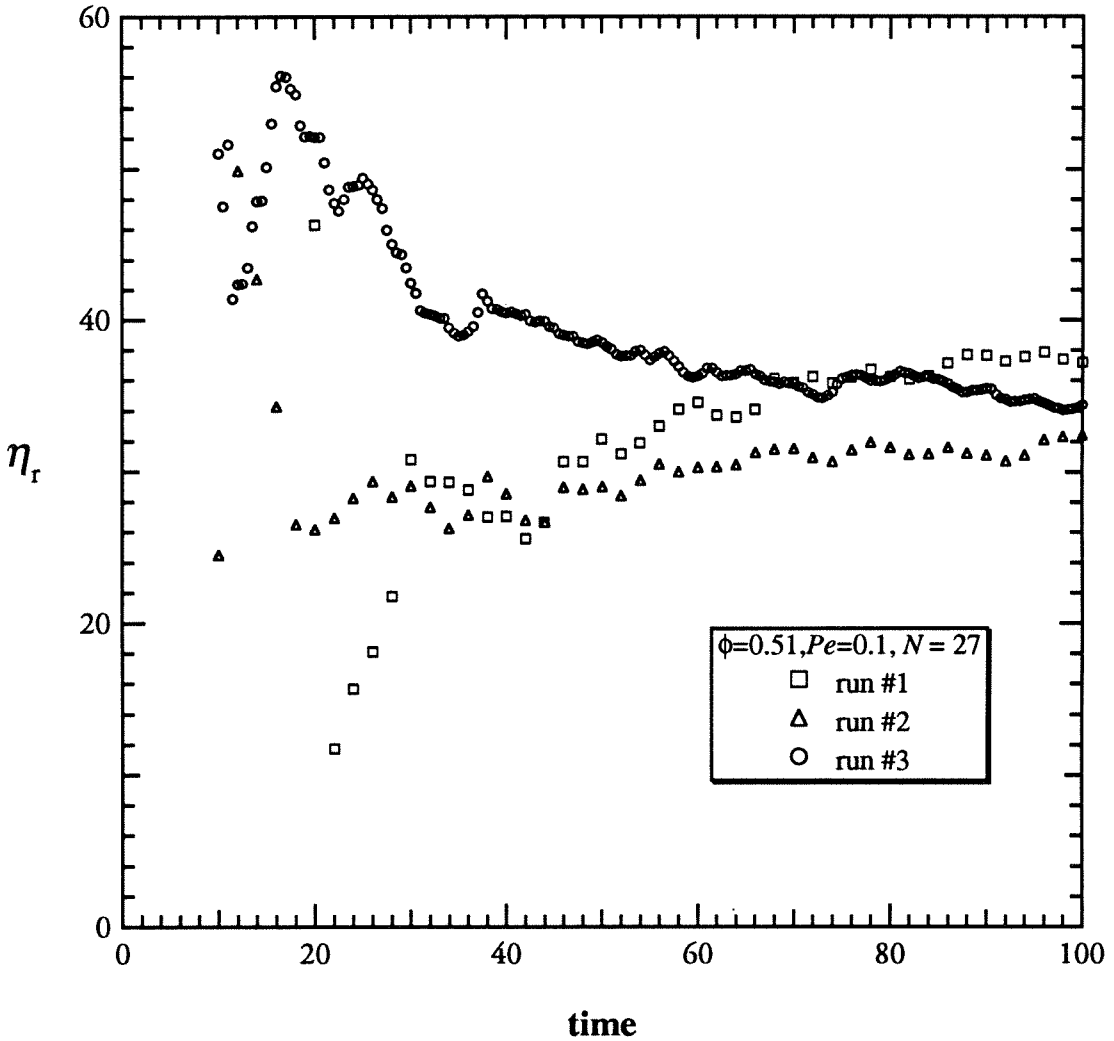

Figure 3.4.d: The steady shear viscosity for hard-sphere suspensions at a volume fraction ϕ=0.51, *Pe*=0.1 and two initial random samples of 27 particles. Run #3 is obtained from run #1 with the same length of 100 time units. There are 20 time units apart between the sample for run #1 (□) and for run #3 (○). The figure shows good convergence for the steady shear viscosity with different initial samples of initial particle configurations (run #1 (□) and run #2 (Δ)) and different time intervals when the samples are taken from one simulation (run #1 and run #3).

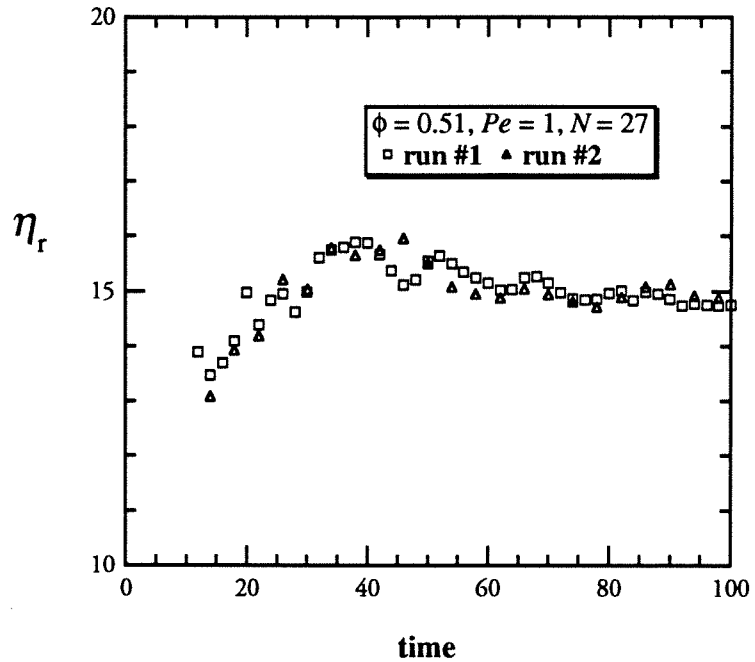

Figure 3.4.e: The shear viscosity η_r of hard spheres at ϕ=0.51 and Pe=1.

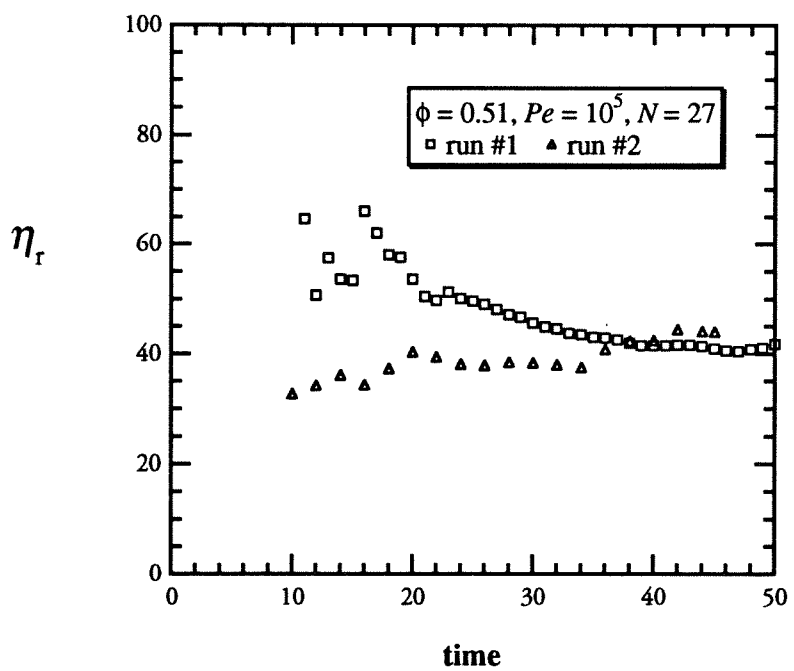

Figure 3.4.f : The shear viscosity η_r of hard spheres at ϕ=0.51 and Pe=10^5.

Figure 3.4.e-f : The shear viscosity η_r of hard-sphere suspensions at ϕ=0.51 with Pe=0.1 (Fig.3.4.e) and 10^5 (Fig.3.4.f) with two initial random samples of 27 particles (run #1 (□) and run #2 (Δ)). Both figures show good convergence for the steady shear viscosity with different initial particle configurations.

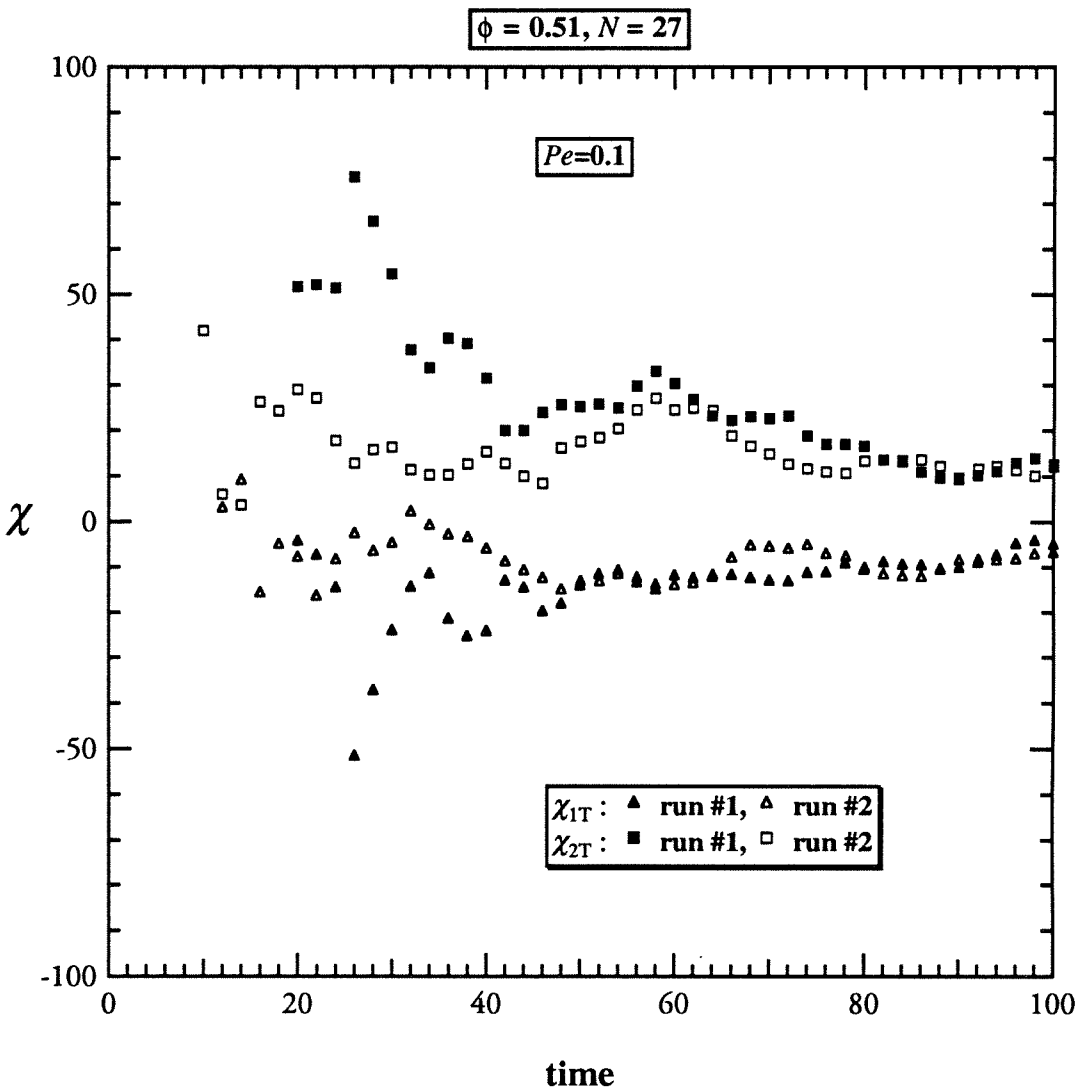

Figure 3.4.g : Plot of the time-averaged first and second normal stress differences χ_{1T} and χ_{2T} versus shear time for hard-sphere suspensions at ϕ=0.51 and Pe=0.1 with two initial random samples of 27 particles. The convergence for both normal stress differences for different initial particle configurations is excellent.

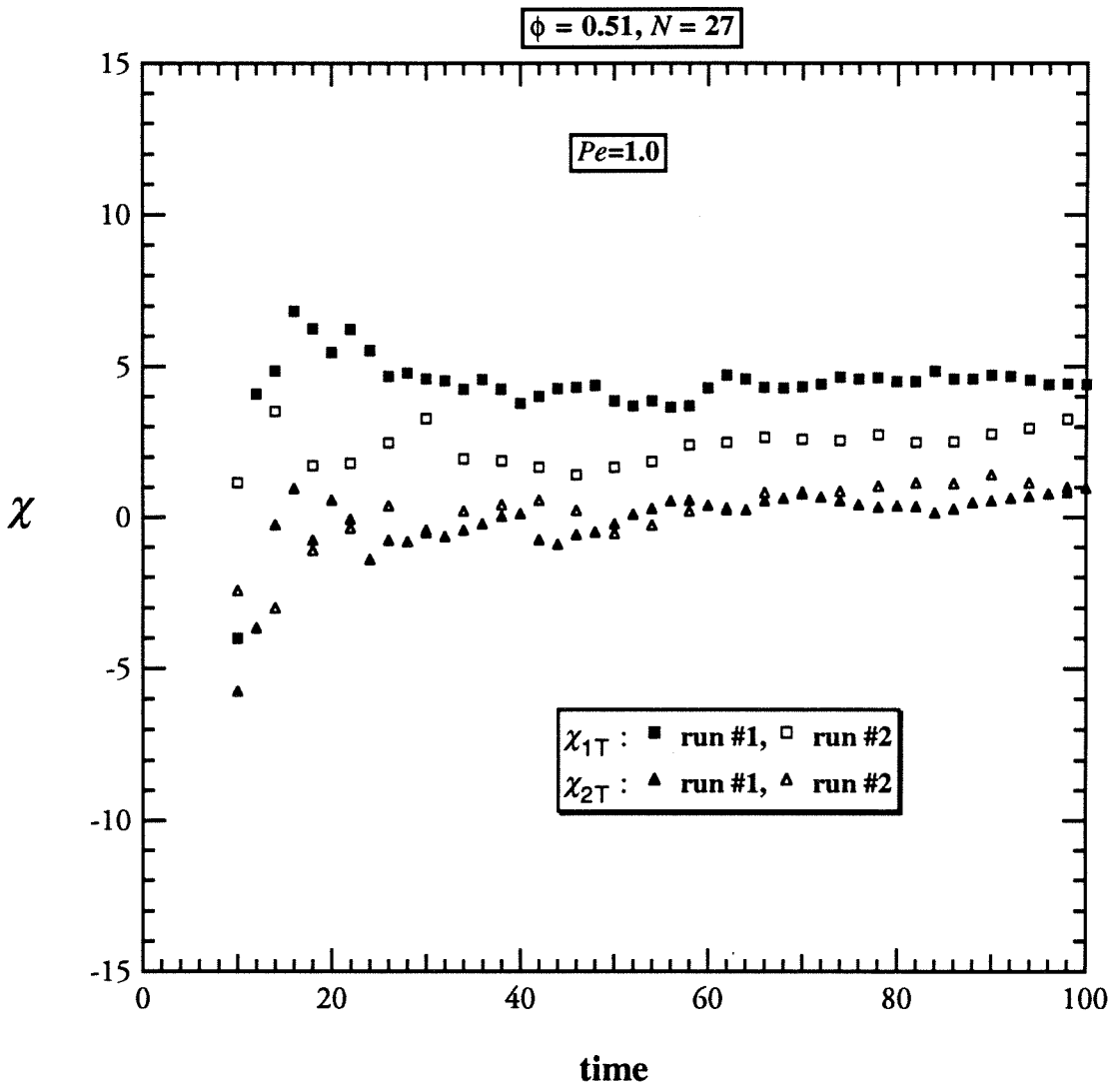

Figure 3.4.h : Plot of the time-averaged first and second normal stress differences χ_{1T} and χ_{2T} versus shear time for hard-sphere suspensions at ϕ=0.51 and Pe=1 with two initial random samples of 27 particles. The convergence for both normal stress differences for different initial particle configurations is excellent.

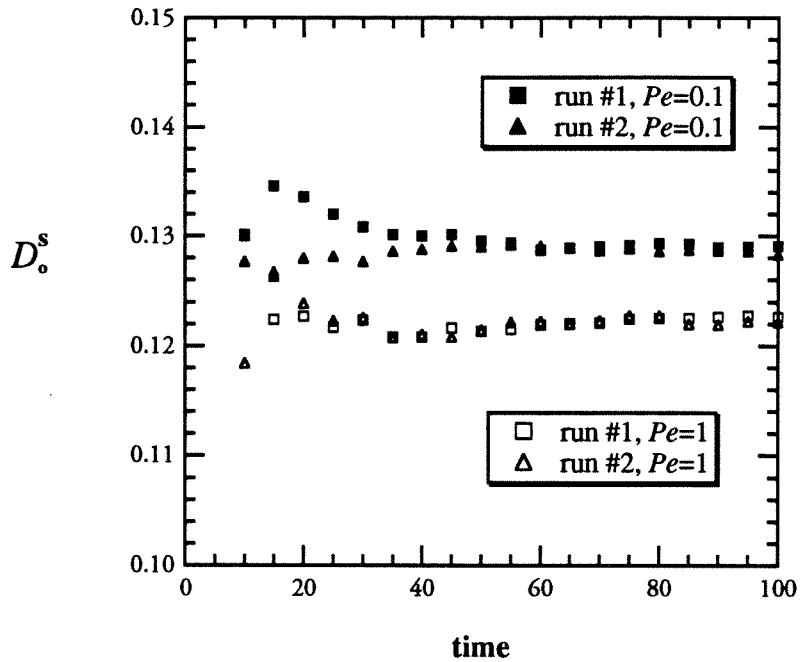

Figure 3.4.i : The short-time translational self-diffusion coefficient of hard-sphere suspensions at volume fraction ϕ=0.51 and Pe=0.1 and 1.0.

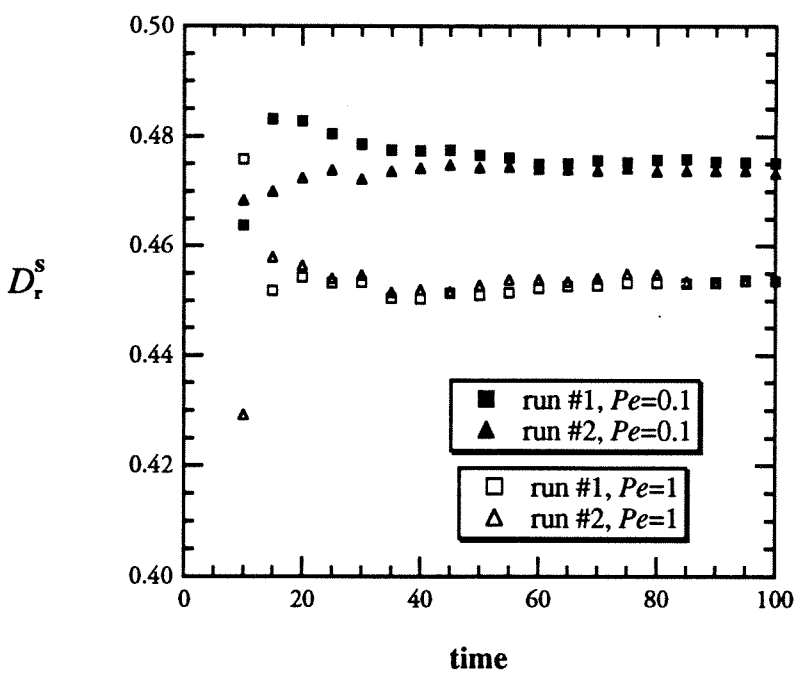

Figure 3.4.j : The short-time rotational self-diffusion coefficient of hard-sphere suspensions at volume fraction ϕ=0.51 and Pe=0.1 and 1.0.

Figure 3.4.i-j: The steady short-time translational (Fig.3.4.i) and rotational (Fig.3.4.j) self-diffusion coefficients of hard-sphere suspensions at ϕ=0.51 and Pe=0.1 and 1.0 with two initial random samples of 27 particles. Both figures show that there is negligible difference in the steady values of both self-diffusion coefficients obtained from different initial particle configurations.

Chapter IV

1. THE EQUILIBRIUM PAIR-DISTRIBUTION FUNCTION OF HARD SPHERES AND 2. THE DYNAMIC SIMULATION OF PERIODIC LATTICES

In this chapter the accuracy of Stokesian dynamics is demonstrated by comparing simulation results with known theories and exact calculations, which generally exist in the limit of infinite dilution or certain restrictive particle configurations such as periodic arrays or an equilibrium distribution of hard spheres. Among critical tests which Brady *et al.* (1988) and Bossis and Brady (1987, 1989) illustrated for the Stokesian dynamics method, the pair-distribution function, $g(r)$, of pure Brownian suspensions ($Pe \to 0$) and macroscopic properties of periodic arrays of non-colloidal spheres ($Pe \to \infty$) in a simple shear flow are important and can be used to calibrate the accuracy of the simulation method. In section IV.1, the equilibrium pair-distribution function of pure Brownian suspension is presented, and in section VI.2 dynamic simulation results for the rheology of three sheared periodic lattices: SCC, BCC and FCC, are presented. The transport properties of unsheared periodic lattices and hard-sphere distribution generated by a Monte-Carlo method (i.e., no dynamics were performed) can be found in Phillips *et al.* (1988).

IV.1 The Equilibrium Pair-Distribution Function of Hard Spheres

In a hard-sphere colloidal suspension, particles are subjected only to an excluded volume force: there exists a hard core region which prevents particles from overlapping. The distribution function for this equilibrium structure is the well-known hard-sphere distribution (Chae, Ree and Ree (1969), McQuarrie (1976), Pusey (1991)). With the inclusion of the proper many-body hydrodynamic interactions, particularly the lubrication interactions, as discussed in chapter II, this hard-sphere repulsive force plays no direct role and we may set the interparticle/external force $\mathbf{F}^P \equiv 0$ in equation (2.1). The par-

ticles are still subject to the thermal Brownian force which is modeled in the Stokesian dynamics method. In the absence of a shear flow ($Pe \rightarrow 0$), the evolution equation (2.7) becomes simply:

$$\Delta \mathbf{x} = \nabla \cdot \mathbf{R}_{FU}^{-1} \, \Delta t + \mathbf{X}(\Delta t) \quad , \tag{4.1}$$

$$\langle \mathbf{X} \rangle = 0 \; , \; \langle \mathbf{X}\mathbf{X} \rangle = 2 \, \mathbf{R}_{FU}^{-1} \Delta t \quad . \tag{4.2}$$

Equation (4.1) gives the evolution of the suspension microstructure over time. From the particle positions, the angularly averaged pair-distribution function, $g(r)$, can be computed and averaged over the course of the simulation. $g(r)$ describes the probability density of finding a particle at a particle center-center spacing r provided that there is a particle at the origin. In general, $g(r)$ depends on the separation vector $\mathbf{r}$, i.e., $g(\mathbf{r})$, but the equilibrium hard-sphere distribution is isotropic; therefore, the pair-distribution function is independent of $\mathbf{r}$ and a function only of the radial distance r. We can generate the hard-sphere $g(r)$ by a simple Monte-Carlo scheme and compare this to the results of actually integrating (4.1) in time.

Figure 4.1 shows a comparison of $g(r)$ obtained by Stokesian dynamics for a pure hard-sphere suspension at volume fraction ϕ=0.45 for different numbers of particle in the unit cell: N = 27 ($\triangle$), 81 ($\square$), 123 ($\circ$) with the hard-sphere $g(r)$ (solid curve) obtained by a Monte-Carlo calculation at identical volume fraction. In the simulation a time step Δt=5×10^{-4} was used and there are 50,000 time steps for the run with 27 and 81 particles and 10,000 time steps for the run with 123 particles. As seen in this figure, $g(r)$ for even the smallest size compares very well with that of hard spheres. There is a small difference

in $g(r)$ at contact r=2 about 8%, and near the second nearest neighbor peak at $r \approx 4$ which is near the edge of the unit cell for 27 particles. When N is raised to 81 and 123, the comparison of $g(r)$ from simulation and the hard sphere distribution is excellent for all particle center-center spacing. At r=2, $g(r)$ for hard spheres is 4.66, while it is 4.57, 4.58 and 4.60 for N=27, 81 and 123, respectively. The very small difference for $g(r)$ at r=2 falls within the statistical uncertainty associated with simulations.

This important test demonstrates the correctness of our calculation for Brownian motion and the precise treatment of both terms: $\nabla \cdot \mathbf{R}_{FU}^{-1}\ \Delta t$ and $\mathbf{X}(\Delta t)$. For a hard-sphere suspension in the absence of a shear flow, the only interactions are hydrodynamic. A correct $g(r)$ can be obtained by simulation only when the model captures correctly the many-body hydrodynamics and the near-field lubrication interactions among the particles. Simulation methods which approximate the hydrodynamic interactions as the pairwise constant forces and attempt to substitute the grand resistance tensor $\mathcal{R}$ by the identity or the pairwise Rotne-Prager tensor (Rotne and Prager (1969), Ermak and McCammon (1978)) will fail to yield correct microstructure of hard-sphere Brownian suspensions, unless a repulsive force is explicitly included ($\mathbf{F}^P \neq 0$). It is the balance of the two terms: $\nabla \cdot \mathbf{R}_{FU}^{-1}$ and $\mathbf{X}$ that produces the proper hard-sphere distribution. $\nabla \cdot \mathbf{R}_{FU}^{-1}$ acts like a repulsive interparticle force and allows the particles that would be stuck together by the strong lubrication force to sample all configurational spaces. It is *important* and *necessary* for a simulation method to capture the physics in the limit $Pe \rightarrow 0$ before it can be used to model the Brownian motion for a perturbed suspension with non-zero Péclet number.

IV.2 The Dynamic Simulation of Periodic Lattices

Among theoretical developments for suspensions, the model of regular arrays of spheres has always been the most popular one since exact solutions exist and can be derived in a close form or numerically computed (Hasimoto (1958), Chwang and Wu (1974), Zick and Homsy (1981), Zuzovsky and Brenner (1983), and Nunan and Keller (1984)). The perfectly symmetric and periodic structures of the lattices enable an analytical solution to Stokes flow and greatly simplify the mathematical details. Brady *et al.* (1988) have successfully pioneered the application of the Stokesian dynamics method for simulating periodic lattices and determined the sedimentation velocity and viscosity for these specific arrangements of the particles. The comparison between simulation results and exact calculations was very good and demonstrated the accuracy of Stokesian dynamics.

Dynamic simulations of periodic lattices of spheres in a simple shear flow is straight forward and relatively simple for Stokesian dynamics and served as an additional bench mark of understanding on the transport properties of microstructured materials, even though there are no other independent calculation with which to compare our results. In this section we report results for the following suspension properties of periodic lattices: the resistivity, K^{-1}, and the steady shear viscosity, η_r.

Simulation results are presented for three lattices: simple cubic (SCC), body-centered cubic (BCC) and faced-center cubic (FCC) in a simple shear flow. There is no Brownian motion and we examine the other limit of Stokesian dynamics ($Pe \rightarrow \infty$). For a periodic lattice, only one particle is needed in the unit cell and its images can be replicated to

fill the space. The dimension of the system matrix needed is greatly reduced to the size of (11×11). The simulation is extremely fast and marked at ≈ 30 seconds for 100 time steps of $\Delta t=10^{-2}$ on a 2-MFLOPS Sun workstation. For periodic lattice models, Stokesian dynamic offers a speed which is far superior over other numerical methods.

The set of basis vectors for the unit cell of each lattice type ($\mathbf{e}_1$, $\mathbf{e}_2$, $\mathbf{e}_3$) is defined as the following:

For SCC:

$$\mathbf{e}_1 = (H,0,0) \quad ; \quad \mathbf{e}_2 = (0,H,0) \quad ; \quad \mathbf{e}_3 = (0,0,H) \ , \tag{4.3.a}$$

$$\tau_o = H^3 \ . \tag{4.3.b}$$

For BCC:

$$\mathbf{e}_1 = (\tfrac{H}{2},\tfrac{H}{2},-\tfrac{H}{2}) \quad ; \quad \mathbf{e}_2 = (-\tfrac{H}{2},\tfrac{H}{2},\tfrac{H}{2}) \quad ; \quad \mathbf{e}_3 = (\tfrac{H}{2},-\tfrac{H}{2},\tfrac{H}{2}) \ , \tag{4.4.a}$$

$$\tau_o = \tfrac{1}{2}H^3 \ . \tag{4.4.b}$$

For FCC:

$$\mathbf{e}_1 = (\tfrac{H}{2},\tfrac{H}{2},0) \quad ; \quad \mathbf{e}_2 = (0,\tfrac{H}{2},\tfrac{H}{2}) \quad ; \quad \mathbf{e}_3 = (\tfrac{H}{2},0,\tfrac{H}{2}) \ , \tag{4.5.a}$$

$$\tau_o = \tfrac{1}{4}H^3 \ . \tag{4.5.b}$$

Here H is the length and τ_o is the volume of the unit cell. Spheres are periodically replicated to fill the infinite space by using the set of basic vectors defined in (4.3) to (4.5) and a set of integers according to the following relation:

$$\mathbf{r}_n = n_1\ \mathbf{e}_1 + n_2\ \mathbf{e}_2 + n_3\mathbf{e}_3\ \ , \tag{4.6}$$

where $n_1, n_2, n_3 = 0, \pm1, \pm2, ...$ The set of the basis vectors ($\mathbf{e}_1$, $\mathbf{e}_2$, $\mathbf{e}_3$) of the unit cell is used as the reference coordinate system. The flow and the velocity gradient direction are defined by the first and second basis vectors $\mathbf{e}_1$ and $\mathbf{e}_2$, respectively. For example with a SCC lattice, the flow direction is the x-axis and the velocity gradient direction is the y-axis. With this shear direction, the lattice will repeat itself periodically in time and the maximum volume fraction which the lattice can still flow along the direction of the basis vector $\mathbf{e}_1$ is 0.5236 for SCC, 0.6802 for BCC and 0.7405 for FCC. If the shear direction is along an arbitrary direction, the lattice will not necessarily repeat itself and the maximum volume fraction at which the lattice can flow will also be different. For a discussion of shear direction and maximum volume fractions, please see Adler and Brenner (1984) and Claeys and Kraynik (1991).

IV.2.1 The Resistivity of Periodic Arrays of Spheres in a Simple Shear Flow

For a porous medium or a fixed bed of particles, Darcy's law relates the mean pressure gradient and the average fluid velocity $\langle \mathbf{U} \rangle$ according to:

$$\nabla\langle p \rangle = -\ K^{-1} \cdot \langle \mathbf{U} \rangle\ \ , \tag{4.7}$$

where p is the pressure, K is the permeability tensor of the medium and its inverse is referred to as the resistivity, which measures the added resistance to the bulk flow due to the presence of the rigid particles. For Stokes flow, the linear momentum balance requires that the pressure gradient equal the average force which the particles exert on

the fluid:

$$\nabla\langle p\rangle = n \langle \mathbf{F}_i^H \rangle = - n \langle \mathbf{R}_{FU} \rangle \cdot \langle \mathbf{U} \rangle \quad , \tag{4.8}$$

where we have used equation (2.3). Here n is the number density of the particles. From (4.7) and (4.8), we have:

$$K^{-1} = \langle \mathbf{R}_{FU} \rangle \, . \tag{4.9}$$

For a spatially periodic lattice, the resistivity is identical to the drag coefficient for arrays of spheres which in turn is inversely proportional to the sedimentation velocity. The two problems can be identically treated only when the particles are identical and arranged in a periodic lattice.

Exact results of the resistivity K^{-1} for the static, unsheared periodic lattices can be found from Zick and Homsy (1981). In our simulations, we study the dynamics by shearing the lattice and compute the resistivity K^{-1} by first averaging the principle diagonal terms of $\mathbf{R}_{FU}$ and then averaging it over one unit time cycle defined as the time when the periodic cell repeats its starting undeformed configuration. Results for the translational resistivity K^{-1} obtained by Stokesian dynamics are summarized in Table 4.1. Particle volume fraction ϕ varies from dilution to close packing. Simulation results for the rotational resistivity, K_{ROT}^{-1}, for all three types of lattices are also reported in this table. Data from Table 4.1 is plotted in Fig.4.2 to illustrate the relation of the time-averaged translational resistivity K^{-1} and ϕ for SCC (•), BCC (△) and FCC (□). The figure shows an exponential decay of the resistivity with increasing volume fraction

for all three lattices. We noted that the resistivity computed along the flow direction (along the basis vector $\mathbf{e}_1$) is about 10% higher than the resistivities computed along the direction of the velocity gradient and vorticity. K^{-1} for BCC and FCC lattice are similar while it is higher for SCC lattice.

Figure 4.3 shows the plot of time-averaged rotational resistivity, K_{ROT}^{-1}, versus ϕ for all lattices. K_{ROT}^{-1} is seen to decrease linearly with a slope of 1.25 for small values of ϕ and then decays rapidly at the maximum packing, ϕ_{max}. While K_{ROT}^{-1} is 0.1451 for SCC at close packing, K_{ROT}^{-1} is very close for BCC and FCC lattice, with 0.0787 for BCC and 0.0824 for FCC.

IV.2.2 The Shear Viscosity of Periodic Arrays of Spheres

Equation (2.18) can be used to compute the particle stresslets, **S**, and is repeated here for convenience:

$$\mathbf{S} = - \mathbf{R}_{SU} \cdot (\mathbf{U}\text{-}\mathbf{U}^{\infty}) + \mathbf{R}_{SE} : \mathbf{E}^{\infty} - \mathbf{r}\mathbf{F}^{P} \quad . \tag{4.10}$$

For a periodic lattice with force/torque free particles, i.e., $\mathbf{F}^{P} = 0$, $\mathbf{U}\text{-}\mathbf{U}^{\infty} \equiv 0$ as the particles move with the fluid velocity due to a simple shear flow. The only contribution to the rheology of the periodic lattice is from the resistance matrix $\mathbf{R}_{SE}$ which relates the particle stresslets to the rate of strain $\mathbf{E}^{\infty}$ imposed by the shear flow on the rigid spheres. Equation (4.10) simplifies to:

$$\mathbf{S} = \mathbf{R}_{SE} : \mathbf{E}^{\infty} \quad . \tag{4.11}$$

Using the reference coordinates based on the set of basis vectors ($\mathbf{e}_1$, $\mathbf{e}_2$, $\mathbf{e}_3$) of the unit cell, the time-averaged shear viscosity η_r is computed according to:

$$\eta_r = 1 + \frac{9}{2}\,\phi\,\overline{\mathbf{S}_{12}^{H}} \quad . \tag{4.12}$$

The subscripts 1 and 2 denote the direction taken from the set of basis vectors $\mathbf{e}_1$ and $\mathbf{e}_2$ and again we shear the unit cell along $\mathbf{e}_1$ with the velocity gradient along the $\mathbf{e}_2$ direction.

The shear viscosity defined in (4.12) is computed by averaging the particle stress in the 1-2 direction, $\mathbf{S}_{12}^{H}$, over one unit time cycle when the lattice repeats its starting configuration. Results for η_r are summarized in Table 4.2. The first column is the volume fraction ϕ, followed by η_r for each lattice type. ϕ varies from dilution to maximum packing ϕ_{max}. We present first the steady rheology in Figures 4.4 and 4.5, followed by the instantaneous rheology in Figures 4.6 to 4.8.

As shown in Fig.4.4, the time-averaged η_r for SCC (•), BCC (□), FCC (△) and random hard-sphere (Monte-Carlo) distributions (○) sampled with 27 particles are plotted against the volume fraction. For random hard spheres, the Monte-Carlo method is used to generate 25 to 50 random samples of 27 particles at each ϕ value and then η_r is computed by following the method presented by Phillips *et al.* (1988):

$$\langle \mathbf{S} \rangle = -\,\mathbf{A} : \mathbf{E}^{\infty} = -\,\langle \mathbf{R}_{SU} \cdot \mathbf{R}_{FU}^{-1} \cdot \mathbf{R}_{FE} - \mathbf{R}_{SE} \rangle : \mathbf{E}^{\infty} \quad . \tag{4.13}$$

For the isotropic hard-sphere distribution, the symmetric and traceless fourth rank order tensor $\mathbf{A}$ must be of the form:

$$\mathbf{A} = \frac{\beta}{2} \left(\delta_{ik} \, \delta_{jl} \; + \; \delta_{il} \, \delta_{jk} \; - \; \frac{2}{3} \, \delta_{ij} \, \delta_{kl} \right) \; . \tag{4.14}$$

From the resistance tensors $\mathbf{R}_{SU}$, $\mathbf{R}_{FU}$ and $\mathbf{R}_{SE}$, we can compute β for each random configuration and average it over the total number of samples. In dimensionless form, η_r for a hard-sphere model is given by:

$$\eta_r = 1 + \frac{5}{2} \, \phi \, \beta \; . \tag{4.15}$$

In Fig.4.4, the vertical lines denote the value of ϕ_{max} at maximum packing for each lattice type with ϕ_{max}= 0.5236, 0.6802, 0.7405 for SCC, BCC and FCC lattices, respectively. We notice that η_r is largest for random hard spheres, followed by FCC, BCC and smallest for SCC for $\phi < 0.5236$. At ϕ_{max} as spheres come in contact, η_r for the periodic lattices diverges. The differences in the shear viscosity among these four models are a direct result of the hydrodynamic interactions which depend on the number of nearest neighbors as well as the relative separation distance among the particles. To illustrate this variation in the shear viscosity, we plot η_r in a linear scale against a smaller range for ϕ from 0 to 0.55 in Fig.4.5. The figure shows the largest variation in η_r for the hard-sphere suspension compared to the SCC lattice. Noticeable differences in η_r are also seen for the three lattices, especially in the region of high ϕ value.

Although the general behavior of η_r which shows shear thickening with increasing volume fraction is seen to be in qualitative agreement with experimental observations, these models cannot be used to represent colloidal dispersions. The highly-restrictive periodic lattice models ($Pe \rightarrow \infty$) and the random hard-sphere model ($Pe \rightarrow 0$) will definitely fail to capture the correct shear-induced microstructure which is a function of

both Pe and ϕ. Suspension macroscopic properties can only be predicted with accuracy when the model does not impose any restriction on the motion of particles and this can be seen from our simulation results for rheology of dense hard-sphere Brownian dispersions presented in chapters VI to IX.

The instantaneous rheology of the lattice models at or near close packing versus the strain are shown in Figures 4.6 to 4.8 for SCC, BCC and FCC lattices, respectively The instantaneous η_r is plotted on a logarithmic scale with two strain units. η_r is periodic with shear time at a strain unit of one as a result of the repeat of the lattice every strain unit. While the two lattices SCC and BCC flow at their maximum packing, the highest volume fraction for a flowing FCC lattice is 0.728 which is below its maximum packing at 0.7405. η_r diverges quickly as ϕ approaches ϕ_{max}. We also find that the normal stress differences which are defined in (2.23) and (2.34) are statistically zero for sheared periodic lattices and it is expected for flowing lattices with highly symmetry.

In this chapter, we have provided the quantitative results with which theories and other simulation methods can be tested. The periodic lattice model is simple and can give reasonable quantitative results. Next we turn our attention to disordered Brownian suspensions where the microstructure is induced by the flow.

Table 4.1: Results for the time-averaged translation and rotational resistivities, K^{-1} and K^{-1}_{ROT}, for sheared periodic lattices: SCC, BCC and FCC obtained by Stokesian dynamics for different particle volume fraction ϕ. Column (1) is ϕ. Columns (2) to (4) are the translational and columns (5) to (7) are the rotational resistivities for SCC, BCC and FCC lattices, respectively. The resistivities are computed from the mean of the diagonal elements of the resistance tensor $\mathbf{R}_{FU}$, the pressure terms, and averaged over a unit time cycle defined as the time when the lattice repeats its starting configuration in a simple shear flow.

	K^{-1}			K^{-1}_{ROT}		
ϕ	**SCC**	**BCC**	**FCC**	**SCC**	**BCC**	**FCC**
0.0010	0.8249	0.8218	0.8218	0.9999	0.9999	0.9999
0.0270	0.4988	0.4893	0.4893	0.9730	0.9730	0.9730
0.0640	0.3591	0.3464	0.3465	0.9360	0.9360	0.9360
0.1250	0.2415	0.2257	0.2257	0.8716	0.8728	0.8724
0.2160	0.1503	0.1313	0.1314	0.7687	0.7738	0.7742
0.3430	0.0872	0.0651	0.0651	0.6051	0.6275	0.6284
0.4500	0.0606	0.0363	0.0364	0.4272	0.4963	0.4997
0.5236	0.0500	0.0245	0.0246	0.1451	0.4006	0.4087
0.6000		0.0167	0.0167		0.2970	0.3122
0.6802		0.0112	0.0134		0.0787	0.2490
0.7200			0.0111			0.1786
0.7405			0.00533			0.0824

Table 4.2: Results of the time-averaged shear viscosity η_r for sheared periodic lattices: SCC, BCC and FCC obtained by Stokesian dynamics simulations with different volume fractions. Particle volume fraction ϕ is shown in the first column with value ranging from dilution to close packing, followed by η_r for SCC, BCC and FCC lattice in column (2), (3) and (4), respectively. The set of basis vectors for the unit cell ($\mathbf{e}_1$, $\mathbf{e}_2$, $\mathbf{e}_3$) of each lattice is used as the reference coordinates. The flow and the velocity gradient directions are defined by the first and second basis vectors $\mathbf{e}_1$ and $\mathbf{e}_2$ of the unit cell, respectively. The shear viscosity η_r is averaged over a unit time cycle defined as the time when the lattice returns to its starting configuration in a simple shear flow.

ϕ	η_r^{SCC}	η_r^{BCC}	η_r^{FCC}
0.0010	1.0025	1.0025	1.0025
0.0270	1.0674	1.0701	1.0699
0.0640	1.1609	1.1754	1.1743
0.1250	1.3259	1.3820	1.3765
0.2160	1.6256	1.8095	1.7840
0.3430	2.2927	2.9107	2.7873
0.4500	3.5256	5.0692	4.7392
0.5000	4.9190	7.2236	6.4015
0.5236	9.6285	8.9091	7.1369
0.6000		25.0330	11.0490
0.6500		54.6890	17.4450
0.6802		9425.0	25.5100
0.7000			36.7670
0.7250			87.9800
0.7280			151.1500

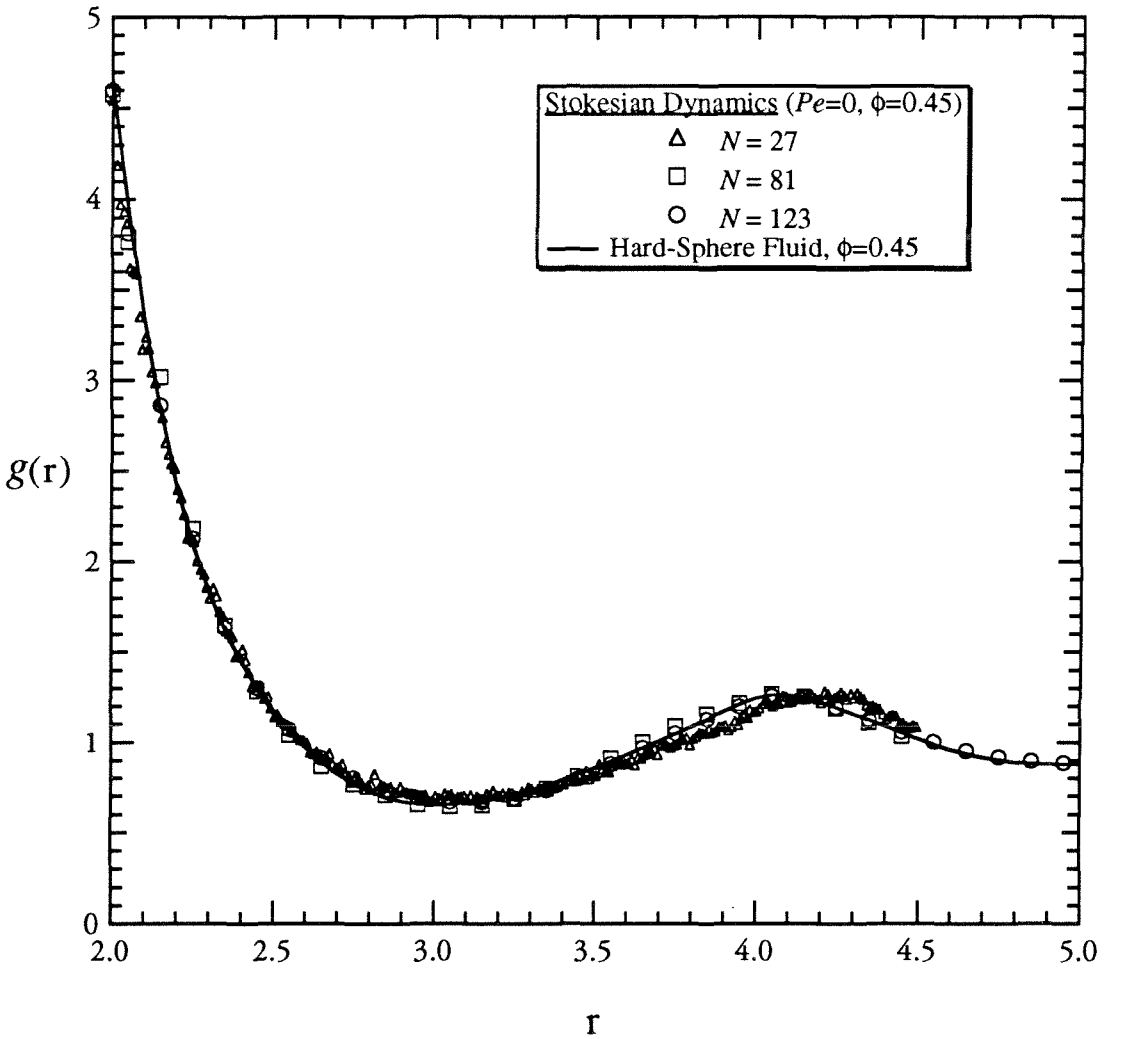

Figure 4.1: Comparison of the radial pair-distribution function for hard-sphere Brownian suspensions at volume fraction ϕ=0.45: (solid curve) hard-sphere distribution computed by the Monte-Carlo method and results obtained by Stokesian dynamics simulation at Pe=0 and different number of particles N = 27 (Δ), 81 (□) and 123 (○) in the unit cell. It is seen from the figure that simulation results for g(r) compare very well with that for hard spheres. At the smallest number of particles N = 27, the influence of the periodicity can be seen in the shift in the location near the second nearest neighbor peak.

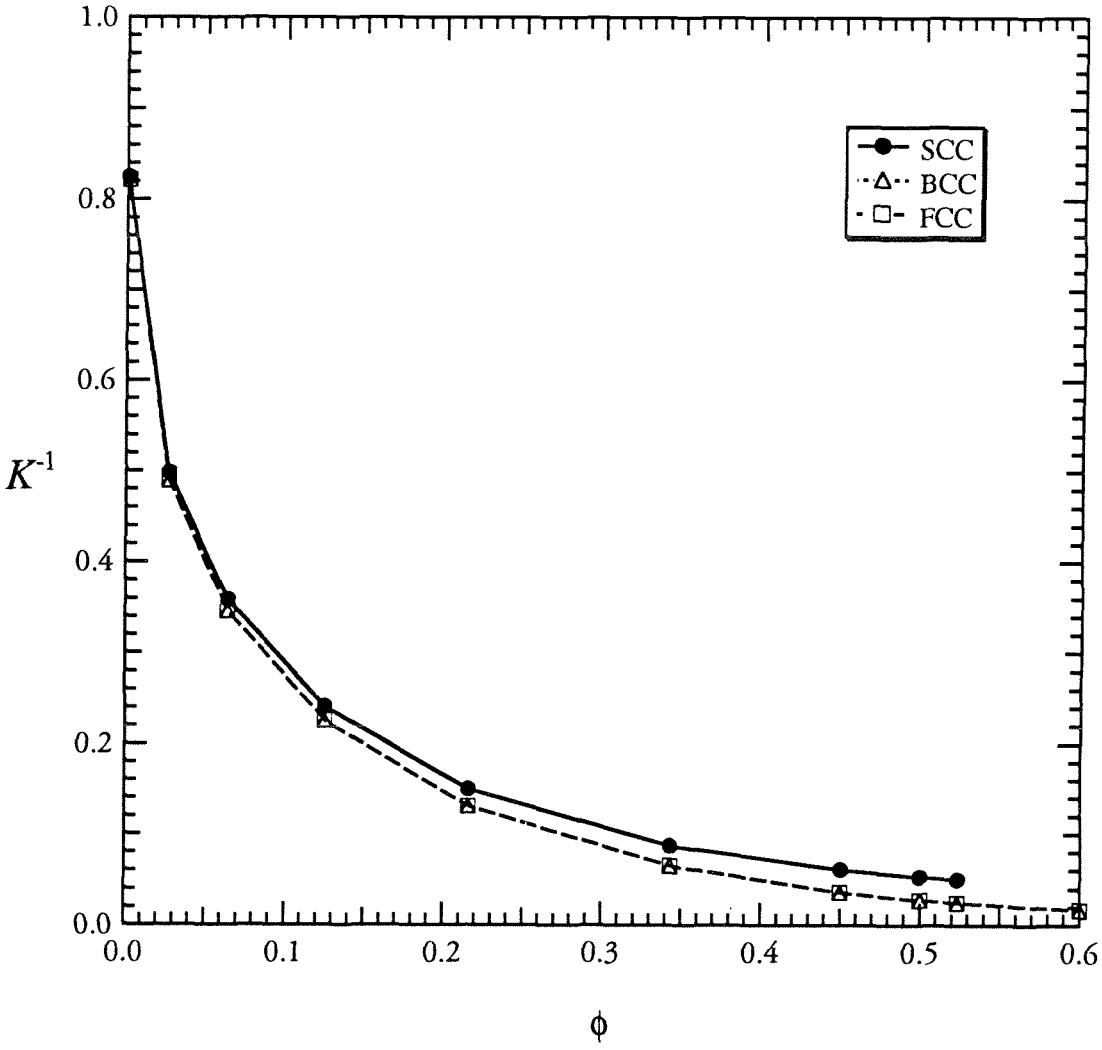

Figure 4.2: The time-averaged translational resistivity of sheared periodic lattices: (●) SCC, (Δ) BCC and (□) FCC obtained by Stokesian dynamics as a function of the volume fraction. The resistivity is averaged for one unit time cycle when the lattice repeats its starting configuration in a simple shear flow. The flow and the velocity gradient directions are defined by the first and second basis vector $\mathbf{e}_1$ and $\mathbf{e}_2$ of the unit cell, respectively. The figure shows a rapid decay of the resistivity with increasing volume fraction.

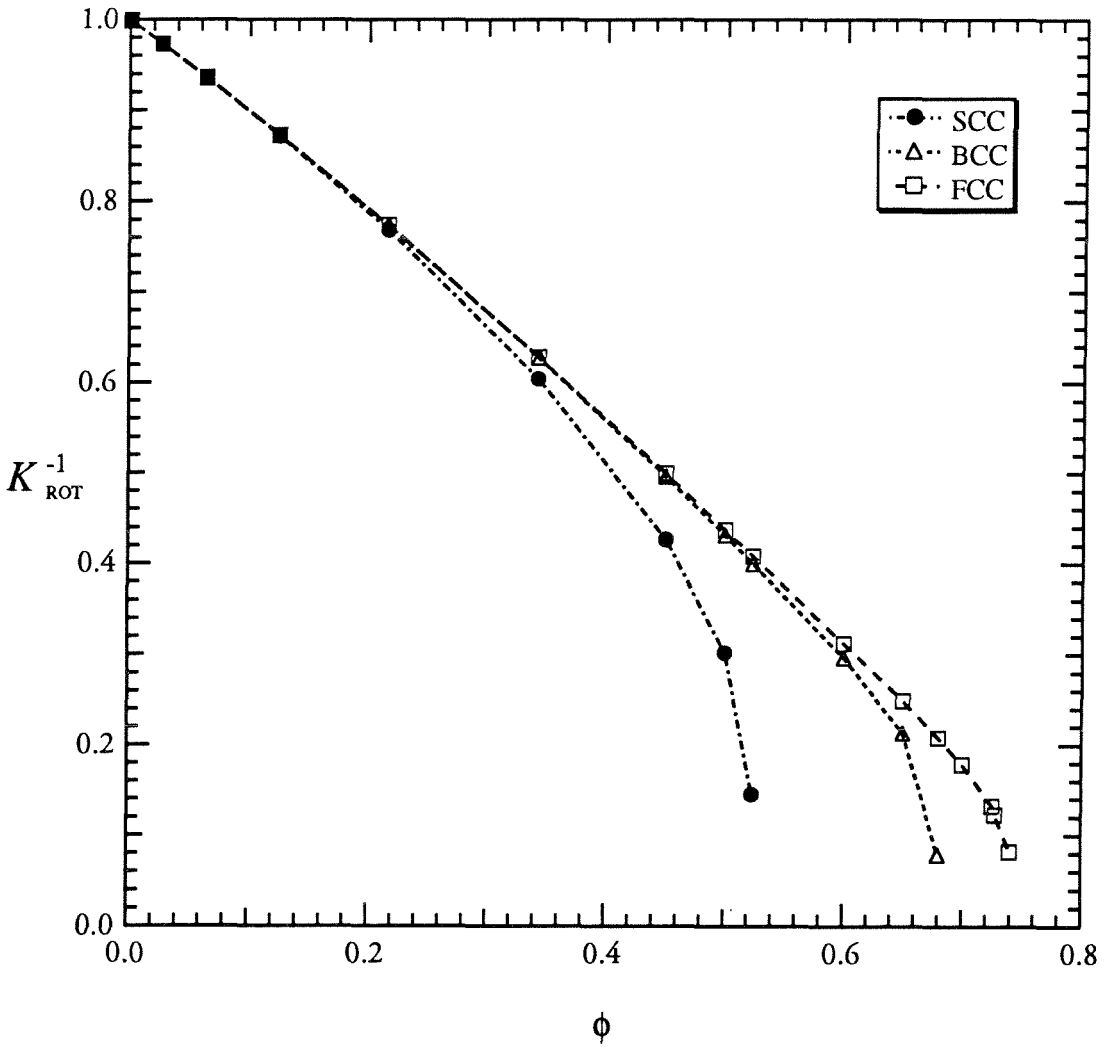

Figure 4.3: The time-averaged rotational resistivity obtained for sheared periodic lattices: (●) SCC, (Δ) BCC and (□) FCC obtained by Stokesian dynamic as a function of the volume fraction. The resistivity is averaged for a unit time cycle when the lattice repeats its starting configuration in a simple shear flow. The flow and the velocity gradient directions are defined by the first and second basis vectors $\mathbf{e}_1$ and $\mathbf{e}_2$ of the unit cell, respectively.

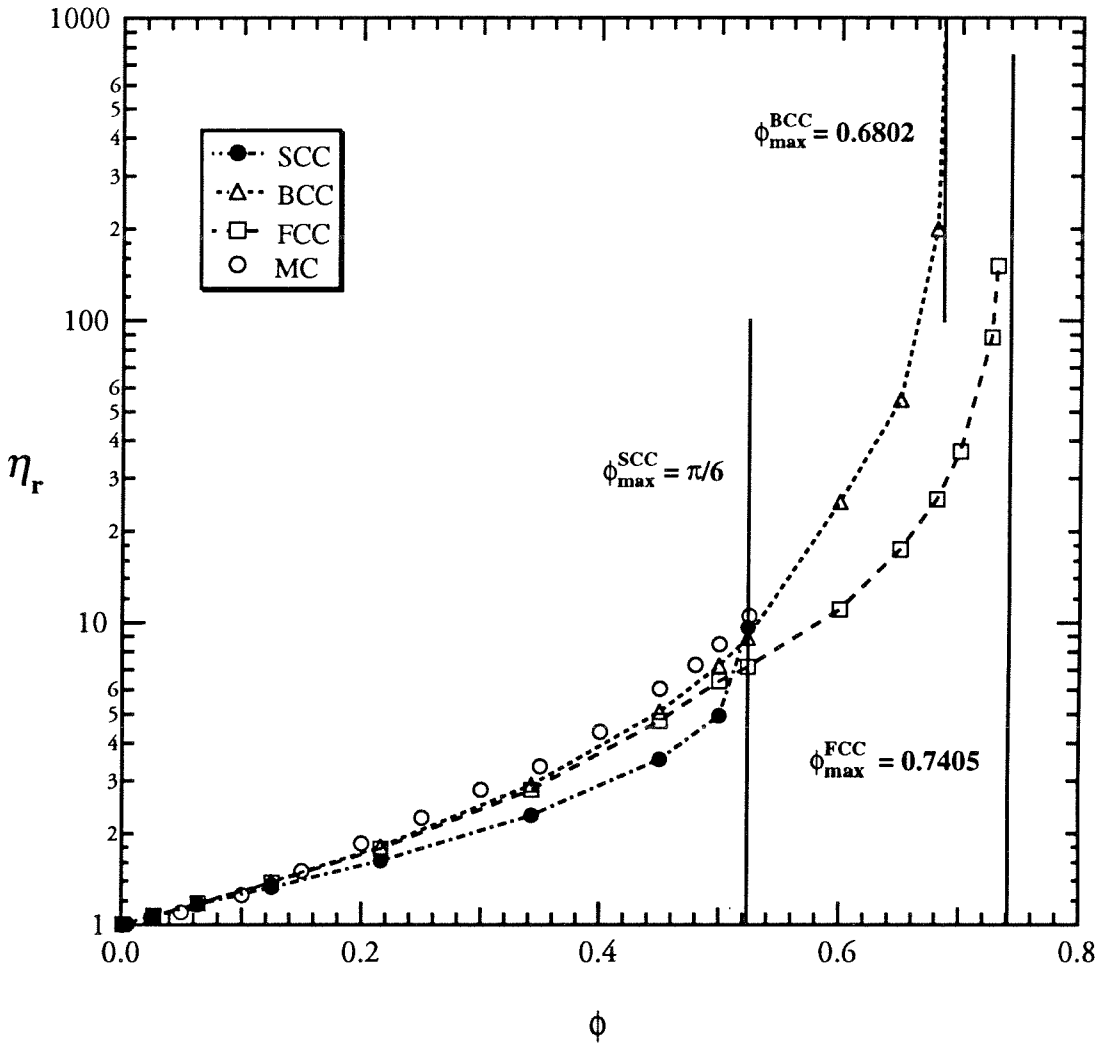

Figure 4.4: The time-averaged shear viscosity for different sheared lattices: SCC (●), BCC (Δ), FCC (□) and a hard-sphere model (MC) (○). The steady shear viscosity for the lattices is averaged over a unit time cycle when the lattice repeats its initial configuration. The flow and the velocity gradient directions are defined by the first and second basis vectors $\mathbf{e}_1$ and $\mathbf{e}_2$ of the unit cell, respectively. It is seen from this figure that for $\phi<0.5$, η_r is smallest for SCC, followed by FCC, then BCC and largest for random hard spheres. At $\phi\approx0.5$ the difference in the steady shear viscosity for these models is small. Random particle configurations for hard spheres are computed by the Monte-Carlo method (MC). Results for the sheared lattices are obtained by Stokesian dynamics simulations.

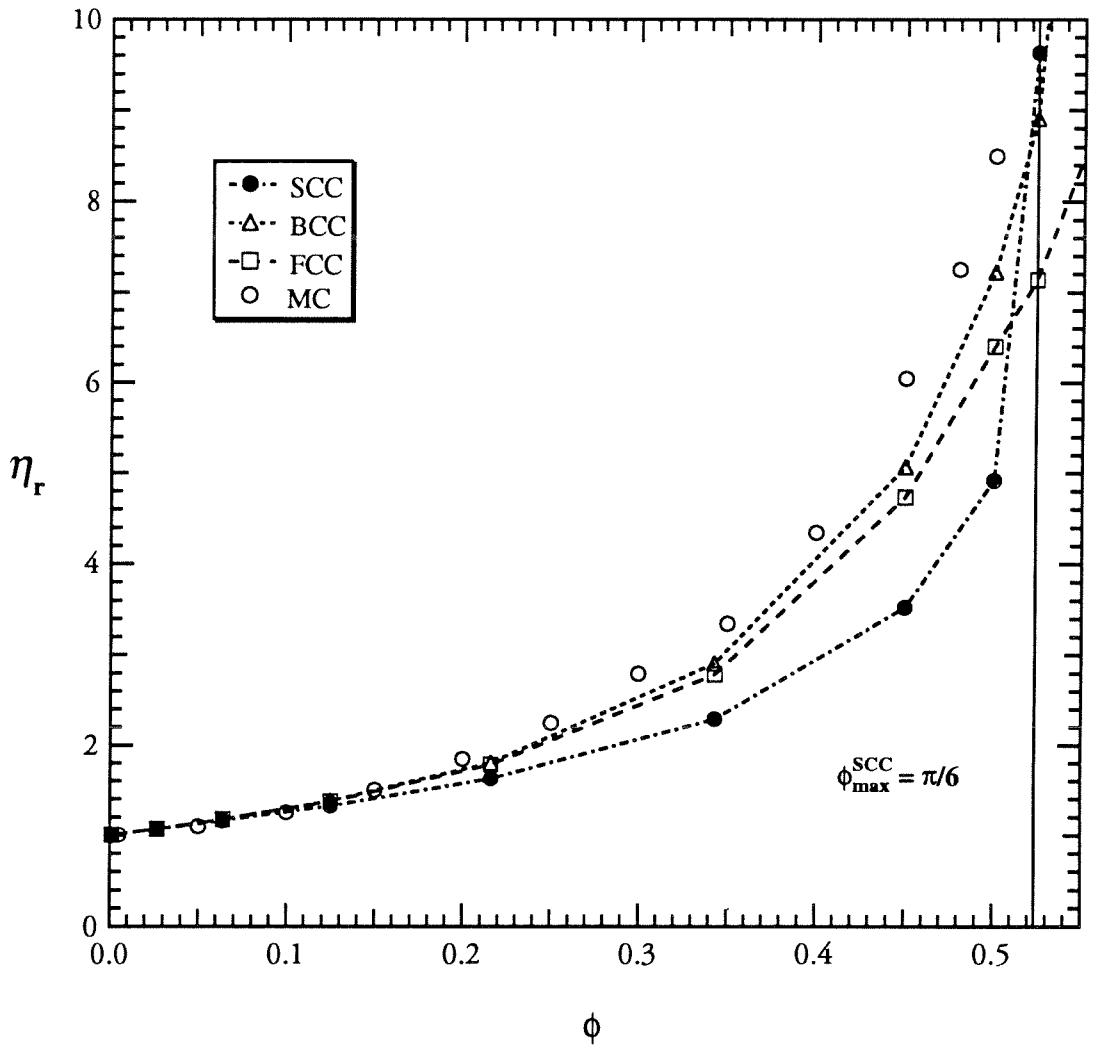

Figure 4.5: The steady shear viscosity for different sheared lattices: SCC (●), BCC (Δ), FCC (□), and a hard-sphere model (MC) (○). The shear viscosity is plotted on a linear scale and with smaller range of particle volume fraction. It can be seen from this plot that the shear viscosity of a hard-sphere model is larger than that of the lattices as ϕ increases. There are noticeable differences in η_r among these models, especially at large particle volume fractions.

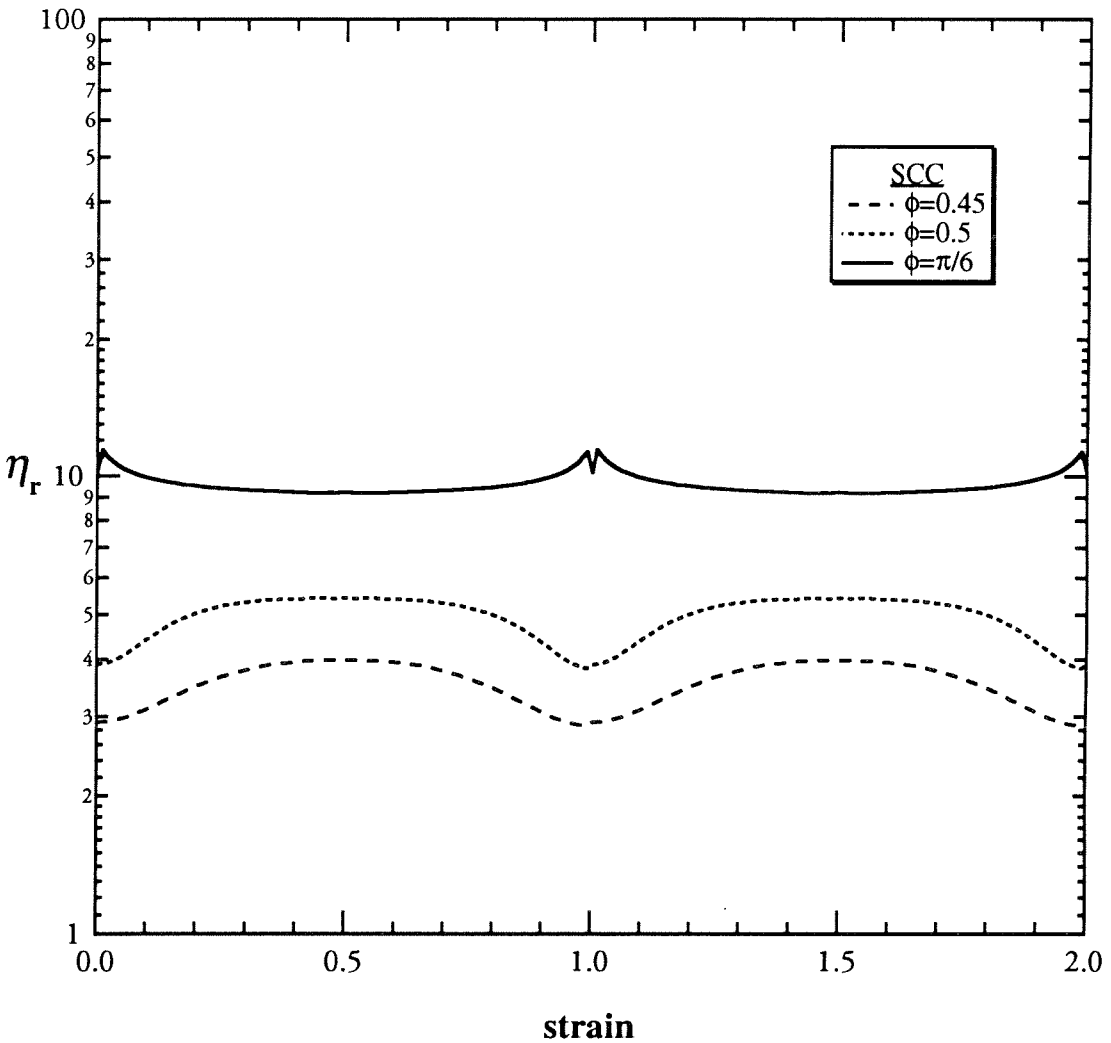

Figure 4.6: Plot of instantaneous shear viscosity versus strain for a sheared SCC lattice with ϕ = 0.45 (dashed curve), 0.5 (dotted curve) and 0.5236 (close packing) (solid curve). The shear viscosity is periodic at a strain of unity as expected from symmetry. The flow and the velocity gradient directions are defined by the first and the second basis vectors $\mathbf{e}_1$ and $\mathbf{e}_2$ of the unit cell, respectively.

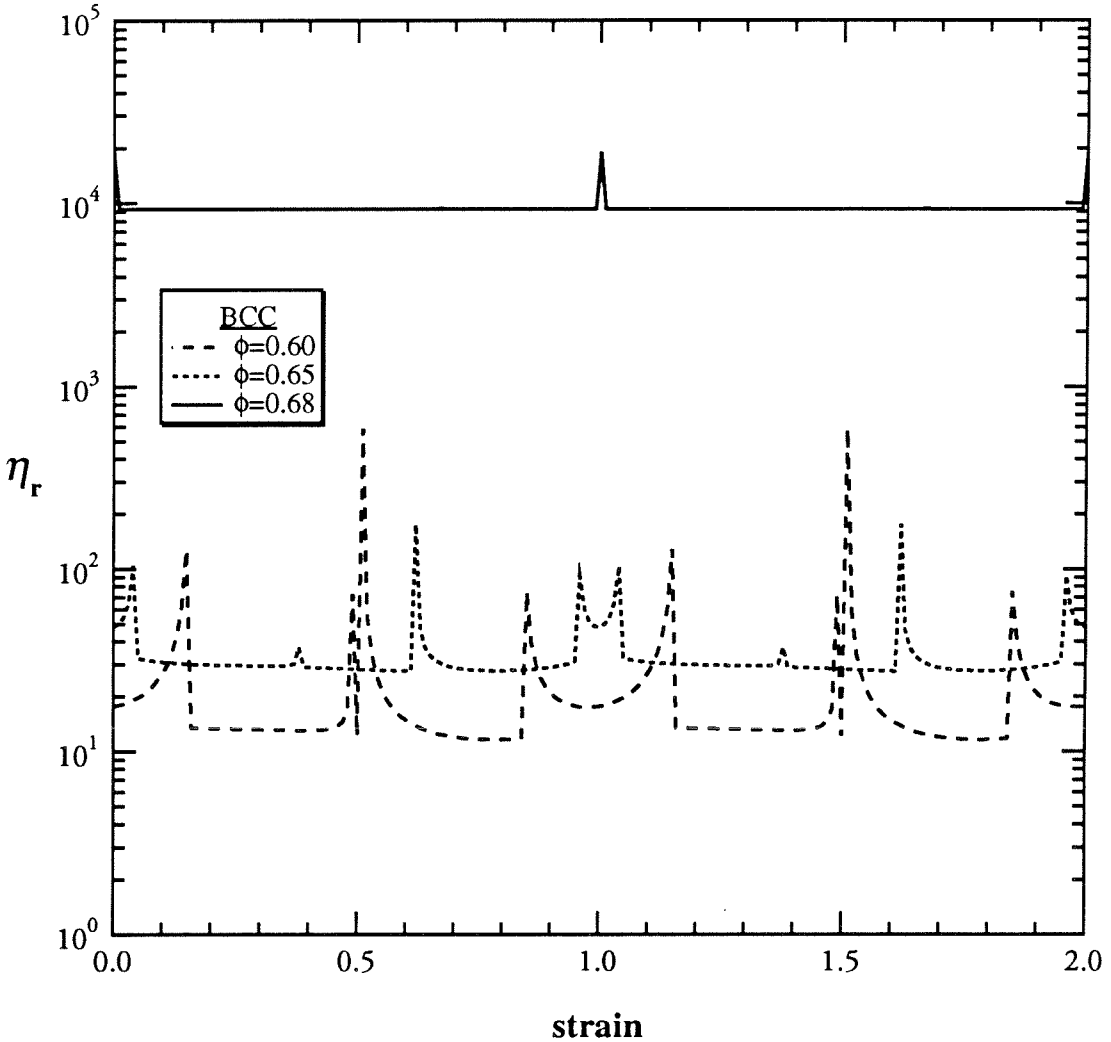

Figure 4.7: Plot of instantaneous shear viscosity versus strain for a sheared BCC lattice with particle volume fraction ϕ = 0.6 (dashed curve), 0.65 (dotted curve), and 0.68 (close packing) (solid curve). The shear viscosity is periodic at a strain of unity. At close packing (ϕ=0.68), the shear viscosity is three orders of magnitude larger than that of a lattice with ϕ=0.65. The flow and the velocity gradient directions are defined by the first and the second basis vectors $\mathbf{e}_1$ and $\mathbf{e}_2$ of the unit cell, respectively.

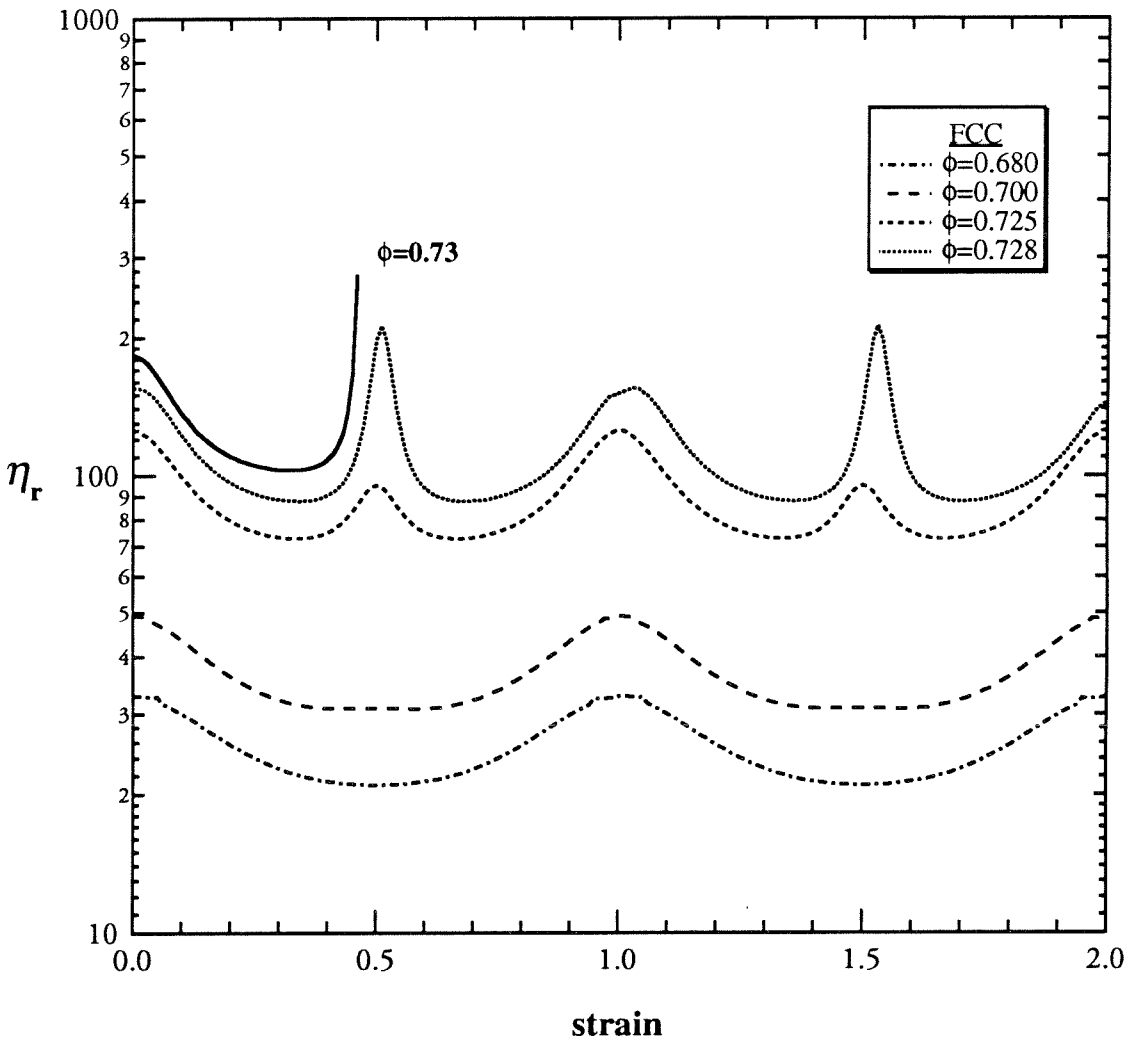

Figure 4.8: Plot of instantaneous shear viscosity versus strain for a sheared FCC lattice with different particle volume fractions: ϕ = 0.68, 0.7, 0.725, 0.728, and 0.73 (close to maximum packing which equals to 0.7405 for FCC lattice). Results are obtained by Stokesian dynamics simulations. The shear viscosity is periodic with a unity strain and diverges at ϕ=0.73. The flow and the velocity gradient directions are defined by the first and the second basis vectors $\mathbf{e}_1$ and $\mathbf{e}_2$ of the unit cell, respectively.

Chapter V

SIMULATION OF DENSE HARD-SPHERE SUSPENSIONS: INTRODUCTION

The purpose of this chapter is to explain our method of presenting results obtained by Stokesian dynamics simulations for dense hard-sphere suspensions in the following chapters, VI to IX. In chapter II, we introduced the two fundamental parameters: the particle volume fraction, ϕ, and the Péclet number, $Pe = 6\pi\eta a^3\dot{\gamma}/kT$, which measures the relative importance of the shear and Brownian forces. For hard-sphere suspensions, the particles are force- and torque-free, i.e., $\mathbf{F}^P = 0$, and they interact uniquely through hydrodynamic and Brownian forces. In our simulations, the particle volume fraction ϕ is varied from 0.316 to 0.6; the specific value studied are: 0.316, 0.37, 0.4, 0.419, 0.45, 0.47, 0.48, 0.49, 0.51, 0.55, 0.58, 0.59 and 0.6. This range of volume fractions spans moderately concentrated regime through the colloidal fluid-colloidal crystalline phase transition at $\phi \approx 0.5$. For each ϕ, the Péclet number is varied from the strong Brownian limit (Pe=0.01) to the pure hydrodynamic limit ($Pe \to \infty$).

The generally observed rheological behavior of dense hard-sphere suspensions is shown schematically in Fig.5.1 to illustrate the dependence of the steady shear viscosity on Pe and ϕ. The nonequilibrium phase diagram is also sketched to show the phase behavior of dense hard-sphere suspensions. For the region of small Péclet number and volume fraction below the "phase transition" (region I), the isotropic colloidal fluid structure is slightly deformed. In this region shear thinning has generally been observed. As the shear rate increases into region II, experimental results have shown that the microstructure changes from an isotropic state at equilibrium to a shear-induced phase where colloidal fluid and colloidal crystals may coexist. Region III encompasses hard-sphere suspension with particle volume fractions above the colloidal fluid-colloidal crystalline phase transition. The strongly ordered crystalline phase has been seen to be

destroyed by a large shearing deformation accompanied with a large increase in the shear viscosity.

We shall present simulation results at a fixed volume fraction with varying Péclet numbers. This is done by traveling along with constant ϕ in Fig.5.1 and we present the change of suspension macroscopic properties with varying Péclet numbers. The hard-sphere suspensions in our studies are divided into three groups according to particle volume fraction: moderately dense, dense and very dense suspensions. The dense suspension with ϕ=0.45 is presented first in chapter VI, followed by the moderately dense suspensions with ϕ from 0.316 to 0.419 in chapter VII, then the very dense suspensions with ϕ ranging from 0.47 to 0.6 in chapter VIII, and finally the summary for the entire dense suspensions in chapter IX.

The suspension at ϕ=0.45 was selected to start our thesis research for three reasons: First, a suspension at ϕ=0.45 is dense and that is important to our interest in investigating and studying behavior of dense hard-sphere suspensions. Second, the volume fraction at 0.45 fits well with the range of particle volume fractions in the experiments of van der Werff and de Kruif (1989) for silica hard spheres. We can compare our results with their results and test the accuracy of Stokesian dynamics. Third, a suspension at ϕ=0.45 is dense and not far below ϕ_F= 0.494±0.002 of the colloidal fluid - colloidal crystalline phase transition at equilibrium. In addition to studying the macroscopic behavior of dense hard-sphere suspensions, we can investigate the influence of the imposed shear on the equilibrium phase transition. These are the reasons that suspension at ϕ=0.45 is a good choice to start our studies and it is discussed first.

In chapters VI to VIII, there are three main sections which contain results for the rheology, microstructure and self-diffusivities. The full set of particle stresses, which include the steady shear viscosities and normal stress differences, are discussed in the rheology section. The shear-induced microstructure section includes the pair-distribution function and the probability density. They are used to probe the flow of particles in detail. By examining the microstructure, we can relate its deformation to suspension macroscopic properties and understand the mechanisms which cause interesting rheological behavior. In this section, results for the structure factors and their comparisons with experimental results are also discussed. With the advancement in optical engineering, spectroscopic techniques such as light scattering and small angle neutron scattering (SANS) are applied to measure the structure factor. This is an opportunity for us to relate our simulation results to experimental measurements. The results for both the short- and the long-time self-diffusion coefficients are presented in the self-diffusivities section.

In chapter IX, results are summarized for the entire range of concentrations. Comparison of simulation results for the steady shear viscosity and self-diffusivities with experiments is shown. Chapter IX is concluded with the results of suspension temperature and the time-correlation function for the particle velocity fluctuations.

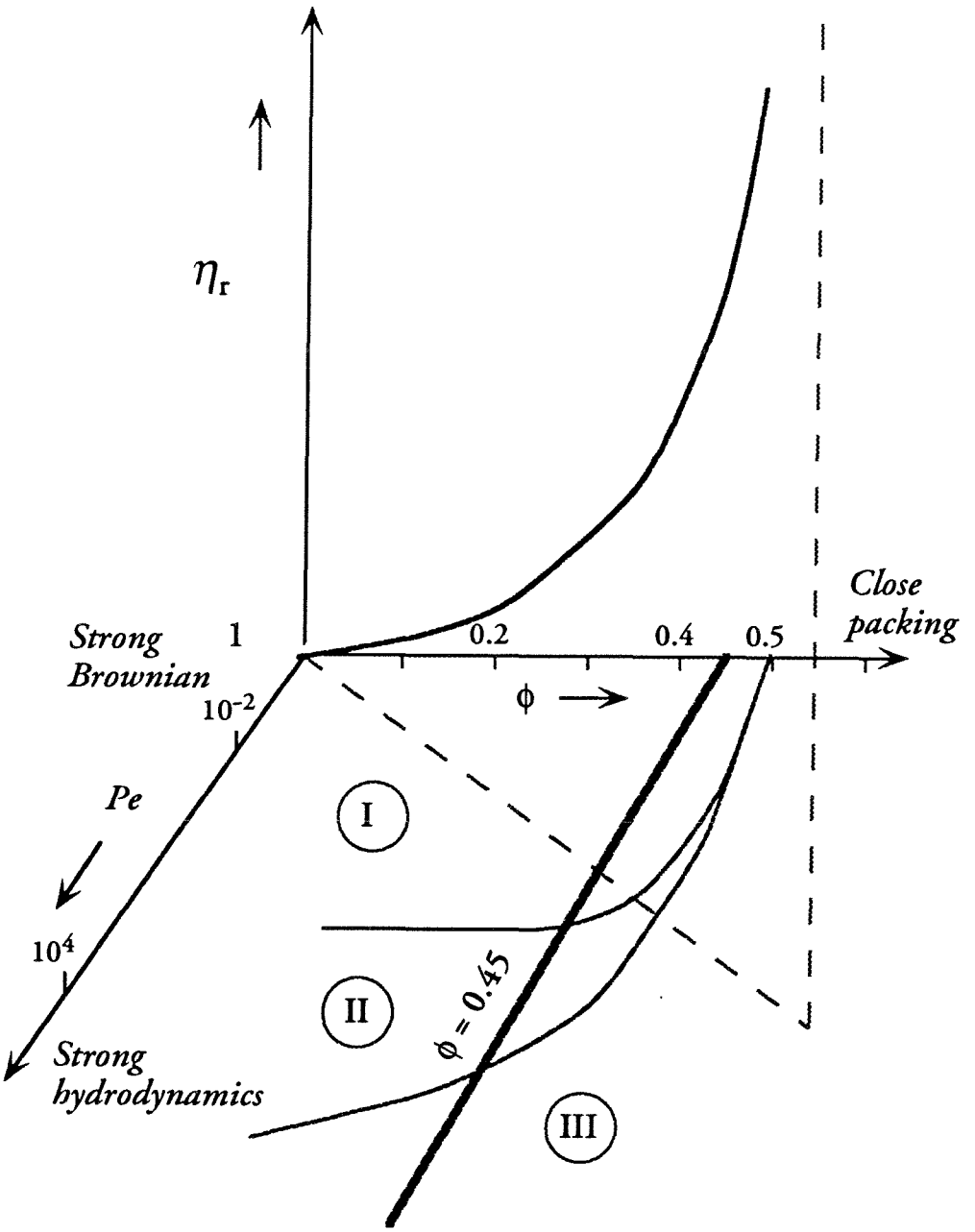

Figure 5.1: The generally observed relation of the steady shear viscosity as a function of the two important dimensionless parameters: particle volume fraction, ϕ, and the Péclet number, *Pe*, which measures the relative importance of the imposed shear and Brownian forces. The nonequilibrium phase diagram for hard-sphere suspensions is sketched with three regions: colloidal fluid (region I), coexisting phase of colloidal fluid and colloidal crystals (region II), and an ordered crystalline phase (region III).

Chapter VI

STOKESIAN DYNAMICS SIMULATION OF HARD-SPHERE SUSPENSIONS: $\phi = 0.45$

The model of hard-sphere suspensions in our simulations implies that the suspended particles are force- and torque-free, i.e., $\mathbf{F}^P = 0$. The particles interact solely by the hydrodynamic and Brownian forces. Details on the unit cell model and the reference coordinates are shown in Fig.3.1 with the flow direction the x-axis, the velocity gradient direction y and the vorticity direction z. These reference coordinates apply to all the runs except one special case in which a different flow direction is tested and it will be clearly stated when its results are reported. For the Brownian dominated limit ($Pe < 1$), the time is scaled with the diffusive time a^2/D_o where D_o is the diffusion coefficient of a sphere at infinite dilution. When the hydrodynamics dominate ($Pe > 1$), the time is scaled with the shear rate, $\dot{\gamma}^{-1}$. Both nondimensionalizations are applicable for the special case of Pe=1. The evolution and the simulation methodology were discussed in chapter II. Here, we discuss the results in detail for hard-sphere suspension at volume fraction ϕ=0.45 only.

Specifications of the runs and the sampling method for hard-sphere suspensions at a particle volume fraction ϕ=0.45 are summarized in Table 6.1.a for 27 particles and in Table 6.1.b for larger numbers of particles with N = 63, 64, 81, 123 and a monolayer model with 25 particles. Column (1) is the Péclet number, Pe, and column (2) is the number of particle, N. Columns (3) and (4) are the starting time, t_{start}, and the ending time, t_{end}, of each run, respectively. Except the two special runs which are denoted by $Pe = ^{*}10$ at the end of Table 6.1.a and a monolayer with 25 particles at the end of Table 6.1.b, all simulations start with a random particle placement and have t_{start}= 0. Initial random samples of N particles are computed by first placing all N spheres in a regular lattice and then each sphere is randomized about 50,000 to 100,000 times using

the Monte-Carlo random method. We compute the angularly averaged pair-distribution function $g(r)$ for these initial samples and compare with that from the hard-sphere distribution to verify that the structure was isotropic. For the runs with 27 and 64 particles, we pick simple cubic (SCC) arrays of spheres and then randomize the particles. Other values of N are also tested to prevent the possible influence of the starting regular arrays or the evenness of number of particles that may fit exactly into periodic lattices in the simulation on suspension macroscopic properties and on the microstructure. The random sample with 81 particles starts with a body-centered cubic (BCC) packing and it is then randomized. For the runs with 123 particles, we first set 125 particles into 5×5×5 simple cubic arrays of spheres in the unit cell at ϕ=0.45. Two particles are randomly removed from 125 particles and the length of the unit cell is reduced to adjust particle volume fraction to ϕ=0.45 for 123 particles. Finally the 123 particle configuration is randomized and used as the initial sample for the subsequent simulations. A similar method is applied for the selection of 63 particles.

The special run which is denoted as $Pe = ^{*}10$ and t_{start}= 100 in the end of Table 6.1.a starts with a particle configuration obtained from the end of a regular run with Pe=10 and t_{end}= 100. The (*) symbol implies a new flow direction is tested along the y-axis. Note that the reported run time is dimensionless as it is scaled properly by the method mentioned earlier. The monolayer runs shown in the end of Table 6.1.b are continuing simulations with the order of the runs specified by the bracketed numbers: Pe = 0.1[1] → 10[2] → 10^{3}[3] →10[4]. From a random sample of 25 particles for a monolayer (2D) with an areal fraction ϕ_A= 0.675 which is comparable to a volume fraction ϕ=0.45 in three dimensions (3D) using the 2/3 rule, the suspension is sheared

for 350 time units (t_{end}= 350) at Pe=0.1 for the first of a four-run series. At the end of the first run, Pe is raised from 0.1 to 10 and the suspension is sheared for another 350 time units (t_{end}= 700) to complete the second run. The third run is started by increasing Pe from 10 to 10^3 and continued for 240 time units (t_{end}= 940). Pe is finally reduced from 10^3 to 10 for the fourth run and the suspension is sheared for the last 300 time units (t_{end}= 1240) to complete this four-run series. This series of runs follows the practice in experiments where the shear rate is step increased and the sample is sheared and then the steady shear viscosity is measured. The aim of these special runs is to investigate the influence of the flow direction and initial particle placements as well as the possibility of hysteresis effects on suspension properties. By raising Pe from 0.1 to 10 in run [2] and lowering Pe from 10^3 to 10 in run [4], we can analyze the results from these two runs to determine if there is hysteresis effect. Column (5) in Tables 6.1.a and 6.1.b is the time step, Δt_{set}, and column (6) is the number of time steps, NSTEPS, for each run. In general, the run time for 27 particles ranges from 50 to 100 time units and is relatively longer than the run time average of 40 time units for the runs with a large number of particles. For Pe=0.1 and 0.01, the suspensions are sheared for 500 time units to allow equilibration for both the shear viscosity and the normal stress differences. The purpose of columns (7), (8) and (9) are best illustrated by the following example. From the 100 time units of the run with Pe=10^3 and N=27 in Table 6.1.a, we discard the first 10 time units and then sample data over 16 time intervals (# *trials* shown in column (8)). Each trial has 60 time units (t_{diff} shown in column (6)) and is successively sampled by shifting in time (t_{shift} shown in column (7)) 2 time units or 2000 time steps.

The 40 dimensionless time units for the runs with 123 particles are relative short and

we are able to sample the results only one time from each run. This explains why t_{shift} is zero for all runs and $\#\ trials = 1$ in Table 6.1.b and the standard deviations for the shear viscosity and normal stress differences are not listed. A dynamic simulation with 40 time units (40 000 time steps with a time step Δt_{set}=10^{-3}) requires 4.3 hours for 27 particles and 334 hours ($\approx$ 2 weeks) for 123 particles on an IBM RiSC/6000 model 530 (rated at 10 MFLOPS). The fast speed of our Stokesian dynamics simulations enables the study of dense hard-sphere suspensions, yet it is still relatively slow for dynamic simulations with $N \approx O(100)$. This is the only reason why runs are shorter for large N.

Monolayer simulations were pioneered and studied in detail by Brady and Bossis (1985), Bossis and Brady (1984, 1987, 1989), Lester (1988) and Bonnecaze and Brady (1992). Their motivation was to save significant computer time with monolayer models, yet obtain appropriate qualitative results. The matrix size for a 2D model is $(6N \times 6N)$ while it is $(11N \times 11N)$ for 3D. Stokesian dynamics method requires an $O(\mathcal{N}^3)$ computations where $\mathcal{N}$ is the size of the matrix. It is a saving of nearly a factor of 6.2 by using a monolayer with the same number of particles as in a 3D model. Our monolayer simulations were done for three reasons: First, 2D models offer a very effective means to graphically visualize the evolution of particle positions. Second, for the same number of particles a larger unit cell is used in 2D than in 3D, which allows meaningful computation of the structure factor at large distance. Note that a monolayer with 100 particles is equivalent to a three dimensional system with 1000 particles in terms of the number of neighboring particles. Third, we will show our simulation results for shear viscosity using both 2D and 3D models at the same volume fraction. These results compare very well, qualitatively and quantitatively indicating that the correct physics is captured in mono-

layer simulations. Using a monolayer for saving computer time is no longer a necessity with the fast speed of our Stokesian dynamics computer programs.

VI.1 Suspension Rheology

VI.1.1 The Steady Shear Viscosity

The results for the steady shear viscosities of hard-sphere suspensions at ϕ=0.45 as a function of Pe are summarized in Table 6.2.a for 27 particles and in Table 6.2.b for N = 63, 64, 81, 123 and a monolayer with 25 particles. Columns (3) to (8) give the mean of the steady shear viscosity and its standard deviation for the hydrodynamic, the Brownian, and total contribution, respectively. For a simple shear flow in the x–y plane the relative viscosity η_r, the viscosity of the suspension normalized by the fluid viscosity, is the relation between the x–y component of the bulk stress $\langle\Sigma\rangle$ and the x–y component of the bulk rate of strain $\langle\mathbf{E}\rangle$. The viscosity of a suspension is defined with the aid of equation (2.21),

$$\eta_r = 1 + \eta_r^H + \eta_r^B \quad . \tag{6.1}$$

η_r^H and η_r^B are given in equation (2.22.a) and (2.22.c), respectively.

Results for the shear viscosities from Table 6.2.a are plotted in Fig.6.1 to show the variation of the hydrodynamic and Brownian contribution to the total shear viscosity as a function of the Péclet number. The total shear viscosity curve resembles quite strikingly experimental curves: shear thinning at low Péclet numbers ($Pe < 1$), a plateau region, $1 < Pe < 10^2$, where the change of the total shear viscosity is small and finally a shear-

thickening region at large Péclet numbers ($Pe > 10^2$). In the plateau region, both the hydrodynamic viscosity η_r^H ($\triangle$) and the Brownian viscosity η_r^B ($\square$) vary noticeably, but their changes are seen to compensate each other to yield a relatively constant total shear viscosity η_r ($\bullet$). The Brownian viscosity decreases quickly as Pe increases from 0.01 to 10 and it has essentially vanished for $Pe > 10^2$. The hydrodynamic viscosity shows an opposite trend: η_r^H remains relatively constant with a value of 4.55±0.15 as shown in Table 6.2.a from Pe=0.01 to $Pe \approx 10$ and then continuously increases with increasing Pe. The increase in η_r^H for $Pe > 10$ is due to the formation of large clusters whose size grows with the Péclet number. In the absence of Brownian motion ($Pe \rightarrow \infty$), experiments (Hoffman (1972), Graham and Bird (1984)) and simulations (Bossis and Brady) on a monolayer have shown similar evidence of clusters. Graham and Bird (1984) observed the constant formation and destruction of clusters of particles in sheared concentrated suspensions of large polymethyl methacrylate (PMMA) spheres with radius $a \approx 0.635$ mm. The spheres were neutrally dispersed in oil/tetrabromoethane solution. The large size of the spheres was designed to study the effect of hydrodynamic forces on particle clusters. They also discovered that even in the dilution suspensions with $\phi = 0.1$, over 25 % of the spheres were observed in clusters of two or more members. Simulation results from Bossis and Brady displayed large and elongated clusters of particles spanning the entire unit cell in the limit of high Péclet numbers. The graphic video animation of the particle positions from our simulations for monolayer with 25 spheres clearly demonstrates the existence of large clusters of particles at high shear rate, Pe=10^3 (run [3]). In section VI.2.3, we present snap shots of particle positions (cf. Figures 6.12 to 6.17) which are obtained from the four-run series of a monolayer model for the three structures

of hard spheres: randomly dispersed particles for slightly deformed suspensions (Pe=0.01 in run [1]), strong ordering of well separated particles for suspensions with a balance of the Brownian and hydrodynamic forces (Pe=10 in run[2] and run [4]) and clusters of particles for hydrodynamically driven suspensions in the shear thickening regime (Pe=10^3 in run [3]).

Figure 6.1 also shows an unique Péclet number in the shear thinning region where the hydrodynamic and the Brownian contribution to the total viscosity is exactly the same. We denote this unique Péclet number as Pe^* and from Fig.6.1, it is seen that $Pe^* \approx 0.6$ and η_r^H and η_r^B are equal to ≈ 4.55. The relation of Pe^* on particle volume fraction is presented in chapter IX, where we finalize the entire dense hard-sphere suspensions. Pe^* is seen to be shifted to a higher value with increasing ϕ. At lower ϕ, Pe^* does not exist as the hydrodynamic viscosity is always greater than the Brownian viscosity for the range of Pe from 0.01 to ∞ in our study. Pe^* thus can be viewed as a rheological signal when the flowing suspension starts to order and the suspension begins to shear thin.

Information from Table 6.2.a and Fig.6.1 offer two conclusive evidences on the shear thinning and shear thickening. First, the shear thinning in the region of $Pe < 1$ is due only to the decrease in the Brownian viscosity since the hydrodynamic viscosity does not change appreciably. Second, the shear thickening at large Péclet number ($Pe > 10^2$) is due to the increase in the hydrodynamic viscosity as the Brownian viscosity decays to zero. The stochastic Brownian motion acts to restore the suspension to an equilibrium state from shearing deformation. As the Péclet number increases, the time scale due to the imposed shear is much smaller than the diffusive time and the Brownian motion

simply does not have sufficient time to counter an increasing deformation to the structure due to the imposed shear. The Brownian motion becomes less and less important relative to the shear and this causes a significant decrease from Brownian contribution to the shear viscosity and to suspension macroscopic properties in general.

In the region with large Péclet number, η_r^H contributes essentially all the total shear viscosity η_r. The increase in η_r^H is associated with clusters of particles at large Péclet number and the particle configuration becomes increasingly anisotropic. Clusters of particles are more resistant to the shearing deformation than particles that are separated in a fluid since in a cluster, a particle cannot translate and/or rotate without first moving and/or rotating with the entire cluster. The existence of these clusters is the cause of the shear thickening as they disrupt the bulk flow. A larger shear force is required to deform the clusters and to shear the clustered suspension; This is reflected as an increase in hydrodynamic viscosity, η_r^H. Even though the direction contribution from Brownian motion to suspension macroscopic properties has vanished in the shear thickening region, the presence of weak Brownian forces perturb and cause the distribution of particles to be anisotropic (see section VI.2.3). More importantly, its random motion destroys large clusters of particles, which reduces the shear viscosity and maintains to the diffusive behavior in the dense suspensions.

Figure 6.2 presents a comparison for the steady total shear viscosity η_r from Fig.6.1 with the experimental results from van der Werff and de Kruif (1989) and van der Werff (1990) for sterically stabilized monodispersed silica particles suspended in cyclohexane. The particle volume fractions in the experiments are ϕ = (+) 0.419±0.01, (⊡) 0.443±0.01

and (△) 0.47±0.01. The range of the Péclet numbers in the experiments is from 0.01 to 10. The curves for ϕ=0.419 and 0.47 show the measurements for the viscosity in a forward and a reverse flow direction. The reproducibility of experimental results is excellent indicating the independence of the steady shear viscosity on the direction of the shear at steady state. The (•) symbols are Stokesian dynamics simulations at $\phi = 0.45$ for N=27. Data from Table 6.2.b are plotted in the same figure for N = (□) 63 and 64, (▲) 81, (◊) 123, monolayer with N = (○) 25 and $N = 27$ at $Pe = 10$ with a shear flow in the y-axis (×). Our results for ϕ=0.45 compare remarkably well with the experiments for ϕ=0.443 and 0.47. The simulation results for different number of particles from 27 to 123 particles in the unit cell show very little change in the shear viscosity indicating that a system size as small as 27 particles is sufficient to model unbounded suspensions for this property. At Pe=10, we observe no difference in η_r for different flow directions as the shear viscosities are similar for run [2] and run [4] with a monolayer of 25 particles. The hysteresis influence on η_r is insignificant at Pe=10 and this is also seen in the experiments of van der Werff and de Kruif with forward and reverse shear directions for samples at ϕ=0.419 and 0.47. The monolayer simulation results compare remarkably well with 3D results as seen in the figure. A dimensionless run time of 40 to 60 allows good equilibration for η_r and standard deviations are small as reported in Tables 6.2.a and 6.2.b. van der Werff and de Kruif reported 2% uncertainty for the measurements of volume fraction and 10% uncertainty for the measurements of the shear viscosity at high ϕ. A 2% uncertainty in measurements for the volume fraction may lead to large uncertainty in the shear viscosity at high ϕ due to extreme sensitivity of the viscosity on the volume fraction, which can be seen in this figure by comparing the narrow gap

between the experimental results for shear viscosity of ϕ=0.419 and 0.443 and the wide spread between the shear viscosities of ϕ=0.443 and 0.47.

Both the experiments and the simulation show the suspension shear thins, and this is seen from our dynamic simulations to be due to the decrease of Brownian contribution to the stress. Our simulations show a shear thickening region for $Pe > 10^2$ and this was not seen in the experiments of van der Werff and de Kruif because experimental limitations did not allow them to continue with high enough shear rates. Shear thickening have been observed in many other systems (Hoffman (1972), Laun (1988), Barne (1989), Boersma *et al.* 1990), however. Shear thickening in Brownian suspensions is due to the formation of large clusters as the Péclet number increases. The necessity for the suspension to shear thicken can also be seen from the viscosity measurement for large spheres ($Pe \rightarrow \infty$) by Jeffery and Acrivos (1976), Gadala-Maria (1979) and Pätzold (1980), which show a viscosity larger than the minimum in the shear thinning viscosity of the Brownian suspensions shown in Fig.6.2; therefore, the suspension *must* shear thicken.

VI.1.2 The Steady Normal Stress Differences

We discuss next the normal stress differences for hard-sphere suspensions. The normal stress differences are important to the field of rheology as they help to characterize the non-Newtonian behavior due to the anisotropic deformation of the microstructure. Tables 6.3.a and 6.3.b summarize the simulation results for the mean of the time-averaged first and the second normal stress differences along with their statistics. Columns (3) to (8) give the first normal stress difference, χ_1, and columns (9) to (14) give the second normal stress difference, χ_2. The hydrodynamic contribution is presented first, followed

by the Brownian contribution and the total contribution last. The standard deviation denoted as σ are computed from a number of samples and shown in Tables 6.1.a and 6.1.b. For a monolayer model, the forces in the z direction are not needed for dynamic simulations, so the second normal stress differences are not known and they are not computed. The first and second normal stress differences, χ_1 and χ_2, are defined according to equation (2.23) and (2.24) and they both are normalized by $\eta\dot{\gamma}$.

Results in Table 6.3.a are plotted in Figures 6.3.a and 6.3.b to show the change of the hydrodynamic and Brownian contribution to the steady normal stress differences χ_1 and χ_2, respectively. In the region of small Péclet number ($Pe < 1$), the deformation of the equilibrium structure is so small that there is a large degree of statistical uncertainty in the Brownian contribution to the stress and it can be seen in Table 6.3.a that the standard deviation for the Brownian contribution to the normal stress difference $\sigma_{\chi_{1B}}$ in column (6) and $\sigma_{\chi_{2B}}$ in column (12) are as large as the mean themselves. These mean values reflect the simulation fluctuations at low Pe. For a hard-sphere suspension of force-free particles, it is expected that there are no normal stress differences in the limit of $Pe \rightarrow 0$. Similarly for the hydrodynamic limit $Pe \rightarrow \infty$, the normal stress differences must be identically zero, a consequence of the flow reversal symmetry. Our simulations at $Pe{=}\infty$ for dense suspensions are not long enough to allow us to verify this as the time step must be set extremely small to avoid severe particle overlapping.

It is seen from Figures 6.3.a and 6.3.b that the hydrodynamic contribution to normal stress differences ($\triangle$), χ_{1H} and χ_{2H} are practically zero for small Pe ($Pe < 1$) and then increase to an asymptotic value ≈ 2 with increasing Pe. Both χ_{1H} and χ_{2H} are positive

for all Péclet numbers. The Brownian contribution to normal stress differences (□), χ_{1B} and χ_{2B} decays rapidly in absolute values with increasing Pe and they are opposite in sign. For $Pe < 1$, the total normal stress differences (●), χ_{1T} and χ_{2T} are essentially the same as χ_{1B} and χ_{2B}, respectively. For large Pe ($Pe > 10^2$), χ_{1H} and χ_{2H} contribute all to χ_{1T} and χ_{2T} as the Brownian contribution has vanished. Similar to the plot of viscosity in Fig.6.1, Figures 6.3.a and 6.3.b show a plateau region with Pe in the range of 1 to 10^2 where both χ_{1T} and χ_{2T} remain unchanged and are minimum in absolute values. In this region, the decrease from the Brownian contribution is compensated by an increase from the hydrodynamic contribution.

Figure 6.4 presents the relation of χ_{1T} and χ_{2T} with different Péclet numbers and shows the range of Pe from 1 to 10^2 where both are minimum in absolute value. As seen in this figure, the normal stress differences are small for hard-sphere suspensions without interparticle and/or external forces. Johnson, de Kruif and May (1988) reported their finding of small normal stress differences for silica hard spheres in a steady shear flow with a range of volume fraction from 0.36 to 0.52 and attributed the small normal stress differences to the local anisotropy of distribution of the particle number density. Unfortunately, they did not report any data, so we could not compare and verify our results with their findings. It is easy to see from a consideration of small departure from equilibrium that the Brownian forces are directly responsible for the normal stress differences, i.e., coming from the term $\mathbf{S}^B$. At high Péclet numbers the Brownian forces are *indirectly* responsible for the normal stress differences by causing the microstructure to be anisotropic.

Our results as well as experiments show very interesting shear thinning and shear thickening behavior of dense hard-sphere suspensions in a simple shear flow. The important task is to determine and to understand the mechanisms which produce these rheological behaviors. In our dynamic simulations, we can trace the particle positions in space and in time to investigate their relative arrangements in a shear flow, the shear-induced microstructure, and this is presented next.

VI.2 The Shear-Induced Microstructure

The method of examining the microstructure is through the pair-distribution function, which gives the probability density for finding a particle at an assigned position provided that there is a particle at the origin. We will focus on the following two forms of the pair-distribution function: the radial pair-distribution function $g(r)$ and the projection of the pair-distribution on a plane. The radial pair-distribution function, $g(r)$, is the angularly averaged $g(\mathbf{r})$, i.e., $g(r) = \int g(\mathbf{r})d\Omega$, which depends only on the particle center-center radial distance. The plane projection distribution function is obtained from the probability of finding a particle at a position in a plane of interest provided that there is a particle at the center of the unit cell. The periodic images of particles from the neighboring cells are excluded to avoid multiple counts for $g(r)$. From the unit cell, the valid range of the particle center-center spacing r is from a value of 2 (when two particles come in contact) to the edge of the unit cell measured diagonally from the center. We will start with the angularly averaged pair-distribution function and follow with the plane projection distribution function and the static structure factor last. The static structure factor, $S(\mathbf{k})$, is the Fourier transform of the radial pair-distribution function

or the plane projection distribution function. We have chosen these two representations because they convey the most information.

VI.2.1 The Angularly Averaged Pair-Distribution Function $g(r)$

The pair-distribution function $g(\mathbf{r})$ is important to the theoretical development of suspension microstructure and properties. Batchelor (1977) has derived a rigorous theory for the pair-distribution function as a perturbation expansion in shear rate about the equilibrium structure employing an exact two-body expression for the hydrodynamic interactions. The theory is exact in the limit of dilution and small shear rates. Russel and Gast (1986) and Wagner and Russel (1989) have extended Batchelor's results to finite volume fractions by introducing the potential of a mean force but still truncate the hydrodynamic interactions at the pair-level. The determination of weakly-perturbed $g(\mathbf{r})$ has been used with success to derive expressions for predicting rheological properties of a suspension in the limit of vanishing small shear rates (Felderhof (1989)). Bossis and Brady (1987) have reported results for the angular dependence of $g(\mathbf{r})$ for a monolayer of hard spheres at an areal fraction $\phi_A = 0.453$. The shear rate was varied from strong Brownian limit ($Pe \rightarrow 0$) to pure hydrodynamic regime ($Pe \rightarrow \infty$). The pair-distribution function $g(\mathbf{r})$ obtained from their simulations show that the random equilibrium structure is first perturbed slightly ($Pe < 1$) and then deformed to a hydrodynamically driven structure, which shows large clusters formed along the compression axis of the flow at high shear rates ($Pe > 10$). The distortion was seen to be linear in the range of small Péclet number ($Pe < 1$).

We are interested in finding the shear-induced microstructure of dense hard-sphere

suspensions at all shear rates. At equilibrium, the structure of the hard-sphere suspension at a volume fraction ϕ=0.45 is amorphous (liquid-like) and the pair-distribution function $g(\mathbf{r})$ depends only on the relative radial center-center distance between two particles, i.e., $g(\mathbf{r}) \rightarrow g(r)$. When the suspension is sheared, the particle structure is deformed and the pair-distribution function develops angular dependence. The radial pair-distribution function $g(r)$ does not contain important information of angular distribution of the particles, but we can extract useful information on the relative separation of the particles.

We can evaluate $g(r)$ from the particle positions obtained during the course of dynamic simulation and examine the suspension microstructure from a close particle center-center spacing r=2 to a distance comparable with several layers of neighboring particles for the runs with 123 particles. Figure 6.5 shows the plot of $g(r)$ for hard spheres at a volume fraction ϕ=0.45 with different Péclet numbers: (dotted curve) 0, (dotted-dash curve) 0.43 , (solid curve) 10 and (dashed curve) 10^3. After the first spike at $r \approx 2$, $g(r)$ shows several smaller peaks at large values of r. The insert figure in the upper left of Fig.6.5 is a plot of $g(r)$ on a logarithmic scale with a much smaller range of r from 2 to 2.2 to illustrate the value of $g(r)$ at contact. Results for the angularly averaged pair-distribution function evaluated at r=2, $g(2)$, are summarized in Table 6.4.a for the runs with 27 particles and in Table 6.4.b for the runs with 63, 64, 81 and 123 particles. It is seen from this figure that $g(2)$ for the equilibrium isotropic structure (Pe=0) and for suspensions with small deformation (Pe=0.43) are similar as the Brownian motion is still the dominant force in both cases. From Table 6.4.b, our simulation results for $g(2)$ with 123 particles are 4.59 for the pure Brownian limit (Pe=0) and 4.94 for Pe=0.43, a slight increase from that for hard spheres at equilibrium. The Monte-Carlo method gives

4.65 for $g(2)$ compared to our 4.59 at Pe=0 showing the accuracy of Stokesian dynamics. The striking difference in $g(2)$ can be seen for the runs with Pe=10 and with Pe=10^3: $g(2)$ for Pe=10 is 0.84, a significant five-fold decrease from $g(2)$ at Pe=0. At Pe=10, near particles do not contact and there exists a small fluid gap between the particles. This can be clearly seen from the insert figure where the first peak of $g(r)$ at Pe=10 is shifted from r=2 to $r \approx 2.025$. As Pe increases to 10^3, $g(2)$ increases to a value of ≈ 48, a nearly fifty-fold increase compared to $g(2)$=0.89 for Pe=10. Large values of $g(2)$ indicate the existence of clusters of particles as seen for the case of strong hydrodynamic interactions.

Figure 6.6 plots the radial dependence of $g(r)$ with a smaller, linear scale from 0.5 to 1.5 for the entire range of r in the unit cell with 123 particles. Similar to Fig.6.5, Fig.6.6 shows a relatively small difference in $g(r)$ between the equilibrium isotropic distribution (Pe=0) (dotted curve (a)) and the suspension with a small deformation (Pe=0.43) (dotted-dash curve (b)). $g(r)$ for Pe=10 (solid curve (c)) follow curves (a) and (b) over this range of r, with the exception of two small peaks at $r \approx 7.2$ and 8.2. One should note that $g(r)$ for $Pe = 0$ (a), 0.43 (b) and 10 (c) show the second nearest neighbor peak at $r \approx 4.1$ in contrast to r=4 for Pe=10^3 (dashed curve (d)). This implies that there is still a small fluid gap between the first and second neighbors with r=4.1. For Pe=10^3 $g(r)$ shows a narrower peak at r=4, which suggests that the flowing particles are more closely packed at high Péclet numbers - a harbinger of cluster formation.

Figures 6.5 and 6.6 provide important information on the suspension microstructure. Suspensions at equilibrium or with small deformations ($Pe < 1$) show a particle

arrangement with small value of $g(2)$ and the broad second peak at $r \approx 4.1$. At Pe=10, particles are relatively well separated as indicated by the smallness of $g(2)$. Finally for suspensions with strong hydrodynamic interaction (Pe=10^3), the probability of having clusters of two or more particles is seen to be high as $g(r)$ shows an intense first nearest neighbor peak at r=2 and the second sharp peak at r=4. We will now examine the pair-distribution function $g(r)$ as particles come in contact with finer increments in the Péclet number.

Results of $g(2)$ from Table 6.4.a for the runs with 27 particles and in Table 6.4.b for the runs with N = 63, 64, 81 and 123 are plotted in Fig.6.7. Note that $g(2)$ is plotted on a logarithmic scale. The figure shows a very small variation in $g(2)$ with a different number of particles in the unit cell at the same Péclet number. $g(2)$ is relatively constant for small Pe ($Pe < 1$), decreases to a minimum value at $Pe \approx 3$ and then increases with increasing Pe. The relation of $g(2)$ and the Péclet number resembles closely the behavior of the steady shear viscosity shown in Fig.6.2. As seen from Fig.6.7 the smallness of $g(2)$ at $Pe \approx 3$, which is the region of minimum shear viscosity, implies that particles are relatively well separated and not in contact with their neighbors. The large value of $g(2)$ for $Pe > 10^2$ indicates on the average we would be able to find two or more particles in contact. Large values of $g(2)$ at high Péclet numbers are consistent with the high shear viscosity observed in the shear thickening region, which we attribute to the existence of clusters. Note that over much of the shear thinning region in Fig.6.1 ($0.01 < Pe < 1$), $g(2)$ is virtually unchanged. Next, we present complete details of the shear-induced microstructure by examining the plane projection of the probability density functions.

VI.2.2 The Probability Density Functions $g(x,y)$, $g(x,z)$ and $g(z,y)$

Recalling the shear thinning and shear thickening behavior of dense hard-sphere suspensions presented in Figures 6.1 and 6.2, we now want to travel along the curve for the steady shear viscosity at each particular Péclet number, and probe the relative particle arrangements and examine the shear-induced microstructure. An effective method to view the flow of particles in the unit cell is to focus our vision separately on each of the three faces of the cubic unit cell: $x-y$, $x-z$ and $z-y$ relative to the reference coordinates. The directions of the flow, velocity gradient and vorticity are the x-, y- and z-axis, respectively. In our simulations, we divide the planes of the unit cell by small squares with dimension of (0.1,0.1) in length. The particle positions are projected onto these squares and the probability density function of finding a particle at a position in a particular square relative to the particle at the origin is computed. To plot the plane projection distribution function, we employ the density plot feature from the *Mathematica* program.

We focus first on the runs with 27 particles. Figure 6.8.a shows the plot of the plane projection distribution function computed on the $x-y$ plane, $g(x,y)$, with different Péclet numbers. Regions of light color represent high probability and regions of dark color represent low probability. The reference axes are shown on the right of the figure. The flow direction is the horizontal x-axis and the velocity gradient is the vertical y-axis. We have the frontal view of the unit cell as the flow direction is from left to right. $g(x,y)$ is shown with increasing Péclet numbers from left to right and from top to bottom. Starting with Pe=0.01 from the top left corner, $g(x,y)$ displays symmetrical bright spots forming a circle. It is equally probable to find a nearest neighbor at one of these sites around

the centered particle and the density plot describes the isotropic structure of a strong Brownian suspension. As the Péclet number increases, the symmetric ring is increasingly distorted and then is opened at Pe=1. At Pe=3, the first sign of horizontal bands with light color is seen and the ring is broken. As Pe increases from 3 to 10, $g(x,y)$ shows clearly the formation of "strings" of flowing particles along the flow direction. The string formation becomes weaker at Pe=100 as fluctuations in $g(x,y)$ are seen near these bands and it is destroyed as Pe increases to 10^3. Here we observe the shear melting process as we approach the hydrodynamic domination limit. There is a significant difference in the density plot of Pe=0.01 and 10^3. Regions outside the symmetric ring from $g(x,y)$ for Pe=0.01 are shown with low probability as a dark color and this implies that particles are random and not in contact. In contrast, regions outside the distorted ring from $g(x,y)$ for Pe=10^3 are marked with high probability as a light color. It is highly probable that particles can be found at every site in this region and it is the signal of clusters of particles. The ring is also thinner for Pe=10^3, which is another evidence of closely spaced or touching particles, compared to the thick and symmetric ring at Pe=0.01.

The most revealing microstructure is a plot of the plane projection distribution function computed on the $z-y$ plane, $g(z,y)$, which is shown in Fig.6.8.b. The vorticity direction is the horizontal z-axis and the velocity gradient direction is the vertical y-axis. The flow direction is perpendicular to the $z-y$ plane and we view the flow of particles directly toward our eyes. The density plots are shown with the same light-high and dark-low scale of the probability and the order of the Péclet number as illustrated in Fig.6.8.a for $g(x,y)$. At Pe=0.01, $g(z,y)$ shows the same symmetric ring pattern seen in Fig.6.8.a, as expected for an essentially equilibrium suspension. The isotropic

structure should not have a preferred orientation and it is correctly shown by Stokesian dynamics. There is very small variation in the plot of $g(z,y)$ as Pe increases from 0.01 to 1. $g(z,y)$ starts to show the high probability light spots at Pe=3. As Pe increases to 10, $g(z,y)$ shows a very striking pattern of bright spots which form a "hexagonal" packing of particles flowing directly out of the $z-y$ plane. At large Pe, the hexagonal packing is weakened and has disappeared completely at Pe=10^3. Again we observe the shear melting effect for suspensions with strong hydrodynamic forces. It is important to note that the plot of $g(z,y)$ at Pe=10 shows a bright spot at the center of the unit cell. This centered bright spot is *not* from the centered particle at the origin. It is rather from the two nearest neighbors of the centered particle and these two neighbors have the same height y and depth z, but different horizontal x value defined in the unit cell; one neighbor is in the front and the other is behind the centered particle, and all three particles flow as a string along the flow direction, the x-axis which is perpendicular to the $z-y$ plane. The formation of strings of particles is also shown in the plot of $g(x,y)$ in Fig.6.8.a. This centered bright spot can only be seen with the distinct "hexagonal" packing from a plot of $g(z,y)$.

A similar plot for the plane projection distribution function on the $x-z$ plane, $g(x,z)$, is shown in Fig.6.8.c. We view the particles from the top of the unit cell with the flow of particles from left to right. $g(x,z)$ resembles closely $g(x,y)$, showing the random structure at Pe=0.01. As the suspension is sheared the strings form along the flow direction at Pe=10 and 20, and finally the strings are melted at high shear rates, Pe=10^3. At Pe=10, the density plot of the steady $g(x,y)$ $g(x,z)$ and $g(z,y)$ reveal the formation of strongly ordered suspensions. Particles line up in "strings", with "hexagonal" packing

along the flow direction. It is of interest to find the Péclet number which signals the onset and destruction of ordered packing, as well as the range of volume fractions over which the suspensions can be sheared into ordered microstructures. Figure 6.8.d shows the relation of $g(z, y)$ with a finer increment of the Péclet number. The ordered hexagonal packing is first detected at Pe=5, but not as clear as that for the run with Pe=10. The shearing melts and destroys the ordered structure at Pe=200. The transitional Péclet number, where the particle configurations change from a random orientation to a strong ordering, is seen at Pe=3.

Figure 6.8.e displays the evolution of the probability density $g(x, z)$ for the special run with 27 particles and a new flow direction along the y-axis. The sample of 27 particles was first sheared in the normal x-direction for 100 dimensionless time units at Pe=10. The shear direction is then changed from the x- to the y-axis and the strongly ordered suspension is sheared with a new shear direction for another 100 time units at the same Péclet number. For this special run the new flow direction, the y-axis, is perpendicular the $x-z$ plane. For the first fifty time units, $g(x, z)$ shows that particles are in a transition to arrange and position themselves to order along the new flow direction. The steady $g(x, z)$, which is averaged for the last fifty time units is shown in the right most figure with a clear hexagonal packing. Our results show that there is no influence of the flow direction as well as the starting particle configurations on the microstructure and the rheology given that there is sufficient time allowing the structure to equilibrate.

The microstructure obtained from dynamic simulations with a large number of particles is presented next. Figures 6.9.a and 6.9.b show $g(x, y)$ and $g(z, y)$ for different

Péclet numbers: 0.01 (upper left), 0.43 (upper right), 10 (lower left) and 10^4 (lower right), respectively. There are 63 or 64 particles in the unit cell. At Pe=10, the string formation and hexagonal packing of particles are again observed.

The time evolution of $g(x, y)$ for 123 particles is plotted in Fig.6.10.a. The flow direction is from left to right along the horizontal x-axis and the velocity gradient is the vertical y-axis. For the first twenty time units, $g(x, y)$ shows fluctuations and a weak string formation as the particles are sheared from a random initial configuration (left and central figure). The steady $g(x, y)$ (right figure) is averaged for the last thirty time units and shows a distinct formation of strings of particles along the flow direction. Figure 6.10.b plots the dynamics of $g(z, y)$ with different shear times. The flow direction is now perpendicular to the $z-y$ plane, with the vorticity the horizontal z-axis and the velocity gradient the vertical y-axis. From left to right, the density plots of $g(z, y)$ show the transition of particle relative arrangement with time under shear. The random structure is sheared into a final strongly ordered structure. The remarkable hexagonal packing of particles along the flow direction is seen quite clearly from the density plot of the steady $g(z, y)$ (right figure) after fifty shear time units. Figure 6.10.c shows the change of $g(x, z)$ with different shear time. For the $x-z$ plane, we view the flow of particles from the top of the unit cell with the flow direction in the horizontal x-axis, and the vorticity direction in the vertical z-axis and the particles flow from left to right. Starting from an isotropic structure, the shear produces a change in the particle relative arrangements to strings of particles flowing along the flow direction. The string formation can be observed from $g(x, y)$ in Fig.6.10.a and from $g(x, z)$ in Fig.6.10.c. Note that there are five strings

of particles shown by $g(x,y)$ but ten strings are counted from a plot of $g(x,z)$. The difference in number of strings is due to the plane with which we view the particles.

The particle arrangement in all three directions is plotted in Fig.6.10.d where the particles are positioned according to the probability information from Figures 6.10.a to 6.10.c. From top to bottom of Fig.6.10.d, the left column shows a density plot of the steady probability densities $g(z,y)$, $g(x,y)$ and $g(x,z)$, respectively; the right column shows the corresponding particle positions determined from these density plots. The upper figures are $g(z,y)$ on the left, and on the right the formation of "hexagonal" packing of particles flowing along the flow direction which is perpendicular to the $z-y$ plane. The hexagonally packed particles flow out of the plane and directly toward the viewer. The hexagonal packing has a perfect six-fold symmetry, allowing the particles to flow with ease relative to one another following the imposed shear flow. The particles do not have to move around one another in this arrangement. This structure can also be rotated by any amount without affecting the smooth flow of particles. There are several hexagons in the unit cell as the ordering is seen to be long ranged. The particle center-center distance from the central particle to its first six hexagonal neighbors is ≈ 2.025 and to its second twelve dodecahedral neighbors is ≈ 4.1, which can also be obtained from $g(z,y)$ and from the pair-distribution $g(r)$ shown in Figures 6.5 and 6.6. The central figures are the density plot of $g(x,y)$ on the left and on the right the formation of "strings" or "bands" of particles along the x-axis. The five strings correspond to the five horizontal layers of particles in the hexagonal packing seen in $g(z,y)$. The lower figures are the density plot $g(x,z)$ on the left and on the right the "strings" of particles flowing along the x-axis. There are 10 strings, corresponding to the ten vertical layers

of particles in the hexagonal packing from $g(z,y)$. The ten strings of particles are drawn to show the staggered position of the strings.

A comparison of the steady plane projection distribution functions $g(x,y)$, $g(x,z)$ and $g(z,y)$ for different Péclet numbers is illustrated in Figures 6.10.e, 6.10.f and 6.10.g, respectively. In these three figures, density plots are shown for three different Péclet numbers: $Pe = 0.43$ (left figure), 10 (central figure) and 10^3 (right figure). There are 123 particles in the unit cell. These figures display a random microstructure with symmetric ring for suspensions with a small deformation (Pe=0.43), the shear-induced ordered microstructure with well separated particles and distinctive "strings" and "hexagonal" packing of flowing particles (Pe=10), and the microstructure with clusters of particles as shown by the sharpening of the first nearest neighbor ring for suspensions at high shear rate (Pe=10^3).

The density plot $g(z,y)$ with 81 particles in Fig.6.11.a shows an interesting feature of the shear-induced microstructure. $g(z,y)$ shows a random structure for $Pe = 0.01$ (upper left) and 0.43 (upper right), shear-ordered packing at Pe=10 (lower left) and structure with regions of clusters at Pe=10^4 (lower right). At Pe=10, we see the hexagonal packing but the pattern is rotated with a small angle relative to the horizontal z-axis and this is illustrated in Fig.6.11, which shows the plot of particle positions according to the density plot of $g(z,y)$. Particles are sheared into order at Pe=10, but 81 particles cannot fit into a hexagonal packing without rotating by a small angle. Ensemble of 81 particles is small to fit into 5×5×5 arrays of spheres in a unit cell and too large for 4×4×4 string arrangement, so it can only fit into a 4×4×5, which precisely what is seen from the

density plot of $g(z, y)$. The rotational angle is made more clear in the section VI.2.4.1 for the structure factor $S(\mathbf{k})$.

VI.2.3 Suspension Microstructure of a Monolayer with 25 Particles

Dynamic simulations of a monolayer offer an effective means to graphically visualize the evolution of the particle positions and can help us to understand the rheological behavior of dense hard-sphere suspensions. In section VI.1, we provided the same results for the steady shear viscosities of monolayers as the three dimensional simulations. The only restriction imposed on a monolayer is that the particles cannot be displaced in the vorticity direction, the z-axis; the computation is kept fully three dimensional. From the dynamic simulations of a monolayer, the particle positions are recorded and animated on a video tape to present the dynamics and evolution of the suspension microstructure. Actual snap shots of the particle positions are presented in Figures 6.12 to 6.17.

Figure 6.12 presents the starting particle configuration of 25 particles in a monolayer model with an areal fraction $\phi_A = 0.675$ which is comparable to a volume fraction ϕ=0.45 if one uses the 2/3 rule. The center square is the unit cell and particles outside the cell are periodic images which are replicated to fill the unbounded space. The isotropic equilibrium structure is slightly deformed with a small shear rate at Pe=0.01 (run [1] in Table 6.1.b) and the particle positions are plotted in Fig.6.13.a at time t=100 time units and in 6.13.b at time t=350. Both figures show only small departure from isotropic equilibrium structure. As the suspensions are sheared into the region of minimum viscosity with a balance of Brownian and hydrodynamic forces at Pe=10 (run [2]), snap shots of the particle positions in Figures 6.14.a to Fig.6.14.c clearly demonstrate very

strong ordering structures with "string" formation of flowing particles along the flow direction, the x-axis. Particles are well separated from each other and flow as strings and rotate with the imposed shear. Figures 6.15.a to 6.15.c show the microstructure of hard spheres in the limit of strong hydrodynamic forces (Pe=10^3 in run[3]). It is clear that particles form large clusters which span the entire unit cell along the compression axis. This creates a temporal and spatial local anisotropy in the distribution of the particle number density in which more particles are found in the cluster along the compression axis. These clusters disrupt the shear flow and are the cause of shear thickening. As the Péclet number decreases from 10^3 to 10 (run [4]), we again observe the string formation of flowing particles as illustrated by snap shots of particle positions in Figures 6.16.a and 6.16.b. Hysteresis is not seen in our simulations as we are able to capture similar shear-induced structures independent of the starting particle configurations. We also return to the same viscosity at Pe=10, which agrees well with the 3D simulation at the comparable volume fraction as shown in Fig.6.2. Finally, we present snap shots of particle positions for three distinct microstructures in Fig.6.17: randomly dispersed particles for slightly deformed suspensions (left figure), alignment of flowing particles as strings for suspensions with a balance of Brownian and hydrodynamic forces (central figure) and clusters of particles for hydrodynamically driven suspensions (right figure).

Before we determine the important relation of suspension rheological behavior to the microstructure and explain the shear thinning and thickening phenomena of hard spheres, a final connection of our findings of the shear-induced structures and that from experiments is necessary to verify that the dynamic simulation results agree with experiments under similar conditions. The static structure factors which can be measured by

optical techniques are used to compare with our calculations and are presented in the following section.

VI.2.4 The Structure Factor $S(\mathbf{k})$

As we discussed in sections VI.2.1 and VI.2.2, the pair-distribution function and the plane projection of the probability density contain valuable information on the deformation of the microstructure in a shear flow. Additional information on the microstructure can also be obtained from the Fourier transform of $g(\mathbf{r})$, the static structure factor $S(\mathbf{k})$. The static structure factor is important for two main reasons. First, $S(\mathbf{k})$ can be directly measured by optical techniques such as the scattering of light, X-rays or neutrons, and its distortion can be related to the deformation of a flowing suspension. Being able to observe and to measure the distortion of $S(\mathbf{k})$, we can understand suspension behavior and improve the predictability of the theories and computer models. Results of the static structure factor from experiments can be used to rigorously test existing and new theories, as well as simulation methods. Second, $S(\mathbf{k})$ is itself a direct result of an analytical solution of the Fourier transform pair-distribution correlation $g(\mathbf{r})$ and the pair-particle convection-diffusion equation of the pair probability density. For these reasons, the static structure factor is of fundamental interest.

Existing theories have focused on the prediction of deformation of the nonequilibrium static structure factor, $S(\mathbf{k})$, and its relation to suspension macroscopic properties. These theories centralize on the perturbation about the equilibrium structure factor $S(k)$. They are applicable to dilute suspensions and to the limit of small shear rates since the models take rigorous account only of the pairwise thermodynamic interactions between particles

and either neglect completely or include only the pairwise hydrodynamic interactions. Johnson *et al.* (1988) and Ackerson (1989) have reported a short review of the theories for the nonequilibrium static structure factor $S(\mathbf{k})$ by Ronis (1984, 1984, 1986), Schwarzl and Hess (1986) and Dhont (1987, 1989). Results of small-wave-vector static structure factor measurements from Ackerson have shown large disagreements with these theories as the volume fraction of the suspension subjected to small shear rates increases.

Since these theories are referenced to the equilibrium state, the general solution of the static structure factor can be expected in the following form:

$$S(\mathbf{k}, Pe) = S(k) + Pe\, S^{1}(\mathbf{k}) + Pe^{2}\, S^{2}(\mathbf{k}) + ... \tag{6.2}$$

Equation (6.2) is truncated after the term with $O(Pe^{2})$ and is valid for $Pe \ll 1$. $S^{1}(\mathbf{k})$ and $S^{2}(\mathbf{k})$ are the first- and second-order nonequilibrium static structure factors, respectively and predictions of them vary among theories. Dhont has employed a singular perturbation analysis method to show that in the limit of small shear rates the explicit Fourier transform of the Smoluchowski equation yields a k-space boundary layer near $k = 0$ whose width scales as $Pe^{\frac{1}{2}}$. In real space this corresponds to the usual, well understood, problem of a singular perturbation for large $r \approx O(Pe^{-1/2})$ when the convective shear motion balances the diffusive motion. Dhont's result predicts that the expansion for $S(\mathbf{k},Pe)$ proceeds as:

$$S(\mathbf{k},Pe) = S_{o}(k) + Pe^{1/2}\, S^{1}(\mathbf{k},Pe) + ... \tag{6.3}$$

However, Brady (*unpublished work*) has shown that although the expansion is singular

with an outer region scaling as $Pe^{-1/2}$, because the inner boundary condition on the pair-distribution function at contact is of a quadrupole character, this causes the singular nature to appear at higher order, specifically,

$$S(\mathbf{k},Pe) = S_o(k) + Pe\, S^1(k) + Pe^{3/2}\, S^2(k) + ... \tag{6.4}$$

Our purposes in this section are to determine the nonequilibrium structure factor for dense hard-sphere suspensions at all shear rates and provide a direct comparison of our calculations with experiments. This comparison will verify the microstructure which is obtained by Stokesian dynamics in agreement with experimental results. For spherical particles, the equilibrium static structure factor, $S(k)$ can be computed according to:

$$S(k) = 1 + 4\pi n \int_0^\infty r^2\, [g(r) - 1]\, \frac{\sin(kr)}{kr} dr \ , \tag{6.5}$$

where k is the scattered wave number and n is the particle number density, i.e., n=$\frac{N}{V}$ with V the volume of the unit cell which contains N particles. The scattered wave number is given by:

$$k = |\,\mathbf{k}\,|\ \frac{4\pi}{\lambda}\ \sin\frac{\theta}{2} \ , \tag{6.6}$$

where $\mathbf{k}$ is the wave vector, λ is the wavelength of the incident radiation and θ is the scattering angle.

Similar to the calculation of the pair-distribution function and the plane projection distribution which is presented in sections VI.2.1 and VI.2.2, we compute the nonequi-

librium static line and plane structure factors. During the course of the dynamic simulations, the particle positions are used to compute the nonequilibrium static structure factor from the following discrete Fourier transform relation:

$$S(\mathbf{k}, Pe) \equiv \frac{1}{N} \sum_{j=1}^{N} \sum_{l=1}^{N} \langle\, exp\,[i\,\mathbf{k}\cdot\mathbf{r}_{jl}]\,\rangle \ , \tag{6.7}$$

where $\mathbf{r}_{jl} = \mathbf{r}_j - \mathbf{r}_l$ is the separation distance between particle j and particle l, i inside the bracket the denotes an imaginary number, $\langle\ \rangle$ implies an ensemble average over all particle configurations and the wave number is nondimensionalized with the particle radius a. From each particle configuration, the structure factors are computed with a selected range of the wave numbers. Small- and large-wave-number structure factors measure the long- and short-range correlation of the particle configurations, respectively. The dynamic simulations with 123 and 126 particles offer correlations of different particle positions up to three particle diameters and they are used to compute $S(\mathbf{k})$.

VI.2.4.1 The Line Structure Factors $S(k_x)$, $S(k_y)$ and $S(k_z)$

The line structure factors $S(k_x)$, $S(k_y)$ and $S(k_z)$ are computed by choosing the wave vector $\mathbf{k}$ parallel to the k_x-, k_y- and k_z-axis, respectively. Recall that the flow direction is the x-axis, the velocity gradient y and the vorticity z. To compute $S(k_x)$ for example, we fix the dimensionless wave numbers k_y=k_z=0 and vary only the wave number k_x. The Cosine Fourier transform is applied in equation (6.7) to compute these line structure factors and they are averaged over time during the course of dynamic simulations.

Figure 6.18 shows a plot of the equilibrium structure factor $S(k)$ for hard-sphere

suspensions at a volume fraction ϕ=0.45 with 81 particles at Pe=0. The dynamic simulations give 500 samples of the particle positions from which we computed the equilibrium structure factor along the k_x-, k_y- and k_z-axis. The three curves $S(k_x)$, $S(k_y)$ and $S(k_z)$ for undeformed hard spheres show small variation for an isotropic random structure of a hard-sphere distribution, which is not expected since 500 samples for 81 particles show a good comparison for the angularly averaged pair-distribution function $g(r)$ with that of a hard-sphere distribution as shown in Fig.4.1. The small variation in the equilibrium structure factor is likely due to the small number of samples of particle positions and small number of particles in the simulation. The first intensity maximum is observed at the dimensionless wave numbers k_x, k_y, $k_z \approx$ 3.5 which is commonly known and labeled as the Debye-Scherrer ring. The peaks at the wave number $k_{max} \approx 3.5$ can be used to compute the particle center-center spacing according to the relation (Laun *et al.* (1992)):

$$d = \frac{4\pi}{\sqrt{3}\, k_{max}} , \tag{6.8}$$

with $k_{max} \approx 3.5$, $d \approx 2.07$ which is in agreement with the value of 2.025 obtained from the distribution function $g(r)$ for hard spheres with Pe=0 and 123 particles reported in section VI.2.1.

Recall that Fig.6.11.b shows the hexagonal packing of strings of particles which are constructed from the plane projection distribution function $g(z, y)$ for 81 particles at Pe=10. The packing pattern is rotated with a small angle θ=-15°. The value of the angle θ is determined by varying the angle shown in equation (6.6) for the incident wave vector and then computing the line structure factor with wave numbers parallel to

these lines. Results are plotted in Fig.6.19 for the nonequilibrium structure factor with different angles: θ ($\triangle$) -15°, (——) 0° (which is $S(k_z)$), ($\square$) 45° and (...) 90° (which is $S(k_y)$). The upper right figure shows angle θ relative to the k_z-axis and is defined in the k_x-k_y plane. The figure shows clearly that the structure factors which are computed with the wave numbers parallel to the -15° and 45° lines give strong scattering light intensity patterns. The strings of particles with their axes on the -15° and 45° lines give the high intensity peaks seen at the wave numbers $k \approx 3.6$, 6.6, and 7.6. As expected for the rotated hexagonal packing, $S(k_y)$ and $S(k_z)$ show negligible scattered intensity. Note that a dimensionless wave number $k \approx 6$ comes from light with a wavelength $\lambda \approx \frac{1}{k}=\frac{1}{6}$ of the particle radius. Therefore, the structure factors with intensity peaks computed at these large wave numbers (short wavelengths) can capture only the short-range correlation of particles in the string formation and not the hexagonal packing. To probe the long-range order of the hexagonally packed particles which extends to several particle diameters, dimensionless wave numbers of $O(2a)$ or smaller must be used to compute the structure factor and this is the main reason why simulations with a large number of particles are necessary as we now show with 123 and 126 particles.

Figures 6.20, 6.21, and 6.22 show a comparison of the nonequilibrium line structure factors $S(k_x)$, $S(k_y)$, and $S(k_z)$ with 123 particles and three different Péclet numbers: ($\square$) 0.43, ($\bullet$) 10 and ($\triangle$) 10^3, respectively. Figure 6.20 shows a small difference for $S(k_x)$ with different Péclet numbers. This is expected due to large and constant changes of the particle positions in the flow direction, the x-axis. $S(k_x)$ for the runs with Pe=10 shows four peaks at regular spacing of the dimensionless wave number k_x, but the intensities of these peaks are relatively small to be attributed to an ordering of particles along the

k_x-axis.

Figure 6.21 illustrates a comparison of $S(k_y)$ for different Péclet numbers. While $S(k_y)$ for Pe = 0.43 and 10^3 shows insignificant scattered intensity, $S(k_y)$ of Pe=10 displays clearly two peaks with intensity maxima: one peak at the wave number $k_y \approx 3.6$ (the Debye-Scherrer ring) with scattered intensity of $O(N)$ and one smaller and less intense peak at larger wave number $k_y \approx 7.4$. It is evident that the two high scattered intensity peaks reflect a strong ordering of the suspensions. The peak at longer wave number $k_y \approx 7.4$ (shorter wave length) must reflect the string formation of the particles. Before the primary intensity maxima can be labeled as the signature of the long-range hexagonal packing, we need to examine and cross check with other evidences, especially to compare with experiments. One concrete piece of information is that $S(k_y)$ with Pe=10 displays the strong ordering of the particles along the k_y-axis.

A similar comparison for $S(k_z)$ can be seen from Fig.6.22 which shows only one intense peak for Pe=10 and very small scattered intensity for Pe = 0.43 and 10^3. The intense peak of $S(k_z)$ with Pe=10 shows up at a larger wave number, $k_z \approx 6$, compared to $k_y \approx 3.6$ for $S(k_y)$ in Fig.6.21. At this large wave number, the line structure factor $S(k_z)$ probes a strong correlation of the stringed particles. $S(k_y)$ and $S(k_z)$ show strong ordering of the particle positions in the k_y- and k_z-direction for hard spheres at Pe=10 and it is consistent with the information obtained from the plane projection distribution function in section VI.2.

Xue and Grest (1990) have reported a similar finding of the layering order of the particles in the presence of an oscillating shear flow. Their results for the anisotropic

structure factors were obtained by Brownian dynamics simulation method which is Stokesian dynamics without hydrodynamic interactions. Because there are no hydrodynamic interactions, short-range repulsive interparticle forces are needed to prevent particle overlap and set the volume fraction. A repulsive Yukawa potential (Robbins *et al.* (1988)) was used in their model. From the ratio of the lengths of a rectangular unit cell which contains 504 particles, it is estimated that the volume fraction of the suspension in their model is $\phi \approx 0.52$ (the interparticle spacing a in their model is equivalent to our particle diameter). The suspension is close packed at rest and the oscillatory shear is applied to melt the equilibrium crystalline structure and randomize it to the string phase. As the suspension changes to a string ordering phase, their results for the structure factor displayed two intense peaks for the velocity gradient direction and one less intense peak for the vorticity direction. In addition, the structure factors show peaks with different intensities for various shear rates at identical wave numbers. Their suspensions are seen to be ordered in an oscillatory shear independent of shear rates which the ordering fashions may not be the same . Their results further show that the string order is independent of the amplitude and the frequency of the oscillatory shear flow, but depends only on the product of the two in the range of dimensionless amplitude from 1 to 6.

To examine the long-range correlation of the hexagonal packing observed for the runs at Pe=10, we compute $S(k_y)$ and $S(k_z)$ with a smaller range of the wave numbers, k_y and k_z, from 0.5 to 2.5 and plot these line structure factors in Figures 6.23.a and 6.23.b, respectively. It is clear from these figures that at Pe=10, particle positions are correlated in a distinct pattern and the correlation is long ranged, as the line structure factors at small wave numbers show broad peaks with high scattered intensity compared to those

for Pe=0.43 and 10^3, which show minimum scattered intensity.

The anisotropic line structure factors can only probe the discrete spacings of the particle positions which are projected on the same axis with the incident wave vectors. To capture the details on the two-dimensional packing pattern, the static plane structure factors can be examined and those are discussed next. The static plane structure factors are computed in the velocity-velocity gradient plane, $S(k_x, k_y)$, in the velocity-vorticity plane, $S(k_x, k_z)$ and in the vorticity-velocity gradient plane, $S(k_z, k_y)$.

VI.2.4.2 The Plane Structure Factors $S(k_x, k_y)$, $S(k_x, k_z)$ and $S(k_z, k_y)$

The plane structure factors $S(k_x, k_y)$, $S(k_x, k_z)$ and $S(k_z, k_y)$ are computed by choosing the wave vector parallel to each of the plane of interest. To compute $S(k_x, k_y)$ for example, we fix the wave number k_z=0 and vary k_x and k_y. The Cosine Fourier transform is again applied in equation (6.7) to compute and average these plane structure factors over time during the course of dynamic simulations. The dimensionless wave numbers k_x, k_y and k_z are varied from $\pm$0.5 to $\pm$4.0. The plane structure factors are plotted in a contour plot with four symmetrical quadrants similar to the topographical plots of the small angle neutron scattering (SANS) measurements of the static plane structure factors reported by Johnson *et al.* (1988), van der Werff (1990) and Laun *et al.* (1992). This allows a comparison of our calculations and the experiments. In the first quadrant, both the wave numbers parallel to the horizontal and vertical axis are positive and vary from 0.5 to 4.0. For the second quadrant, the wave number parallel to the vertical axis is unchanged and the wave number parallel to the horizontal axis is now negative and ranges from -4.0 to -0.5. The third and fourth quadrants are mirror

images of the first and the second quadrant, respectively.

Figure 6.24 illustrates a comparison of the plane structure factor computed in the $x-y$ plane (the velocity-velocity gradient plane), $S(k_x, k_y)$, with 123 particles and different Péclet numbers:Pe = 0 (upper left), 0.43 (upper right), 10 (lower left) and 10^3 (lower right) obtained by Stokesian dynamics. Regions of light color represent high scattering light intensity and regions of dark color represent low scattering light intensity. Starting from the upper left, $S(k_x, k_y)$ shows the primary intensity of the symmetric Debye-Scherrer ring for hard spheres at equilibrium (Pe=0). The dynamic simulations for 123 particles at Pe=0 give 100 particle configurations for run with 10,000 time steps and these samples are used to compute $S(k_x, k_y)$. The symmetric ring reflects the random structure at rest for hard-sphere suspensions at a volume fraction ϕ=0.45. $S(k_x, k_y)$ shows the slight distortion of the Debye-Scherrer ring to an elliptical shape for suspensions with a small deformation at Pe=0.43 (upper right). In the k-space, the deformation is seen as a mirror image of the real r-space. Small-wave-vector measurements of the structure factors for hard-sphere colloidal dispersions in a weak shear flow by Johnson *et al.* (1988), Ackerson (1989) and Ronis (1984) have shown similar distortion of the structure factor in the region of small shear rate.

As Pe increases into the string ordered phase ($Pe \approx 10$), $S(k_x, k_y)$ changes from the elliptical formation into circular regions of high scattered intensity along the horizontal line with wave numbers $k_y \approx \pm 4$ and two "bands" of strong intensity along the vertical lime with wave numbers $k_x \approx \pm 3$. Recall that in Fig.6.10.d we present the striking evidence of the particle positions which are constructed with the information obtained

from the plane projection distribution function $g(z,y)$, $g(x,y)$ and $g(x,z)$. Indeed if we compare the particle positions for the $x-y$ plane in Fig.6.10.d and this figure for a contour plot of $S(k_x,k_y)$ with Pe=10, then the "bands" of high scattered intensity are the spectroscopic signature of the horizontal strings of particles (the middle right figure in Fig.6.10.d) and the circular regions of intensity maxima are the spectroscopic signature of the vertical strings of particles (the upper right and middle right figure in Fig.6.10.d). The horizontal and vertical strings of flowing particles are combined to assemble the complete hexagonal packing as seen in Fig.6.10.d in the real r-space. There are also several narrow regions with strong scattered intensity at smaller wave numbers inside the primary ring. Their presence implies the strong ordering is long ranged.

At much higher shear rate (Pe=10^3), the hydrodynamic interactions are dominant over the Brownian forces and destroy the particle order. A contour plot of $S(k_x,k_y)$ with Pe=10^3 (lower right) shows large distortion of the Debye-Scherrer ring in the k_x-k_y space. In contrast to $S(k_y)$ for Pe=0 which shows regions of minimum scattered intensity outside the Debye-Scherrer ring (dark color regions), $S(k_x,k_y)$ for 10^3 shows scattered intensity everywhere in this region and reflects the presence of clustered particles in a hydrodynamic dominated suspension. Note that the region inside the Debye-Scherrer ring with small wave numbers shows insignificant scattered intensity, which is expected as this region probes the long range correlation of the particle positions. Our largest simulation size of 123 or 126 particles is limited to a three-particle-diameter correlation. Only when the strong ordering persists during the entire time of dynamic simulations such as seen at Pe=10, the plane structure factors show some long-range packing of the particles.

Contour plots of the static plane structure factors in the $z-y$ plane (the vorticity-velocity gradient plane) with different Péclet numbers are presented in Fig.6.25. The light-high and dark-low color scale for scattering light intensity and the range of wave numbers are the same as shown in Fig.6.24. k_z is the horizontal axis and k_y is the vertical axis. Again starting from the upper left, $S(k_z, k_y)$ shows primary scattered intensity of the Debye-Scherrer ring for suspensions at a rest state (Pe=0) and for suspensions with a small deformation, Pe=0.43 (upper right). As Pe increases to 10, $S(k_z, k_y)$ shows a distinct "hexagonal" pattern of scattered intensity maxima which is superimposed on the halo ring (lower left). Another six smaller intensity maxima in the region of smaller wave numbers indicates that the strong ordering is indeed long ranged. In reference to the particle positions in the $z-y$ plane shown in the upper right figure of Fig.6.10.d, we observe a clear evidence that the nonequilibrium structure factor $S(k_z, k_y)$ probes the "hexagonal" packing of strings of particles flowing directly out of the $z-y$ plane. The halo pattern is destroyed at strong shear rates, as seen in a contour plot of $S(k_z, k_y)$ with Pe=10^3 (lower right). The most recent SANS measurements for the plane structure factors by Laun *et al.* (1992) for suspensions of electrostatically stabilized styrene-ethylacrylate-copolymer spheres in glycol and in water at a similar volume fraction ϕ=0.434 (labeled as system "A4G" in their experiments) in both Poiseuille and Couette flows have shown the same halo ring of intensity maxima patterns for strongly ordered structures in the shear thinning region. However, in the plateau region where the viscosity is minimum, the halo ring was destroyed (Figures 9, 23, and 24 from Laun *et al.* are copied and shown in Figures 6.34 and 6.35 for comparison.) This is different to our findings which display a strongly ordered structure in the region of minimum viscosity and not in the

shear thinning region. However, the important goal is to find the SANS pattern of the structure factor relating to the microstructural order. From their experiments, the halo ring pattern is the spectroscopic signature of an ordered suspension and our results for the structure factors at Pe=10 show an identical pattern of scattering light intensity. The shift of the region where the shear viscosity is minimum is likely due to that the particles in the experiments may not be completely force-free, i.e., not a true hard-sphere suspension, and this can clearly be seen by examining the experimental results for the shear viscosity. In the region of minimum viscosity, Laun *et al.* obtained a dimensional viscosity $\eta \approx 1$ Pa s (cf. Fig.6.34) (or a dimensionless viscosity $\eta_r \approx 50$ using 20 mPa s glycol solvent at 20 $^{\circ}C$) at a shear rate $\dot{\gamma} = 100\ sec^{-1}$ (or equivalent to our dimensionless Péclet number of ≈ 50). Their minimum shear viscosity is about seven times higher than our simulation results and experimental results from van der Werff and de Kruif for hard spheres.

The microstructure is very special at $Pe \approx 10$ as the influences of the shear and the Brownian force balance and induce the flowing particles into strong ordering. Figure 6.26 shows a comparison of the static plane structure factors computed on three planes: $S(k_x, k_y)$ (left figure), $S(k_x, k_z)$ (central figure) and $S(k_z, k_y)$ (right figure). This figure is the the k-space spectroscopic microstructure (the Fourier transform) of the particle positions shown in Fig.6.10.d. We have already discussed $S(k_x, k_y)$ and $S(k_z, k_y)$ in Figures 6.24 and 6.25, respectively. With Fig.6.26, it is made more clear that the circular regions of intensity maxima from a contour plot of $S(k_x, k_y)$ is the scattered intensity obtained from the "hexagonal" packing. By comparing $S(k_x, k_y)$ with $S(k_x, k_z)$, it is seen that $S(k_x, k_z)$ shows two "bands" of high scattered intensity along the wave numbers

$k_y \approx \pm 4$ which are very similar to the two bands seen from $S(k_x, k_y)$. What is absent from $S(k_x, k_z)$ are the regions of primary maxima intensity. Horizontal strings of flowing particles are staggered into a body-centered fashion in the $x-z$ plane as constructed in the lower right figure of Fig.6.10.d and this pattern enables the "hexagonal" packing of strings of particles to be seen in the $z-y$ plane. The two vertical bands of high scattered intensity from $S(k_x, k_z)$ probe the correlation of horizontal strings of particles and so do the two vertical bands from $S(k_x, k_y)$. The circular regions of intensity maxima from $S(k_x, k_y)$ probe the hexagonal packing and in the $x-y$ plane the hexagonal packing is mapped into the horizontal lines in k-space. The halo ring with intensity maxima is clearly seen from a contour plot of $S(k_z, k_y)$.

To examine only the contribution from the shear-induced ordering, we compute and plot the perturbed structure factors, $S^{'}(\mathbf{k},Pe)$, which is defined as $S^{'}(\mathbf{k}, Pe) \equiv S(\mathbf{k}, Pe) - S(k)$ for hard spheres at Pe=10 in Fig.6.27. The left column shows the unperturbed static $S(\mathbf{k}, Pe)$ and the right column shows the perturbed static structure factors $S^{'}(\mathbf{k}, Pe)$. The first row displays the structure factors computed in the $x-z$ plane, followed by the the structure factors computed in the $z-y$ plane on the second row. It is clear that the ordering spectroscopic signatures are not disturbed by the pure random Brownian contribution as the perturbed structure factors display similar scattered intensity pattern as the unperturbed structure factors. This is expected since our spheres are identical and there is no back scattering due to polydispersity as is commonly observed in experiments (Pusey (1987), van Veluwen *et al.* (1988)). Both the vertical bands from $S(k_x, k_z)$ and the halo intensity maxima are seen from their corresponding perturbed structure factors.

The static structure factors show clearly three different spectroscopic signatures of the hard spheres and these signals can be mapped to the real space and related to the deformation of the suspension. The equilibrium structure which is amorphous at rest for ϕ=0.45 is slightly distorted at small shear rates. As the hard spheres are sheared past the shear thinning region, the microstructure is strongly ordered and the flowing particles are packed into strings in a "hexagonal" pattern. At stronger shear rates in the shear thickening region, the hydrodynamic influence is dominant, the shear-induced ordering is completely destroyed, and the microstructure shows clustering of particles. The microstructure obtained by the spectroscopic static structure factors in k-space is very consistent with the information obtained by the plane projection distribution function in the real r-space. It is important to note that our static structure factors for the microstructure is confirmed by the SANS measurements. Before we address the important question of the relation of the shear thinning and shear thickening to the microstructure, there is one more fundamental property of the suspensions, the self-diffusion of the suspended particles, that we need to examine, and it is discussed in the next section.

VI.3 The Self-Diffusivities

In this section we focus on the particle motions by examining the short- and long-time self-diffusion coefficients of Brownian particles in dense suspensions. Theoretical predictions and experimental measurements of self-diffusivity have been a concern to scientists for years (Eckstein, Bailey and Shapiro (1977), Kops-Werkhoven *et al.* (1981, 1982), Snook *et al.* (1983), van Megen *et al.* (1986), Rallison and Hinch (1986), Leighton

and Acrivos (1987), Qiu *et al.* (1988), Cichoki and Felderhof (1988), Phan and Leighton (1992)). The short-time self-diffusivity measures the instantaneous mobility of the particles in the suspension: the time scale is so short that the particles do not have time to move a distance comparable to their own size or to the interparticle spacing. It conveys the static information of the local structure and mobility of the suspension. In contrast to the short-time self-diffusivity, the long-time self-diffusivity measures the dynamic behavior of the suspension as particles must travel a distance far from its starting location, deform the local structure and exchange places with neighbors. The long-time self-diffusivity also describes the internal mixing at the particle level.

VI.3.1 The Short-Time Self-Diffusion Coefficients

We denote the short-time translational and rotational self-diffusion coefficient as D_o^* and D_r^*, respectively. D_o^* is normalized by the infinite dilution diffusion coefficient of a sphere $D_o = kT/(6\pi\eta a)$ and D_r^* is normalized by $D_r = kT/(8\pi\eta a^3)$. The short-time self-diffusion coefficients D_o^* and D_r^* are reported in Table 6.5.a for the runs with 27 particles and Table 6.5.b for the runs with 63, 64, 81 and 123 particles and also for a monolayer with 25 particles. Columns (3) to (6) are the steady short-time translational self-diffusion coefficients computed in the x-direction, $D_{o_{xx}}^*$, in the y-direction, $D_{o_{yy}}^*$, in the z-direction, $D_{o_{zz}}^*$, the mean, i.e., $D_o^* = \frac{1}{3}(D_{o_{xx}}^* + D_{o_{yy}}^* + D_{o_{zz}}^*)$ and its standard deviation. Similarly, columns (8) to (12) are the short-time rotational self-diffusion coefficients $D_{r_{xx}}^*$, $D_{r_{yy}}^*$, $D_{r_{zz}}^*$, the mean D_r^* and its standard deviation. For the monolayer model, the z-component of the short-time self-diffusivities are not computed and the mean is simply the x and y average, i.e., $D_o^* = \frac{1}{2}(D_{o_{xx}}^* + D_{o_{yy}}^*)$. The short-time self-diffusion coefficient

is defined in equations (2.25) and (2.26). Note that D_o^* is not a true diffusivity in the sense of the mean-square displacement growing linearly with time, except at $Pe \equiv 0$. At finite Pe, the instantaneous motion is not necessarily diffusive, but nevertheless D_o^* gives a measure of the local mobility of a particle.

Results of the steady D_o^* from Table 6.5.a are plotted in Fig.6.28.a as a function of the Péclet number. The short-time translational self-diffusion coefficient is relatively constant for $Pe < 1$, decreases slightly as Pe increases to 1, increases to a maximum at $Pe \approx 10$ and then decreases with increasing Péclet number. The behavior of the short-time self-diffusion coefficient D_o^* can be explained by relating it to the deformation of the suspension. The structure of hard spheres which is liquid-like at rest, is slightly deformed at small shear rates ($Pe < 1$). In this strong Brownian region, Brownian motion is still the dominating force and capable of restoring the isotropic structure from a small departure from equilibrium. The result is a relatively constant D_o^*. The region with $Pe \approx 10$ is very special; recall that it is the ordered region. In this region, D_o^* increases to a maximum value, which implies that the particles are most mobile and are relatively well dispersed. This is consistent with the microstructure which we described in section VI.2. The balance of Brownian and hydrodynamic forces induces a strongly ordered suspension with strings of flowing hexagonally packed particles. The particles are not only very well separated relative to each others but uniformly spaced in strings. As a consequence, the mobility of particles in the packing is greatly enhanced and as a result, we observe the maximum of the short-time self-diffusion coefficient.

As the shear rate increases ($Pe > 10$), the hydrodynamic influence becomes increas-

ingly important and dominates over the diminishing Brownian force. Large deformations of the suspensions in this region are seen due to the formations of particle clusters whose size grows with the Péclet number. Owing to the formation of close pairs and larger aggregates (cf. Figures 6.15.a-c), the short-time self-diffusion coefficient decreases with increasing Pe. Because of lubrication forces, closely spaced or touching particles should move as if they were a single larger particle on a short time scale, and there is a corresponding decrease in the mobility of the suspension, and hence in the short-time self-diffusivities. Note that since the mobility scales with the inverse of particle size, the drop from 0.217 to 0.021 would indicate a characteristic size of 10 particles.

In Fig.6.28.a, the two asymptotes of D_o^* in the limit of pure Brownian motion ($Pe \to 0$) and pure hydrodynamics ($Pe \to \infty$) are plotted. At Pe=0.01, D_o^* equals to 0.17 and is well below the limit of D_o^*=0.217 at $Pe \to 0$. Even a negligibly small contribution from the convective shear at Pe=0.01 seems to influence and disturb the random structure of hard spheres. Similarly, D_o^* equals to 0.07 at Pe=10^4 and is well above the limit of D_o^*=0.021 at $Pe \to \infty$. A minute Brownian contribution at Pe=10^3 still strongly dictates by rupturing the large clusters giving an enhanced local mobility. The relation of D_r^* as a function of the Péclet number is plotted in Fig.6.28.b, and we observe a behavior of the short-time rotational self-diffusion coefficient which is very similar with the short-time translational self-diffusion coefficient. D_r^* is seen to decrease with increasing Pe except in the region of $Pe \approx 10$ at which it is maximum.

Table 6.5.b shows small variations in D_o^* and D_r^* with an increasing number of particles. The only noticeable variation is in the short-time translational self-diffusion coeffi-

cients computed in different directions and shown in Fig.6.29. $D^{*}_{o_{xx}}$ is seen consistently slightly larger ($\approx$ 2 to 5%) than $D^{*}_{o_{yy}}$ and $D^{*}_{o_{zz}}$. The flow direction is the x-axis and we see here the advective effect which increases the mobility of the particles along the flow direction. This trend is not seen for the rotational mode of the self-diffusivities as shown in Fig.6.30.

The most noticeable difference in the short-time self-diffusivities is that results of D^{*}_{o} obtained from a monolayer are as much as two times larger than that of a three-dimension model and this is shown in Table 6.5.b for the monolayer runs with 25 particles. There is no difference in D^{*}_{r} obtained by both models. For a monolayer, particles are restricted to movements only in the x- and the y-axis and can only rotate in the z-axis. These restrictions are likely to enhance the instantaneous mobility of the particles in the x and y-directions to compensate for zero mobility in the z-direction. Next, we examine the dynamics of particle diffusive behavior in a simple shear flow by focusing on the long-time self-diffusivity.

VI.3.2 The Long-Time Self-Diffusion Coefficients

The long-time self-diffusion coefficients are reported in Table 6.6 for the runs with 27 particles. Column (1) is the Péclet number. As seen from this table, 80 to 100 time units are required for the sampling of particle positions for the computing of long-time self-diffusivities. Simulations with larger number of particles (N = 63, 64 ,81 and 123) are relatively short and do not provide sufficient numbers of particle configurations, and this is the reason why we can only compute the long-time self-diffusivities with runs of 27 particles. In Table 6.6, columns (2) to (5) are the steady long-time self-diffusion

coefficients computed in the velocity gradient direction, $D^{s}_{\infty,yy}$, its standard deviation, the steady long-time self-diffusion coefficient computed in the vorticity direction, $D^{s}_{\infty,zz}$ and its standard deviation, respectively. These coefficients are normalized by the infinite dilution diffusion coefficient $D_o = kT/(6\pi\eta a)$. The long-time self-diffusion coefficients are defined in equation (2.27) and computed from the mean-square displacements of the particle positions obtained by dynamic simulation. The final mean value of these coefficients are sampled from a number of time intervals shown in column (7) and the length of time for each sample is displayed in column (6). Note that the reported values for the normalized $D^{s}_{\infty,yy}$ and $D^{s}_{\infty,zz}$ in Table 6.6 are scaled with the diffusive time.

The mean-square displacements have the following long-time behavior:

$$\langle\, (y(t) - y(t_{ref}))^2 \,\rangle \;=\; 2\, D^{s}_{\infty,yy}\, (t - t_{ref}) \;, \tag{6.9}$$

$$\langle\, (z(t) - z(t_{ref}))^2 \,\rangle \;=\; 2\, D^{s}_{\infty,zz}\, (t - t_{ref}) \;. \tag{6.10}$$

$D^{s}_{\infty,yy}$ and $D^{s}_{\infty,zz}$ are computed by first plotting the mean-square displacements of the particles against the elapsed time. The asymptotic value is obtained and then averaged over a number of samples to improve the statistics of these coefficients. The particle trajectories are followed during the course of dynamic simulations and the sudden jumps in positions associated with periodic boundary conditions are removed by mapping the particle trajectories as those would occur in the unbounded fluid. Bossis and Brady (1987) have reported details of the self-diffusivities of Brownian particles for a monolayer model at an areal fraction $\phi_A = 0.453$ which is comparable to ϕ=0.302. Their results

show a remarkable transition from a Brownian motion dominated regime ($Pe < 1$) to a hydrodynamic dominated regime ($Pe > 10$) with a significant change in the behavior of the long-time self-diffusion coefficient computed in the velocity gradient direction.

Figure 6.31 is a log-log plot of the simulation results for $D^*_{\infty,yy}/D_o$ as a function of the Péclet number. For $Pe > 1$, the time should scale with $\dot{\gamma}^{-1}$ and this is equivalent to multiplying $D^*_{\infty,yy}$ and $D^*_{\infty,zz}$ reported in Table 6.6 with Pe. Recall that the velocity gradient of the shear flow is in the y-direction. For $Pe < 1$, the suspension is essentially all Brownian and the dimensionless diffusion coefficient is relatively constant as shown with the limit of $D^*_{\infty,yy}/D_o \approx 0.06$ as $Pe \to 0$. It is seen from Table 6.6 that $D^*_{\infty,yy}$ is smaller than the short-time D^*_o which equals to 0.217 at Pe=0 (cf. Table 6.5.a). This is expected because the diffusing particle must move a distance away from its starting position, deform the local structure and exchange places with near neighbors. Such behavior has recently been measured by van Megen, Underwood and Snook (1986) in concentrated hard-sphere colloidal dispersions. Their values for the dimensionless short- and long-time self-diffusion coefficient of unperturbed suspensions at an effective volume fraction ϕ_E= 0.444 are 0.22 and 0.07, respectively. We obtained 0.217 for the short-time and 0.06 for the long-time self-diffusivities for hard spheres at ϕ=0.45. The comparison is clearly excellent.

At much higher Péclet number ($Pe > 10^2$), Fig.6.31 shows a very different relation of $D^*_{\infty,yy}/D_o$ which grows linearly with increasing Pe. This is expected based on the purely dimensional analysis: as $Pe \to \infty$, the only proper scale for diffusion is $\dot{\gamma}a^2$; therefore, $D^*_{\infty,yy}$ which is nondimensionalized by D_o, should scale with Pe as $Pe \to \infty$. Our

results indeed show this behavior remarkably well with $D^{*}_{\infty,yy}/D_o \approx 0.065$ for $Pe \rightarrow \infty$. Experiments by Eckstein *et al.* (1977) and by Leighton and Acrivos (1987) have quantified the hydrodynamic dispersion of non-Brownian particles in a shear flow. This shear-induced diffusive motion arises from the deterministic chaos displayed by the highly nonlinear evolution equation for the particle positions (equation (2.7) as $Pe \rightarrow \infty$). The two sets of experiments agree only at low volume faction ($\phi < 0.2$), but at higher ϕ, while the results from Eckstein *et al.* show an asymptotic value $D^{*}_{\infty} \approx 0.03$ for $\phi > 0.2$, Leighton and Acrivos obtain increasing D^{*}_{∞} with large ϕ. The most recent experiment from Phan and Leighton (1992) shows the long-time self-diffusivity saturated at a value of 0.09 for ϕ=0.3. Our result, 0.065 lies between the results of these two groups and agrees reasonably well with the new experiments of Phan and Leighton.

Figure 6.31 also shows clearly the transitional Péclet number $\approx$ 10, where the behavior of the long-time self-diffusion coefficient changes from a strong Brownian regime to a hydrodynamic dominated regime. At Pe=10, $D^{*}_{\infty,yy}$ decreases to a minimum value which is two orders of magnitude less than that of $Pe < 1$. It is again the special region where the suspension strongly orders. Because of the order, the long-time self-diffusivity drops dramatically as the particles cannot break out of their strings. Results of Brownian dynamic simulations by Xue and Grest have also shown the similar minimum of long-time self-diffusivities of ordered suspensions in an oscillating shear flow.

The long-time self-diffusion coefficient computed in the vorticity direction, the z-axis, is plotted in Fig.6.32 as a function of the Péclet number. We observe a behavior similar to that of $D^{*}_{\infty,yy}/D_o$ in Fig.6.31. For slightly deformed hard spheres ($Pe < 1$), $D^{*}_{\infty,zz}$ is

relatively constant and for hydrodynamic dominated suspensions, the dimensional $D^{s}_{\infty,zz}$ scales with Pe. The two asymptotic values of $D^{s}_{\infty,zz}$ at $Pe \to 0$ and at $Pe \to \infty$ are similar to that of $D^{s}_{\infty,yy}$. Our results for $D^{s}_{\infty,zz}/D_o \approx 0.057$ in the limit of $Pe \to \infty$ compared well to 0.067 from most recent measurements of Phan and Leighton. In the special region of $Pe \approx 10$, $D^{s}_{\infty,zz}$ decreased to a minimum value, but it remains close to that of $Pe < 1$ in contrast to a more pronounced decrease of $D^{s}_{\infty,yy}$ in this region.

Our study of self-diffusion for dense hard-sphere suspensions shows a clear distinction between the diffusive regime ($Pe \to 0$) and a limit of strong hydrodynamics ($Pe \to \infty$) with a transition region with $Pe \approx 10$. The long-time self-diffusion coefficients D^{s}_{∞}, which are constant at small Péclet numbers, decrease to minimum value at the transitional region where the structure is strongly ordered and then grow linearly with increasing Pe. In this special transitional region, the short-time self-diffusion is maximum as the particles are relatively well separated and evenly spaced from each other. At high Pe, the reduction of the short-time self-diffusion coefficient is seen as a direct result of large particle clusters: particles cannot move without moving all members of the compact cluster even on the short time scale.

VI.4 Conclusions

We have seen the shear thinning and shear thickening behavior in dense suspensions, evidenced by the change of the steady shear viscosity with the Péclet numbers shown in section VI.1. In section VI.2 the dynamics of the shearing deformation to suspension microstructure was presented with details of the flowing particles in the real and Fourier space. In section VI.3 the diffusive motion of particles in a simple shear flow

was illustrated by examining the self-diffusivities. We can now combine all valuable information and address the important question of the relation of suspension macroscopic properties to the shear-induced microstructure. Recall that the suspension shear thins well before the ordering takes place at $Pe \approx 10$. The hexagonally packed particles slide relative to one another and flow with the bulk shear flow. This string formation has been observed experimentally in oscillatory shear (Ackerson and Pusey (1988) and Ackerson (1988, 1990)). Nonequilibrium molecular dynamic (NEMD) simulations of atomic liquids (Erpenbeck (1984), Heyes (1988), Weider *et al.* (1991), Laun *et al.* (1992)) and Brownian dynamic simulations (Xue and Grest (1990), Wilemski (1991), Rigors and Wilemski (1992), Cook and Wilemski (1992)) for hard spheres have also shown the ordered structures, but the string-like formation occurs in the shear thinning region compared to ours which can be seen only after termination of shear thinning. Furthermore, the results from these simulation methods, which neglect the many-body hydrodynamic interactions and must rely on some form of the repulsive force to avoid the particle overlap, tend to show structural order for a wider range of volume fraction. As we shall see in the next chapter where we discuss the rheological and microstructural behavior for moderately dense suspensions with a range of volume fraction from 0.316 to 0.419, the string formation could not be seen for hard spheres with volume fraction below 0.419 for a similar range of Péclet numbers from 0.01 to 10^5.

The tendency of the particles to flow as strings has been used to explain the shear thinning phenomenon observed in NEMD and Brownian dynamics. Although the Brownian suspensions in our study appear to form string-like order, the shear thinning is *not* due to this structural packing. It is rather due to the decrease of the direct Brownian

contribution to the stress since the hydrodynamic contribution to the stress is virtually unchanged from its zero Péclet number value even though the microstructure is significantly different (cf. Fig.6.1). This argument is made more clear with a plot of both the steady shear viscosity η_r and the long-time self-diffusion coefficient $D^*_{\infty,yy}/D_o$ as a function of the Péclet number in Fig.6.33. The left axis is for the steady shear viscosity (●) and the right axis is for the long-time self-diffusion coefficient (△). The figure shows clearly that the suspension has essentially completed the shear thinning process at Pe=3, while the long-time self-diffusion coefficient starts to decrease at Pe=3 and attains a minimum value at Pe=10. Strongly ordered structure occurs at Pe=10 as shown by the minimum $D^*_{\infty,yy}/D_o$ and in Fig.6.8.c but this shear-induced order *does not* cause the suspension to further shear thin. At Pe=3, we do not observe any ordered structure (cf. Fig.6.8.c) yet the steady shear viscosity is as small as that of Pe=10, where the string-like formation is found. This can also be seen from the results of Laun *et al.* which are shown in Figures 6.34 and 6.35. In Fig. 6.34, the upper figure is a plot of the shear viscosity obtained with different flow devices and the bottom figure is SANS measurements for the structure factor on the plane normal to the flow with different shear rates for Couette flow and in Fig.6.35 the structure factors measured in a Poiseuille flow. Their "A4G" system, which is a suspension of electrostatically stabilized styrene-ethylacrylate-copolymer at ϕ=0.434, is close to the volume fraction ϕ=0.45 in this study. The figures show clearly that strongly ordered structure, which were seen with halo rings of intensity maxima (at shear rates of $\dot{\gamma} = 0.6\ sec^{-1}$ and $1\ sec^{-1}$ for Couette flow, and $\dot{\gamma} = 0.1\ sec^{-1}$ for Poiseuille flow) in the shear thinning region, completely disappeared in the plateau region of minimum shear viscosity (at $\dot{\gamma} = 50\ sec^{-1}$ for Couette flow, and $\dot{\gamma} = 83\ sec^{-1}$

for Poiseuille flow). The minimum shear viscosity does not necessarily reflect an ordered structure as seen in their experiments.

The shear thickening phenomenon can be explained by relating the high steady shear viscosity to the formation of large clusters of particles which disrupt the imposed shear flow. This flow blockage has also been seen in recent experiments by Boersma *et al.* for suspensions of large particles ($Pe \rightarrow \infty$). The steady shear viscosity for an isotropic structure is shown in Fig.4.4 and its value $\eta_r \approx 6$ is well below $\eta_r \approx 12$ at $Pe=10^4$ seen in Fig.6.2. Our results which are presented with the actual snap shots of the particle positions in a monolayer model at $Pe=10^3$ (cf. Figures 6.15.a-c) and large values of the pair-distribution function evaluated for touching particles for large Péclet numbers (cf. Fig.6.7) evidently show that for hard spheres the shear thickening is associated with the formation of elongated clusters of particles. This can also be argued from the fact that the viscosity scales as the cube of the largest length, and for a given number density of particles the only way to increase the viscosity is pack them into elongated clusters. Compact spherical clusters will not increase the viscosity. The lack of any observations of an ultimate shear thickening region with increasing shear rates in the experiments of van der Werff and de Kruif for silica hard spheres are probable due to a small range of shear rates. For Brownian hard spheres studied here, a Péclet number greater than 10^2 is needed in order to observe the shear thickening.

In this chapter, we have presented the Stokesian-dynamics simulation method and applied it to investigate the rheology, microstructure and self-diffusivities of dense hard-sphere suspensions at a volume fraction $\phi=0.45$ in a simple shear flow. The remarkably

good agreement between the computer simulation and experiment for the evolution of the steady shear viscosity and for the static structure factor with the Péclet number vindicates that Stokesian dynamics is well capable of excellent *quantitative* as well as *qualitative* predictive ability. More importantly, the method provides a detailed understanding of the fundamental mechanisms causing interesting rheological behavior and its important relation to the shear-induced microstructure.

Table 6.1.a: Statistics for simulations of hard-sphere suspensions at a volume fraction ϕ=0.45 and different Péclet numbers. Tables 6.1.a and 6.1.b give the necessary details of each run and the sampling statistics for the rheology. Column (1) is the Péclet number, Pe, and column (2) is the number of particles, N. Columns (3) and (4) are the starting time and the end time of the run, respectively. Column (5) is the time step and column (6) is the number of time steps. Column (7) is the length of time which is allowed for each sample interval and column (8) is the time units which sampling intervals are successively shifted in time. Column (9) is the total number of samples which is used to compute the mean and statistics for suspension rheology. Initial particle configurations of all the runs in the table are random except the special case with $Pe = ^{*}10$ shown at the end of the table. For the run with $Pe = ^{*}10$, the initial particle placement is obtained from the end of the run with Pe=10 and t_{end}= 100. The symbol (*) denotes that a new shear direction is tested along the y-axis. Results for the runs with larger number of particles and with monolayers are shown in Table 6.1.b. The first 5,000 to 10,000 time steps were discarded for the computing of suspension rheology.

Pe	N	t_{start}	t_{end}	Δt_{set}	NSTEPS	t_{diff}	t_{shift}	# *trials*
0.01	27	0.0	500.0	5×10^{-4}	10^6	130.0	10.0	25
0.10	27	0.0	500.0	10^{-3}	500000	100.0	10.0	35
0.43	27	0.0	50.0	10^{-3}	50000	40.0	1.0	5
1.00	27	0.0	100.0	10^{-3}	100000	80.0	2.0	11
3.00	27	0.0	150.0	10^{-3}	150000	60.0	2.0	41
6.00	27	0.0	50.0	10^{-3}	50000	40.0	1.0	6
7.00	27	0.0	50.0	10^{-3}	50000	40.0	1.0	6
10.00	27	0.0	100.0	10^{-3}	100000	60.0	2.0	16
20.00	27	0.0	60.0	10^{-3}	60000	40.0	1.0	16
10^2	27	0.0	100.0	10^{-3}	100000	60.0	2.0	16
2×10^2	27	0.0	60.0	10^{-3}	60000	40.0	1.0	11
10^3	27	0.0	100.0	10^{-3}	100000	60.0	2.0	16
10^4	27	0.0	70.0	10^{-3}	70000	50.0	1.0	11
10^5	27	0.0	100.0	10^{-3}	100000	60.0	6.0	9
10^6	27	0.0	46.0	5×10^{-4}	90000	40.0	1.0	6
∞	27	0.0	26.0	10^{-4}	250000	20.0		1
$^{*}10.00$	27	100.0	200.0	10^{-3}	100000	60.0	2.0	16

Table 6.1.b: Statistics for simulations of hard-sphere suspensions at a volume fraction ϕ=0.45 and different Péclet numbers. Table captions are the same as shown in Table 6.1.a. Initial particle configurations of all the runs with N = 63, 64, 81 and 123 are random. A series of four continuing runs for a monolayer model with 25 particles follows the order of bracketed numbers from [1] to [4] which are shown in the upper left of Pe in column (1).

Pe	N	t_{start}	t_{end}	Δt_{set}	NSTEPS	t_{diff}	t_{shift}	# *trials*
0.01	63	0.0	40.0	5×10^{-4}	80000	30.0	1.0	5
0.43	63	0.0	40.0	10^{-3}	40000	30.0	1.0	5
10.00	63	0.0	100.0	10^{-3}	100000	60.0	2.0	15
10.00	64	0.0	100.0	10^{-3}	100000	60.0	2.0	15
10^4	63	0.0	50.0	10^{-3}	50000	40.0	1.0	6
∞	64	0.0	30.0	10^{-4}	300000	26.0		1
0.01	81	0.0	60.0	5×10^{-4}	120000	46.0	1.0	6
0.43	81	0.0	60.0	10^{-3}	60000	46.0	1.0	6
10.00	81	0.0	60.0	10^{-3}	60000	46.0	1.0	6
10^4	81	0.0	56.0	10^{-3}	55000	40.0	1.0	6
0.43	123	0.0	40.0	5×10^{-4}	80000	36.0		1
10.00	123	0.0	50.0	10^{-3}	50000	46.0		1
10^3	123	0.0	40.0	10^{-3}	40000	36.0		1
[1] 0.01	25,2D	0.0	350.0	5×10^{-4}	700000	100.0	10.0	5
[2] 10.00	25,2D	350.0	700.0	10^{-3}	350000	60.0	10.0	30
[4] 10.00	25,2D	940.0	1240.0	10^{-3}	300000	60.0	10.0	27
[3] 10^3	25,2D	700.0	940.0	10^{-3}	240000	60.0	10.0	19

Table 6.2.a: Results of the steady shear viscosities obtained by Stokesian dynamics for hard-sphere suspensions at a volume fraction ϕ=0.45 and different Péclet numbers. Results are shown in this table for runs with 27 particles. Column (1) is the the Péclet number, Pe, and column (2) is the number of particles, N. Columns (3) to (8) are the mean and the standard deviation of the hydrodynamic, the Brownian and total viscosity, respectively. The run with $Pe = {}^{*}10$ denotes a new shear direction is tested along the y-axis. Simulation results with larger number of particles (N = 63, 64, 81 and 123) and a monolayer (2D) with 25 particles are shown in Table 6.2.b.

Pe	N	η_H	σ_{η_H}	η_B	σ_{η_B}	η_T	σ_{η_T}
0.01	27	4.611	0.005	9.052	9.111	14.644	9.114
0.10	27	4.573	0.035	7.128	0.623	12.701	0.646
0.43	27	4.713	0.008	6.289	0.056	11.001	0.608
1.00	27	4.795	0.009	3.737	0.018	9.531	0.025
3.00	27	4.512	0.082	1.465	0.068	6.977	0.149
6.00	27	4.468	0.015	1.317	0.017	6.786	0.032
7.00	27	4.321	0.122	1.294	0.069	6.615	0.191
10.00	27	4.514	0.057	1.082	0.026	6.597	0.082
20.00	27	6.052	0.162	0.399	0.037	6.451	0.199
10^2	27	6.592	0.054	0.184	0.005	7.776	0.058
2×10^2	27	7.096	0.051	0.108	0.002	8.204	0.052
10^3	27	9.225	0.100	0.030	0.001	10.256	0.101
10^4	27	10.889	0.094	0.003	0.000	11.892	0.094
10^5	27	13.870	1.680	2.7×10^{-4}	0.000	14.871	1.680
10^6	27	19.717	3.292	4.1×10^{-5}	0.000	20.717	3.292
∞	27	60.235				61.235	
${}^{*}10.00$	27	4.643	0.049	0.798	0.022	6.441	0.071

Table 6.2.b: Results of the shear viscosities obtained by Stokesian dynamics for hard-sphere suspensions at a volume fraction ϕ=0.45 and different Péclet numbers. Results are shown in the table with the following order of number of particles: N = 63, 64, 81 and 123. Results for a monolayer model with 25 particles are shown at the end of the table. Table captions are the same as shown in Table 6.2.a. The relatively short runs with 123 particles produce only one sample of results; therefore, the statistics were not computed and listed in the table.

Pe	N	η_H	σ_{η_H}	η_B	σ_{η_B}	η_T	σ_{η_T}
0.01	63	4.425	0.011	10.168	8.150	16.594	8.152
0.43	63	4.776	0.018	6.480	0.130	11.256	0.147
10.00	63	4.595	0.073	1.171	0.001	6.766	0.073
10.00	64	4.359	0.014	1.175	0.006	6.434	0.020
10^4	63	10.065	0.195	0.003	0.000	11.068	0.195
∞	64	67.151				68.151	
0.01	81	4.775	0.006	9.870	3.833	16.644	3.839
0.43	81	4.789	0.003	6.630	0.046	11.419	0.049
10.00	81	4.592	0.040	1.286	0.018	6.878	0.057
10^4	81	10.542	0.031	0.003	0.000	11.546	0.031
0.43	123	4.654		5.446		11.550	
10.00	123	4.333		1.144		6.477	
10^3	123	8.591		0.025		9.516	
[1] 0.01	25,2D	4.816	0.041	9.185	6.600	16.000	6.684
[2] 10.00	25,2D	4.873	0.430	1.012	0.112	6.473	0.541
[4] 10.00	25,2D	4.702	0.400	1.066	0.103	6.767	0.504
[3] 10^3	25,2D	9.458	0.336	0.025	0.002	10.483	0.338

Table 6.3.a: Results of the normal stress differences obtained by Stokesian dynamics for hard-sphere suspensions at a volume fraction ϕ=0.45 and different Péclet numbers. Column (1) is the the Péclet number, Pe, and column (2) is the number of particles, N. Columns (3) to (8) are the mean and the standard deviation of the hydrodynamic, the Brownian and total first normal stress differences, respectively. Similarly, columns (9) to (14) are the mean and the standard deviation for the hydrodynamic, the Brownian and total second stress differences, respectively. The run with $Pe = {}^{*}10$ denotes a new shear direction is tested along the y-axis. Table 6.3.b gives results for simulations with larger number of particles (N = 63, 64, 81 and 123) and a monolayer (2D) with 25 particles.

Pe	N	χ_{1H}	$\sigma_{\chi_{1H}}$	χ_{1B}	$\sigma_{\chi_{1B}}$	χ_{1T}	$\sigma_{\chi_{1T}}$	χ_{2H}	$\sigma_{\chi_{2H}}$	χ_{2B}	$\sigma_{\chi_{2B}}$	χ_{2T}	$\sigma_{\chi_{2T}}$
0.01	27	0.204	0.009	-20.852	14.903	-20.658	14.896	0.092	0.011	10.339	5.108	10.431	5.100
0.10	27	0.247	0.055	-6.434	4.039	-6.189	4.046	0.019	0.026	2.463	3.302	2.482	3.311
0.43	27	0.271	0.009	-1.833	0.091	-1.563	0.091	0.288	0.011	1.892	0.069	2.180	0.066
1.00	27	0.287	0.017	-0.746	0.075	-0.458	0.090	0.548	0.011	1.320	0.056	1.868	0.062
3.00	27	0.491	0.049	-0.028	0.101	0.463	0.125	0.523	0.031	0.335	0.164	0.858	0.176
5.00	27	0.447	0.023	-0.160	0.031	0.287	0.054	0.415	0.007	0.211	0.051	0.626	0.048
7.00	27	0.388	0.029	-0.522	0.040	-0.134	0.044	0.454	0.043	0.311	0.030	0.765	0.020
10.00	27	0.391	0.079	-0.239	0.057	0.152	0.135	0.450	0.065	0.126	0.048	0.576	0.112
20.00	27	0.374	0.110	-0.449	0.041	-0.075	0.146	0.830	0.096	0.266	0.034	1.096	0.130
10^2	27	0.882	0.150	-0.184	0.025	0.698	0.175	1.354	0.069	0.070	0.019	1.424	0.087
2×10^2	27	1.606	0.096	-0.029	0.006	1.605	0.096	0.913	0.065	0.029	0.006	0.942	0.067
10^3	27	1.657	0.071	-0.012	0.001	1.646	0.072	2.153	0.049	0.003	0.001	2.156	0.049
10^4	27	1.722	0.089	-0.002	0.000	1.720	0.089	2.450	0.114	2.4×10^{-5}	0.000	2.450	0.143
10^5	27	-3.839	2.218	-0.001	0.000	-3.840	2.218	2.124	1.188	1.8×10^{-4}	0.000	2.124	1.188
10^6	27	-5.468	5.962	-5.0×10^{-5}	0.000	-5.469	5.962	2.866	1.197	1.9×10^{-5}	0.000	2.866	1.197
${}^{*}10.00$	27	0.230	0.010	-0.093	0.095	0.137	0.109	0.602	0.071	0.299	0.069	0.901	0.138

Table 6.3.b: Results of the normal stress differences obtained by Stokesian dynamic for a hard-sphere suspension at volume fraction ϕ=0.45 and different Péclet numbers. Results are shown in the following order of number of particles N = 63, 64, 81 and 123. Results from a monolayer (2D) with 25 particles are summarized at the end of the table. Table captions are the same as shown in Table 6.3.a.

Pe	N	χ_{1H}	$\sigma_{\chi_{1H}}$	χ_{1B}	$\sigma_{\chi_{1B}}$	χ_{1T}	$\sigma_{\chi_{1T}}$	χ_{2H}	$\sigma_{\chi_{2H}}$	χ_{2B}	$\sigma_{\chi_{2B}}$	χ_{2T}	$\sigma_{\chi_{2T}}$
0.43	63	0.145	0.008	-1.003	0.090	-0.857	0.096	0.339	0.005	0.996	0.105	1.336	0.105
10.00	63	0.422	0.042	-0.037	0.001	0.385	0.042	0.854	0.047	0.033	0.001	0.821	0.047
10.00	64	0.374	0.013	-0.284	0.013	0.089	0.026	0.564	0.009	0.036	0.022	0.600	0.030
10^4	63	1.508	0.156	-0.003	0.000	1.505	0.156	2.224	0.225	5.5×10^{-4}	0.000	2.224	0.247
0.43	81	0.131	0.007	-1.875	0.181	-1.744	0.188	0.427	0.005	1.198	0.044	1.625	0.041
10.00	81	0.171	0.025	-0.980	0.275	-1.151	0.053	0.442	0.216	0.280	0.122	0.722	0.033
10^4	81	1.595	0.084	-0.002	0.000	1.593	0.084	2.240	0.022	1.0×10^{-4}	0.000	2.240	0.022
0.43	123	0.0.108		-1.151		-1.043		0.327		0.990		1.313	
10.00	123	0.323		-0.360		-0.037		0.792		0.427		1.128	
10^3	123	1.902		-0.005		1.897		1.420		-0.005		1.415	
[1] 0.01	25,2D	-0.163	0.056	-75.218	38.791	-75.381	38.758						
[2] 10.00	25,2D	0.079	0.199	-0.190	0.253	-0.111	0.446						
[4] 10.00	25,2D	0.064	0.147	-0.123	0.212	-0.059	0.356						
[3] 10^3	25,2D	1.764	0.423	-0.008	0.009	1.756	0.431						

Table 6.4.a: The angularly averaged pair-distribution function evaluated at particle center-center spacing r=2, $g(2)$, for different ϕ and Pe. Column (1) is Pe and columns (2) to (11) are $g(2)$ for different particle volume fractions ϕ. The runs for ϕ=0.55 are with 28 particles. The symbol (**) denotes runs with 123 or 126 particles. All other runs are with 27 particles.

Pe	$\phi = 0.316$	$\phi = 0.37$	$\phi = 0.4$	$\phi = 0.419$	$\phi = 0.45$	$\phi = 0.47$	$\phi = 0.48$	$\phi = 0.49$	$\phi = 0.51$	$\phi = 0.55$
0.01	2.38	3.02	3.70	3.84	4.20	4.79		4.91	5.70	8.87
0.10	2.49	3.06	3.55	3.87	4.44	4.76		5.49	6.02	10.50
0.43					4.94					
**0.43					4.94		6.11			
1.00	2.71	3.54	4.06	4.57	5.60	6.07		7.25	7.94	16.69
2.00								2.32		
3.00				0.83	0.95	0.62		1.00	1.40	11.51
5.00		0.24	0.29	0.52	0.59					
7.00			0.38	0.41	0.73	0.02				
10.00	0.05	0.22	0.43	0.56	0.98	0.01		0.02	0.12	14.49
**10	0.06			0.74	0.84		0.21	0.48	0.54	15.01
15.00		1.37	1.06							
20.00		1.87	2.83	3.22	7.26	8.31				
30.00				10.79				17.76		30.57
50.00				19.70						
10^2	17.03	22.26	24.00	28.20	32.61	35.65		37.93	35.08	43.50
$2x10^2$				37.71	40.44					
10^3	31.15	35.11	40.88	48.37	48.98	51.90		54.43	57.21	60.64
$**10^3$					47.88		53.76			
10^4	38.63	43.25	46.76	50.73	56.56	59.53		62.63	64.08	69.50
10^5					66.01	71.10		78.08	78.71	78.49
10^6	38.63	47.21	56.74	63.88	73.24					
∞	55.56	62.14	74.19	83.96	93.00					

Table 6.4.b: The angularly averaged pair-distribution function evaluated at particle center-center spacing r=2, $g(2)$, for hard-sphere suspensions at a volume fraction ϕ=0.45 and different Péclet numbers. Columns (1) to (3) are the Péclet number, Pe, the number of particles, N, and the angularly averaged $g(2)$, respectively. The symbol (**) denotes that $g(2)$ is computed by the Monte-Carlo method.

Pe	N	$g(2)$
0.01	63	4.51
0.43	63	4.46
10.00	63,64	1.35
10^4	63	54.36
0.01	81	4.53
0.43	81	5.05
10.00	81	1.30
10^4	81	56.19
(**) 0.00		4.65
0.00	123	4.59
0.43	123	4.94
10.00	123	0.84
10^3	123	47.88

Table 6.5.a: Results of the short-time self-diffusion coefficients obtained by Stokesian dynamics for hard-sphere suspensions at a volume fraction ϕ=0.45 and different Péclet numbers. Column (1) is Pe and column (2) is N. Columns (3) to (5) are the short-time translational self-diffusion coefficients computed in the x-, y- and z-directions, respectively. Columns (6) and (7) are the mean and standard deviation of the short-time translational self-diffusion coefficient D_o^s. Similarly, columns (8) to (12) give the short-time rotational self-diffusion coefficients in the x-, y-, z-directions, the mean D_r^s and its standard deviation. The self-diffusion coefficients are normalized by the infinite dilution diffusion coefficient D_o. Results of runs with larger number of particles (N = 63, 64, 81 and 123) and a monolayer with 25 particlwes are reported in Table 6.5.b. Note that D_o^s is only truely a diffusivity at Pe=0. At finite Pe, it gives a measure of the local mobility of a particle.

Pe	N	$D^s_{o_{xx}}$	$D^s_{o_{yy}}$	$D^s_{o_{zz}}$	$\langle D^s_o \rangle$	$\sigma_{D^s_o}$	$D^s_{r_{xx}}$	$D^s_{r_{yy}}$	$D^s_{r_{zz}}$	$\langle D^s_r \rangle$	$\sigma_{D^s_r}$
0.00	27	0.218	0.217	0.217	0.217	0.001	0.603	0.604	0.604	0.604	0.001
0.01	27	0.174	0.171	0.172	0.172	0.001	0.553	0.553	0.553	0.553	0.001
0.10	27	0.179	0.175	0.177	0.177	0.001	0.554	0.555	0.554	0.555	0.001
0.43	27	0.173	0.168	0.170	0.170	0.000	0.545	0.545	0.542	0.544	0.001
1.00	27	0.167	0.163	0.165	0.165	0.001	0.533	0.534	0.531	0.533	0.001
3.00	27	0.184	0.178	0.178	0.180	0.001	0.567	0.564	0.560	0.563	0.002
5.00	27	0.180	0.175	0.171	0.175	0.001	0.556	0.549	0.551	0.552	0.002
7.00	27	0.170	0.157	0.158	0.162	0.001	0.526	0.532	0.527	0.528	0.002
10.00	27	0.168	0.158	0.152	0.159	0.003	0.519	0.519	0.524	0.521	0.005
20.00	27	0.166	0.140	0.132	0.146	0.001	0.475	0.494	0.507	0.492	0.003
10^2	27	0.119	0.112	0.110	0.114	0.001	0.411	0.416	0.409	0.412	0.002
2×10^2	27	0.110	0.104	0.101	0.105	0.000	0.386	0.384	0.386	0.385	0.001
10^3	27	0.094	0.088	0.089	0.091	0.001	0.331	0.333	0.326	0.330	0.004
10^4	27	0.077	0.068	0.065	0.070	0.001	0.252	0.254	0.256	0.251	0.002
10^5	27	0.057	0.053	0.054	0.055	0.004	0.215	0.209	0.206	0.210	0.008
10^6	27	0.044	0.042	0.045	0.044	0.000	0.175	0.174	0.166	0.171	0.001
∞	27	0.020	0.022	0.022	0.021	0.002	0.113	0.108	0.111	0.111	0.004

Table 6.5.b: Results of the short-time translational and rotational self-diffusion coefficients obtained by Stokesian dynamics for hard-sphere suspensions at volume fraction ϕ=0.45 and different Péclet numbers. The self-diffusion coefficients are normalized by the infinite dilution diffusion coefficient D_o. The symbol (*) shown next to N in column (2) denotes a monolayer run. Captions of the table are the same as shown in Table 6.5.a.

Pe	N	$D^{s}_{o_{xx}}$	$D^{s}_{o_{yy}}$	$D^{s}_{o_{zz}}$	$\langle D^{s}_{o} \rangle$	$\sigma_{D^{s}_{o}}$	$D^{s}_{r_{xx}}$	$D^{s}_{r_{yy}}$	$D^{s}_{r_{zz}}$	$\langle D^{s}_{r} \rangle$	$\sigma_{D^{s}_{r}}$
0.00	64	0.204	0.205	0.204	0.204	0.001	0.570	.569	0.569	0.569	0.001
0.01	63	0.198	0.194	0.197	0.196	0.001	0.557	0.560	0.557	0.558	0.001
0.43	63	0.185	0.185	0.183	0.184	0.000	0.541	0.540	0.542	0.541	0.000
10.00	63	0.184	0.172	0.174	0.177	0.001	0.520	0.529	0.522	0.524	0.002
10.00	64	0.187	0.173	0.171	0.177	0.000	0.520	0.529	0.529	0.526	0.000
10^4	63	0.093	0.080	0.076	0.083	0.004	0.268	0.288	0.289	0.282	0.006
∞	64	0.020	0.022	0.024	0.022	0.002	0.120	0.112	0.112	0.114	0.004
0.01	81	0.191	0.190	0.191	0.191	0.000	0.551	0.550	0.549	0.549	0.000
0.43	81	0.191	0.188	0.188	0.189	0.000	0.539	0.543	0.541	0.541	0.000
10.00	81	0.217	0.181	0.188	0.195	0.002	0.536	0.569	0.559	0.555	0.004
10^4	81	0.092	0.084	0.082	0.086	0.000	0.272	0.281	0.279	0.277	0.000
0.43	123	0.206	0.203	0.203	0.204		0.550	0.552	0.551	0.551	
10.00	123	0.189	0.182	0.184	0.185		0.520	0.526	0.517	0.521	
10^3	123	0.116	0.111	0.105	0.110		0.340	0.342	0.342	0.341	
0.01	25*	0.336	0.329		0.333	0.000			0.582	0.582	0.001
10.00	25*	0.335	0.332		0.333	0.011			0.582	0.582	0.018
10.00	25*	0.338	0.335		0.336	0.010			0.589	0.589	0.016
10^3	25*	0.213	0.215		0.214	0.003			0.316	0.316	0.004

Table 6.6: Results of the long-time self-diffusion coefficients obtained by Stokesian dynamics for hard-sphere suspensions at a volume fraction ϕ=0.45 and different Péclet numbers. Column (1) is Pe. Columns (2) to (5) are the long-time self-diffusion coefficient computed in the y-direction, $D^s_{\infty,yy}/D_o$, its standard deviation, the long-time self-diffusion coefficient computed in the z-direction, $D^s_{\infty,zz}/D_o$, and its standard deviation, respectively. The long-time self-diffusion coefficients are normalized by the infinite dilution diffusion coefficient D_o. Columns (6) and (7) are the length of time of each sample and the number of samples which are used to compute these long-time self-diffusion coefficients, respectively. All runs in the table are with 27 particles. As shown in columns (6) and (7) in this table, the long-time self-diffusivity requires long run times of 100 or more and the relatively short runs with a large number of particles (N = 64, 81, 123 and 126) do not provide sufficient data for the particle positions which are needed for the computing of the long-time self-diffusion coefficients.

Pe	$D^s_{\infty,yy}$	σ_{yy}	$D^s_{\infty,zz}$	σ_{zz}	t_{diff}	# trials
0.00	0.059	0.012	0.055	0.010	100.0	9
0.01	0.068	0.003	0.058	0.008	185.0	4
0.10	0.076	0.015	0.065	0.005	120.0	16
0.43	0.105	0.005	0.079	0.010	100.0	19
1.00	0.148	0.033	0.179	0.035	100.0	19
3.00	0.054	0.005	0.055	0.009	100.0	13
5.00	0.020	0.002	0.020	0.003	50.0	6
7.00	0.008	0.002	0.015	0.002	50.0	6
10.00	3×10^{-4}	0.000	0.004	0.000	250.0	11
20.00	0.018	0.001	0.020	0.002	85.0	11
10^2	0.029	0.003	0.025	0.002	50.0	6
2×10^2	0.028	0.003	0.027	0.004	85.0	11
10^3	0.039	0.004	0.046	0.003	85.0	11
10^4	0.058	0.016	0.054	0.009	100.0	16

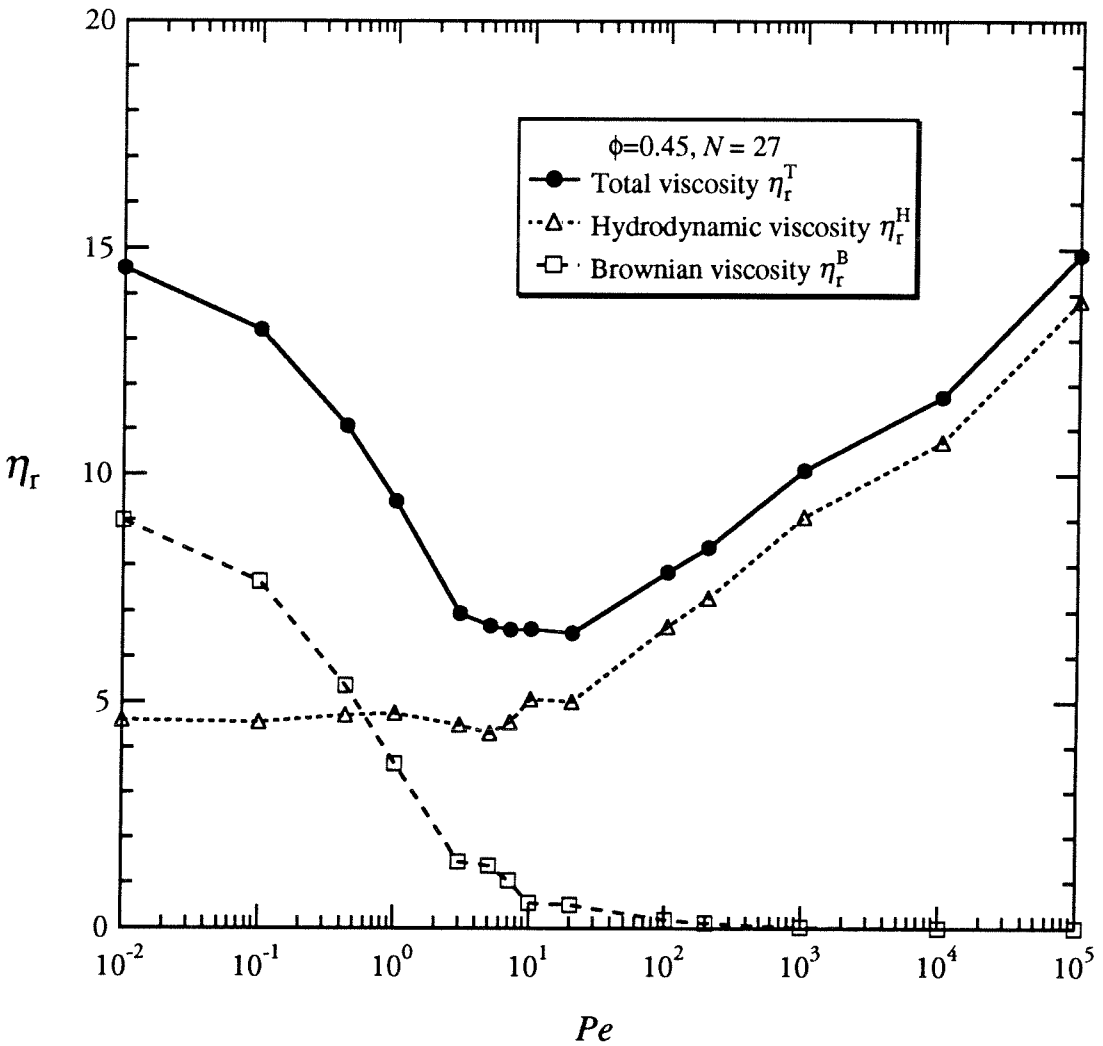

Figure 6.1: The relative viscosity η_r of hard-sphere suspensions at a volume fraction ϕ=0.45 obtained by Stokesian dynamics as a function of Pe: total (●) viscosity, hydrodynamic (Δ) viscosity and Brownian (□) viscosity.

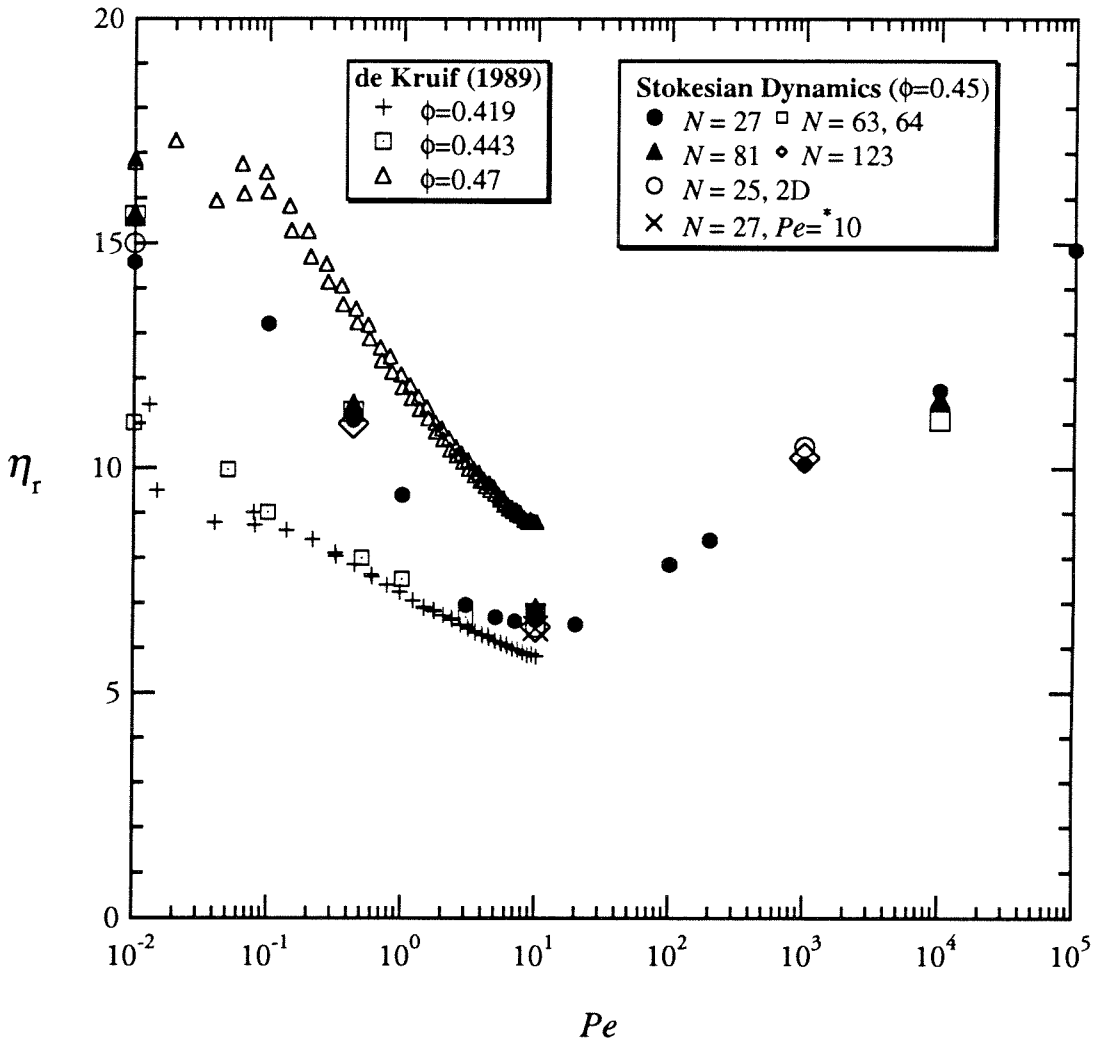

Figure 6.2: Comparison of the simulation results for the steady shear viscosity as a function of Pe at a particle volume fraction ϕ=0.45 (N = 27, 63, 64, 81 and 123; monolayers with N = 25; and (×) at Pe=10 denotes the shear direction along the y-axis) with the experiments of van der Werff and de Kruif (1989) for ϕ=0.419, 0.443 and 0.47.

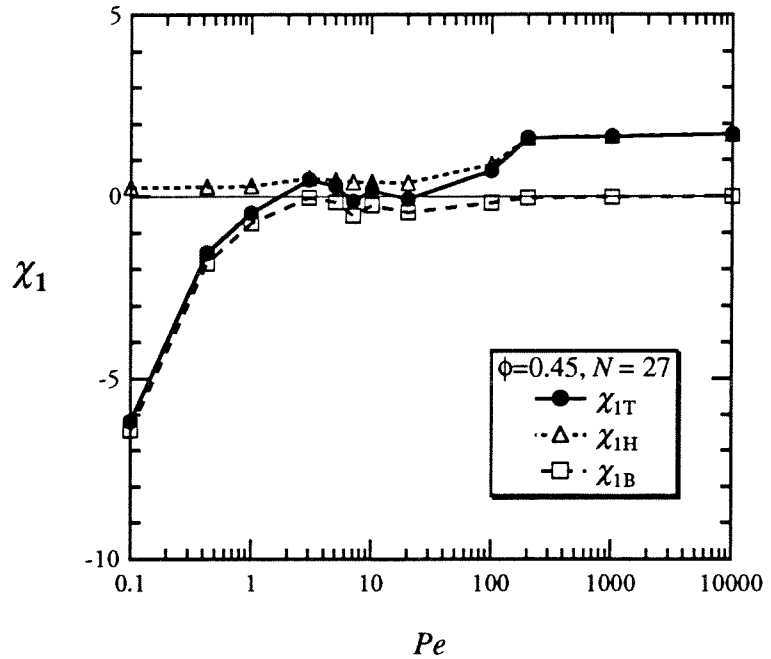

Figure 6.3.a: Plot of the first normal stress differences χ_1 versus Pe.

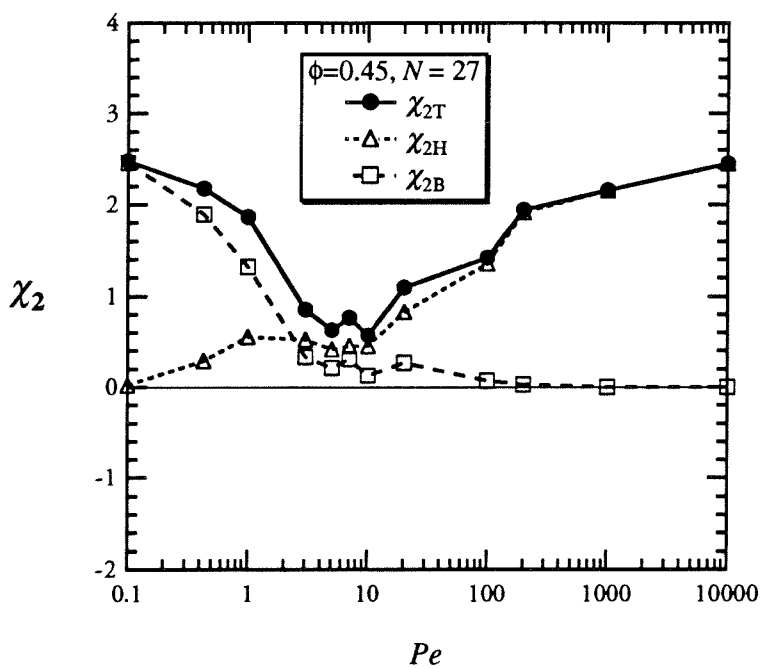

Figure 6.3.b: Plot of the second normal stress differences χ_2 versus Pe.

Figure 6.3.a-b: The first (Fig.6.3.a) and second (Fig.6.3.b) normal stress differences of hard spheres at a volume fraction ϕ=0.45 obtained by Stokesian dynamics as a function of the Péclet number: total (●) normal stress differences, hydrodynamic (Δ) and Brownian (□) contribution.

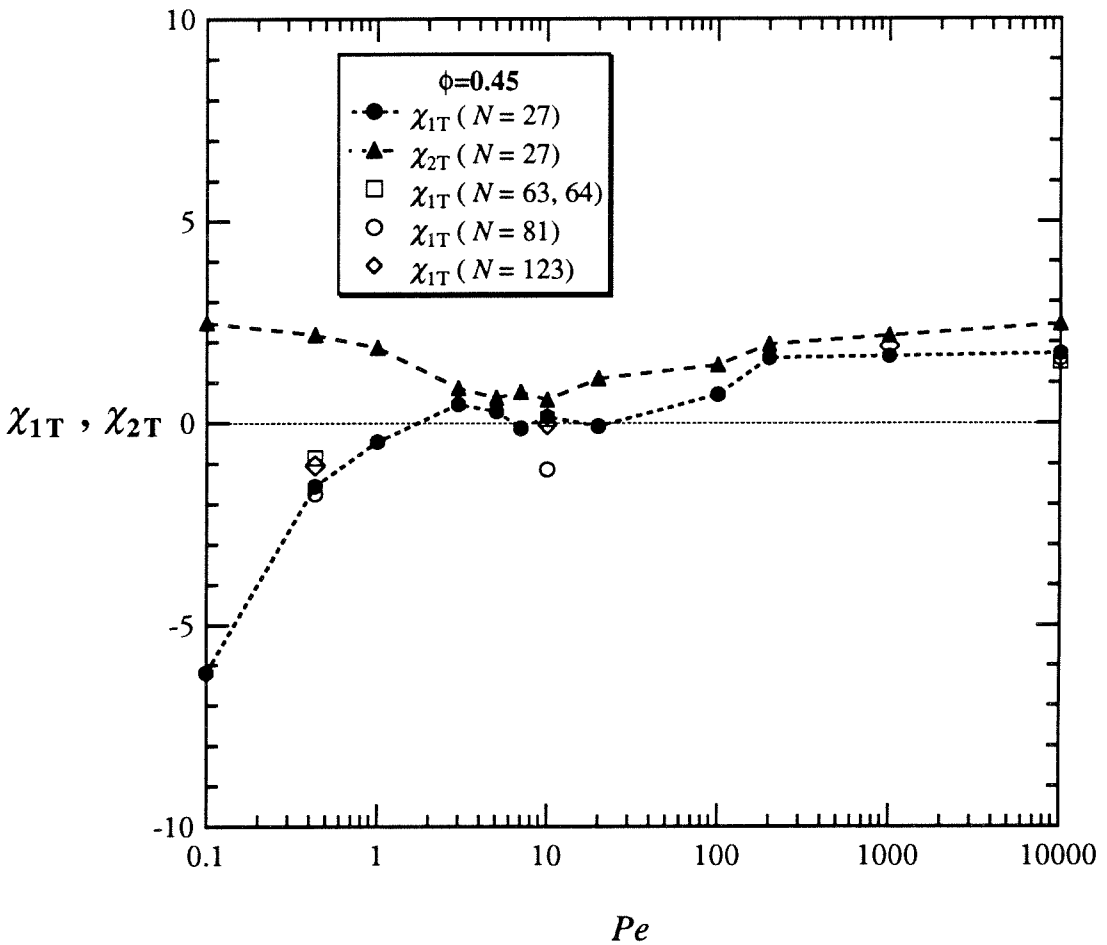

Figure 6.4: The steady first and second total normal stress differences for hard spheres at a volume fraction ϕ=0.45 and N = 27 obtained by Stokesian dynamics as a function of *Pe*: the first (●) and the second (▲) total normal stress differences. The horizontal dotted line through zero is drawn to guide the eyes. The first total normal stress differences are also plotted for runs with larger number of particles: N = 63, 64 (□), 81 (○) and 123 (◇).

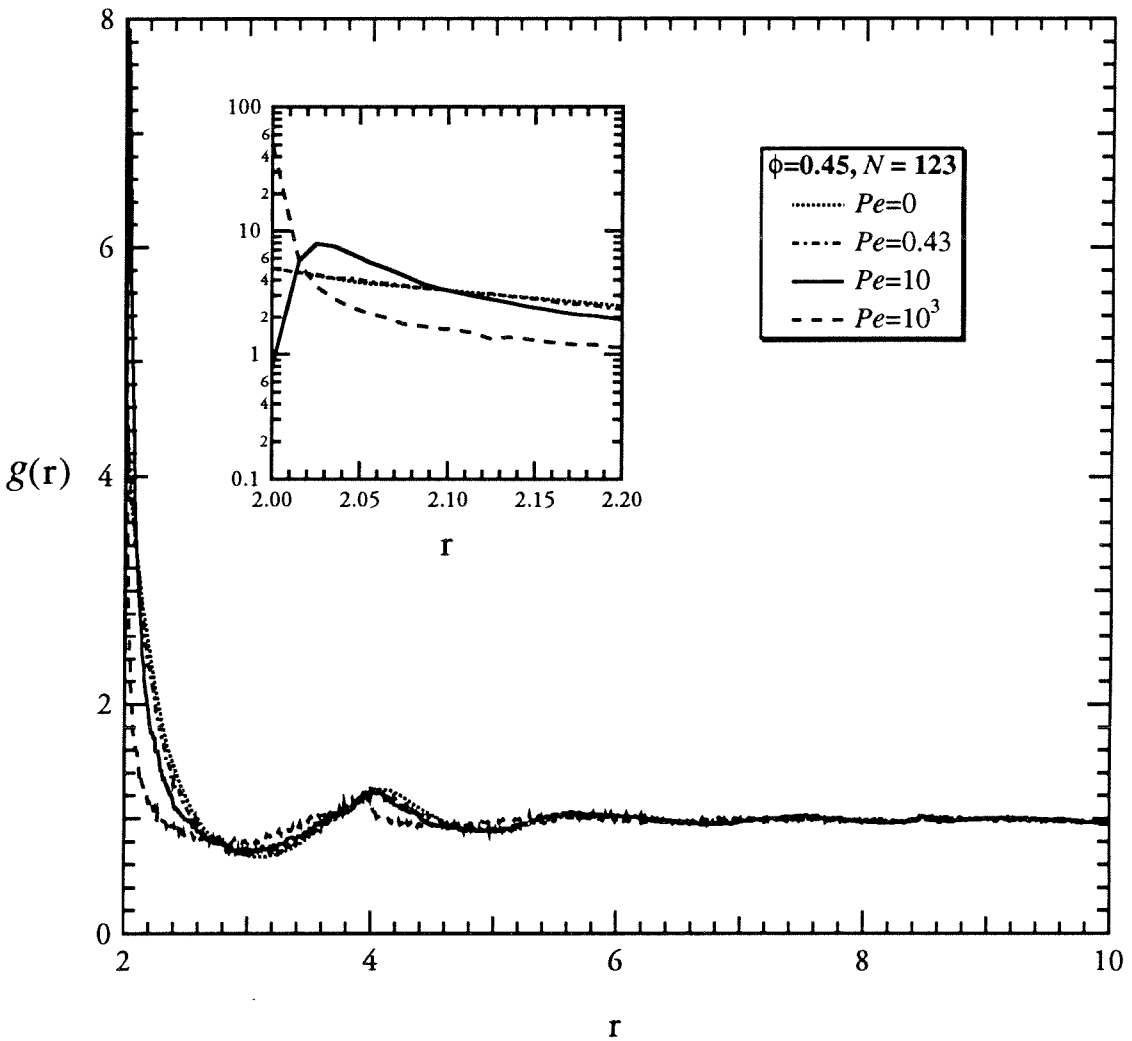

Figure 6.5: The radial dependence of the pair-distribution function $g(r)$ determined by Stokesian dynamics for hard-sphere suspensions with a volume fraction ϕ=0.45, N = 123, and different Pe numbers: (dotted curve) 0, (dotted-dash curve) 0.43, (solid curve) 10, and (dashed curve) 1000. The insert figure in the upper left corner is the plot of $g(r)$ on a logarithmic scale for a small range of r. At r=2 (when two particles are in contact), $g(2)$ is smallest for Pe=10, largest for Pe=1000, and there is a very small difference between the equilibrium (Pe=0) and slightly deformed suspensions (Pe=0.43).

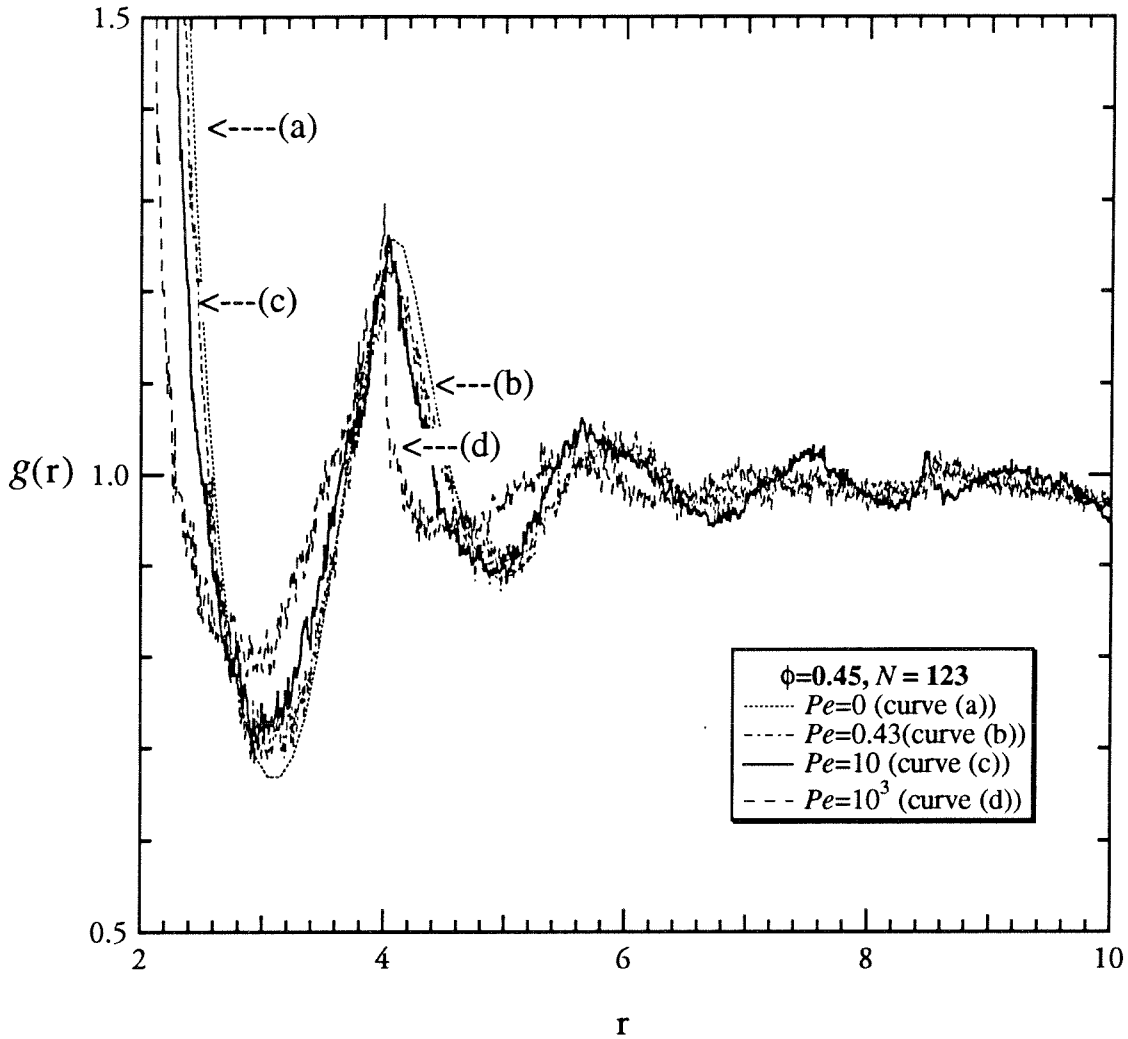

Figure 6.6: Plot of the angularly averaged pair-distribution function versus the particle center-center spacing distance r for different *Pe* numbers: (dotted curve (a)) 0, (dotted-dash curve (b)) 0.43, (solid curve (c)) 10 and (dashed curve (d)) 1000. It is seen from the figure that the spike of $g(r)$ at r=4 is sharp for the curve with *Pe*=1000. For the curves with *Pe*=0.0, 0.43 and 10 the peak is broad and r is slightly shifted to the larger value ($r \approx 4.1$ to 4.2).

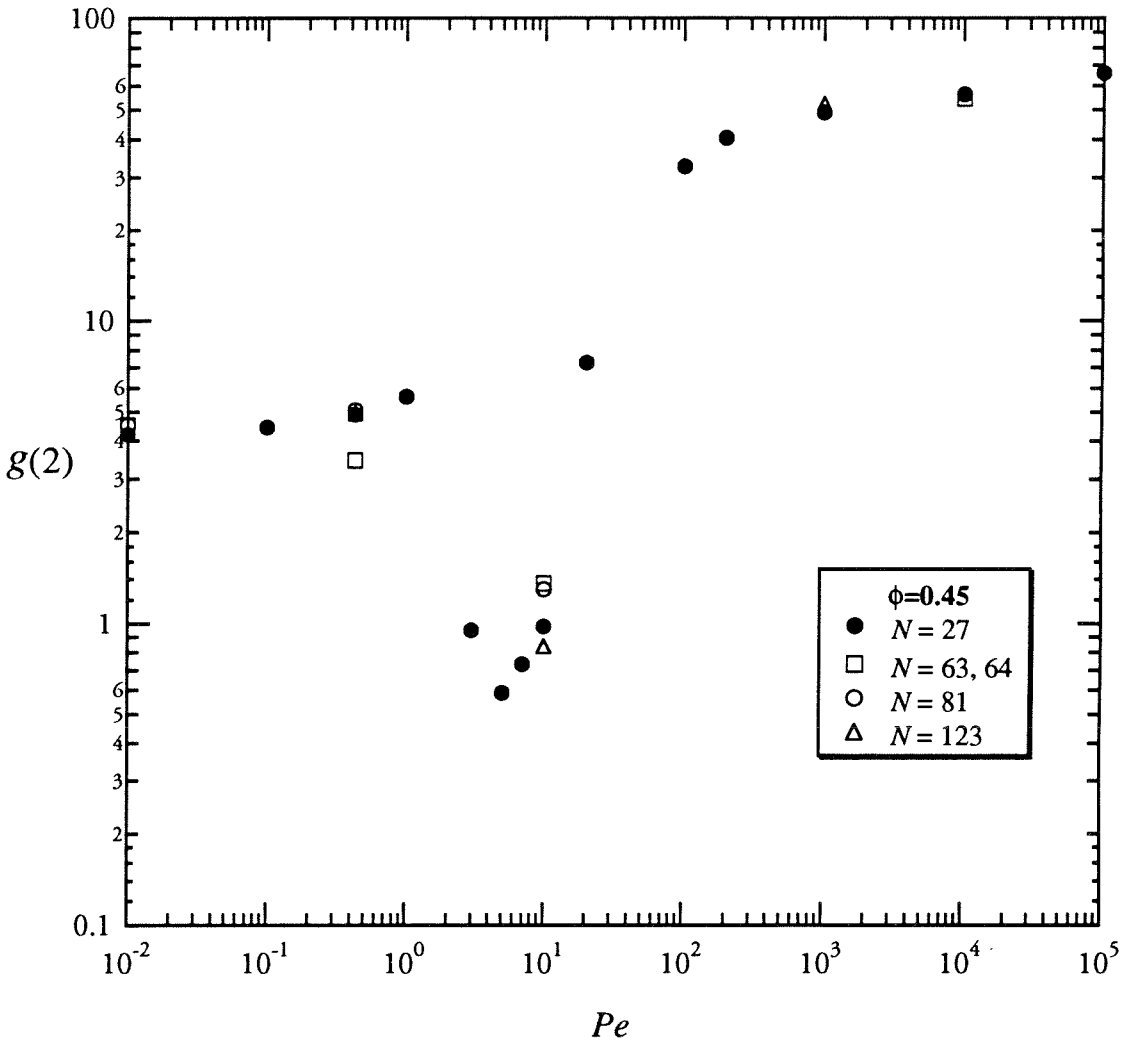

Figure 6.7: The angularly averaged pair-distribution function $g(r)$ evaluated at particle center-center spacing r=2 (when particles are in contact), $g(2)$, obtained by Stokesian dynamics for hard spheres at volume fraction ϕ=0.45 as a function of the Péclet number. $g(2)$ is plotted with various sizes of number of particles: N = 27 (●), 63, 64 (□), 81 (○) and (Δ) N=123. For suspensions with small deformation (Pe<1), $g(2)$ is relatively constant. As Pe increases, $g(2)$ first decreases to a minimum at $Pe\approx3$, increases with large Pe, and approaches an asymptotic limit for $Pe\geq10000$. Note that $g(2)$ is plotted on a logarithmic scale.

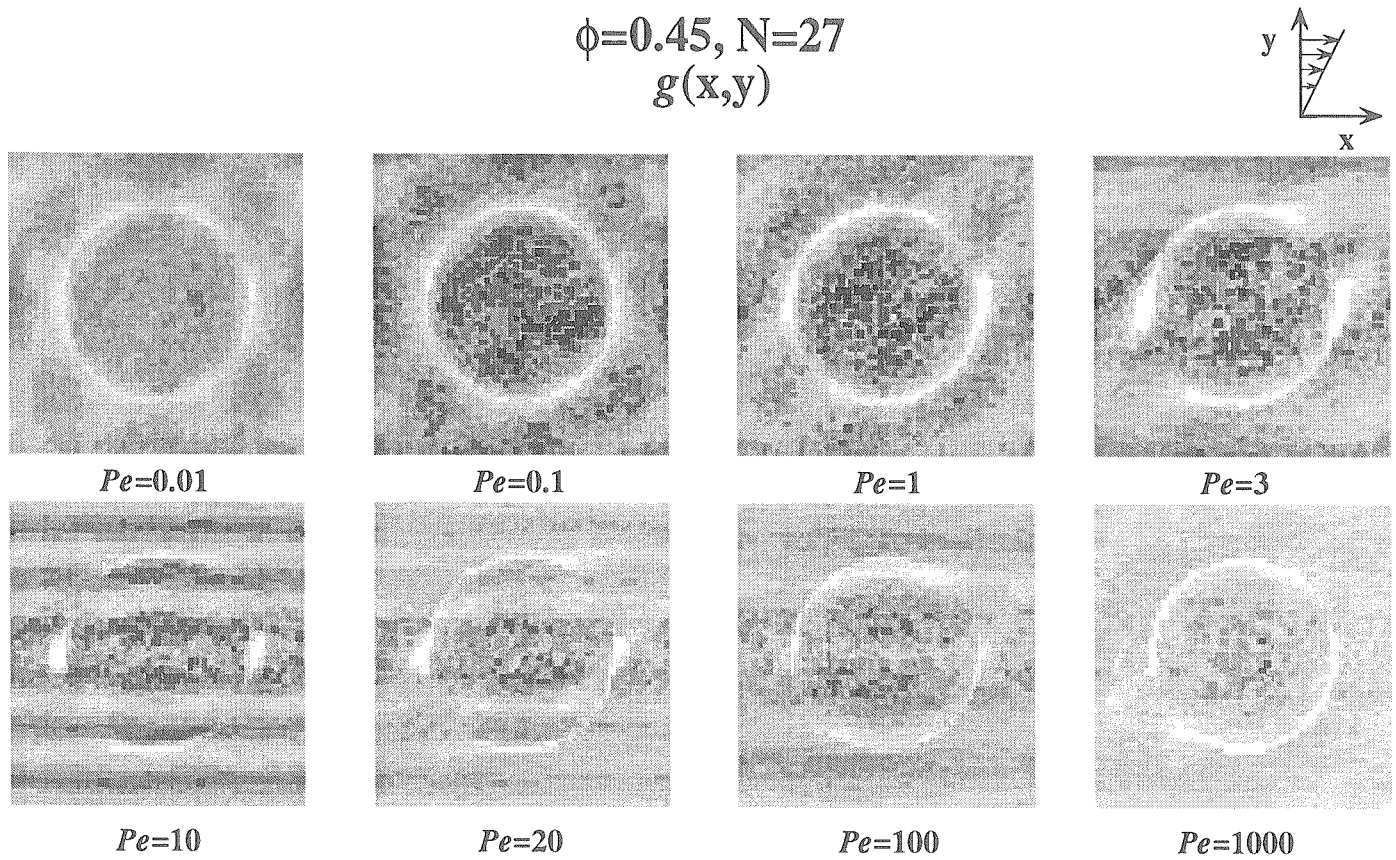

Figure 6.8.a: A plot of probability density for finding a particle in the x-y plane given that there is a particle at the origin, $g(x,y)$, for hard-sphere suspensions at a volume fraction ϕ=0.45 and different Péclet numbers. There are 27 particles in the unit cell. Regions of light color represent high probability and regions of dark color represent low probability. The horizontal x-axis is the flow direction and the vertical y-axis is the velocity gradient direction. $g(x,y)$ shows distinct string formation of flowing particles along the flow direction for *Pe*=10, 20 and 100. The high shear rates at *Pe*=1000 destroy the string formation and note aslo the sharpening of the first nearest neighboring compared to the symmetric ring at *Pe*=0.01.

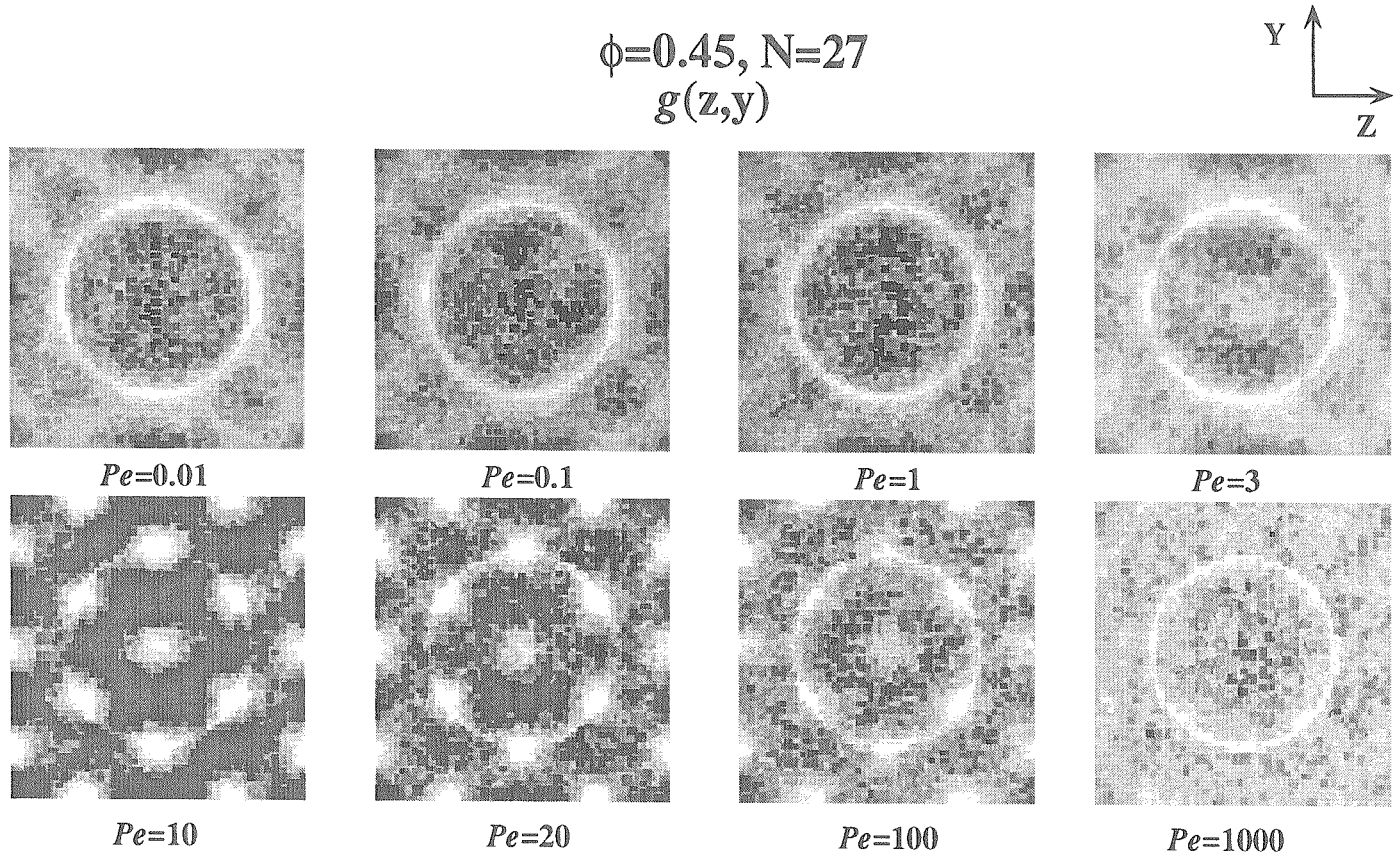

Figure 6.8.b: A plot of probability density for finding a particle in the z-y plane given that there is a particle at the origin, $g(z,y)$, for hard spheres at a volume fraction of ϕ=0.45 with 27 particles and different Péclet numbers. Regions of light color represent high probability and regions of dark color represent low probability. The flow direction is perpendicular to the z-y plane. The horizontal z-axis is the vorticity direction and the vertical y-axis is the velocity gradient direction. $g(z,y)$ shows a distinct "hexagonal" packing of strings of flowing particles for Pe=10, 20 and 100. The hexagonal formation is destroyed by the high shear rates at Pe=1000.

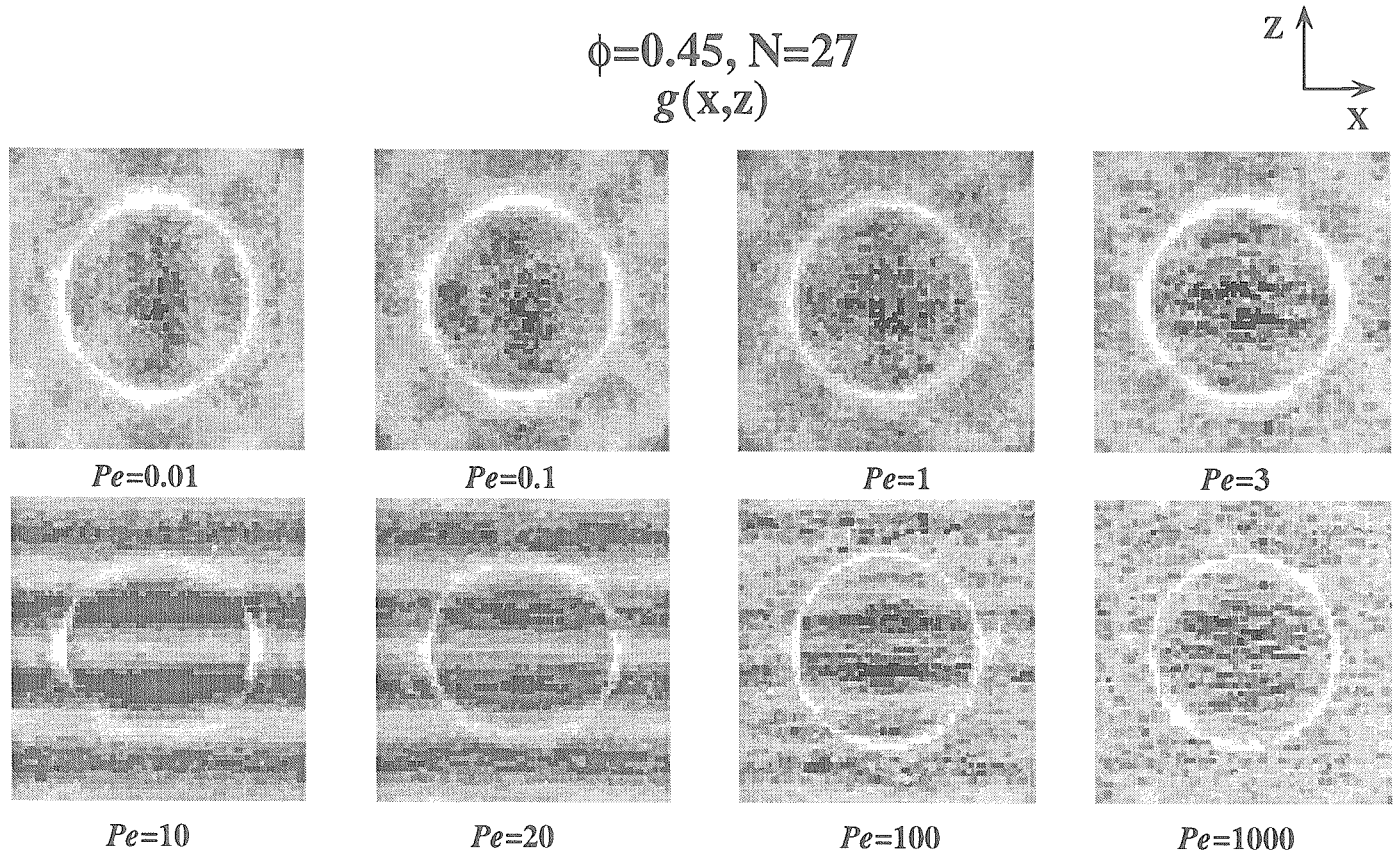

Figure 6.8.c: A plot of probability density for finding a particle in the x-z plane given that there is a particle at the origin, $g(x,z)$, for hard spheres at a volume fraction ϕ=0.45 and different Péclet numbers. There are 27 particles in the unit cell. Regions of light color represent high probability and regions of dark color represent low probability. The flow direction is the horizontal x-axis and the vorticity direction is the vertical z-axis. $g(x,z)$ shows strings of flowing particles for Pe=10 and 20. The string formation begins to fluctuate at Pe=100 and is destroyed by Pe=1000.

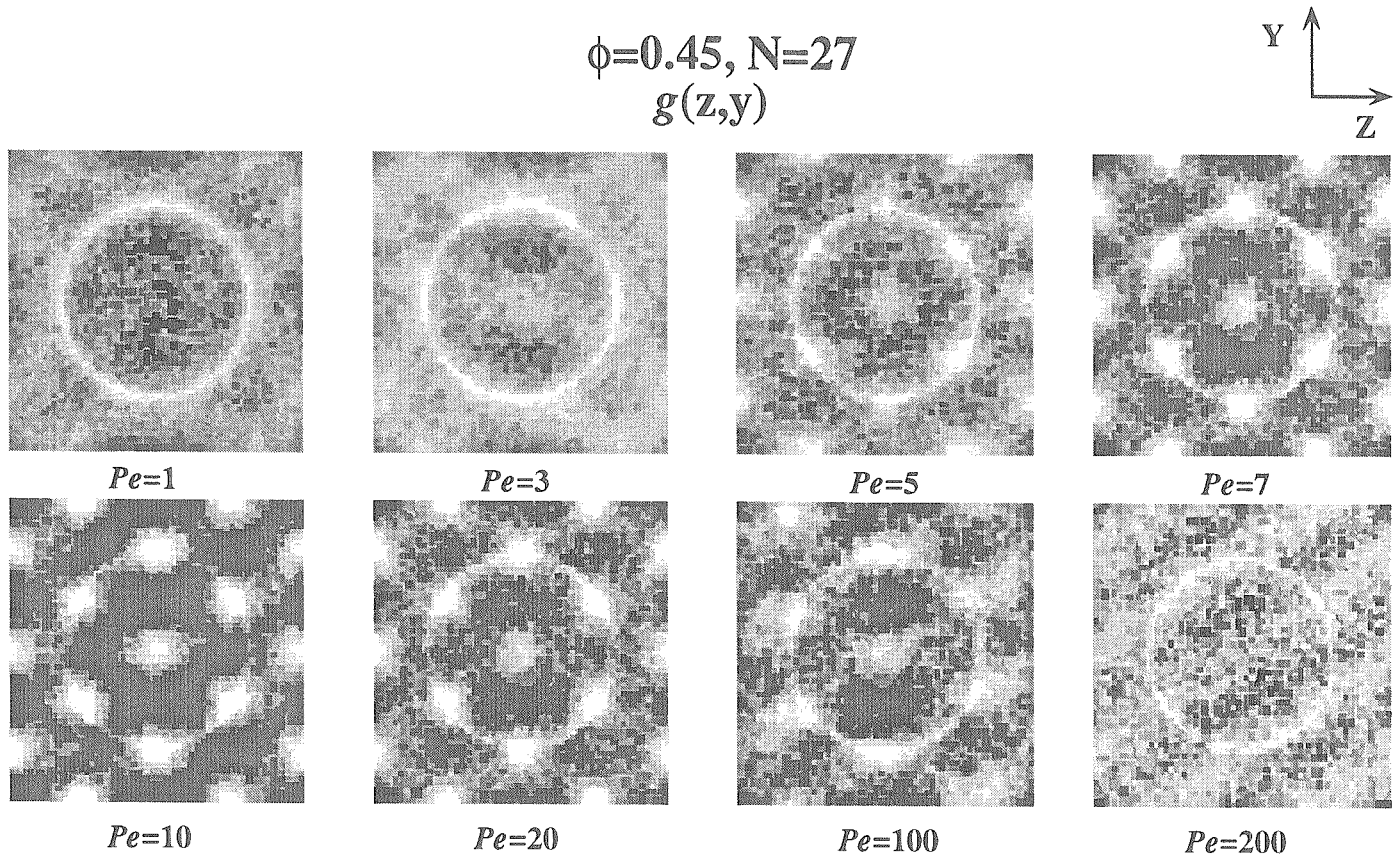

Figure 6.8.d: A plot of probability density $g(z,y)$ for a hard-sphere suspension at volume fraction of ϕ=0.45 with 27 particles and a small range of the Péclet number: from 1 to 200. Regions of light color represent high probability and regions of dark color represent low probability. The flow direction is perpendicular to the z-y plane. The horizontal z-axis is the vorticity direction and the vertical y-axis is the velocity gradient direction. The flowing particles begin to order at *Pe*=5 and the strongly ordered microstructure can be seen for *Pe*=10 and 20 with a distinct "hexagonal" packing. The hexagonal packing formation is destroyed by *Pe*=200.

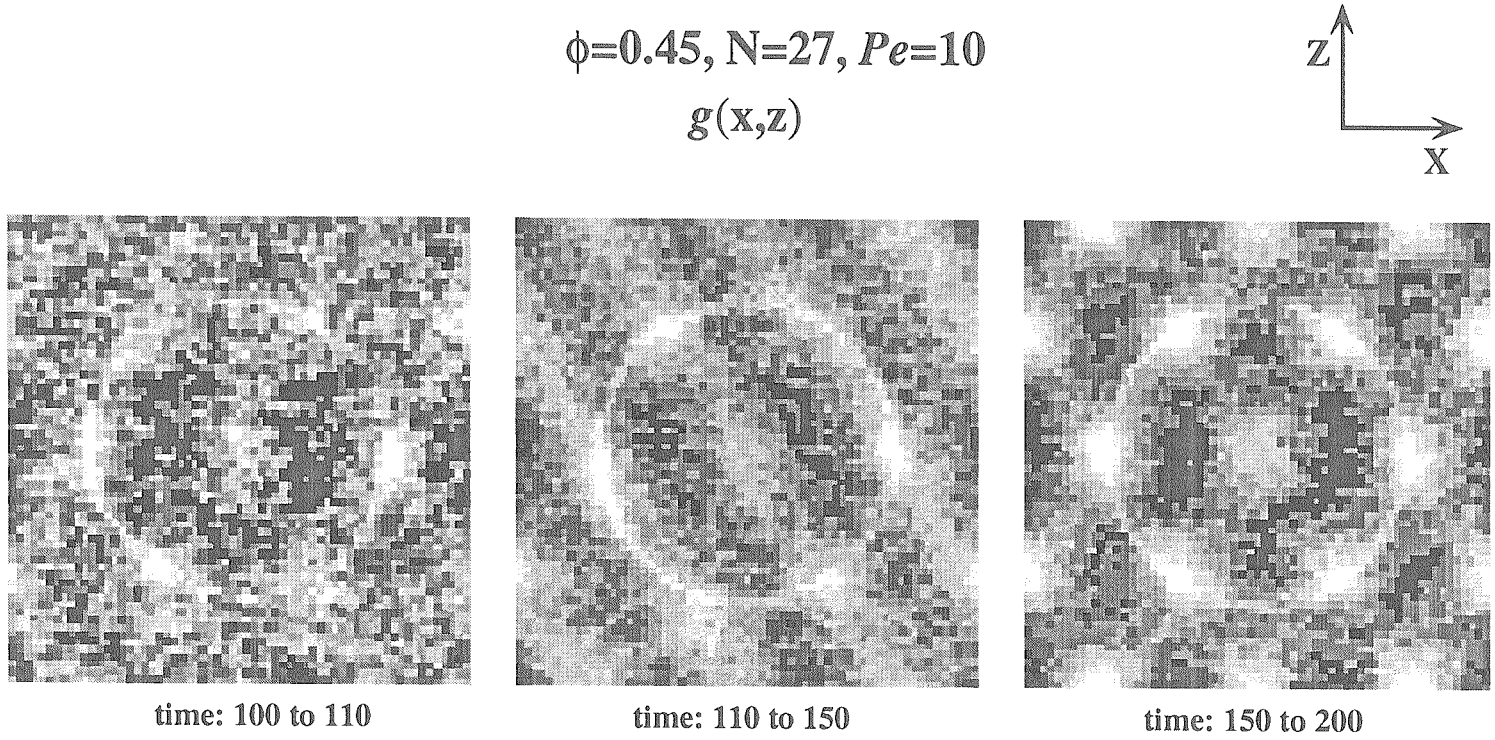

Figure 6.8.e : A plot of probability density for finding a particle in the x-z plane given that there is a particle at the origin, $g(x,z)$, for hard spheres at a volume fraction of ϕ=0.45 with 27 particles and Pe=10. Regions of light color represent high probability and regions of dark color represent low probability. The figure shows the time evolution of structure on changing the flow direction from x to y. The new flow direction, y, is perpendicular to the x-z plane. Note the formation of a similar "hexagonal" pattern which was observed for the density plot $g(z,y)$ with the flow direction in the x-axis shown in Fig. 6.8.b.

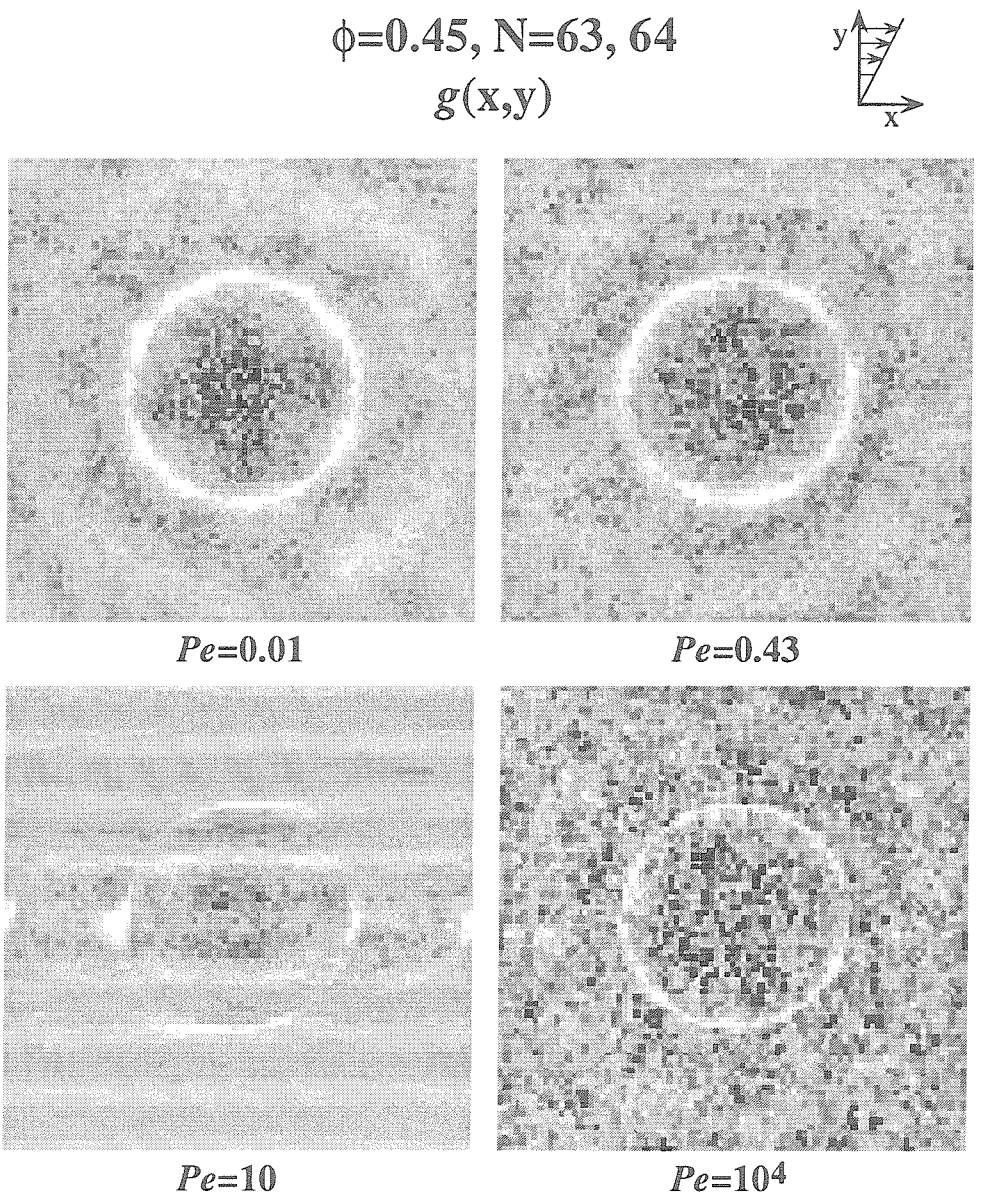

Figure 6.9.a: A plot of probability density for finding a particle in the x-y plane given that there is a particle at the origin, $g(x,y)$, for hard spheres at a volume fraction ϕ=0.45 and different Péclet numbers. There are 63 or 64 particles in the unit cell. Regions of light color represent high probability and regions of dark color represent low probability. The flow direction is the horizontal x-axis and the velocity gradient direction is the vertical y-axis. $g(x,y)$ shows a string formation of flowing particles for Pe=10.

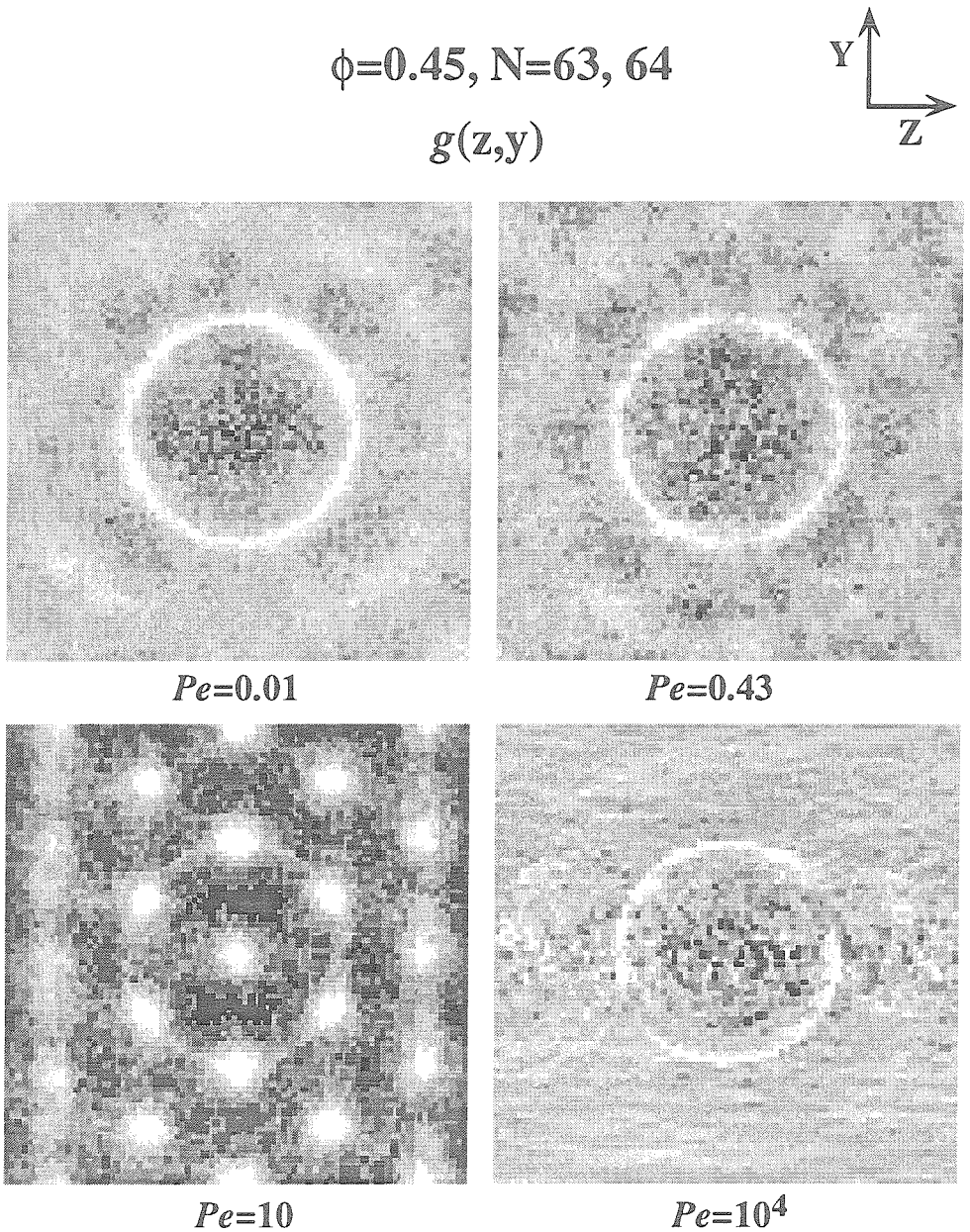

Figure 6.9.b: A plot of probability density for finding a particle in the z-y plane given that there is a particle at the origin, $g(z,y)$, for hard spheres at a volume fraction ϕ=0.45 and different Péclet numbers. There are 63 or 64 particles in the unit cell. Regions of light color represent high probability and regions of dark color represent low probability. The flow direction is perpendicular to the z-y plane. The horizontal z-axis is the vorticity direction and the vertical y-axis is the velocity gradient direction. $g(z,y)$ shows a distinct hexagonal packing of strings of flowing particles for Pe=10.

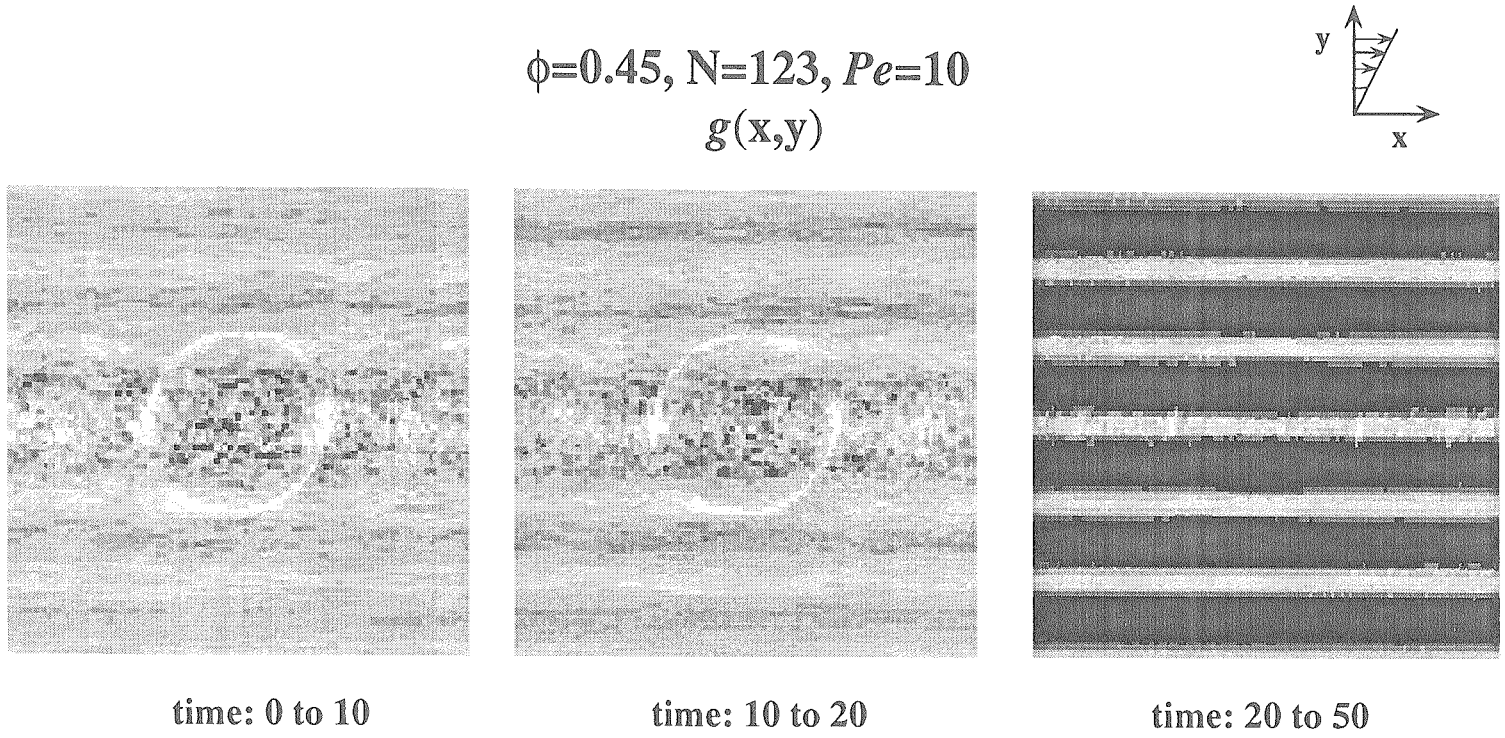

Figure 6.10.a: The time evolution of the probability density $g(x,y)$ for a hard-sphere suspension at volume fraction ϕ=0.45 with 123 particles and Pe=10 obtained by Stokesian dynamics. Regions of light color represent high probability and regions of dark color represent low probability. The flow direction is the horizontal x-axis and the velocity gradient direction is the vertical y-axis. The probability density function $g(x,y)$ is shown for different times. The right most figure is the steady $g(x,y)$, which shows clearly the "bands" or "strings" of particles flowing along the flow direction after a dimensionless time of 50.

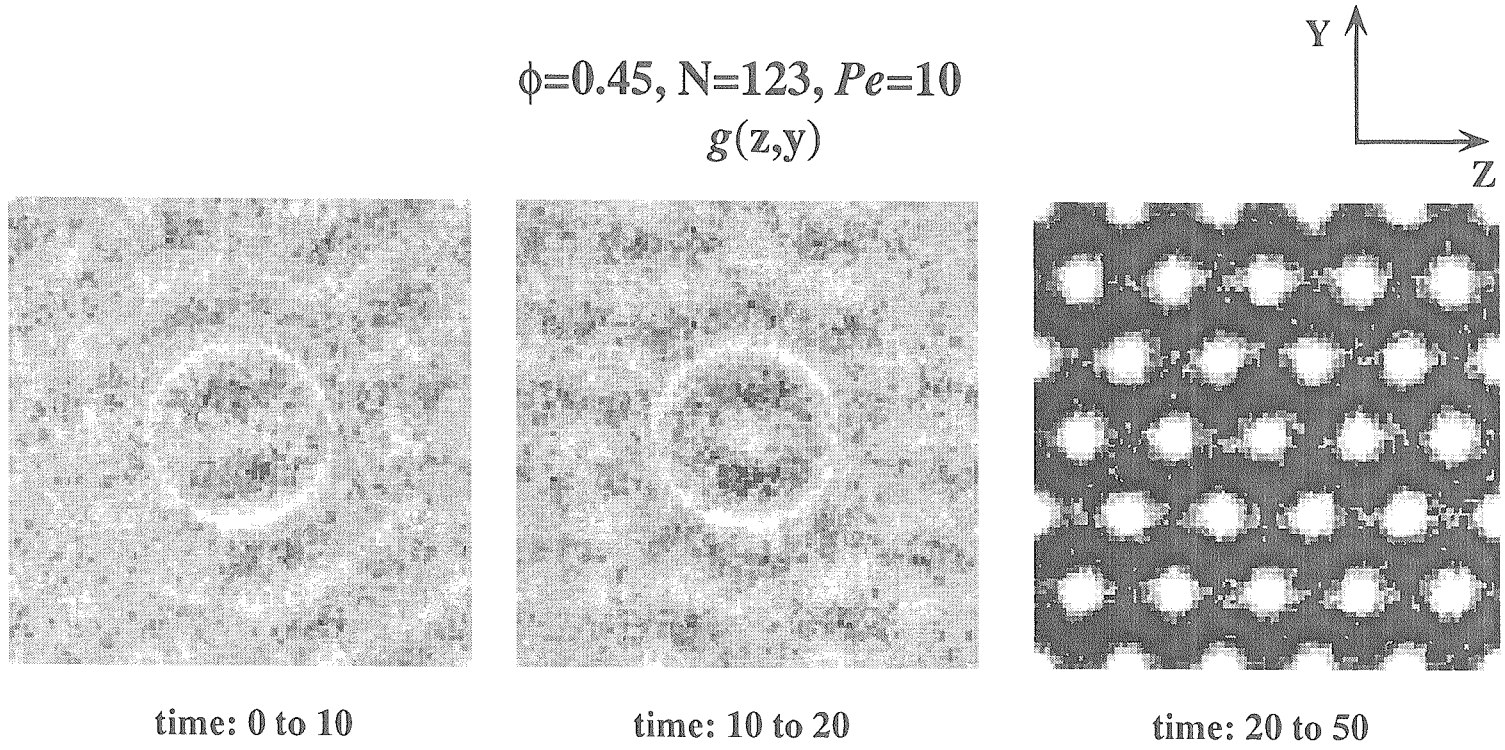

Figure 6.10.b: The evolution of the probability density $g(z,y)$ for a hard-sphere suspension at volume fraction ϕ=0.45 with 123 particles and Pe=10 obtained by Stokesian dynamics. Regions of light color represent high probability and regions of dark color represent low probability. The flow direction is perpendicular to the z-y plane. The vorticity direction is the horizontal z-axis and the velocity gradient direction is the vertical y-axis. The probability density function $g(z,y)$ is shown for different times. The right most figure is the steady probability density function $g(z,y)$ after a dimensionless time of 50. The figure shows the formation of a distinct "hexagonal" packing of strings of particles flowing out of the z-y plane.

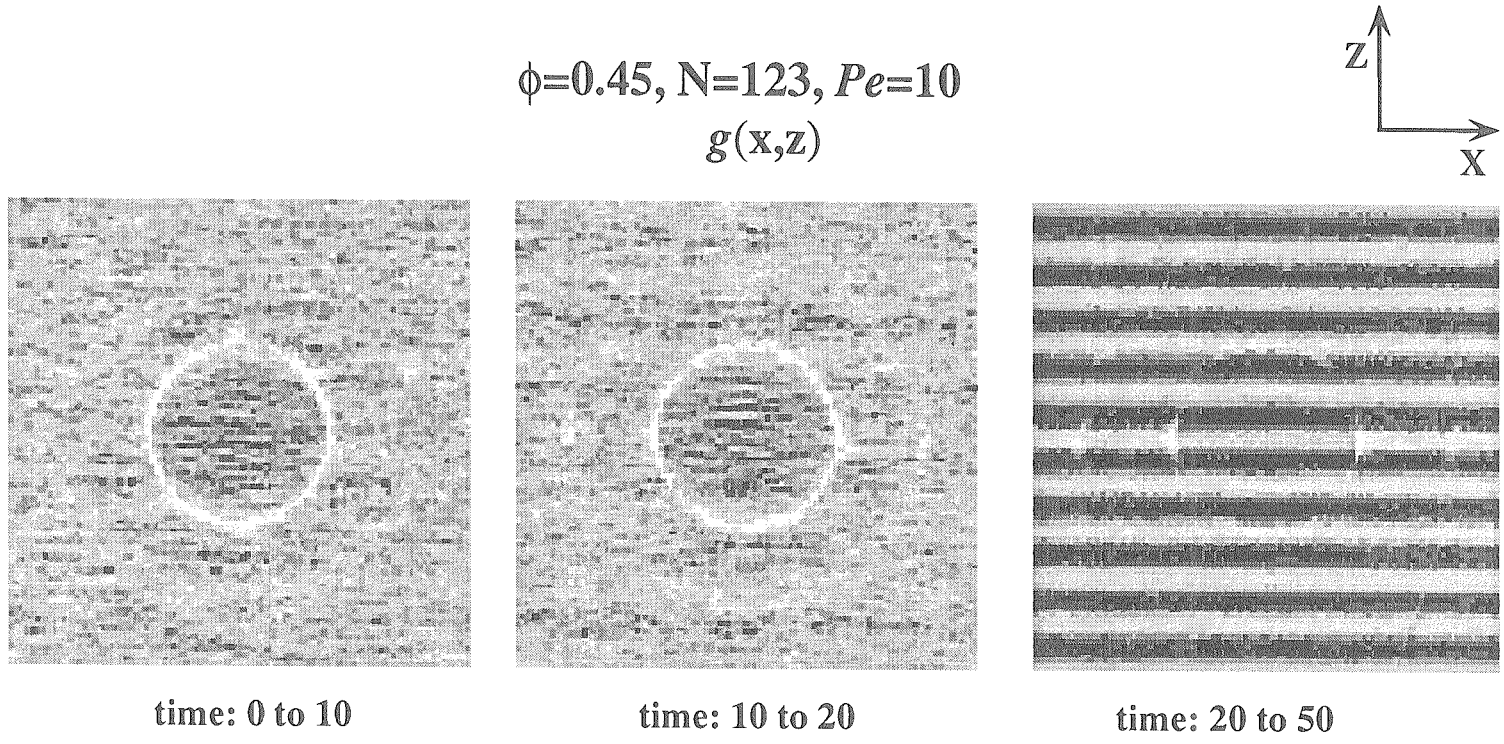

Figure 6.10.c: The time evolution of the probability density $g(x,z)$ for a hard-sphere suspension at volume fraction $\phi=0.45$ with 123 particles and $Pe=10$ obtained by Stokesian dynamics. Regions of light color represent high probability and regions of dark color represent low probability. The flow direction is the horizontal x-axis and the vorticity direction is the vertical z-axis. The probability density function $g(x,z)$ is shown for different times. The right most figure is the steady probability density function $g(x,z)$ after a dimensionless time of 50 and shows clearly the "strings" of particles flowing along the flow direction.

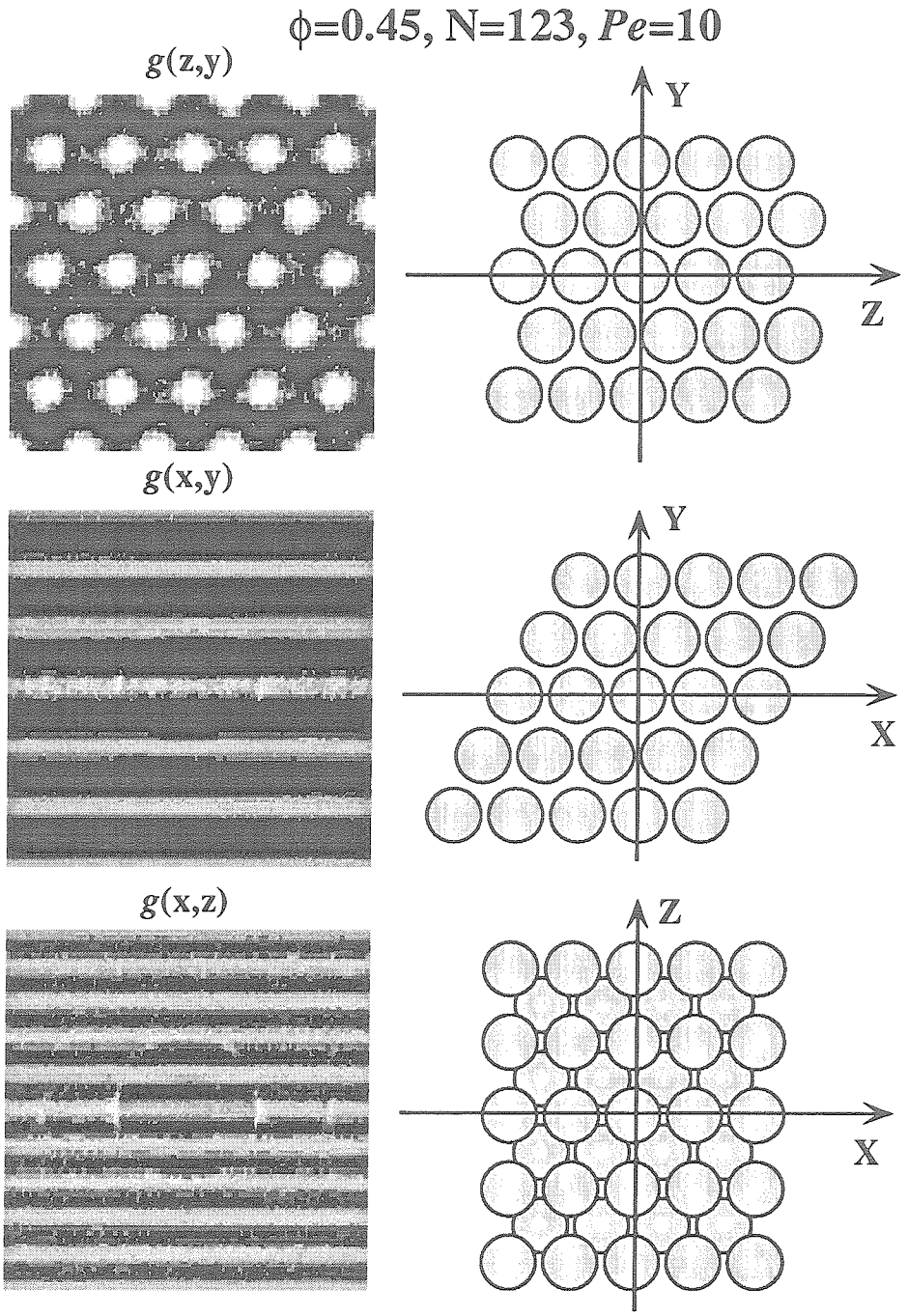

Figure 6.10.d: Plots of the particle positions obtained by Stokesian dynamics for a hard-sphere suspension at volume fraction ϕ=0.45 with 123 particles and Pe=10. From top to bottom: the left column shows a plot of the steady probability density functions g(z,y), g(x,y), and g(x,z) and on the right the corresponding particle positions determined from these density plots.

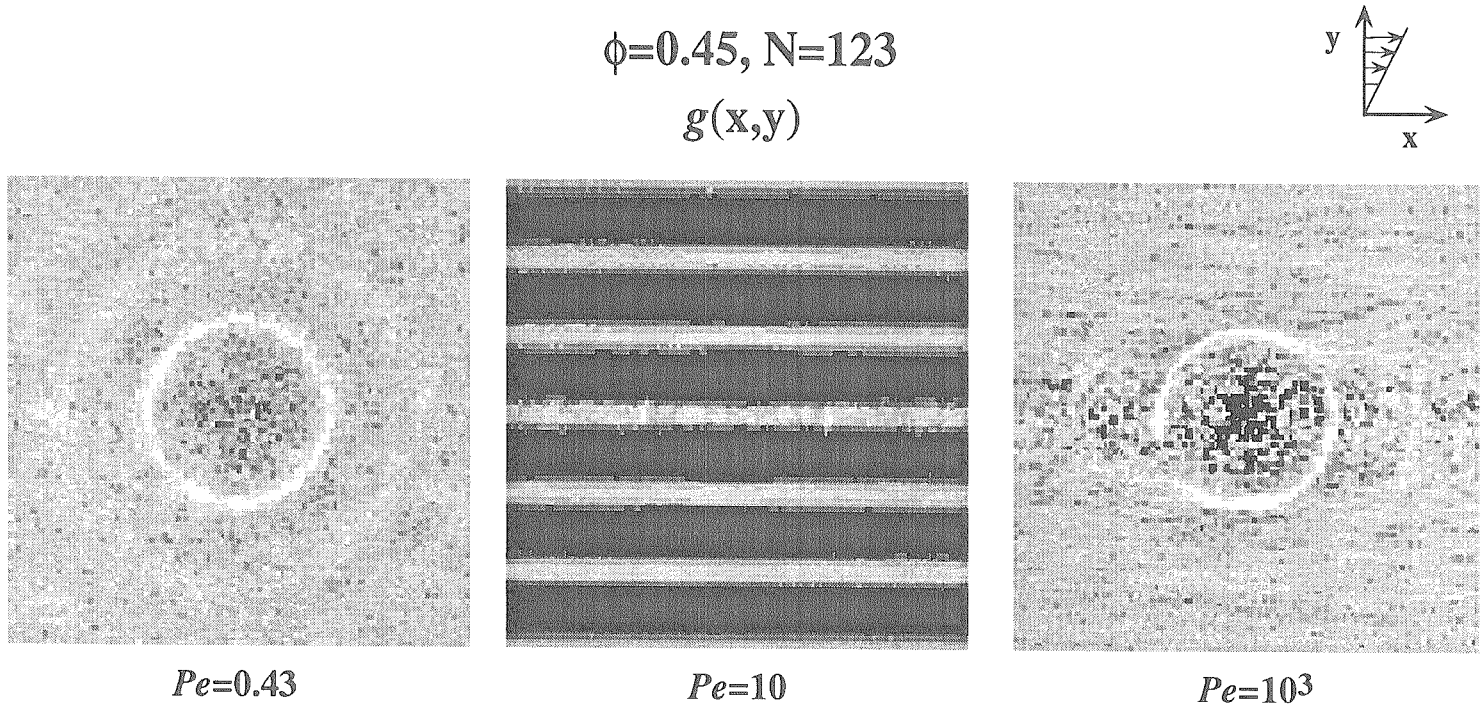

Figure 6.10.e: A comparison of the steady probability density $g(x,y)$ for hard-sphere suspensions at a volume fraction $\phi=0.45$ with 123 particles and different Peclet numbers: 0.43 (left figure), 10 (central figure) and 1000 (right figure) obtained by Stokesian dynamics. Regions of light color represent high probability and regions of dark color represent low probability. The flow direction is the horizontal x-axis and the velocity gradient is the vertical y-axis. For suspensions with a small deformation (Pe=0.43), the steady $g(x,y)$ shows a random structure with a slightly distorted symmetric ring. The formation of "strings" of flowing particles in the flow direction can only be seen for Pe=10. At higher shear rates (Pe=1000), the string formation is destroyed. Note also the sharpening of the first nearest neighbor ring.

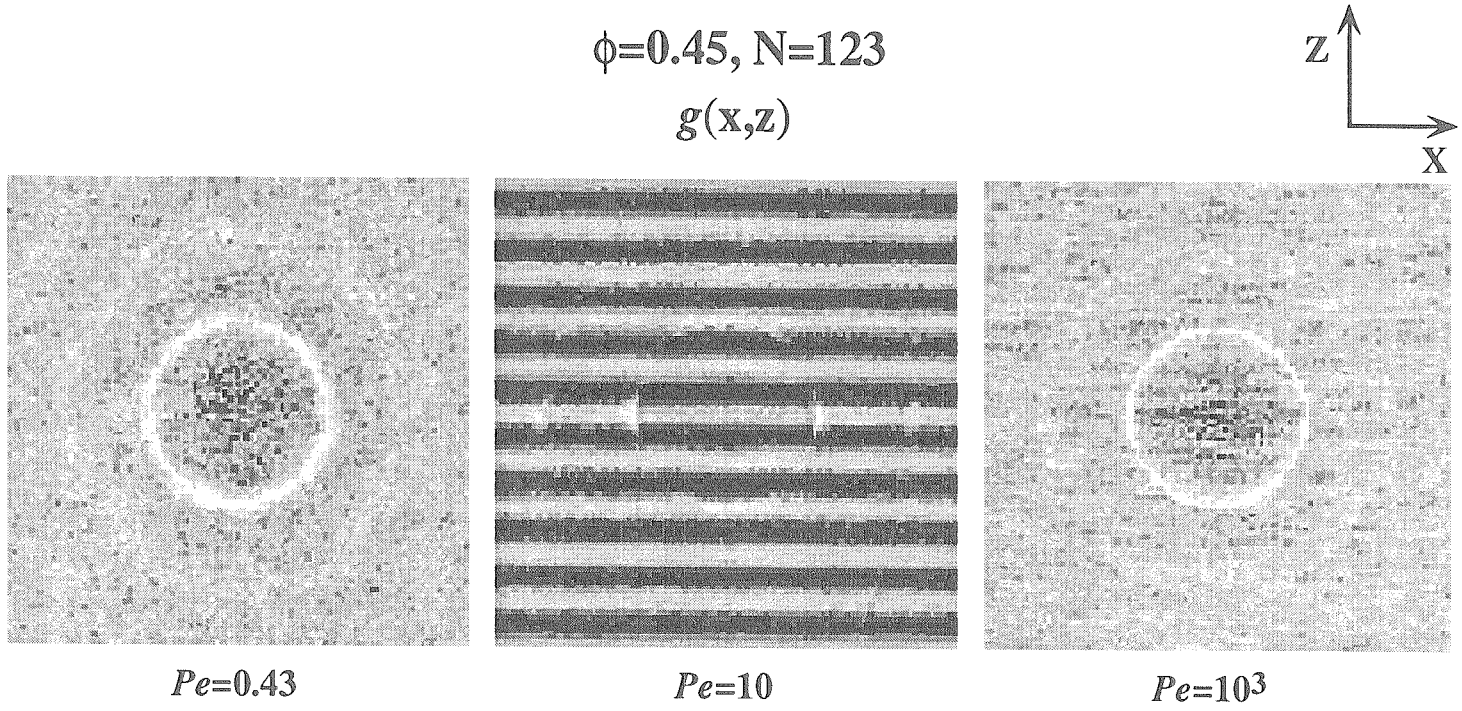

Figure 6.10.f: A comparison of the steady probability density $g(x,z)$ for hard-sphere suspensions at a volume fraction ϕ=0.45 with 123 particles and different Péclet numbers: 0.43 (left figure), 10 (central figure) and 1000 (right figure) obtained by Stokesian dynamics. Regions of light color represent high probability and regions of dark color represent low probability. The flow direction is the horizontal x-axis and the vorticity direction is the vertical z-axis. The formation of "strings" of particles along the flow direction can only be seen for Pe=10 (central figure).

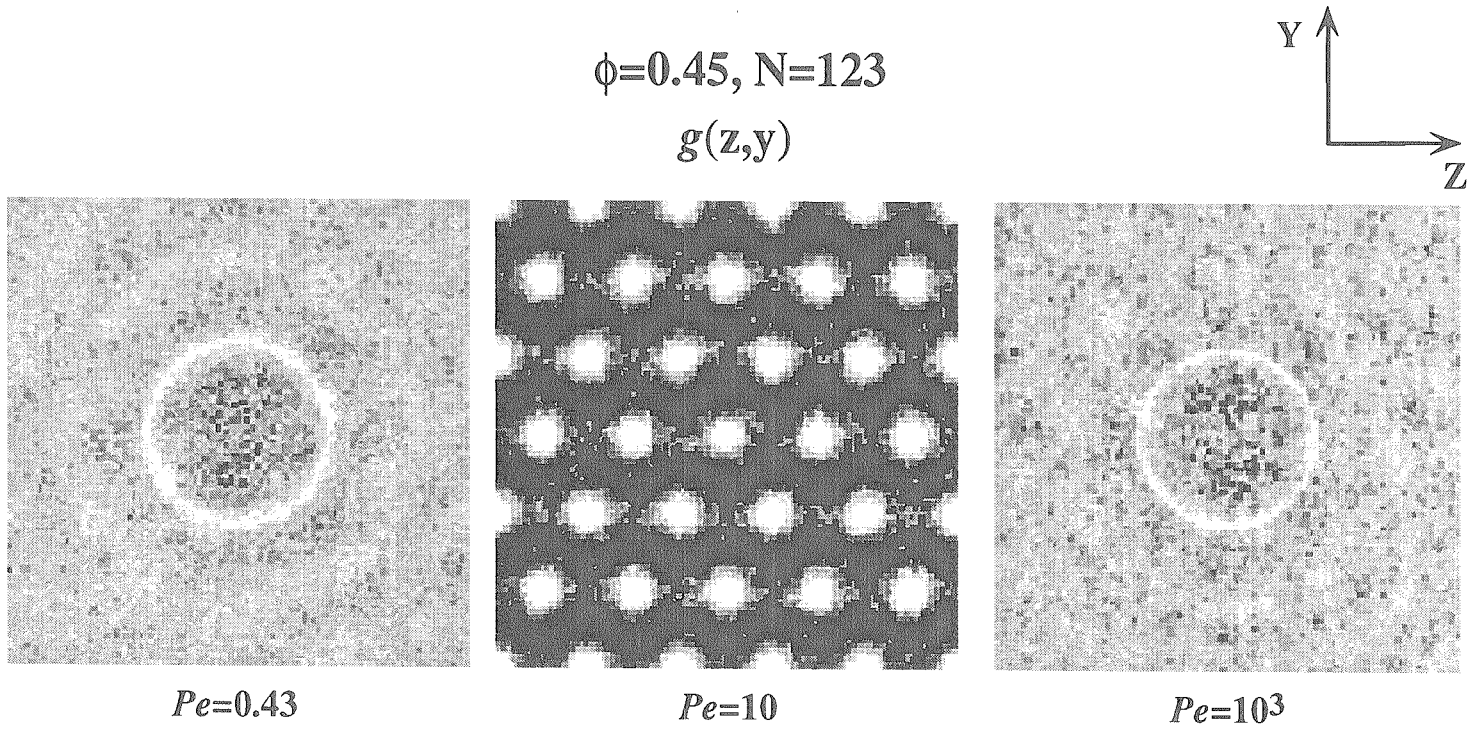

Figure 6.10.g: A comparison of the steady probability density $g(z,y)$ for hard-sphere suspensions at a volume fraction ϕ=0.45 with 123 particles and different Péclet numbers: 0.43 (left figure), 10 (central figure) and 1000 (right figure) obtained by Stokesian dynamics. Regions of light color represent high probability and regions of dark color represent low probability. The flow direction is perpendicular to the z-y plane with the vorticity direction in the horizontal z-axis and the velocity gradient direction in the vertical y-axis. At Pe=10, the balance of the shear and Brownian forces induce the flowing suspension to strong ordering with a distinct "hexagonal" packing of strings of flowing particles.

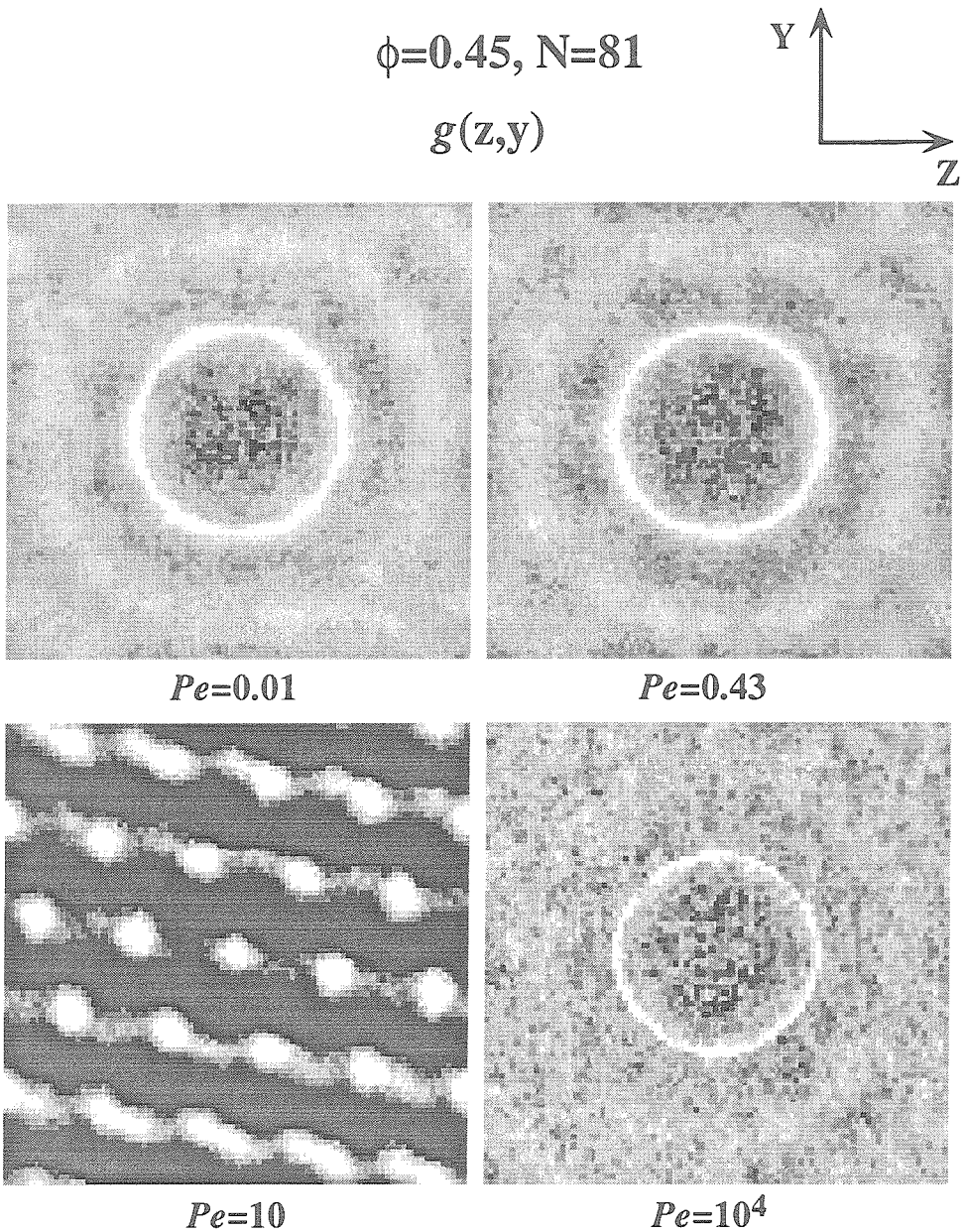

Figure 6.11.a: A plot of probability density $g(z,y)$ for hard spheres at a volume fraction ϕ=0.45 and different Péclet numbers. There are 81 particles in the unit cell. Regions of light color represent high probability and regions of dark color represent low probability. The flow direction is perpendicular to the z-y plane. The vorticity direction is the horizontal z-axis and the velocity gradient direction is the vertical y-axis. In the region of string formation, the hexagonal string arrangement cannot be accommodated within the unit cell for 81 particles. It is inclined as illustrated in Fig.6.11.b.

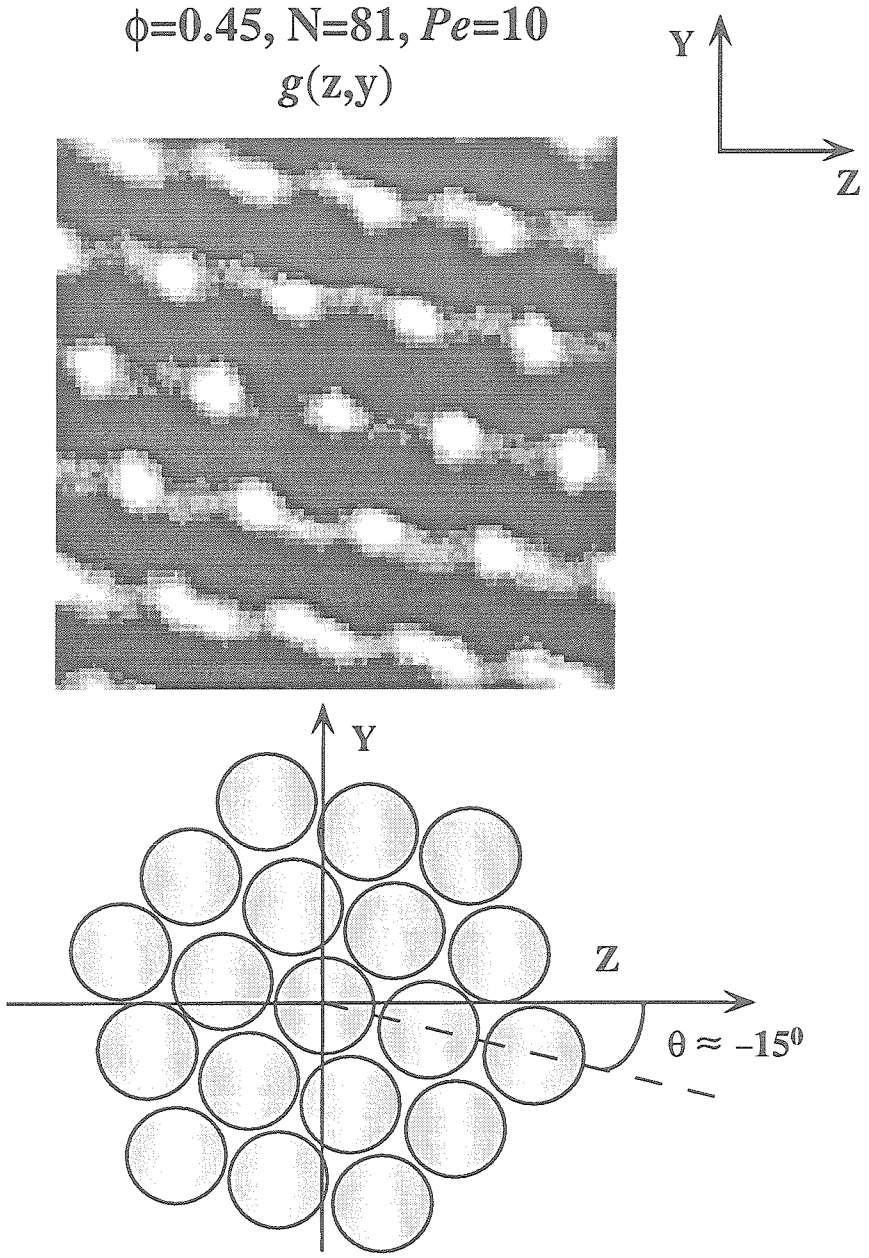

Figure 6.11.b: A plot of particle positions determined from the density plot of Fig.6.11.a for $g(z,y)$ with Pe=10, N=81 and ϕ=0.45. The upper figure is the density plot for $g(z,y)$. The lower figure is the particle positions which shows the formation of the hexagonal packing and "strings" of particles in the flow direction. The hexagonal pattern is rotated by an angle $\theta \approx$-15 degrees relative to the horizontal z-axis, the vorticity direction, in order to accommodate the packing with the unit cell. The flow direction is perpendicular to the z-y plane.

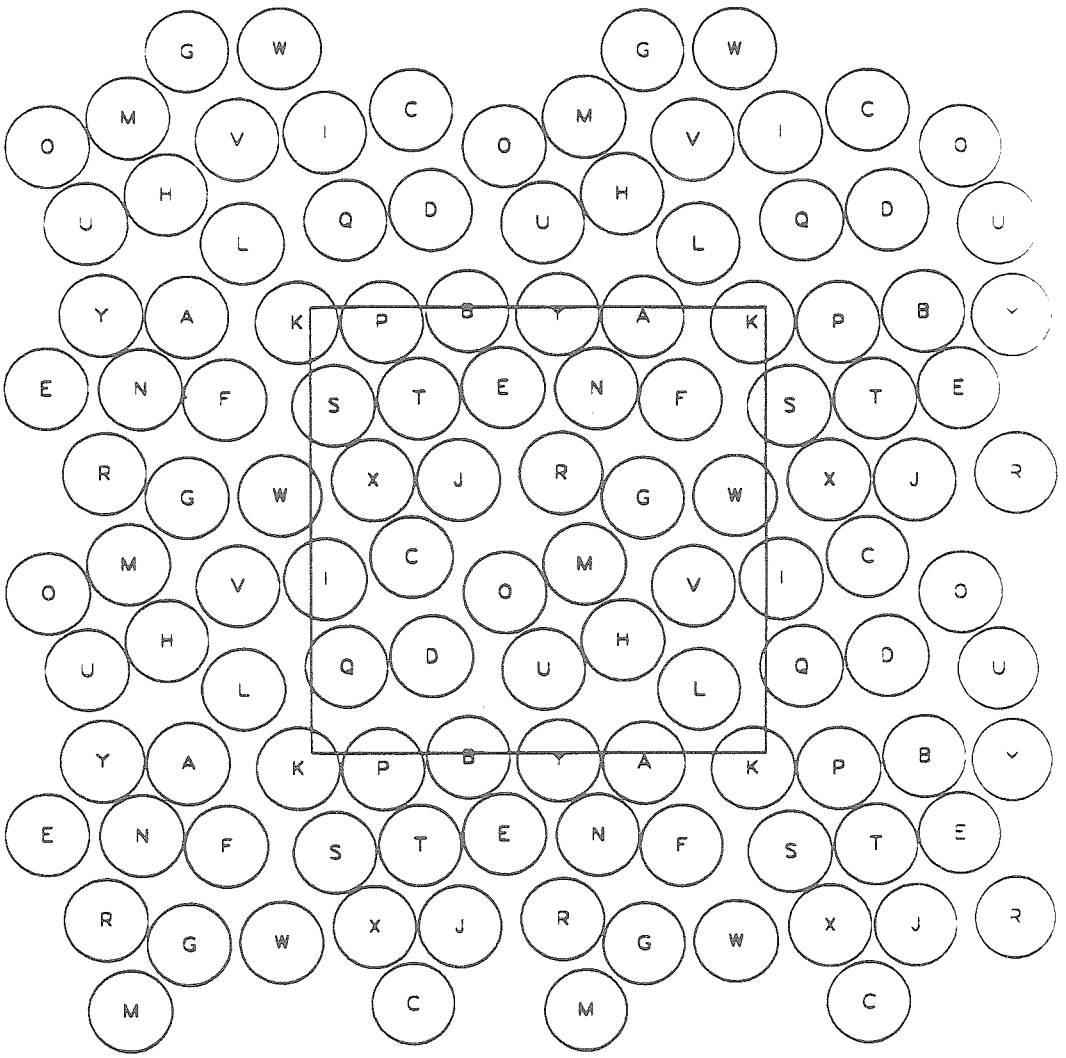

Figure 6.12: A snap shot of the starting configuration for 25 particles in a monolayer model for hard spheres at an areal fraction ϕ_A=0.675 which is comparable to a volume fraction ϕ=0.45. The center square is the unit cell. The particles outside the unit cell are periodic images.

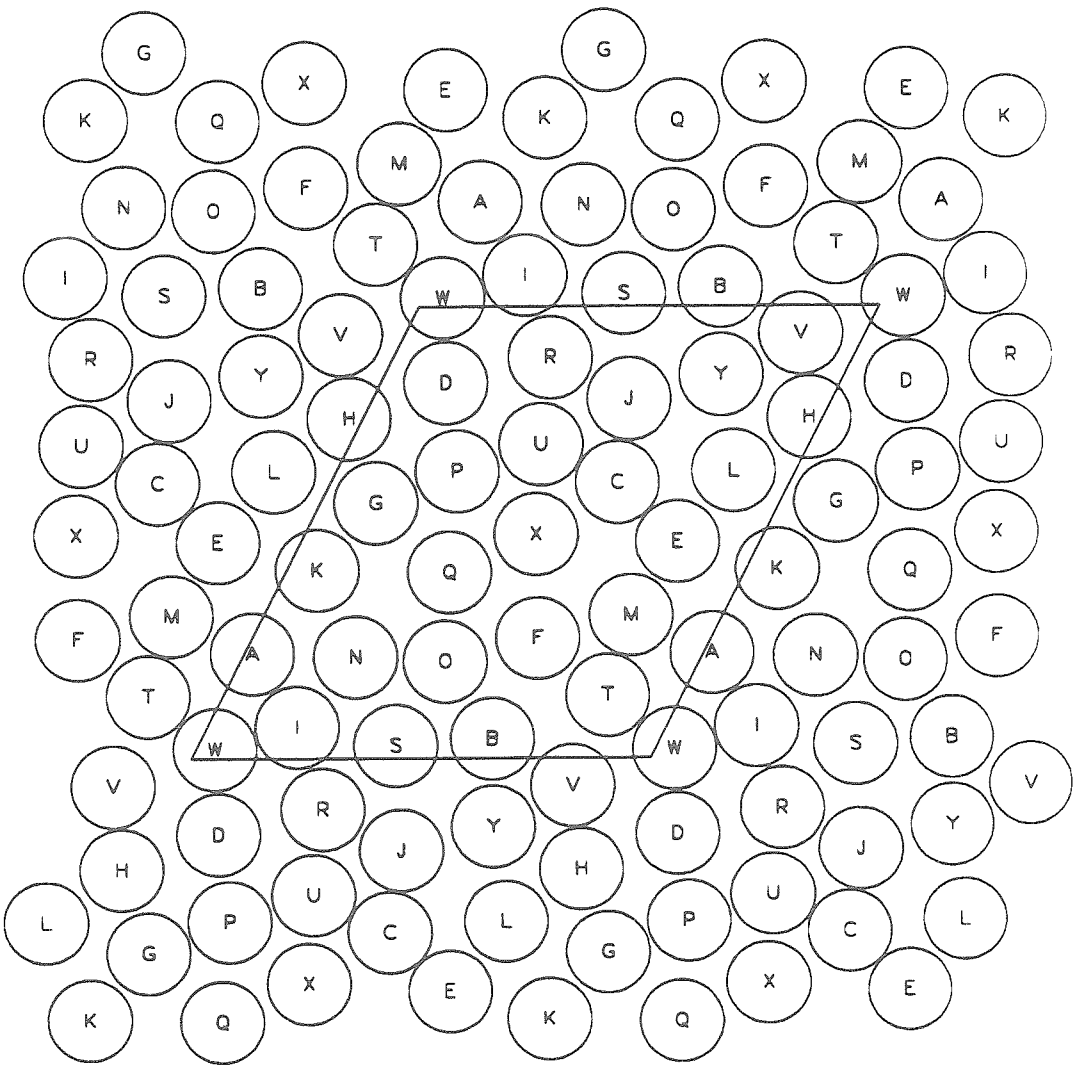

Figure 6.13.a: A snap shot of the particle positions at time t=100. The suspension is sheared with Pe=0.01 and it is seen from the figure that the particle configuration is "random" as expected for suspensions with strong Brownian motion.

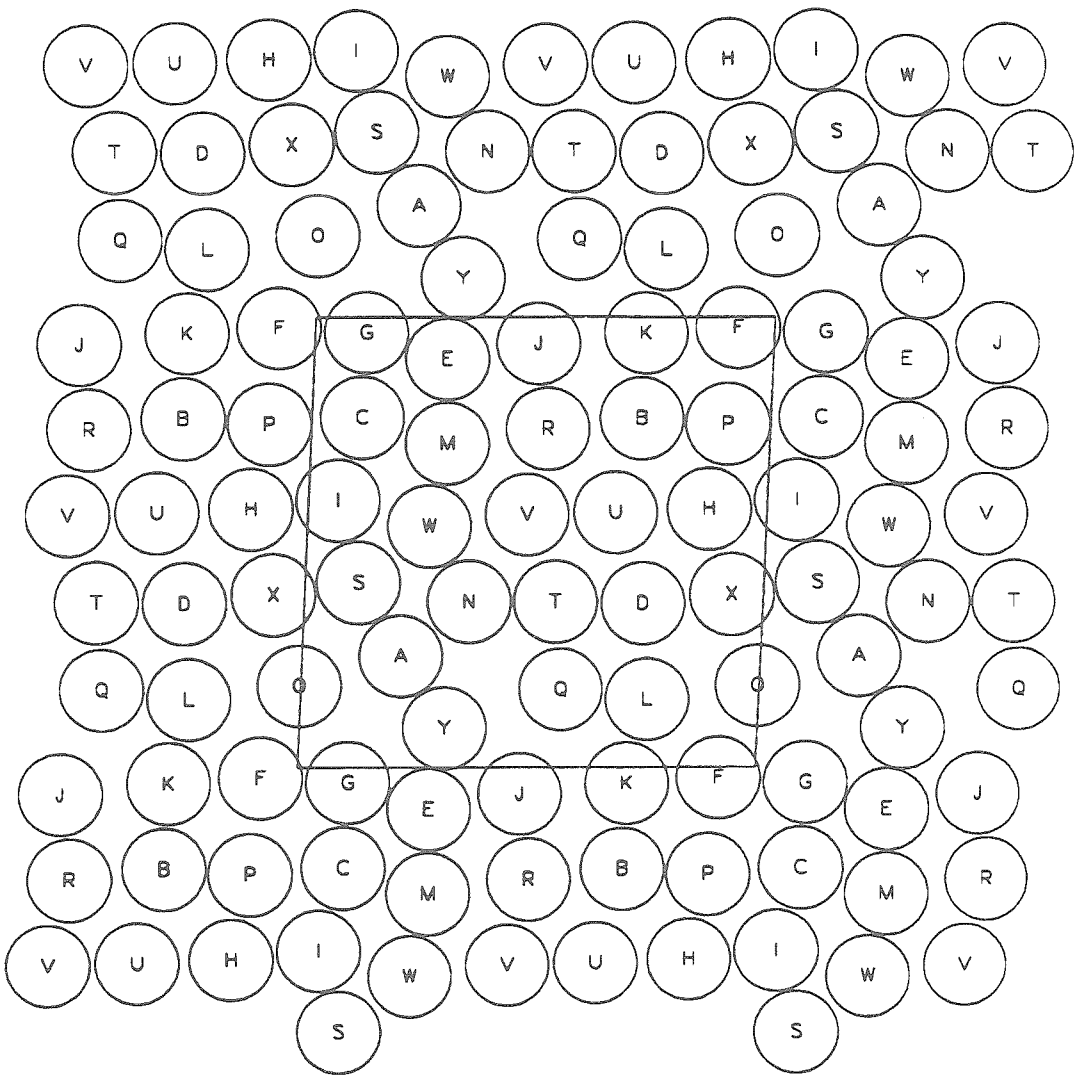

Figure 6.13.b: A snap shot of the positions of 25 particles at time t=350. The figure shows a random structure for suspensions with a small deformation (Pe=0.01). The particles are well dispersed in the Brownian domination limit.

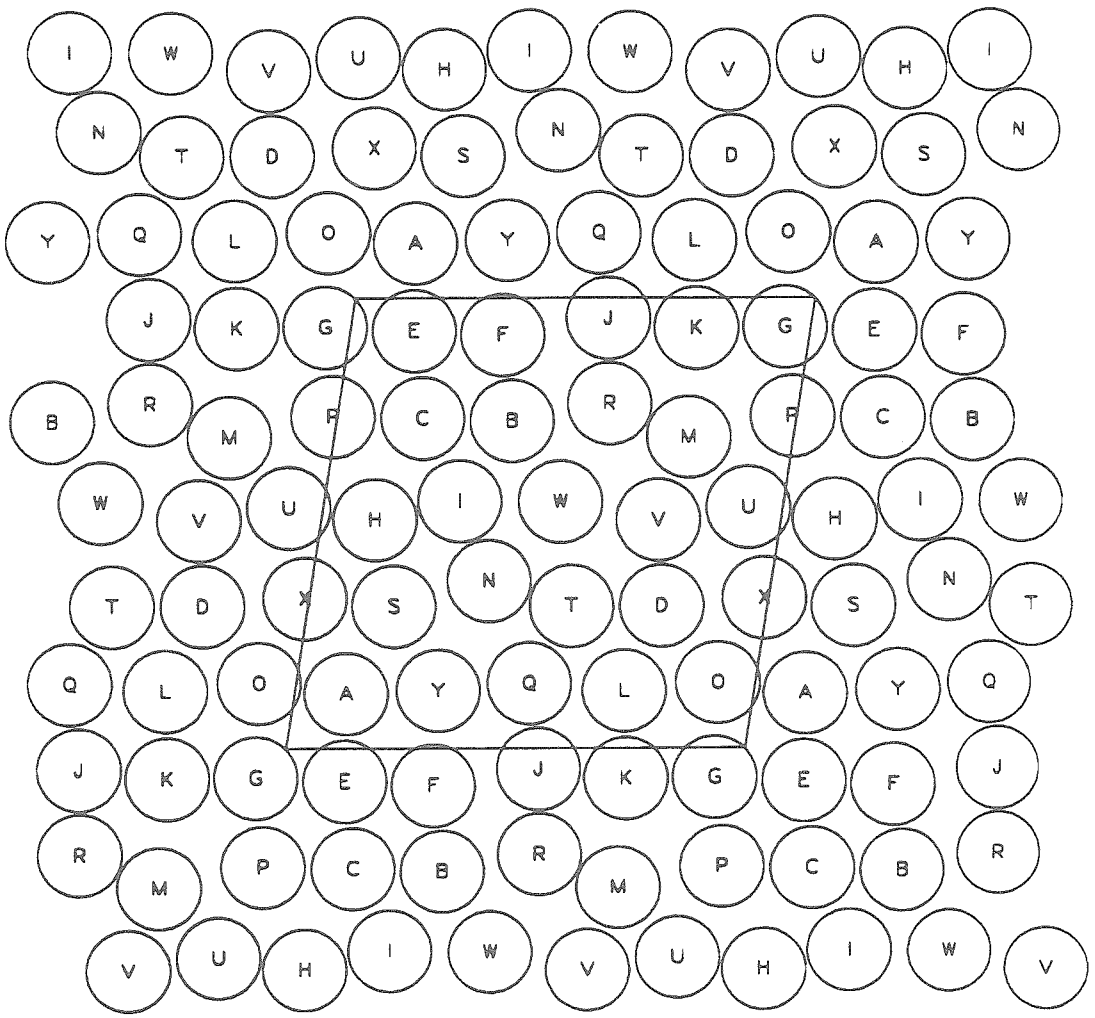

Figure 6.14.a: A snap shot of the particle positions at time t=450. The suspension is sheared at Pe=10 and the figure shows clearly the horizontal "string" formation of flowing particles. The particles are relatively well separated from each other. The flow direction is the horizontal x-axis and the velocity gradient direction is the vertcial y-axis.

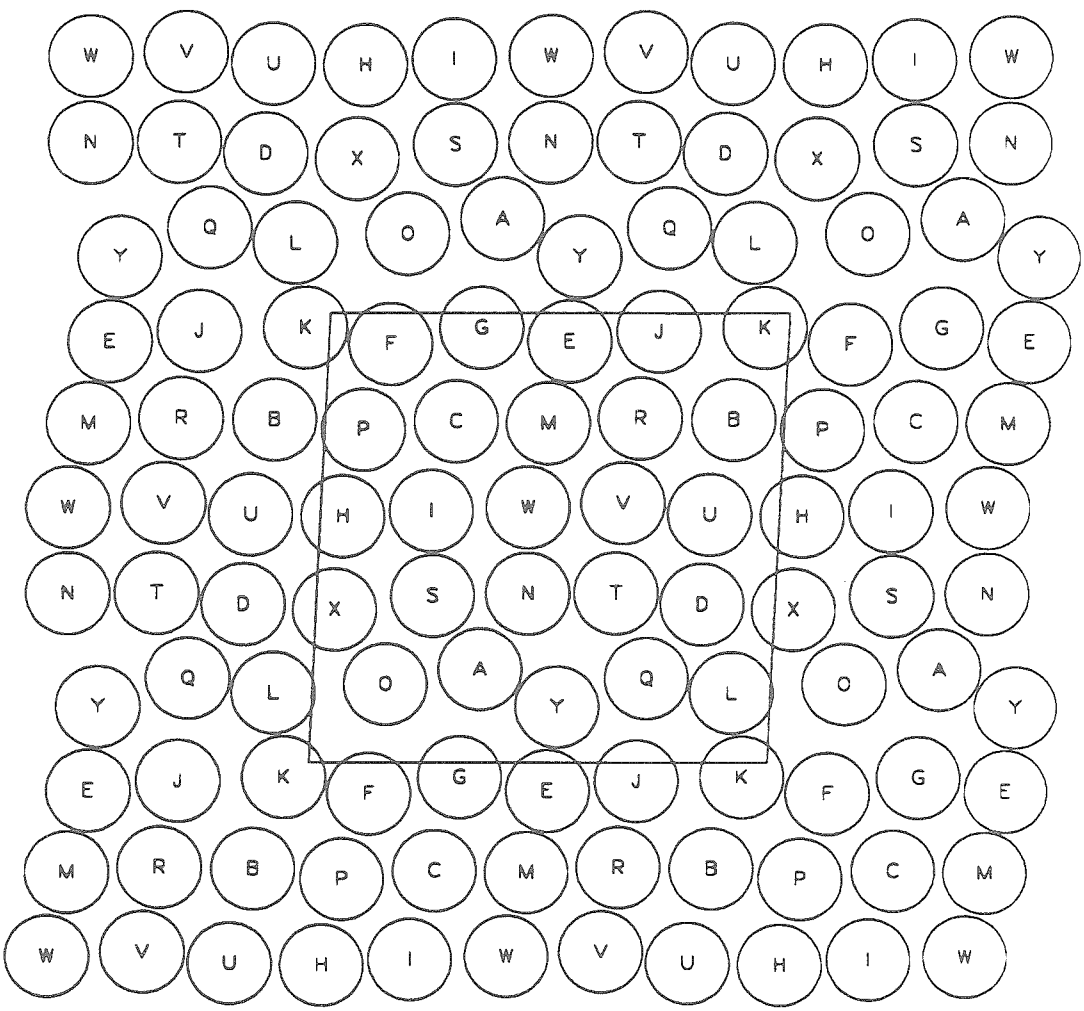

Figure 6.14.b: A snap shot of the particle positions at time t=550. At Pe=10, the microstructure displays a distinct formation of horizontal strings of flowing particles.

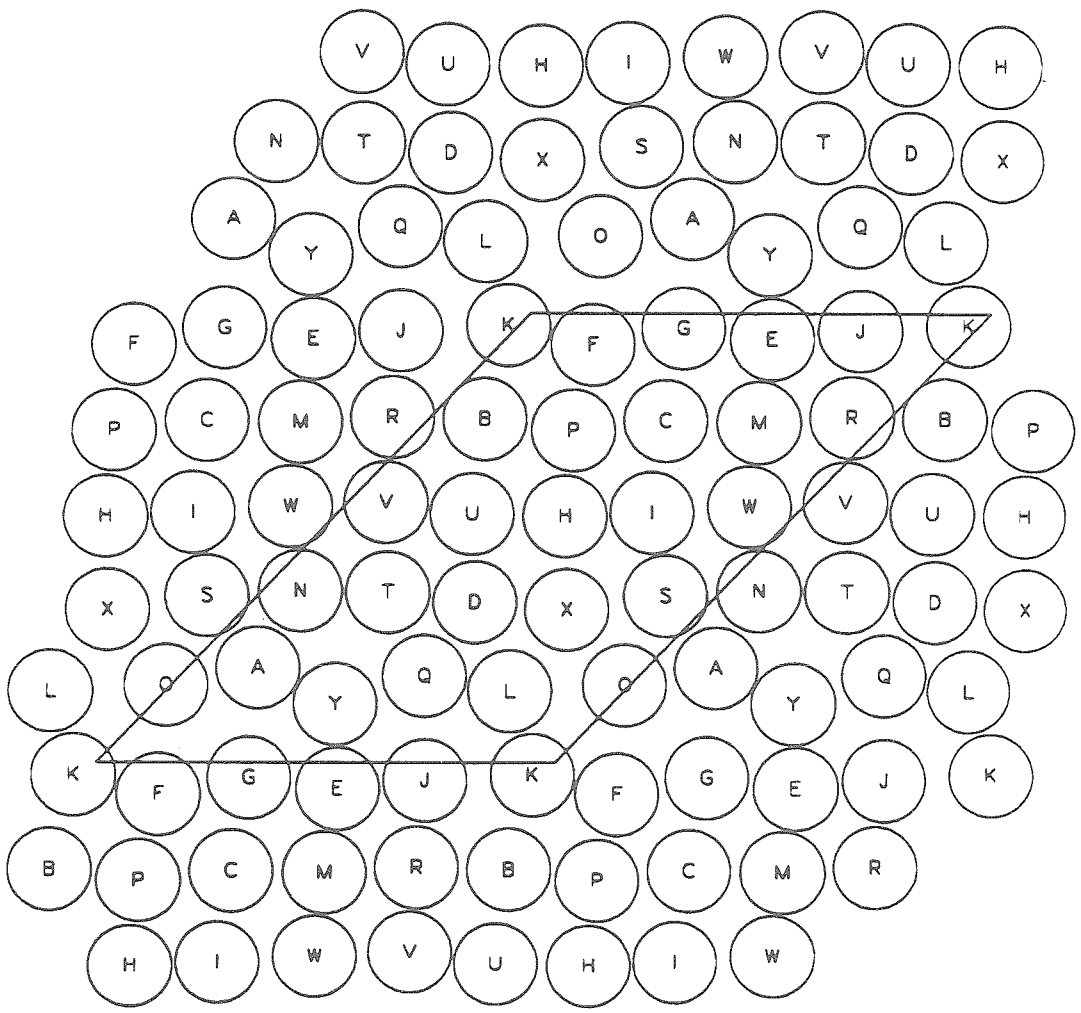

Figure 6.14.c: A snap shot of the particle positions at time t=700. The strong ordering microstructure with string formation of flowing particles is stable as the shear rate is kept constant at Pe=10.

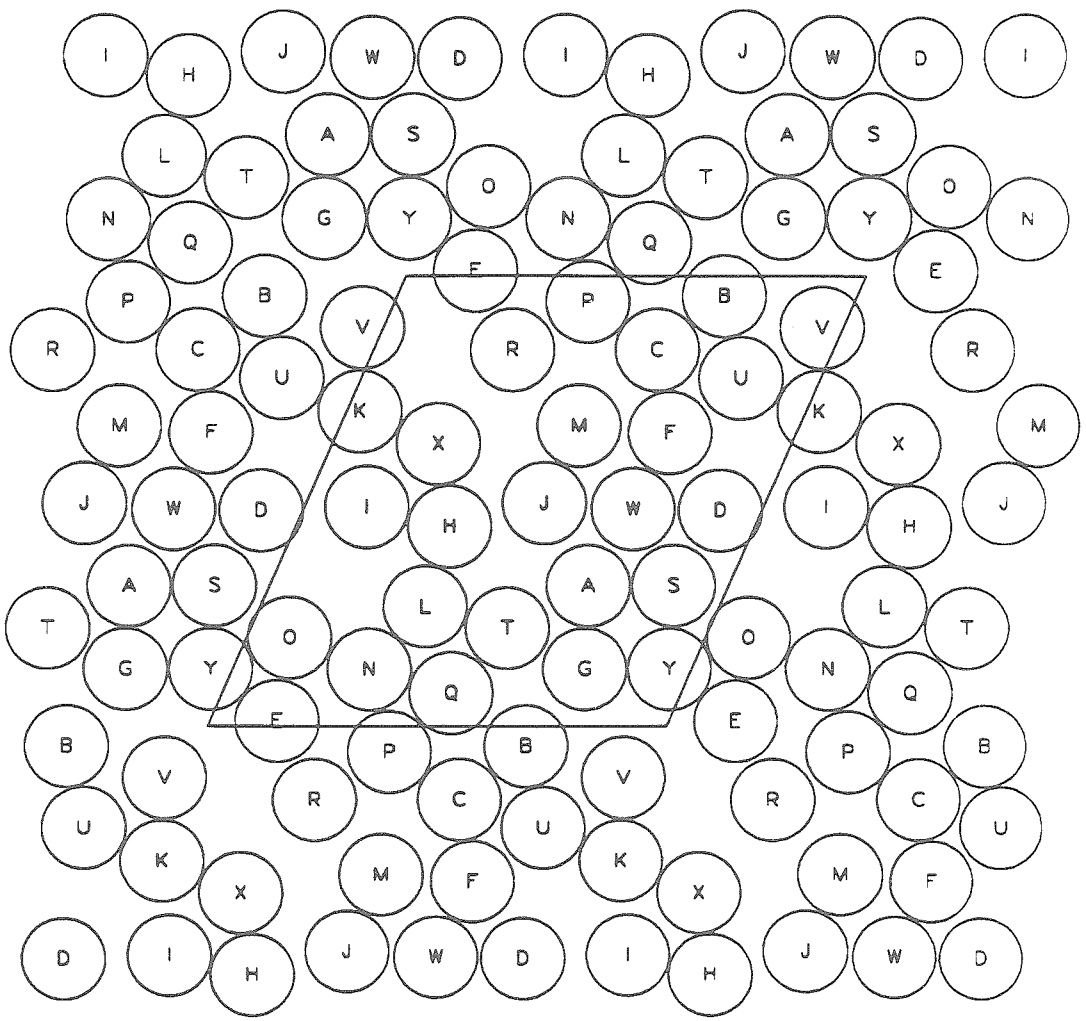

Figure 6.15.a: A snap shot of the particle positions at time t=750. Strong shear rates (Pe=10^3) are seen to destroy the string formation of the flowing particles and the hydrodynamically driven microstructure clearly shows large clusters of particles.

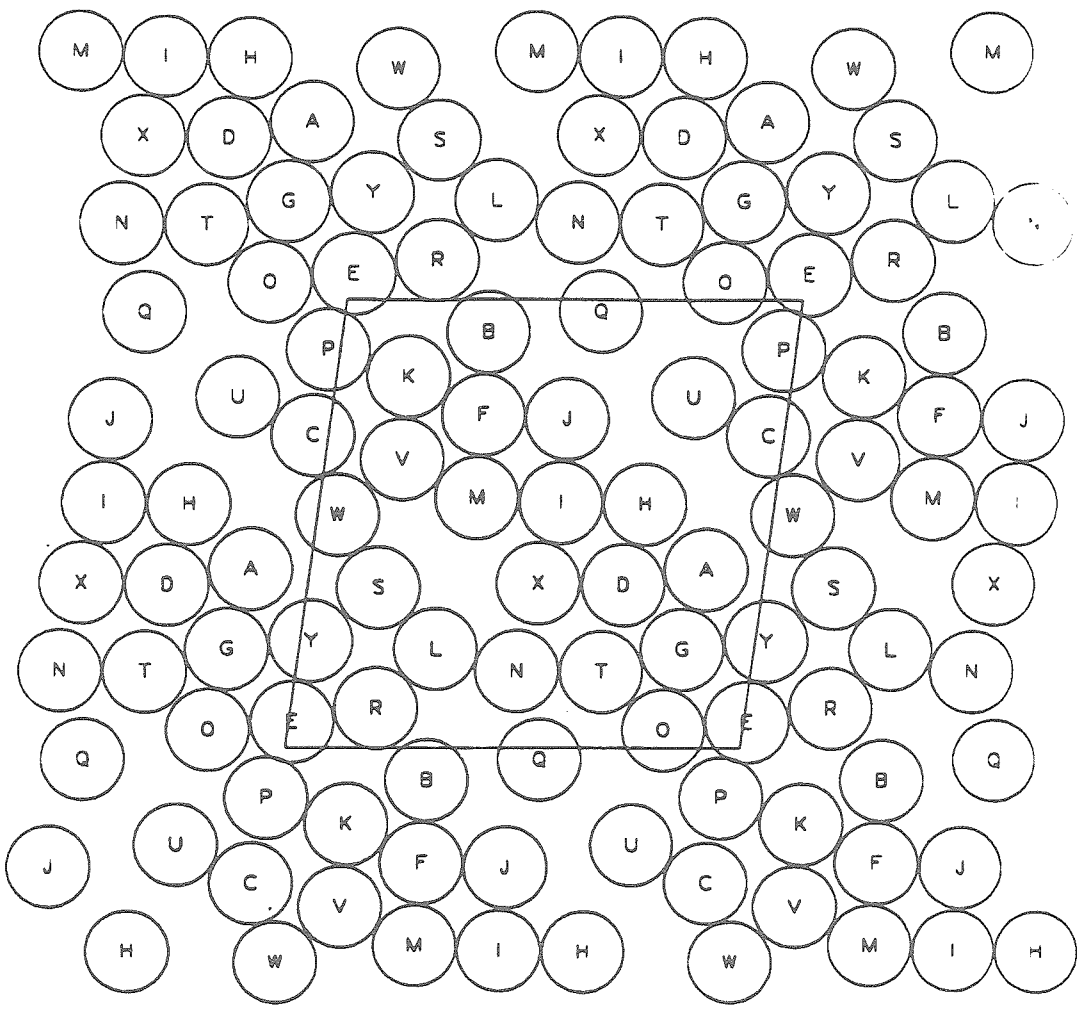

Figure 6.15.b: A snap shot of the particle positions at time t=850 for hard spheres with Pe=10^3. Note the very large spanning cluster of the particles along the compression axis (135°) of the shear flow for strong hydrodynamic interactions.

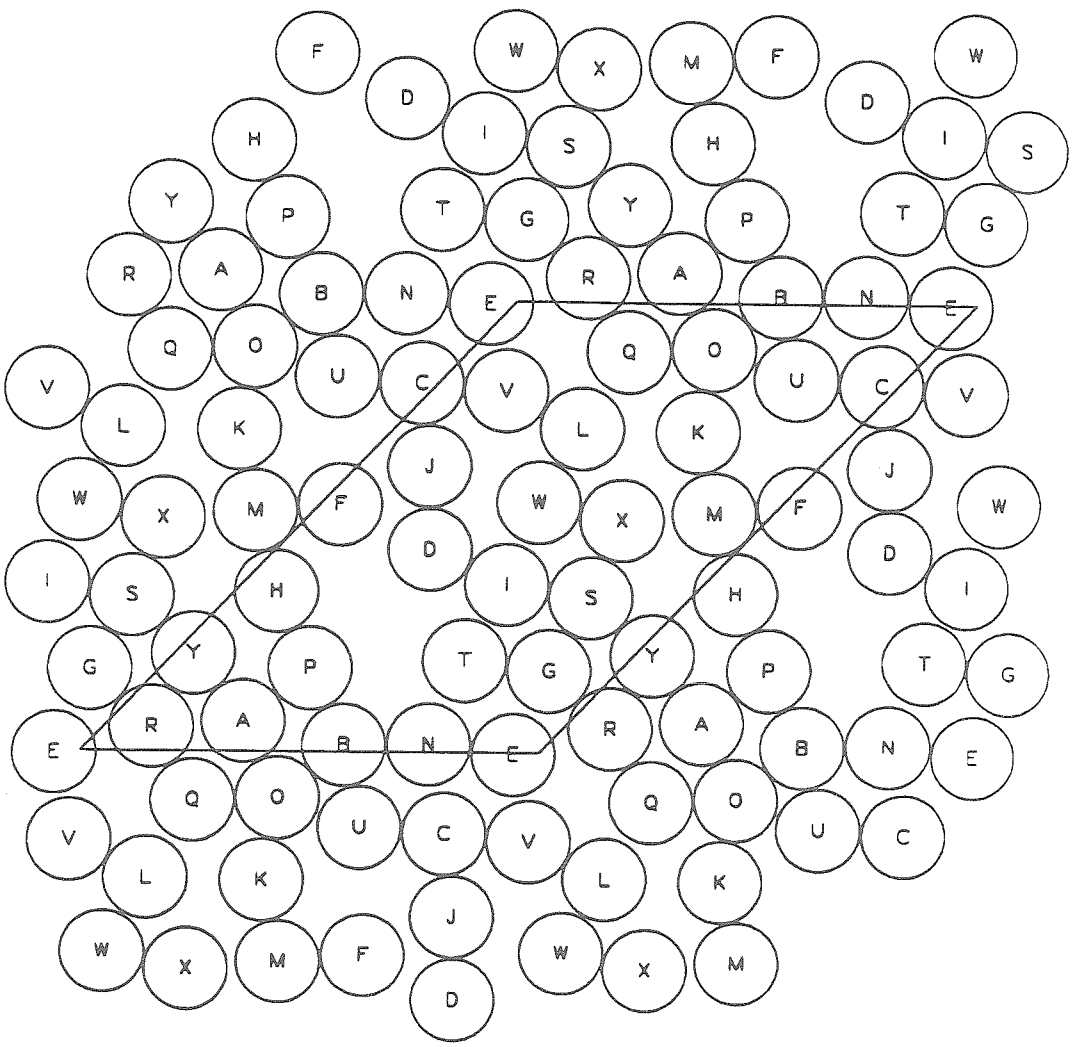

Figure 6.15.c: A snap shot of the particle positions at time t=940 for hard spheres with Pe=10^3. The suspension structure is observed with chains of clusters of the particles which span the entire unit cell.

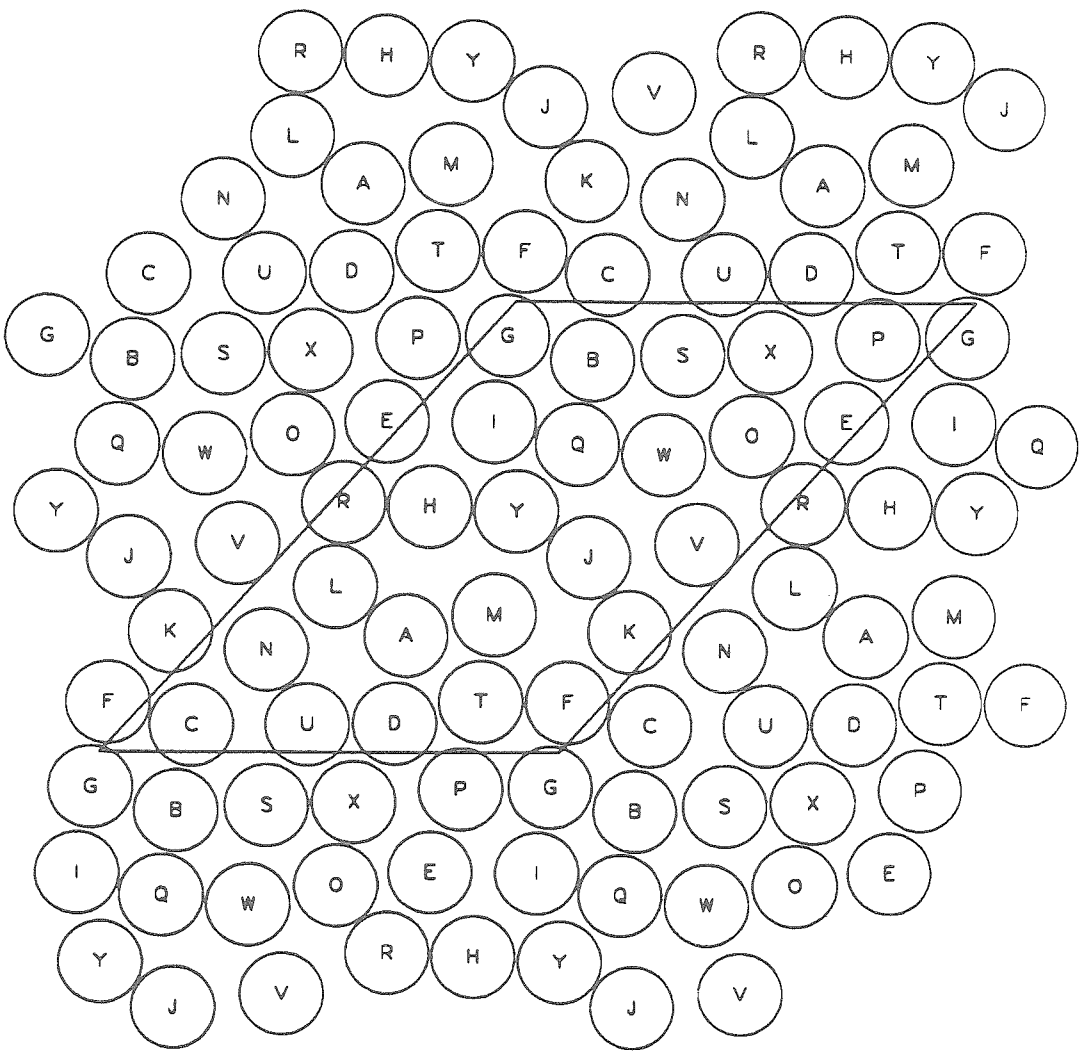

Figure 6.16.a: A snap shot of the particle positions at time t=1100 for hard spheres with Pe=10. Note the absence of the large cluster as the Péclet number is reduced from Pe=10^3 to Pe=10. The particles flow as strings along the flow direction and are very well dispersed.

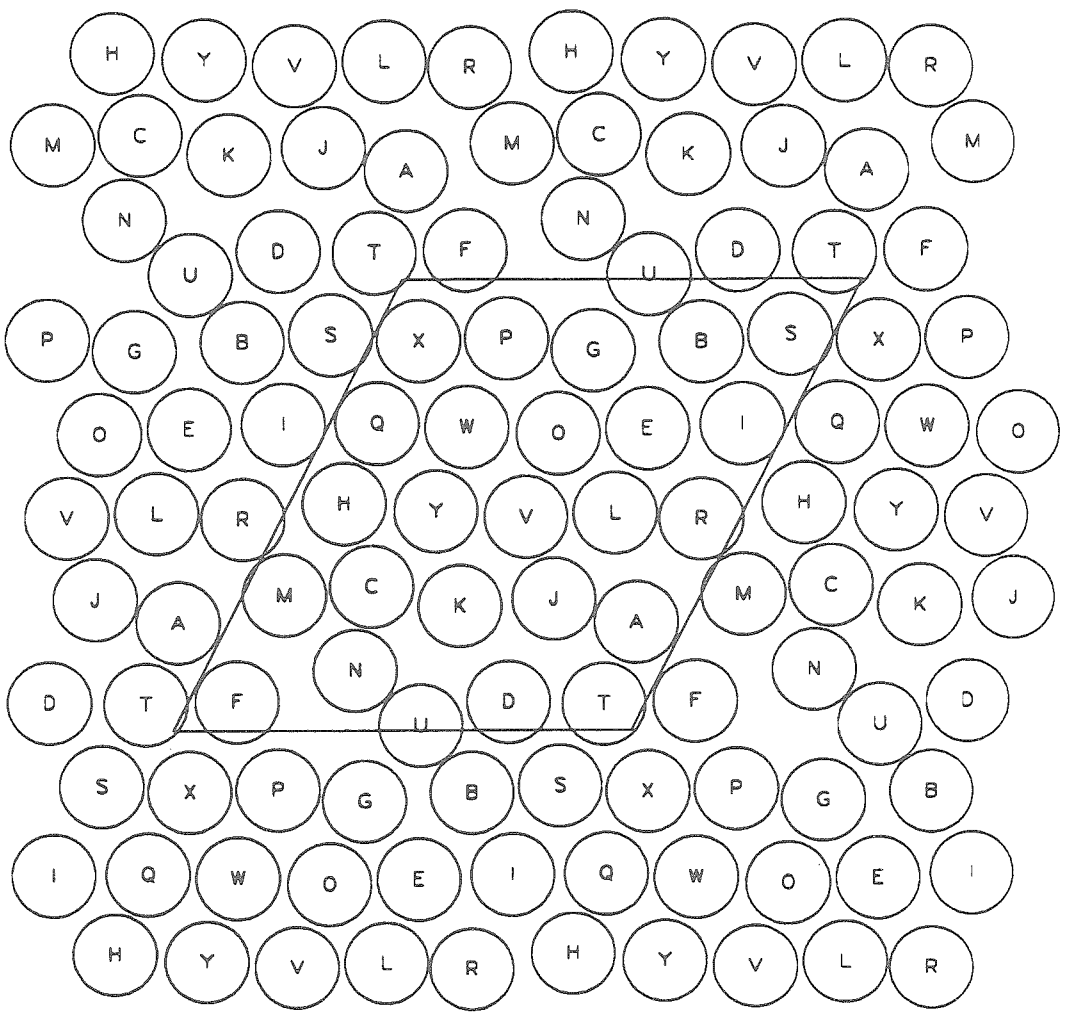

Figure 6.16.b: A snap shot of the particle positions at time t=1240 for hard spheres with Pe=10. The figure displays a suspension microstructure with distinct string formation of flowing particles.

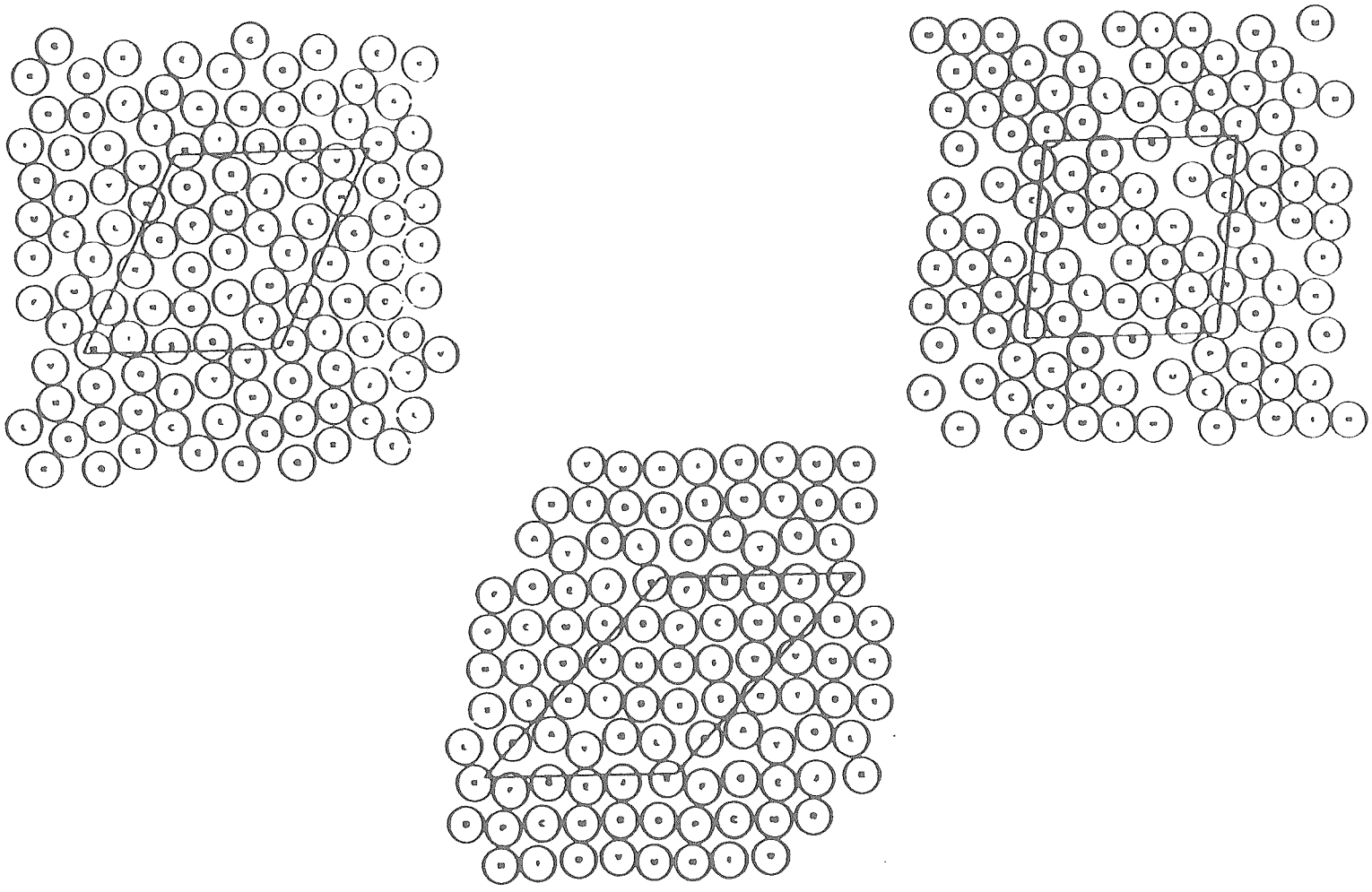

Figure 6.17: Snap shots of the particle positions in three distinct microstructures: (left) well dispersed particles in slightly deformed suspensions at Pe=0.01, (central) "strings" of flowing particles for suspensions with a balance of Brownian and hydrodynamic forces at Pe=10 and (right) large clusters of particles in hydrodynamcially driven suspensions at Pe=10^3.

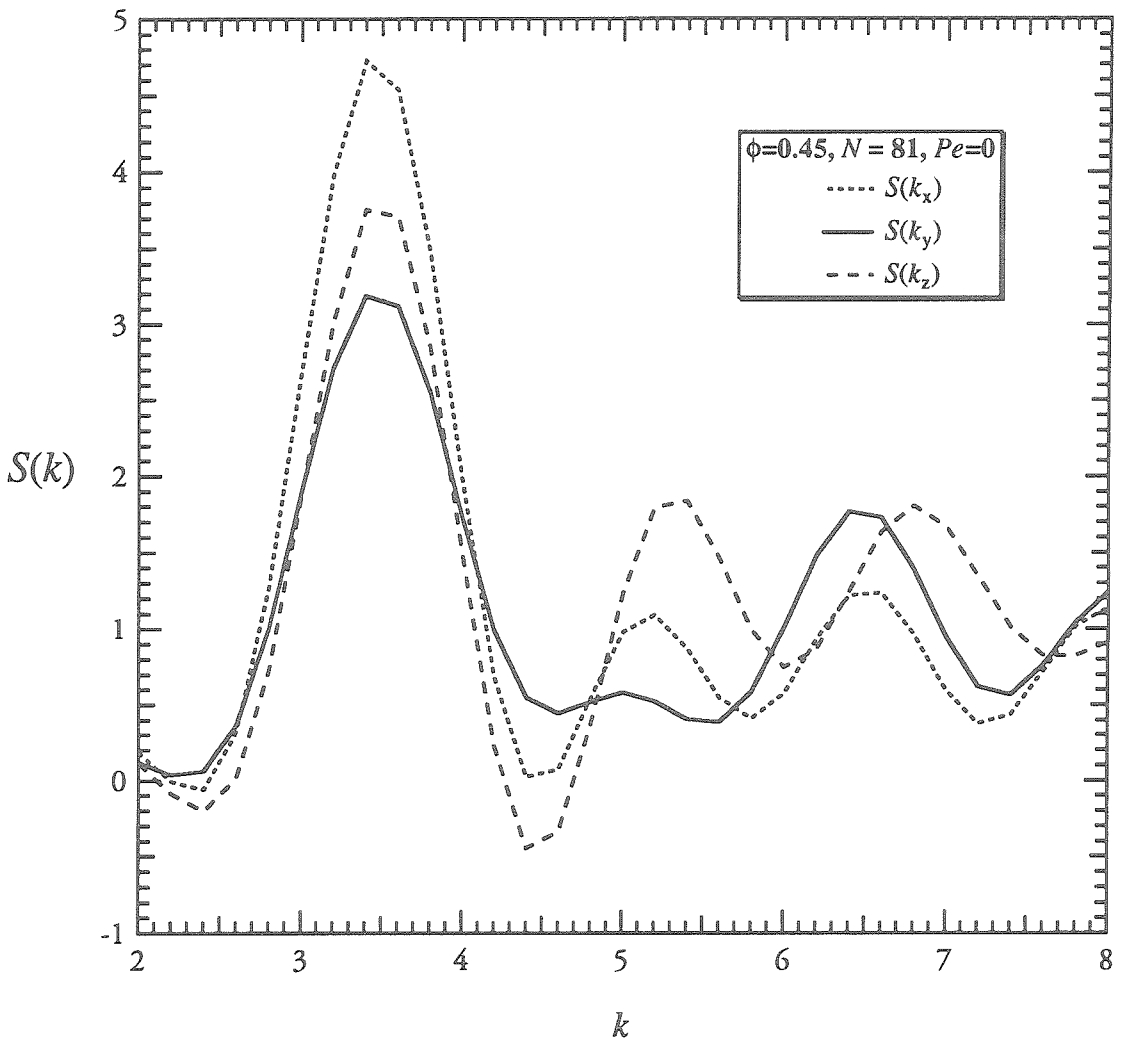

Figure 6.18: The equilibrium structure factor $S(k)$ of hard-sphere suspensions at a volume fraction ϕ=0.45 and 81 particles obtained by Stokesian dynamics at Pe=0 with different dimensionless wave numbers : (dotted curve) $S(k_x)$, (solid curve) $S(k_y)$ and (dashed curve) $S(k_z)$. The equilibrium structure factors computed along different directions show small variations due to a relatively small number of 500 samples of particle configurations .

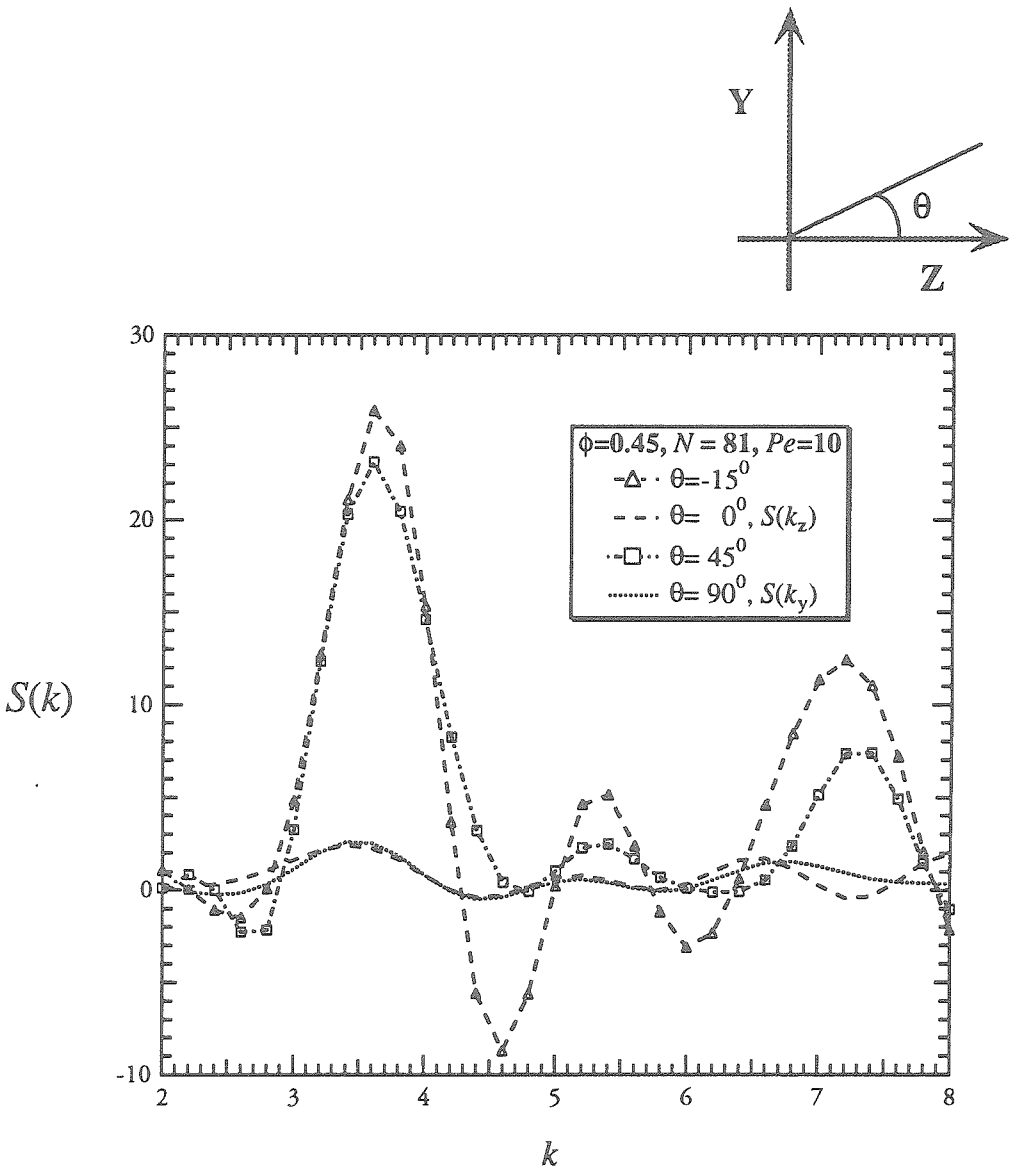

Figure 6.19: The structure factor $S(k)$ for hard-sphere suspensions at a volume fraction ϕ=0.45, Pe=10, and 81 particles computed with different angles θ of the incident light: (Δ) -15 degrees, (----) 0 degrees ($S(k_z)$), ($\square$) 45 degrees and (.....) 90 degrees ($S(k_y)$). The figure clearly shows strong intensity maxima for $S(k)$ which are computed with wave numbers parallel to the -15 and 45 degrees line. The angle θ is shown in the upper right of this figure.

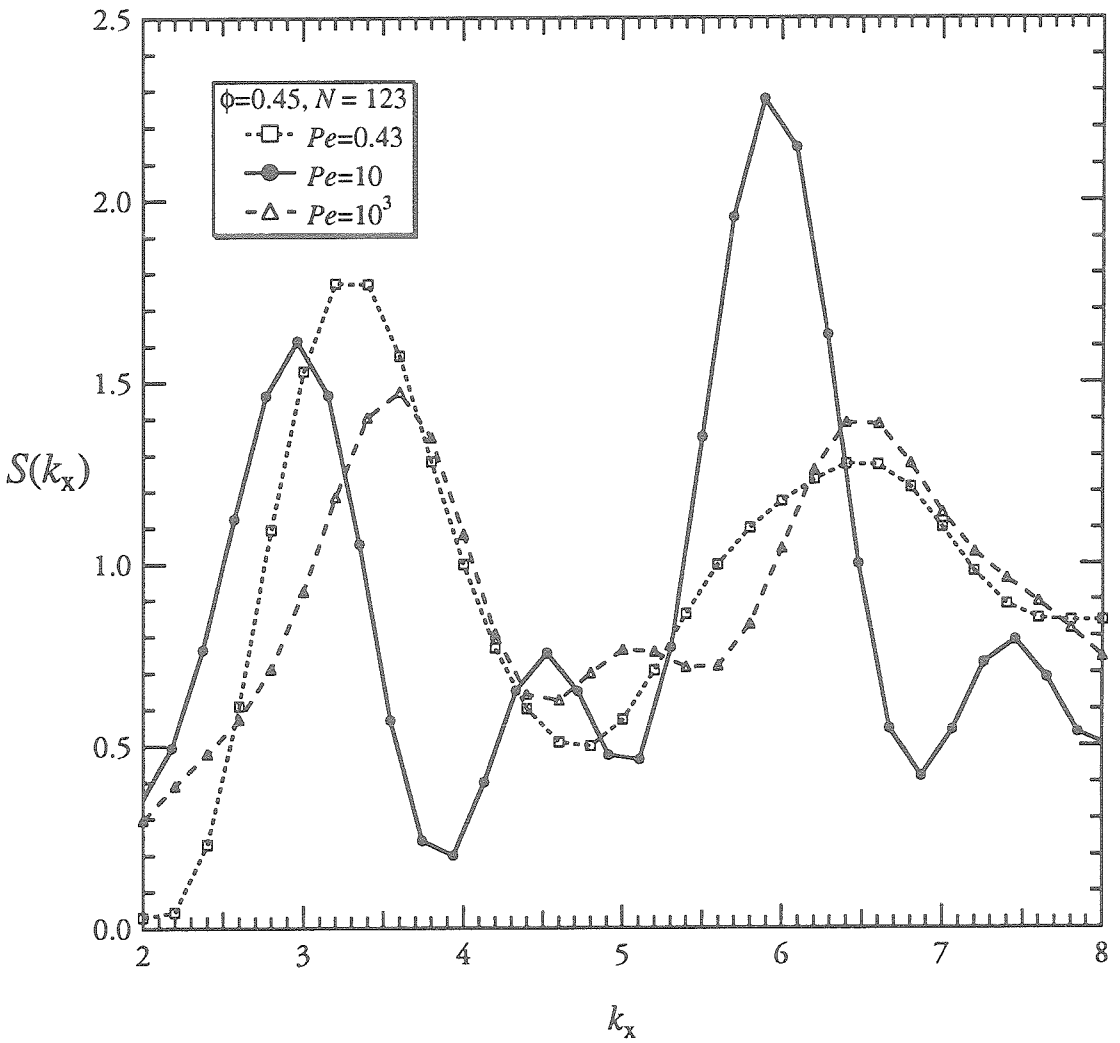

Figure 6.20: The line structure factor $S(k_x)$ for hard-sphere suspensions at a volume fraction ϕ=0.45 and 123 particles obtained by Stokesian dynamics for different Péclet numbers: (△) 0.43, (●) 10, and (□) 1000. The dimensionless wave number k_x is parallel to the flow direction, the x-axis.

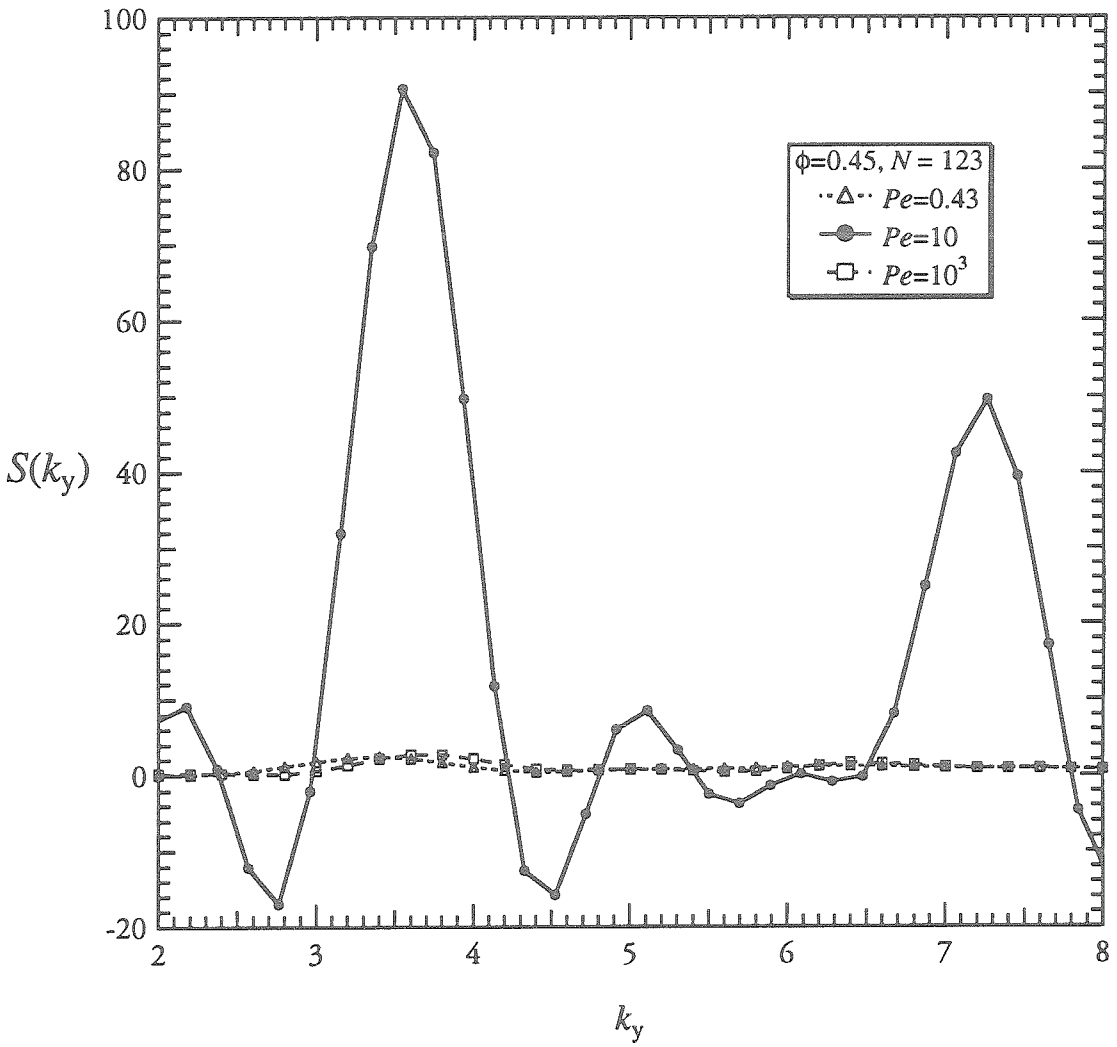

Figure 6.21: The static line structure factor $S(k_y)$ for hard-sphere suspensions at a volume fraction ϕ=0.45 and 123 particles obtained by Stokesian dynamics for different Péclet numbers: (Δ) 0.43, (●) 10 and (□) 1000. The dimensionless wave number k_y is parallel to the velocity gradient direction, the y-axis. It is seen from the figure that $S(k_y)$ for Pe=10 shows the highest scattered intensity at wave numbers k_y≈3.6 and 7.4 compared to $S(k_y)$ for Pe=0.43 and 1000 which show insignificant scattering light intensity for this range of k_y.

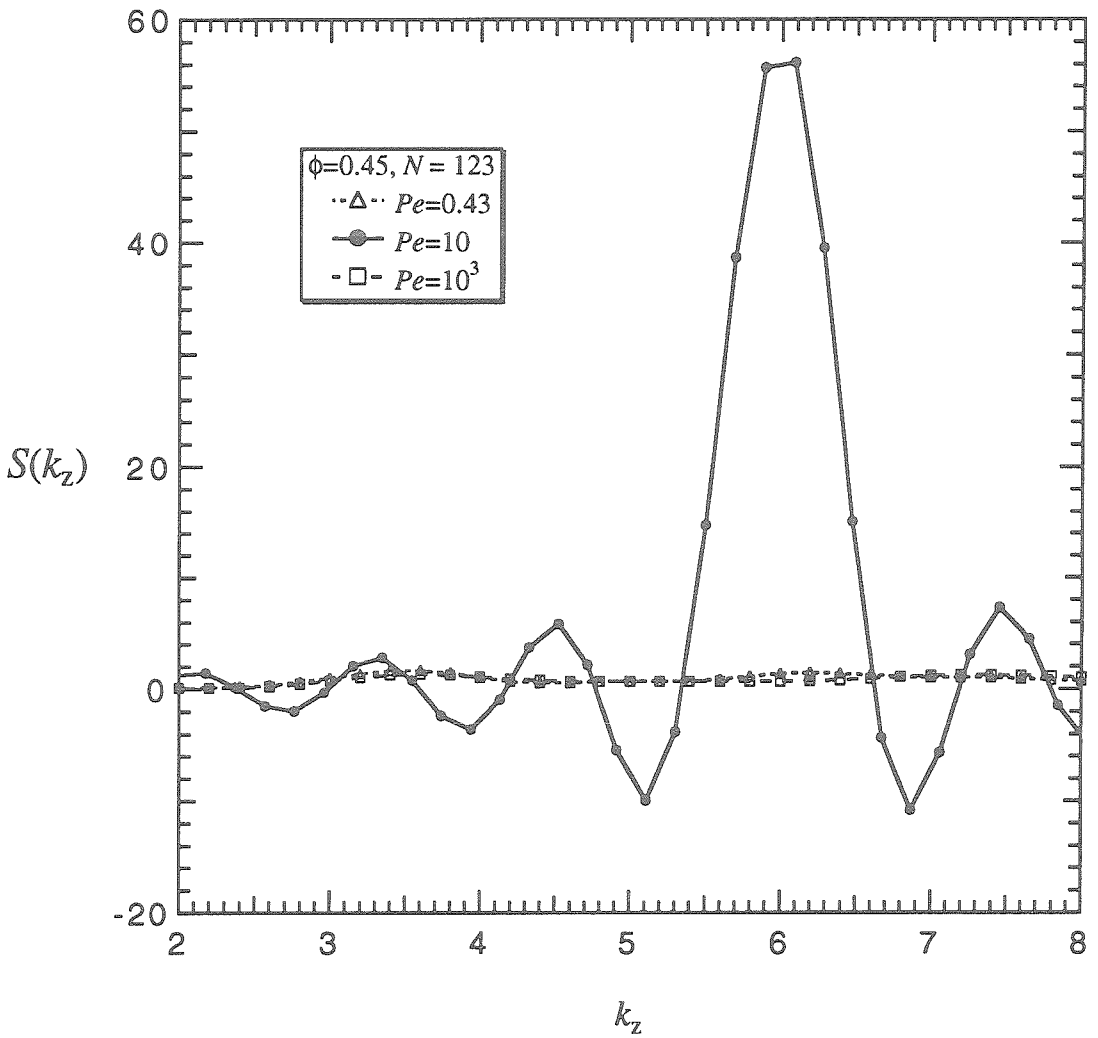

Figure 6.22: The line structure factor $S(k_z)$ for hard-sphere suspensions at a volume fraction ϕ=0.45 and 123 particles obtained by Stokesian dynamics for different Péclet numbers: (Δ) 0.43, (●) 10, and (□) 1000. The dimesionless wave number k_z is parallel to the vorticity direction, the z-axis. The structure factor $S(k_z)$ for Pe=10 shows a high peak of scattered intensity at the dimensionless wave number $k_z \approx 6$.

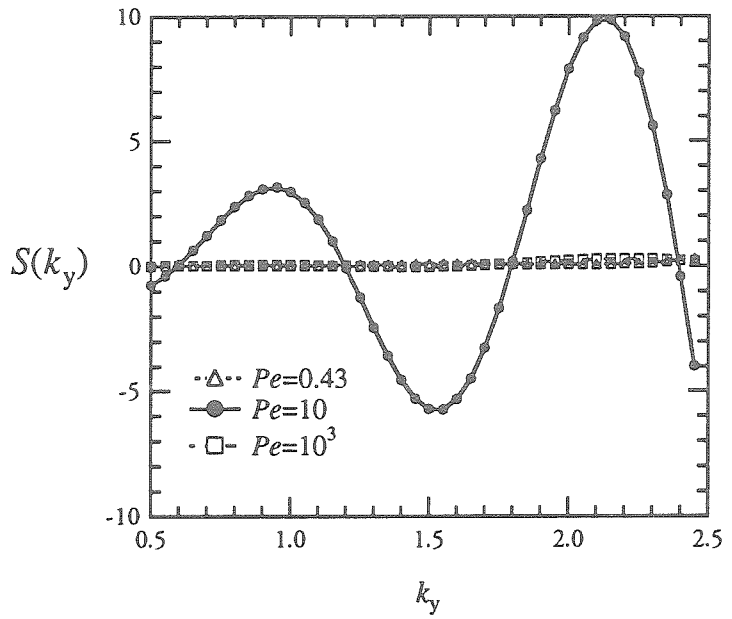

Figure 6.23.a

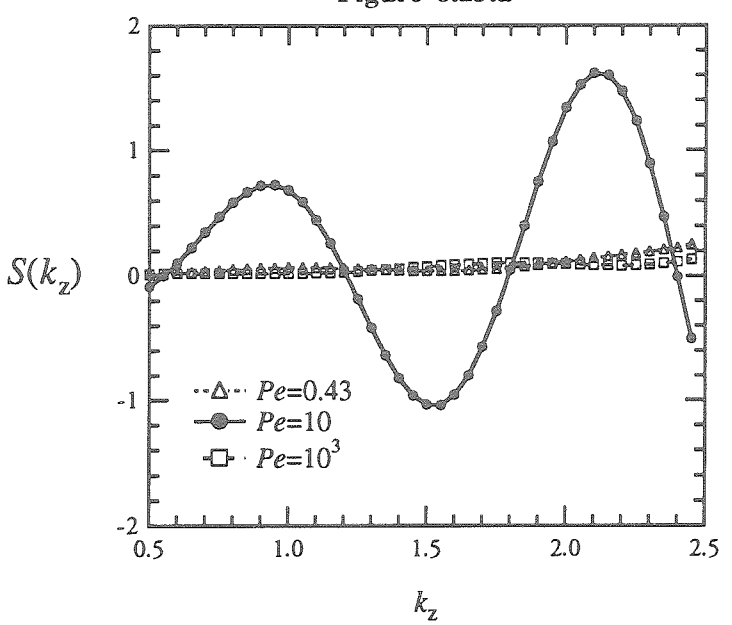

Figure 6.23.b

Figure 6.23.a-b: The structure factors $S(k_y)$ and $S(k_z)$ for hard-sphere suspensions at a volume fraction ϕ=0.45 with N = 123 and different Pe numbers: (Δ) 0.43, (●) 10 and (□) 1000. The structure factors are computed with small wave numbers ranging from 0.5 to 2.5. $S(k_y)$ and $S(k_z)$ for Pe=10 show the long-ranged correlation of the flowing particles.

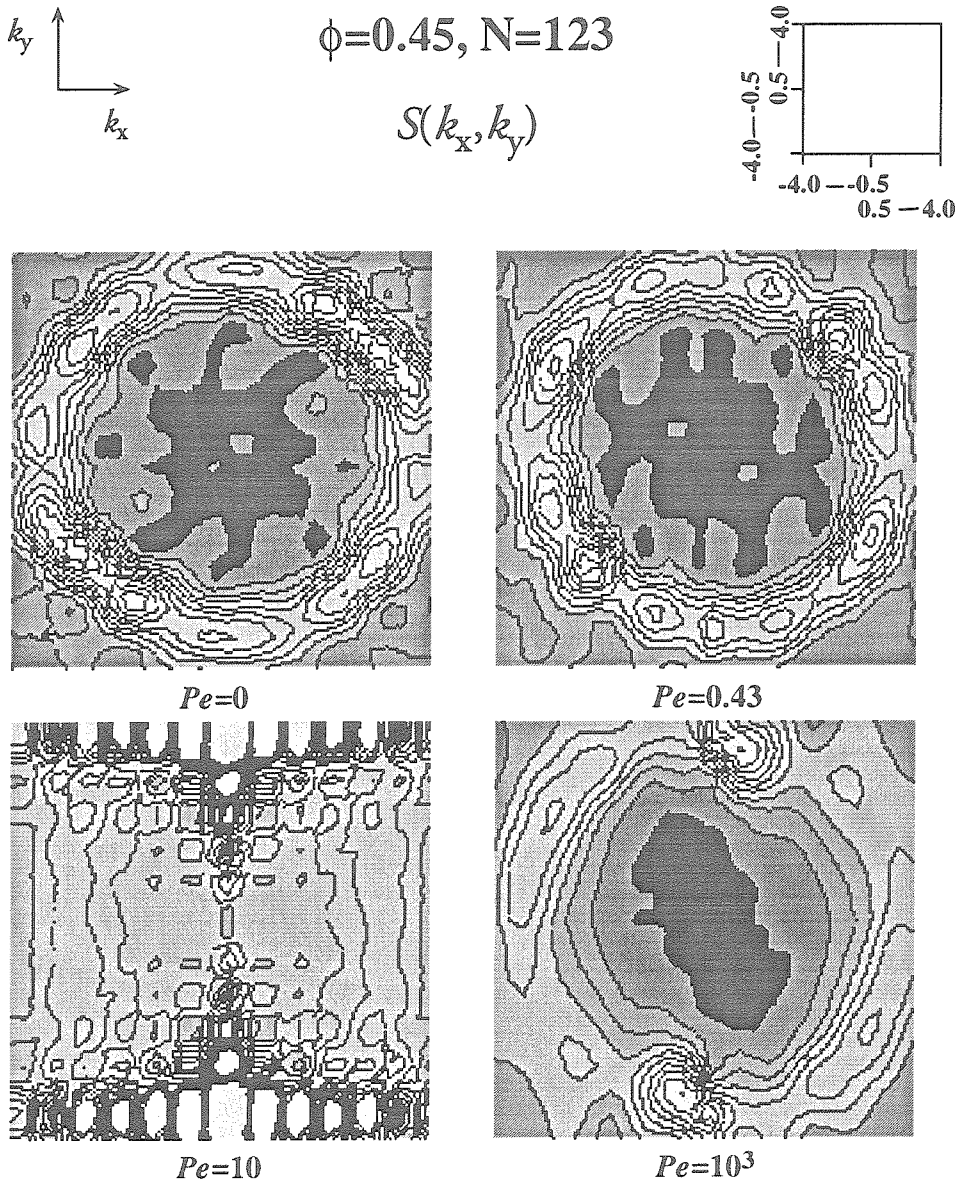

Figure 6.24: The structure factor $S(k_x,k_y)$ obtained by Stokesian dynamics for hard spheres at a volume fraction ϕ=0.45 with 123 particles and four different Péclet numbers: 0 (upper left), 0.43 (upper right), 10 (lower left), and 1000 (lower right). Regions of light color represent high and regions of dark color represent low scattering light intensity. The upper right figure displays the range of the dimensionless wave numbers k_x and k_y. A contour plot of $S(k_x,k_y)$ with Pe=10 shows circular regions of high intensity along the horizontal lines with wave numbers $k_y \approx$ +/- 4 and two "bands" of high scattered intensity along the vertical lines with wave numbers $k_x \approx$ +/- 3.5.

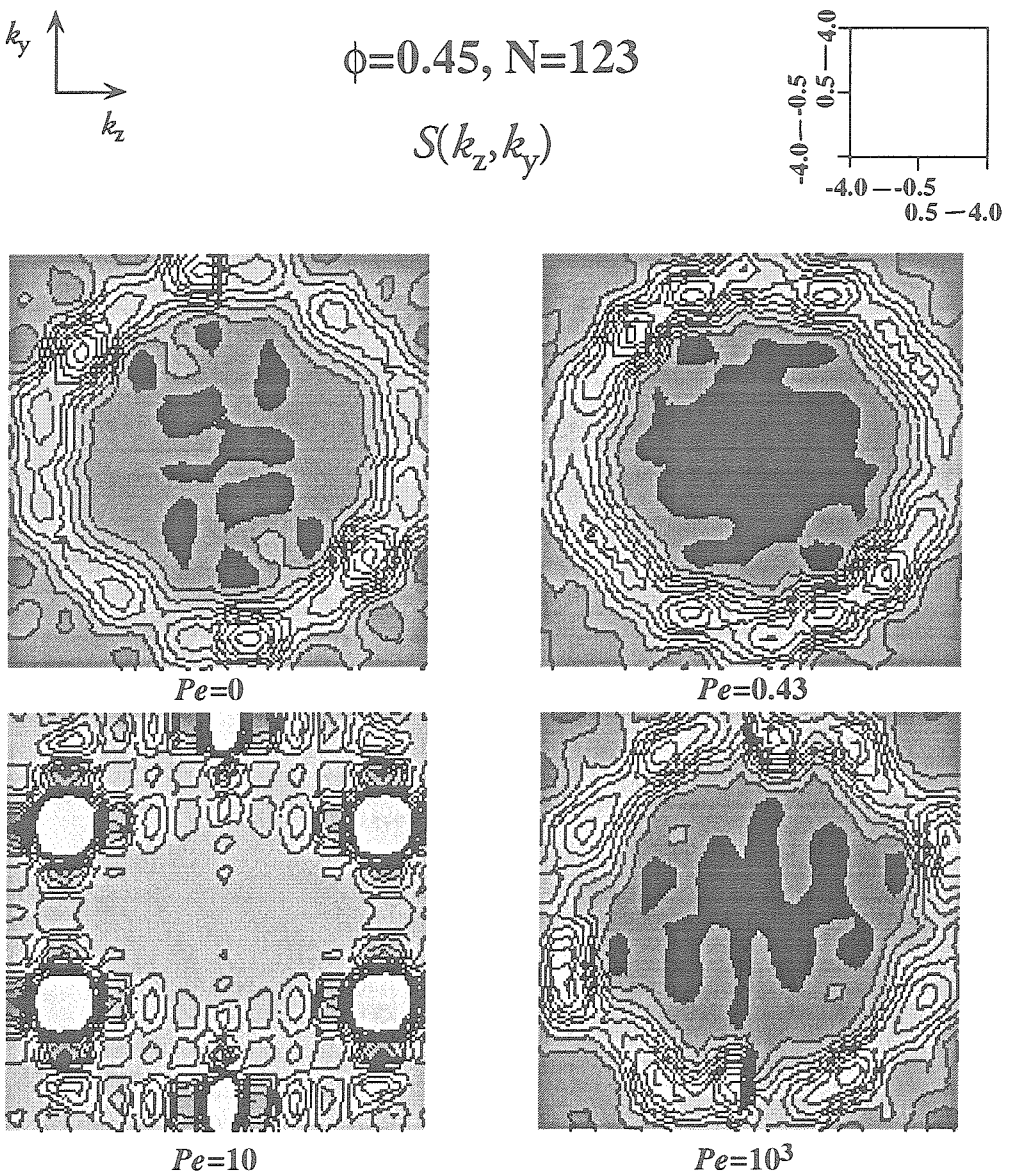

Figure 6.25: The structure factor $S(k_z,k_y)$ obtained by Stokesian dynamics for hard spheres at a volume fraction ϕ=0.45 with 123 particles and four different Péclet numbers: 0 (upper left), 0.43 (upper right), 10 (lower left), and 1000 (lower right). Regions of light color represent high scattering light intensity and regions of dark color represent low scattering light intensity. The upper right figure displays the range of the dimensionless wave numbers k_z and k_y. A contour plot of $S(k_z,k_y)$ shows a distinct "hexagonal" pattern of six intensity maxima which is superimposed on the halo ring for Pe=10. Another six smaller intensity maxima at smaller wave numbers shows the long range order.

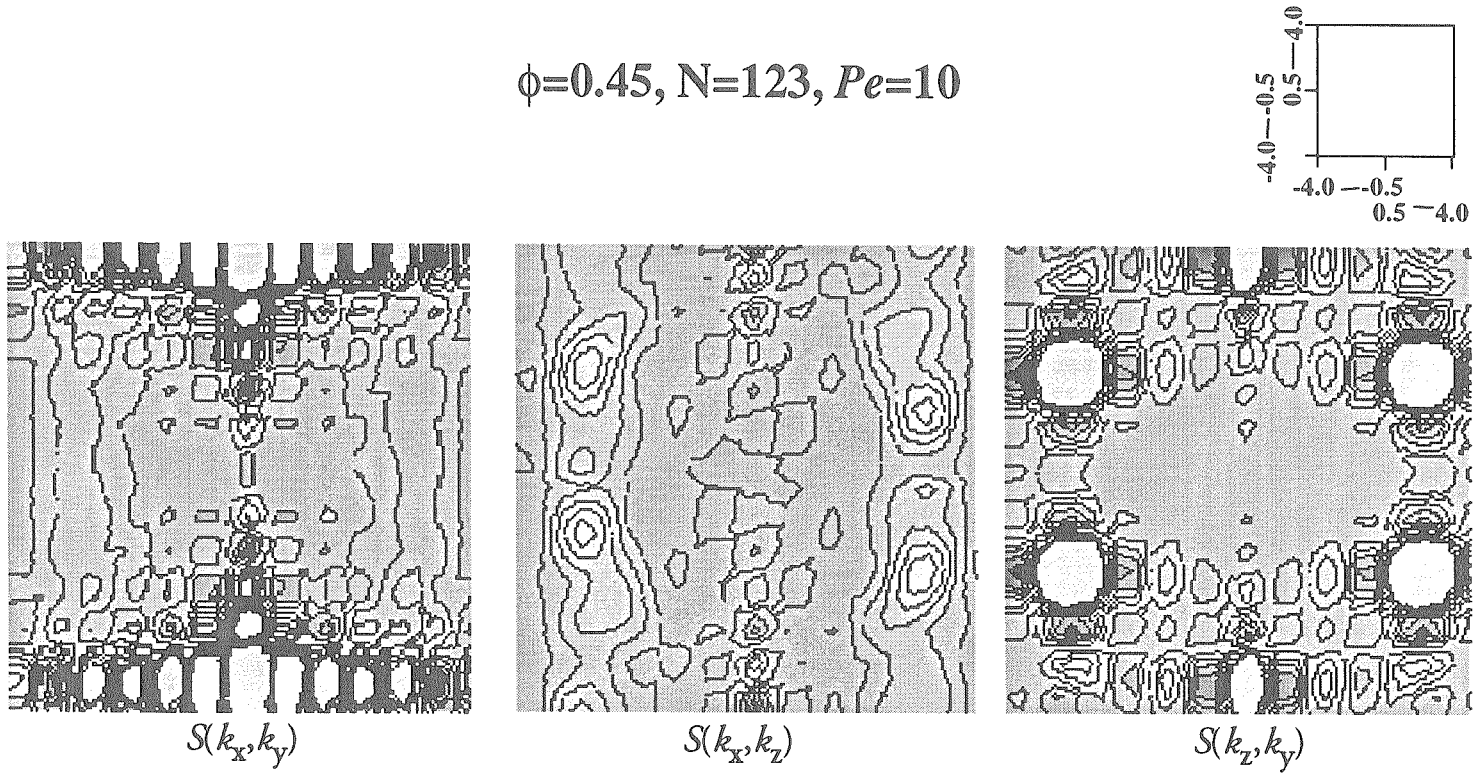

Figure 6.26: The structure factors: $S(k_x,k_y)$ (left), $S(k_x,k_z)$ (central) and $S(k_z,k_y)$ (right) for hard spheres at ϕ=0.45 with 123 particles and Pe=10. Regions of light color represent high scattering light intensity and regions of dark color represent low scattering light intensity. The upper right figure displays the range of the dimensionless wave numbers k_x, k_y and k_z. $S(k_x,k_y)$ shows the intensity maxima along the horizontal lines with $k_y \approx$ +/-4 and two "bands" of high scattered intensity along the vertical k_y-axis. $S(k_x,k_z)$ shows only the "bands" of high scattered intensity along the vertical k_z-axis. Note the absence of circular regions of high intensity along the the horizontal lines $k_y \approx$ +/- 4 in a plot of $S(k_x,k_z)$. $S(k_z,k_y)$ displays a distinct "hexagonal" pattern of six intensity maxima which is superimposed on the halo ring. These striking patterns of high scattering light intenisty are the spectroscopic signatures of a strongly ordered suspension at Pe=10.

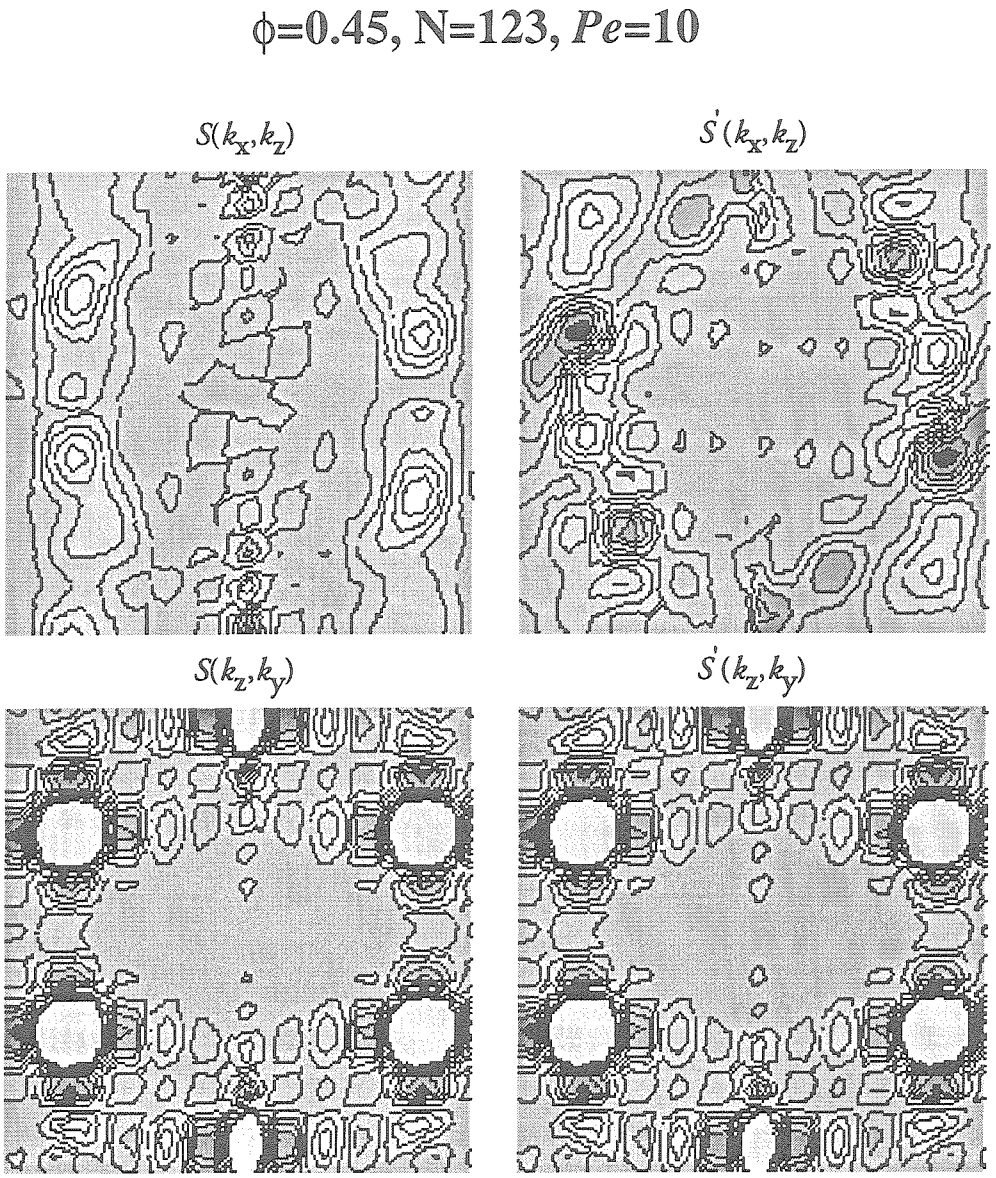

Figure 6.27: A comparison of the nonequilibrium unperturbed (left column) and the perturbed structure factors (right column) obtained by Stokesian dynamics for hard spheres at a volume fraction ϕ=0.45 with 123 particles and Pe=10. The perturbed structure factor is defined as $S'(k) \equiv S(k,Pe) - S(k)$. $S(k_x,k_z)$ and $S'(k_x,k_z)$ are shown in the top row and $S(k_z,k_y)$ and $S'(k_z,k_y)$ are shown in the bottom row. The range of the dimesionless wave numbers k_x, k_y and k_z is from +/-0.5 to +/-4.0. Regions of light color represent high scattering light intensity and region of dark color represent low scattering intensity.

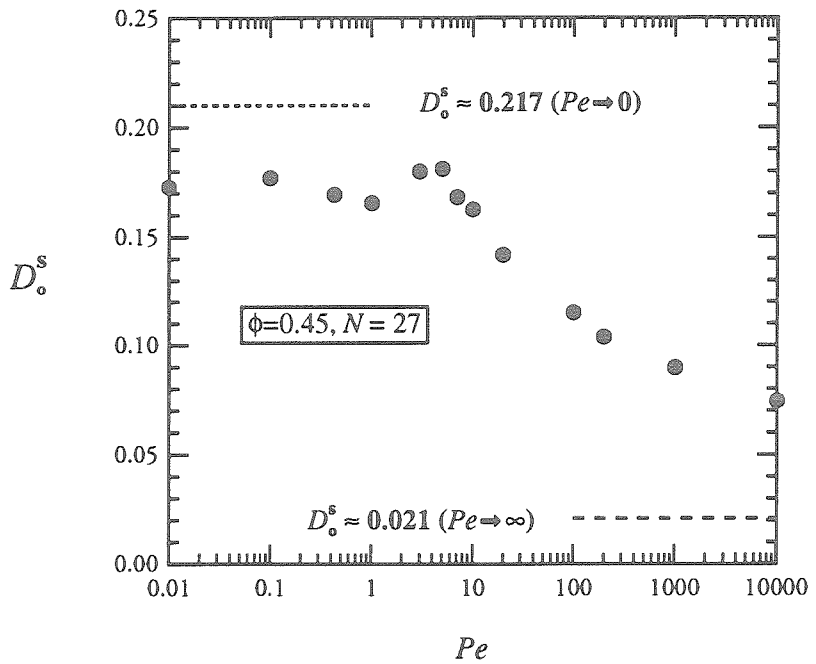

Figure 6.28.a

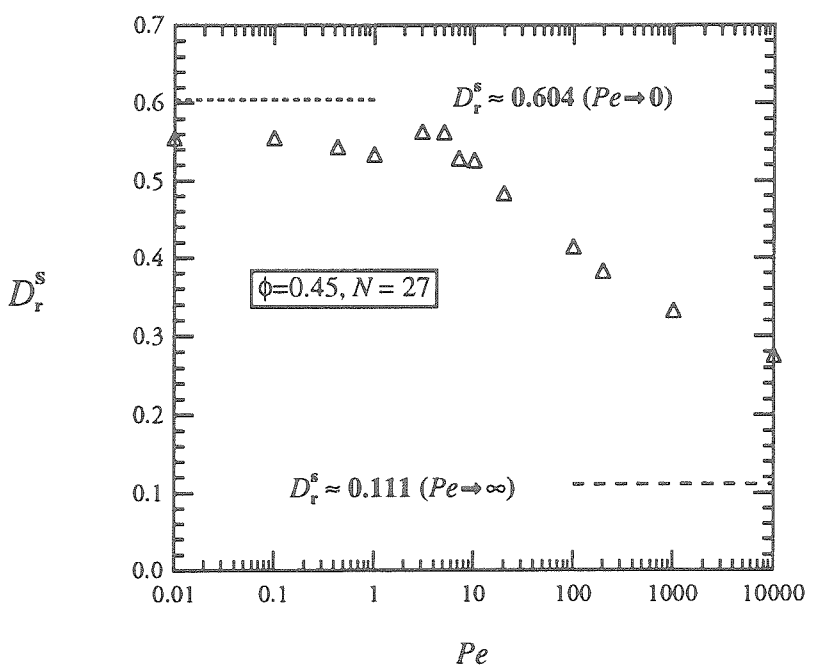

Figure 6.28.b

Figure 6.28.a-b: The steady short-time translational (●) and rotational (Δ) self-diffusion coefficients of hard spheres at a volume fraction ϕ=0.45 with 27 particles obtained by Stokesian dynamics as a function of the Péclet number. It is seen from the plots that both the self-diffusion coefficients remain relatively constants at low Peclet numbers (Pe<1), increase slightly at (Pe≈10) and finally decrease noticeably with increasing Pe. Both coefficients are normalized by the infinite dilution diffusivity D_o.

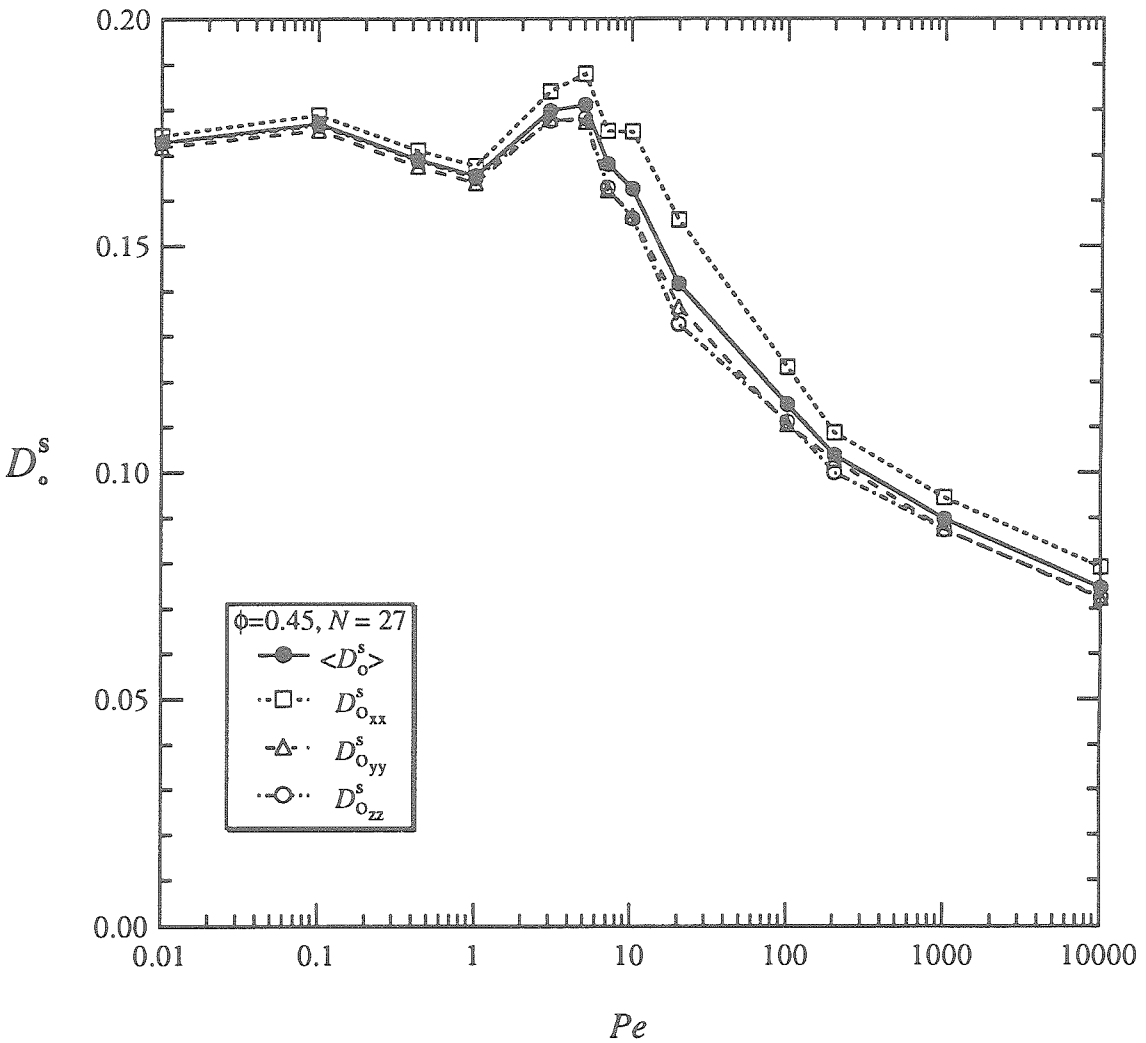

Figure 6.29: The steady short-time translational self-diffusion coefficients: the mean (●), and the coefficients computed for the x-axis (□) (the flow direction), the y-axis (Δ) (the velocity gradient direction) and the z-axis (○) (the vorticity direction) of hard spheres at a volume fraction ϕ=0.45 and 27 particles obtained by Stokesian dynamics as a function of the Péclet number. It is seen from the figure that the self-diffusion coefficient computed in the flow direction, $D^s_{o_{xx}}$, is consistently slightly larger than the coefficients computed in the directions of the velocity gradient and vorticity.

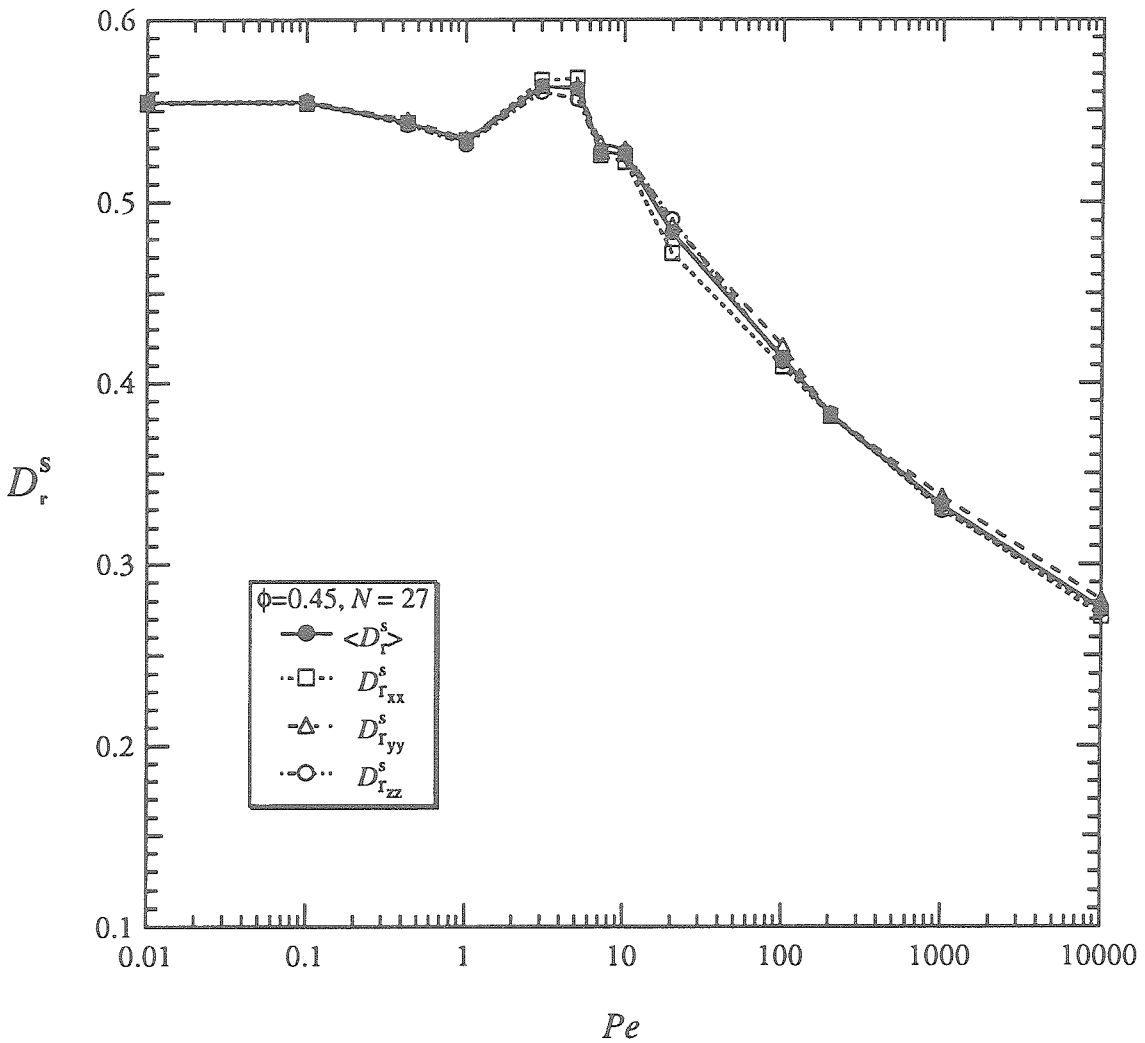

Figure 6.30: The steady short-time rotational self-diffusion coefficients: the mean (●), and the coefficients computed for the x-axis (□), the y-axis (Δ) and the z-axis (○) of hard spheres at a volume fraction ϕ=0.45 and 27 particles obtained by Stokesian dynamics as a function of the Péclet number. The short-time rotational self-diffusion coefficients computed for different directions show negligible variations for the entire range of Pe.

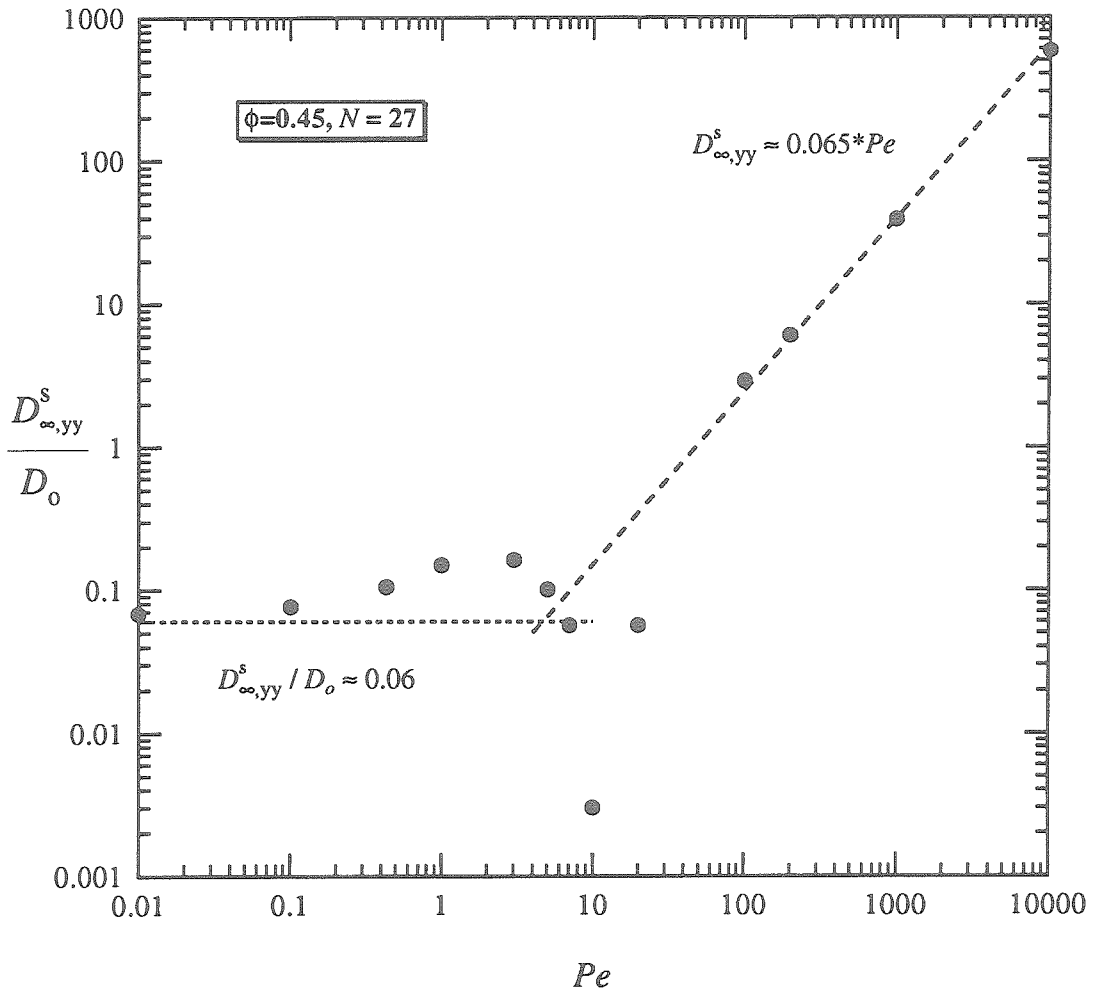

Figure 6.31: The long-time self-diffusivity computed in the velocity gradient direction, the y-axis, normalized by the infinite dilution diffusivity D_o is plotted as a function of the Péclet number for hard spheres at a volume fraction ϕ=0.45. The limiting asymptotes for the long-time self-diffusivity are: $D^s_{\infty,yy} / D_o \approx 0.06$ as $Pe \to 0$ and $D^s_{\infty,yy} \approx 0.065*Pe$ for $Pe \to \infty$. Note that the dimensional long-time self-diffusivity $D^s_{\infty,yy}$ scales as γa^2 for the limit $Pe \to \infty$.

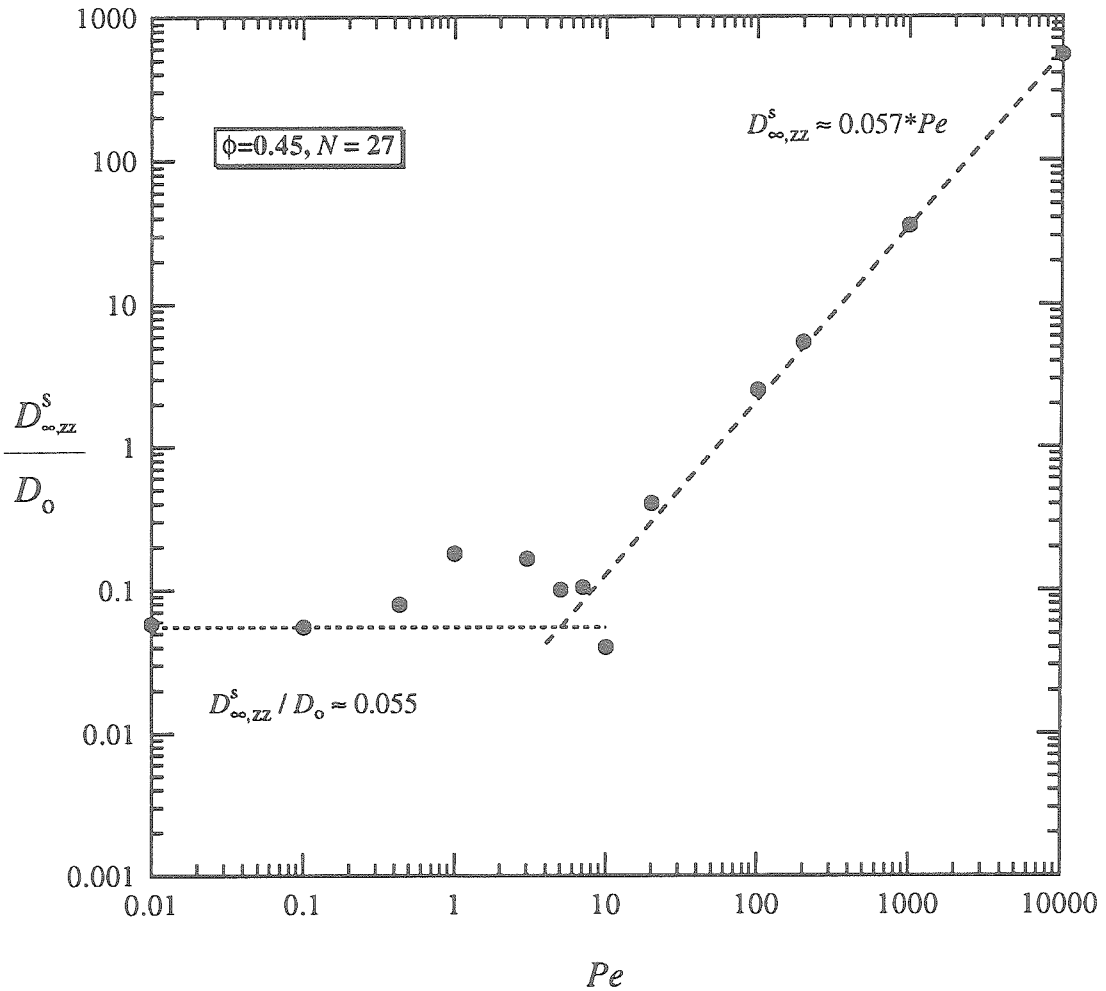

Figure 6.32: The long-time self diffusivity computed in the vorticity direction, the z-axis, normalized by the infinite dilution diffusivity D_0 is plotted as a function of the Péclet number for hard spheres at a volume fraction ϕ=0.45. The limiting asymptotes for the long-time self-diffusivity are: $D^s_{\infty,zz} / D_0 \approx 0.055$ as $Pe \to 0$ and $D^s_{\infty,zz} \approx 0.057*Pe$ for the limit of $Pe \to \infty$. Note that as $Pe \to \infty$, the dimensional long-time self-diffusivity $D^s_{\infty,zz}$ scales as γa^2.

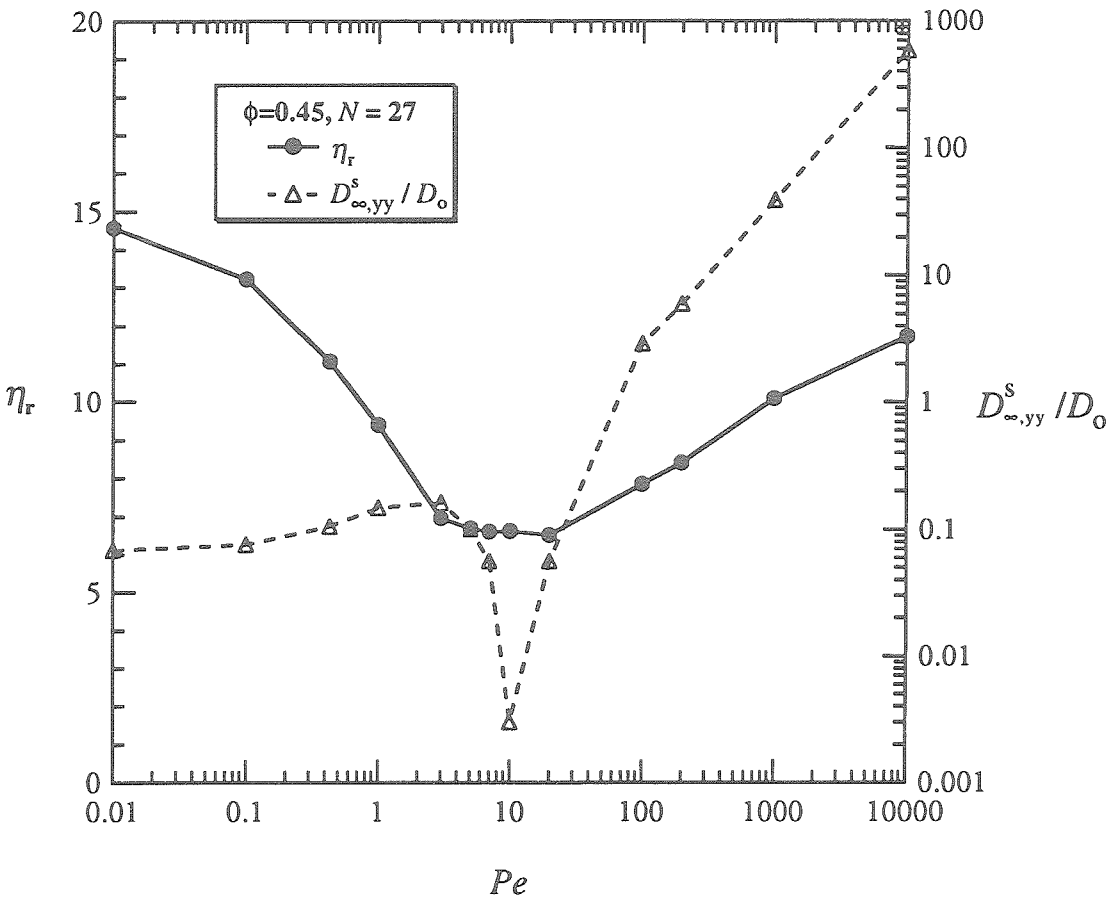

Figure 6.33: The steady shear viscosity η_r and the long-time self-diffusion coefficient $D^s_{\infty,yy}/D_o$ of hard spheres at a volume fraction ϕ=0.45 with 27 particles obtained by Stokesian dynamics as a function of the Péclet number. The left axis is for the steady shear viscosity and the right axis with a logarithmic scale is for the long-time self-diffusion coefficient. It is seen from the figure that while the suspension stops shear thinning at Pe=3, the long-time self-diffusion coefficient begins to decrease at Pe=3 and attains a minimum value at Pe=10.

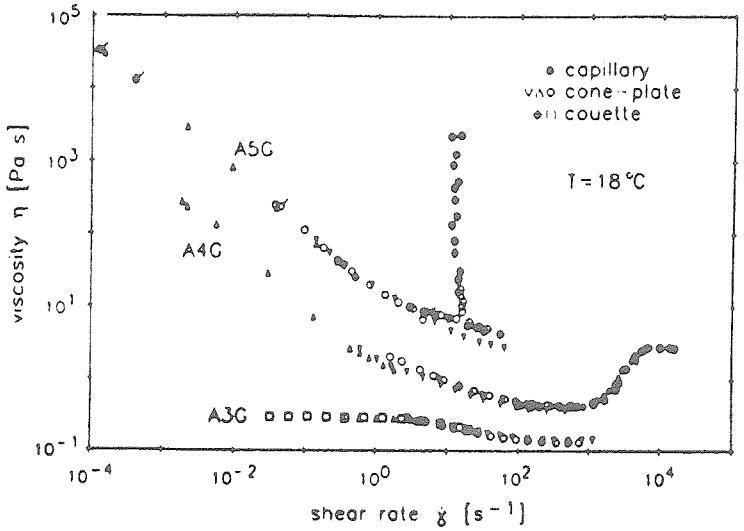

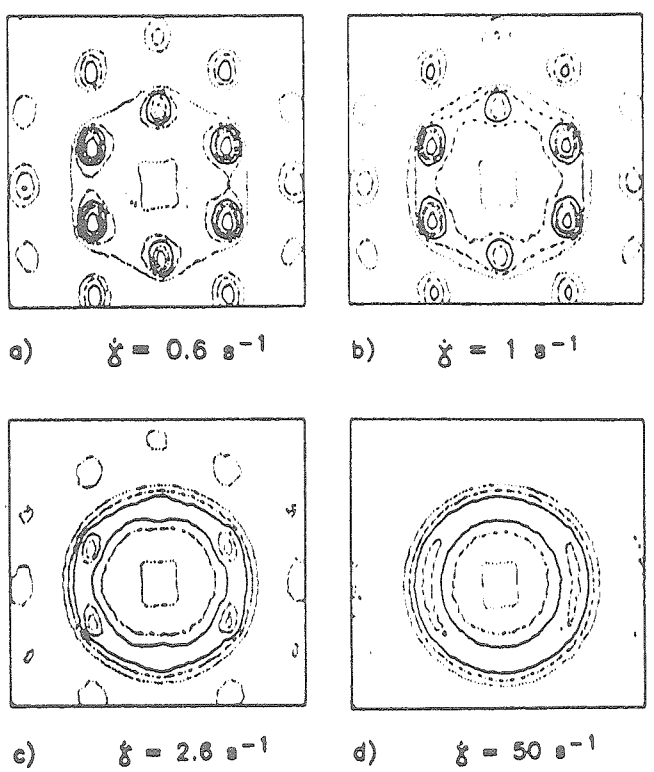

Figure 6.34: Experimental results of Laun *et al.* for (top figure) the steady shear viscosity (Fig.9) and (bottom figure) contour plots of the structure factor measured for "A4G" system in a Couette flow with different shear rates (Fig.24). The flow direction is normal to the vorticity-velocity gradient plane. The "A4G" system is a suspension of electrostatically stabilized styrene-ethylacrylate-coplymer dispersed in glycol at ϕ=0.434. (Figures 9 and 24 are taken from Laun *et al.*, *J. Rheol.*, 36, 743,1992)

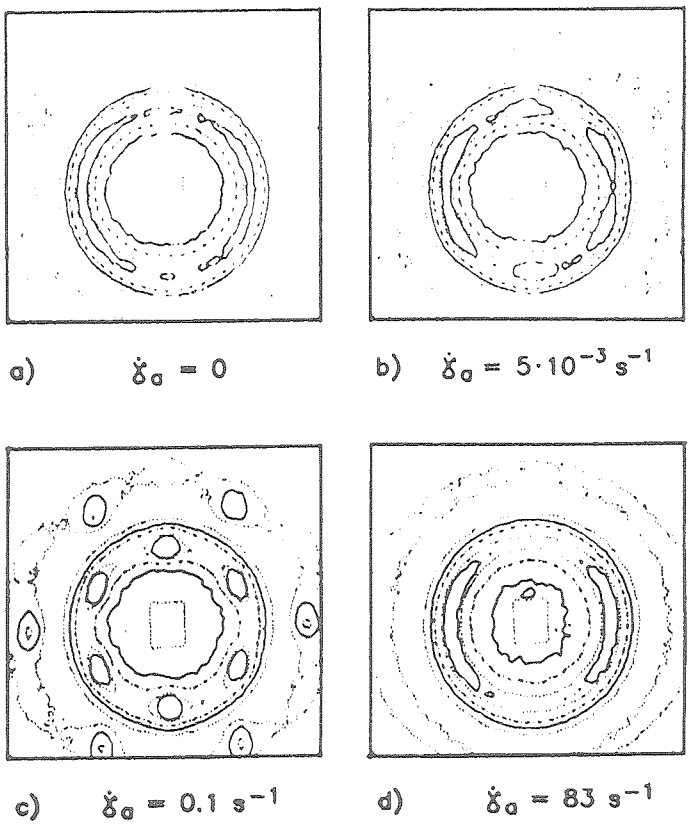

Figure 6.35: Experimental results of Laun *et al.* for the structure factor measured for "A4G" system in a Poiseuille flow with different shear rates (Fig.23). The flow direction is normal to the vorticity-velocity gradient plane. (Figure 23 is taken from Laun *et al.*, *J. Rheol.*, 36, 743,1992)

Chapter VII

STOKESIAN DYNAMICS SIMULATION OF MODERATELY DENSE HARD-SPHERE SUSPENSIONS

In this chapter, we investigate the rheological and microstructural behavior of moderately dense hard-sphere suspensions with a range of volume fraction ϕ from 0.316 to 0.419. At equilibrium, the structure of these suspensions is isotropic as the range of volume fraction is below the freezing phase transition of hard spheres. Hoover and Ree (1968) and Kose and Hachisu (1974) have measured the phase transition of hard spheres at equilibrium and obtained $\phi_F = 0.494 \pm 0.002$ for the fluid phase and $\phi_M = 0.545 \pm 0.002$ for the crystalline phase. A detailed study of the equilibrium phase behavior of a hard-sphere model has also been reported by Pusey and van Megen (1986) and Pusey (1991). As the suspensions are sheared, the changing microstructure causes change in suspension macroscopic properties. The influence of the imposed shear on the macroscopic properties was discussed for dense hard-sphere suspensions at particle volume fraction ϕ=0.45 in chapter VI. It is of our interest to study the dynamics of shearing deformation to the suspension and to predict the macroscopic properties based on the shear-induced microstructure.

The simulation results are presented for four hard-sphere suspensions with volume fractions ϕ=0.316, 0.37, 0.4 and 0.419. For these moderately dense suspensions, we focus on determining the transitional volume fraction which hard-sphere suspensions can be sheared to order and the transitional Péclet number where the suspension behavior changes from a strong Brownian limit to a hydrodynamically dominated regime. The outline of this chapter is identical to chapter VI and the results for ϕ=0.45 are used in this chapter as a reference to compare with these moderately dense suspensions. Suspension rheology is discussed first, followed by the shear-induced microstructure and the self-diffusivities.

Details of the dynamic simulations and the sampling statistics for the rheology are reported in Tables 7.1 to 7.4 for ϕ=0.316, 0.37, 0.4 and 0.419, respectively. Column (1) is the Péclet number, Pe, and column (2) is the number of particles, N. Columns (3) to (6) are the starting time, ending time, the time step and number of time steps for each run, respectively. Column (7) is the elapsed time of each sample and column (8) is the dimensionless time units by which each sample is successively shifted in time. Column (9) is the number of samples which are used to compute the steady shear viscosities and normal stress differences.

Initial random samples of particle configuration are selected for the runs of suspensions at ϕ=0.316, 0.37 and 0.4. For the runs with ϕ=0.419, after an initial sample of particle configuration is chosen the suspension is sheared from Pe=0.01 to Pe=10^4. At the end of each of the thirteen-run series, the Péclet number is step increased and the suspension is sheared for an average dimensionless time of 60. These continuing runs which follow the measurement practice in experiments are tested for the influence of starting particle configurations on suspension properties. In addition to runs with 27 particles, there are two special runs with 123 particles at Pe=10 for suspensions at ϕ=0.316 and 0.419.

VII.1 Suspension Rheology

VII.1.1 The Steady Shear Viscosity

Results for the steady shear viscosities of these four hard-sphere suspensions obtained by Stokesian dynamics for different Péclet numbers are summarized in Tables 7.5 to 7.8.

Column (1) is Pe and column (2) is N. Columns (3) to (8) are the steady hydrodynamic viscosity, its standard deviation, the steady Brownian viscosity, its standard deviation, the steady total viscosity and its standard deviation, respectively.

Results of the steady shear viscosities from Table 7.5 for ϕ=0.316 and from Table 7.6 for ϕ=0.37 are plotted in Figures 7.1 and 7.2, respectively. The figures show the change of the hydrodynamic ($\triangle$) and Brownian ($\square$) contribution to the total ($\bullet$) shear viscosity with varying Péclet numbers. A small decrease in the total shear viscosity in the shear thinning region with $Pe < 10$ corresponds to a decrease in the Brownian viscosity as the hydrodynamic viscosity is constant. The total shear viscosity shows a small increase at large Péclet number ($Pe > 10^2$) which is due to small increase in the hydrodynamic viscosity since the Brownian viscosity has essentially vanished for $Pe > 10$.

The relation of the steady shear viscosities and the Péclet number are shown in Fig.7.3 for ϕ=0.4 and in Fig.7.4 for ϕ=0.419. Data for the two plots are obtained from Tables 7.7 and 7.8, respectively. Figures 7.3 and 7.4 display the same trend of the total shear viscosity, but the shear thinning and shear thickening are more pronounced than that of suspensions at ϕ=0.316 and 0.37. In the shear thinning region ($Pe < 10$) the hydrodynamic viscosity remains relatively constant, while the Brownian viscosity decreases and causes the suspension to shear thin. In the region of large Péclet number, hydrodynamic viscosity contributes all total viscosity and the suspension shear thickens. Figure 7.4 for ϕ=0.419 shows a small plateau region with $Pe \approx 10$ where the total shear viscosity is minimum. The plateau region was not seen for suspensions at ϕ=0.316, 0.37 and 0.4.

In the shear thinning region with small Péclet number ($Pe < 10$), the stochastic Brownian forces act to counter the shearing deformation to the suspension due to the imposed shear. As the shear rate increases, the time scale decreases and Brownian forces do not have sufficient time to restore the deformed suspension to the equilibrium isotropic structure. The Brownian contribution to particle stress, and to macroscopic properties in general, decreases significantly causing the suspension to shear thin, and Brownian motion becomes less important relative to the imposed shear. For the shear thickening region with large Péclet number ($Pe > 10^2$), the hydrodynamics play a dominant role and dictate suspension behavior. An increase in hydrodynamic contribution to particle stress in this region associates with formation of clustered particles causing the suspension to shear thicken. Results from our studies for ϕ=0.45 in chapter VI and experiments of Hoffman (1972), Graham and Bird (1984), Boersma and Laven (1990) and simulations from Bossis and Brady (1984, 1987) on a monolayer have all shown similar evidence of clusters.

As shown in Figures 7.1 and 7.2, the Brownian viscosity is always less than hydrodynamic viscosity for hard-sphere suspensions at ϕ=0.316 and 0.37 for all Péclet numbers. As the volume fraction increases, there exists an unique Péclet number, Pe^*, where the Brownian viscosity is identical to hydrodynamic viscosity and this can be seen at $Pe^* \approx 0.01$ for ϕ=0.4 in Fig.7.3, at $Pe^* \approx 0.2$ for ϕ=0.419 in Fig.7.4, and at $Pe^* \approx 0.6$ for ϕ=0.45 in Fig.6.1 of chapter VI.

Figure 7.5 presents a comparison of the steady shear viscosity η_r for these four suspensions and the experimental results of van der Werff and de Kruif (1989) for silica

hard spheres. The steady shear viscosity for suspension at ϕ=0.45 from Fig.6.2 is also plotted in this figure for our reference of comparison. The volume fractions in the experiments are ϕ = (×) 0.316±0.01, (+) 0.419±0.01, (⊡) 0.443±0.01 and (△) 0.47±0.01. The range of the Péclet numbers in the experiment was from 0.01 to 10. The curves for ϕ=0.419 and 0.47 show the measurements for the viscosity in a forward and a reverse shear direction. The reproducibility of experimental results is excellent indicating the independence of the steady shear viscosity on the direction of the shear at steady state. Stokesian dynamics simulation results are shown for suspensions at ϕ = (▲) 0.316, (◆) 0.37, (○) 0.4, (■) 0.419 and (●) 0.45. A comparison of the steady shear viscosity from Stokesian dynamics and the experiments at the same volume fraction ϕ=0.316 and 0.419 is excellent. The two viscosities are indistinguishable at ϕ=0.316 and change inappreciably for all Péclet numbers. For suspensions at ϕ=0.419, Stokesian dynamics results compare very well with the experiments for $Pe < 10$, but for $Pe \approx 10$ simulation results are seen to be consistently smaller than experimental results in the region of minimum shear viscosity. At Pe=10, our result for the shear viscosity is 4.51 for 27 particles and 4.90 for 123 particles (Table 7.8) compared to 5.90 from the experiments. This noticeable difference between Stokesian dynamics and the experiments is relatively small compared to the large uncertainty in the measurements of the volume fraction in the experiments which leads to large uncertainty in the viscosity as it is very sensitive on the volume fraction. Our results of the steady shear viscosity for suspension at ϕ=0.45 resembles very well with the experimental curves at ϕ=0.443 and 0.47. Figure 7.5 shows a small change in the total relative viscosity for suspensions at ϕ=0.316 and 0.37, a transitional behavior with noticeable change at Pe=10 for suspension at ϕ=0.4, and a shear thinning

and shear thickening behavior for suspensions at ϕ=0.419 and 0.45. Before we examine the shear-induced microstructure for these hard spheres, the normal stress differences are reported and discussed next to complete the section of suspension rheology.

VII.1.2 The Steady Normal Stress Differences

Tables 7.9 to 7.12 summarize the results for the steady first and second normal stress differences for hard-sphere suspensions at ϕ=0.316, 0.37, 0.4 and 0.419, respectively. Column (1) is Pe and column (2) is N. Columns (3) to (8) give the first and columns (9) to (14) give the second normal stress differences, respectively. The hydrodynamic contribution is presented first, followed by Brownian contribution and the the total normal stress differences. The standard deviation σ is computed from a number of samples shown in Tables 7.1 to 7.4.

Results from Tables 7.9 to 7.12 are plotted in pairs of figures to show the change of the first and second normal stress differences with Péclet number. Figures 7.6.a, 7.7.a, 7.8.a, and 7.9.a show the first and Figures 7.6.b, 7.7.b, 7.8.b, and 7.9.b show the second normal stress differences for hard spheres at ϕ=0.316, 0.37, 0.4 and 0.419, respectively. As seen in these figures, the first and second total (●) normal stress differences, χ_{1T} and χ_{2T}, are small and less then 2 units in absolute value for the moderately dense hard spheres. In the region of small Péclet number ($Pe < 1$), the first and second hydrodynamic (△) normal stress differences, χ_{1H} and χ_{2H}, are small compared to the dominant Brownian (□) contribution. As the Péclet number increases, both χ_{1B} and χ_{2B} decay in absolute values quickly and have essentially vanished for $Pe > 10^2$. In this large Péclet number region, χ_{1H} and χ_{2H} increase to a maximum and contribute all χ_{1T} and χ_{2T}, respectively.

While both χ_{1H} and χ_{2H} are positive for all Péclet numbers, χ_{1B} is negative and χ_{2B} is positive. For suspensions at ϕ=0.4 and 0.419, the region at $Pe \approx 10$ shows an interesting behavior of the total normal stress differences. χ_{1T} and χ_{2T} are minimum in absolute value due to noticeable decrease of both hydrodynamic and Brownian contribution to the normal stress differences and this is the plateau region where the steady shear viscosity is minimum.

Figures 7.10.a and 7.10.b present a comparison for the first and second total normal stress differences for hard spheres with ϕ = (▲) 0.316, (◆) 0.37, (○) 0.4, and (□) 0.419. The normal stress differences of hard-sphere suspensions at ϕ=0.45 (●) which was presented in chapter VI are also shown in these two figures as a reference of comparison. As expected for these four moderately dense hard spheres, χ_{1T} and χ_{2T} are relatively smaller than the small normal stress differences of hard spheres at ϕ=0.45. The transitional volume fraction at which a hard-sphere suspension first shows minimum normal stress differences (in absolute value) at $Pe \approx 10$ is ϕ=0.4. A suspension at this volume fraction also shows the first rheological signal of shear thinning and shear thickening (cf. Fig.7.5).

In this rheology section, we have seen a small change in the steady shear viscosity for hard spheres at a volume fraction $\phi < 0.4$. At the transitional volume fraction ϕ=0.4, the suspension begins to show shear thinning and shear thickening behavior. For hard-sphere suspensions at volume fraction $\phi \geq 0.4$, the Brownian motion is important and its contribution influences the macroscopic properties and the deformation of the suspension structure, especially in the region of small Péclet number ($Pe < 1$). Next, we

examine the microstructure of these hard spheres and determine its relation to suspension macroscopic properties.

VII.2 The Shear-Induced Microstructure

VII.2.1 The Angularly Averaged Pair-Distribution Function $g(r)$

The angularly averaged pair-distribution functions $g(r)$ for the runs with 123 particles are plotted in Figures 7.11 and 7.12 for hard spheres at Pe=10 and volume fraction ϕ = (dotted curve) 0.316, (dashed curve) 0.419 and the reference curve for ϕ=0.45 (solid curve). As shown in Fig.7.11, there is negligible difference in $g(r)$ for large particle center-center spacing (r>4). At $r \approx 2$ and $r \approx 4$, $g(r)$ displays small variations which can be seen from the insert figure, where $g(r)$ is plotted with a small range of r from 2 to 2.2 for closely spaced particle pairs. The first peak of $g(r)$ is seen at $r \approx 2.03$ and the peak intensity increases with increasing ϕ. The radial distance where the intense peak occurs is shifted to smaller value from $r \approx 2.04$ for ϕ=0.316 to $r \approx 2.02$ for ϕ=0.45. As the volume fraction increases, the probability of finding the first nearest neighbors at a smaller radial distance also increases, but in this region with $Pe = 10$ the particles are still very well separated from each other as shown by the small value of $g(r)$ at $r \approx 2$. Figure 7.12 shows a plot of $g(r)$ with a smaller scale from 0.5 to 1.5 for all particle center-center spacing r. $g(r)$ for ϕ=0.316 shows a fluid-like behavior as its values fluctuate about 1.0 compared to a distinct peak pattern of $g(r)$ for ϕ=0.45. Hard-sphere suspension at volume fraction ϕ=0.419 shows the onset of microstructural order, but the order is not long ranged as seen from the curve of $g(r)$ for ϕ=0.419. After showing a second peak at $r \approx 4.2$, which is similar but less intense than that of $g(r)$ for ϕ=0.45, $g(r)$ for ϕ=0.419

fluctuates about 1.0 for $r > 5$ and shows the same fluid-like behavior as $g(r)$ for ϕ=0.316 in this range of large particle center-center spacing.

Figure 7.13 displays a comparison of the angularly averaged pair-distribution function evaluated at particle center-center spacing r=2, $g(2)$, for these moderately dense hard spheres at ϕ= (▲) 0.316, (◆) 0.37, (○) 0.4, (□) 0.419, and the reference curve for ϕ=0.45 (●) with a fine increment of Péclet numbers. Data for this plot are obtained from Table 6.4.a for the runs with 27 particles. For suspensions with small deformation ($Pe < 1$), $g(2)$ varies insignificantly. As the Péclet number increases, $g(2)$ first decreases to a minimum value at $Pe \approx 10$ and then increases quickly with increasing Pe and approaches an asymptotic limit at large Péclet number ($Pe > 10^4$). At Pe=10, $g(2)$ for ϕ=0.316 is smallest which implies large spacing between the particles at this volume fraction. The figure also show large $g(2)$ with increasing volume fraction at the same Péclet number.

The angularly averaged pair-distribution function $g(r)$ shows important information on the local structure of the suspension. The equilibrium isotropic structure of hard spheres at a rest state is deformed by the imposed shear and changed to less random, but well dispersed particles at $Pe \approx 10$ as noted by small values of $g(2)$. For large Péclet numbers ($Pe > 10^3$), the hydrodynamics are dominant over the Brownian forces and large shearing deformation causes the particles to form clusters corresponding to large values for $g(2)$. In the following section, we present the details of the shearing deformation to suspension microstructure by examining the plane projection of the probability density functions $g(x, y)$, $g(x, z)$ and $g(z, y)$.

VII.2.2 The Probability Density Functions $g(x,y)$, $g(x,z)$ and $g(z,y)$

To examine the microstructure of the suspension, we travel along the steady shear viscosity curves shown in Fig.7.5 and probe the relative arrangement of the flowing particles at different Péclet numbers. Recall from chapter VI that the probability density functions $g(x,y)$, $g(x,z)$, and $g(z,y)$ reveal striking and very valuable information on the shear-induced microstructure for a hard-sphere suspension at ϕ=0.45. $g(x,y)$, $g(x,z)$ and $g(z,y)$ give the probability of finding a particle in the $x-y$, $x-z$ and $z-y$ plane given that there is a particle at the origin, respectively. The directions of the flow, the velocity gradient, and the vorticity are the x-, y-, and z-axis, respectively. For the $x-y$ plane, we have the frontal view of the flow of particles with the flow direction from left to right and along the horizontal x-axis. The top view of the flow of particles is shown by the $x-z$ plane with the horizontal x-axis is the flow direction. Another effective view of the flow of particles is given by the $z-y$ plane which is perpendicular to the flow.

A plot of the probability density function $g(x,y)$ with different Péclet numbers for a hard-sphere suspension at ϕ=0.316 in shown in Fig.7.14. Regions of light color represent high probability and regions of dark color represent low probability. Starting from the top to bottom and from left to right of Fig.7.14, the Péclet number is shown with an increasing order from 0.01 to 10^4. $g(x,y)$ shows a thick and symmetric ring for a random suspension with a small deformation ($Pe < 1$) and a thinner ring for an hydrodynamic dominated suspension ($Pe > 10^2$). The pattern of thin ring implies the high probability of finding closely spaced or touching particles - the existence of clusters. It is important to note that the ring is always close in this range of the Péclet number. At volume fraction

ϕ=0.316, the suspension is relatively less dense and there is fluid space for particles to move. $g(x,y)$ does not show any ordered structure even though the pair-distribution function $g(2)$ is minimum (cf. Fig.7.13).

Figure 7.15 displays the probability densities $g(z,y)$ (first row) and $g(x,y)$ (second row) for hard spheres at ϕ=0.37 for a small range of the Péclet number from 5 to 20. $g(z,y)$ begins to show signal of structural order at Pe=10, but the shear-induced structure is weak, not well formed, and unstable as large fluctuations are seen near the ordered regions.

Figures 7.16 and 7.17 show the probability densities $g(x,y)$ and $g(z,y)$ for a hard-sphere suspension at ϕ=0.4, respectively. Compared to the microstructure of suspensions at ϕ=0.316 and 0.37 (cf. Figures 7.14 and 7.15), the signal of an ordered structure is gaining strength with increasing volume fraction. $g(x,y)$ displays string formation of particles in the flow direction for a very narrow range of the Péclet number from 10 to 13 as seen in Fig.7.14. The string formation is unclear compared to the sharp string formation for ϕ=0.45 (cf. Fig.6.8.a). Similar to $g(x,y)$, $g(z,y)$ displays weakly ordered structure in a narrow range of the Péclet numbers from 5 to 15. The structure is unstable and destroyed at relatively small shear rate (Pe=20) as shown in Fig.7.15 and also in Fig.7.14. The transitional microstructural signature which shows the first sign of shear-induced order of the particle positions is consistent with the transitional rheological signature which begins to show shear thinning and shear thickening behavior for a hard-sphere suspension at ϕ=0.4.

The probability densities $g(x,y)$ and $g(z,y)$ of a hard sphere at ϕ=0.419 are shown

in Figures 7.18 and 7.19 with different Péclet numbers, respectively. For a small range of the Péclet number from 10 to 20, the flowing suspension is ordered with well formed strings of particles in the $x-y$ plane (Fig.7.18) and hexagonally packed strings of flowing particles in the $z-y$ plane (Fig.7.19). The structural order is destroyed at a relatively small Péclet number of 50.

The microstructure can be seen with more detail from the runs with 123 particles. A comparison of $g(x,y)$ and $g(z,y)$ for three different volume fractions ϕ=0.316 (left figure), 0.419 (central figure) and 0.45 (right figure) with 123 particles at Pe=10 is shown in Figures 7.20 and 7.21, respectively. Although the dimensionless run time of 40 for the runs with 123 particles is shorter than an average of 100 time units for the runs with 27 particles, the microstructure and the rheology were carefully checked and verified to be steady. There is clear evidence that the shear-induced order of the flowing particles at Pe=10 develops in increasingly dense suspensions. The structure for suspensions at ϕ=0.316 and 0.419 are weak and fluctuated compared to the well formed and distinct structure for ϕ=0.45.

Our results for the microstructure showed that suspensions of colloidal particles at volume fraction $\phi < 0.4$ cannot be sheared into order. For a range of volume fraction from 0.4 to 0.419, transitional signature of a shear-induced structure is seen. The microstructure still fluctuates between a slightly deformed random structure and an ordered state which occurs in a very narrow range of the Péclet number. In the following section, we examine the microstructure by analyzing the structure factor $S(\mathbf{k})$. The line and plane structure factors are computed from the runs with 123 particles for ϕ=0.316 and 0.419

at Pe=10 and compared with the structure factors from the runs with 123 particles for ϕ=0.45 which was presented in chapter VI.

VII.2.3 The Line Structure Factors $S(k_x)$, $S(k_y)$ and $S(k_z)$

The line structure factor computed in the flow direction, $S(k_x)$, is plotted in Fig.7.22 with different dimensionless wave numbers for hard-sphere suspensions at Pe=10 and three volume fractions: ϕ= ($\triangle$) 0.316, ($\circ$) 0.419 and the reference curve ϕ=0.45 ($\bullet$). There are 123 particles in the unit cell. $S(k_x)$ shows a small variation in the weak scattering light patterns. In the flow direction, the particles constantly change the positions causing change in the pattern of scattering light. It is difficult to label and attribute the weakly scattered intensity of $S(k_x)$ to a structural order in the x-axis. The peaks of scattered intensity from $S(k_x)$ are much smaller than that of the structure factors computed in the velocity gradient direction, $S(k_y)$, and in the vorticity direction, $S(k_z)$, as shown in Figures 7.23 and 7.24, respectively.

The line structure factors $S(k_y)$ in Fig.7.23 and $S(k_z)$ in Fig.7.24 for ϕ = ($\triangle$) 0.316 and ($\circ$) 0.419 show insignificant scattered intensity compared to the intensity maxima of $O(N)$ for ϕ=0.45 ($\bullet$). A pattern of weak scattered intensity is consistent with the information obtained from the plot of the probability density functions $g(x,y)$ and $g(z,y)$ (cf. Figures 7.20 and 7.21) which show an unstable and fluctuated structure for ϕ=0.316 and 0.419.

VII.2.4 The Plane Structure Factors $S(k_x,k_z)$ and $S(k_z,k_y)$

Figure 7.25 shows contour plots of the plane structure factors computed in the velocity

- velocity gradient plane, $S(k_x, k_y)$, (first row) and in the vorticity - velocity gradient plane, $S(k_z, k_y)$, (second row) for hard spheres at Pe=10 and three different volume fractions: ϕ=0.316 (left column), 0.419 (central column) and 0.45 (right column). There are 123 particles in the unit cell. Regions of light color represent high scattering light intensity and regions of dark color represent low scattering light intensity. The directions of the dimensionless wave numbers k_x, k_y and k_z are displayed on the right of this figure. The range of these wave numbers is from $\pm$0.5 to $\pm$4.0. $S(k_x, k_y)$ and $S(k_z, k_y)$ for ϕ=0.316 and 0.419 display weak scattered intensity of slightly deformed Debye-Scherrer ring compared to $S(k_x, k_y)$ and $S(k_z, k_y)$ for ϕ=0.45 which shows a distinct scattered intensity pattern with two vertical bands in the k_x-k_z plane and halo ring with six intensity maxima in the k_z-k_y plane reflecting a strongly order suspension. The evidence that we examine here is the microstructure of a random suspension at volume fraction less than 0.45 in the transition to order at Pe=10. The transitional signal of structural order is stronger with increasing volume fraction but at ϕ=0.419 the shear still cannot process and induce the flowing suspension into a strong ordering as seen for the suspension at ϕ=0.45. In the next section, we examine the self-diffusivities of these hard-sphere suspensions and present the results of the short- and long-time self-diffusion coefficients.

VII.3 The Self-Diffusivities

The self-diffusivities are important to suspension mechanics since they contain valuable information on particle mobility. The short-time self-diffusivities measure the instant mobility of the suspended particles, and the long-time self-diffusivities measure the dynamic behavior of the suspensions as the particles must travel a distance comparable

to theirs own size, deform the local structure, and exchange places with neighbors. The long-time self-diffusivity also describes the internal mixing at the particle scale level.

VII.3.1 The Short-Time Self-Diffusion Coefficients

Simulation results for the short-time translational and rotational self-diffusion coefficients are summarized in Tables 7.13 to 7.16 for ϕ=0.316, 0.37, 0.4 and 0.419, respectively. Column (1) is Pe and column (2) is N. Columns (3) to (6) are the steady short-time translational self-diffusion coefficients computed in the x-axis, $D^s_{o_{xx}}$, in the y-axis, $D^s_{o_{yy}}$, in the z-axis, $D^s_{o_{zz}}$, the mean, i.e., $D^s_o = \frac{1}{3}\,(D^s_{o_{xx}}+D^s_{o_{yy}}+D^s_{o_{zz}})$, and its standard deviation. Similarly, columns (8) to (12) are the short-time rotational self-diffusion coefficients $D^s_{r_{xx}}$, $D^s_{r_{yy}}$, $D^s_{r_{zz}}$, the mean D^s_r, and its standard deviation. D^s_o and D^s_r are normalized by the infinite dilution diffusion coefficients $D_o = kT/(6\pi\eta a)$ and $D_r = kT/(8\pi\eta a^3)$, respectively.

Results from these four tables are plotted in Fig.7.26 for D^s_o and in Fig.7.27 for D^s_r as a function of the Péclet number and different volume fractions ϕ = (▲) 0.316, (◆) 0.37, (○) 0.4, (□) 0.419, and (●) 0.45. These two figures show a general behavior of the short-time self-diffusion coefficients. Both D^s_o and D^s_r remain relatively constant in the Brownian dominated limit ($Pe < 1$) as the equilibrium isotropic structure is slightly deformed by small shear rates. At large Péclet number ($Pe > 10$), both D^s_o and D^s_r decrease with increasing Péclet number and imply a reduction in the mobility of the particles owing to the formation of closely spaced or touching particles. In the special region with $Pe \approx 10$, the behavior of the short-time self-diffusion coefficients depends on the volume fraction. For hard spheres at $\phi < 0.4$, the transition behavior in this region of the Péclet number is smooth as there is not much change in the local structure.

For hard spheres at ϕ=0.419 and 0.45, a small increase of D_o^s and D_r^s is a direct result of enhanced local mobility due to well separated particles in a suspension. In chapter VI, we show that the strong ordering of the microstructure for ϕ=0.45 with hexagonally packed strings of flowing particles is accompanied by an increase in D_o^s and D_r^s. In an hexagonal packing, the particles are not only relatively well separated from each other but also are evenly spaced. The particles in the hexagonal arrangement are very mobile and as a result, the short-time self-diffusion coefficients are maximum. Figures 7.26 and 7.27 also show a decrease of D_o^s and D_r^s as the volume fraction increases for hard spheres at the same Péclet number. For relatively less dense suspension at ϕ=0.316, the short-time mean translational self-diffusion coefficient, $\langle D_o^s \rangle$, for a pure Brownian suspension (Pe=0) and for a slightly deformed suspension (Pe=0.01) is the same as shown in Table 7.13. As the volume fraction increases, a small shear at low Péclet number can influence and disturb the random structure and this can be seen by comparing $\langle D_o^s \rangle$ = 0.269 at Pe=0 which is larger than $\langle D_o^s \rangle$ = 0.221 at Pe=0.01 for ϕ=0.4 (cf. Table 7.15). A similar trend can be observed in the hydrodynamic dominated limit. The presence of very small Brownian motion (Pe=10^6) can perturb and induce diffusive behavior, and this is seen by comparing $\langle D_o^s \rangle$ = 0.1 at Pe=10^6 which is larger than a small D_o^s = 0.044 for a pure hydrodynamic suspension (Pe=∞) for ϕ=0.4 (cf .Tables 7.15). Data from these four tables also show a consistent trend which the short-time translational self-diffusion coefficient computed in the flow direction, $D_{o_{xx}}^s$, is slightly larger than $D_{o_{yy}}^s$ and $D_{o_{zz}}^s$. The imposed shear increases the instantaneous mobility of the particles in the flow direction compared to the directions of the velocity gradient and the vorticity.

VII.3.2 The Long-Time Self-Diffusion Coefficients

The long-time self-diffusion coefficients are reported in Tables 7.17 to 7.20 for the runs with 27 particles of hard spheres at ϕ=0.316, 0.37, 0.4 and 0.419, respectively. Column (1) is *Pe*. Columns (2) to (5) are the steady long-time self-diffusion coefficient computed in the velocity gradient direction, $D^s_{\infty,yy}$, its standard deviation, in the vorticity direction, $D^s_{\infty,zz}$, and its standard deviation, respectively. These coefficients are normalized by the infinite dilution diffusion coefficient $D_o = kT/(6\pi\eta a)$. The mean value of these coefficients is computed from a number of samples shown in column (7) and each sample interval has a time unit displayed in column (6). Note that the time has been scaled with a diffusive time for these coefficients. For the method of computing the long-time self-diffusion coefficients, please see section VI.3.2.

Figure 7.28 is a log-log plot of $D^s_{\infty,yy}/D_o$ as a function of the Péclet number for hard spheres at ϕ = (▲) 0.316, (♦) 0.37, (○) 0.4, (□) 0.419 and (●) 0.45 as a reference for comparison. Recall that the y-axis is the velocity gradient direction. For strong Brownian suspension ($Pe < 1$), the dimensionless diffusion coefficient is relatively constant and has an asymptotic limit of $D^s_{\infty,yy} \approx O(D_o)$ as $Pe \to 0$. The influence of the imposed shear can be seen by comparing $D^s_{\infty,yy}$ for a pure Brownian suspension and for a slightly deformed suspension at *Pe*=0.01. Table 7.17 gives $D^s_{\infty,yy}$= 0.160 at *Pe*=0 compared to $D^s_{\infty,yy}$= 0.204 at *Pe*=0.1 for ϕ=0.316. Similarly, Table 7.19 for ϕ=0.4 shows $D^s_{\infty,yy}$= 0.103 at *Pe*=0 compared to $D^s_{\infty,yy}$= 0.120 at *Pe*=0.1. A small amount of the shear force is seen to disturb the Brownian suspension and enhance the diffusivity of particles in the velocity gradient direction. The long-time self-diffusion coefficient, $D^s_{\infty,yy}$,

is also smaller than the short-time self-diffusion coefficient, D_o^s, at Pe=0 as shown in Tables 7.17 and 7.19. This behavior of the self-diffusivities has been measured in the tracer diffusion experiments by van Megen, Underwood and Snook (1986). Their experimental results of the short- and long-time self-diffusion coefficients for hard spheres at equilibrium are: D_o^s= 0.34 and $D_{\infty,yy}^s$= 0.13 for ϕ=0.384, and D_o^s= 0.22 and $D_{\infty,yy}^s$= 0.11 for ϕ=0.411 (cf. Table 1 and Fig.6 from van Megen, Underwood and Snook (1986)). Stokesian dynamics simulation results are D_o^s= 0.269 (Table 7.15) and $D_{\infty,yy}^s$= 0.103 (cf. Table 7.19) for ϕ=0.4 and Pe=0. Our values compare remarkably well with their experimental results for pure Brownian suspensions illustrating the excellent accuracy of the Stokesian dynamics simulation method.

In the limit of large Péclet number ($Pe > 10^2$), $D_{\infty,yy}^s$ increases linearly with increasing Pe as predicted by the dimensional analysis of the time scale for the diffusion. As $Pe \rightarrow \infty$, the proper scale for the diffusion is $\dot{\gamma}a^2$; therefore, $D_{\infty,yy}^s$ which is nondimensionalized by D_o should scale with Pe as $Pe \rightarrow \infty$. Figure 7.28 displays the correct relation of $D_{\infty,yy}^s$ in the region of large Péclet number ($Pe > 10^2$). The asymptotic limit as $Pe \rightarrow \infty$ for the long-time self-diffusion coefficient is $D_{\infty,yy}^s/D_o \approx$ 0.06 which compares very close to the new experiments of Phan and Leighton (1992). We shall present a final comparison of the complete dense suspension with their experiments in chapter IX.

Figure 7.28 shows clearly the transitional Péclet number $Pe \approx 10$, where the behavior of the $D_{\infty,yy}^s$ changes from a strong Brownian limit to the hydrodynamic dominated regime. At Pe=10, $D_{\infty,yy}^s$ of hard spheres with $\phi \geq 0.4$ decreases to a minimum implying that the particles are packed in an ordered formation and flow as strings. Figure 7.28 also

shows the transitional volume fraction ϕ=0.4 as suspensions with a volume fraction below 0.4 display insignificant change of $D^s_{\infty,yy}$ in this special region of the Péclet number.

A similar behavior of the long-time self-diffusion coefficient computed in the vorticity direction, $D^s_{\infty,zz}$, is seen in Fig.7.29. Recall that the z-axis is the direction of the vorticity. $D^s_{\infty,zz}$ changes inappreciably in the Brownian dominated limit ($Pe < 1$) and increases linearly with increasing Pe for hydrodynamic dominated regime ($Pe > 10^2$). In the special region of the Péclet number ($Pe \approx 10$), $D^s_{\infty,zz}$ for hard spheres with a volume fraction $\phi \geq 0.4$ decreases to a minimum value but the decrease of $D^s_{\infty,zz}$ is not as pronounced as that of $D^s_{\infty,yy}$.

VII.4 Conclusions

In this chapter, we showed that hard spheres at volume fraction $\phi < 0.4$ cannot be sheared into order and the change of the steady shear viscosity with the Péclet number is small. As the volume fraction increases, the flowing suspension is in the transition to form a structural order in the special region with $Pe \approx 10$, but the microstructure is weak and fluctuated between a slightly deformed isotropic structure and an ordered state. The suspension shear thins for $Pe < 10$ and shear thicken for $Pe > 10$. For $Pe \approx 10$, the steady shear viscosity is minimum and no further shear thinning is found in this special region.

Our results for the moderately dense hard-sphere suspensions agree with the experimental findings of Pusey and van Megen (1986) for the equilibrium phase transition of hard spheres. Hard spheres, which are below the colloidal fluid - colloidal crys-

talline phase transition (ϕ_F= 0.494), are isotropic at rest and experimentally do not show structural order in a simple shear flow. Near this phase transition, the suspension, which shows the coexistence of colloidal fluid and colloidal crystals at equilibrium, can be sheared into strong ordering as recently observed in experiments from Laun (1988) and Laun *et al.* (1992). This study provides the fruitful capability of Stokesian dynamics in modeling particulate flow and improves our understanding of the behavior of moderately concentrated colloidal suspensions.

In contrast to Stokesian dynamics which does not show shear thinning and shear thickening behavior and strong ordering of the flowing particles for suspensions at volume fractions $\phi < 0.4$, computer simulations with nonequilibrium molecular dynamics by Laun *et al.* (1992) and with Brownian dynamics method by Erpenbeck (1983), Heyes (1988), Weider *et al.* (1991), Wilemski (1991) tend to predict the shear thinning along with the string formation of flowing particles for all volume fractions. On of the main reason for this poor prediction is that these simulations are incapable of treating the important many-body hydrodynamic interactions and depend on the interparticle forces to set the structure and the rheology. Stokesian dynamics with hydrodynamics accurately produces the behavior of hard-sphere suspensions from dilution to close packing without the need of interparticle forces. In the next chapter, we present and discuss the rheological and microstructural behaviors of very dense hard-sphere suspensions at particle volume fraction $\phi > 0.45$.

Table 7.1: Statistics for simulations of a hard-sphere suspension at volume fraction ϕ=0.316 and different Péclet numbers. Table captions are the same as shown in Table 6.1.a. Initial particle configurations of all runs in the table are random.

Pe	N	t_{start}	t_{end}	Δt_{set}	NSTEPS	t_{diff}	t_{shift}	# *trials*
0.01	27	0.0	100.0	5×10^{-4}	200000	95.0	1.0	6
0.10	27	0.0	200.0	10^{-3}	200000	60.0	5.0	58
1.00	27	0.0	200.0	10^{-3}	200000	60.0	5.0	58
10.00	27	0.0	100.0	10^{-3}	100000	60.0	1.0	41
10^2	27	0.0	100.0	10^{-3}	100000	60.0	2.0	21
10^3	27	0.0	100.0	10^{-3}	100000	60.0	2.0	21
10^4	27	0.0	100.0	10^{-3}	100000	60.0	2.0	21
10^5	27	0.0	200.0	10^{-3}	200000	100.0	10.0	20
10^6	27	0.0	60.0	10^{-3}	60000	50.0	1.0	11
∞	27	0.0	40.0	10^{-4}	400000	30.0		1
10.00	123	0.0	40.0	10^{-3}	40000	35.0		1

Table 7.2: Statistics for simulations of a hard-sphere suspension at volume fraction ϕ=0.37 and different Péclet numbers. Table captions are the same as shown in Table 6.1.a. Initial particle configurations of all the runs in the table are random.

Pe	N	t_{start}	t_{end}	Δt_{set}	NSTEPS	t_{diff}	t_{shift}	# *trials*
0.01	27	0.0	200.0	5×10^{-4}	400000	195.0	1.0	6
0.10	27	0.0	60.0	10^{-3}	60000	50.0	1.0	11
1.00	27	0.0	60.0	10^{-3}	60000	50.0	1.0	11
5.00	27	0.0	60.0	10^{-3}	60000	50.0	1.0	11
10.00	27	0.0	60.0	10^{-3}	60000	50.0	1.0	11
15.00	27	0.0	60.0	10^{-3}	60000	50.0	1.0	11
20.00	27	0.0	60.0	10^{-3}	60000	50.0	1.0	11
10^2	27	0.0	60.0	10^{-3}	60000	50.0	1.0	11
10^3	27	0.0	60.0	10^{-3}	60000	50.0	1.0	11
10^4	27	0.0	60.0	10^{-3}	60000	50.0	1.0	11
10^6	27	0.0	60.0	10^{-3}	60000	50.0	1.0	11
∞	27	0.0	40.0	10^{-4}	400000	30.0		1

Table 7.3: Statistics for simulations of a hard-sphere suspension at volume fraction ϕ=0.4 and different Péclet numbers. Table captions are the same as shown in Table 6.1.a. Initial particle configurations of all the runs in the table are random.

Pe	N	t_{start}	t_{end}	Δt_{set}	NSTEPS	t_{diff}	t_{shift}	# *trials*
0.01	27	0.0	110.0	5×10^{-4}	220000	100.0	1.0	11
0.10	27	0.0	60.0	10^{-3}	60000	50.0	1.0	11
1.00	27	0.0	60.0	10^{-3}	60000	50.0	1.0	11
5.00	27	0.0	60.0	10^{-3}	60000	50.0	1.0	11
7.00	27	0.0	60.0	10^{-3}	60000	50.0	1.0	11
10.00	27	0.0	60.0	10^{-3}	60000	50.0	1.0	11
13.00	27	0.0	60.0	10^{-3}	60000	50.0	1.0	11
15.00	27	0.0	60.0	10^{-3}	60000	50.0	1.0	11
20.00	27	0.0	60.0	10^{-3}	60000	50.0	1.0	11
10^2	27	0.0	60.0	10^{-3}	60000	50.0	1.0	11
10^3	27	0.0	60.0	10^{-3}	60000	50.0	1.0	11
10^4	27	0.0	60.0	10^{-3}	60000	50.0	1.0	11
10^6	27	0.0	60.0	10^{-3}	60000	50.0	1.0	11
∞	27	0.0	40.0	10^{-4}	400000	30.0		1

Table 7.4: Statistics for simulations of a hard-sphere suspension at volume fraction ϕ=0.419 and different Péclet numbers. Table captions are the same as shown in Table 6.1.a. Initial random samples of particles are selected for the runs with Pe=0.01, 30, 10^6, and ∞. A series of 13 continuing runs is started with Pe=0.01 [1] and ended with Pe=10^4 [13].

Pe	N	t_{start}	t_{end}	Δt_{set}	NSTEPS	t_{diff}	t_{shift}	# *trials*
[1] 0.01	27	0.0	100.0	5×10^{-4}	200000	75.0	5.0	6
[2] 0.10	27	100.0	200.0	10^{-3}	100000	80.0	2.0	11
[3] 1.00	27	200.0	300.0	10^{-3}	100000	80.0	2.0	11
[4] 3.00	27	300.0	360.0	10^{-3}	60000	50.0	1.0	11
[5] 5.00	27	360.0	420.0	10^{-3}	60000	50.0	1.0	11
[6] 7.00	27	420.0	480.0	10^{-3}	60000	50.0	1.0	11
[7] 10.00	27	480.0	540.0	10^{-3}	60000	50.0	1.0	11
[8] 15.00	27	540.0	600.0	10^{-3}	60000	50.0	1.0	11
[9] 20.00	27	600.0	660.0	10^{-3}	60000	50.0	1.0	11
30	27	0.0	60.0	10^{-3}	60000	50.0	1.0	11
[10] 50.00	27	660.0	720.0	10^{-3}	60000	50.0	1.0	11
[11] 2×10^2	27	720.0	780.0	10^{-3}	60000	50.0	1.0	11
[12] 10^3	27	780.0	840.0	10^{-3}	60000	50.0	1.0	11
[13] 10^4	27	840.0	900.0	10^{-3}	60000	50.0	1.0	11
10^6	27	0.0	60.0	10^{-4}	600000	50.0	1.0	6
∞	27	0.0	50.0	10^{-4}	500000	40.0		1
10.00	123	0.0	40.0	10^{-3}	40000	35.0		1

Table 7.5: Results of the shear viscosities obtained from Stokesian dynamics for a hard-sphere suspension at volume fraction ϕ=0.316 and different Péclet numbers. Table captions are the same as shown in Table 6.2.a.

Pe	N	η_H	σ_{η_H}	η_B	σ_{η_B}	η_T	σ_{η_T}
0.01	27	1.868	0.001	1.161	0.673	4.029	0.673
0.10	27	1.865	0.003	0.768	0.087	3.632	0.089
1.00	27	1.845	0.004	0.601	0.006	3.447	0.006
10.00	27	1.907	0.015	0.176	0.003	3.083	0.019
10^2	27	2.258	0.027	0.029	0.001	3.287	0.028
10^3	27	2.654	0.077	0.003	0.000	3.656	0.078
10^4	27	2.888	0.019	$2.1\text{x}10^{-4}$	0.000	3.889	0.019
10^5	27	2.988	0.032	$1.9\text{x}10^{-5}$	0.000	3.986	0.032
10^6	27	3.044	0.090	$1.1\text{x}10^{-6}$	0.000	4.004	0.090
∞	27	3.673				4.673	
10.00	123	1.779		0.151		2.930	

Table 7.6: Results of the shear viscosities obtained from Stokesian dynamics for hard-spheres suspensions at volume fraction ϕ=0.37 and different Péclet numbers. Table captions are the same as shown in Table 6.2.a.

Pe	N	η_H	σ_{η_H}	η_B	σ_{η_B}	η_T	σ_{η_T}
0.01	27	2.660	0.002	1.810	0.670	5.470	0.673
0.10	27	2.671	0.007	1.704	0.178	5.375	0.177
1.00	27	2.689	0.005	1.169	0.013	4.857	0.015
5.00	27	2.629	0.011	0.543	0.008	4.172	0.015
10.00	27	2.676	0.025	0.293	0.009	3.969	0.034
15.00	27	2.799	0.015	0.292	0.004	4.090	0.019
20.00	27	2.909	0.007	0.208	0.002	4.117	0.008
10^2	27	3.479	0.017	0.062	0.001	4.541	0.018
10^3	27	3.739	0.055	0.006	0.000	4.744	0.055
10^4	27	4.297	0.040	$5.7\text{x}10^{-4}$	0.000	5.297	0.036
10^6	27	4.696	0.031	$4.0\text{x}10^{-6}$	0.000	5.696	0.031
∞	27	6.366				7.366	

Table 7.7: Results of the shear viscosities obtained from Stokesian dynamics for a hard-sphere suspension at volume fraction ϕ=0.4 and different Péclet numbers. Table captions are the same as shown in Table 6.2.a.

Pe	N	η_H	σ_{η_H}	η_B	σ_{η_B}	η_T	σ_{η_T}
0.01	27	3.284	0.005	3.224	1.126	7.507	1.131
0.10	27	3.290	0.006	2.680	0.123	6.970	0.119
1.00	27	3.303	0.005	1.808	0.013	6.111	0.016
5.00	27	2.965	0.018	0.617	0.007	4.853	0.022
7.00	27	2.964	0.018	0.550	0.010	4.513	0.027
10.00	27	2.886	0.027	0.292	0.020	4.178	0.039
13.00	27	3.467	0.059	0.408	0.023	4.875	0.082
15.00	27	3.583	0.048	0.365	0.012	4.948	0.060
20.00	27	3.905	0.031	0.339	0.006	5.244	0.040
10^2	27	4.570	0.036	0.104	0.003	5.674	0.039
10^3	27	5.084	0.026	0.010	0.000	6.094	0.026
10^4	27	6.012	0.046	0.002	0.000	7.003	0.046
10^6	27	6.959	0.095	$9.0\text{x}10^{-6}$	0.000	7.959	0.095
∞	27	14.507				15.507	

Table 7.8: Results of the shear viscosities obtained from Stokesian dynamics for a hard-sphere suspension at volume fraction ϕ=0.419 and different Péclet numbers. Table captions are the same as shown in Table 6.2.a.

Pe	N	η_H	σ_{η_H}	η_B	σ_{η_B}	η_T	σ_{η_T}
[1] 0.01	27	3.779	0.018	4.930	3.916	9.709	3.916
[2] 0.10	27	3.726	0.070	4.235	0.342	8.961	0.347
[3] 1.00	27	3.824	0.007	2.402	0.014	7.226	0.017
[4] 3.00	27	3.612	0.017	1.314	0.007	5.925	0.022
[5] 5.00	27	3.542	0.038	0.870	0.027	5.412	0.065
[6] 7.00	27	3.377	0.042	0.537	0.025	4.913	0.066
[7] 10.00	27	3.184	0.069	0.323	0.024	4.507	0.094
[8] 15.00	27	3.385	0.089	0.270	0.020	4.655	0.095
[9] 20.00	27	3.523	0.032	0.236	0.009	4.758	0.040
30.00	27	4.421	0.033	0.307	0.007	5.727	0.040
[10] 50.00	27	4.860	0.051	0.221	0.005	6.081	0.055
[11] $2\text{x}10^2$	27	5.972	0.023	0.080	0.001	7.052	0.024
[12] 10^3	27	6.486	0.106	0.017	0.001	7.503	0.106
[13] 10^4	27	7.283	0.053	0.002	0.000	8.284	0.053
10^6	27	9.374	0.412	$1.1\text{x}10^{-5}$	0.000	10.374	0.412
∞	27	24.151				25.151	
10.00	123	3.431		0.465		4.896	

Table 7.9: Results of the normal stress differences obtained by Stokesian dynamics for hard spheres at volume fraction ϕ=0.316 and different Péclet numbers. Table captions are the same as shown in Table 6.3.a.

Pe	N	χ_{1H}	$\sigma_{\chi_{1H}}$	χ_{1B}	$\sigma_{\chi_{1B}}$	χ_{1T}	$\sigma_{\chi_{1T}}$	χ_{2H}	$\sigma_{\chi_{2H}}$	χ_{2B}	$\sigma_{\chi_{2B}}$	χ_{2T}	$\sigma_{\chi_{2T}}$
0.01	27	0.024	0.004	-1.673	1.041	-1.650	1.038	0.008	0.001	2.509	0.484	2.517	0.485
0.10	27	0.027	0.008	-0.688	0.177	-0.661	0.181	0.016	0.003	0.786	0.178	0.802	0.178
1.00	27	0.054	0.003	-0.130	0.020	-0.076	0.036	0.126	0.003	0.271	0.120	0.397	0.123
10.00	27	0.243	0.014	-0.109	0.009	0.134	0.023	0.202	0.021	0.101	0.015	0.303	0.036
10^2	27	0.329	0.020	-0.026	0.003	0.303	0.023	0.282	0.024	0.012	0.002	0.294	0.026
10^3	27	0.316	0.031	-0.006	0.001	0.310	0.031	0.257	0.025	0.001	0.001	0.259	0.024
10^4	27	0.284	0.029	-0.001		0.283	0.029	0.171	0.023	$3.2\text{x}10^{-4}$		0.171	0.023
10^5	27	0.253	0.031	$-5.4\text{x}10^{-5}$		0.253	0.031	0.181	0.014	$5.6\text{x}10^{-6}$		0.181	0.014
10^6	27	0.230	0.018	$-5.0\text{x}10^{-6}$		0.229	0.018	0.044	0.006	$2.7\text{x}10^{-7}$		0.044	0.006

Table 7.10: Results of the normal stress differences obtained from Stokesian dynamics for hard spheres at volume fraction ϕ=0.37 and different Péclet numbers. Table captions are the same as shown in Table 6.3.a.

Pe	N	χ_{1H}	$\sigma_{\chi_{1H}}$	χ_{1B}	$\sigma_{\chi_{1B}}$	χ_{1T}	$\sigma_{\chi_{1T}}$	χ_{2H}	$\sigma_{\chi_{2H}}$	χ_{2B}	$\sigma_{\chi_{2B}}$	χ_{2T}	$\sigma_{\chi_{2T}}$
0.01	27	0.083	0.002	-24.204	8.830	-24.120	8.850	0.024	0.002	23.282	8.240	23.306	8.250
0.10	27	0.032	0.012	-0.839	0.280	-0.808	0.282	0.021	0.005	1.021	0.226	1.042	0.235
1.00	27	0.110	0.010	-0.789	0.041	-0.679	0.033	0.222	0.009	0.639	0.045	0.861	0.054
5.00	27	0.132	0.019	-0.438	0.016	-0.306	0.034	0.307	0.004	0.470	0.003	0.777	0.007
10.00	27	0.186	0.009	-0.277	0.005	-0.091	0.014	0.391	0.020	0.237	0.023	0.628	0.043
15.00	27	0.336	0.008	-0.185	0.008	0.151	0.015	0.463	0.024	0.114	0.014	0.577	0.038
20.00	27	0.457	0.022	-0.010	0.014	0.360	0.036	0.355	0.009	0.066	0.005	0.420	0.012
10^2	27	0.474	0.013	-0.047	0.001	0.427	0.013	0.627	0.014	0.020	0.005	0.646	0.020
10^3	27	0.531	0.029	-0.007		0.524	0.029	0.590	0.053	0.003		0.594	0.053
10^4	27	0.546	0.039	$-8.8\text{x}10^{-4}$		0.546	0.039	0.550	0.022	$2.9\text{x}10^{-4}$		0.550	0.022
10^6	27	0.328	0.027	$-1.3\text{x}10^{-5}$		0.328	0.027	0.312	0.034	$5.6\text{x}10^{-6}$		0.312	0.034

Table 7.11: Results of the normal stress differences obtained from Stokesian dynamics for hard spheres at volume fraction ϕ=0.4 and different Péclet numbers. Table captions are the same as shown in Table 6.3.a.

Pe	N	χ_{1H}	$\sigma_{\chi_{1H}}$	χ_{1B}	$\sigma_{\chi_{1B}}$	χ_{1T}	$\sigma_{\chi_{1T}}$	χ_{2H}	$\sigma_{\chi_{2H}}$	χ_{2B}	$\sigma_{\chi_{2B}}$	χ_{2T}	$\sigma_{\chi_{2T}}$
0.01	27	0.082	0.011	-38.377	6.881	-38.296	6.892	0.010	0.013	26.221	1.529	26.232	1.529
0.10	27	0.018	0.007	-0.954	1.007	-0.936	1.010	0.052	0.006	1.893	1.490	1.944	1.496
1.00	27	0.239	0.012	-0.499	0.069	-0.260	0.078	0.280	0.012	0.238	0.042	0.517	0.051
5.00	27	0.310	0.023	-0.313	0.044	-0.003	0.066	0.294	0.020	0.175	0.051	0.468	0.071
7.00	27	0.465	0.022	-0.226	0.028	0.239	0.045	0.324	0.029	0.145	0.026	0.470	0.054
10.00	27	0.317	0.017	-0.224	0.021	0.093	0.038	0.288	0.033	0.160	0.024	0.448	0.056
13.00	27	0.471	0.041	-0.174	0.029	0.297	0.070	0.522	0.024	0.092	0.013	0.615	0.017
15.00	27	0.473	0.010	-0.211	0.009	0.262	0.014	0.537	0.010	0.034	0.005	0.572	0.010
20.00	27	0.609	0.041	-0.146	0.019	0.463	0.060	0.598	0.028	0.099	0.008	0.697	0.035
10^2	27	0.702	0.064	-0.056	0.007	0.646	0.071	0.832	0.019	0.041	0.006	0.873	0.023
10^3	27	0.530	0.032	-0.013	0.001	0.518	0.032	1.002	0.052	0.003	0.001	1.005	0.053
10^4	27	0.583	0.033	-0.002		0.581	0.033	1.466	0.028	$1.8\text{x}10^{-4}$		1.466	0.028
10^6	27	0.413	0.068	$-1.4\text{x}10^{-5}$		0.413	0.068	0.886	0.078	$3.7\text{x}10^{-6}$		0.886	0.078

Table 7.12: Results of the normal stress differences obtained from Stokesian dynamics for hard spheres at volume fraction ϕ=0.419 and different Péclet numbers. A sequence of 13 continuing runs is started with Pe=0.01 [1] and ended with Pe=10^4 [13]. Table captions are the same as shown in Table 6.3.a.

Pe	N	χ_{1H}	$\sigma_{\chi_{1H}}$	χ_{1B}	$\sigma_{\chi_{1B}}$	χ_{1T}	$\sigma_{\chi_{1T}}$	χ_{2H}	$\sigma_{\chi_{2H}}$	χ_{2B}	$\sigma_{\chi_{2B}}$	χ_{2T}	$\sigma_{\chi_{2T}}$
[1] 0.01	27	0.139	0.010	-66.760	21.138	-66.461	21.135	0.109	0.021	72.905	26.979	73.014	26.999
[2] 0.10	27	0.172	0.008	-1.096	0.714	-0.924	0.710	0.056	0.015	0.876	0.726	0.932	0.714
[3] 1.00	27	0.276	0.007	-0.743	0.071	-0.467	0.073	0.290	0.005	0.625	0.063	0.915	0.065
[4] 3.00	27	0.359	0.009	-0.381	0.036	-0.022	0.044	0.513	0.018	0.464	0.020	0.978	0.036
[5] 5.00	27	0.610	0.019	-0.056	0.026	0.554	0.039	0.427	0.022	0.307	0.017	0.734	0.037
[6] 7.00	27	0.129	0.042	-0.538	0.044	-0.409	0.086	0.481	0.051	0.432	0.047	0.913	0.098
[7] 10.00	27	0.278	0.020	-0.397	0.008	-0.119	0.026	0.043	0.066	0.269	0.046	0.312	0.112
[8] 15.00	27	0.324	0.025	-0.330	0.010	-0.005	0.035	0.185	0.050	0.043	0.002	0.228	0.052
[9] 20.00	27	0.625	0.013	-0.245	0.010	0.380	0.020	0.180	0.015	0.088	0.009	0.268	0.022
30.00	27	0.828	0.027	-0.046	0.006	0.782	0.024	0.699	0.007	0.064	0.005	0.764	0.011
[10] 50.00	2	0.845	0.021	-0.044	0.005	0.707	0.024	0.990	0.038	0.082	0.004	1.076	0.041
[11] $2\text{x}10^2$	27	0.844	0.037	-0.045	0.003	0.799	0.039	1.394	0.027	0.026	0.002	1.420	0.028
[12] 10^3	27	0.895	0.058	-0.015	0.001	0.880	0.059	1.428	0.046	0.003	0.001	1.431	0.047
[13] 10^4	27	0.914	0.055	-0.002	0.001	0.912	0.055	1.633	0.049	$3.1\text{x}10^{-4}$		1.632	0.049
10^6	27	-2.798	0.198	$-1.0\text{x}10^{-4}$		-2.798	0.198	0.476	0.150	$1.3\text{x}10^{-4}$		0.476	0.150
10.00	123	0.397		-0.190		0.207		0.557		0.247		0.803	

Table 7.13: Results of the short-time self-diffusion coefficients obtained by Stokesian dynamics for hard spheres at volume fraction ϕ=0.316 and different Péclet numbers. Table captions are the same as shown in Table 6.5.a.

Pe	N	$D^s_{o_{xx}}$	$D^s_{o_{yy}}$	$D^s_{o_{zz}}$	$\langle D^s_o \rangle$	$\sigma_{D^s_o}$	$D^s_{r_{xx}}$	$D^s_{r_{yy}}$	$D^s_{r_{zz}}$	$\langle D^s_r \rangle$	$\sigma_{D^s_r}$
0.00	27	0.304	0.304	0.303	0.304	0.001	0.718	0.718	0.716	0.717	0.000
0.01	27	0.306	0.300	0.303	0.303	0.001	0.715	0.716	0.715	0.715	0.000
0.10	27	0.306	0.301	0.303	0.304	0.000	0.715	0.716	0.715	0.715	0.001
1.00	27	0.306	0.300	0.301	0.303	0.001	0.709	0.711	0.710	0.710	0.000
10.00	27	0.305	0.286	0.290	0.294	0.001	0.688	0.702	0.692	0.694	0.001
10^2	27	0.267	0.247	0.251	0.255	0.001	0.598	0.622	0.610	0.610	0.002
10^3	27	0.301	0.264	0.266	0.277	0.008	0.558	0.606	0.595	0.586	0.011
10^4	27	0.266	0.241	0.236	0.248	0.002	0.498	0.543	0.539	0.527	0.004
10^5	27	0.223	0.205	0.206	0.211	0.002	0.461	0.494	0.489	0.481	0.005
10^6	27	0.224	0.205	0.211	0.213	0.001	0.462	0.498	0.489	0.483	0.003
∞	27	0.166	0.173	0.171	0.170	0.006	0.405	0.361	0.359	0.375	0.013
10.00	123	0.306	0.308	0.301	0.305		0.703	0.717	0.708	0.709	

Table 7.14: Results of the short-time self-diffusion coefficients obtained by Stokesian dynamics for hard spheres at volume fraction ϕ=0.37 and different Péclet numbers. Table captions are the same as shown in Table 6.5.a.

Pe	N	$D^s_{o_{xx}}$	$D^s_{o_{yy}}$	$D^s_{o_{zz}}$	$\langle D^s_o \rangle$	$\sigma_{D^s_o}$	$D^s_{r_{xx}}$	$D^s_{r_{yy}}$	$D^s_{r_{zz}}$	$\langle D^s_r \rangle$	$\sigma_{D^s_r}$
0.01	27	0.253	0.248	0.250	0.250	0.001	0.652	0.654	0.652	0.653	0.001
0.10	27	0.253	0.250	0.250	0.251	0.000	0.655	0.654	0.654	0.654	0.000
1.00	27	0.251	0.243	0.245	0.246	0.001	0.640	0.646	0.642	0.643	0.001
5.00	27	0.253	0.239	0.239	0.244	0.001	0.640	0.650	0.645	0.645	0.001
10.00	27	0.250	0.225	0.234	0.236	0.001	0.619	0.640	0.625	0.628	0.001
15.00	27	0.231	0.214	0.215	0.220	0.000	0.589	0.606	0.598	0.598	0.001
20.00	27	0.227	0.213	0.216	0.219	0.000	0.588	0.600	0.591	0.593	0.001
10^2	27	0.204	0.187	0.189	0.193	0.001	0.520	0.543	0.529	0.530	0.001
10^3	27	0.186	0.168	0.169	0.175	0.001	0.458	0.488	0.473	0.473	0.002
10^4	27	0.161	0.147	0.149	0.152	0.001	0.395	0.418	0.411	0.408	0.002
10^6	27	0.152	0.135	0.133	0.140	0.001	0.346	0.384	0.380	0.370	0.001
∞	27	0.113	0.111	0.107	0.110	0.006	0.282	0.279	0.293	0.285	0.015

Table 7.15: Results of the short-time self-diffusion coefficients obtained by Stokesian dynamics for hard spheres at volume fraction ϕ=0.4 and different Péclet numbers. Table captions are the same as shown in Table 6.5.a.

Pe	N	$D^s_{o_{xx}}$	$D^s_{o_{yy}}$	$D^s_{o_{zz}}$	$\langle D^s_o \rangle$	$\sigma_{D^s_o}$	$D^s_{r_{xx}}$	$D^s_{r_{yy}}$	$D^s_{r_{zz}}$	$\langle D^s_r \rangle$	$\sigma_{D^s_r}$
0.00	27	0.269	0.269	0.270	0.269	0.001	0.668	0.668	0.667	0.667	0.001
0.01	27	0.224	0.218	0.221	0.221	0.001	0.616	0.619	0.618	0.618	0.001
0.10	27	0.224	0.220	0.223	0.222	0.001	0.617	0.615	0.615	0.616	0.001
1.00	27	0.218	0.214	0.214	0.216	0.000	0.603	0.605	0.605	0.604	0.001
5.00	27	0.230	0.216	0.215	0.220	0.001	0.614	0.623	0.619	0.619	0.001
7.00	27	0.222	0.206	0.207	0.212	0.000	0.598	0.606	0.601	0.602	0.001
10.00	27	0.230	0.209	0.212	0.217	0.000	0.606	0.615	0.606	0.609	0.001
13.00	27	0.207	0.192	0.193	0.197	0.002	0.567	0.578	0.572	0.572	0.004
15.00	27	0.260	0.234	0.235	0.242	0.002	0.613	0.629	0.624	0.622	0.003
20.00	27	0.238	0.222	0.223	0.228	0.000	0.593	0.604	0.597	0.598	0.001
10^2	27	0.170	0.155	0.158	0.161	0.001	0.476	0.494	0.481	0.484	0.002
10^3	27	0.151	0.134	0.137	0.141	0.002	0.406	0.435	0.420	0.420	0.003
10^4	27	0.120	0.109	0.109	0.113	0.000	0.329	0.347	0.341	0.339	0.001
10^6	27	0.107	0.098	0.095	0.100	0.001	0.272	0.285	0.296	0.284	0.002
∞	27	0.043	0.045	0.045	0.044	0.002	0.156	0.143	0.151	0.150	0.005

Table 7.16: Results of the short-time self-diffusion coefficients obtained by Stokesian dynamics for hard spheres at volume fraction ϕ=0.419 and different Péclet numbers. Table captions are the same as shown in Table 6.5.a.

Pe	N	$D^s_{o_{xx}}$	$D^s_{o_{yy}}$	$D^s_{o_{zz}}$	$\langle D^s_o \rangle$	$\sigma_{D^s_o}$	$D^s_{r_{xx}}$	$D^s_{r_{yy}}$	$D^s_{r_{zz}}$	$\langle D^s_r \rangle$	$\sigma_{D^s_r}$
0.01	27	0.206	0.200	0.203	0.203	0.001	0.592	0.596	0.593	0.593	0.001
0.10	27	0.204	0.202	0.203	0.203	0.001	0.594	0.592	0.592	0.593	0.001
1.00	27	0.200	0.195	0.196	0.197	0.001	0.577	0.579	0.578	0.578	0.001
3.00	27	0.207	0.200	0.200	0.202	0.000	0.595	0.600	0.594	0.597	0.000
5.00	27	0.204	0.197	0.197	0.199	0.001	0.589	0.590	0.585	0.588	0.001
7.00	27	0.213	0.190	0.197	0.200	0.000	0.580	0.597	0.583	0.587	0.000
10.00	27	0.212	0.185	0.177	0.191	0.001	0.558	0.575	0.585	0.573	0.002
15.00	27	0.203	0.176	0.174	0.185	0.001	0.544	0.563	0.564	0.557	0.001
20.00	27	0.198	0.170	0.168	0.179	0.002	0.531	0.549	0.552	0.544	0.002
30.00	27	0.169	0.161	0.160	0.163	0.000	0.508	0.511	0.507	0.509	0.001
50.00	27	0.164	0.148	0.150	0.154	0.000	0.479	0.496	0.486	0.487	0.001
$2x10^2$	27	0.137	0.126	0.127	0.130	0.001	0.417	0.432	0.419	0.423	0.001
10^3	27	0.121	0.111	0.109	0.114	0.001	0.364	0.379	0.374	0.372	0.002
10^4	27	0.111	0.099	0.099	0.103	0.000	0.318	0.335	0.332	0.328	0.000
10^6	27	0.067	0.058	0.062	0.062	0.000	0.207	0.210	0.215	0.211	0.001
∞	27	0.036	0.040	0.038	0.038	0.002	0.148	0.135	0.145	0.143	0.004
10.00	123	0.217	0.206	0.208	0.211		0.579	0.587	0.578	0.581	

Table 7.17: Results of the long-time self-diffusion coefficients obtained by Stokesian dynamics for hard spheres at volume fraction ϕ=0.316 and different Péclet numbers. Table captions are the same as shown in Table 6.6. The runs are with 27 particles.

Pe	$D^s_{\infty,yy}$	σ_{yy}	$D^s_{\infty,zz}$	σ_{zz}	t_{diff}	# trials
0.00	0.160	0.015	0.158	0.025	100.0	19
0.01	0.187	0.017	0.126	0.015	90.0	6
0.10	0.204	0.013	0.100	0.005	100.0	19
1.00	0.326	0.030	0.179	0.027	100.0	19
10.00	0.022	0.002	0.012	0.001	85.0	11
10^2	0.011	0.001	0.010	0.001	85.0	11
10^3	0.049	0.004	0.008	0.001	85.0	11
10^4	0.051	0.004	0.011	0.001	85.0	11
10^5	0.038	0.009	0.007	0.001	85.0	11
10^6	0.038	0.009	0.007	0.001	85.0	11

Table 7.18: Results of the long-time self-diffusion coefficients obtained by Stokesian dynamics for hard spheres at volume fraction ϕ=0.37 and different Péclet numbers. Table captions are the same as shown in Table 6.6. The runs are with 27 particles.

Pe	$D^s_{\infty,yy}$	σ_{yy}	$D^s_{\infty,zz}$	σ_{zz}	t_{diff}	# trials
0.01	0.105	0.022	0.114	0.040	90.0	6
0.10	0.131	0.011	0.124	0.015	50.0	6
1.00	0.184	0.017	0.164	0.005	50.0	6
5.00	0.032	0.005	0.054	0.006	50.0	6
10.00	0.019	0.001	0.013	0.001	50.0	6
15.00	0.028	0.004	0.029	0.002	50.0	6
20.00	0.027	0.003	0.028	0.003	50.0	6
10^2	0.022	0.002	0.019	0.002	50.0	6
10^3	0.028	0.003	0.014	0.001	50.0	6
10^4	0.036	0.004	0.015	0.002	50.0	6
10^6	0.045	0.003	0.008	0.002	50.0	6

Table 7.19: Results of the long-time self-diffusion coefficients obtained by Stokesian dynamics for hard spheres at volume fraction ϕ=0.4 and different Péclet numbers. Table captions are the same as shown in Table 6.6. The runs are with 27 particles.

Pe	$D^{s}_{\infty,yy}$	σ_{yy}	$D^{s}_{\infty,zz}$	σ_{zz}	t_{diff}	# trials
0.00	0.103	0.016	0.131	0.029	95.0	13
0.01	0.115	0.013	0.101	0.014	95.0	13
0.10	0.120	0.004	0.104	0.009	50.0	6
1.00	0.135	0.012	0.144	0.015	50.0	6
5.00	0.018	0.002	0.040	0.002	50.0	6
7.00	0.022	0.002	0.023	0.001	50.0	6
10.00	0.008	0.001	0.016	0.001	50.0	6
13.00	0.033	0.002	0.029	0.001	50.0	6
15.00	0.030	0.003	0.038	0.003	50.0	6
20.00	0.043	0.001	0.046	0.007	50.0	6
10^2	0.039	0.003	0.015	0.002	50.0	6
10^3	0.023	0.002	0.024	0.002	50.0	6
10^4	0.065	0.006	0.016	0.002	50.0	6

Table 7.20: Results of the long-time self-diffusion coefficients obtained by Stokesian dynamics for hard spheres at volume fraction ϕ=0.419 and different Péclet numbers. Table captions are the same as shown in Table 6.6. The runs are with 27 particles.

Pe	$D^s_{\infty,yy}$	σ_{yy}	$D^s_{\infty,zz}$	σ_{zz}	t_{diff}	# *trials*
0.01	0.074	0.010	0.071	0.011	90.0	6
0.10	0.085	0.011	0.087	0.010	90.0	6
1.00	0.210	0.018	0.153	0.023	90.0	6
3.00	0.093	0.003	0.059	0.005	50.0	6
5.00	0.044	0.005	0.048	0.007	50.0	6
7.00	0.009	0.001	0.015	0.001	50.0	6
10.00	0.007	0.003	0.007	0.002	50.0	6
15.00	0.007	0.001	0.009	0.001	50.0	6
20.00	0.008	0.002	0.009	0.002	50.0	6
30.00	0.017	0.003	0.026	0.004	50.0	6
50.00	0.030	0.003	0.039	0.002	50.0	6
$2x10^2$	0.048	0.007	0.029	0.004	50.0	6
10^3	0.030	0.001	0.018	0.004	50.0	6
10^4	0.046	0.003	0.027	0.006	50.0	6

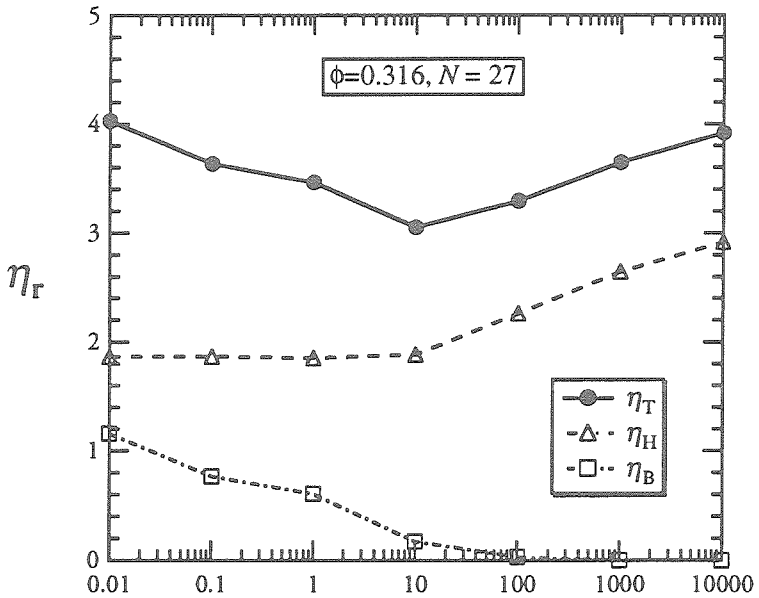

Figure 7.1

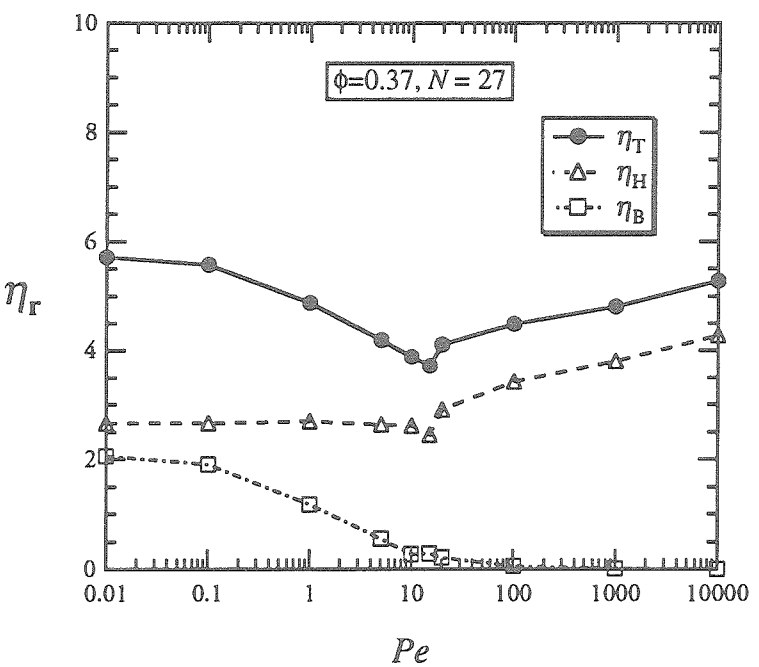

Figure 7.2

Figure 7.1-2: The steady shear viscosities: total (●) viscosity η_T, hydrodynamic (Δ) viscosity η_H and Brownian (□) viscosity η_B, obtained by Stokesian dynamics as a function of the Péclet number for hard spheres at particle volume fraction ϕ=0.316 (Fig.7.1) and 0.37 (Fig.7.2).

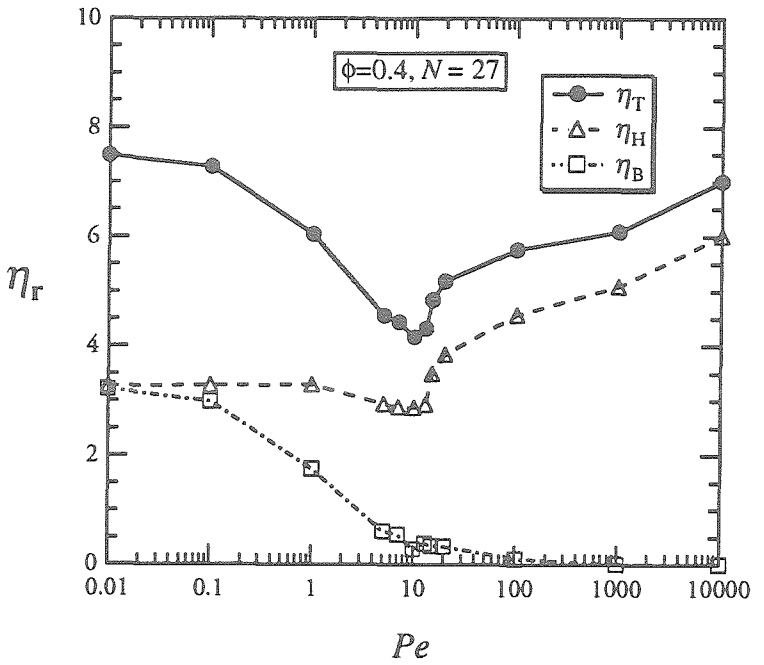

Figure 7.3

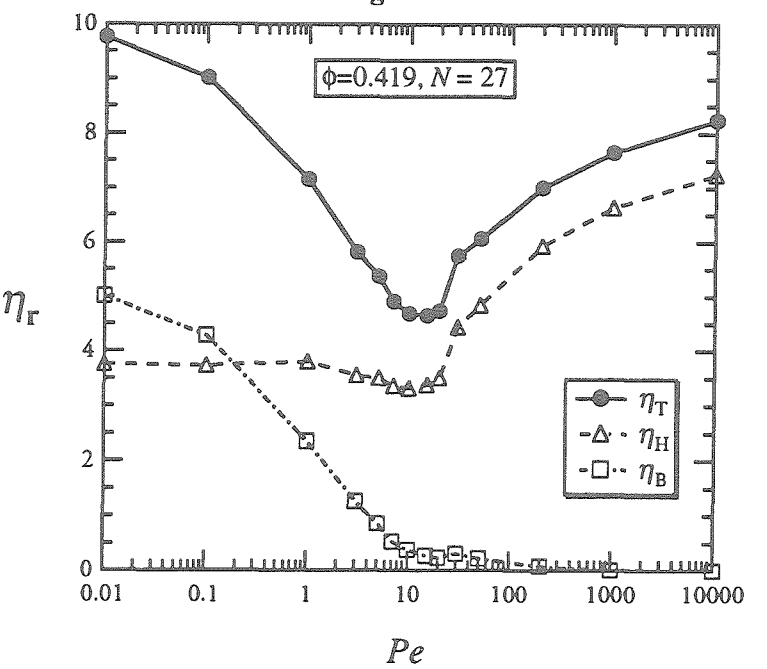

Figure 7.4

Figure 7.3-4: The steady shear viscosities: total (●) viscosity η_T, hydrodynamic (Δ) viscosity η_H and Brownian (□) viscosity η_B, obtained by Stokesian dynamics as a function of the Péclet number for hard spheres at particle volume fraction ϕ=0.4 (Fig.7.3) and 0.419 (Fig.7.4).

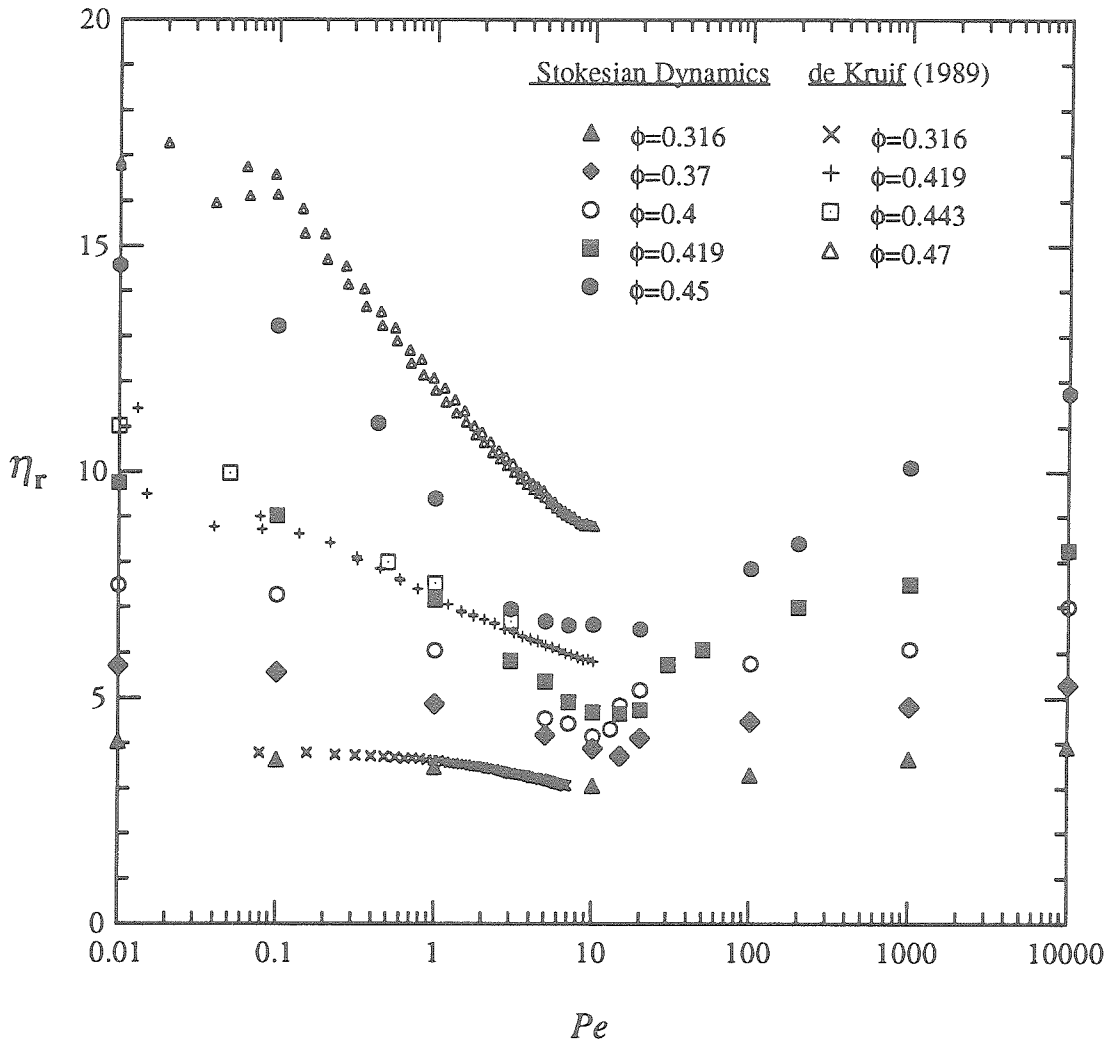

Figure 7.5: Comparison of the simulation results for the steady shear viscosity as a function of the Péclet number for hard-sphere suspensions at volume fractions: ϕ = (▲) 0.316, (◆) 0.37, (○) 0.4, (■) 0.419, and (●) 0.45 with the experiments from van der Werff and der Kruif (1989) for silica hard spheres with ϕ = 0.316 (×), 0.419 (+), 0.443 (□), and (△) 0.47.

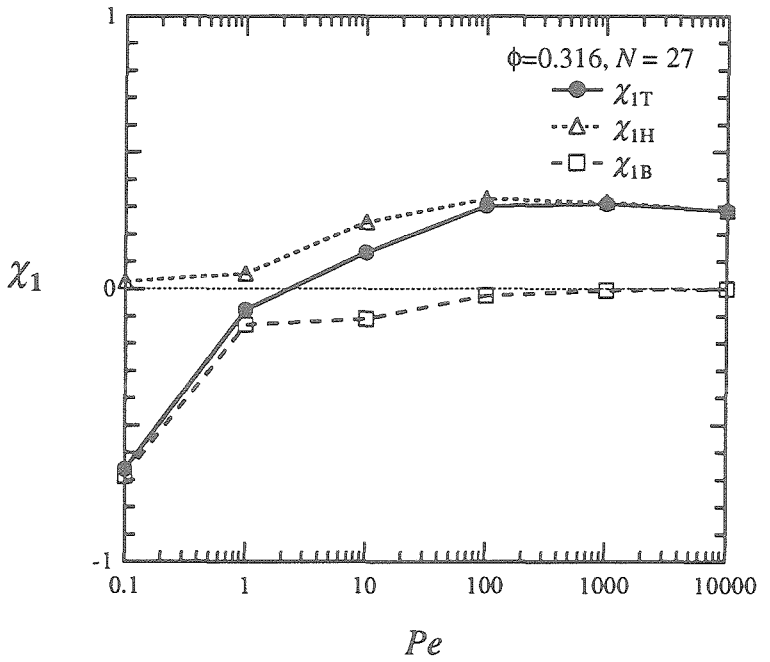

Figure 7.6.a

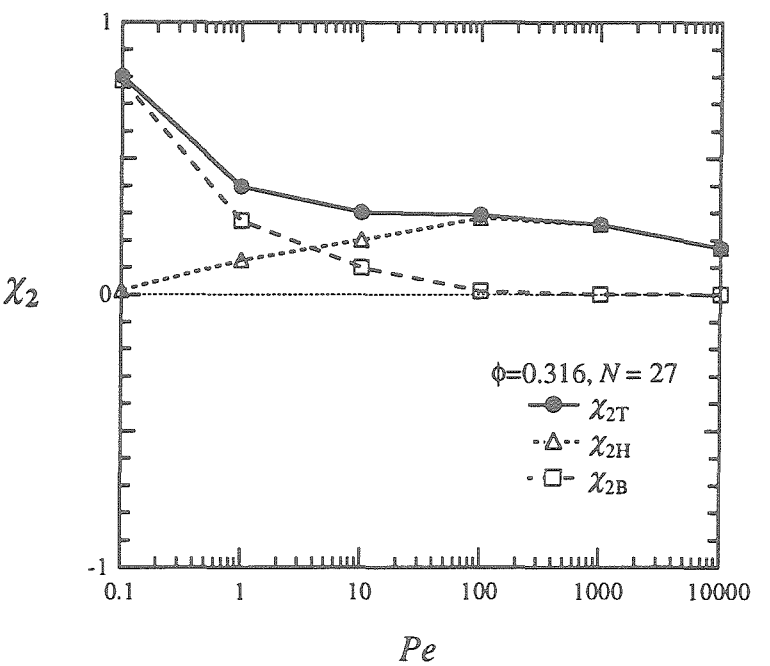

Figure 7.6.b

Figure 7.6.a-b: The first (Fig.7.6.a) and second (Fig.7.6.b) normal stress differences for hard spheres at a volume fraction ϕ=0.316 obtained by Stokesian dynamics as a function of the Péclet number. The plot symbols are: the total (●), hydrodynamic (Δ) and Brownian (□) normal stress differences.

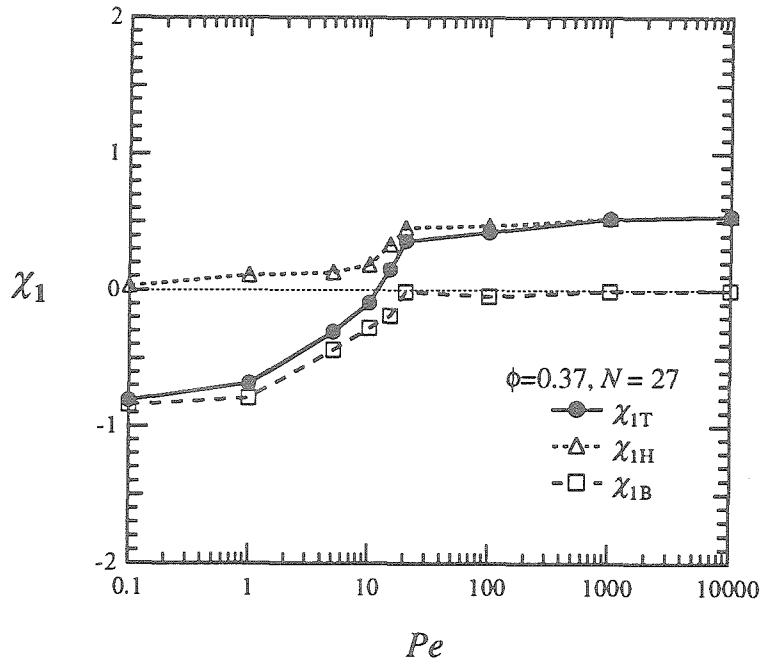

Figure 7.7.a

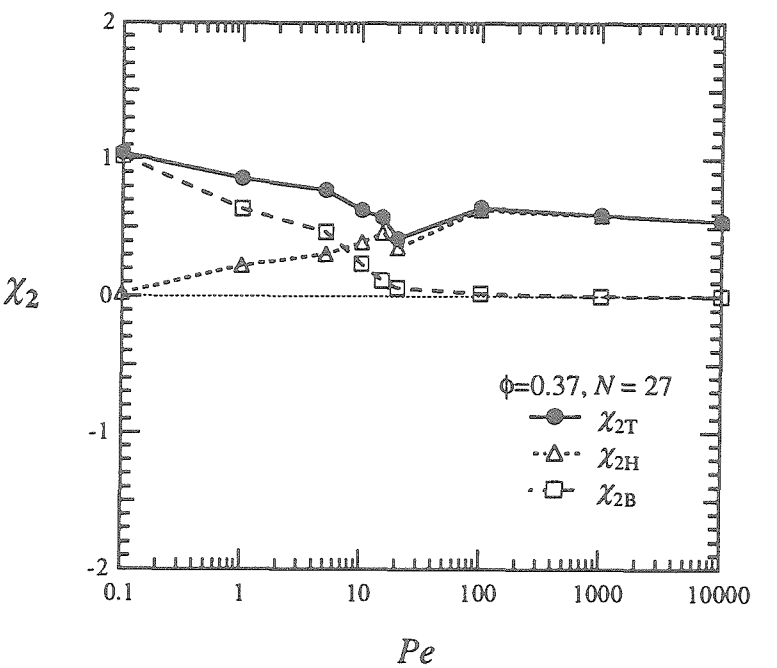

Figure 7.7.b

Figure 7.7.a-b: The first (Fig.7.7.a) and second (Fig.7.7.b) normal stress differences for hard spheres at a volume fraction ϕ=0.37 obtained by Stokesian dynamics as a function of the Péclet number. The plot symbols are: the total (●), hydrodynamic (Δ) and Brownian (□) normal stress differences.

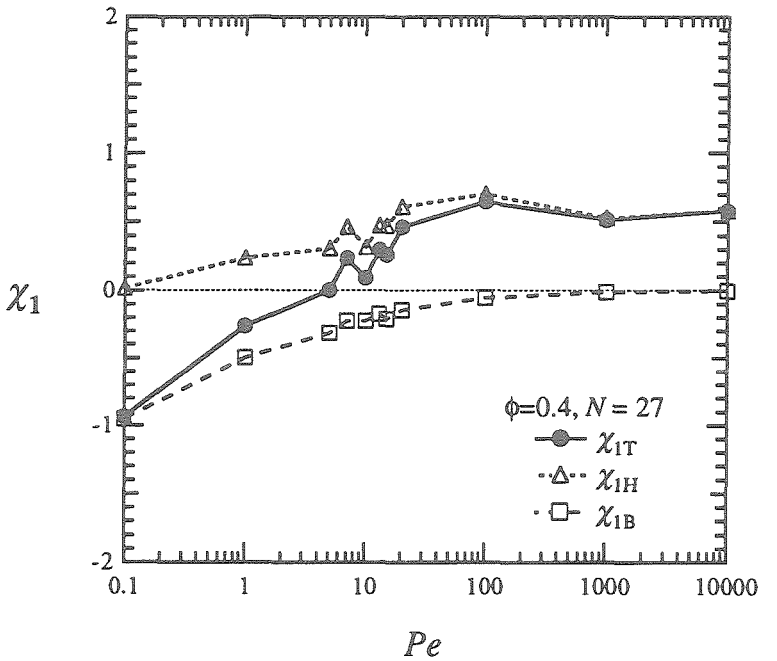

Figure 7.8.a

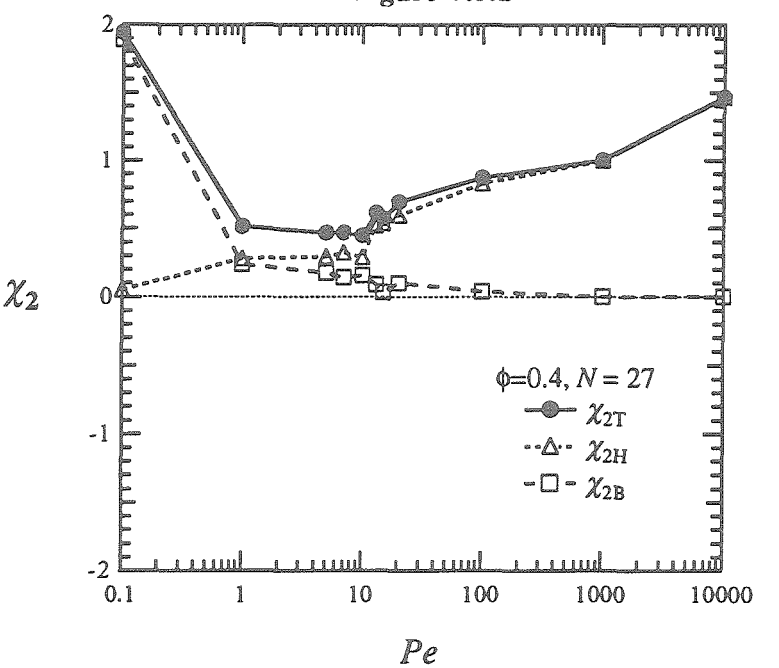

Figure 7.8.b

Figure 7.8.a-b: The first (Fig.7.8.a) and second (Fig.7.8.b) normal stress differences for hard spheres at a volume fraction ϕ=0.4 obtained by Stokesian dynamics as a function of the Peclet number. The plot symbols are: the total (●), hydrodynamic (Δ) and Brownian (□) normal stress differences.

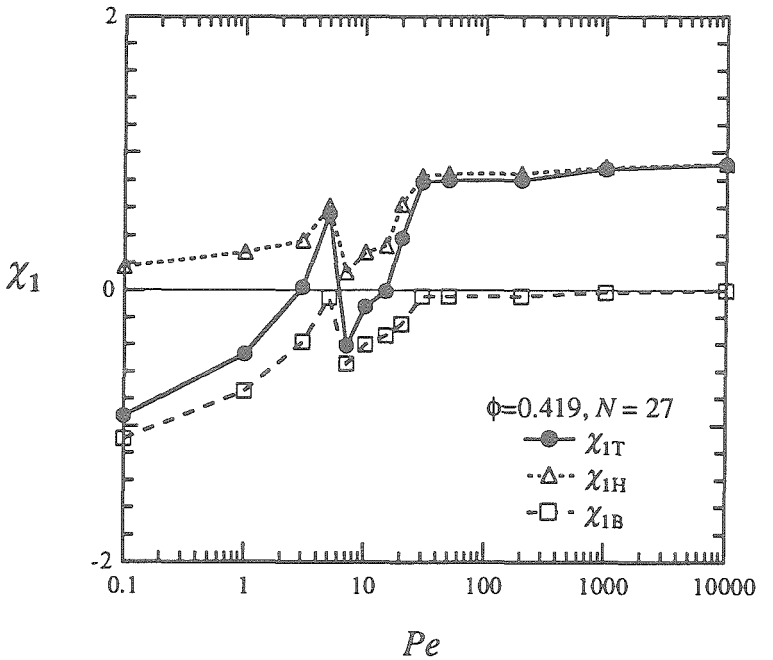

Figure 7.9.a

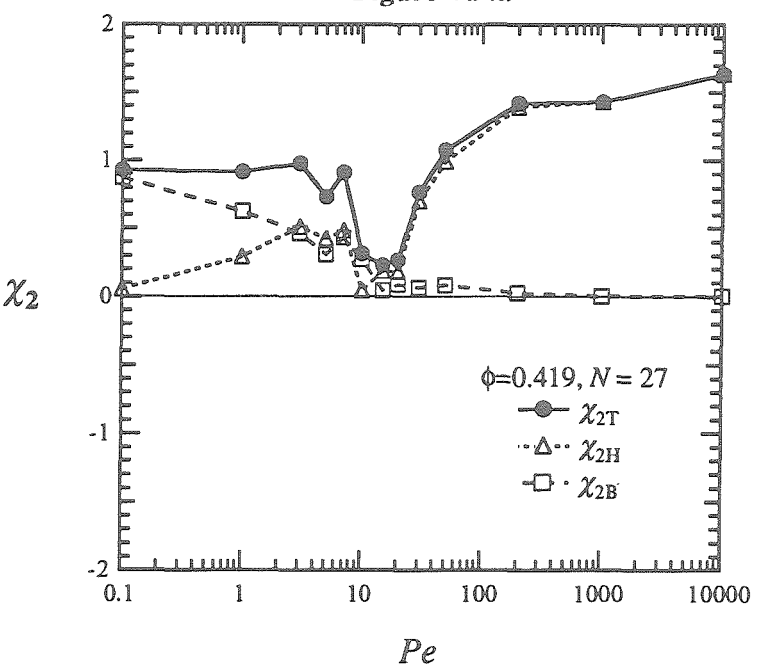

Figure 7.9.b

Figure 7.9.a-b: The first (Fig.7.9.a) and second (Fig.7.9.b) normal stress differences for hard spheres at a volume fraction ϕ=0.419 obtained by Stokesian dynamics as a function of the Péclet number. The plot symbols are: the total (●), hydrodynamic (Δ) and Brownian (□) normal stress differences.

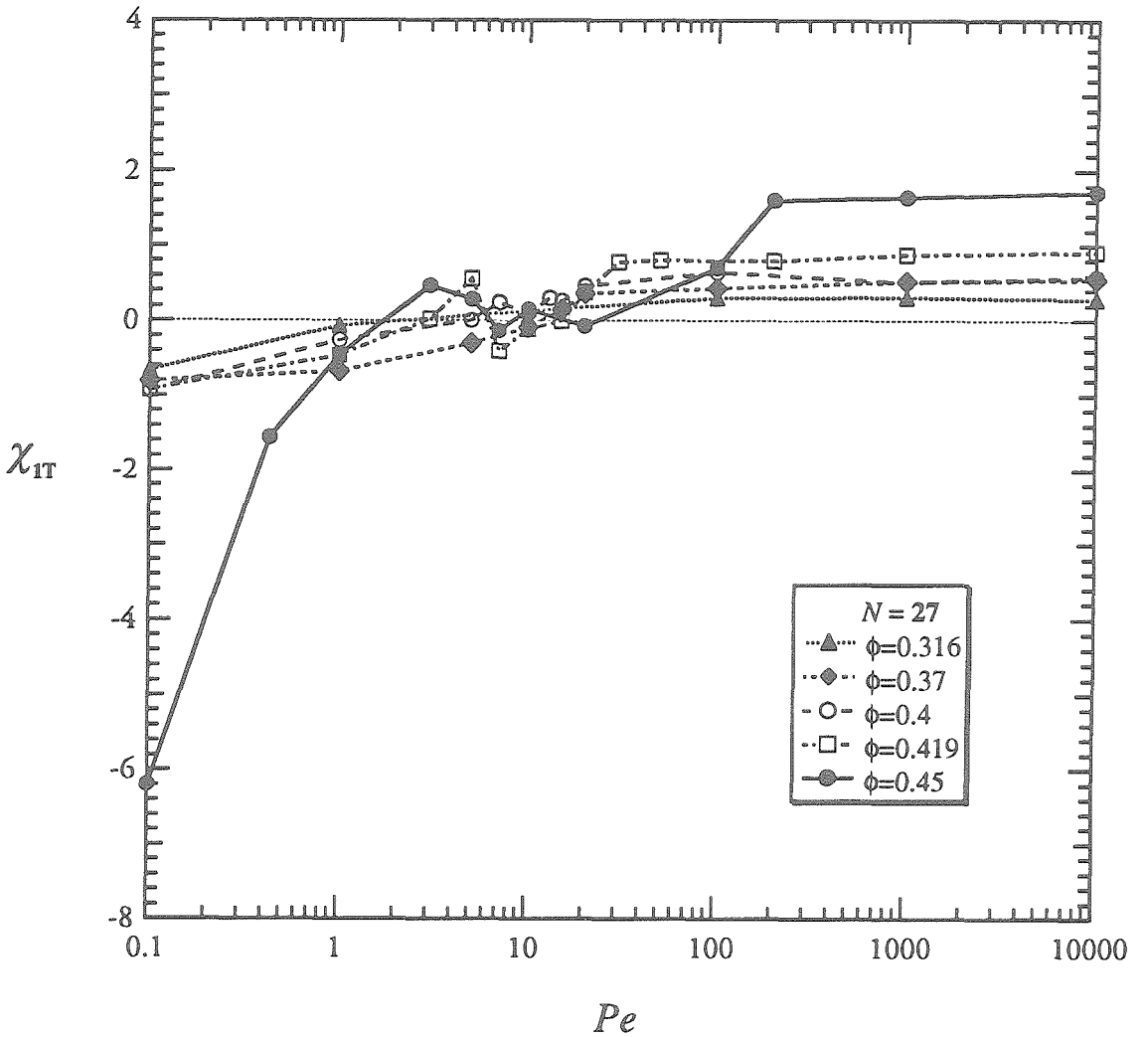

Figure 7.10.a: A comparison of the first normal stress difference χ_{1T} for hard spheres obtained by Stokesian dynamics at different volume fractions: ϕ = (▲) 0.316, (◆) 0.37, (○) 0.4, (□) 0.419 and (●) 0.45.

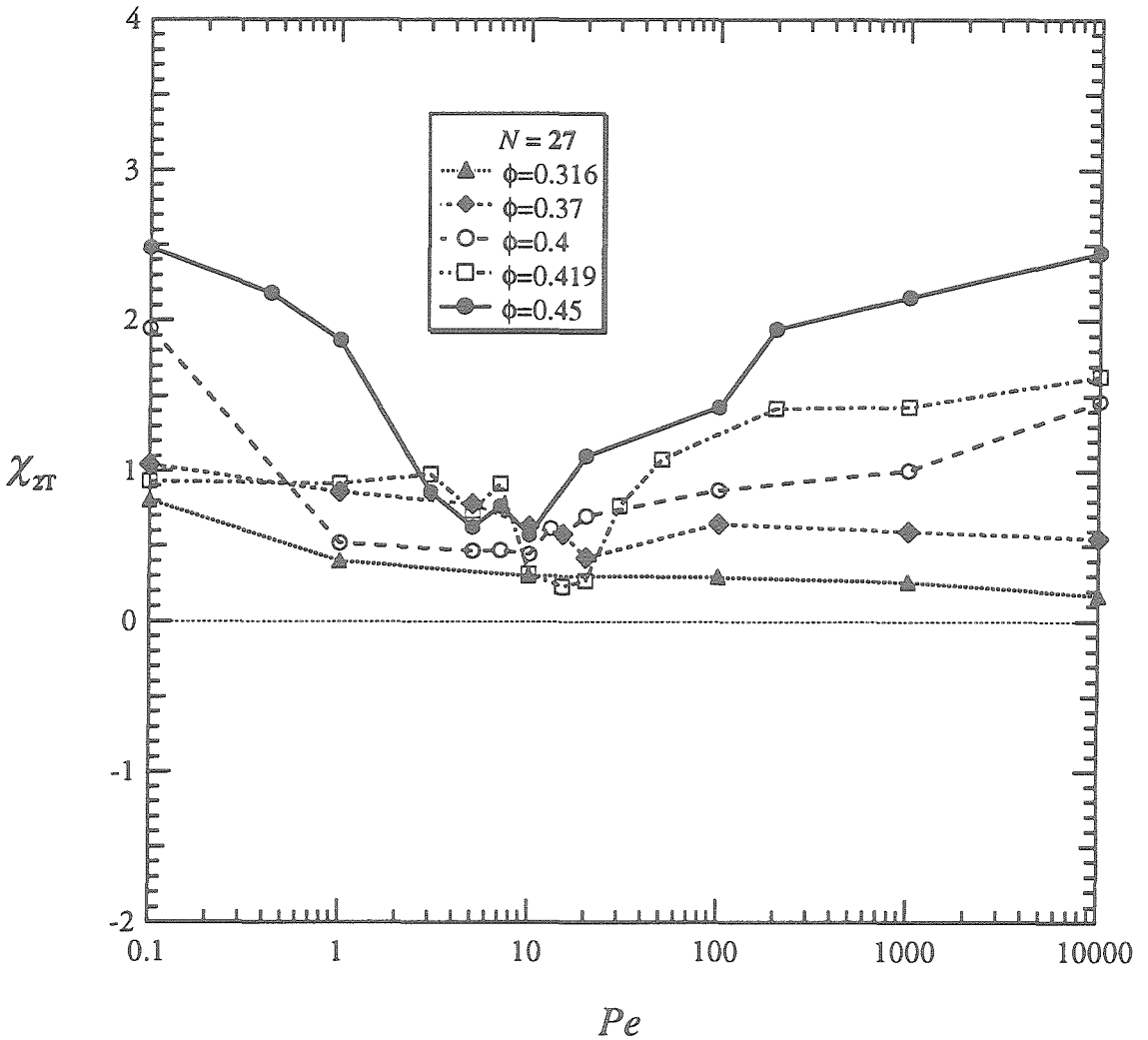

Figure 7.10.b: A comparison of the second normal stress difference χ_{2T} for hard spheres obtained by Stokesian dynamics at different volume fractions: ϕ = (▲) 0.316, (◆) 0.37, (○) 0.4, (□) 0.419 and (●) 0.45.

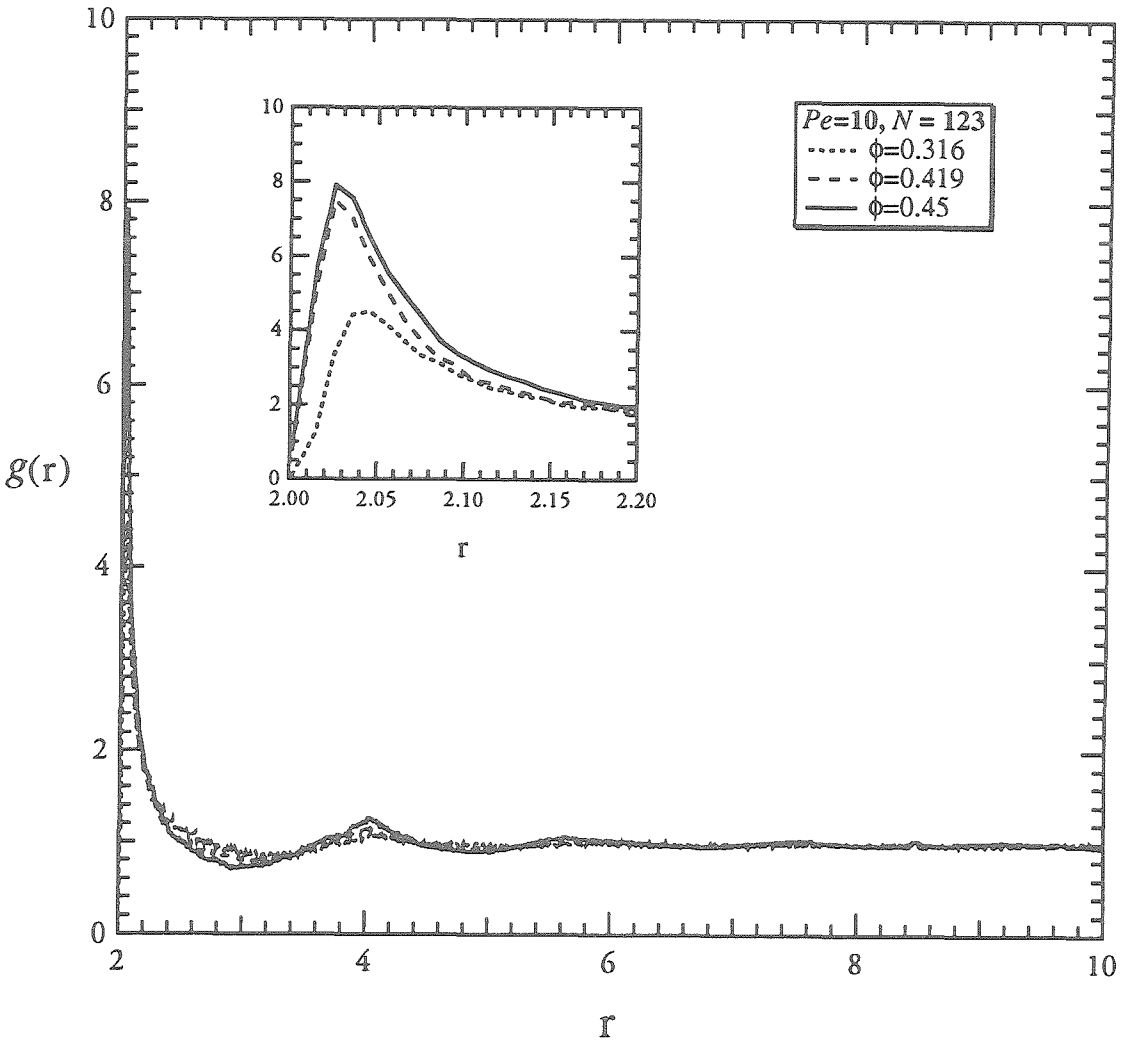

Figure 7.11: The radial dependence of the pair-distribution function $g(r)$ determined by Stokesian dynamics for hard spheres with Pe=10 and different volume fractions: ϕ = (dotted curve) 0.316, (dashed curve) 0.419 and (solid curve) 0.45. The insert figure in the upper left corner is a plot of $g(r)$ with small range of the particle center-center spacing r. The figure shows $g(r)$ increases with increasing volume fraction at near contact (r≈2.03). The pair-distribution function evaluated at r=2 for touching particles, $g(2)$, are small for hard spheres at Pe=10.

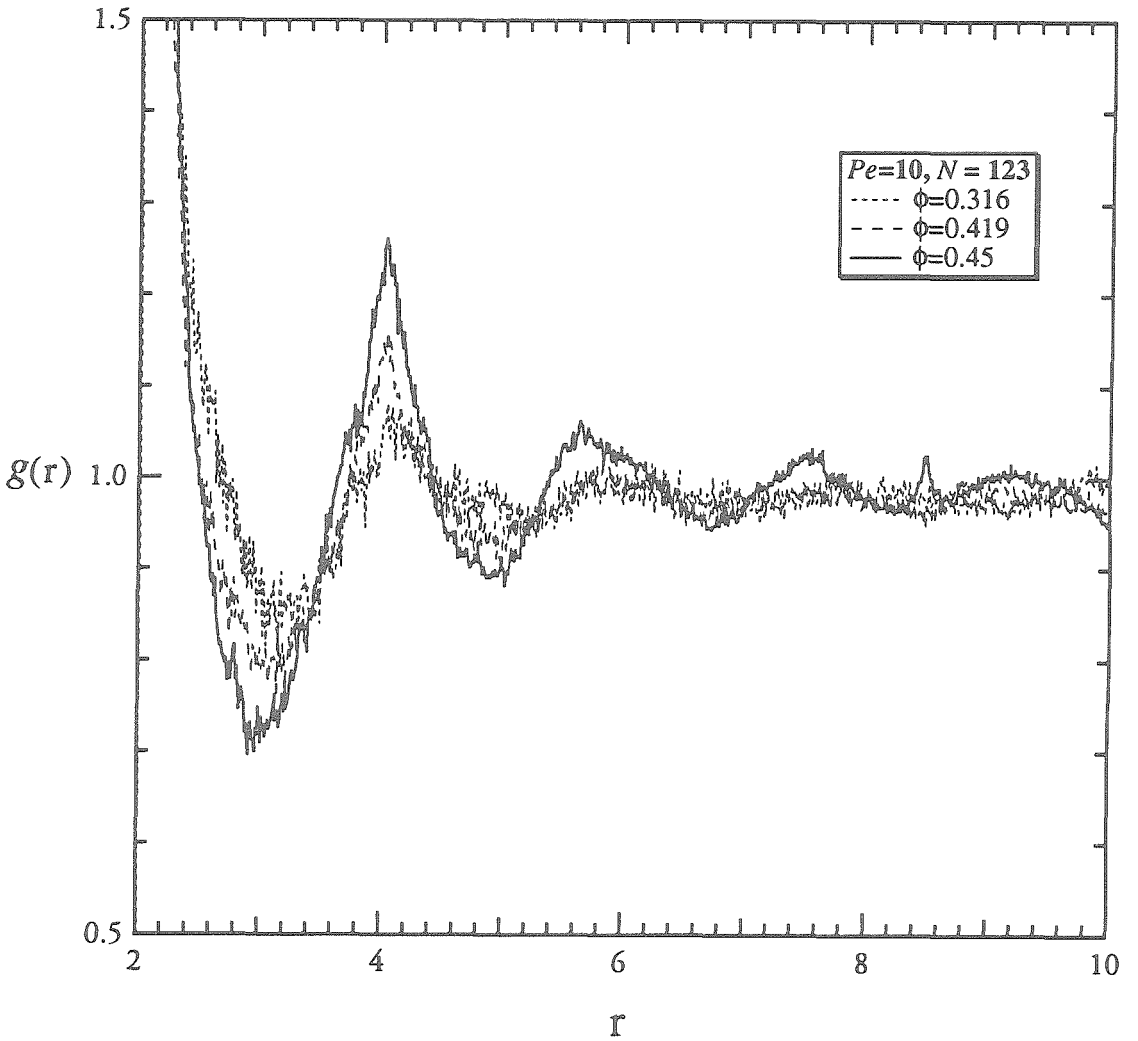

Figure 7.12: A plot of the radial pair-distribution function $g(r)$ versus the particle center-center spacing r for hard spheres with Pe=10 and different volume fractions: ϕ = (dotted curve.) 0.316, (dashed curve) 0.419, and (solid curve) 0.45. There are 123 particles in the unit cell.

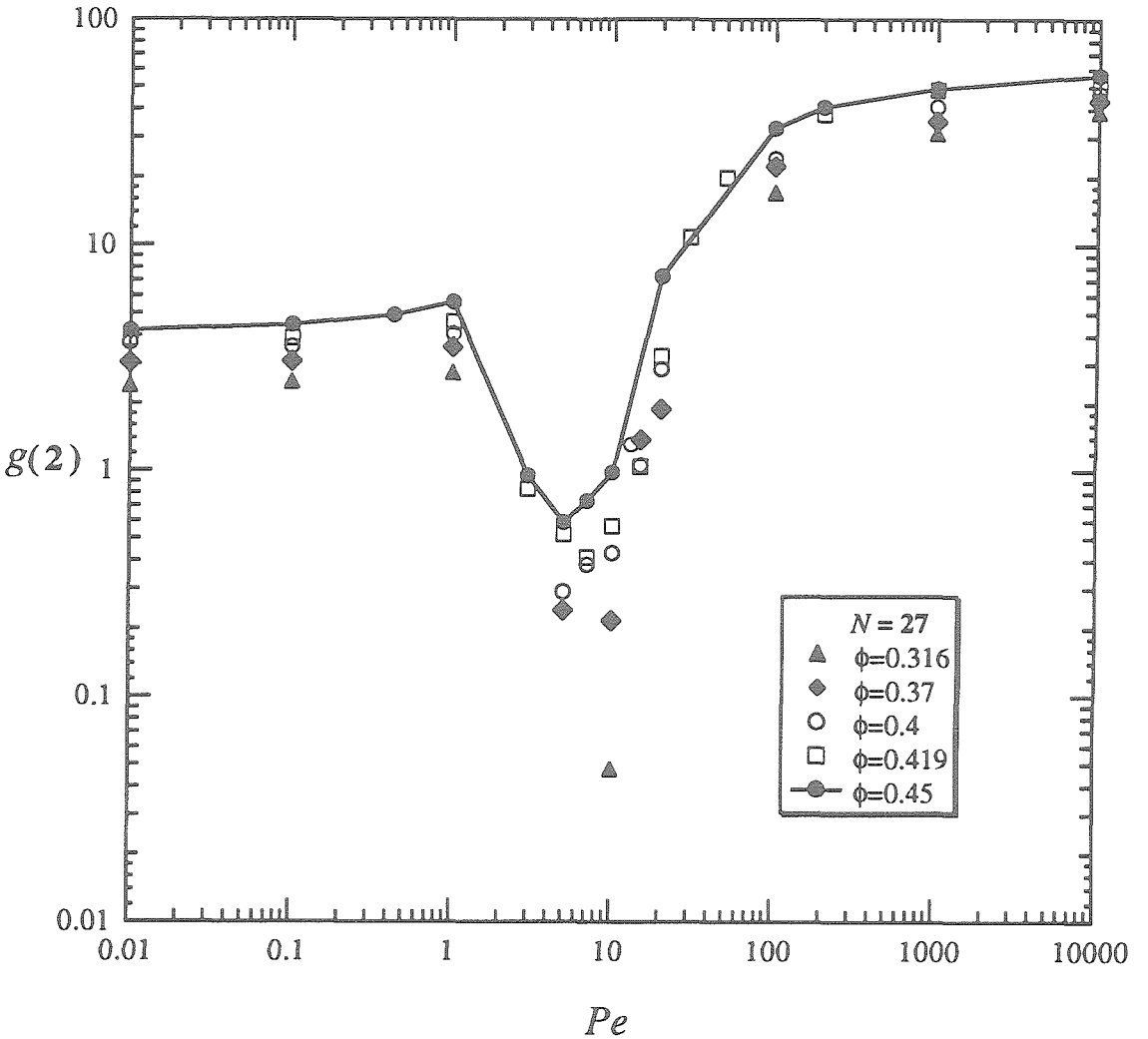

Figure 7.13: The radial pair-distribution function $g(r)$ evaluated at particle center-center spacing r=2 (when particles are in contact), $g(2)$, obtained by Stokesian dynamics for hard spheres as a function of the Péclet number at different volume fractions: ϕ = (▲) 0.316, (◆) 0.37, (○) 0.4, (□) 0.419 and (●) 0.45. $g(2)$ increases with increasing volume fraction for hard spheres at the same Peclet number. For suspensions with a small deformation (Pe<1), $g(2)$ changes inappreciably. As the Péclet number increases, $g(2)$ first decreases to a minimum value at Pe≈10, increases quickly with large Pe and approaches an asymptotic value at Pe≈10000.

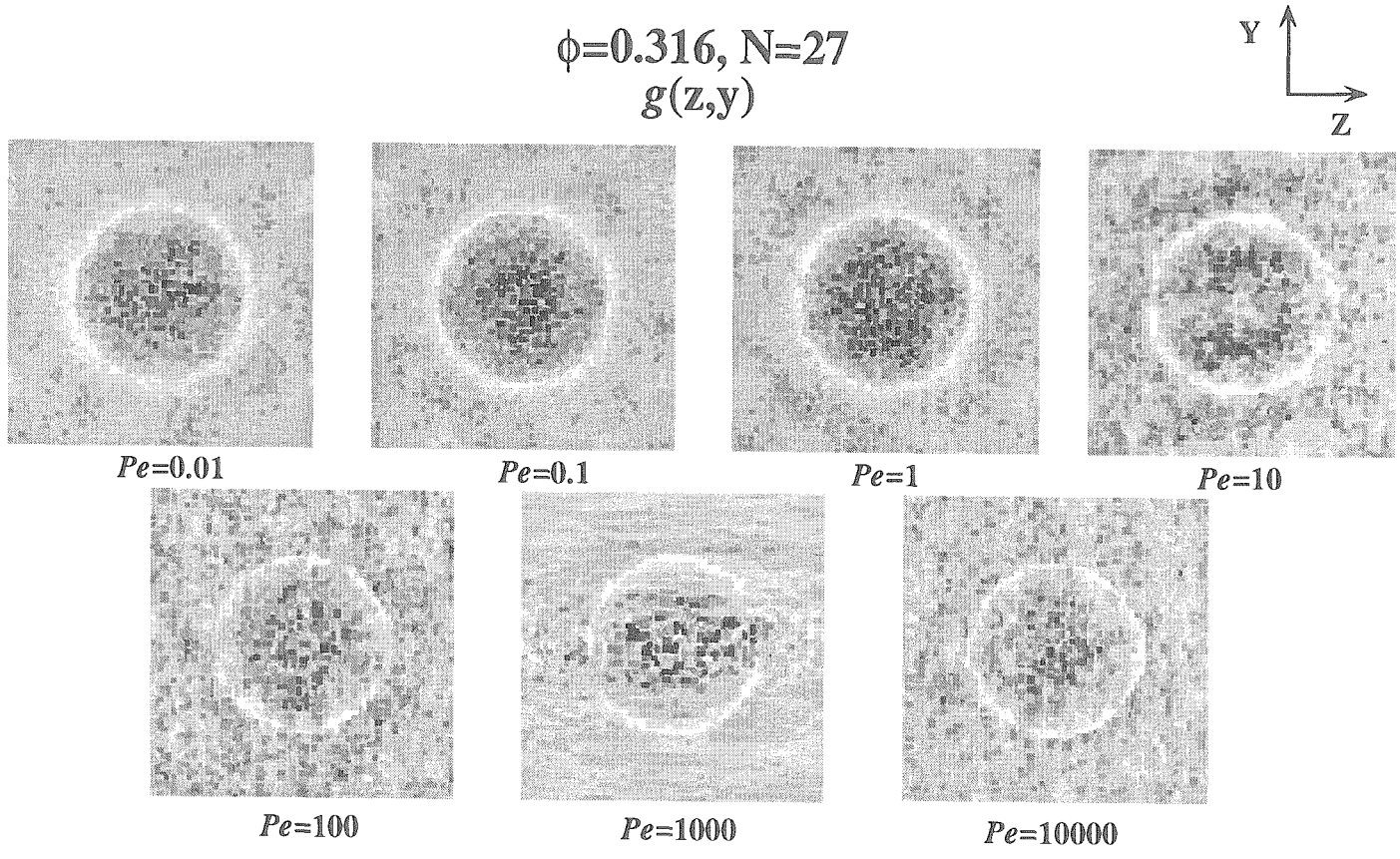

Figure 7.14: The probability density $g(z,y)$ for a hard-sphere suspension at volume fraction ϕ=0.316 with 27 particles obtained by Stokesian dynamics for different Péclet numbers. Regions of light color represent high probability and regions of dark color represent low probability. The flow direction is perpendicular to the z-y plane. The horizontal z-axis is the vorticity direction and the vertical y-axis is the velocity gradient direction. $g(z,y)$ does not show an ordered structure for Pe in the range of 0.01 to 10000.

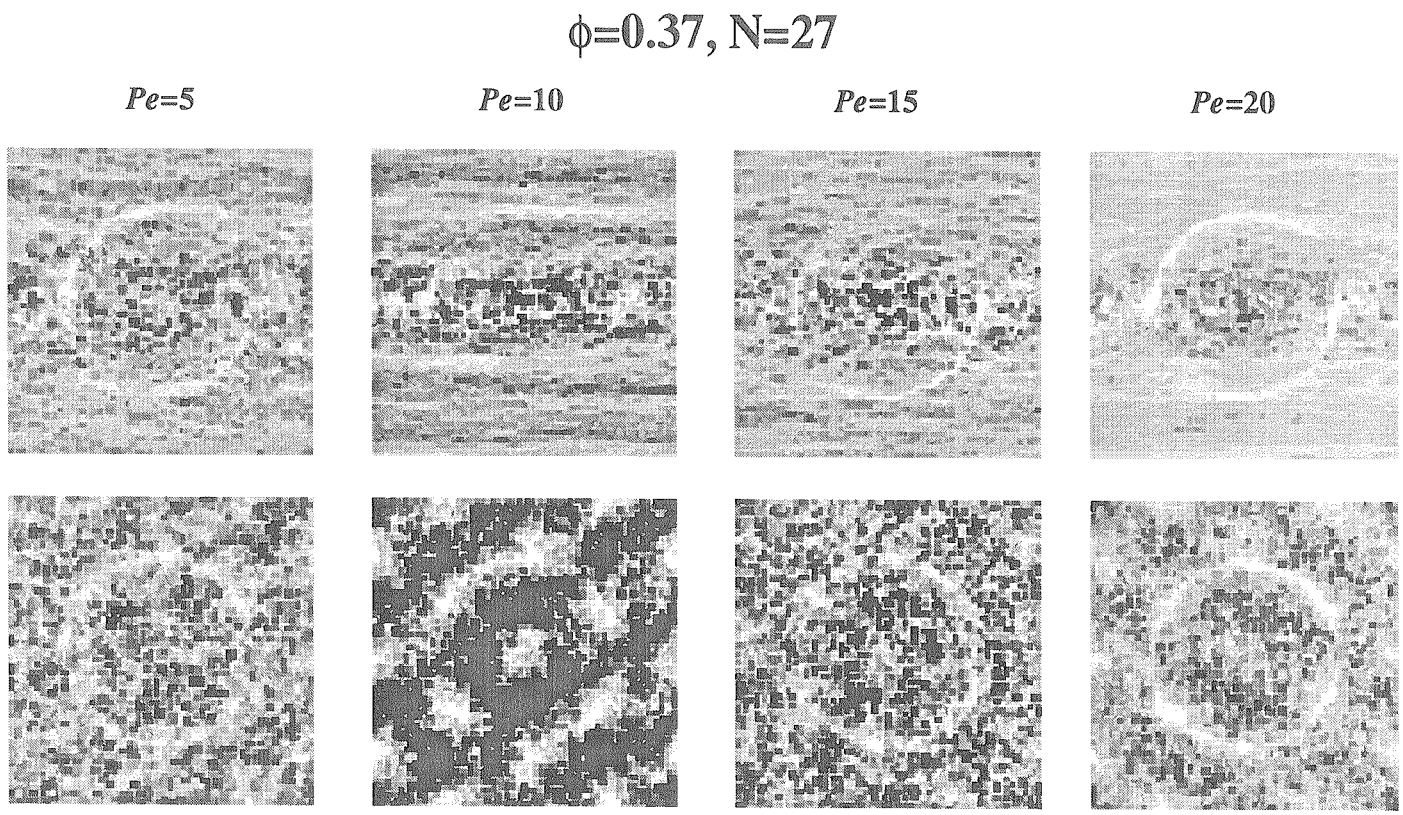

Figure 7.15: The probability density function $g(z,y)$ (top row) and $g(x,y)$ (bottom row) for hard spheres at a volume fraction ϕ=0.37 with 27 particles obtained by Stokesian dynamics for four different Péclet numbers: 5 , 10, 15 and 20. Regions of light color represent high probability and regions of dark color represent low probability. The flow direction is perpendicular to z-y plane (top row) and along the horizontal x-axis (bottom row). The shear-induced microstructure is unclear and fluctuated in this small range of Péclet number.

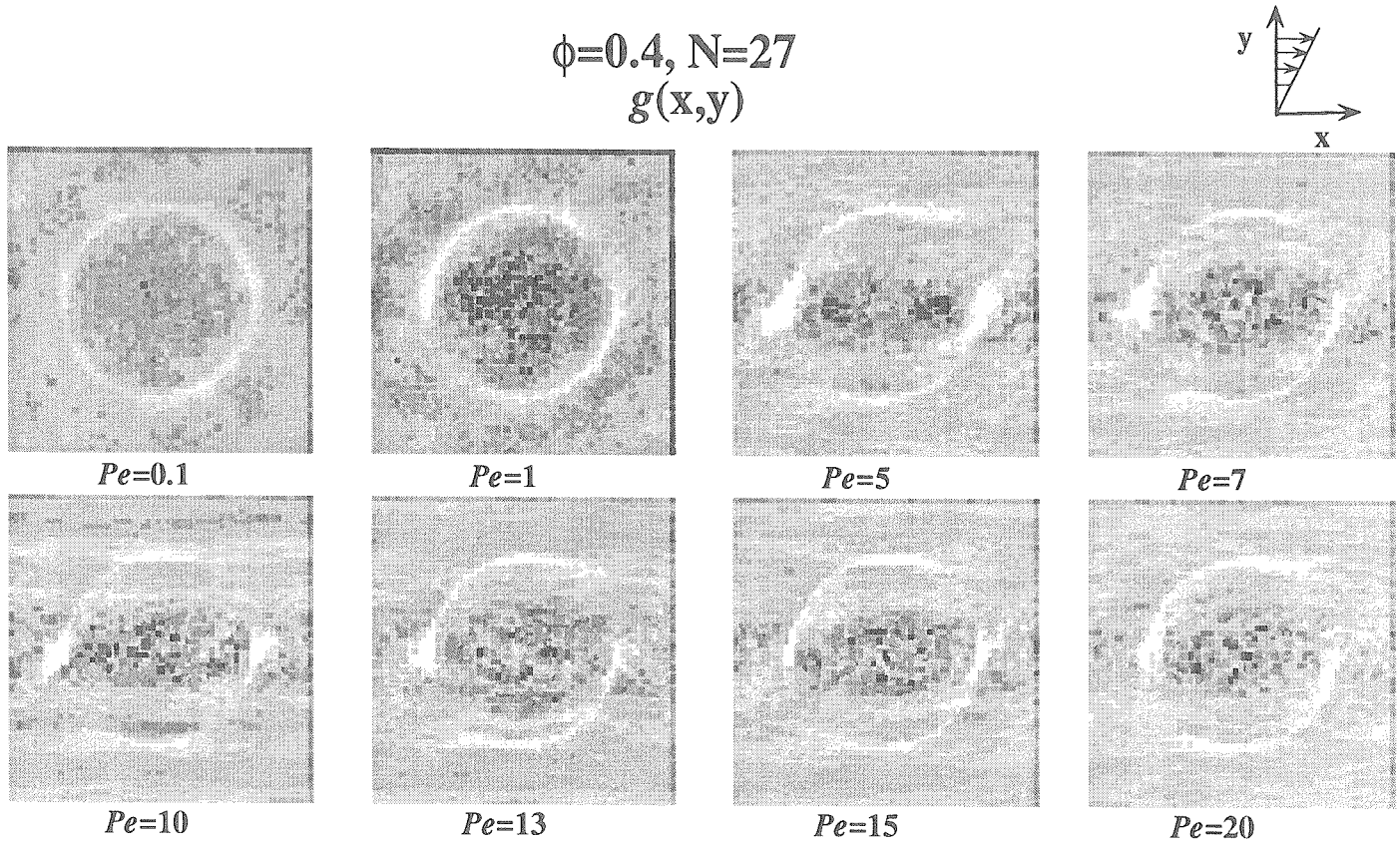

Figure 7.16: The probability density function $g(x,y)$ for hard spheres at volume fraction ϕ=0.4 with 27 particles obtained by Stokesian dynamics for different Péclet numbers. Regions of light color represent high probability and regions of dark color represent low probability. The flow direction is the horizontal x-axis and the velocity gradient direction is the vertical y-axis. $g(x,y)$ shows an onset of stringed particles along the flow direction for a very small range of Péclet number from 10 to 13. The string formation is unclear and fluctuated, compared to the string formation for ϕ=0.45 (cf. Fig.6.8.a). The weakly ordered structure is destroyed by moderate shear rates at Pe=20.

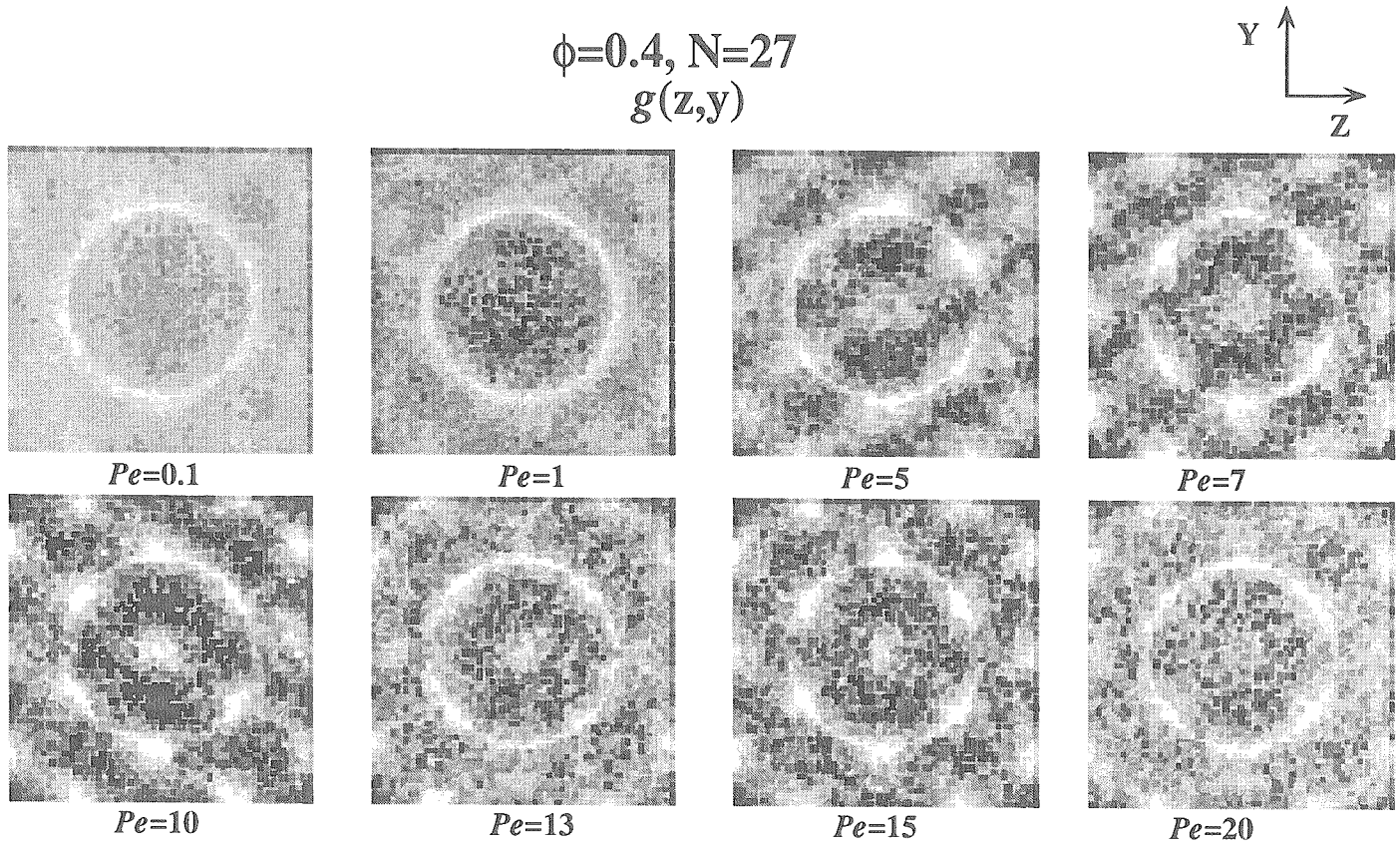

Figure 7.17: The probability density function $g(z,y)$ for hard spheres at volume fraction ϕ=0.4 with 27 particles obtained by Stokesian dynamics for different Péclet numbers. Regions of light color represent high probability and regions of dark color represent low probability. The flow direction is perpendicular to the z-y plane with the vorticity direction the z-axis and the velocity gradient direction the y-axis. $g(z,y)$ shows an "hexagonal" packing of flowing particles for a very small range of Péclet numbers from 5 to 15. The hexagonal formation is not well formed, unclear and fluctuated, compared to the hexagonal packing for ϕ=0.45 (cf. Fig.6.8.b). The weakly ordered structure is destroyed by Pe=20.

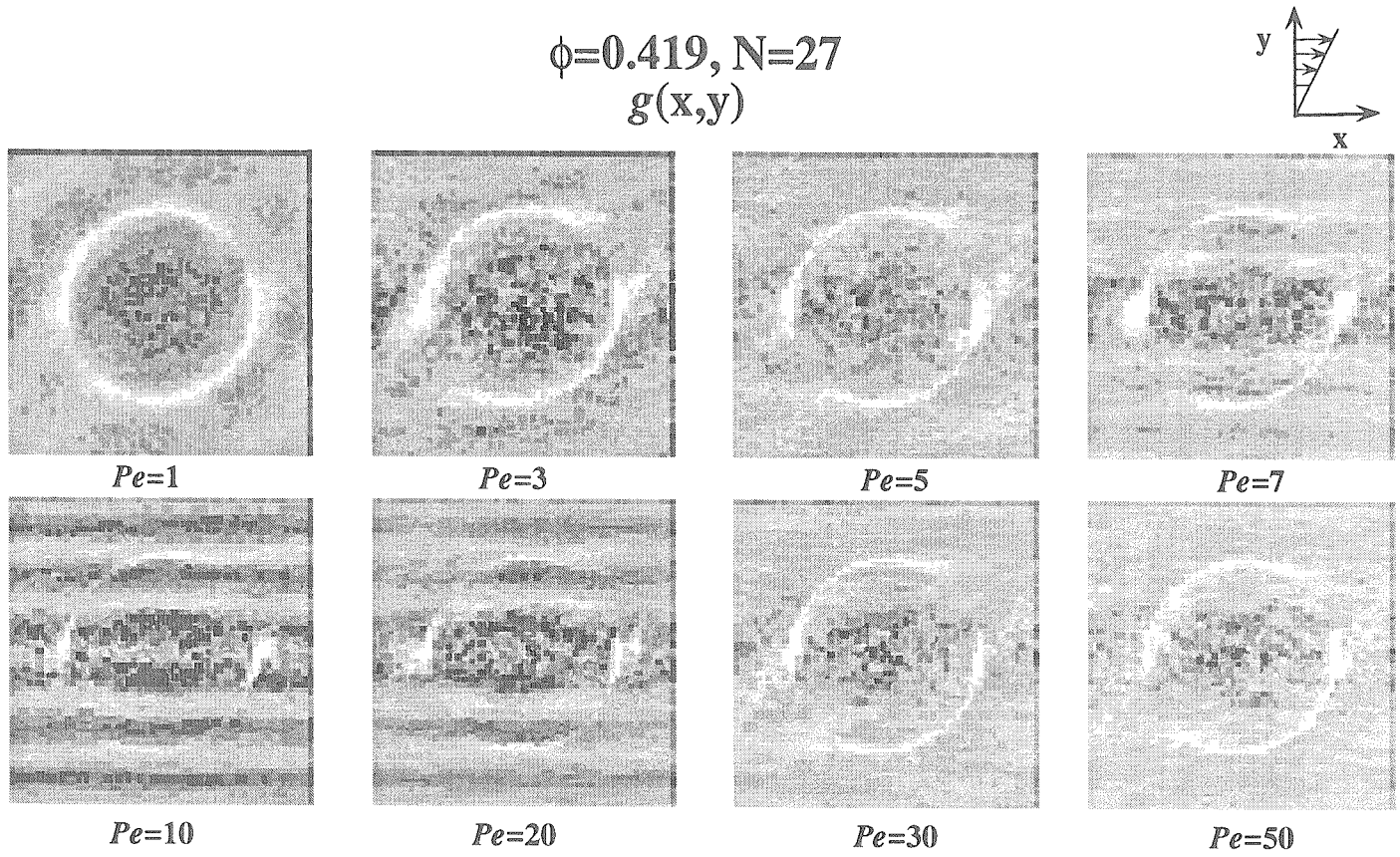

Figure 7.18: The probability density function $g(x,y)$ for hard spheres at a volume fraction ϕ=0.419 with 27 particles obtained by Stokesian dynamics for different Péclet numbers. Regions of light color represent high probability and regions of dark color represent low probability. The horizontal x-axis is the flow direction and the vertical y-axis is the velocity gradient direction. Strings of flowing particles along the flow direction can clearly be seen for *Pe*=10 and 20. The ordered microstructure is seen for a small range of *Pe* from 7 to 20. The string formation is destroyed by moderate shear rates at *Pe*=50.

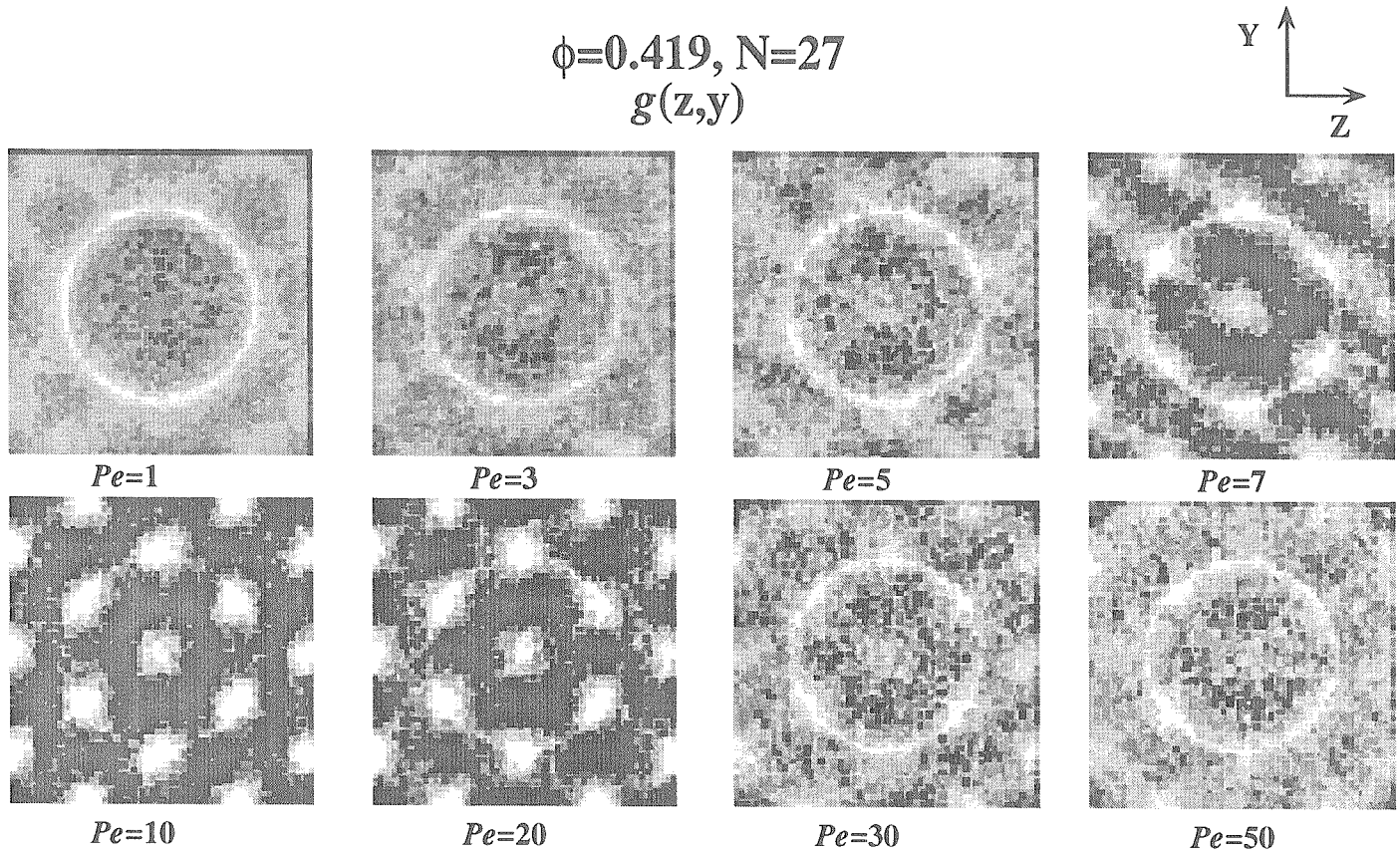

Figure 7.19: The probability density function $g(z,y)$ for hard spheres at a volume fraction ϕ=0.419 with 27 particles obtained by Stokesian dynamics for different Péclet numbers. Regions of light color represent high probability and regions of dark color represent low probability. The flow direction is perpendicular to the z-y plane. The horizontal z-axis is the vorticity direction and the vertical y-axis is the velocity gradient direction. $g(z,y)$ shows an "hexagonal" packing of strings of particles flowing along the flow direction at Pe=10 and 20. The ordered microstructure with hexagonal packing, which occurs in a small range of Pe from 7 to 20, is destroyed by Pe=50.

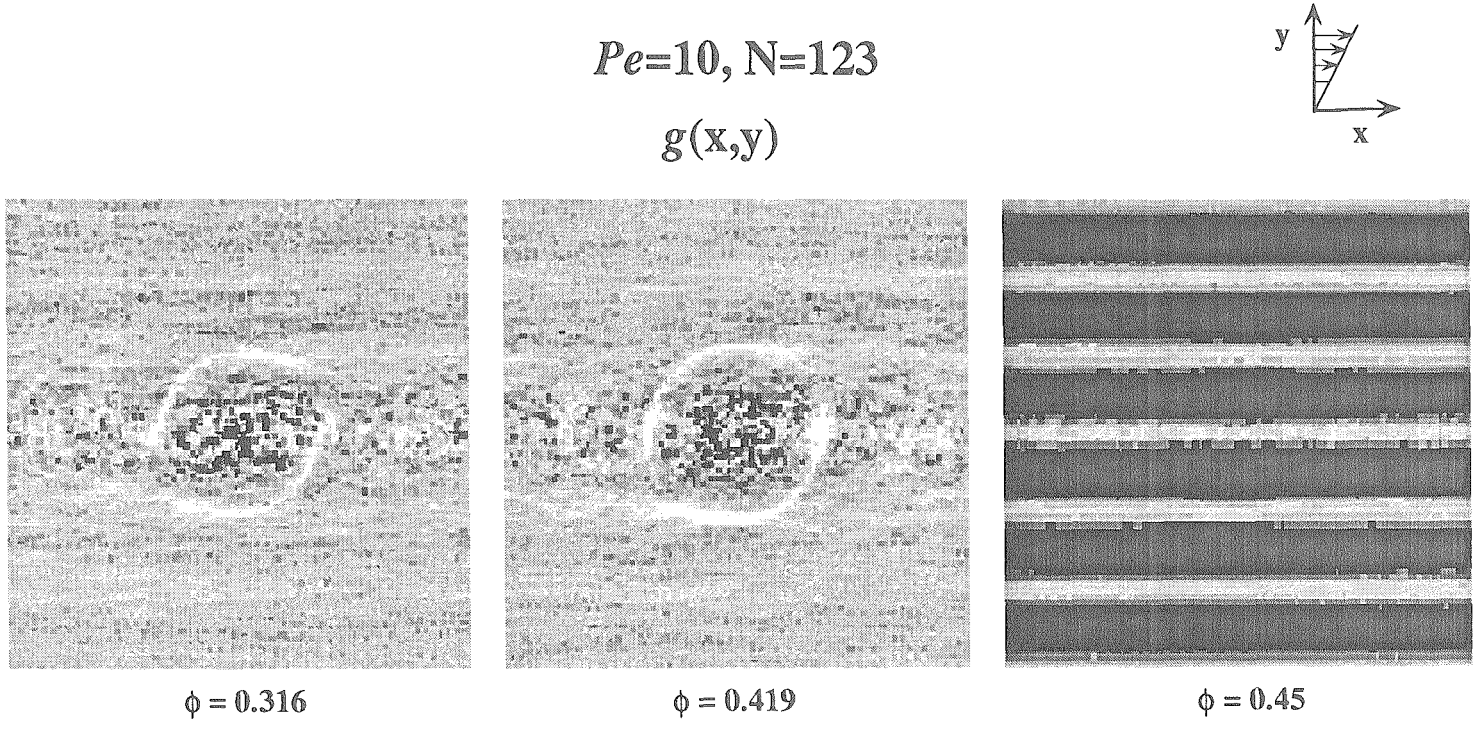

Figure 7.20: A comparison of the probability density $g(x,y)$ of hard spheres with Pe=10 obtained by Stokesian dynamics for three different volume fractions: ϕ=0.316 (left figure), 0.419 (central figure) and 0.45 (right figure). There are 123 particles in the unit cell. Regions of light color represent high probability and regions of dark color represent low probability. The flow direction is the horizontal x-axis and the velocity gradient direction is the vertical y-axis. $g(x,y)$ for suspensions at ϕ= 0.316 and 0.419 show a weak and fluctuated "string" formation of flowing particles compared to the sharp and clear "string" formation of hard spheres at ϕ=0.45 (right most figure).

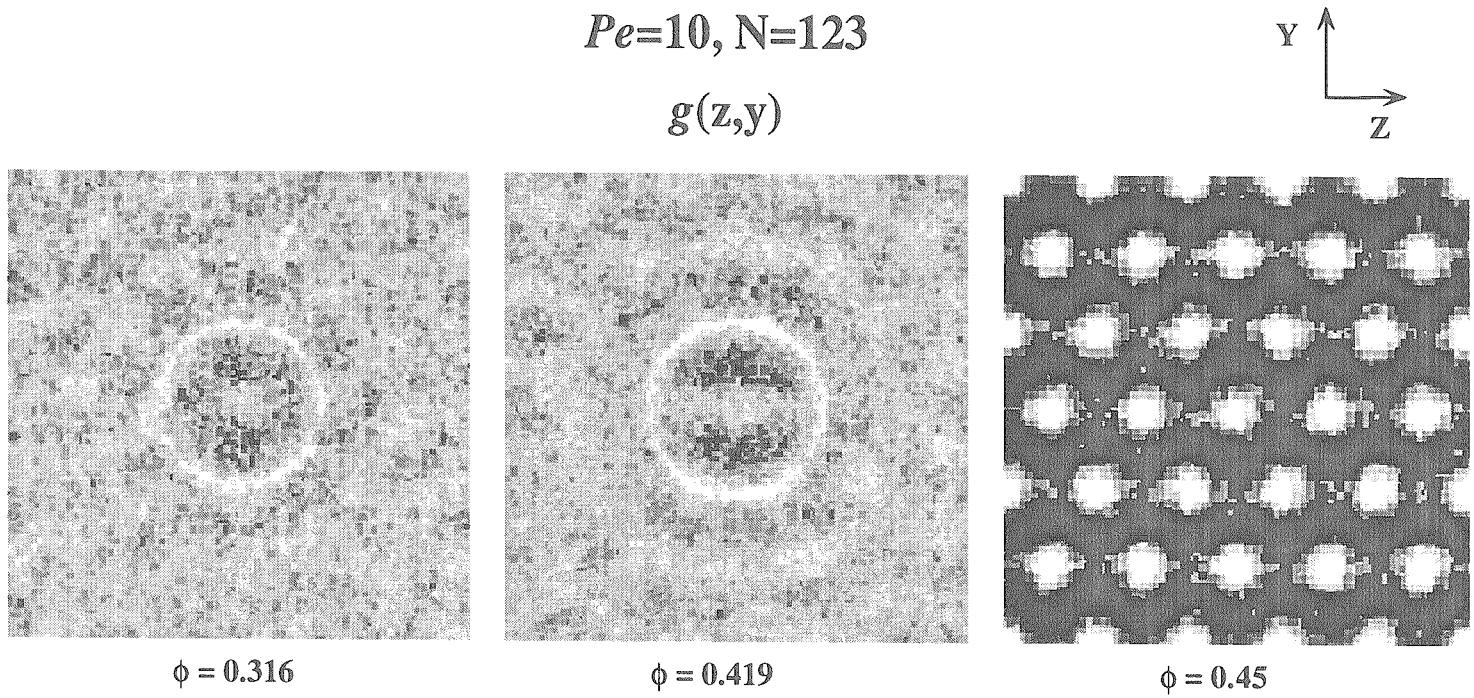

Figure 7.21: A comparison of the probability density $g(z,y)$ of hard spheres with Pe=10 obtained by Stokesian dynamics for three different volume fractions: ϕ=0.316 (left figure), 0.419 (central figure) and 0.45 (right figure). There are 123 particles in the unit cell. Regions of light color represent high probability and regions of dark color represent low probability. The flow direction is perpendicular to the z-y plane withthe horizontal z-axis the vorticity direction and the vertical y-axis the velocity gradient direction. $g(z,y)$ for suspensions at ϕ=0.316 and 0.419 show transitional signals of particle ordering with fluctuations near the regions of string order compared to the clear and distinct "hexagonal" packing of hard spheres at ϕ=0.45.

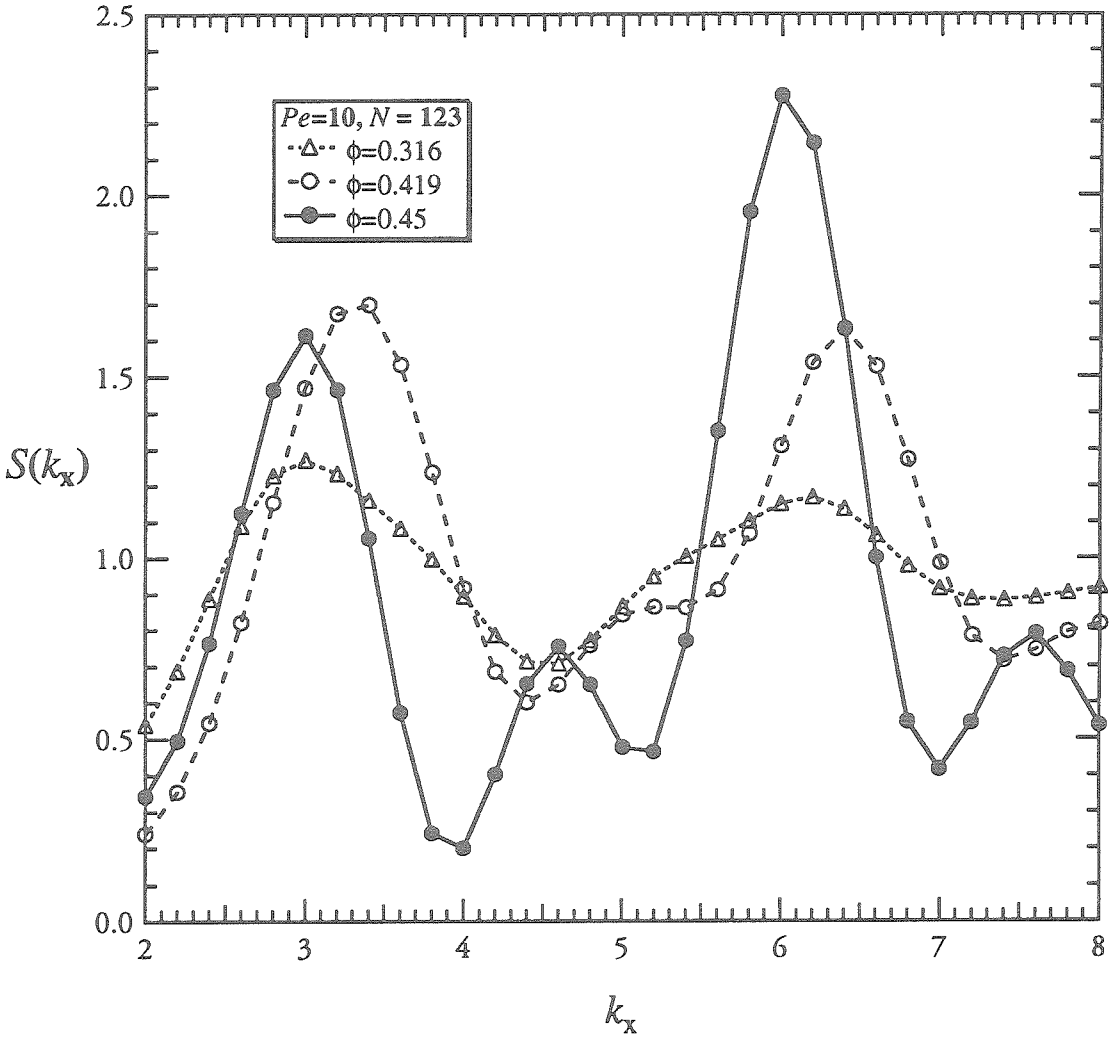

Figure 7.22: The line structure factor $S(k_x)$ determined by Stokesian dynamics for hard spheres with Pe=10 and volume fractions ϕ = (Δ) 0.316, (○) 0.419 and (●) 0.45. k_x is the dimensionless wave number in the flow direction, the x-axis. There are 123 particles in the unit cell. $S(k_x)$ shows small variation in scattered intensity due to constant and large change of particle positions in the flow direction.

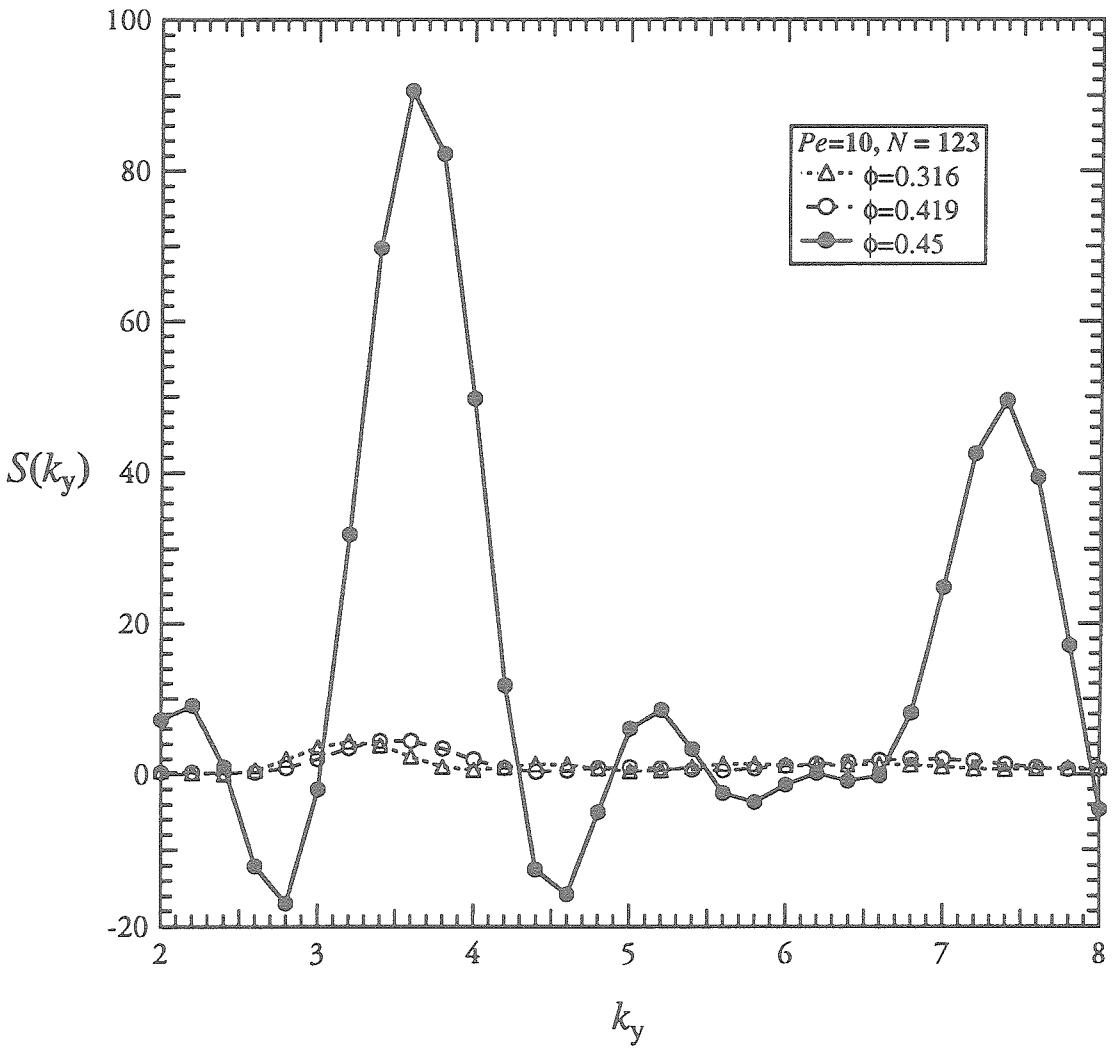

Figure 7.23: The line structure factor $S(k_y)$ determined by Stokesian dynamics for hard spheres with Pe=10 and volume fractions ϕ = (Δ) 0.316, (○) 0.419 and (●) 0.45. k_y is the dimensionless wave number in the direction of the velocity gradient, the y-axis. There are 123 particles in the unit cell. The line structure factor for hard spheres with ϕ=0.45 displays two scattered intensity peaks at the wave numbers $k_y \approx 3.6$ and ≈ 7.4. Suspensions at ϕ=0.316 and 0.419 show insignificant scattered intensity compared to that of a suspension at ϕ=0.45.

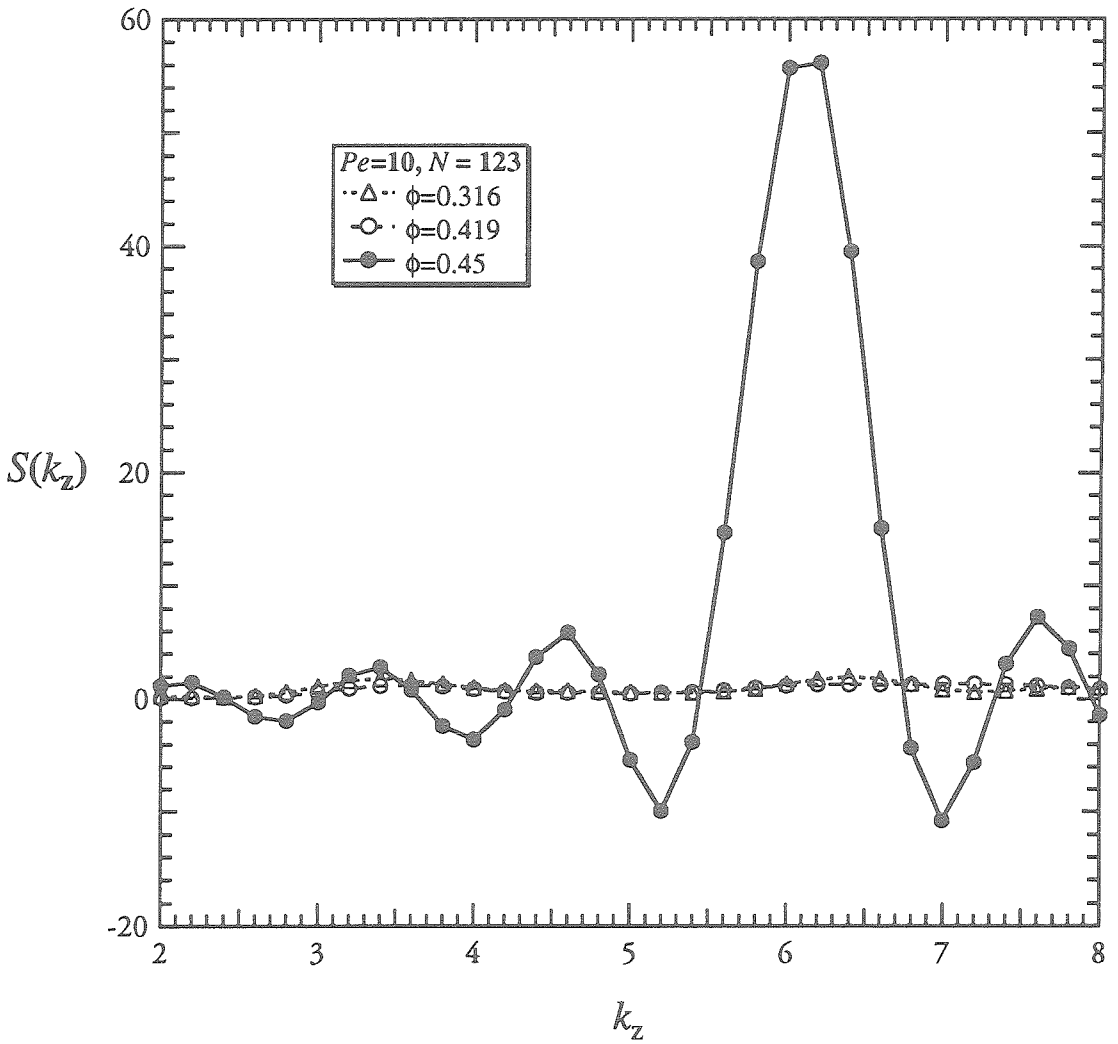

Figure 7.24: The line structure factor $S(k_z)$ determined by Stokesian dynamics for hard spheres with Pe=10 and volume fractions ϕ = (Δ) 0.316, (○) 0.419 and (●) 0.45. k_z is the dimensionless wave number in the direction of the vorticity, the z-axis. There are 123 particles in the unit cell. The line structure factor for hard spheres at ϕ=0.45 displays an intensity peak at the wave number $k_y \approx 6$. Suspensions at ϕ=0.316 and 0.419 show insignificant scattered intensity compared to that of a suspension at ϕ=0.45.

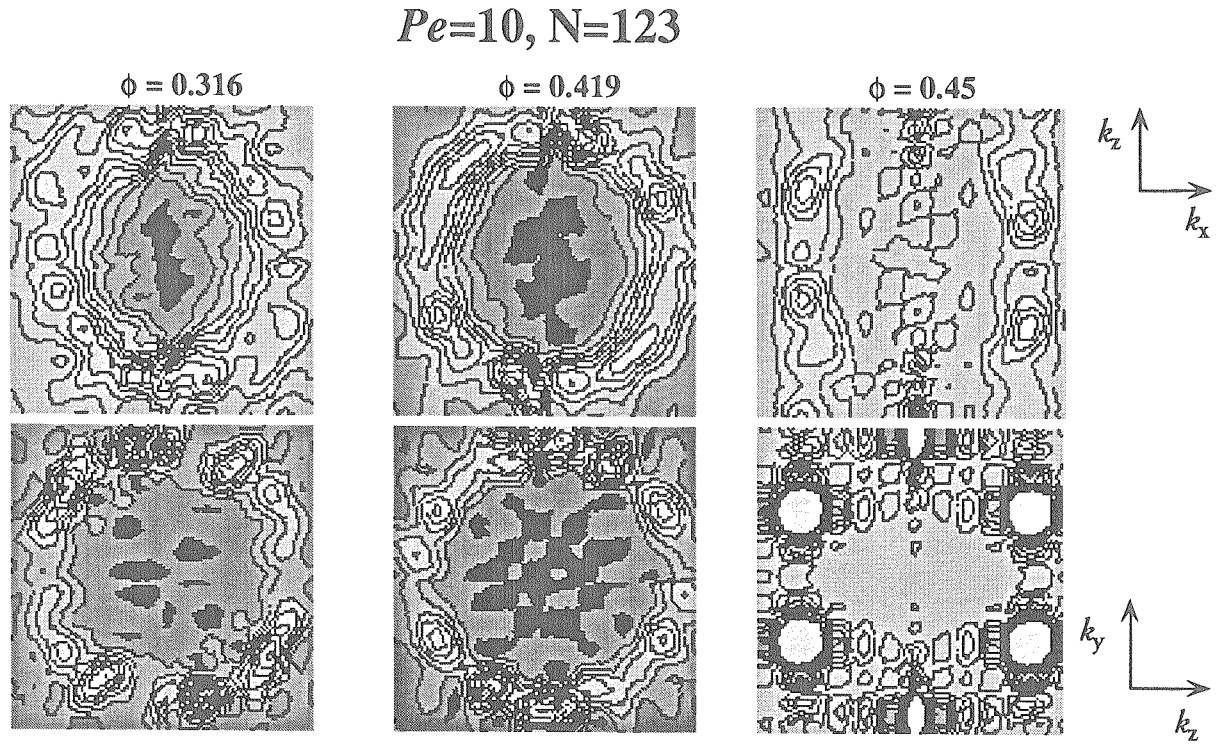

Figure 7.25: A comparison of the structure factors $S(k_x,k_z)$ (top row) and $S(k_z,k_y)$ (bottom row) for hard spheres at Pe=10 and three different volume fractions: ϕ=0.316 (left column), 0.419 (central column) and 0.45 (right column). Regions of light color represent high scattering light intensity and regions of dark color represent low scattering light intensity. The range of the dimesionless wave numbers k_x, k_y and k_z is from +/-0.5 to +/-4.0. The high scattered intensity patterns with two vertical bands in the k_x-k_z plane and halo ring with six intensity maxima in the k_z-k_y plane can only be seen for ϕ=0.45.

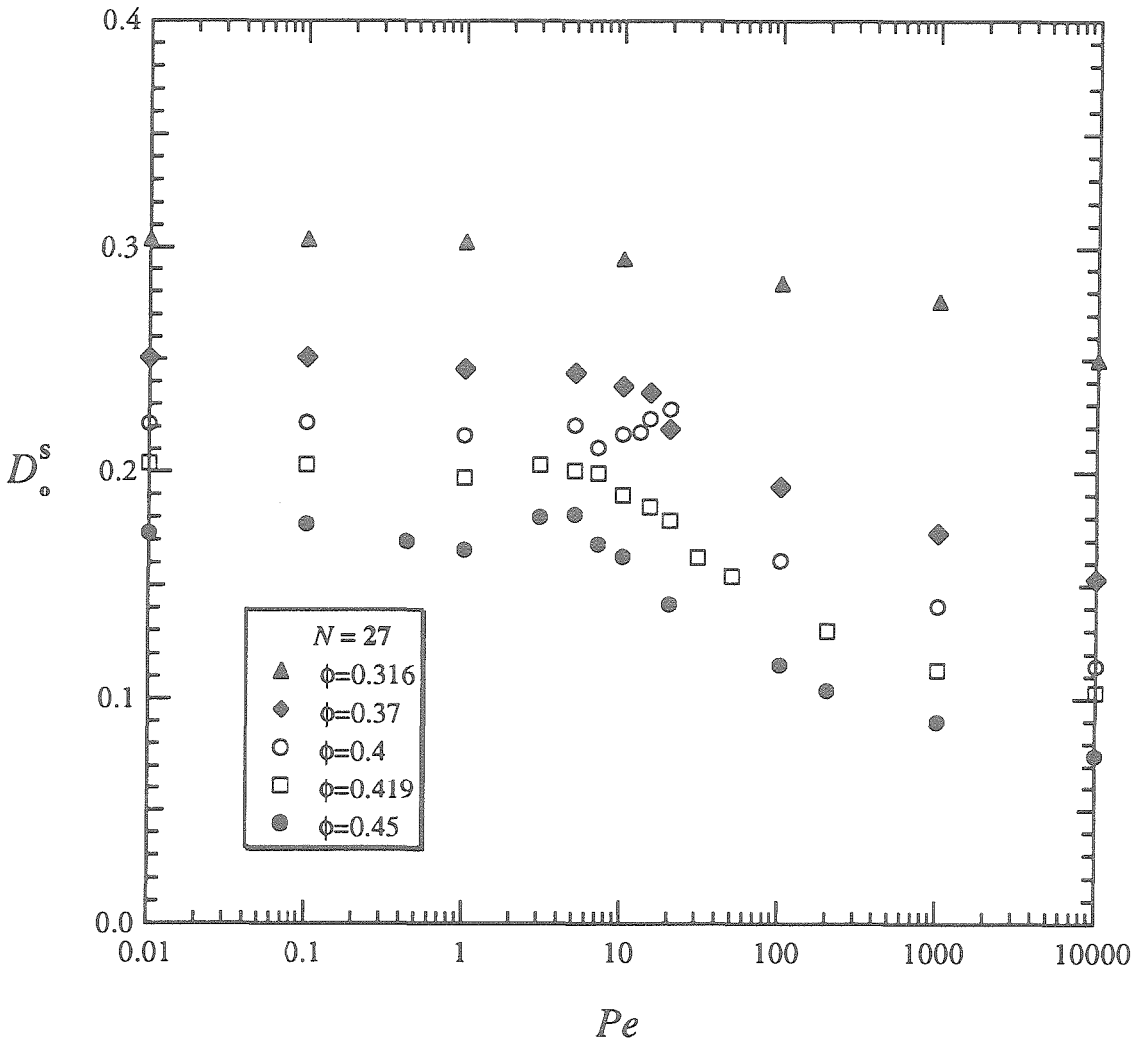

Figure 7.26: The short-time translational self-diffusion coefficient D_o^s normalized by the infinite dilution diffusion coefficient D_o obtained by Stokesian dynamics as a function of the Péclet number for hard spheres at volume fractions ϕ: (▲) 0.316, (◆) 0.37, (○) 0.4, (□) 0.419 and (●) 0.45. The short-time translational self-diffusion coefficient is relatively constant for small Péclet number ($Pe<1$) and decreases with increasing Pe. At the same Péclet number, the short-time self-diffusion coefficient decreases with increasing volume fraction.

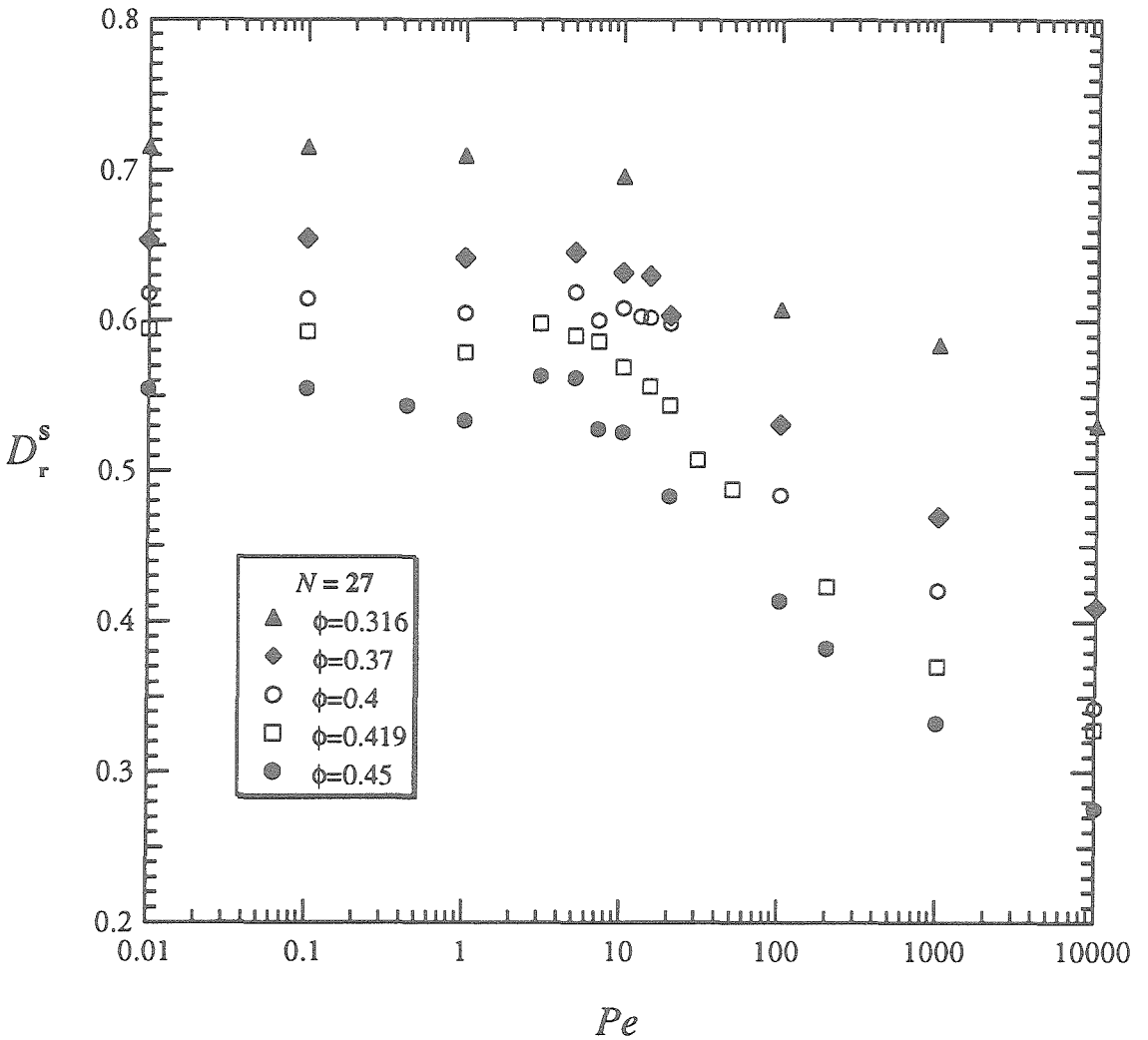

Figure 7.27: The short-time rotational self-diffusion coefficient D_r^s normalized by the infinite dilution diffusion coefficient D_o obtained by Stokesian dynamics as a function of the Péclet number for hard spheres at volume fractions ϕ: (▲) 0.316, (◆) 0.37, (○) 0.4, (□) 0.419 and (●) 0.45. It is seen from the figure that the short-time rotational self-diffusion coefficient is relatively constant for small Péclet number ($Pe<1$) and decreases with increasing Pe. As the volume fraction increases, the short-time self-diffusion coefficient decreases.

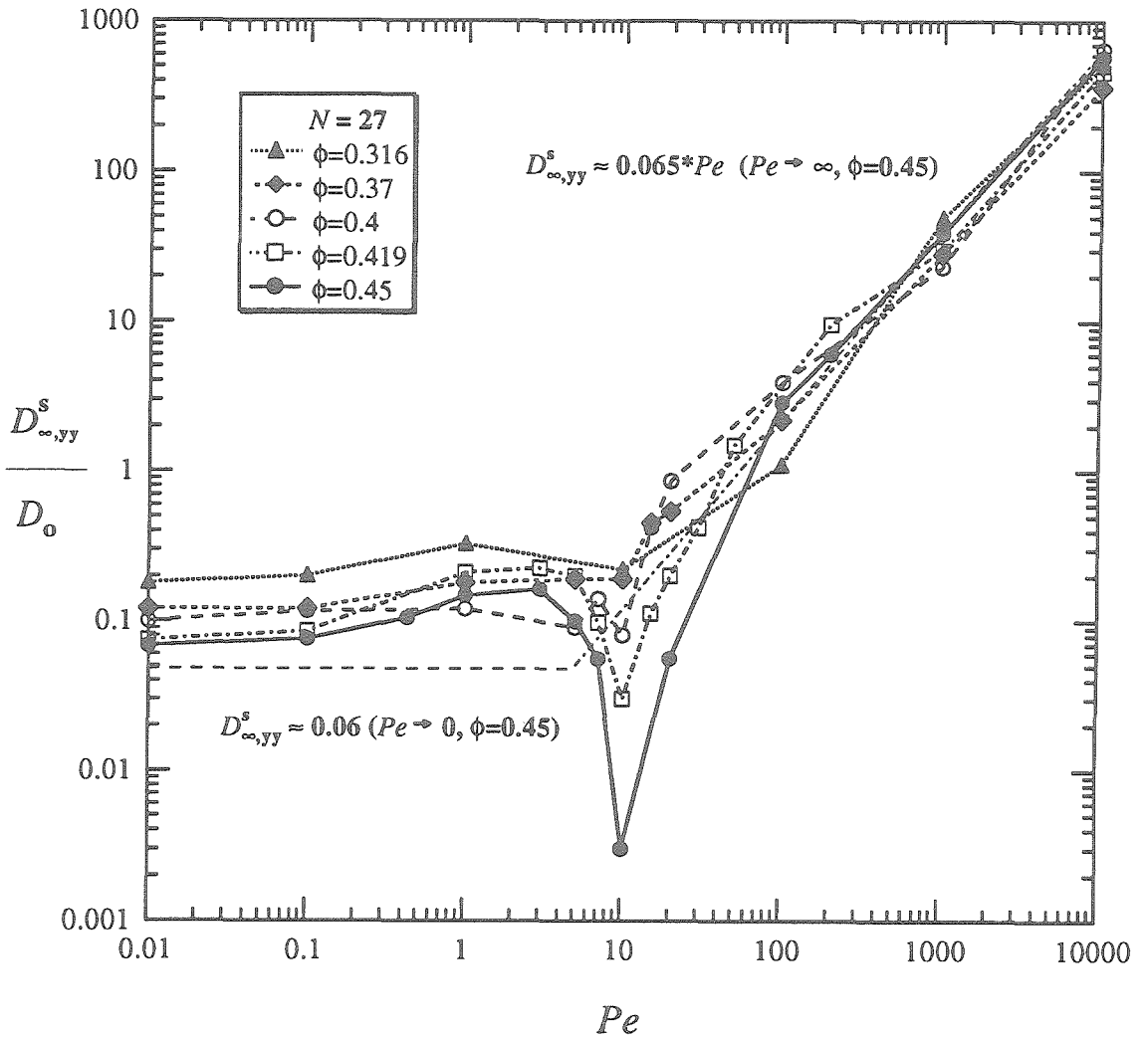

Figure 7.28: The long-time self-diffusion coefficient $D^s_{\infty,yy}$ normalized by the infinite dilution value D_o is plotted as a function of the Péclet number for hard spheres at volume fractions: ϕ = 0.316 (▲), 0.37 (◆), 0.4 (○), 0.419 (□) and 0.45 (●). The limiting asymptotes are: $D^s_{\infty,yy} \approx O(D_o)$ as $Pe \to 0$ and $D^s_{\infty,yy} \approx 0.06 \times Pe$ as $Pe \to \infty$. Note that as $Pe \to \infty$, the dimensional long-time self-diffusion coefficient scales as $\dot{\gamma}a^2$. The transition from the strong Brownian regime to the hydrodynamic domination limit occurs for $Pe \approx 10$. The two limits of $D^s_{\infty,yy}$ at $Pe \to 0$ and at $Pe \to \infty$ are shown in the figure for hard spheres at ϕ=0.45.

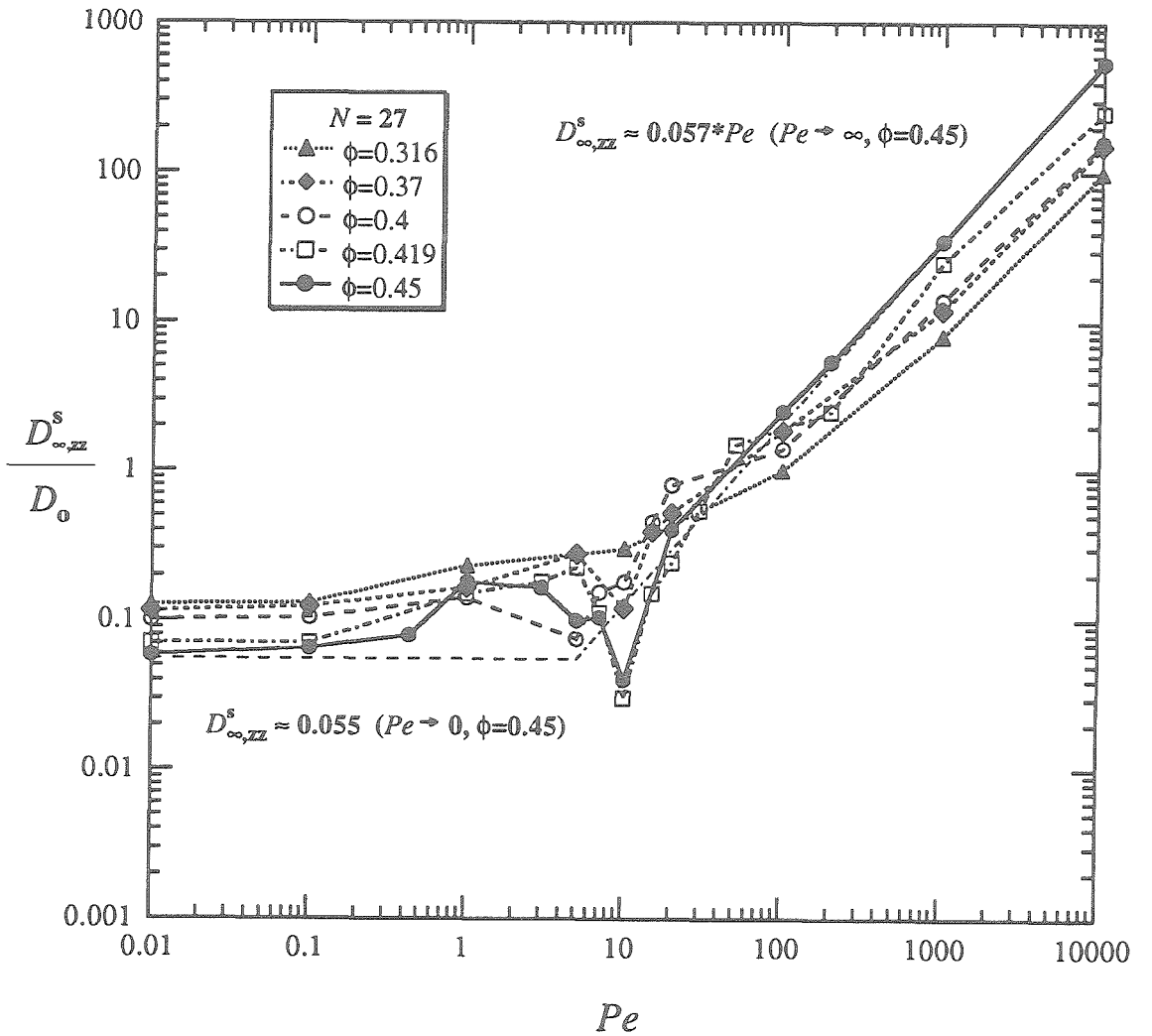

Figure 7.29: The long-time self-diffusion coefficient $D^s_{\infty,zz}$ normalized by the infinite dilution value D_o is plotted as a function of the Péclet number for hard spheres at volume fractions: $\phi = 0.316$ (▲), 0.37 (◆), 0.4 (○), 0.419 (□) and 0.45 (●). The limiting asymptotes are: $D^s_{\infty,zz} \approx O(D_o)$ as $Pe \to 0$ and $D^s_{\infty,zz} \approx 0.057 \times Pe$ as $Pe \to \infty$. Note that as $Pe \to \infty$, the dimensional long-time self-diffusion coefficient scales as $\dot{\gamma}a^2$. The transition from the strong Brownian regime to the hydrodynamic domination limit occurs for $Pe \approx 10$. The two limits of $D^s_{\infty,zz}$ at $Pe \to 0$ and at $Pe \to \infty$ are shown in the figure for hard spheres at ϕ=0.45.

Chapter VIII

STOKESIAN DYNAMICS SIMULATION OF VERY DENSE HARD-SPHERE SUSPENSIONS

Before we proceed to present the results and to discuss the behavior of very dense hard-sphere suspensions, let's briefly review our results for the dense and moderately dense colloidal suspensions. In chapter VI, we presented the complete details of our study for the behavior of dense hard-sphere suspensions at a volume fraction ϕ=0.45. In the Brownian dominated limit ($Pe < 1$), the suspension shear thins and the decrease of the steady shear viscosity corresponds to the decrease of Brownian contribution to the stress. The equilibrium isotropic structure is slightly perturbed, but particles are still very well dispersed. In the special plateau region ($Pe \approx 10$), a balance of Brownian and hydrodynamic forces induce a strongly ordered suspension with distinct "hexagonal" packing of strings of particles flowing with the shear flow. The steady shear viscosity remains relatively unchanged and is a minimum. In this region, a decrease of Brownian contribution to particle stress is compensated by an increase of hydrodynamic contribution. Most importantly, our results show that the shear-induced structure *does not* cause further shear thinning of the suspension (cf. Fig.6.33). The nonlinear behavior of the direct Brownian contribution to the stress, which comes directly from the highly nonlinear deformation of the local structure, is the main cause of the shear thinning. The ordered structure is controlled by the Brownian forces which act as short-ranged repulsive forces and counter the shearing deformation of the suspension. At high shear rates ($Pe > 10^2$), the suspension shear thickens and the hydrodynamics contribute all particle stress. In the shear thickening region, the hexagonal packing is destroyed and the suspended particles become closely spaced or touch and form elongated clusters disrupting the bulk flow and this is the main cause of shear thickening.

In comparison to hard spheres at a volume fraction ϕ=0.45, the moderately dense

colloidal suspensions at volume fractions in the range of 0.316 to 0.419 show a very weak shear thinning and shear thickening behavior and the results were presented in chapter VII. Hard-sphere suspensions with volume fraction ϕ below 0.4 cannot be sheared to order and the change in the steady shear viscosity is small. As the volume fraction increases (ϕ=0.4 and 0.419), the suspensions did show a signature of shear-induced structure for $Pe \approx 10$, but the order is weak, unstable and occurs in a narrow range of the Péclet number. The transitional volume fraction is found to be approximately ϕ=0.4, where the suspension begins to display shear thinning and shear thickening and the microstructural arrangements suggest the start of ordering.

In this chapter, we investigate the behavior of very dense hard-sphere suspensions with volume fractions above 0.45. The range of volume fraction in our study is from 0.47 to 0.6. At equilibrium, these hard spheres span the colloidal fluid-colloidal crystalline phase transition, with $\phi_F = 0.494 \pm 0.002$ for the fluid phase and $\phi_M = 0.545 \pm 0.002$, and go beyond the the glass region, where the glass transition occurs at $\phi_G \approx 0.58$. In addition to determining the influence of the shear on the deformation of the microstructure and relating this to suspension macroscopic properties, we endeavor to study the shear melting effect which disturbs and destroys the equilibrium crystalline structure of very dense hard spheres and induces the flowing particles to a different ordered pattern. The relaxation time of a string-ordered microstructure is also studied. Similar to the outline of chapters VI and VII, we present the suspension rheology first, the shear-induced microstructure second, and the self-diffusivities last.

Details of the simulations and the sampling statistics for the rheology are summarized

in Tables 8.1 to 8.5 for hard spheres at ϕ=0.47, 0.48, 0.49, 0.51 and 0.55, respectively. Column (1) is the Péclet number, Pe, and column (2) is the number of particles, N. Columns (3) to (6) are the starting time, ending time, the time step and number of time steps for each run, respectively. Column (7) is the elapsed time for each sample and column (8) is the time units which each sample is successively shifted in time. Column (9) is the number of samples which are used to compute the rheology.

Table 8.1 for ϕ=0.47 shows a nine-run series which begins with the run at Pe=0.1 [1] and ends with the run at Pe=10^4 [9]. The bracketed number, which is shown in column (1) next to the Péclet number, specifies the order of the run series. Initial samples of particles are selected randomly for the runs with Pe=0.01, 0.1 and 10^5. All of these runs are with 27 particles and an average of dimensionless run time is 100.

Details of dynamic simulations for hard spheres at a volume fraction ϕ=0.48 are reported in Table 8.2. In addition to a three-run series with 123 particles, a monolayer model with 80 and 120 particles at an areal fraction ϕ_A= 0.72, which is comparable to a volume fraction ϕ=0.48 using the 2/3 rule, is also simulated. At the end of the run with 80 particles and Pe=10 [1], the microstructure is verified for strings of particles in the flow direction, the x-axis. The influence of the shear on the order of flowing particles is tested with high shear rates at Pe=10^3 [2] and 10^4 [2]. In a different run starting with strings of flowing particles, the shear is stopped (in the run with Pe=0 [2]) and the string formation at Pe=10 [1] is allowed to relax to an equilibrium state, so we can study the relaxation of a string-ordered structure. A monolayer model with 80 and 120 particles provides a large number of neighboring particles which are needed for the computing of

the structure factors at small wave numbers (large wave lengths). In a monolayer with 100 particles, a particle has up to 5 particle diameters of different neighbors and it is equivalent to a three dimensional model with 1000 particles, which is prohibitively costly to run on a workstation.

Table 8.3 gives details of the runs for hard spheres at ϕ=0.49. The Péclet number ranges from 0.01 to 10^5 and these runs start with a random initial sample of 27 particles. A special run with 123 particles at Pe=10 is shown at the end of this table. Details of the runs for hard spheres at a volume fraction ϕ=0.51 are reported in Table 8.4. There are two series of continuing runs for 27 particles and the order of the run series is denoted by the bracketed numbers shown in column (1). The first run series follows the order of Pe=10 [1], 10^2 [2], 10^3 [3+], 2000 [4+] and 10^4 [5+]. The second run series follows the order of Pe=10 [1], 10^2 [2], 0.1 [3-] and 0.01 [4-]. All other runs in this table start with random sample of the particles. Table 8.5 shows details of the runs with 28 particles for ϕ=0.55. Initial random particle configurations are chosen for the runs with Pe=0.01, 3, 10, 30 and 10^5. A series of continuing runs are carried out with the following order of Pe=10 [1], 10^2 [2] and 10^3 [3]. The particle configuration at the end of the run with Pe=10^3[3] is used for the runs with Pe=0.1, 1 and 10^4. A special run with 126 particles at Pe=10 is shown at the end of Table 8.5. To select a random particle configuration for a hard-sphere suspension with a volume fraction above 0.55, we set 28 or 126 particles in a BCC or FCC lattice and then randomize the spheres for approximately 10^6 moves. Note that a volume fraction 0.55 is above the maximum close packing $\phi_{max}^{SCC} = 0.5236$ for a SCC lattice and 27 or 123 particles cannot be assembled into a BCC or FCC lattice. This is the reason why the runs for $\phi \geq 0.55$ are with 28 or 126 particles.

VIII.1 Suspension Rheology

VIII.1.1 The Steady Shear Viscosity

Results of the steady shear viscosities of hard-sphere suspensions at volume fractions ϕ=0.47, 0.48, 0.49, 0.51 and 0.55 obtained by Stokesian dynamics for different Péclet numbers are summarized in Tables 8.6 to 8.10, respectively. Column (1) is Pe and column (2) is N. Columns (3) to (8) are the steady hydrodynamic viscosity, its standard deviation, the steady Brownian viscosity, its standard deviation, the steady total shear viscosity and its standard deviation, respectively. Results of the steady shear viscosities from Table 8.6 for ϕ=0.47 are plotted in Fig.8.1 to show the change of Brownian ($\Box$) and hydrodynamic contribution ($\triangle$) to the total shear viscosity ($\bullet$) with varying Péclet numbers. The total shear viscosity curve shows a strong shear thinning and shear thickening behavior and resembles quite strikingly experimental curves. The steady total shear viscosity, η_r, decreases noticeably in the shear thinning region ($Pe < 5$) from $\eta_r \approx 21.1$ at Pe=0.01 to a minimum viscosity $\eta_r \approx 4.2$ in a small plateau region ($5 \leq Pe \leq 10$) and then increases with increasing Péclet numbers in the shear thickening region with $Pe > 10$. The cause of the shear thinning in the region of $Pe < 1$ is due only to the decrease in the Brownian contribution to the stress since the hydrodynamic contribution remains unchanged in this region. For $1 \leq Pe \leq 5$, the suspension continuously shear thins and the shear thinning in this region is due not only to a decrease in the Brownian contribution to particle stress but also due to a small reduction in the hydrodynamic contribution as well. The reduction in hydrodynamic viscosity was not seen for suspensions at ϕ=0.45 (cf. Fig.6.1). Figure 8.1 shows a small plateau region ($5 \leq Pe \leq 10$)

where the total shear viscosity is minimum. A further shear thickening region is seen at $Pe > 10$ where hydrodynamics contribute all to the total shear viscosity. At $Pe^* \approx 0.7$, Brownian and hydrodynamic viscosities are the same.

The rheological behavior of the two hard-sphere suspensions at volume fractions ϕ=0.48 and 0.49 are plotted in Figures 8.2 and 8.3 with data for these two figures taken from Tables 8.7 and 8.8, respectively. The two hard spheres show the same trend seen for hard spheres at ϕ=0.47. In the first shear thinning region ($Pe < 1$), the decrease in the Brownian viscosity, η_r^B, is a direct cause of the shear thinning. For $1 \leq Pe \leq 5$, the decrease of both η_r^B and η_r^H drives a further decrease of the total viscosity, η_r, to a minimum value in the second shear thinning region. The suspension shear thickens for $Pe > 10$ as η_r^H increases quickly and contributes essentially all to the total shear viscosity since η_r^B has decayed and vanished for $Pe > 10^2$. As seen in Fig 8.2, the total shear viscosity shows little variation for a monolayer with 80 particles (●) and 120 particles (⊠) at Pe=10. The comparison for the total viscosity of a monolayer with 80 particles (●) and a 3D model with 123 particles (○) at Pe=0.43, 10 and 10^3 is excellent. The negligible change of total viscosity with different number of particles: 27 and 123, in the simulation can also be seen in Fig.8.3 for ϕ=0.49. At $Pe^* \approx 0.9$, Brownian and hydrodynamic viscosities are the same for the two hard-sphere suspensions.

Results from Table 8.9 for ϕ=0.51 are plotted in a log-log plot in Fig.8.4 to show the relation of the relative viscosities as a function of the Péclet number. As the Péclet number increases from the Brownian dominated limit (Pe=0.01), the suspension strongly shear thins for $Pe < 10$ and shear thickens for $Pe > 10$. The plateau region, which is

seen for hard spheres at ϕ=0.45 (cf. Fig.6.1) where the steady total shear viscosity is minimum, has reduced to a very narrow region at Pe=10. The figure shows a decrease in η_r^H and η_r^B for $1 \leq Pe \leq 10$ which causes the suspension to further shear thin. At Pe=10, both η_r^H and η_r^B are a minimum value. A good comparison is obtained for η_r from the run with 27 particles (●) and 123 particles (⊠) at Pe=10. Figure 8.4 shows identical Brownian and hydrodynamic viscosities at $Pe^* \approx 1$.

Figure 8.5 displays the relation of the relative viscosities for hard spheres at a volume fraction ϕ=0.55 with different Péclet numbers in a log-log scale. Data for the figure are taken from Table 8.10. For a slightly perturbed dense hard-sphere suspension (Pe=0.01), the steady total shear viscosity is large. As the Péclet number increases, the dense suspension shows very strong shear thinning as the total shear viscosity decreases from $\eta_r \approx O(1000)$ at Pe=0.01 to $\eta_r \approx 10$ at Pe=10. In the plateau region ($30 \leq Pe \leq 10^2$), the total shear viscosity is unchanged and minimum as the decrease of the Brownian contribution to the stress is balanced by the increase of hydrodynamic contribution, which is the same behavior obtained for hard spheres at ϕ=0.45. For large Péclet numbers ($Pe > 10^3$), the suspension shear thickens due to an increase of hydrodynamic viscosity. Note that the Brownian viscosity is small compared to hydrodynamic viscosity, but it has not completely vanished in the shear thickening region as seen for hard spheres at smaller volume fractions. Figure 8.5 shows a delay of the transition from shear thinning to shear thickening and the plateau region is shift to larger Péclet number, from $Pe \approx 10$ at $\phi \leq 0.51$ to $30 \leq Pe \leq 10^2$ for ϕ=0.55. The variation in the total shear viscosity for 28 particles (●) and for 126 particles (⊠) at Pe=10 is negligibly small. At $Pe^* \approx 2$, the contribution of Brownian and hydrodynamic to particle stress are identical.

A comparison of the simulation results for the steady total viscosity and experimental results from van der Werff and de Kruif (1989) for silica hard spheres is shown in Fig.8.6 with a log-log scale. Stokesian dynamics results are plotted for hard spheres at ϕ = (●) 0.45 as a reference for comparison, (■) 0.47, (◇) 0.48, (▲) 0.49, (○) 0.51 and (⊠) 0.55. The volume fractions in the experiments are: ϕ = (+) 0.419±0.01, (⊡) 0.443±0.01, (△) 0.47±0.01 and (×) 0.488±0.01. In the region with $Pe \leq 1$, Stokesian dynamic results for ϕ=0.47 and 0.49 compare remarkably well with experiments at identical or similar volume fractions: ϕ=0.47 and 0.488. In the region of $Pe \approx 10$, simulation results are noticeably twice as small as the experimental results. This noticeable difference in the total viscosity is rather peculiar since the comparison for our results for ϕ=0.45 with their experiments is excellent as shown in chapter VI. The uncertainty of our results is small as shown in Tables 8.6 to 8.10 for the shear viscosities in this region.

The newly noticeable difference is due largely to the small reduction of the hydrodynamic viscosity which is found for these very dense hard spheres. In the experiments, van der Werff and de Kruif reported an approximate 2% uncertainty for the measurements of the viscosities and another 2% for the measurements of the volume fractions. The 2% uncertainty for the shear viscosities is standard, but a 2% uncertainty in the volume fractions may lead to large uncertainty in the viscosity, especially at high ϕ values due to extreme sensitivity of the viscosity on the volume fraction. This can be seen by noting the large difference in the shear viscosity curves at ϕ=0.419, 0.47, and 0.488 from their experiments.

Our results also show that the total shear viscosity for ϕ=0.47 is smallest at Pe=10

and smaller than the minimum viscosity for ϕ=0.45. This trend has not yet been seen in experiments or reported. There is clearly a need for further experiments as well as simulations of well characterized dense colloidal dispersions. As the Péclet number increases, our viscosity curves recover quickly for $Pe > 10$ and would have matched the trend of the experiments in the region of large Péclet number if the shear rates were increased. The suspension shows a shear thickening region for $Pe > 10^2$ and this was not seen in the experiments of van de Werff and de Kruif which were limited to highest shear rates at Pe=10. Shear thickening have been observed in many other systems (Hoffman (1972), Laun (1988), Barnes (1989), Boersma *et al.* (1990)). The viscosities, which are measured for large spheres ($Pe \rightarrow \infty$) by Jeffery and Acrivos (1976), Gadala-Maria (1979) and Pätzold (1980), are larger than the minimum in the shear thinning viscosity of the Brownian suspensions shown in Fig.8.6; therefore, the suspension *must* shear thicken. In the next section, we present our findings for the steady normal stress differences.

VIII.1.2 The Steady Normal Stress Differences

Results of the steady first and second normal stress differences and its statistics are summarized in Tables 8.11 to 8.15 for these very dense hard-sphere suspensions at volume fractions ϕ=0.47, 0.48, 0.49, 0.51 and 0.55, respectively. Column (1) is Pe and column (2) is N. Columns (3) to (8) give the first and columns (9) to (14) give the second normal stress differences, respectively. In these columns, results for the hydrodynamic contribution are presented first, followed by the Brownian contribution, and the total normal stress differences last. The standard deviation computed from the number of samples shown in Tables 8.1 to 8.5 is denoted by σ. For the runs of a monolayer with 80

and 120 particles shown in Table 8.12, the forces in the z direction are not needed for dynamic simulations, so the second normal stress differences are not computed. Results from Tables 8.11 to 8.15 are plotted in pairs of figures for each ϕ to show the change of the hydrodynamic ($\triangle$) and Brownian contribution ($\square$) to the total normal stress differences ($\bullet$) with varying Péclet numbers. For a monolayer with 80 particles, only the first normal stress differences are plotted in Fig.8.8.

Figures 8.7.a, 8.8, 8.9.a, 8.10.a and 8.11.a show the first and Figures 8.7.b, 8.9.b, 8.10.b and 8.11.b show the second normal stress differences for hard spheres at ϕ=0.47, 0.48, 0.49, 0.51 and 0.55, respectively. For the region with small Péclet number, the hydrodynamic ($\triangle$) first and second normal stress differences, χ_{1H} and χ_{2H}, are small and negligible compared to the dominant Brownian contribution ($\square$) χ_{1B} and χ_{2B}, respectively. In the region of small Péclet number ($Pe < 1$), the statistical uncertainty in the Brownian contribution to stress is large as shown in Tables 8.11 to 8.15. The standard deviation for the Brownian contribution to the normal stress difference $\sigma_{\chi_{1B}}$ (column (6)) and $\sigma_{\chi_{2B}}$ (column (12)) are large, and the mean values of normal stress differences reflect the simulation fluctuations at low Pe. The large fluctuations in Brownian contribution to the stress in the region of small Péclet number are due to small deformation of the equilibrium structure for relatively short runs. Simulations with longer run times are necessary for the region of small Péclet numbers. For a hard-sphere distribution of force-free particles, it is expected that there are no normal stress differences in the limit of $Pe \rightarrow 0$.

As the Péclet number increases, χ_{1B} and χ_{2B} decay in absolute value and have essen-

tially vanished for $Pe > 10^2$. In this large Péclet number region, χ_{1H} and χ_{2H} increase and contribute totally to χ_{1T} and χ_{2T}, respectively. Note that while both χ_{1H} and χ_{2H} are positive for all Péclet numbers, χ_{1B} is negative and χ_{2B} is positive. The special regions at $Pe \approx 10$ for hard spheres at $\phi \leq 0.51$ (cf. Figures 8.7 to 8.10) and at $Pe \approx 100$ for hard spheres at ϕ=0.55 (Fig.8.11.a-b) show a large decrease in absolute value for both normal stress differences, and recall that in these special regions, the total viscosities are also minimum. The minimum in absolute value of χ_{1T} and χ_{2T} in this region is due to a noticeable decrease of both the hydrodynamic and Brownian contribution to the normal stress differences. A shift of the transition from shear thinning to shear thickening to larger Péclet number as the volume fraction increases to ϕ=0.55 (cf. Fig.8.5) is seen to be consistent with a similar shift of the region where both the normal stress differences are minimum as shown in Figures 8.11.a and 8.11.b.

Figure 8.12.a and 8.12.b illustrate a comparison for the total first and second normal stress differences with different volume fractions ϕ = (□) 0.47, (♦) 0.48, (△) 0.49, (○) 0.51 and (⊠) 0.55. The normal stress differences of hard-sphere suspensions at ϕ=0.45 (●) are also shown in these two figures as a reference for comparison. In the region of $1 \leq Pe \leq 10^4$, χ_{1T} and χ_{2T} for dense hard spheres at volume fraction $\phi \leq 0.51$ are relatively the same as the normal stress differences of hard spheres at ϕ=0.45 which are of $O(1)$ and small compared to the normal stress differences for suspensions at ϕ=0.55 which are positive and of $O(10)$.

Our results and experiments show pronounced shear thinning and shear thickening behavior of very dense hard-sphere suspensions in simple shear flow. The important

challenge to us is to determine and to understand the mechanisms which produce these interesting rheological behaviors, especially in the special region with $Pe \approx 10$, where the minimum viscosity of hard spheres at a range of volume fraction from 0.47 to 0.51 is smaller than the minimum viscosity of hard-sphere suspensions at ϕ=0.45. This is a great opportunity for us to study and to understand the relation of certain shear-induced order patterns of the flowing particles to the pronounced shear thinning behavior. In the following section, the shear-induced microstructure is presented.

VIII.2 The Shear-Induced Microstructure

VIII.2.1 The Angularly Averaged Pair-Distribution Function $g(r)$

Figure 8.13.a shows the radial dependence of the angularly averaged pair-distribution function, $g(r)$, with Pe=10 for hard-sphere suspensions at volume fractions ϕ = (dotted curve) 0.48, (dashed curve) 0.49 and (dotted-dash curve) 0.51. There are 123 particles in the unit cell. In comparison to $g(r)$ for ϕ=0.45 (solid curve) which displays strong single peaks at the particle center-center radial spacing $r \approx 4$, 6 and 8, $g(r)$ for these denser hard spheres shows a strikingly different pattern with two strong twin peaks at $r \approx 4$ and $r \approx 6$ and two intense single peaks at $r \approx 7$ and 9. These sharp peaks with high intensity are the signature of the strong ordering of the flowing particles at Pe=10. Recall that the pattern of $g(r)$ for ϕ=0.45 reflects the hexagonal packing of strings of flowing particle which we discussed in detail in chapter VI. As the volume fraction increases, one would expect the location of the intense peaks to be shifted to a slightly smaller r for denser suspensions. Figure 8.13.a displays this shift from $r \approx 4.2$ for ϕ=0.45 to $r \approx 3.8$ for ϕ=0.48, 49 and 0.51, but the peak at $r \approx 4.2$ is also seen for these denser suspensions.

The twin peaks of $g(r)$ at these two radial spacings suggest that the hexagonal ring is not symmetrical and the packing pattern of the flowing particles may be stretched or distorted. $g(r)$ offers information from which we can identify the location of distortion. In the region of strong ordering, there are two distinct arrangements of the particles: hexagonal formation for particles on the $z-y$ plane and string formation for particles in the flow direction, which can be seen from the $x-y$ and $x-z$ planes. By analyzing the peaks of $g(r)$, we can identify that the stretching must be from the particle positions at the apex of the hexagon and not from the stringed particles in the flow direction. This is because that at $r \approx 3.8$, which is less than 4 for two particle diameters, the two particles in a string formation (the first and second nearest neighbors of the particle at the origin) must have been overlapped and the program would have terminated which it did not occur. Particles in the hexagonal formation do not overlap for $r \approx 3.8$ due to their staggered positions in this packing. The double-peaked $g(r)$ gives the location of the particles on the second ($r \approx 3.8$) and third ($r \approx 4.2$) distorted hexagonal rings. This can also be seen from the plot of the probability density computed in the $z-y$ plane, $g(z,y)$ (cf. Fig.8.21.c).

Similar to the plot of $g(r)$ in Fig.8.13.a, we plot the radial dependence of $g(r)$ for denser hard-sphere suspensions at ϕ = (dotted curve) 0.55, (dashed curve) 0.58 and (dotted-dash curve) 0.6 in Fig.8.13.b, and the results are obtained from simulations with 126 particles. $g(r)$ for ϕ=0.49 and 123 particles (solid curve) is also plotted in this figure for our comparison. The twin-peaked $g(r)$ for $0.47 \leq \phi \leq 0.51$ becomes less strong as ϕ increases to the range of 0.55 to 0.6 and comparing to $g(r)$ for ϕ=0.45 (cf. Fig.8.13.a), we observe a reversal trend of $g(r)$ which changes from a pattern with double peaks

to a similar pattern of strong single peaks of ϕ=0.45. The degree of the distortion and stretching of the particle order is less for hard spheres with a volume fraction in the range of 0.55 to 0.6 compared to the distortion of the structure for ϕ in the range of 0.48 to 0.51. While the stretching and distortion may be related to the small size of the unit cell as the volume fraction increases, it is a strong evidence that the suspensions in this range of volume fraction are induced to a strong ordering state at $Pe \approx 10$ by the balance of shear and Brownian forces. For the current computing power of workstations and small unit times on the Cray Y-MP supercomputer, we are limited to simulations with less than 150 particles. It is of our interest to bring the Stokesian dynamics simulation method to the full speed of parallel computing so that simulations with $O(10^3)$ particles can be performed.

Figure 8.13.c illustrates the pair-distribution function for a small range of r from 2.0 (when the particles come in contact) to 2.1 and with Pe=10. There are 123 or 126 particles in the unit cell. Note that $g(r)$ is plotted with a logarithmic scale. The plot symbols for different volume fractions are: ϕ = (□) 0.48, (△) 0.49, (○) 0.51, (▲) 0.55, (⊠) 0.58, and (⧫) 0.6. As the volume fraction ϕ increases from 0.45 (●), the pair-distribution function evaluated at r=2, $g(2)$, first decreases to a minimum for ϕ = 0.48 and then increases with increasing volume fraction. In chapter VI, we determined the relation of the steady shear viscosity to the deformation of the microstructure, which in a dense suspension can be represented by the pair-distribution function evaluated at r=2 (cf. Fig.6.5). The minimum shear viscosity in the special region $Pe \approx 10$ corresponds to the minimum of $g(2)$ and, in the shear thickening region with large Péclet numbers, the large value of the steady shear viscosity corresponds to the large value of $g(2)$. $g(2)$ for ϕ in

the range of 0.48 to 0.51 is indeed smaller than the small $g(2)$ of ϕ=0.45 indicating that the relatively well separation of strings of the flowing particles produces a more efficient flow than the string order at ϕ=0.45, and as a result the steady shear viscosity should be less, which is observed for these very dense suspensions. The first peak of $g(r)$ is seen at $r \approx 2.02$ and for very dense suspension at ϕ=0.58 and 0.6, it is shifted to=$r \approx 2$ as particles are closely spaced or touch.

A comparison of $g(r)$ for different Péclet numbers: (dotted curve) 0.43, (solid curve) 10 and (dashed curve) 10^3 is presented in Fig.8.14 for ϕ=0.48 with 123 particles. Intense peaks for strong ordering microstructure can only be seen for Pe=10. The insert figure shows $g(r)$ with a logarithmic scale for a smaller range of the particle center-center spacing r from 2.0 to 2.1. For a slightly deformed suspension (Pe=0.43), our results for $g(2)$ is 5.81 which compares very well with the value of 6.1 of a random suspension (Pe=0) computed by a Monte-Carlo simulation. At Pe=10, $g(2)$ is small and then increases 100 fold for Pe=10^3 in the shear thickening region. The large value of $g(2)$ in the region of strong hydrodynamics ($Pe > 10^2$) is a direct result of the formation of particle clusters.

Figure 8.15 shows the relation of $g(2)$ with a finer increment of the Péclet number from 0.01 to 10^4 for hard spheres at different volume fractions: ϕ = (●) 0.45, (□) 0.47, (△) 0.49, (○) 0.51 and (⊠) 0.55. $g(2)$ are computed from the runs with 27 or 28 particles in the unit cell and data for the plot are taken from Table 6.4.a. In the region of small Péclet numbers ($Pe < 1$), $g(2)$ is relatively constant and increases with large ϕ. As the Péclet number increases, $g(2)$ decreases sharply for $Pe \approx 10$ and increases quickly and approaches an asymptotic value in the hydrodynamic dominated limit ($Pe \rightarrow \infty$). The

special region at Pe=10 shows a remarkable behavior of $g(2)$ which it first decreases to a minimum at ϕ=0.47 and then increases with increasing ϕ. $g(2)$ displays little variation for different numbers of particles as shown in Table 6.4.a.

The steady shear viscosity and the pair-distribution function show a clear evidence of the two types of suspension behavior in the special region ($Pe \approx 10$). For the volume fraction in the range of 0.47 to 0.51 which spans the colloidal crystalline-colloidal fluid phase transition of hard spheres at equilibrium, the steady shear viscosity is small. The flowing particles are largely separated from each other and the packing order is distorted or stretched as shown by the double peaked pattern of $g(r)$ compared to single-peaked pattern of suspensions at ϕ=0.45. As the volume fraction increases into the glass transition ($0.55 \leq \phi \leq 0.6$), the rheological behavior returns to the behavior for suspensions at ϕ=0.45 and the suspension shows a delay to larger Péclet number of the shear thinning-shear thickening transition. In the following section, we examine the shear-induced microstructure with more detail by traveling along the steady shear viscosity curves (cf. Figures 8.1 to 8.5) and probing the relative arrangement of the particles at each particular Péclet number where the viscosities are computed.

VIII.2.2 The Probability Density Functions $g(x,y)$, $g(x,z)$ and $g(z,y)$

Our computer simulations for very dense hard spheres include two systems of different number of particles. In this section, the simulation results for 27 or 28 particles are presented first, followed by the simulation results with large N which include 123 or 126 particles, and a monolayer model with 80 and 120 particles last.

VIII.2.2.1 $g(x,y)$, $g(x,z)$ and $g(z,y)$ for 3-D models with 27 or 28 particles

The microstructure of the first group of hard spheres at ϕ=0.47, 0.49 and 0.51 is presented by the probability density functions computed in the $x-y$ plane, $g(x,y)$, in the $x-z$ plane, $g(x,z)$ and in the $z-y$ plane, $g(z,y)$ in Figures 8.16, 8.17 and 8.18, respectively. The are 27 particles in the unit cell. The flow direction is the x-axis, the velocity gradient direction is the y-axis, and the vorticity direction is the z-axis. Regions of light color represent high probability and regions of dark color represent low probability. The probability density functions are plotted with a range of the Péclet numbers shown with the increasing order from left to right and from top to bottom.

Figures 8.16.a, 8.16.b and 8.16.c show the change of $g(x,y)$, $g(x,z)$ and $g(z,y)$ for ϕ=0.47 with varying Pe ranging from 0.1 to 10^3, respectively. Starting from Pe=0.1 in the upper left, the microstructure is seen with a slightly deformed symmetric ring for strong Brownian suspension (Pe=0.1 and 1). For Pe in the range of 3 to 100, the flowing suspension is strongly ordered with strings of particles in the flow direction shown by $g(x,y)$ and $g(x,y)$ and two different patterns of hexagonal packing of strings of flowing particles shown by $g(z,y)$ in Fig.8.16.c. $g(z,y)$ shows a slightly stretched and distorted hexagonal at Pe=10 compared to the symmetrical hexagonal packing at Pe=20 which is the packing order for the flowing particles obtained for ϕ=0.45 (cf. Fig.6.8.b). The important difference between the two patterns *is not* the orientation of the hexagonal packing but it is the separation of the particles in the packing. Figure 8.16.c shows that the separating distance of the particles in the hexagonal formation is larger at Pe=10 compared to that of Pe=20. This trend can also be seen from Fig.8.15 for the plot of

the pair-distribution function evaluated for particle center-center spacing r=2, $g(2)$. For ϕ=0.47, $g(2)$ at Pe=10 is 0.01 compared to 8.31 for Pe=20 which is nearly 1000 fold increase (cf. Table 6.4.a). Referring to the steady shear viscosity curve of ϕ=0.47 (cf. Fig.8.1), the shear viscosity is smaller and minimum at Pe=10 than at Pe=20. The order of the flowing particles is destroyed at large shear rates (Pe=10^3).

The microstructure of hard spheres at a volume fraction ϕ=0.49 is displayed in Figures 8.17.a-c and it is very similar to the microstructure of ϕ=0.47. In the regions of strong ordering (Pe=3 and 30), $g(x,y)$ in Fig.8.17.a and $g(x,z)$ in Fig.8.17.b show strings of flowing particles in the flow direction, and $g(z,y)$ in Fig.8.17.c. shows a distinct hexagonal packing of strings of flowing particles. $g(z,y)$ clearly shows a very well formed hexagonal at Pe=10. Note that there are only three strings of particles in the z-axis compared to five strings of the hexagonal packing at Pe=30. The difference in the number strings of the particles at Pe=10 and Pe=30 can also be seen from $g(x,z)$. If we view the flow of the particles from the top of the unit cell, the $x-z$ plane, with the flow direction from our left to our right, then we would see three distinct sheets of particles with large fluid space between the sheets at Pe=10. In this packing, the separating distance between the particles is largest and as expected the shear viscosity is minimum (cf. Fig.8.3). The microstructural order of the flowing particles are destroyed by high shear rates at Pe=10^3.

The microstructures of the last hard-sphere suspension in the first group are presented by the density plot of $g(x,y)$ in Fig.8.18.a and $g(z,y)$ in Fig.8.18.b for ϕ=0.51. Regions of string order are seen for Pe=3, 10 and 10^2. Again we observe two different patterns of

hexagonal packing at Pe=10 and 100, with the particles more separated in the new type of hexagonal packing at Pe=10. The transitional Péclet number which the suspension begins to order is seen at Pe=3 and the string formation is destroyed at considerably large shear rates (Pe=10^4).

Figures 8.19.a-c display the microstructures of hard spheres at ϕ=0.55 for Pe ranging from 0.1 to 10^4. There are now 28 particles in the unit cell. $g(x,y)$ in Fig.8.19.a and $g(x,z)$ in Fig.8.19.b show a string formation of particles for a large range of the Péclet number from 10 to 10^4. $g(z,y)$ shows an interesting type of packing in the region of string order. The stretched hexagonal is inclined and rotated with a small positive angle relative to the vorticity direction, the z-axis, to accommodate all 28 particles within the unit cell, which is similar to the inclination of the packing of 81 particles for ϕ=0.45 (cf. Fig.6.11.a). Only one type of hexagonal packing is seen for ϕ=0.55. More interestingly, as shown by the steady shear viscosity curve in Fig.8.5 the suspension starts to shear thicken for Pe from 10 to 10^3, yet the microstructure begins to order for this range of the Péclet number. The string order of hexagonally packed particles *does not* necessarily produce the minimum viscosity as we see clearly for this very dense suspension.

For very dense hard-sphere suspensions, the results of the runs with 27 or 28 particles reveal a remarkable shear-induced microstructure which helps us to envision the shearing deformation of the suspension and gain the physical understanding of the mechanisms which induce the rheological behavior. This is a great motivation for us to pursue dynamic simulations with a larger number of particles which provide more detail of the microstructure, especially its long-ranged order and the necessity of a large number of

particles for the computation of the structure factors. In the next section, we present the details of our finding for the microstructure of dense hard spheres modeled with a large number of particles.

VIII.2.2.2 $g(x,y)$, $g(x,z)$ and $g(z,y)$ for Suspensions with 123 or 126 Particles

In this section, the microstructure of the flowing suspensions is determined from the runs with 123 or 126 particles. This allows a comparison with the microstructure of a hard-sphere suspension at ϕ=0.45 which we presented in detail in Chapter VI (cf. Figures 6.10.a to 6.10.g). As shown in Figures 8.20.a-c, the steady probability density functions $g(x,y)$, $g(x,z)$ and $g(z,y)$are plotted for ϕ=0.48 and three different Péclet numbers: Pe=0.43 (left figure), 10 (central figure) and 10^3 (right figure). There are 123 particles in the unit cell. The flow direction is the x-axis, the velocity gradient direction is the y-axis and the vorticity direction is the z-axis. Regions of light color represent high probability and regions of dark color represent low probability. These figures display three representative microstructures of the hard spheres. At low Péclet number (Pe=0.43), the small shear rate can only slightly perturb the equilibrium structure since the Brownian motion is strong and the particle motion is diffusive. The structure is very close to that of suspension at rest state which is isotropic for ϕ=0.48 and this is correctly shown by Stokesian dynamics in these three figures. The probability density functions show a symmetric ring with small deformation for Pe=0.43 in all three planes. As the Péclet number increases into the ordered region (Pe=10), the flowing suspension is strongly ordered with strings of particles in the flow direction shown by $g(x,y)$ in Fig.8.20.a and $g(x,z)$ in Fig.8.20.b and a distinct "hexagonal" packing of strings of flow-

ing particles shown by $g(z,y)$ in Fig.8.20.c. The order is long ranged as shown by several hexagonal packing of the particles within the unit cell. For a hydrodynamic dominated suspension (Pe=10^3), the hexagonal packing of strings of particles is destroyed. Large clusters of particles are formed as seen by the sharpening first nearest neighbor ring for Pe=10^3.

The most revealing microstructure in the ordered region with Pe=10 is shown in Figures 8.21.a-c for hard spheres at ϕ = (top left) 0.45, (top central) 0.48, (top right) 0.49, (bottom left) 0.51, (bottom central) 0.55 and (bottom right) 0.58. There are 123 or 126 particles in the unit cell. $g(x,y)$ in Fig.8.21.a and $g(x,z)$ in Fig.8.21.b clearly show strings of particles in the flow direction, the x-axis, for ϕ from 0.45 to 0.51. For ϕ=0.55 and 0.58, the structure has not equilibrated after a dimensionless time of 40, but the particles are seen in transition to order as $g(x,y)$ and $g(x,z)$ show less intense signals of a string formation. Note the striking difference in the patterns of string formation in the density plots of $g(x,y)$ and $g(x,z)$ for ϕ=0.45 compared to ϕ in the range of 0.48 to 0.58. This comparison shows a clear evidence of the switching in the packing order from the $x-y$ and $x-z$ packing for ϕ=0.45 to the $x-z$ and $x-y$ for larger ϕ, respectively. As shown in Fig.8.21.a, $g(x,y)$ changes from a 5-stringed formation for ϕ=0.45 to a 9-stringed pattern for larger ϕ. Similarly, $g(x,z)$ in Fig.8.21.b shows a reversal trend which it changes from a 9-stringed formation for ϕ=0.45 to a 5-stringed pattern for denser hard spheres. The more effective means to observe the change of the order microstructure at Pe=10 is shown in Fig.8.21.c for the probability density function $g(z,y)$. $g(z,y)$ displays the hexagonal packing of strings of flowing particles. A closer examination of these hexagonal patterns shows a noticeable difference among these packing. As ϕ increases

from 0.45 to the range of 0.48 to 0.51, the symmetric hexagonal packing for ϕ=0.45 is rotated by an angle of 90 degrees and slightly stretched in the velocity gradient direction, the vertical y-axis. The distortions of the hexagons are seen from this figure as well as from the pair-distribution function $g(r)$ which shows two twin peaks (cf. Figures 8.13.a and 8.13.b). The new hexagonal packing is consistent with the new packing in the $x-y$ and $x-z$ plane. As the volume fraction increases to 0.55 and 0.58, the new hexagonal packing is further inclined by a small angle relative to the vorticity direction, the z-axis, to accommodate 126 particles within the unit cell. The switching of the orientation of the strings is most likely influenced by the small size of the unit cell as the volume fraction increases.

Figure 8.21.d shows our most recent results for dynamic simulations with 126 particles at volume fractions ϕ=0.59 (left column) and 0.6 (right column). $g(x,y)$ is shown in the top row and $g(z,y)$ is shown in the bottom row. Initial particle samples are selected randomly and the dimensionless run time is 50. The microstructure has not yet equilibrated, but the onset of particle order can be seen from this figure. These runs demonstrate the capability of Stokesian dynamics in simulating very dense suspensions. The theoretical volume fraction for an hexagonal packing of strings of particles in three dimensions is 0.605. From a random sample of 126 particles at ϕ=0.6, which is in the glass transition at rest state and essentially theoretical maximum volume fraction of hexagonally packed particles, we can shear the suspension to order.

VIII.2.2.3 $g(x,y)$ for a Monolayer with 80 Particles

The probability density function $g(x,y)$ is plotted in Fig.8.22.a for a monolayer with

80 particles at an areal fraction ϕ_A= 0.72, which is comparable with ϕ=0.48 in three dimensions, for different Péclet numbers. The flow direction is the horizontal x-axis and the velocity gradient direction is the vertical y-axis. The initial sample of 80 particles is selected by first setting 80 particles in a square array 8×10 and then the particles are randomized by a Monte-Carlo calculation for 10^6 moves with a small random displacement step. Note that at equilibrium, the microstructure displays a crystalline phase as shown in the upper left most figure at Pe=0. Alder and Wainwright (1962) have studied and found the phase transition of a hard-disk fluid starting at an areal fraction ϕ_A^F= 0.62 (comparable to ϕ=0.41 which is less than ϕ_F= 0.494 of the phase transition of a hard-sphere model). This is consistent with our finding for the equilibrium crystalline microstructure at ϕ_A= 0.72. The small shear rate at Pe=0.01 is seen to perturb, but it is not sufficiently strong to melt the crystalline phase. At Pe=1, we observe the shear melting effect which destroys the equilibrium crystalline phase. As the Péclet number increases, the shear begins to induce the string order of particles in the flow direction as can be seen for Pe in the range of 10 to 10^4. The string formation is destroyed at very high shear rates (Pe=10^5) and again we observe the shear melting effect on the colloidal crystals.

VIII.2.2.4 The Relaxation of a String-Ordered Microstructure

In addition to studying the shear melting effect, we investigate the relaxation time of a string-order microstructure. The monolayer is first sheared to string order at Pe=10 as shown in Fig.8.22.a, then the shear rate is discontinued and we perform a dynamic simulation with pure Brownian motion at Pe=0. As the microstructure equilibrates,

Stokesian dynamics is expected to capture the process of recrystallization of the monolayer at $\phi_A = 0.72$. The evolution of the microstructure at different times is shown in Fig.8.22.b. The suspension recrystallizes after a sufficiently long dimensionless time of 80 and the figure shows the excellent comparison of crystalline phase obtained by Stokesian dynamics simulation at Pe=0 and computed by a Monte-Carlo calculation. Note that the time is scaled with diffusive time and for a typical colloidal diffusive time of $O(10^{-2}\text{sec})$, it should take approximately 2 hours for the suspension to relax and return to a crystalline phase. The large relaxation times have also been confirmed in experiment of Ackerson and Pusey (1988) and Pusey and van Megen (1986). In the following section, we present simulation results for the line and plane structure factors.

VIII.2.3 The Structure Factor $S(\mathbf{k})$

Our goals are to provide a comparison of the structure factors obtained by Stokesian dynamics and measured from experiments. Furthermore, we need to determine the spectroscopic signature of an ordered suspension and understand the relation of the scattering light pattern to the deformation of the flowing suspension. In the following sections, the line structure factors $S(k_x)$, $S(k_y)$ and $S(k_z)$ are presented first, followed by the plane structure factors $S(k_x, k_y)$, $S(k_x, k_z)$ and $S(k_z, k_y)$.

VIII.2.3.1 The Line Structure Factors $S(k_x)$, $S(k_y)$ and $S(k_z)$

The line structure factors $S(k_x)$, $S(k_y)$ and $S(k_z)$ are computed by choosing the wave vector parallel to the k_x-, k_y- and k_z-axis, respectively. To compute $S(k_x)$ for example, we fix the dimensionless wave numbers k_y=k_z=0 and vary only the wave number k_x.

The computing method for the structure factors is presented in chapter VI.

Figures 8.23.a-c show $S(k_x)$, $S(k_y)$ and $S(k_z)$ for dense hard spheres in the ordered region with Pe=10 for different volume fractions: ϕ = (□) 0.48, (△) 0.49 and (○) 0.51. The structure factors for hard spheres at ϕ=0.45 (●) are also plotted in these three figures for a reference of comparison. There are 123 particles in the unit cell and the dimensionless wave numbers k_x, k_y and k_z range from 2 to 8. As shown in Fig.8.23.a, the structure factors computed in the flow direction, $S(k_x)$, show small variation due to constant and large changes of the particle positions. The scattering light intensities of $S(k_x)$ are small compared to that of $S(k_y)$ and $S(k_z)$ computed in the directions of the velocity gradient and the vorticity as shown in Figures 8.23.b and 8.23.c, respectively. $S(k_y)$ shows a single peak with high intensity at the dimensionless wave number $k_y \approx 6.4$ and $S(k_z)$ shows two intense peaks at the dimensionless wave numbers $k_z \approx 3.5$ and $k_z \approx 7$. The peak intensities of $S(k_y)$ and $S(k_z)$ are less for ϕ=0.51 compared to the high intensity of ϕ=0.48 and 0.49. These intensity maxima probe the string order of the particles in the flow direction at Pe=10. The most striking revealing of a change of the microstructure at Pe=10 as the volume fraction increases from 0.45 to the range of 0.48 to 0.51 is by comparing the structure factors $S(k_y)$ and $S(k_z)$ of these denser hard spheres to $S(k_z)$ and $S(k_y)$ for ϕ=0.45 shown in Figures 8.23.b and 8.23.c, respectively. The striking resemblance of these curves clearly demonstrates a switching in the packing order of the flowing particles along the y- and the z-axis for ϕ=0.45 to the z- and the y-axis for denser suspensions, respectively. This switching of the packing pattern is also seen from a plot of the probability density functions $g(x,y)$ and $g(x,z)$ (cf. Figures 8.21.a and 8.21.b).

Figure 8.23.d plots the structure factor which is computed with an angle θ=-15° relative to the z-axis for ϕ = (△) 0.55 and (□) 0.58 at Pe=10. There are 126 particles in the unit cell and to accommodate all 126 hexagonally packed particles, the hexagon is inclined as shown in Fig.8.21.c. Figure 8.23.d reinforces this claim and shows that strong scattering light intensity can only be seen along the $\theta = -15^{\circ}$ line. The structure factor computed with θ=0°, $S(k_z)$, shows a negligible scattering for all wave numbers.

A comparison for the structure factors $S(k_y)$ and $S(k_z)$ with three different Péclet numbers: Pe = (□) 0.43, (●) 10 and (△) 10^3, is shown in Figures 8.24.a and 8.24.b for hard spheres at ϕ=0.48, respectively. The strong scattered intensity which is the spectroscopic signature of strongly ordered flowing particles can only be seen for Pe=10 as shown in these two figures.

VIII.2.3.2 The Line Structure Factor $S(k_y)$ for a Monolayer

At equilibrium, the monolayer at an areal fraction ϕ_A= 0.72 shows the crystalline phase as presented in Figures 8.22.a and 8.22.b. To display the intensity pattern of the shear melting effect, the structure factor computed in the direction of the velocity gradient, $S(k_y)$, is plotted in Fig.8.25 for different Péclet numbers: Pe = (○) 0.01, (□) 1,(●) 10, (⊠) 10^3 and (△) 10^5. $S(k_y)$ shows an intensity maxima peak at the dimensionless wave number $k_y \approx 3.5$ and a less intense peak at $k_y \approx 6.5$ for Pe=10 and 10^3 which are seen as the spectroscopic signature for strings of flowing particles in the flow direction. The colloidal crystals at equilibrium are sheared to melt and induced into strings of particles for Péclet number in the range of 10 to 10^3. The string formation is destroyed at very high shear rate (Pe=10^5) and shows minimal scattering.

The relaxation of a string-order suspension is probed by plotting the evolution of $S(k_y)$ for different dimensionless times as shown in Fig.8.26. $S(k_y)$ shows one intense peak at $k_y \approx 3.5$ and one smaller peak at $k_y \approx 6.5$ for the starting string-ordered suspension at time=0 (●). The intensity at these two peaks decreases sharply with time. After a dimensionless time of 80, $S(k_y)$ displays intensity maxima for the crystalline phase (⊠) as the suspension recrystallizes and returns to a rest state.

The anisotropic line structure factors were effectively used to probe the strings formation of the flowing suspension in the ordered region with Pe=10. The most striking evidence was presented to show a change in the microstructure as the volume fraction increases from 0.45 to the range of 0.48 to 0.51. The packing order has switched from the y- and z-axis for ϕ=0.45 to the z- and y-axis for denser hard spheres, respectively. These denser hard-sphere suspensions also show a small shear viscosity for Pe=10. To probe two different patterns of hexagonal formation and examine the deformation of the microstructure, the two-dimensional plane structure factors are computed and presented in the following section.

VIII.2.4 The Plane Structure Factors $S(k_x, k_y)$, $S(k_x, k_z)$ and $S(k_z, k_y)$

The plane structure factors $S(k_x, k_y)$, $S(k_x, k_z)$ and $S(k_z, k_y)$ are computed by choosing the wave vectors parallel to each of the plane of interest. To compute $S(k_x, k_y)$ for example, we fix the wave number k_z=0 and vary k_x and k_y. The dimensionless wave numbers k_x, k_y and k_z are varied from $\pm$0.5 to $\pm$4.0. This range of wave numbers is used to compute the nonequilibrium plane structure factors which are plotted in a contour plot with four symmetrical quadrants similar to the topographical plots of the small angle

neutron scattering (SANS) measurements of the static plane structure factors reported by Johnson *et al.* (1988), van der Werff and de Kruif (1989) and Laun *et al.* (1992). In the first quadrant, both the wave numbers parallel to the horizontal and vertical axes are positive and vary from 0.5 to 4.0. For the second quadrant, the wave number parallel to the vertical axis is unchanged and the wave number parallel to the horizontal axis is negative and ranges from -4.0 to -0.5. The third and fourth quadrant are mirror images of the first and the second quadrant, respectively.

VIII.2.4.1 The Plane Structure Factor $S(k_x, k_y)$ of a Monolayer

The dynamic simulations with monolayer of 80 and 120 particles provide a large number of neighboring particles within the cell which are necessary for the computation of the structure factor with both large and small wave numbers probing the short- and long-ranged order of the flowing suspension, respectively. Figures 8.27.a-c show the plane structure factor computed in the $x-y$ plane, $S(k_x, k_y)$, for a monolayer of 80 particles at an areal fraction $\phi_A = 0.72$ with different Péclet numbers. The range of the dimensionless wave numbers k_x and k_y is from ± 0.5 to ± 4.0 and these three figures display the surface plots of $S(k_x, k_y)$ as a function of k_x and k_y. Starting from the top of Fig.8.27.a, $S(k_x, k_y)$ shows random regions of strong scattering light intensity for the crystals of an equilibrium hard-disk fluid. There is little variation in $S(k_x, k_y)$ for a suspension with small deformation at Pe=0.01 (bottom figure) compared to the equilibrium $S(k_x, k_y)$ (top figure). The scattered intensity pattern of $S(k_x, k_y)$ becomes increasingly distinct as the Péclet number increases. At Pe=1 (top figure in Fig.8.27.b), $S(k_x, k_y)$ begins to form bands and the regions of random scattered intensity seen at Pe=0.01 completely disappears.

The two vertical bands along the wave numbers $k_x \approx \pm 3.5$ are clearly seen for Pe=10 (bottom figure in Fig.8.27.b) and at Pe=10^3 (top figure in Fig.8.27.c). These bands with intensity maxima are the signature of strings of flowing particles. The pattern of high intensities is destroyed at high shear rates (Pe=10^5) (bottom figure in Fig.8.27.c). The surface plot of $S(k_x, k_y)$ provides a clear comparison of the microstructure for a strong Brownian suspension with random regions of high intensity (Pe=0.01) and a hydrodynamic dominated suspension with distorted ring of intensity maxima, which is the signature of clusters of particles in the high Péclet number limit.

To capture the long-ranged order of the flowing suspension, we compute $S(k_x, k_y)$ with a smaller range of the dimensionless wave numbers k_x and k_y from 0.5 to 1.5 and plotted in Figures 8.28.a-c. At Pe=10, the long-ranged order of strings of particles can be seen with vertical bands of high intensity along the wave numbers $k_x \approx 0.75$ and $k_x \approx 1.5$ (bottom figure in Fig.8.28.b). $S(k_x, k_y)$ with small wave numbers at Pe=10^3 (top figure in Fig.8.28.c) does not show the long-ranged string formation. This is due to the deficiency in number of particles for the computation of small-wave-number structure factors. Results from the run with a monolayer of 120 particles at Pe=10 and the same areal fraction are plotted in Fig.8.29 for $S(k_x, k_y)$ with small (top figure) and large (bottom figure) wave numbers. The intensity pattern of $S(k_x, k_y)$ are much higher, especially for the small wave numbers for 120 particles compared to $S(k_x, k_y)$ for 80 particles. It is clear that for small-wave-number structure factors, simulations with monolayer of $O(10^2)$ particles are needed; it is equivalent with simulations of $O(10^3)$ particles in three dimensions, which is beyond the present 100-MFLOPS rated workstations.

VIII.2.4.2 The Plane Structure Factors $S(k_x, k_y)$, $S(k_x, k_z)$ and $S(k_z, k_y)$

Figures 8.30.a, 8.30.b and 8.30.c show the comparison for the plane structure factors $S(k_x, k_y)$, $S(k_x, k_z)$ and $S(k_z, k_y)$ with different Péclet numbers for hard spheres at ϕ=0.48, respectively. For Pe=0.43 (left figure), the isotropic Debye-Scherrer ring for the equilibrium structure is slightly distorted to an elliptic in the Fourier k-space. For the strongly ordered region with Pe=10 (central figure) $S(k_x, k_y)$ and $S(k_x, k_z)$ displays vertical bands of intensity maxima for strings of flowing particles. Furthermore, $S(k_x, k_z)$ displays circular regions of high intensity for the order of flowing particles in a hexagonal packing which can also be seen clearly with $S(k_z, k_y)$. At Pe=10^3 (right figure), the patterns of high scattering light are destroyed.

The microstructures of the flowing suspensions in the special shear region with Pe=10 are compared for hard-sphere suspensions with different volume fractions and they are shown in Figures 8.31.a and 8.31.b. There are 123 or 126 particles in the unit cell and the volume fraction ϕ varies from 0.45 to 0.58. The two figures show conclusive evidence of a strongly ordered microstructure with bands of high intensity from contour plots of $S(k_x, k_y)$ and a halo ring of six intensity maxima from contour plots of $S(k_z, k_y)$. Note that the circular regions of intensity maxima can only be seen for ϕ=0.45 in Fig.8.31.a. Recall that we report our findings of a switching in the packing order of flowing particles from y- and z-axis for ϕ=0.45 to z and y-axis for ϕ in the range of 0.48 to 0.51. The absence of circular regions of high intensity in $S(k_x, k_y)$ for denser hard spheres can now be seen from $S(k_x, k_z)$ shown in Fig.8.30.b. Note also that the difference in the halo pattern shown in Fig.8.31.b. The halo ring for ϕ=0.45 is rotated by an angle 90 degrees

for ϕ in the range of 0.48 and 0.51 and it is further inclined by a small angle with respect to the horizontal k_z-axis due to the accommodation of 126 particles within the unit cell. The rotation of the halo ring is also evidence of the switching in the packing pattern as ϕ becomes larger than 0.45.

The most recent SANS measurements for the plane structure factors by Laun *et al.* (1992) for both plane Poiseuille and Couette flows have shown the halo ring patterns in the shear thinning region, and the halo ring disappears as the shear rate increases into the shear thickening region (cf. Fig.24 from Laun *et al.* (1992) and shown in Figures 6.34 and 6.35 in chapter VI) for suspensions of electrostatically stabilized styrene-ethylacrylate-copolymer spheres in glycol and in water at a volume fraction of ϕ=0.434. Results from the experiments with plane Poiseuille flow for denser hard spheres do not reveal a change in the pattern of the halo ring or a stronger shear thinning behavior. There was only one experiment with Couette flow for hard spheres at ϕ=0.434 reported. Our results for the plane structure factors in the velocity gradient-velocity plane show the same halo ring pattern of scattering light for strongly ordered suspensions as measured by Laun *et al.*. We needs more experiments with well characterized and dense colloidal hard spheres in shear flow to verify the interesting change of the microstructure and pronounced shear thinning behavior.

The question that needs to be addressed is whether the new orientation of the hexagonal packing induces a more efficient flow of the particles for ϕ in the range of 0.48 to 0.51 which shows smaller shear viscosities at Pe=10 than the small viscosity of suspensions at ϕ=0.45. In chapter VI, we showed that the orientation of the symmetric hexagonal

packing does not influence the rheology as seen from the indistinguishable difference in shear viscosity given by 27, 81 and 123 particles at ϕ=0.45. The shear viscosity depends on the deformation of the suspension and the relative separation distance between the particles. In this aspect, we see clearly a connection of the steady shear viscosity and the pair-distribution function evaluated for closely spaced particles at r=2, $g(2)$, which is a function of the two important dimensionless parameters, the volume fraction and the Péclet number. For hard spheres with ϕ in the range of 0.48 to 0.51, $g(2)$ at Pe=10 is smaller than $g(2)$ for ϕ=0.45 (cf. Fig.8.15) and thus we obtained small shear viscosities for denser hard spheres. The stretching of the new hexagonal packing allows a larger separation of the particles in the packing and induces a more efficient flow of strings of hexagonally packed particles.

VIII.3 The Self-Diffusivities

In this section, we focus on the short- and long-time self-diffusion coefficients of Brownian particles in dense suspensions. The short-time self-diffusivities measure the instantaneous mobility of the particles on a small time scale so small that the particles do not have to move a distance comparable to its own size. In contrast to the short-time self-diffusivities, the long-time self-diffusivities measure the dynamic behavior of the suspensions as the particles must travel a distance far from their starting locations, deform the local structure and exchange places with neighbors.

VIII.3.1 The Short-Time Self-Diffusion Coefficients

The short-time translational and rotational self-diffusion coefficient are denoted by D_o^s

and D_r^s, respectively. D_o^s is normalized by the infinite dilution coefficient $D_o = kT/(6\pi\eta a)$ and D_r^s is normalized by $D_r = kT/(8\pi\eta a^3)$. The short-time self-diffusion coefficients D_o^s and D_r^s are reported in Tables 8.16 to 8.20 for ϕ=0.47, 0.48, 0.49, 0.51 and 0.55, respectively. Column (1) is Pe and column (2) is N. Columns (3) to (6) are the steady short-time translational self-diffusion coefficients computed in the x-axis, $D_{o_{xx}}^s$, in the y-axis, $D_{o_{yy}}^s$, in the z-axis, $D_{o_{zz}}^s$, the mean, i.e., $D_o^s = \frac{1}{3}(D_{o_{xx}}^s + D_{o_{yy}}^s + D_{o_{zz}}^s)$, and its standard deviation. Similarly, columns (8) to (12) are the short-time rotational self-diffusion coefficients $D_{r_{xx}}^s$, $D_{r_{yy}}^s$, $D_{r_{zz}}^s$, the mean D_r^s, and its standard deviation. For the monolayer model, the z-component of the short-time self-diffusivities is not computed and the mean is defined as the x and y average, i.e., $D_o^s = \frac{1}{2}(D_{o_{xx}}^s + D_{o_{yy}}^s)$.

Results of the steady D_o^s and D_r^s from these five tables are plotted in Figures 8.32.a and 8.32.b as a function of the Péclet number, respectively. The plot symbols for different volume fractions ϕ are: (□) 0.47,(△) 0.49, (○) 0.51 and (⊠) 0.55. There are 27 or 28 particles in the unit cell. D_o^s and D_r^s for ϕ=0.45 (●) are also plotted in these two figures as a reference for comparison. As shown in these two figures, D_o^s and D_r^s are relatively constant for $Pe < 1$, decrease slightly at $Pe \approx 1$, increase to a maximum at $Pe \approx 10$, and finally decrease with increasing Pe. The behavior of the short-time self-diffusion coefficients can be explained by referring to the shearing deformation of the suspensions. In the region of small shear rates ($Pe < 1$), the equilibrium structure, whether it is random or a crystalline phase, is slightly perturbed and the strong Brownian motion dominates and maintains the diffusive behavior of the suspension. The microstructure in this region is very close to that of a rest state and as a result the short-time self-diffusion coefficients do not change.

For the region of $Pe \approx 1$, the stronger shear force begins to influence the deformation of the suspension and the particles are less diffusive than pure Brownian particles at Pe=0. In this region, we observe a slight decrease of the short-time self-diffusion coefficients. D_o^s and D_r^s also decrease as the volume fraction increases for $Pe < 10$. In the ordered region with $Pe \approx 10$, the figure shows an increase of D_o^s and D_r^s to a maximum value which implies the enhancement of instantaneous mobility due to a large separation of particles. This is consistent with the microstructure described in section VIII.2. The proper balance of Brownian and hydrodynamic forces induces an ordered structure with well separated and relatively uniform spaced particles packed in the strings along the flow direction. As a consequence, the particles are very mobile at Pe=10 and we observe the maximum of the short-time self-diffusion coefficients. In this region, the short-time self-diffusion coefficients for ϕ=0.47 and 0.49 are also larger than that for ϕ=0.45. Again this is consistent with the behavior of the pair-distribution function evaluated for touching pairs of particles, $g(2)$, (cf. Fig.8.15) and the behavior of the steady shear viscosity (cf. Fig.8.6).

In the region of large Péclet number ($Pe > 10^2$), the high shearing deformation causes particles to cluster. The mobility of the flowing particles in the clusters is greatly reduced and as a result we have a decrease in the short-time self-diffusion coefficients as shown in these two figures. Summarized results from Tables 8.16 to 8.20 also show that D_o^s computed in the x-axis, $D_{o_{xx}}^s$, is slightly larger than D_o^s computed in the y- and the z-axis, $D_{o_{yy}}^s$ and $D_{o_{zz}}^s$.

VIII.3.2 The Long-Time Self-Diffusion Coefficients

Results of the long-time self-diffusion coefficients are reported in Tables 8.21 to 8.24 for the runs with 27 or 28 particles for ϕ=0.47, 0.49, 0.15 and 0.55. Column (1) is the Péclet number. Columns (2) to (5) are the steady long-time self-diffusion coefficient computed in the velocity gradient direction, $D^s_{\infty,yy}$, its standard deviation, the steady long-time self-diffusion coefficient computed in the vorticity direction, $D^s_{\infty,zz}$, and its standard deviation, respectively. The mean value of these coefficients are computed from the number of samples shown in column (7) and each sample interval has a time unit displayed in column (6). These coefficients are normalized by the infinite dilution diffusion coefficient $D_o = kT/(6\pi\eta a)$. Note that the reported values for the normalized $D^s_{\infty,yy}$ and $D^s_{\infty,zz}$ in these tables are scaled with the diffusive time. Long run times of the simulations with 27 or 28 particles are needed for $D^s_{o_{yy}}$ and $D^s_{o_{zz}}$ which equilibrate after an average of a dimensionless time of 80 as shown in these tables. The relatively shorter run times for simulations with 123 and 126 particles do not provide sufficient particle positions and this is why these runs are not used to compute $D^s_{o_{yy}}$ and $D^s_{o_{zz}}$. The velocity gradient direction is the y-axis and the vorticity direction is the z-axis. For Pe>1, the time is scaled with $\dot{\gamma}^{-1}$ and this is equivalent to multiplying $D^s_{\infty,yy}$ and $D^s_{\infty,zz}$ reported in Tables 8.21 to 8.24 with Pe.

Figure 8.33.a shows a log-log plot of the simulation results for $D^s_{\infty,yy}/D_o$ as a function of the Péclet number. For $Pe < 1$, the suspension is essentially all Brownian and the dimensionless diffusion coefficient is relatively constant and $D^s_{\infty,yy} \approx O(D_o)$ as shown in the limit of $Pe \rightarrow 0$. At much higher Péclet number (Pe>10^2), Fig.8.33.a shows a

very different relation of $D^s_{\infty,yy}/D_o$ which is linear with increasing Pe. This is expected based on the dimensional analysis: as $Pe \rightarrow \infty$, the only scale for the diffusion is $\dot{\gamma}a^2$; therefore, the dimensional $D^s_{\infty,yy}$ should scale with Pe as $Pe \rightarrow \infty$. Our results indeed show this behavior remarkably well with $D^s_{\infty,yy} \approx 0.065 \times Pe$ for $Pe \rightarrow \infty$. Figure 8.33.a also shows clearly the transitional Péclet number $Pe \approx 10$, where the behavior of the long-time self-diffusion coefficient changes from a strong Brownian limit to a hydrodynamic dominated regime. At Pe=10, the nondimensionalized $D^s_{\infty,yy}$ decreases to a minimum value which is two orders of magnitude less than that of $Pe < 1$. It is again the ordered region where the steady shear viscosity is also minimum. Referring to the shear-induced ordered structure at Pe=10, the minimum value of $D^s_{\infty,yy}$ indicates that the particles are least diffusive in the y-axis. Equivalently, the minimum value of $D^s_{\infty,yy}$ must imply a strongly ordered structure and in string formations, the particles can not break away. Note also that at Pe=10, $D^s_{\infty,yy}$ for ϕ = (□) 0.47 and (△) 0.49 are smaller than that of ϕ = (●) 0.45 which is the same as $D^s_{\infty,yy}$ for ϕ = (○) 0.51. Results of Brownian dynamic simulations by Xue and Grest (1990) have also shown the similar minimum in the long-time self-diffusivities of ordered suspensions in an oscillating shear flow. $D^s_{\infty,yy}$ for ϕ=0.55 shows a different behavior with a plateau region with Pe in the range of 10 to 100 where $D^s_{\infty,yy}$ remains minimum and then increases with large Pe. A shift of the Brownian-hyrodynamic transition from Pe=10 to Pe=100 as seen in this figure and is consistent with the small shift of the shear thinning-shear thickening transition as shown in Fig.8.6.

The long-time self-diffusion coefficient computed in the vorticity direction, the z-axis is plotted in Fig.8.33.b as a function of the Péclet number for the same hard-sphere sus-

pensions. We observe a behavior of $D^s_{\infty,zz}/D_o$ similar to that of $D^s_{\infty,yy}/D_o$ in Fig.8.33.a in the strong Brownian and strong hydrodynamic regimes. For slightly deformed hard spheres ($Pe < 1$), $D^s_{\infty,zz}/D_o$ is relatively constant and for hydrodynamically driven suspensions, the dimensional $D^s_{\infty,zz}$ scales with Pe. The two asymptotic limits of $D^s_{\infty,zz}$ at $Pe \rightarrow 0$ and at $Pe \rightarrow \infty$ are similar to that of $D^s_{\infty,yy}$. In the ordered region with $Pe \approx 10$, $D^s_{\infty,zz}$ decreases to a minimum value but it is less pronounced than the significant decrease of $D^s_{\infty,yy}$. We observe the same behavior for $D^s_{\infty,zz}$ as $D^s_{\infty,yy}$ for ϕ=0.55 which shows a plateau region with Pe in the range of 10 to 1000 where $D^s_{\infty,zz}$ changes inappreciably and a shift to larger Péclet number of the transition from the Brownian to hydrodynamic domination. In chapter IX, we provide the comparison of our simulation results for the long-time self-diffusion coefficients in the limit of pure hydrodynamics ($Pe \rightarrow \infty$) with the experimental findings from Eckstein *et al.* (1977), Leighton and Acrivos (1987), and the most recent results from Phan and Leighton (1992).

Our study of the self-diffusivities for dense hard sphere suspensions shows a clear distinction between the diffusive Brownian regime ($Pe \rightarrow 0$) and a hydrodynamic dominated regime ($Pe \rightarrow \infty$) with a transition region near $Pe \approx 10$. The long-time self-diffusion coefficients D^s_∞ are constant at small Péclet numbers, decrease to minimum value at transitional region where the structure is strongly ordered and then grow linearly with increasing Pe. In this special transitional region, the short-time self-diffusion is maximum due to enhanced instantaneous mobility of the suspended particles. At high Pe, the reduction of the short-time self-diffusion coefficients is a direct result of large particle clusters: a particle cannot move without moving all members of the compact cluster even at short time scales.

VIII.4 Conclusions

In this chapter, we detailed our study for very dense hard-sphere suspensions with volume fraction ranging from 0.47 to 0.6. In a simple shear flow, these dense hard-sphere suspensions displayed interesting rheological and microstructural behaviors. The suspensions with volume fraction from 0.47 to 0.51 strongly shear thinned for $Pe < 1$, and in the special region with Pe=10 the steady shear viscosity was minimum and smaller than the steady shear viscosity of hard spheres at ϕ=0.45. In the region of large Péclet number ($Pe > 10^2$), these very dense suspensions shear thickened. The pronounced minimum shear viscosities in the special region at Pe=10 corresponded to not only a decrease in the Brownian but also a small reduction in hydrodynamic viscosity. This was not seen for suspensions at ϕ=0.45, where the hydrodynamic contribution to the stress remains unchanged for $Pe < 10$.

Our results for microstructure show clearly the evolution of the flowing particles as a function of both the Péclet number and volume fraction. In the region of low Péclet number ($Pe < 1$), the microstructure is that of a slightly deformed suspension near equilibrium. Both the short- and long-time self-diffusivities showed little variation as the flowing suspension was still strongly diffusive and Brownian motion plays a dominant role in this low Péclet number regime. In the ordered region ($Pe \approx 10$), the proper balance of the Brownian and hydrodynamic forces induced the flowing suspension into strong ordering with hexagonally packed strings of particles in the flow direction. The short-time self-diffusion coefficients were maximum as the flowing particles are very mobile. The long-time self-diffusion coefficients were minimum due to the packing formation of

flowing particles which are locked into strings.

The distinct hexagonal packing for ϕ=0.45 with 123 particles was rotated by 90 degrees as the volume fraction increases to the range of 0.47 to 0.51, which may be related to the size of the unit cell. However, it is important to note that it *is not* the orientation of the packing which produces a smaller minimum viscosity for these dense hard spheres than the minimum viscosity for ϕ=0.45. The small minimum viscosities are directly related to the deformation of the structure which gives relatively large separation among the particles in the hexagon. The new hexagonal packing for very dense hard spheres was stretched slightly in the velocity gradient direction allowing the particles in this packing to be further apart than the particles in the hexagonal packing for ϕ=0.45. The particles moved more efficiently in the new packing and for this new flow pattern, we obtained the lowest shear viscosity. This is a great opportunity for processing optimization where dense suspensions can be made to flow with homogeneous order and least resistance.

We have successfully applied the Stokesian dynamics simulation method for studying the rheological and microstructural behaviors of very dense hard sphere suspensions. Our results provide the necessary physical understanding of the mechanisms which cause interesting suspension microscopic and macroscopic behavior. The accurate treatments for both the hydrodynamic and Brownian forces in dense suspension were demonstrated by good comparison of simulation results for the steady shear viscosities with experimental measurements. The accuracy of the method was also illustrated by reproducing the recrystallization process when a string-ordered suspension relaxed and returned to the crystalline phase at equilibrium. The shear melting of the crystals at equilibrium

and of the crystals which we produced by a shear-induced process at Pe=10 for dense hard-sphere suspensions were presented in detail. At the theoretical maximum packing of $\phi^{max} = 0.605$ of the hexagonally packed particles, Stokesian dynamics is well capable of simulating a random particle configuration and inducing a flow of ordered particles. The simulations provide vast amount of information and results from which can be used to test theories as well as other simulation methods.

Table 8.1: Statistics for simulations of hard spheres at volume fraction ϕ=0.47 and different Péclet numbers. Table captions are the same as shown in Table 6.1.a. Random samples of particle configurations are selected for Pe=0.01, 0.1 and 10^5. The running order of a series of nine continuing runs from [1] to [9] is given by bracketed numbers which are shown in column (1) next to Pe.

Pe	N	t_{start}	t_{end}	Δt_{set}	NSTEPS	t_{diff}	t_{shift}	# *trials*
0.01	27	0.0	200.0	5×10^{-4}	400000	190.0	1.0	11
[1] 0.10	27	0.0	100.0	5×10^{-4}	200000	80.0	1.0	11
[2] 1.00	27	100.0	200.0	10^{-3}	100000	70.0	2.0	16
[3] 3.00	27	200.0	300.0	10^{-3}	100000	60.0	2.0	21
[4] 7.00	27	300.0	400.0	10^{-3}	100000	60.0	2.0	21
[5] 10.00	27	400.0	500.0	10^{-3}	100000	60.0	2.0	21
[6] 20.00	27	500.0	600.0	10^{-3}	100000	60.0	2.0	21
[7] 10^2	27	600.0	700.0	10^{-3}	100000	60.0	2.0	21
[8] 10^3	27	700.0	800.0	10^{-3}	100000	60.0	2.0	21
[9] 10^4	27	800.0	900.0	10^{-3}	100000	60.0	2.0	21
10^5	27	0.0	50.0	10^{-4}	500000	40.0	1.0	5

Table 8.2: Statistics for simulations of hard-sphere suspensions at a volume fraction ϕ=0.48 and different Péclet numbers. Table captions are the same as shown in Table 6.1.a. For the runs with 123 particles, a series of three-continuing runs begins with Pe=0.43 [1] and ends with Pe=10^3 [3]. For simulations of monolayer with 80 particles, initial particle configuration of the run with Pe=10^2, 10^5 and 0 are taken from the end of the run with Pe=10. The run of a monolayer with 120 particles is started with a random particle configuration.

Pe	N	t_{start}	t_{end}	Δt_{set}	NSTEPS	t_{diff}	t_{shift}	# *trials*
[1]0.43	123	0.0	40.0	5×10^{-4}	80000	35.0		1
[2]10.00	123	40.0	80.0	10^{-3}	40000	35.0		1
[3]10^3	123	80.0	120.0	10^{-3}	40000	35.0		1
0.01	80,2D	0.0	30.0	10^{-4}	300000			
1.00	80,2D	0.0	30.0	10^{-4}	300000	20.0		1
[1]10.00	80,2D	0.0	40.0	10^{-3}	40000	30.0		1
20.00	80,2D	0.0	25.0	10^{-3}	25000	20.0		1
10^3	80,2D	0.0	23.0	10^{-3}	23000	20.0		1
[2]10^4	80,2D	40.0	70.0	10^{-4}	300000	25.0		1
[2]10^5	80,2D	40.0	50.0	10^{-4}	100000	10.0		1
[2]0.00	80,2D	40.0	90.0	10^{-4}	500000			
10.00	120,2D	0.0	40.0	10^{-3}	40000	35.0		1

Table 8.3: Statistics for simulations of hard spheres at volume fraction ϕ=0.49 and different Péclet numbers. Table captions are the same as shown in Table 6.1.a. Random particle configurations are selected for all the runs.

Pe	N	t_{start}	t_{end}	Δt_{set}	NSTEPS	t_{diff}	t_{shift}	# *trials*
0.01	27	0.0	140.0	5×10^{-4}	280000	90.0	1.0	5
0.10	27	0.0	100.0	10^{-3}	100000	80.0	1.0	11
1.00	27	0.0	100.0	10^{-3}	100000	80.0	1.0	11
2.00	27	0.0	100.0	10^{-3}	100000	80.0	1.0	11
3.00	27	0.0	100.0	10^{-3}	100000	80.0	1.0	11
10.00	27	0.0	100.0	10^{-3}	100000	80.0	1.0	11
30.00	27	0.0	100.0	10^{-3}	100000	60.0	5.0	7
10^2	27	0.0	100.0	10^{-3}	100000	60.0	5.0	7
10^3	27	0.0	100.0	10^{-3}	100000	60.0	5.0	7
10^4	27	0.0	100.0	10^{-3}	100000	60.0	5.0	7
10^5	27	0.0	85.0	10^{-4}	850000	60.0	5.0	5
10.00	123	0.0	40.0	10^{-3}	40000	35.0		1

Table 8.4: Statistics for simulations of hard spheres at volume fraction ϕ=0.51 and different Péclet numbers. Table captions are the same as shown in Table 6.1.a. Initial random samples of particles are selected for the runs with Pe=1, 10 and 10^5 with 27 particles and Pe=10 with 123 particles. There are two series of continuing runs for 27 particles and the orders of the run series are given by the bracketed numbers shown in column (1). The first run series follows the order of [1], [2], [3+], [4+] and [5+] and the second run series follows the order of [1], [2], [3-] and [4-].

Pe	N	t_{start}	t_{end}	Δt_{set}	NSTEPS	t_{diff}	t_{shift}	# *trials*
[4−] 0.01	27	300.0	400.0	10^{-4}	10^6	90.0	1.0	11
[3−] 0.10	27	200.0	300.0	10^{-4}	10^6	90.0	1.0	11
1.00	27	0.0	100.0	10^{-3}	100000	70.0	2.0	16
[4−] 3.00	27	300.0	400.0	10^{-3}	100000	70.0	2.0	16
[1] 10.00	27	0.0	100.0	10^{-3}	100000	70.0	2.0	16
[2] 10^2	27	100.0	200.0	10^{-3}	100000	70.0	2.0	16
[4−] $3x10^2$	27	300.0	400.0	10^{-3}	100000	70.0	2.0	16
[3+] 10^3	27	200.0	300.0	10^{-3}	100000	70.0	5.0	9
[4+] $2x10^3$	27	300.0	400.0	10^{-3}	100000	70.0	5.0	9
[5+] 10^4	27	400.0	500.0	10^{-3}	100000	70.0	5.0	9
10^5	27	0.0	45.0	10^{-4}	450000	30.0	1.0	6
10.00	123	0.0	40.0	10^{-3}	40000	35.0		1

Table 8.5: Statistics for simulations of hard spheres at volume fraction ϕ=0.55 and different Péclet numbers. Table captions are the same as shown in Table 6.1.a. Initial random particle configurations are chosen for the run with Pe=0.01, 3, 10, 30 and 10^5. A series of continuing runs are carried out with the order of Pe from [1] to [4] as shown in column (1). Except a special run with 126 particles at Pe=10, all other runs are with 28 particles.

Pe	N	t_{start}	t_{end}	Δt_{set}	NSTEPS	t_{diff}	t_{shift}	# *trials*
0.01	28	0.0	100.0	10^{-4}	10^6	90.0	1.0	11
[4] 0.10	28	300.0	400.0	10^{-4}	10^6	80.0	2.0	11
[4] 1.00	28	300.0	400.0	5×10^{-4}	200000	80.0	2.0	11
3.00	28	0.0	100.0	10^{-3}	100000	90.0	1.0	11
[1] 10.00	28	0.0	100.0	10^{-3}	100000	60.0	5.0	9
30.00	28	0.0	100.0	10^{-3}	100000	60.0	5.0	9
[2] 10^2	28	100.0	200.0	10^{-3}	100000	60.0	5.0	9
[3] 10^3	28	200.0	300.0	10^{-3}	100000	60.0	5.0	9
[4] 10^4	28	300.0	360.0	5×10^{-4}	120000	50.0	1.0	11
10^5	28	0.0	60.0	10^{-5}	600000	50.0	1.0	6
10.00	126	0.0	40.0	10^{-3}	40000	35.0		1

Table 8.6: Results of the shear viscosities obtained by Stokesian dynamics for hard spheres at volume fraction ϕ=0.47 and different Péclet numbers. Table captions are the same as shown in Table 6.2.a.

Pe	N	η_H	σ_{η_H}	η_B	σ_{η_B}	η_T	σ_{η_T}
0.01	27	5.191	0.033	14.937	10.187	21.127	10.231
[1] 0.10	27	5.156	0.013	14.244	3.063	20.399	3.103
[2] 1.00	27	6.804	0.092	6.501	1.751	14.305	1.845
[3] 3.00	27	3.930	0.061	1.092	0.074	6.022	0.135
[4] 7.00	27	3.140	0.012	0.147	0.005	4.287	0.017
[5] 10.00	27	3.084	0.030	0.097	0.017	4.181	0.042
[6] 20.00	27	5.536	0.316	0.586	0.073	7.122	0.389
[7] 10^2	27	7.604	0.523	0.240	0.028	8.844	0.551
[8] 10^3	27	11.146	0.186	0.042	0.001	12.188	0.187
[9] 10^4	27	13.922	1.438	0.005	0.000	14.927	1.438
10^5	27	22.877	3.092	0.001	0.000	23.877	3.092

Table 8.7: Results of the shear viscosities obtained by Stokesian dynamics for hard spheres at volume fraction ϕ=0.48 and different Péclet numbers. Table captions are the same as shown in Table 6.2.a. The last section of the table give the results of the simulations for a monolayer (2D) with 80 and 120 particles.

Pe	N	η_H	σ_{η_H}	η_B	σ_{η_B}	η_T	σ_{η_T}
[1] 0.43	123	6.001		8.752		15.757	
[2] 10.00	123	4.673		0.876		6.549	
[3] 10^3	123	11.408		0.043		12.451	
0.01	80,2D	6.029		18.751		25.780	
1.00	80,2D	5.956		5.949		12.905	
[1] 10.00	80,2D	3.898		0.853		5.751	
20.00	80,2D	7.203		0.755		8.958	
10^3	80,2D	13.084		0.038		14.122	
[2] 10^4	80,2D	15.736		0.004		16.740	
[2] 10^5	80,2D	22.632		0.001		23.633	
10.00	120,2D	3.769		1.115		5.884	

Table 8.8: Results of the shear viscosities obtained by Stokesian dynamics for hard spheres at volume fraction ϕ=0.49 and different Péclet numbers. Table captions are the same as shown in Table 6.2.a.

Pe	N	η_H	σ_{η_H}	η_B	σ_{η_B}	η_T	σ_{η_T}
0.01	27	6.052	0.504	22.670	13.723	29.721	13.800
0.10	27	6.011	1.245	15.111	5.007	22.122	5.850
1.00	27	6.246	0.030	5.947	0.069	13.193	0.099
2.00	27	4.933	0.014	2.451	0.018	8.384	0.032
3.00	27	4.329	0.216	1.172	0.256	6.501	0.472
10.00	27	4.031	0.014	0.595	0.002	5.626	0.014
30.00	27	6.645	0.083	0.569	0.018	8.173	0.101
10^2	27	8.623	0.266	0.298	0.023	9.921	0.289
10^3	27	12.375	1.373	0.051	0.002	13.426	1.375
10^4	27	18.643	3.291	0.008	0.000	19.651	3.292
10^5	27	31.097	5.238	0.001	0.000	30.098	5.238
10.00	123	4.239		0.351		5.590	

Table 8.9: Results of the shear viscosities obtained by Stokesian dynamics for hard spheres at volume fraction ϕ=0.51 and different Péclet numbers. Table captions are the same as shown in Table 6.2.a.

Pe	N	η_H	σ_{η_H}	η_B	σ_{η_B}	η_T	σ_{η_T}
$^{[4-]}0.01$	27	6.841	0.009	134.500	51.083	142.340	51.091
$^{[3-]}0.10$	27	6.696	0.052	21.757	8.197	29.454	8.243
1.00	27	6.804	0.021	6.501	0.265	14.305	0.266
$^{[4-]}3.00$	27	5.083	0.041	1.653	0.065	7.737	0.106
$^{[1]}10.00$	27	4.107	0.015	0.147	0.001	5.525	0.015
$^{[2]}10^2$	27	8.450	0.070	0.265	0.008	9.715	0.079
$^{[4-]}3\text{x}10^2$	27	12.512	0.565	0.179	0.015	13.691	0.581
$^{[3+]}10^3$	27	16.778	1.447	0.084	0.004	17.862	1.450
$^{[4+]}2\text{x}10^3$	27	17.504	3.149	0.044	0.001	18.548	3.150
$^{[5+]}10^4$	27	21.992	5.572	0.001	0.041	22.993	5.613
10^5	27	44.556	8.560	0.001	0.000	45.557	8.560
10.00	123	5.035		0.290		6.325	

Table 8.10: Results of the shear viscosities obtained by Stokesian dynamics for hard spheres at volume fraction ϕ=0.55 and different Péclet numbers. Table captions are the same as shown in Table 6.2.a.

Pe	N	η_H	σ_{η_H}	η_B	σ_{η_B}	η_T	σ_{η_T}
0.01	28	11.346	0.157	774.575	63.685	786.925	63.837
[4]0.10	28	11.298	0.062	70.526	12.870	82.824	13.066
[4]1.00	28	12.945	0.114	20.982	0.327	34.927	0.437
3.00	28	11.559	0.150	8.767	0.202	21.325	0.348
[1]10.00	28	8.305	0.083	1.929	0.060	11.234	0.141
30.00	28	8.178	0.075	0.769	0.023	9.947	0.097
[2]10^2	28	8.787	0.051	0.301	0.007	10.088	0.058
[3]10^3	28	13.806	0.148	0.090	0.003	14.895	0.151
[4]10^4	28	47.299	2.349	0.035	0.003	48.344	2.351
10^5	28	55.981	5.362	0.003	0.001	56.984	5.362
10.00	126	8.429		2.123		11.552	

Table 8.11: Results of the normal stress differences obtained by Stokesian dynamics for hard spheres at volume fraction ϕ=0.47 and different Péclet numbers. Table captions are the same as shown in Table 6.3.a.

Pe	N	χ_{1H}	$\sigma_{\chi_{1H}}$	χ_{1B}	$\sigma_{\chi_{1B}}$	χ_{1T}	$\sigma_{\chi_{1T}}$	χ_{2H}	$\sigma_{\chi_{2H}}$	χ_{2B}	$\sigma_{\chi_{2B}}$	χ_{2T}	$\sigma_{\chi_{2T}}$
0.01	27	0.044	0.001	-103.230	21.241	-103.180	21.243	0.027	0.013	8.076	0.806	8.104	0.817
[1] 0.10	27	0.188	0.013	-7.470	1.179	-7.282	1.180	0.244	0.163	3.750	0.883	3.994	0.889
[2] 1.00	27	0.379	0.034	-3.862	0.444	-3.483	0.421	0.956	0.013	1.954	0.185	2.910	0.188
[3] 3.00	27	0.298	0.024	-0.942	0.073	-0.644	0.062	0.445	0.029	0.786	0.142	1.231	0.139
[4] 7.00	27	0.282	0.013	-1.105	0.035	1.387	0.045	0.110	0.006	0.588	0.013	0.698	0.016
[5] 10.00	27	0.370	0.076	-0.823	0.108	1.243	0.094	0.048	0.012	0.304	0.106	0.352	0.112
[6] 20.00	27	0.057	0.245	-0.685	0.178	-0.628	0.421	0.131	0.409	0.323	0.252	0.454	0.655
[7] 10^2	27	1.208	0.189	-0.118	0.041	1.090	0.228	1.088	0.474	0.038	0.045	1.126	0.518
[8] 10^3	27	1.903	0.304	-0.244	0.003	1.879	0.306	2.180	0.214	0.003	0.005	2.183	0.218
[9] 10^4	27	1.944	0.254	-0.003		1.940	0.254	3.149	0.298	0.002		3.149	0.298

Table 8.12: Results of the normal stress differences obtained by Stokesian dynamics for hard spheres at volume fraction ϕ=0.48 and different Péclet numbers. Table captions are the same as shown in Table 6.3.a.

Pe	N	χ_{1H}	$\sigma_{\chi_{1H}}$	χ_{1B}	$\sigma_{\chi_{1B}}$	χ_{1T}	$\sigma_{\chi_{1T}}$	χ_{2H}	$\sigma_{\chi_{2H}}$	χ_{2B}	$\sigma_{\chi_{2B}}$	χ_{2T}	$\sigma_{\chi_{2T}}$
[2] 10.00	123	0.002	0.001	0.524	0.034	0.526	0.036	0.199	0.121	0.368	0.065	0.567	0.186
[3] 10^3	123	2.182	0.094	-0.013	0.002	2.056	0.096	2.056	0.150	0.013	0.004	2.069	0.154
1.00	80,2D	0.232	0.032	-1.472	0.153	-1.240	0.179						
[1] 10.00	80,2D	0.610	0.086	-0.177	0.163	0.433	0.205						
20.00	80,2D	0.807	0.332	-0.289	0.106	0.518	0.438						
10^3	80,2D	0.798	0.140	-0.033	0.001	0.765	0.142						
[2] 10^4	80,2D	1.731	0.419	-0.002	0.001	1.729	0.419						
[2] 10^5	80,2D	4.378	2.154	-0.001		4.377	2.154						
10.00	120,2D	0.020	0.002	0.535	0.150	0.555	0.180						

Table 8.13: Results of the normal stress differences obtained by Stokesian dynamics for hard spheres at volume fraction ϕ=0.49 and different Péclet numbers. Table captions are the same as shown in Table 6.3.a.

Pe	N	χ_{1H}	$\sigma_{\chi_{1H}}$	χ_{1B}	$\sigma_{\chi_{1B}}$	χ_{1T}	$\sigma_{\chi_{1T}}$	χ_{2H}	$\sigma_{\chi_{2H}}$	χ_{2B}	$\sigma_{\chi_{2B}}$	χ_{2T}	$\sigma_{\chi_{2T}}$
0.01	27	0.189	0.015	-67.939	4.356	-67.750	4.368	0.133	0.006	75.514	9.308	75.674	9.311
0.10	27	0.212	0.018	-1.302	0.667	-1.090	0.673	0.278	0.006	2.914	0.689	3.192	0.692
1.00	27	0.511	0.020	-0.544	0.095	-0.033	0.082	0.765	0.009	0.688	0.092	1.453	0.100
2.00	27	0.436	0.009	2.816	0.128	3.252	0.136	0.661	0.006	0.410	0.106	1.071	0.109
3.00	27	0.149	0.032	2.116	0.400	2.265	0.374	0.628	0.079	0.268	0.127	0.896	0.110
10.00	27	0.212	0.008	1.778	0.042	1.990	0.042	0.083	0.004	0.620	0.038	0.703	0.040
30.00	27	0.281	0.056	-0.638	0.089	-0.357	0.141	0.020	0.132	-0.245	0.048	-0.226	0.176
10^2	27	0.466	0.200	-0.249	0.074	0.218	0.273	0.940	0.284	-0.046	0.070	0.894	0.353
10^3	27	1.388	0.156	-0.050	0.003	1.338	0.157	1.775	0.488	-0.009	0.008	1.767	0.497
10^4	27	2.994	0.488	-0.004	0.001	2.994	0.488	3.267	0.193	-0.002	0.001	3.265	0.194
10.00	123	0.002		0.276		0.278		0.087		0.334		0.421	

Table 8.14: Results of the normal stress differences obtained by Stokesian dynamics for hard spheres at volume fraction ϕ=0.51 and different Péclet numbers. Table captions are the same as shown in Table 6.3.a.

Pe	N	χ_{1H}	$\sigma_{\chi_{1H}}$	χ_{1B}	$\sigma_{\chi_{1B}}$	χ_{1T}	$\sigma_{\chi_{1T}}$	χ_{2H}	$\sigma_{\chi_{2H}}$	χ_{2B}	$\sigma_{\chi_{2B}}$	χ_{2T}	$\sigma_{\chi_{2T}}$
[4−]0.01	27	0.261	0.034	-120.300	5.898	-120.040	5.920	0.127	0.014	54.861	7.848	54.988	7.838
[3−]0.10	27	0.403	0.009	-9.161	1.322	-8.758	1.325	0.212	0.063	8.686	2.954	8.898	2.907
1.00	27	0.956	0.013	-1.954	0.185	-0.998	0.188	0.379	0.035	3.862	0.444	4.241	0.421
[4−]3.00	27	0.757	0.029	0.006	0.228	0.763	0.203	0.354	0.028	3.985	0.220	4.340	0.194
[1]10.00	27	0.173	0.009	0.738	0.063	0.911	0.067	0.219	0.025	2.929	0.280	3.148	0.257
[2]10^2 ,	27	0.538	0.102	0.036	0.024	0.574	0.118	0.007	0.148	-0.147	0.044	-0.140	0.190
[4−]$3\text{x}10^2$	27	2.009	0.322	-0.011	0.015	2.020	0.326	0.681	0.347	-0.141	0.022	0.540	0.36
[3+]10^3	27	2.178	0.214	-0.015	0.011	2.164	0.224	0.718	0.189	-0.074	0.008	0.643	0.194
[4+]$2\text{x}10^3$	27	2.880	0.409	-0.001	0.004	2.880	0.411	0.436	0.355	-0.053	0.008	0.383	0.362
[5+]10^4	27	4.381	0.690	-0.155	0.207	4.226	0.893	0.728	0.849	-1.019	0.161	-0.291	0.849
10.00	123	0.158		0.370		0.528		1.032		0.061		1.093	

Table 8.15: Results of the normal stress differences obtained by Stokesian dynamics for hard spheres at volume fraction ϕ=0.55 and different Péclet numbers. Table captions are the same as shown in Table 6.3.a.

Pe	N	χ_{1H}	$\sigma_{\chi_{1H}}$	χ_{1B}	$\sigma_{\chi_{1B}}$	χ_{1T}	$\sigma_{\chi_{1T}}$	χ_{2H}	$\sigma_{\chi_{2H}}$	χ_{2B}	$\sigma_{\chi_{2B}}$	χ_{2T}	$\sigma_{\chi_{2T}}$
0.01	28	1.931	0.152	-1173	21.866	-1171	21.995	0.852	0.138	1308	47.843	1309	47.951
[4] 0.10	28	1.381	0.074	-48.746	6.158	-47.366	6.108	0.453	0.091	2.461	8.477	2.913	8.524
[4] 1.00	28	1.271	0.059	-2.463	0.956	-1.193	0.905	2.109	0.031	4.162	0.702	6.271	0.720
3.00	28	1.587	0.125	4.340	0.510	5.927	0.517	2.142	0.094	4.516	0.526	2.188	0.614
[1] 10.00	28	0.568	0.052	7.155	0.200	7.723	0.183	1.200	0.046	-1.169	0.094	0.032	0.124
30.00	28	1.532	0.106	5.877	0.527	7.409	0.627	0.469	0.065	-1.309	0.090	-0.841	0.151
[2] 10^2	28	3.708	0.122	3.964	0.130	7.672	0.233	0.027	0.089	-0.792	0.071	-0.765	0.153
[3] 10^3	28	10.324	0.919	1.939	0.208	12.263	1.120	0.488	0.441	-0.237	0.017	0.251	0.456
[4] 10^4	28	8.076	0.444	0.020	0.001	8.096	0.444	9.884	0.767	-0.003	0.001	9.881	0.768
10.00	126	1.782		9.848		11.630		-0.681		-3.616		4.297	

Table 8.16: Results of the short-time self-diffusion coefficients obtained by Stokesian dynamics for hard spheres at volume fraction ϕ=0.47 and different Péclet numbers. Captions of the table are the same as shown in Table 6.4.a.

Pe	N	$D^{s}_{o_{xx}}$	$D^{s}_{o_{yy}}$	$D^{s}_{o_{zz}}$	$\langle D^{s}_{o} \rangle$	$\sigma_{D^{s}_{o}}$	$D^{s}_{r_{xx}}$	$D^{s}_{r_{yy}}$	$D^{s}_{r_{zz}}$	$\langle D^{s}_{r} \rangle$	$\sigma_{D^{s}_{r}}$
0.01	27	0.163	0.160	0.162	0.162	0.000	0.530	0.532	0.532	0.531	0.001
0.10	27	0.162	0.160	0.161	0.161	0.001	0.530	0.529	0.531	0.530	0.002
1.00	27	0.156	0.154	0.155	0.155	0.001	0.516	0.513	0.511	0.514	0.001
3.00	27	0.180	0.175	0.176	0.177	0.002	0.570	0.554	0.546	0.557	0.002
7.00	27	0.202	0.192	0.198	0.197	0.000	0.612	0.575	0.550	0.579	0.001
10.00	27	0.202	0.195	0.197	0.198	0.001	0.611	0.572	0.551	0.578	0.000
20.00	27	0.141	0.120	0.115	0.115	0.001	0.442	0.459	0.466	0.455	0.002
10^2	27	0.107	0.097	0.094	0.100	0.001	0.384	0.390	0.390	0.388	0.003
10^3	27	0.078	0.072	0.070	0.074	0.001	0.301	0.306	0.302	0.303	0.001
10^4	27	0.062	0.059	0.058	0.060	0.001	0.245	0.247	0.243	0.245	0.004
10^5	27	0.033	0.029	0.032	0.032	0.000	0.165	0.163	0.161	0.163	0.001

Table 8.17: Results of the short-time self-diffusion coefficients obtained by Stokesian dynamics for hard spheres at volume fraction ϕ=0.48 and different Péclet numbers. (*) denotes a monolayer run. Captions of the table are the same as shown in Table 6.4.a.

Pe	N	$D^s_{o_{xx}}$	$D^s_{o_{yy}}$	$D^s_{o_{zz}}$	$\langle D^s_o \rangle$	$\sigma_{D^s_o}$	$D^s_{r_{xx}}$	$D^s_{r_{yy}}$	$D^s_{r_{zz}}$	$\langle D^s_r \rangle$	$\sigma_{D^s_r}$
0.43	123	0.170	0.168	0.168	0.169		0.503	0.505	0.503	0.503	
10.00	123	0.194	0.161	0.156	0.170		0.494	0.516	0.526	0.512	
10^3	123	0.085	0.079	0.075	0.080		0.292	0.295	0.295	0.294	
0.01	80*	0.306	0.304		0.305	0.000			0.533	0.533	0.001
1.00	80*	0.288	0.281		0.284	0.000			0.491	0.491	0.000
10.00	80*	0.291	0.271		0.281	0.000			0.497	0.497	0.000
20.00	80*	0.282	0.265		0.274	0.001			0.483	0.483	0.001
10^3	80*	0.174	0.174		0.174	0.001			0.276	0.276	0.002
10^4	80*	0.146	0.157		0.152	0.002			0.221	0.221	0.002
10^5	80*	0.118	0.118		0.118	0.006			0.148	0.148	0.007
10.00	120*	0.318	0.350		0.333	0.002			0.570	0.570	0.003

Table 8.18: Results of the short-time self-diffusion coefficients obtained by Stokesian dynamics for hard spheres at volume fraction ϕ=0.49 and different Péclet numbers. Captions of the table are the same as shown in Table 6.4.a.

Pe	N	$D^s_{o_{xx}}$	$D^s_{o_{yy}}$	$D^s_{o_{zz}}$	$\langle D^s_o \rangle$	$\sigma_{D^s_o}$	$D^s_{r_{xx}}$	$D^s_{r_{yy}}$	$D^s_{r_{zz}}$	$\langle D^s_r \rangle$	$\sigma_{D^s_r}$
0.01	27	0.148	0.146	0.147	0.147	0.000	0.506	0.507	0.510	0.508	0.000
0.10	27	0.144	0.141	0.142	0.142	0.000	0.500	0.500	0.500	0.500	0.001
1.00	27	0.135	0.133	0.133	0.134	0.001	0.480	0.478	0.477	0.478	0.002
2.00	27	0.152	0.151	0.149	0.151	0.001	0.522	0.504	0.509	0.512	0.001
3.00	27	0.162	0.158	0.160	0.160	0.000	0.544	0.522	0.510	0.525	0.000
10.00	27	0.182	0.171	0.179	0.177	0.000	0.582	0.529	0.501	0.537	0.001
30.00	27	0.119	0.100	0.098	0.105	0.002	0.407	0.419	0.420	0.415	0.004
10^2	27	0.097	0.085	0.084	0.089	0.003	0.364	0.372	0.371	0.369	0.007
10^3	27	0.068	0.060	0.059	0.062	0.001	0.280	0.286	0.285	0.284	0.001
10^4	27	0.049	0.046	0.044	0.046	0.001	0.218	0.219	0.219	0.219	0.002
10^5	27	0.026	0.023	0.025	0.025	0.001	0.151	0.148	0.145	0.148	0.001
10.00	123	0.188	0.155	0.152	0.165		0.489	0.508	0.514	0.504	

Table 8.19: Results of the short-time self-diffusion coefficients obtained by Stokesian dynamics for hard spheres at volume fraction ϕ=0.51 and different Péclet numbers. Captions of the table are the same as shown in Table 6.4.a.

Pe	N	$D^*_{o_{xx}}$	$D^*_{o_{yy}}$	$D^*_{o_{zz}}$	$\langle D^*_o \rangle$	$\sigma_{D^*_o}$	$D^*_{r_{xx}}$	$D^*_{r_{yy}}$	$D^*_{r_{zz}}$	$\langle D^*_r \rangle$	$\sigma_{D^*_r}$
0.01	27	0.134	0.135	0.134	0.134	0.001	0.489	0.488	0.491	0.489	0.001
0.10	27	0.131	0.132	0.132	0.132	0.001	0.480	0.477	0.479	0.479	0.001
1.00	27	0.125	0.124	0.123	0.124	0.001	0.460	0.450	0.456	0.455	0.002
3.00	27	0.140	0.140	0.138	0.139	0.002	0.504	0.477	0.479	0.487	0.003
10.00	27	0.155	0.150	0.153	0.153	0.000	0.536	0.483	0.462	0.494	0.002
10^2	27	0.089	0.079	0.081	0.083	0.001	0.364	0.357	0.350	0.357	0.001
$3x10^2$	27	0.066	0.061	0.060	0.062	0.001	0.301	0.301	0.298	0.300	0.004
10^3	27	0.053	0.048	0.045	0.049	0.002	0.251	0.254	0.257	0.254	0.004
$2x10^3$	27	0.051	0.045	0.044	0.047	0.001	0.239	0.245	0.243	0.242	0.002
10^4	27	0.041	0.038	0.036	0.038	0.001	0.205	0.204	0.204	0.204	0.002
10^5	27	0.019	0.019	0.019	0.019	0.000	0.143	0.131	0.136	0.137	0.001
10.00	123	0.135	0.124	0.123	0.128		0.436	0.441	0.440	0.439	

Table 8.20: Results of the short-time self-diffusion coefficients obtained by Stokesian dynamics for hard spheres at volume fraction ϕ=0.55 and different Péclet numbers. Captions of the table are the same as shown in Table 6.4.a.

Pe	N	$D^s_{o_{xx}}$	$D^s_{o_{yy}}$	$D^s_{o_{zz}}$	$\langle D^s_o \rangle$	$\sigma_{D^s_o}$	$D^s_{r_{xx}}$	$D^s_{r_{yy}}$	$D^s_{r_{zz}}$	$\langle D^s_r \rangle$	$\sigma_{D^s_r}$
0.01	28	0.101	0.089	0.101	0.097	0.001	0.416	0.434	0.413	0.421	0.003
0.10	28	0.093	0.089	0.090	0.091	0.000	0.397	0.402	0.400	0.400	0.001
1.00	28	0.080	0.078	0.078	0.079	0.000	0.366	0.366	0.366	0.366	0.001
3.00	28	0.082	0.082	0.080	0.081	0.000	0.384	0.374	0.376	0.378	0.001
10.00	28	0.082	0.081	0.078	0.081	0.000	0.387	0.358	0.358	0.367	0.000
30.00	28	0.076	0.075	0.070	0.073	0.000	0.368	0.329	0.332	0.343	0.001
10^2	28	0.066	0.066	0.061	0.064	0.000	0.341	0.295	0.300	0.312	0.001
10^3	28	0.043	0.040	0.035	0.039	0.001	0.248	0.221	0.227	0.232	0.002
10^4	28	0.021	0.021	0.020	0.021	0.001	0.164	0.157	0.158	0.160	0.002
10.00	126	0.094	0.093	0.082	0.090		0.377	0.356	0.376	0.370	

Table 8.21: Results of the long-time self-diffusion coefficients obtained by Stokesian dynamics for hard spheres at volume fraction ϕ=0.47 and different Péclet numbers. All runs are with 27 particles. Captions for the table are the same as shown in Table 6.5.

Pe	$D^*_{\infty,yy}$	σ_{yy}	$D^*_{\infty,zz}$	σ_{zz}	t_{diff}	# *trials*
0.01	0.042	0.014	0.043	0.010	80.0	12
0.10	0.078	0.008	0.040	0.004	80.0	16
1.00	0.150	0.018	0.097	0.007	80.0	16
3.00	0.009	0.001	0.015	0.002	80.0	16
7.00	$2.4\text{x}10^{-4}$	0.000	$7.0\text{x}10^{-4}$	0.000	80.0	16
10.00	$4.9\text{x}10^{-4}$	0.000	$5.8\text{x}10^{-4}$	0.000	80.0	16
20.00	0.007	0.001	0.008	0.001	80.0	16
10^2	0.015	0.001	0.022	0.002	80.0	16
10^3	0.030	0.003	0.036	0.007	80.0	16
10^4	0.039	0.006	0.033	0.003	80.0	16

Table 8.22: Results of the long-time self-diffusion coefficients obtained by Stokesian dynamics for hard spheres at volume fraction ϕ=0.49 and different Péclet numbers. All runs are with 27 particles. Captions for the table are the same as shown in Table 6.5.

Pe	$D^s_{\infty,yy}$	σ_{yy}	$D^s_{\infty,zz}$	σ_{zz}	t_{diff}	# trials
0.01	0.023	0.001	0.043	0.001	90.0	11
0.10	0.041	0.006	0.060	0.007	80.0	16
1.00	0.160	0.011	0.089	0.007	80.0	16
2.00	0.030	0.003	0.032	0.004	80.0	16
3.00	0.021	0.001	0.020	0.003	80.0	16
10.00	$1.7\text{x}10^{-4}$	0.000	$1.8\text{x}10^{-4}$	0.000	95.0	4
30.00	0.003	0.000	0.002	0.000	85.0	11
10^2	0.010	0.001	0.021	0.002	80.0	16
10^3	0.020	0.003	0.042	0.005	80.0	16
10^4	0.052	0.004	0.048	0.003	80.0	16

Table 8.23: Results of the long-time self-diffusion coefficients obtained by Stokesian dynamics for hard spheres at volume fraction ϕ=0.51 and different Péclet numbers. All runs are with 27 particles. Captions for the table are the same as shown in Table 6.5.

Pe	$D^*_{\infty,yy}$	σ_{yy}	$D^*_{\infty,zz}$	σ_{zz}	t_{diff}	# *trials*
0.01	0.017	0.001	0.030	0.003	80.0	16
0.10	0.032	0.004	0.051	0.002	80.0	16
1.00	0.084	0.004	0.011	0.016	80.0	16
3.00	0.006	0.000	0.017	0.000	80.0	16
10.00	$3.0\text{x}10^{-4}$	0.000	$5.0\text{x}10^{-4}$	0.000	80.0	16
10^2	0.002	0.000	0.002	0.000	80.0	16
$3\text{x}10^2$	0.022	0.002	0.024	002	80.0	16
10^3	0.031	0.004	0.020	0.003	80.0	16
$2\text{x}10^3$	0.033	0.003	0.036	0.002	80.0	16
10^4	0.030	0.005	0.031	0.002	80.0	16

Table 8.24: Results of the long-time self-diffusion coefficients obtained by Stokesian dynamics for suspensions with ϕ=0.55 and different Péclet numbers. All runs are with 28 particles. Captions for the table are the same as shown in Table 6.5.

Pe	$D^{*}_{\infty,yy}$	σ_{yy}	$D^{*}_{\infty,zz}$	σ_{zz}	t_{diff}	# trials
0.01	0.010	0.001	0.013	0.001	90.0	6
0.10	0.031	0.006	0.027	0.004	80.0	16
1.00	0.149	0.017	0.136	0.020	80.0	16
3.00	0.029	0.004	0.062	0.003	80.0	16
10.00	0.002	0.000	0.010	0.002	80.0	16
30.00	0.001	0.000	0.005	0.001	80.0	16
10^2	$4.8\text{x}10^{-4}$	0.000	0.003	0.000	80.0	16
10^3	$5.2\text{x}10^{-4}$	0.000	0.002	0.000	80.0	16
10^4	0.065	0.009	0.087	0.001	50.0	6

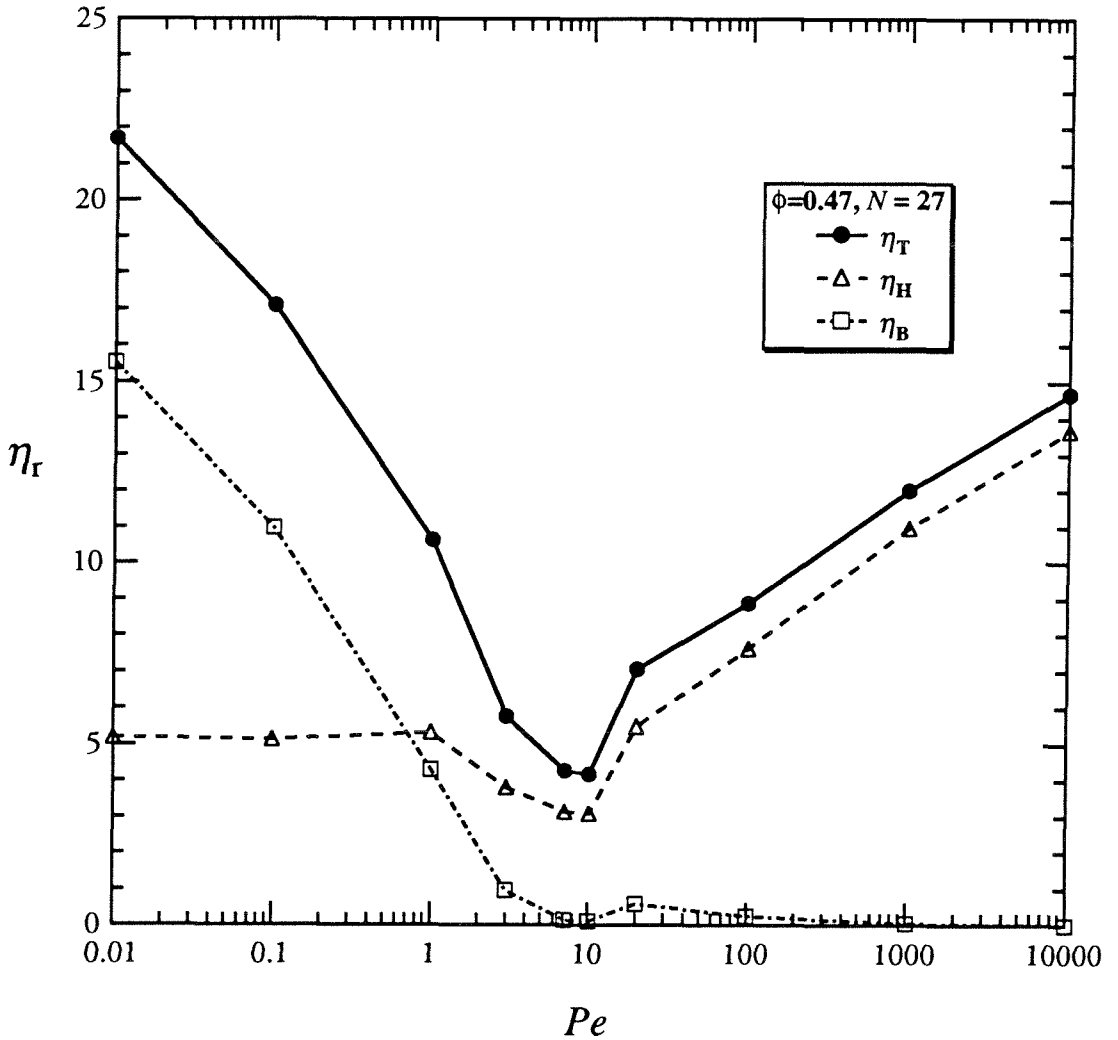

Figure 8.1: The relative viscosity η_r of hard-sphere suspensions at a volume fraction ϕ=0.47 obtained by Stokesian dynamics as a function of the Péclet number: total (●) shear viscosity η_T, hydrodynamic (Δ) viscosity η_H and Brownian (□) viscosity η_B.

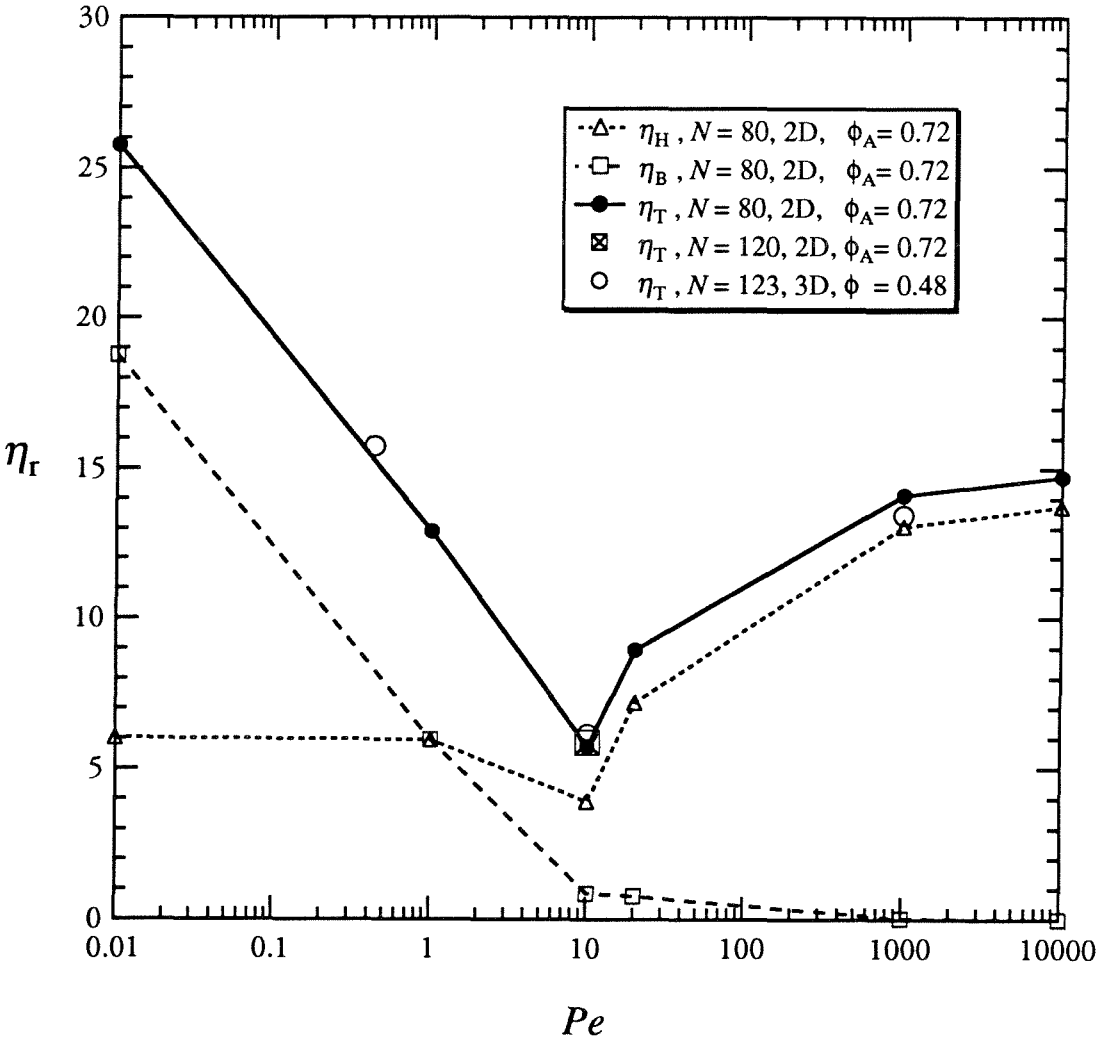

Figure 8.2: The relative viscosity of a monolayer at areal fraction ϕ_A= 0.72 and hard-sphere suspensions at a comparable volume fraction ϕ=0.48 obtained by Stokesian dynamics as a function of the Péclet number: total (●) shear viscosity, hydrodynamic (Δ) viscosity η_H and Brownian (□) viscosity η_B. The variation of the total shear viscosity is negligibly small for a monolayer with (●) 80 particles and (⊠) 120 particles at *Pe*=10 and a 3D model with 123 particles (○) at a comparable volume fraction ϕ=0.48 and *Pe*=0.43, 10 and 1000.

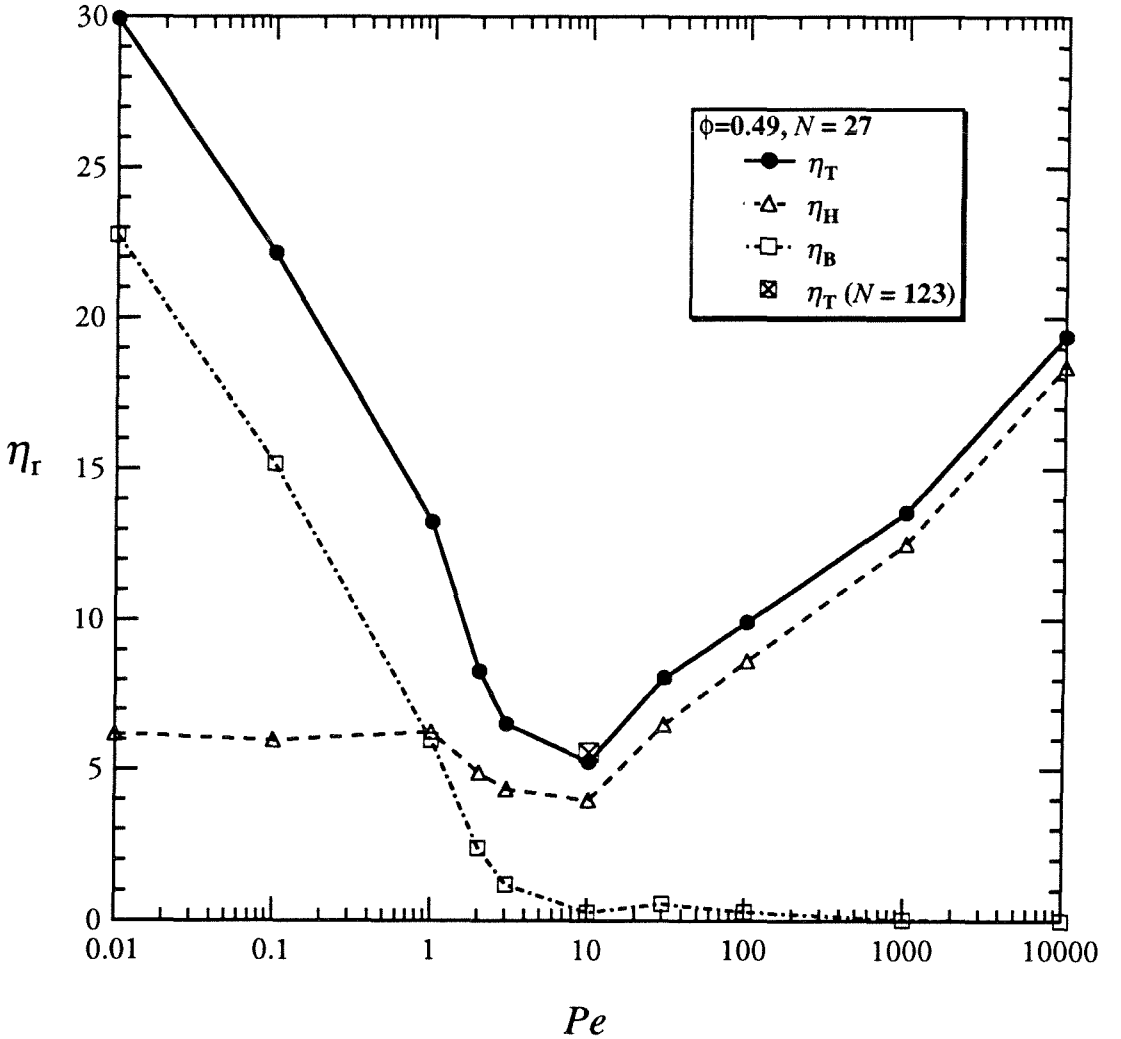

Figure 8.3: The relative viscosity η_r of a hard-sphere suspension at volume fraction ϕ=0.49 obtained by Stokesian dynamics as a function of the Péclet number: total (●) shear viscosity, hydrodynamic (Δ) viscosity η_H and Brownian (□) viscosity η_B. A comparison of the total shear viscosity at Pe=10 for 27 particles (●) and for 123 particles (⊠) at the same volume fraction shows negligible difference.

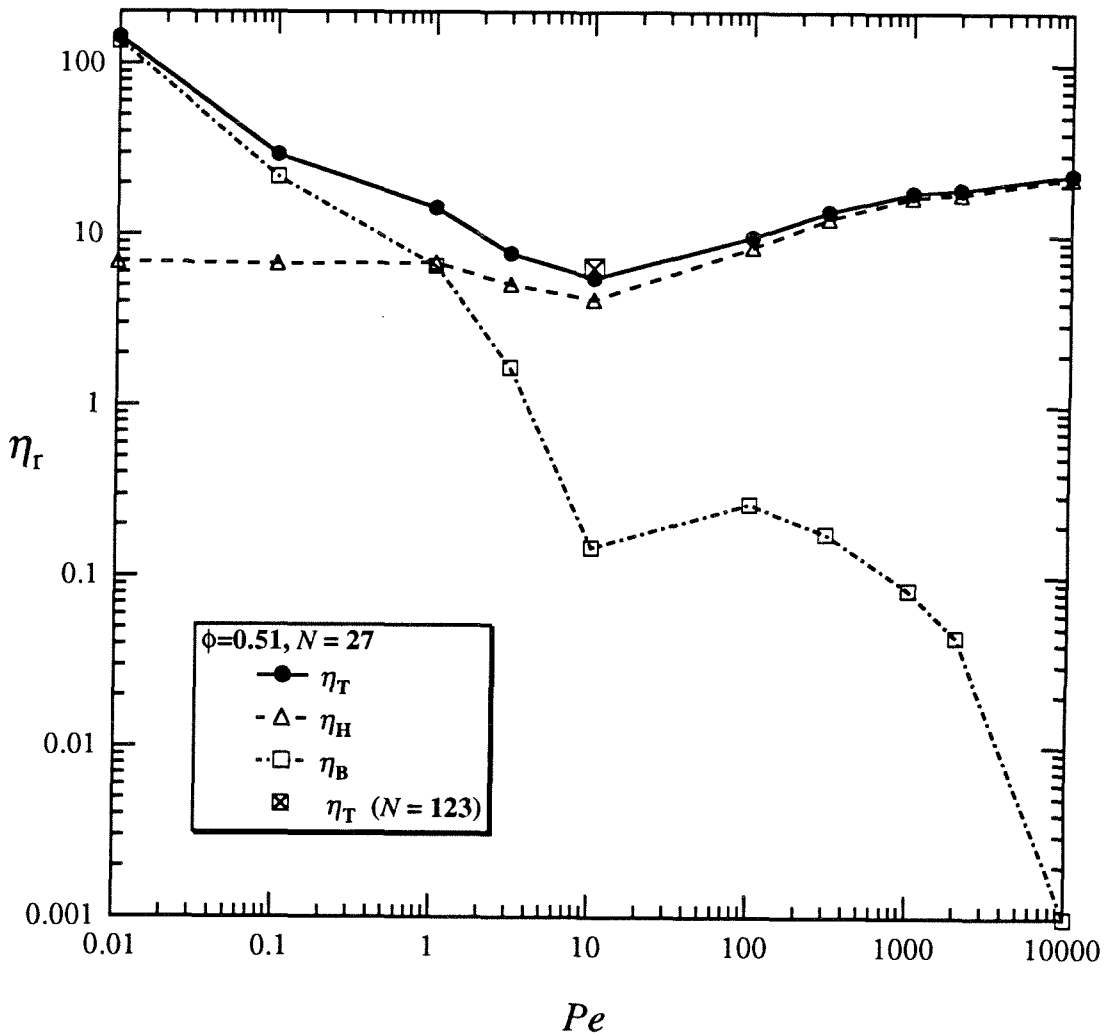

Figure 8.4: A log-log plot of the relative viscosity η_r of hard spheres at a volume fraction ϕ=0.51 obtained by Stokesian dynamics as a function of the Péclet number: total (●) shear viscosity, hydrodynamic (Δ) viscosity η_H and Brownian (□) viscosity η_B. A comparison of the total shear viscosity at Pe=10 for (●) 27 particles and for (⊠) 123 particles at the same volume fraction shows negligible variation.

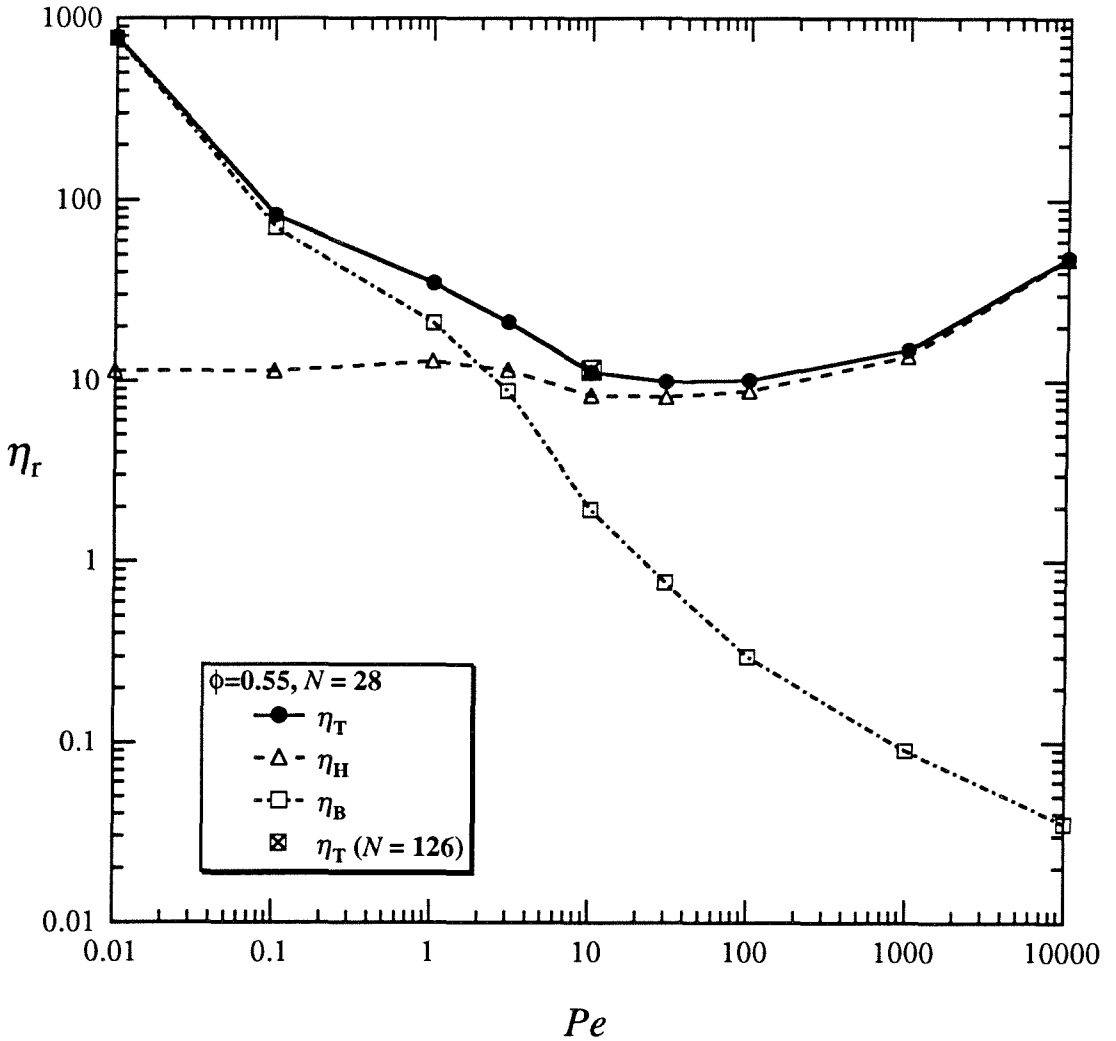

Figure 8.5: A log-log plot of the relative viscosity η_r of hard-sphere suspensions at a volume fraction ϕ=0.55 obtained by Stokesian dynamics as a function of the Péclet number: total (●) shear viscosity, hydrodynamic (Δ) viscosity η_H and Brownian (□) viscosity η_B. The total shear viscosity shows lilltle variation in changing the number of particles from 28 (●) to 126 particles (⊠) at Pe=10.

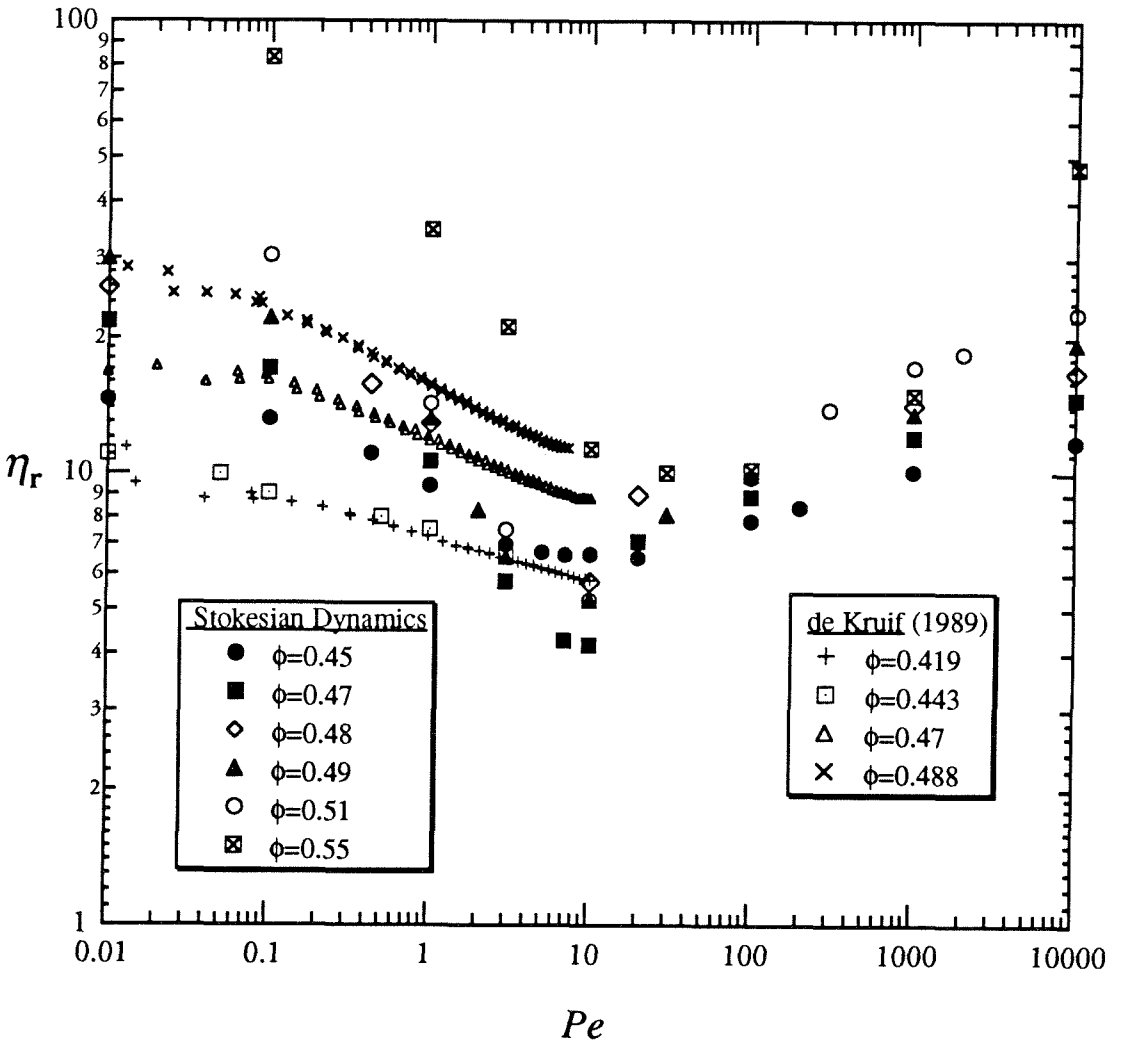

Figure 8.6: Comparison of the simulation results for the steady shear viscosity as a function of the Péclet number and different volume fractions: ϕ = (●) 0.45, (■) 0.47, (◊) 0.48, (▲) 0.49, (○) 0.51 and (⊠) 0.55 with the experiments of van der Werff and de Kruif (1989): (+) 0.419±0.01, (⊡) 0.443±0.01, (△) 0.47±0.01 and (×) 0.488±0.01.

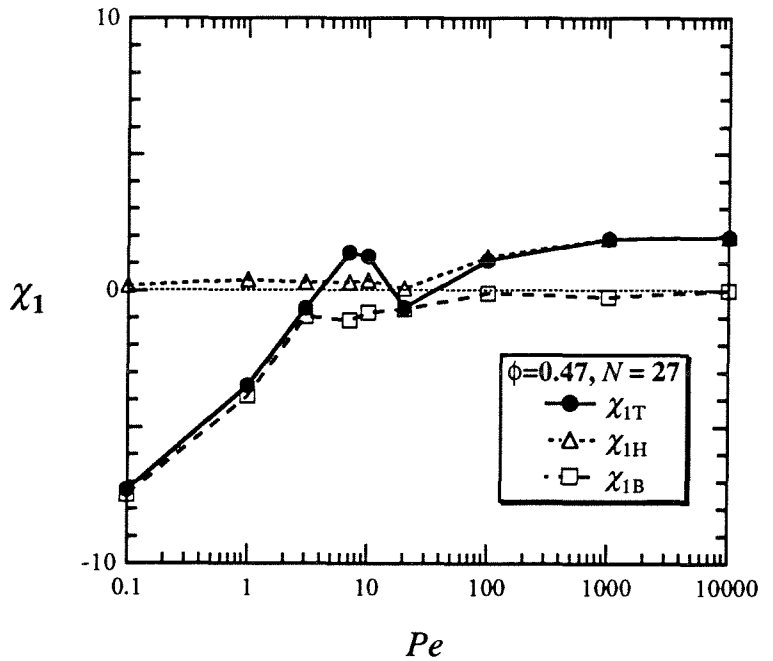

Figure 8.7.a

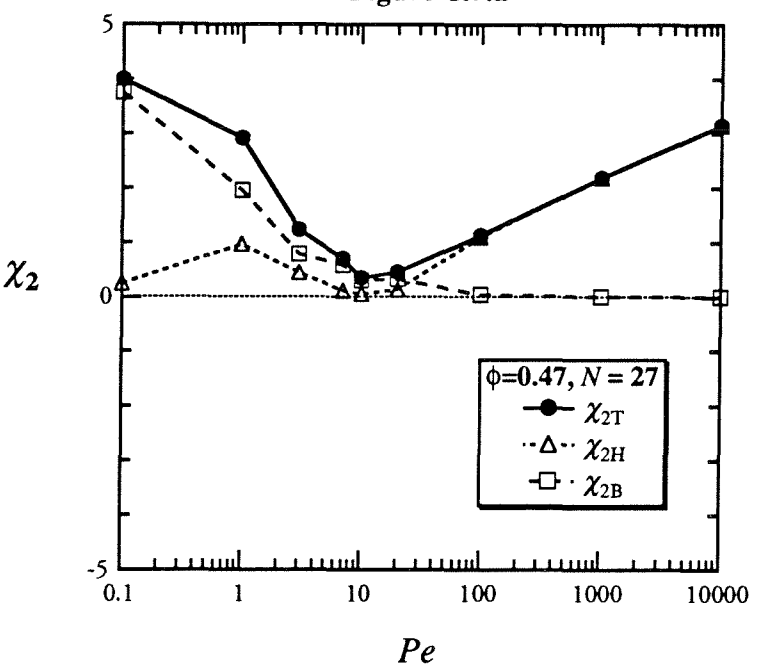

Figure 8.7.b

Figure 8.7.a-b: The first (Fig.8.7.a) and second (Fig.8.7.b) normal stress differences for hard spheres at volume fraction ϕ=0.47 obtained by Stokesian dynamics as a function of the Péclet number: total (●) normal stress differences, hydrodynamic (Δ) and Brownian (□) contribution.

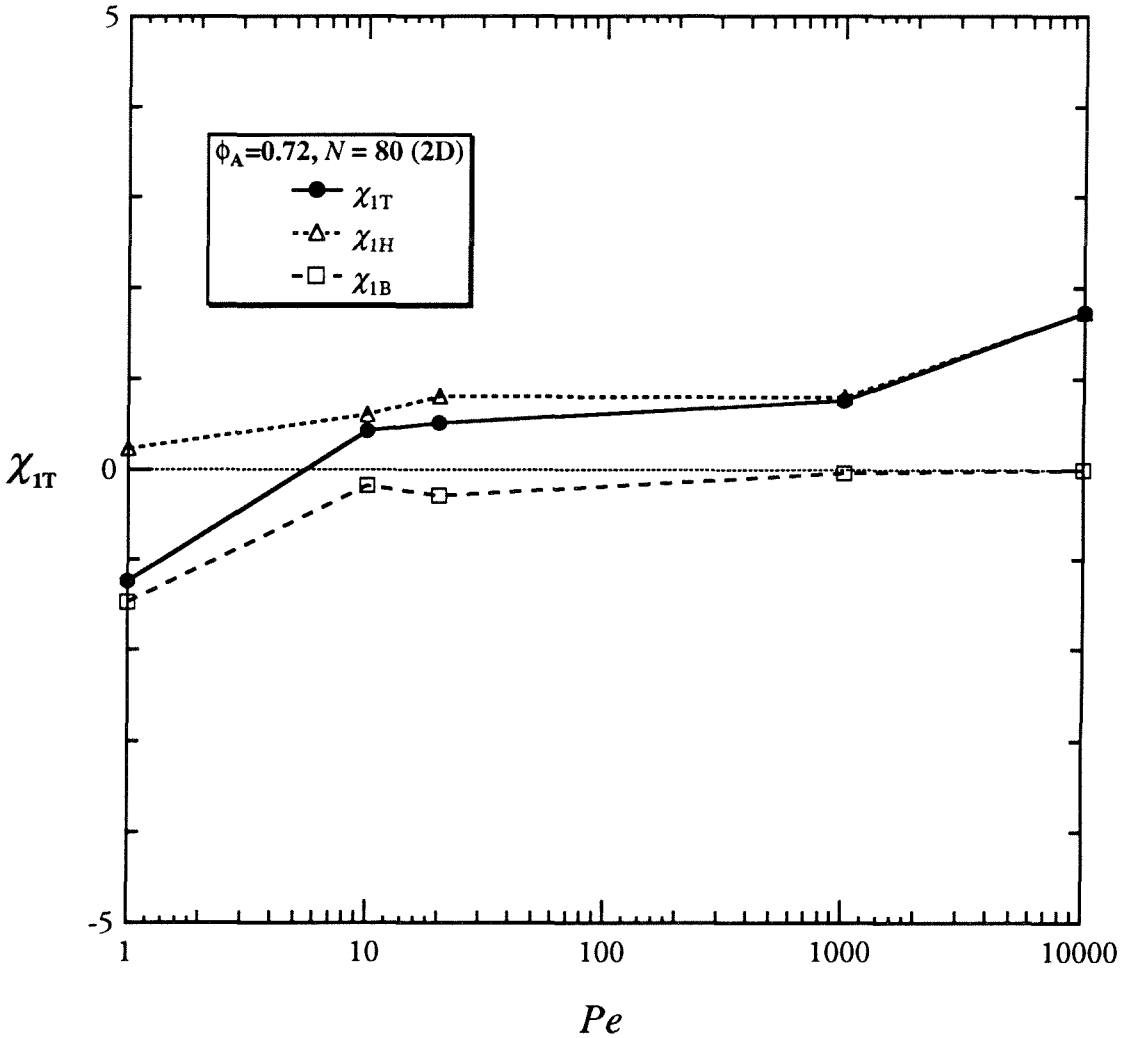

Figure 8.8: The first normal stress difference χ_1 for a monolayer with 80 particles at areal fraction ϕ_A= 0.72 obtained by Stokesian dynamics as a function of the Péclet number: total (●) first normal stress difference, hydrodynamic (Δ) and Brownian (□) contribution.

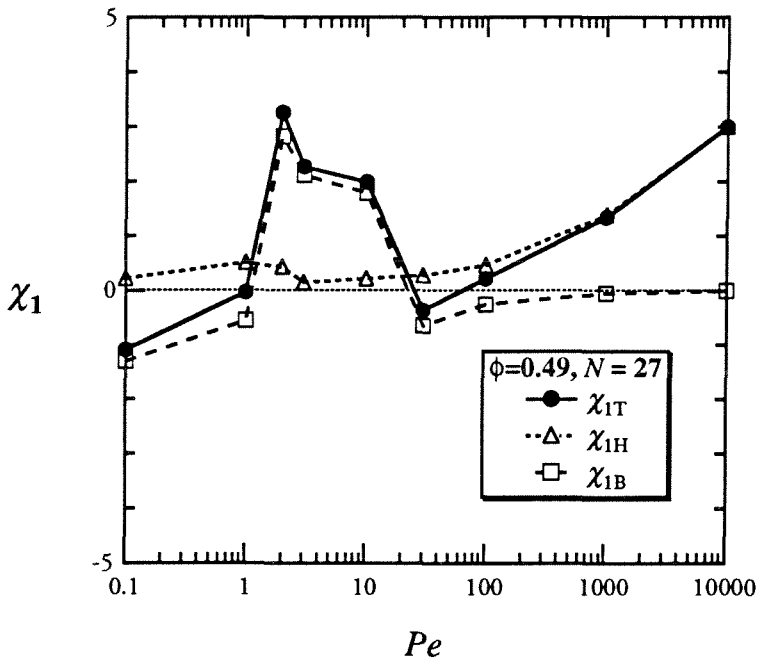

Figure 8.9.a

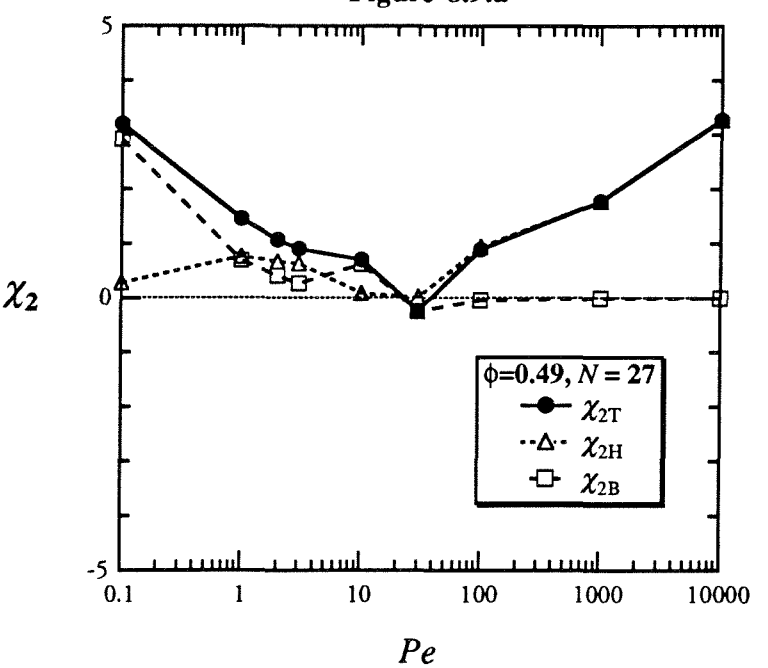

Figure 8.9.b

Figure 8.9.a-b: The first (Fig.8.9.a) and second (Fig.8.9.b) normal stress differences for hard spheres at volume fraction ϕ=0.49 obtained by Stokesian dynamics as a function of the Péclet number: total (●) normal stress differences, hydrodynamic (Δ) and Brownian (□) contribution.

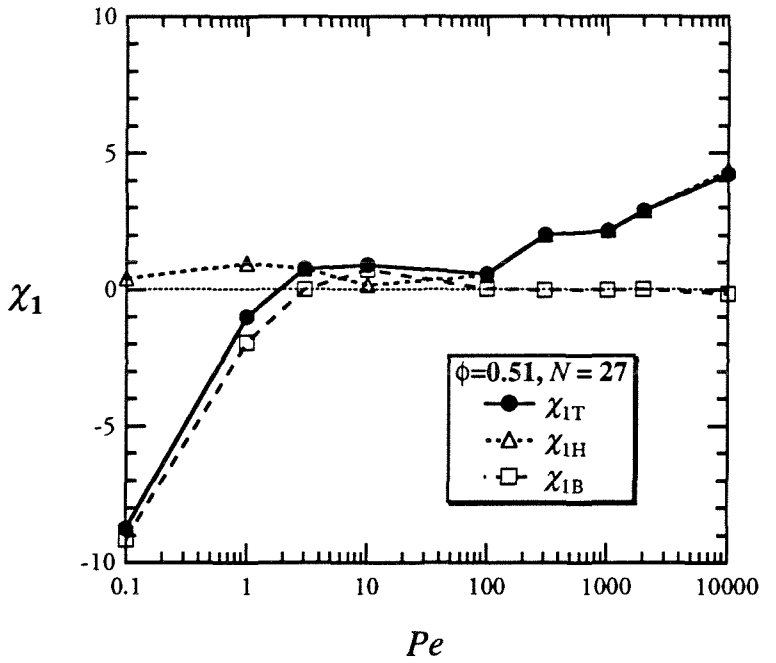

Figure 8.10.a

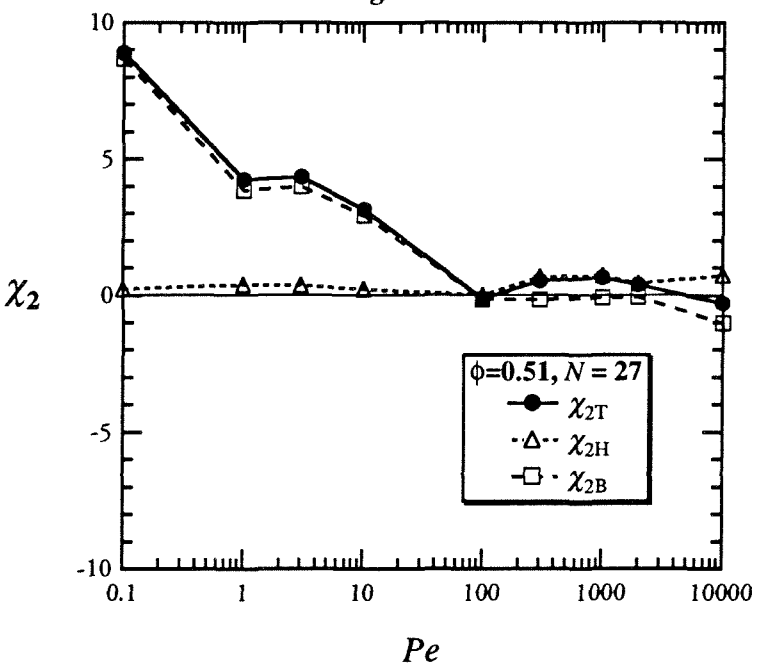

Figure 8.10.b

Figure 8.10.a-b: The first (Fig.8.10.a) and second (Fig.8.10.b) normal stress differences for hard spheres at volume fraction ϕ=0.51 obtained by Stokesian dynamics as a function of the Péclet number: total (●) normal stress differences, hydrodynamic (Δ) and Brownian (□) contribution.

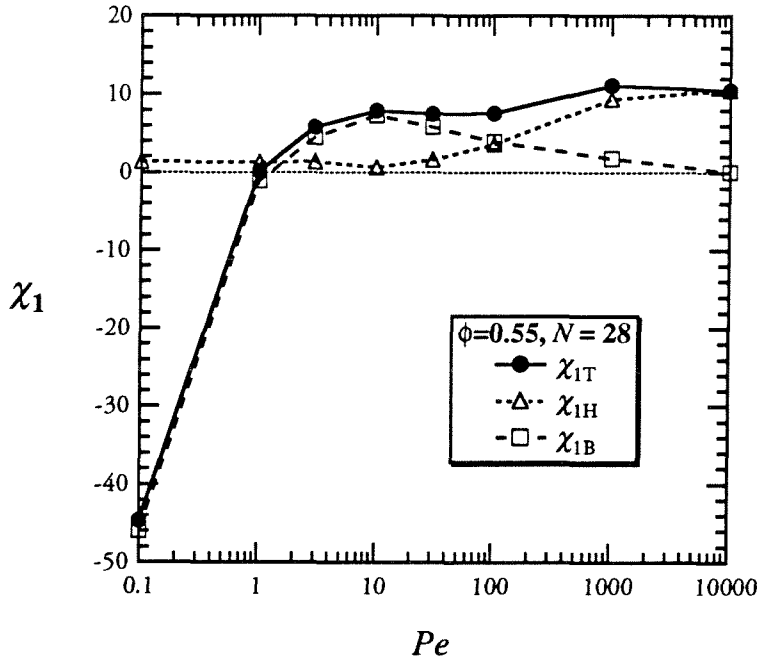

Figure 8.11.a

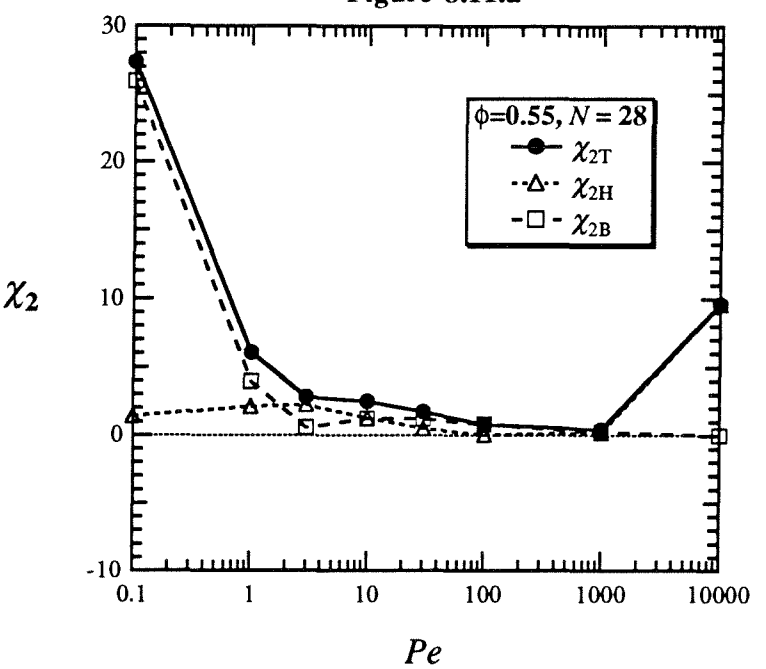

Figure 8.11.b

Figure 8.11.a-b: The first (Fig.8.11.a) and second (Fig.8.11.b) normal stress differences for hard spheres at volume fraction ϕ=0.55 obtained by Stokesian dynamics as a function of the Péclet number: total (●) normal stress differences, hydrodynamic (Δ) and Brownian (□) contribution.

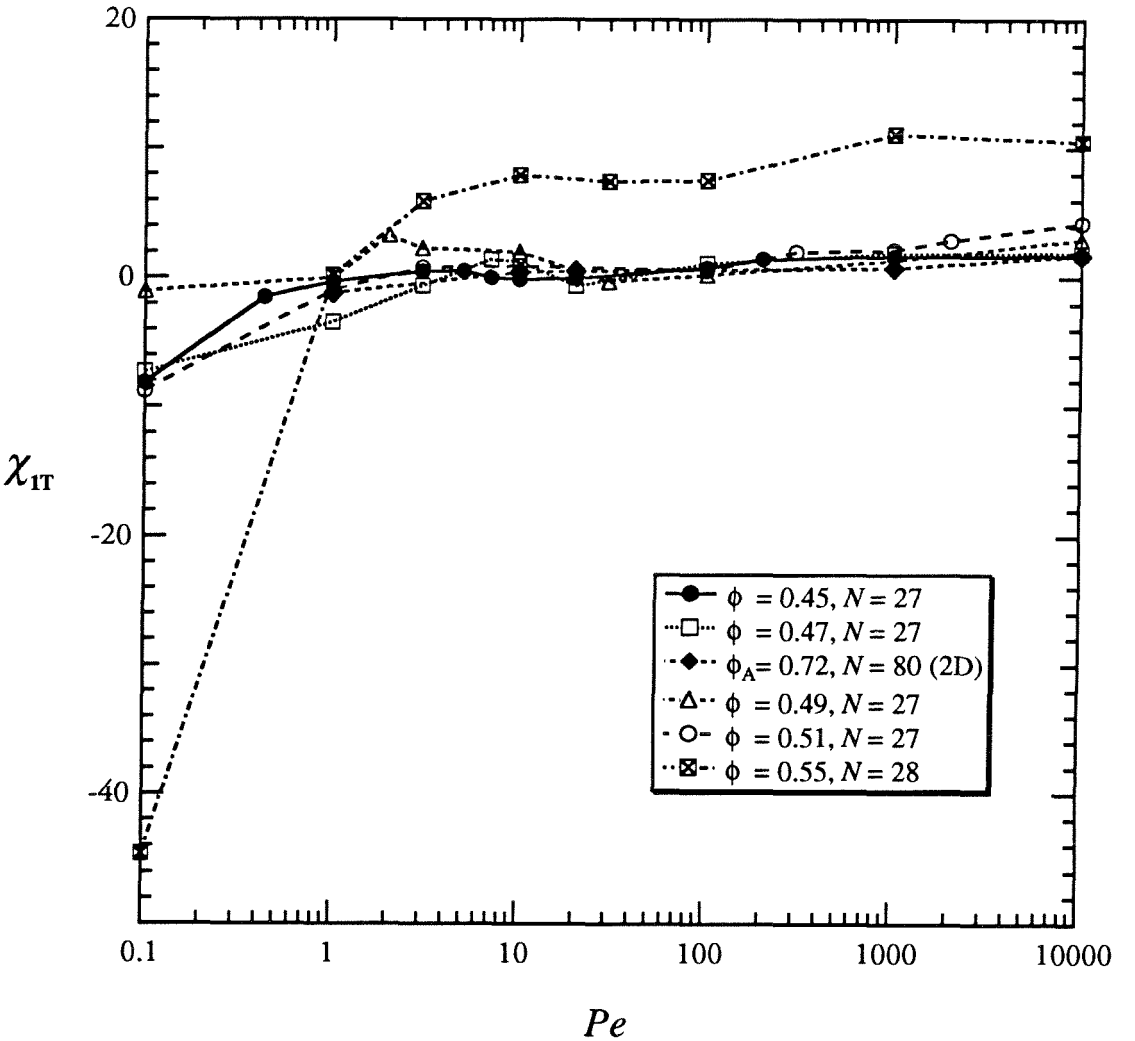

Figure 8.12.a: The total first normal stress differences χ_{1T} for hard spheres obtained by Stokesian dynamics as a function of the Péclet number and different volume fractions ϕ = (●) 0.45, (□) 0.47, (Δ) 0.49, (○) 0.51 and (⊠) 0.55. Results for the first total normal stress differences of a monolayer with 80 particles (◆) at areal fraction ϕ_A= 0.72 (comparable to a volume fraction ϕ=0.48) is also plotted in the figure.

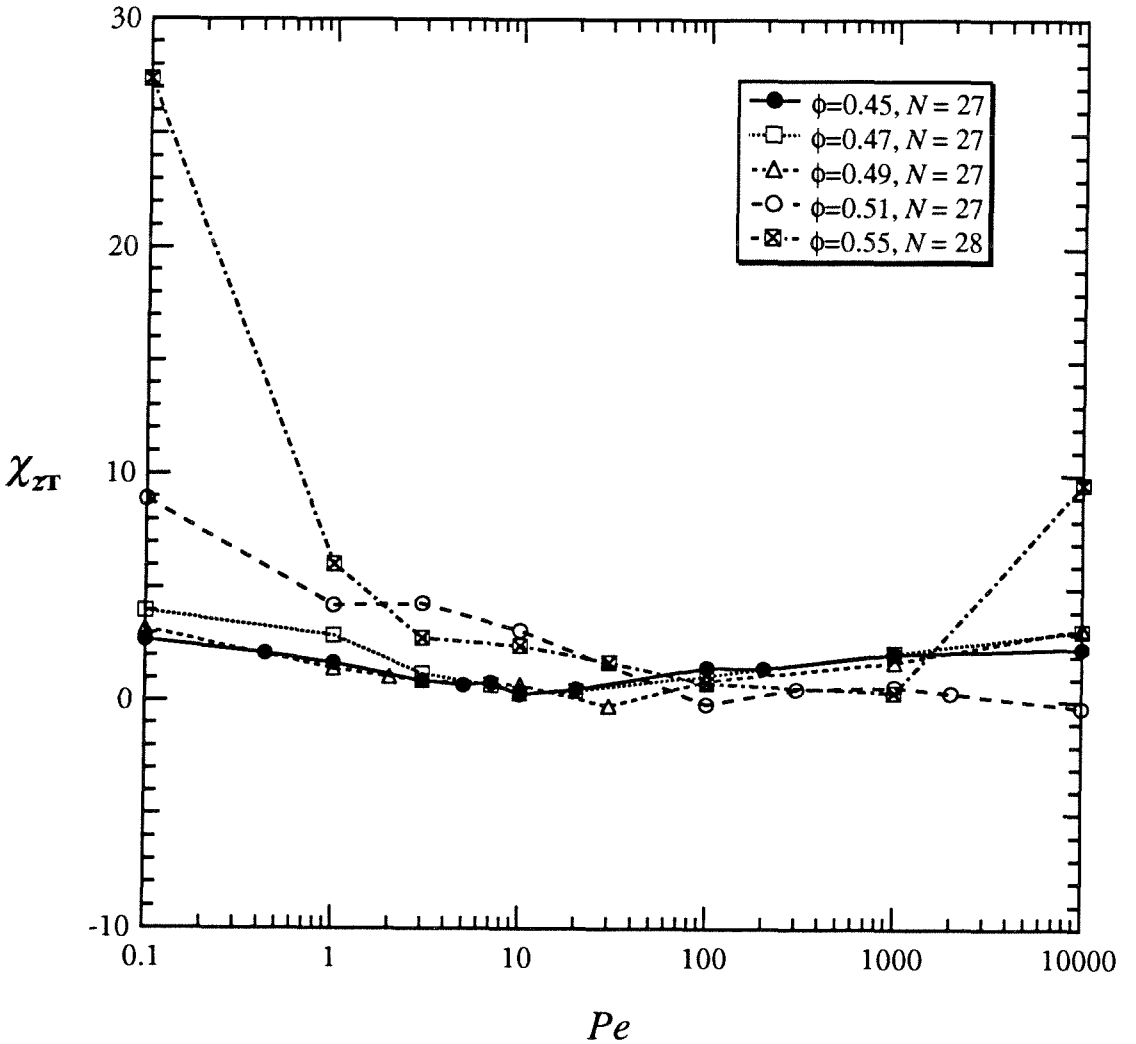

Figure 8.12.b: The total second normal stress differences χ_{2T} for hard spheres obtained by Stokesian dynamics as a function of the Péclet number and different volume fractions ϕ = (●) 0.45, (□) 0.47, (Δ) 0.49, (○) 0.51 and (⊠) 0.55.

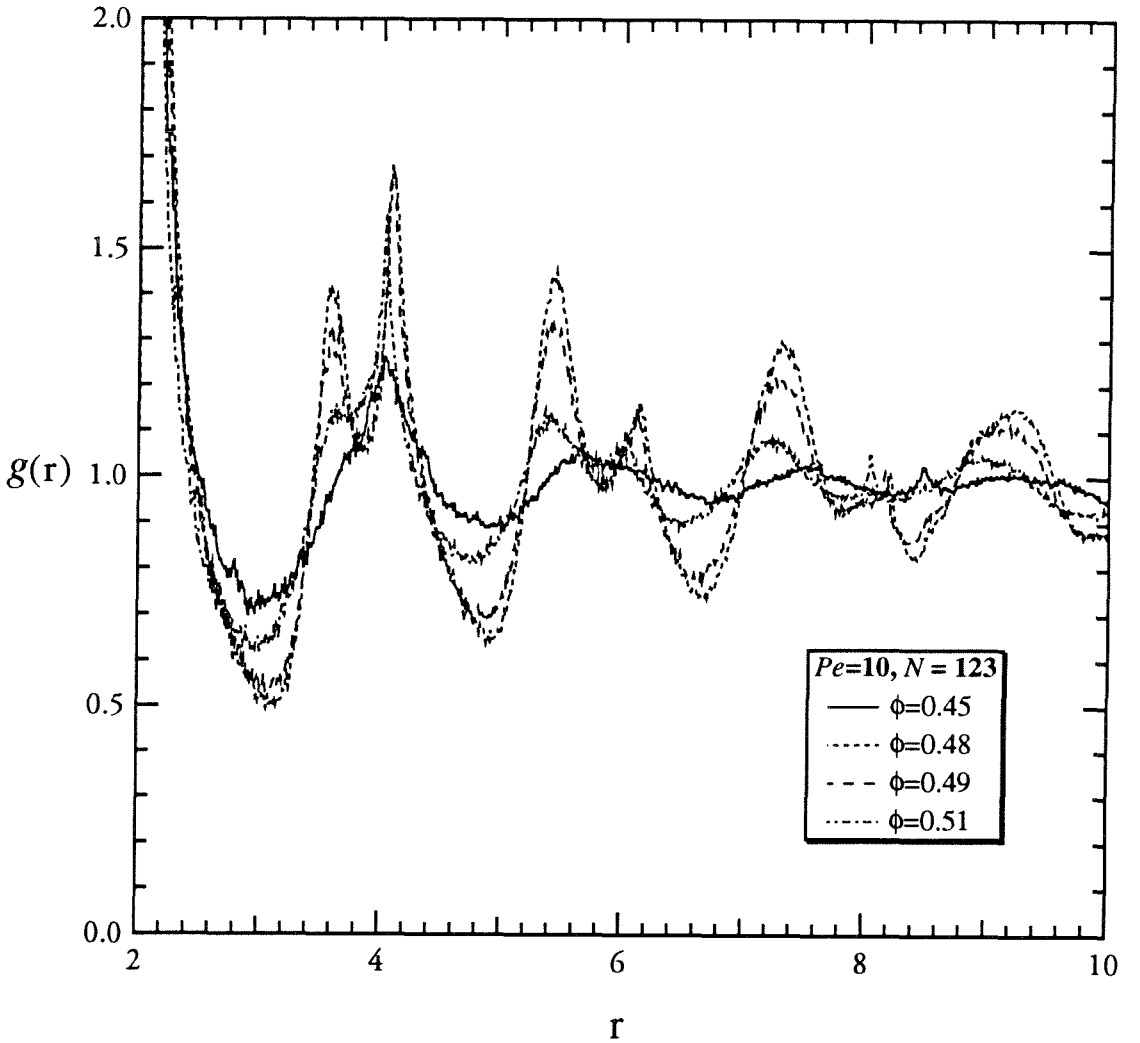

Figure 8.13.a: The radial dependence of the pair-distribution function $g(r)$ determined by Stokesian dynamics for hard-sphere suspensions with Pe=10 and different volume fractions ϕ = (solid curve) 0.45, (dotted curve) 0.48, (dashed curve) 0.49 and (dotted-dash curve) 0.51. There are 123 particles in the unit cell. Note the change of the radial pair-distribution function as the volume fraction increases from 0.45. $g(2)$ for ϕ=0.48, 0.49 and 0.51 shows two strong double peaks at the particle center-center radial spacing $r\approx4$ and $r\approx6$ and two less intense single peaks at $r\approx7$ and $r\approx9$. In comparison to $g(r)$ for ϕ=0.45, the twin-peaked pattern of $g(r)$ for these dense hard spheres reflects a slight distortion and stretching to the symmetry of the hexagonal packing for ϕ=0.48, 0.49 and 0.51 (cf. Fig.8.21.c).

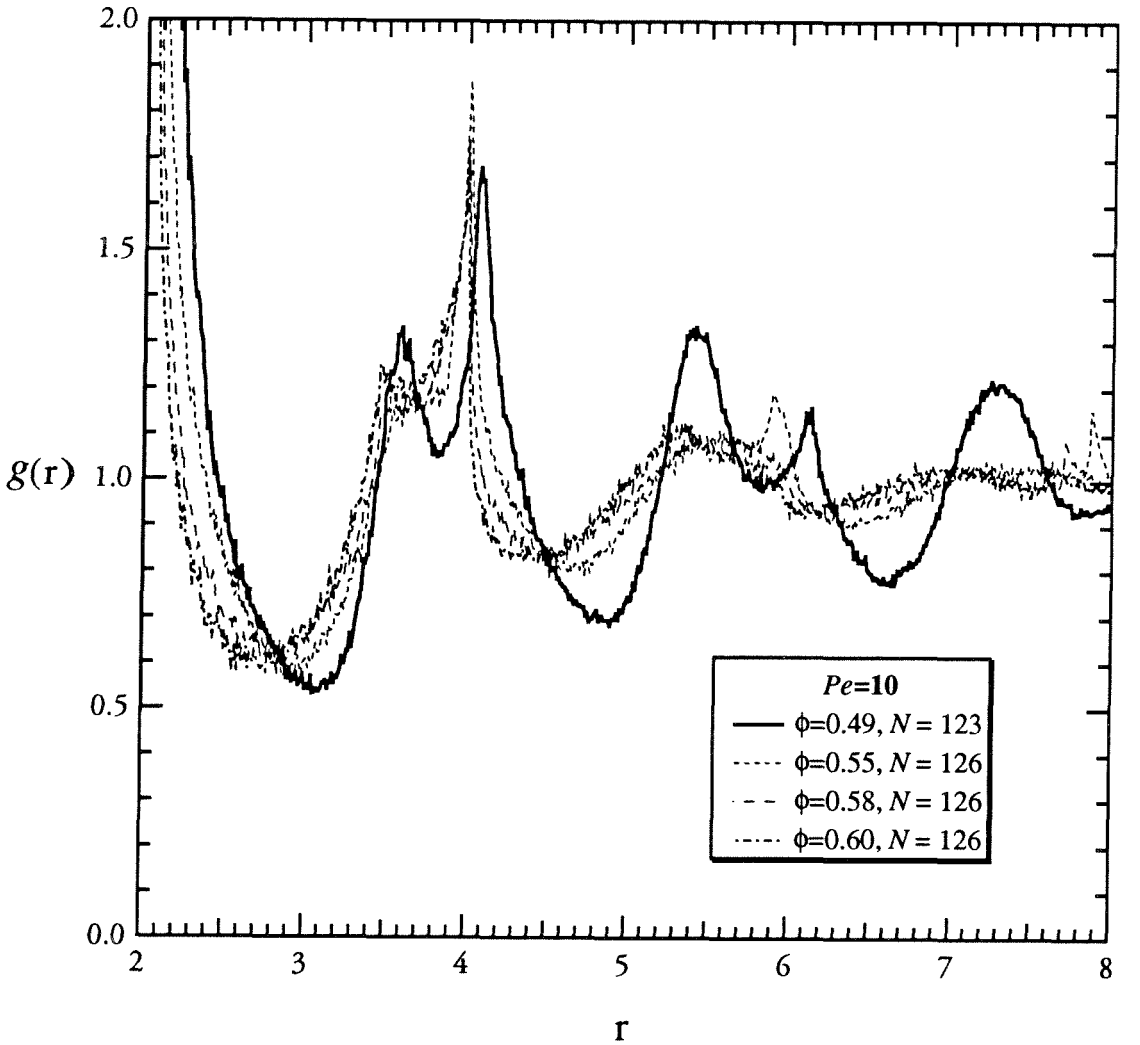

Figure 8.13.b: The radial dependence of the pair-distribution function $g(r)$ determined by Stokesian dynamics for hard-sphere suspensions with Pe=10 and different volume fractions ϕ = (dotted curve) 0.55, (dashed curve) ϕ=0.58, and (dotted-dash curve) 0.6. There are 126 particles in the unit cell. $g(r)$ for ϕ=0.49 (solid curve) (cf. Fig.8.13.a) is plotted as a reference for comparison. As the volume fraction increases from 0.49 to 0.6, the twined-peak pattern, which is seen for ϕ=0.49 indicating a distortion to the symmetric of the hexagonal packing, is less pronounced. $g(2)$ for very dense hard spheres at ϕ=0.55, 0.58 and 0.6 shows a sharp and more intense peak at r≈4 and smaller peaks at larger radial distances r≈6 and r≈7.

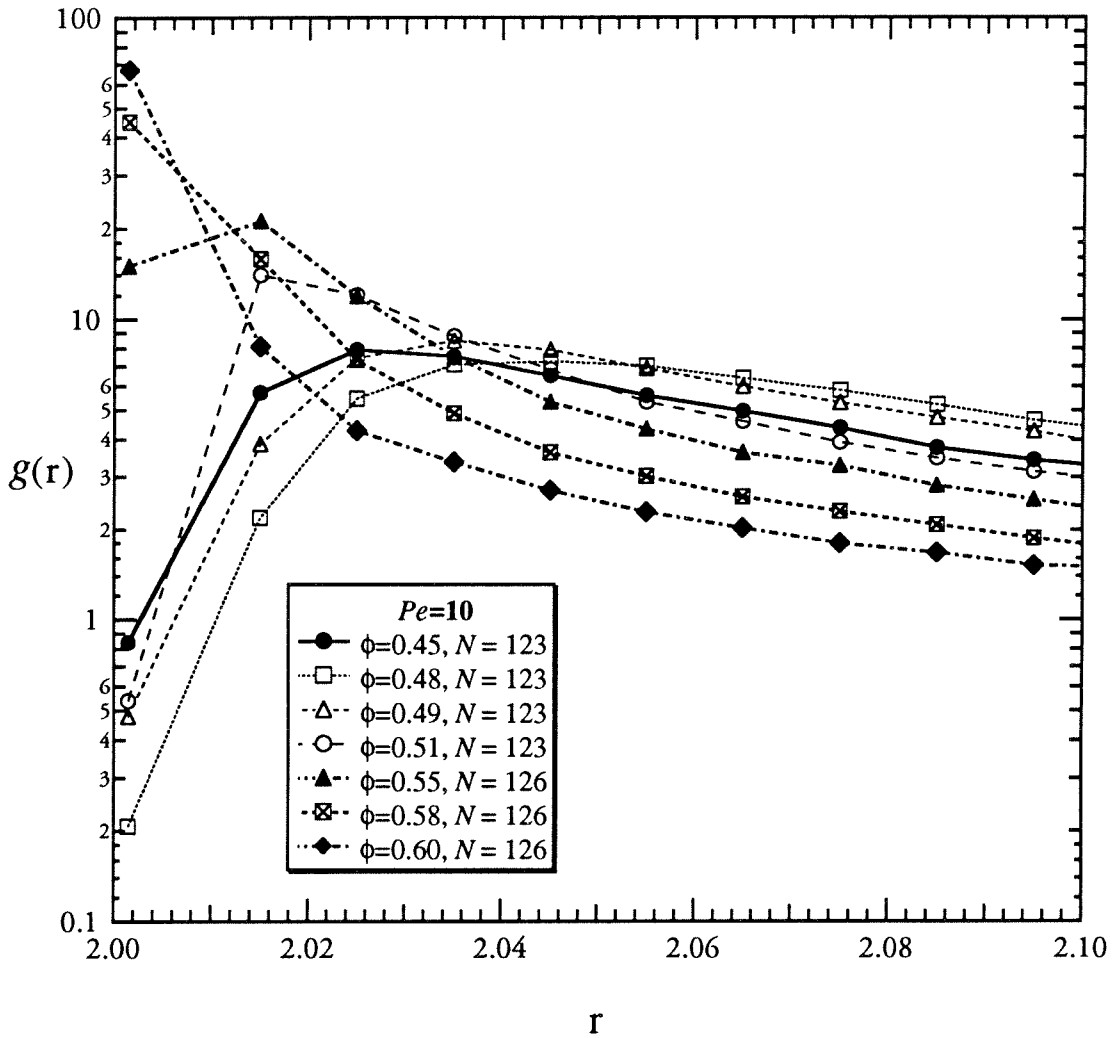

Figure 8.13.c: The radial dependence of the pair-distribution function $g(r)$ obtained by Stokesian dynamics for hard spheres at Pe=10 with a small range of the particle center-center spacing r from 2 (when the particles come in contact) to 2.1. The plot symbols are for suspensions at different volume fractions ϕ = (●) 0.45, (□) 0.48, (Δ) 0.49, (○) 0.51, (▲) 0.55, (⊠) 0.58 and (◆) 0.6. There are 123 or 126 particles in the unit cell. At r≈2, $g(2)$ first decreases as the volume fraction ϕ increases from 0.45 to 0.47 and then increases with increasing ϕ. Note that $g(r)$ is plotted with a logarithmic scale.

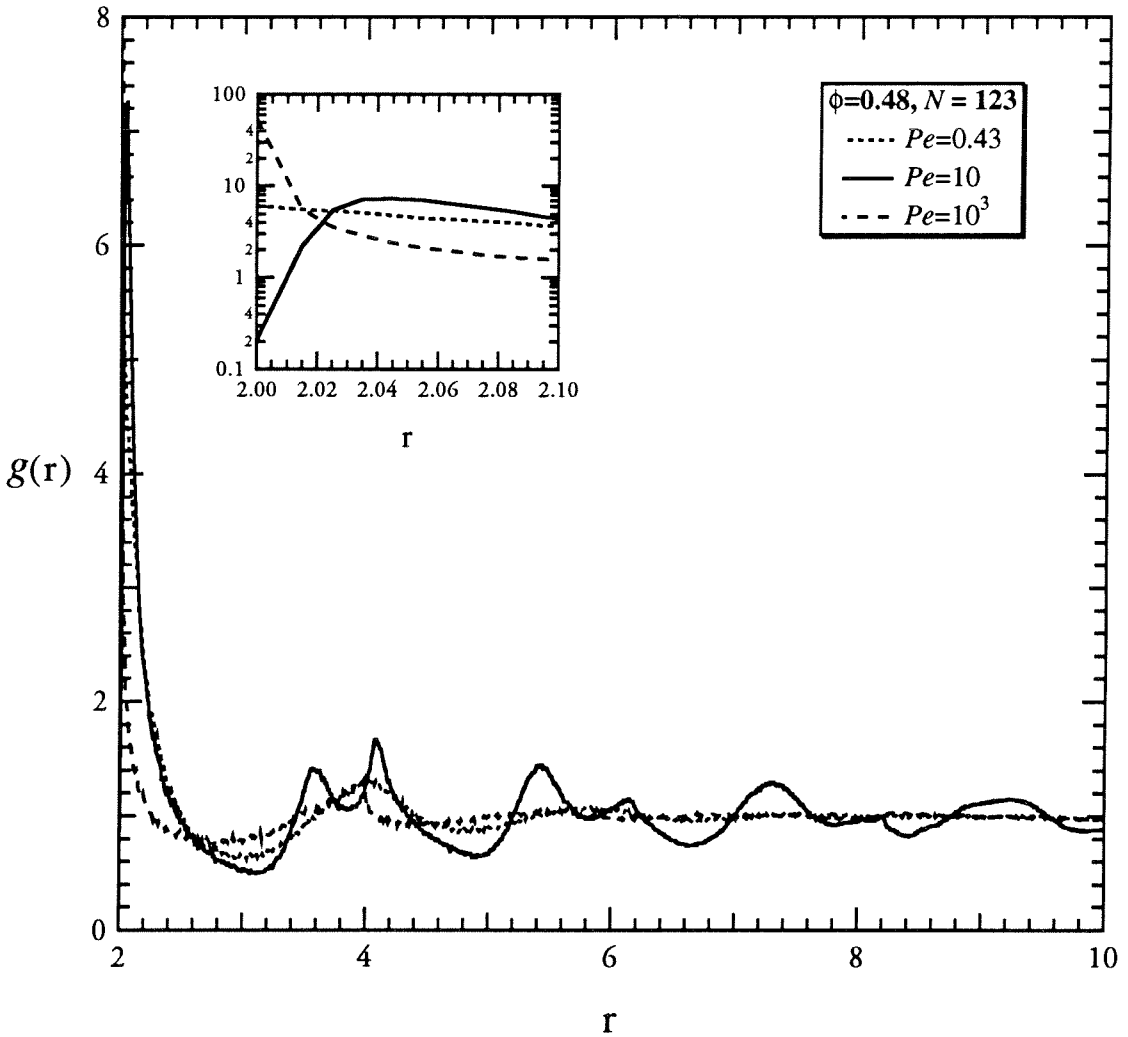

Figure 8.14: The radial dependence of the pair-distribution function $g(r)$ obtained by Stokesian dynamics for hard spheres at a volume fraction ϕ=0.48 with 123 particles and different *Pe*: (dotted curve) 0.43, (solid curve) 10 and (dashed curve) 1000. $g(r)$ at *Pe*=10 shows intense peaks at regular spacing r. The insert figure in the upper left of this figure shows a semi-log plot of $g(r)$ with a smaller range of r from 2 to 2.1. The pair-distribution function evaluated for r≈2, $g(2)$, is smallest for *Pe*=10 and largest for *Pe*=1000. The shearing deformation to the suspension is small at *Pe*=0.43 as shown by $g(2)$≈6.1 which changes slightly from $g(2)$=5.81 for the isotropic hard-sphere distribution obtained by a Monte-Carlo calculation.

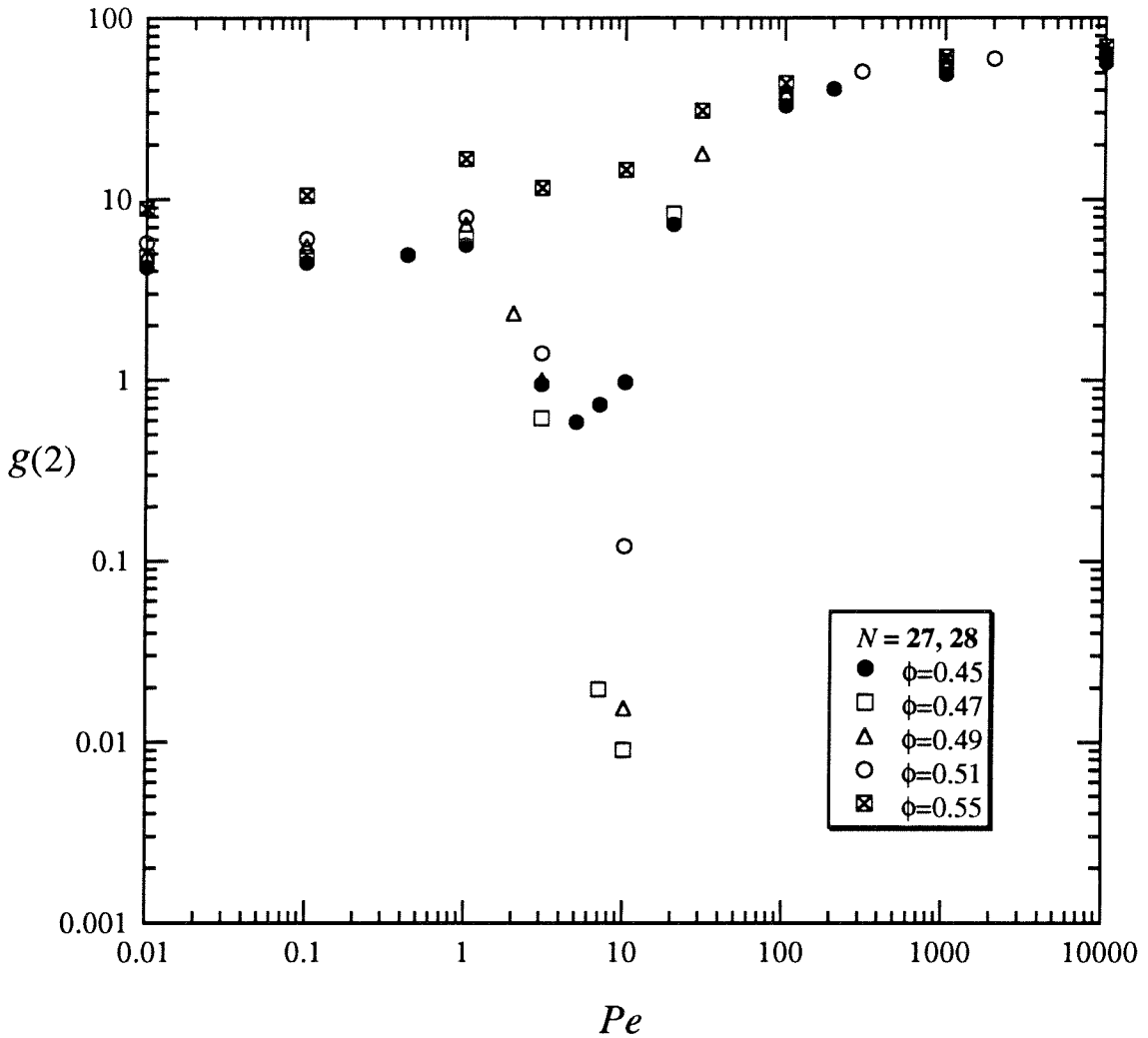

Figure 8.15: A log-log plot of the radial pair-distribution function $g(r)$ evaluated at particle center-center spacing r=2 (when particles are in contact), $g(2)$, obtained by Stokesian dynamics for hard spheres as a function of the Péclet number at different volume fractions: ϕ = (□) 0.47, (Δ) 0.49, (○) 0.51 and (⊠) 0.55. There are 27 or 28 particles in the unit cell. $g(2)$ for ϕ=0.45 (●) is also plotted in this figure as a reference for comparison. For suspensions with a small deformation (Pe<1), $g(2)$ changes inappreciably. As the Péclet number increases, $g(2)$ first decreases to a minimum value at Pe≈10, then increases quickly with large Pe and approaches an asymptotic value for Pe>1000. Note that at Pe≈10, $g(2)$ first decreases as ϕ increases from 0.45 to 0.47 and then increases with increasing ϕ.

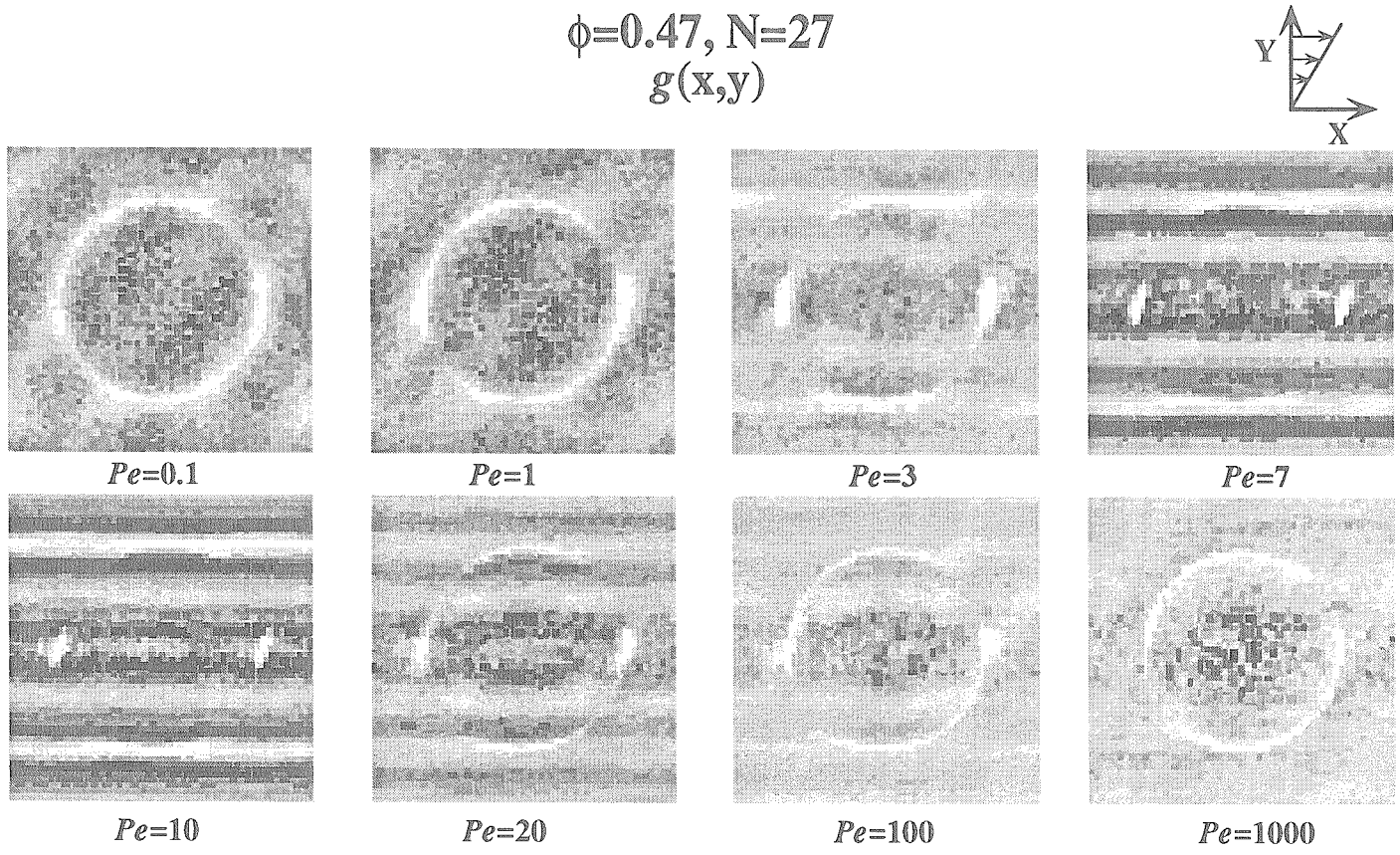

Figure 8.16.a: The probability density function $g(x,y)$ for hard spheres at a volume fraction ϕ=0.47 with 27 particles obtained by Stokesian dynamics for different Péclet numbers. Regions of light color represent high probability and regions of dark color represent low probability. The flow direction is the horizontal x-axis and the velocity gradient direction is the vertical y-axis. $g(x,y)$ shows a "string" formation of flowing particles for *Pe* in the range of 3 to 100. The string order is destroyed by *Pe*=1000. Note also the sharpening of the first nearest neighbor ring of *Pe*=100 and 1000 compared to the slightly distorted symmetric ring of *Pe*=0.1 and 1.

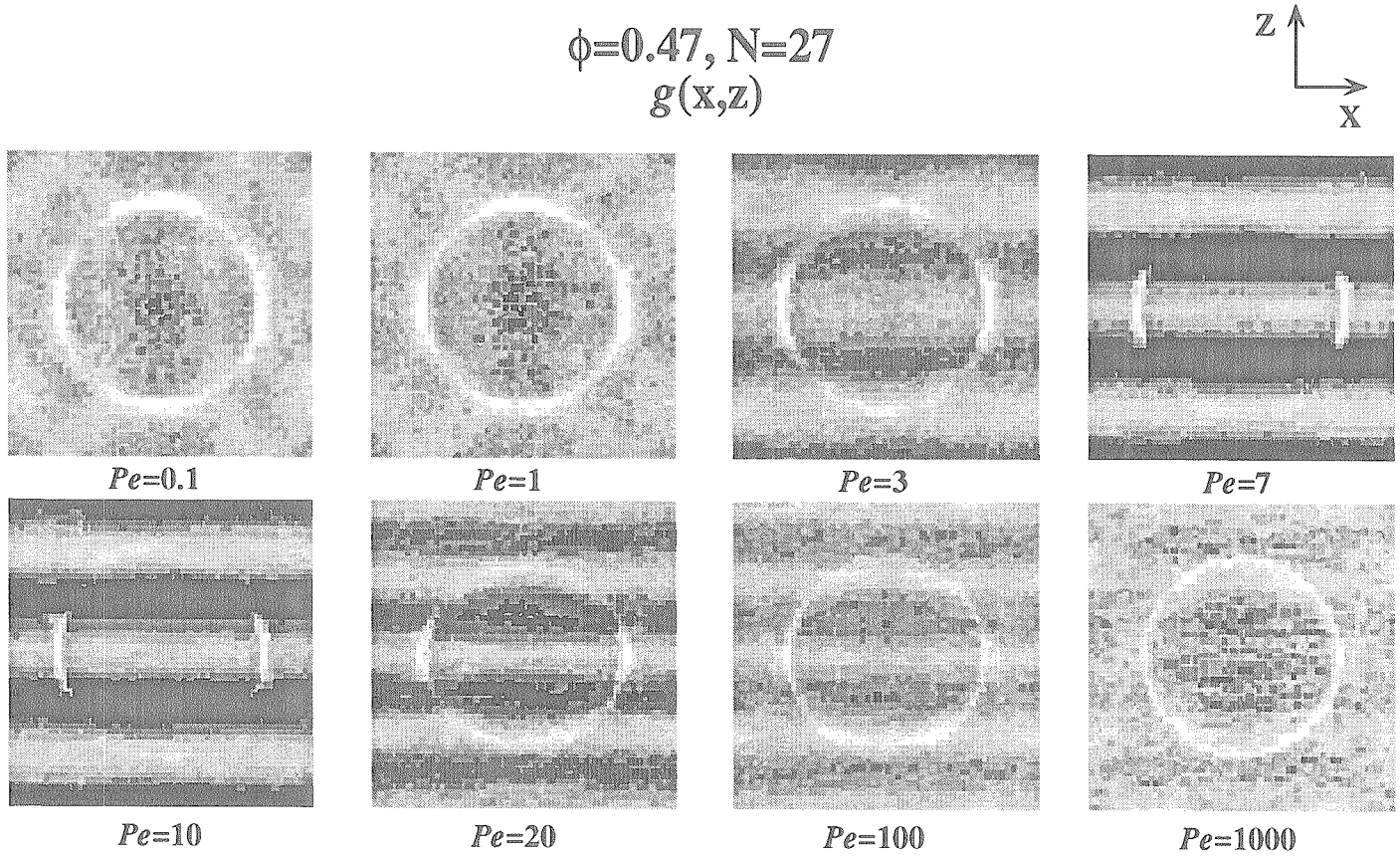

Figure 8.16.b: The probability density function $g(x,z)$ for hard spheres at a volume fraction ϕ=0.47 with 27 particles obtained by Stokesian dynamics for different Péclet numbers. Regions of light color represent high probability and regions of dark color represent low probability. The flow direction is the horizontal x-axis and the vorticity direction is the vertical z-axis. $g(x,z)$ shows clearly a "string" formation of flowing particles for *Pe* in the range of 3 to 100. Note that $g(x,z)$ changes from a 3-stringed formation at *Pe*=3, 7 and 10 to a 5-stringed pattern at *Pe*=20 and 100. The string order is destroyed by *Pe*=1000.

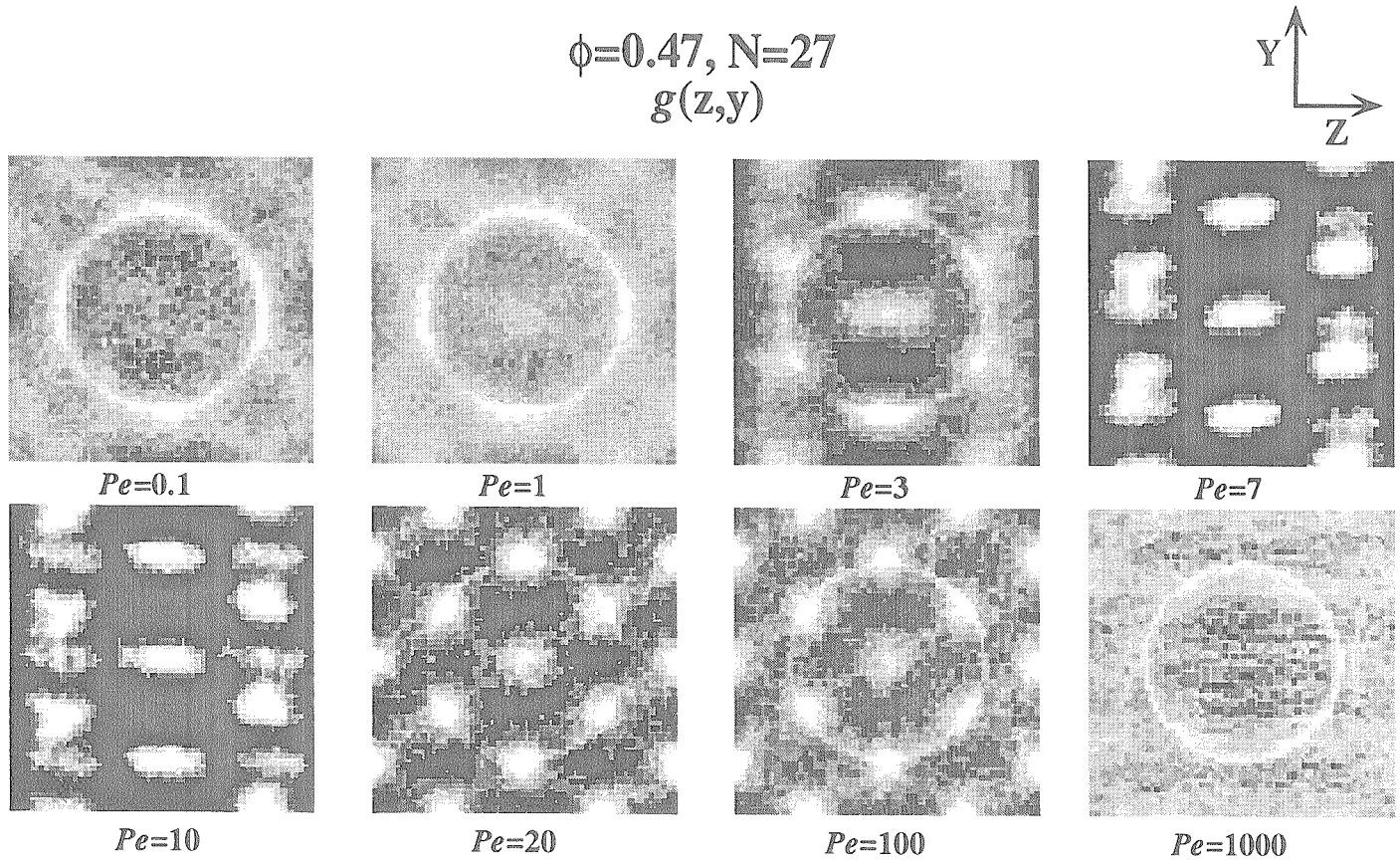

Figure 8.16.c: The probability density function $g(z,y)$ for hard spheres at a volume fraction ϕ=0.47 with 27 particles obtained by Stokesian dynamics for different Péclet numbers. Regions of light color represent high probability and regions of dark color represent low probability. The flow direction is perpendicular to the z-y plane. The vorticity direction is the z-axis and the velocity gradient direction is the y-axis. $g(z,y)$ shows a distinct "hexagonal" packing of strings of flowing particles for *Pe* from 3 to 100. The high shear rate at *Pe*=1000 destroys the hexagonal formation and cause particles to cluster as shown by the sharpening of the first nearest neighbor ring.

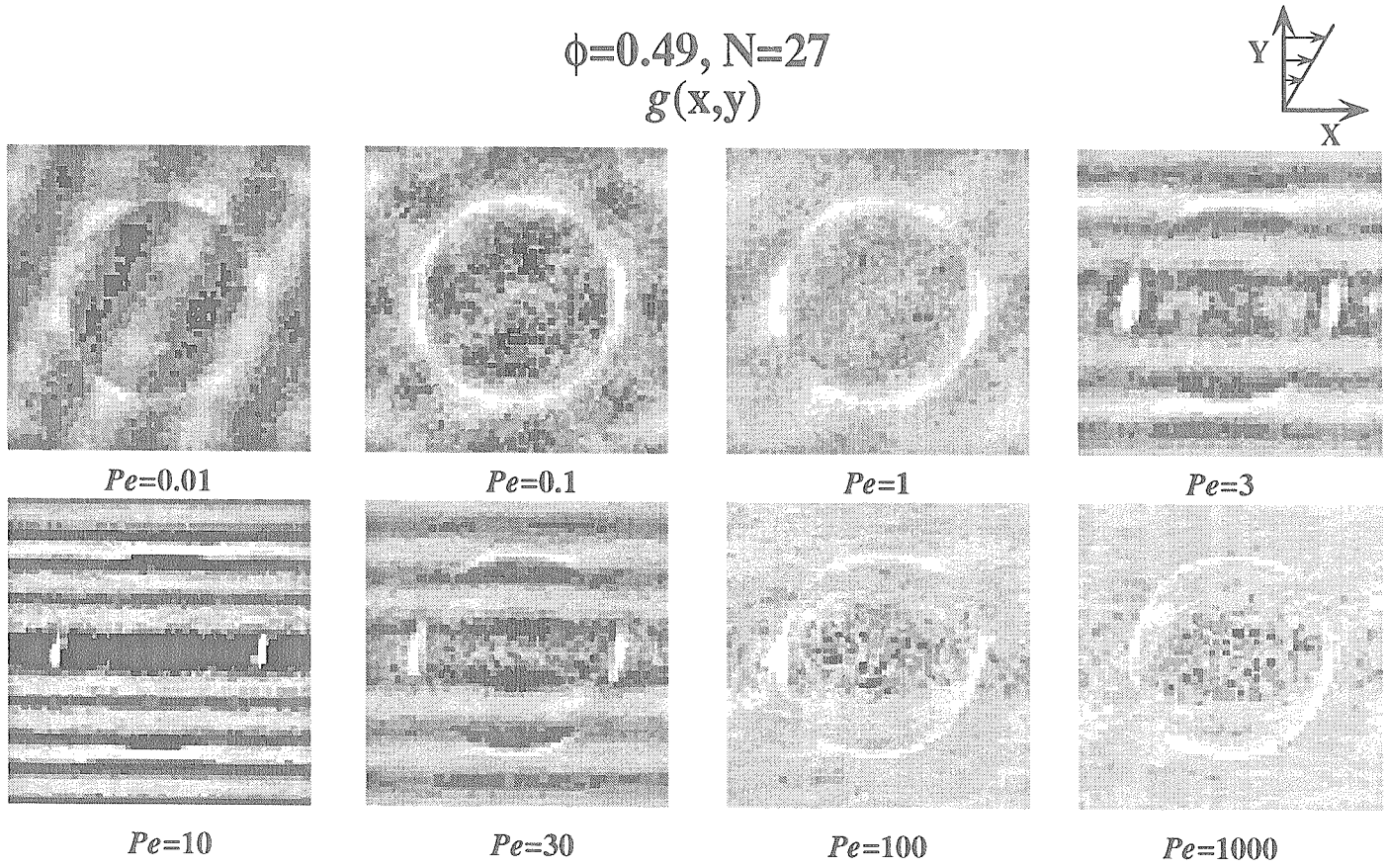

Figure 8.17.a: The probability density function $g(x,y)$ for hard spheres at a volume fraction ϕ=0.49 with 27 particles obtained by Stokesian dynamics for different Péclet numbers. Regions of light color represent high probability and regions of dark color represent low probability. The flow direction is the horizontal x-axis and the velocity gradient direction is the vertical y-axis. $g(x,y)$ shows stringed particles in the flow direction for *Pe* from 3 to 30. The string formation is destroyed by *Pe*=1000.

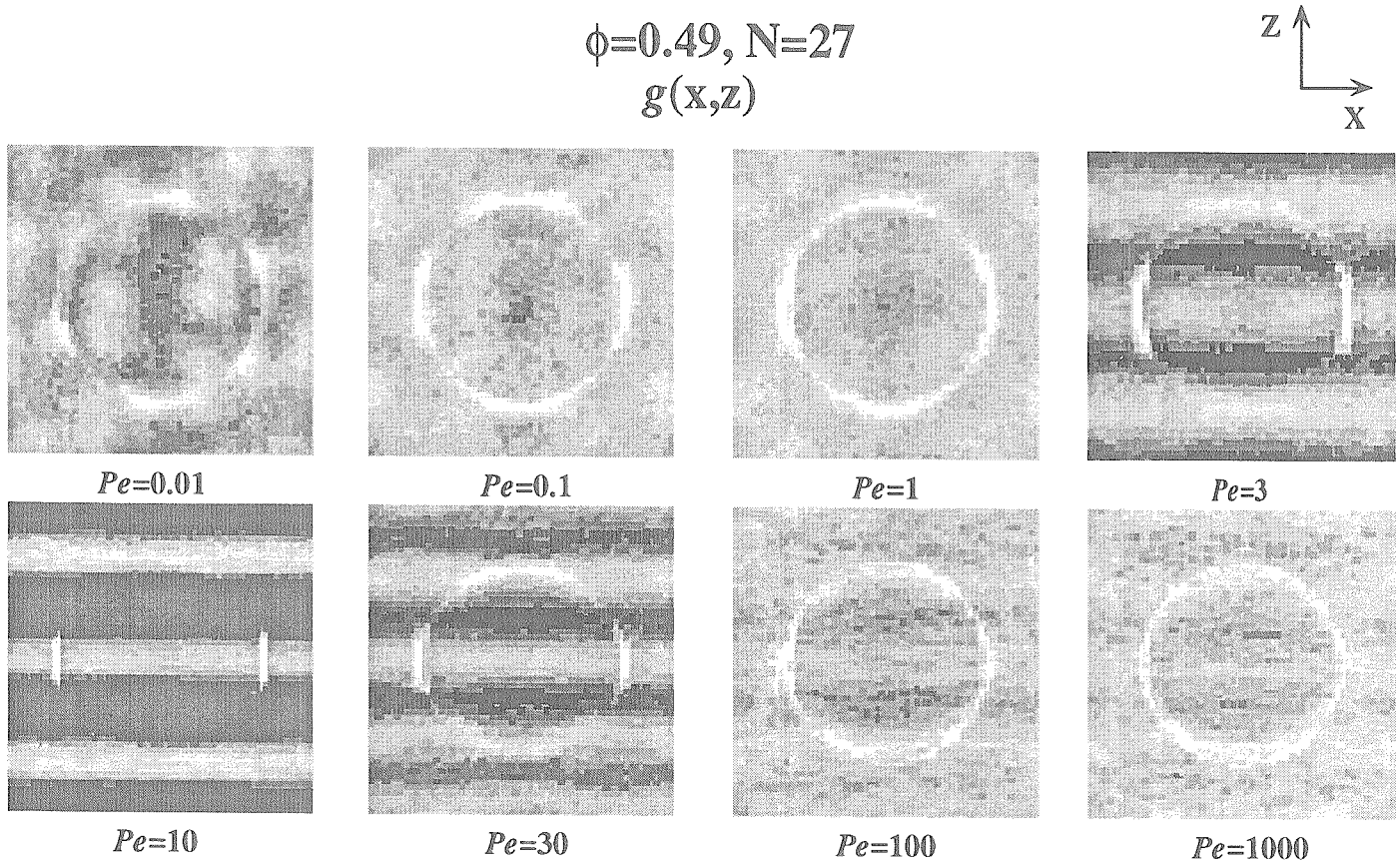

Figure 8.17.b: The probability density function $g(x,z)$ for hard spheres at a volume fraction ϕ=0.49 with 27 particles obtained by Stokesian dynamics for different Péclet numbers. Regions of light color represent high probability and regions of dark color represent low probability. The flow direction is the horizontal x-axis and the vorticity direction is the vertical z-axis. Strings of flowing particles can clearly be seen for *Pe* from 3 to 30. Note also the change of $g(x,z)$ from a 3-stringed pattern at *Pe*=3 and 10 to a 5-stringed pattern at *Pe*=30. The string order is destroyed by *Pe*=1000.

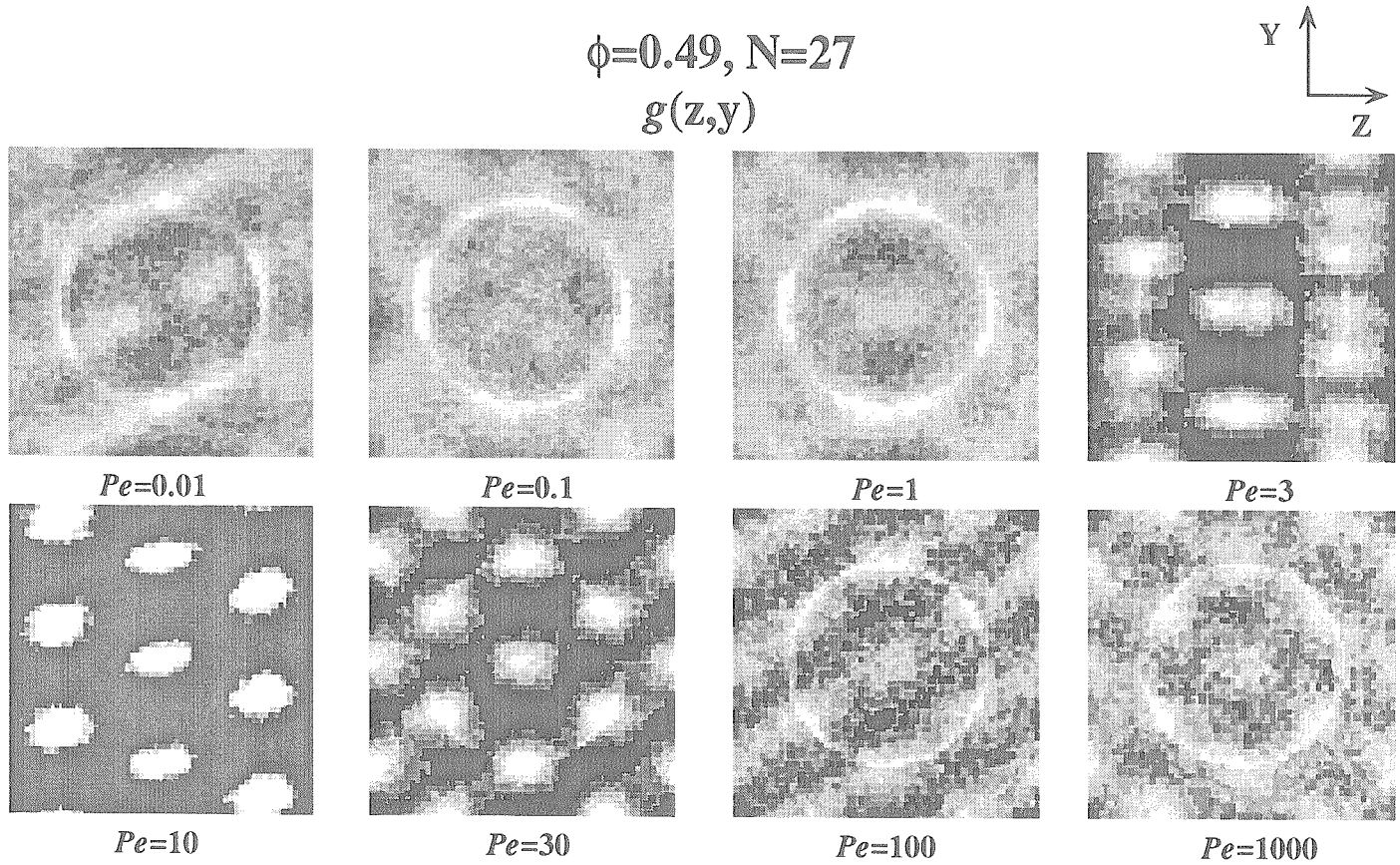

Figure 8.17.c: The probability density function $g(z,y)$ for hard spheres at volume fraction ϕ=0.49 with 27 particles obtained by Stokesian dynamics for different Péclet numbers. Regions of light color represent high probability and regions of dark color represent low probability. The flow direction is perpendicular to the z-y plane. The vorticity direction is the horizontal z-axis and the velocity gradient direction is the vertical y-axis. $g(z,y)$ shows a distinct "hexagonal" packing of strings of flowing particles for *Pe* from 3 to 30. Note also a small inclination of the hexagonal pattern of $g(z,y)$ at *Pe*=10. The hexagonal order is destroyed by *Pe*=1000.

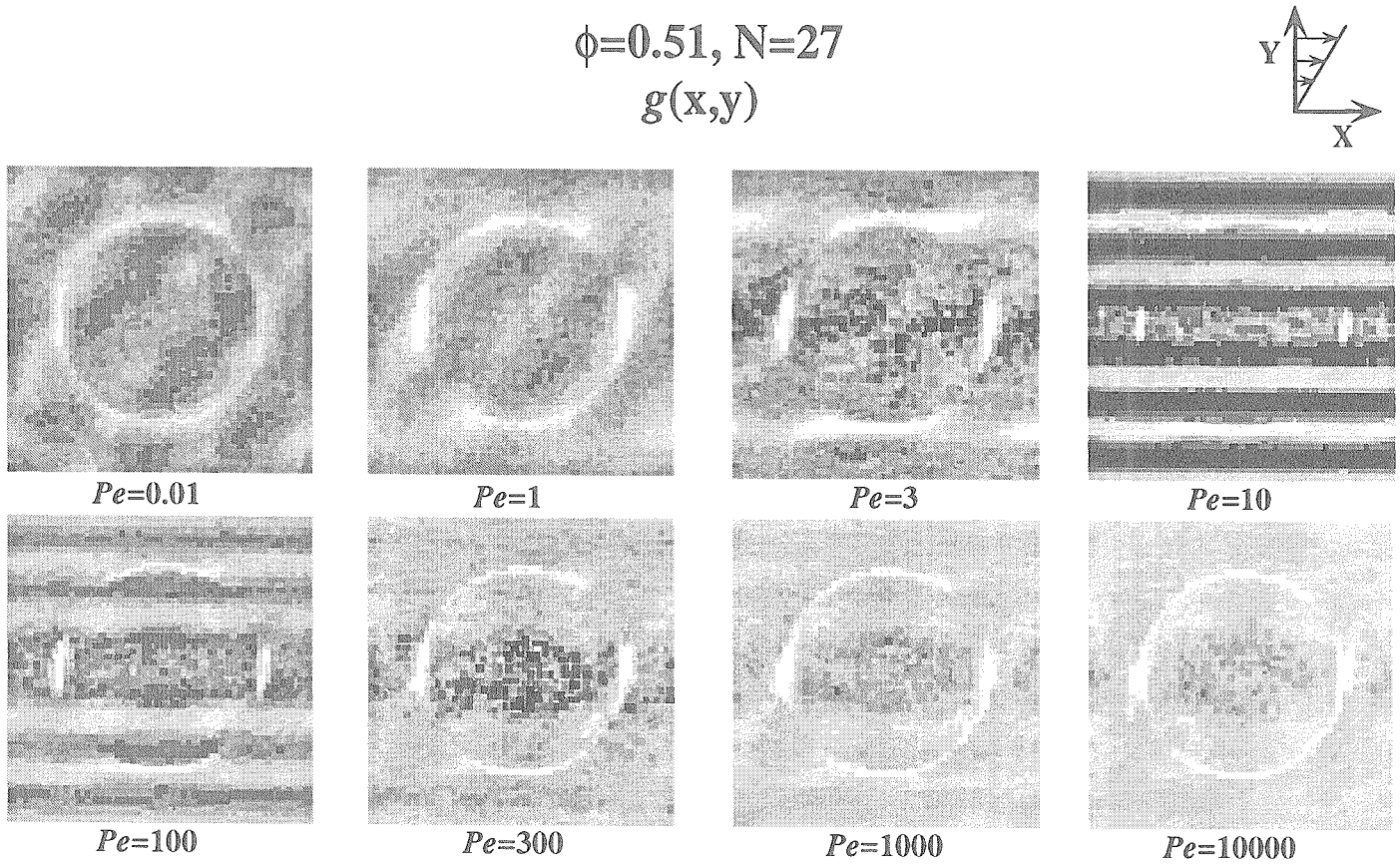

Figure 8.18.a: The probability density function $g(x,y)$ for dense hard spheres at a volume fraction ϕ=0.51 with 27 particles obtained by Stokesian dynamics for different Péclet numbers. Regions of light color represent high probability and regions of dark color represent low probability. The flow direction is the horizontal x-axis and the velocity gradient direction is the vertical y-axis. Strings of flowing particles can be seen for *Pe* from 3 to 100. The string order begins to fluctuate at *Pe*=300 and is destroyed by *Pe*=10000. $g(x,y)$ shows a 5-stringed pattern for *Pe*=10 and 100.

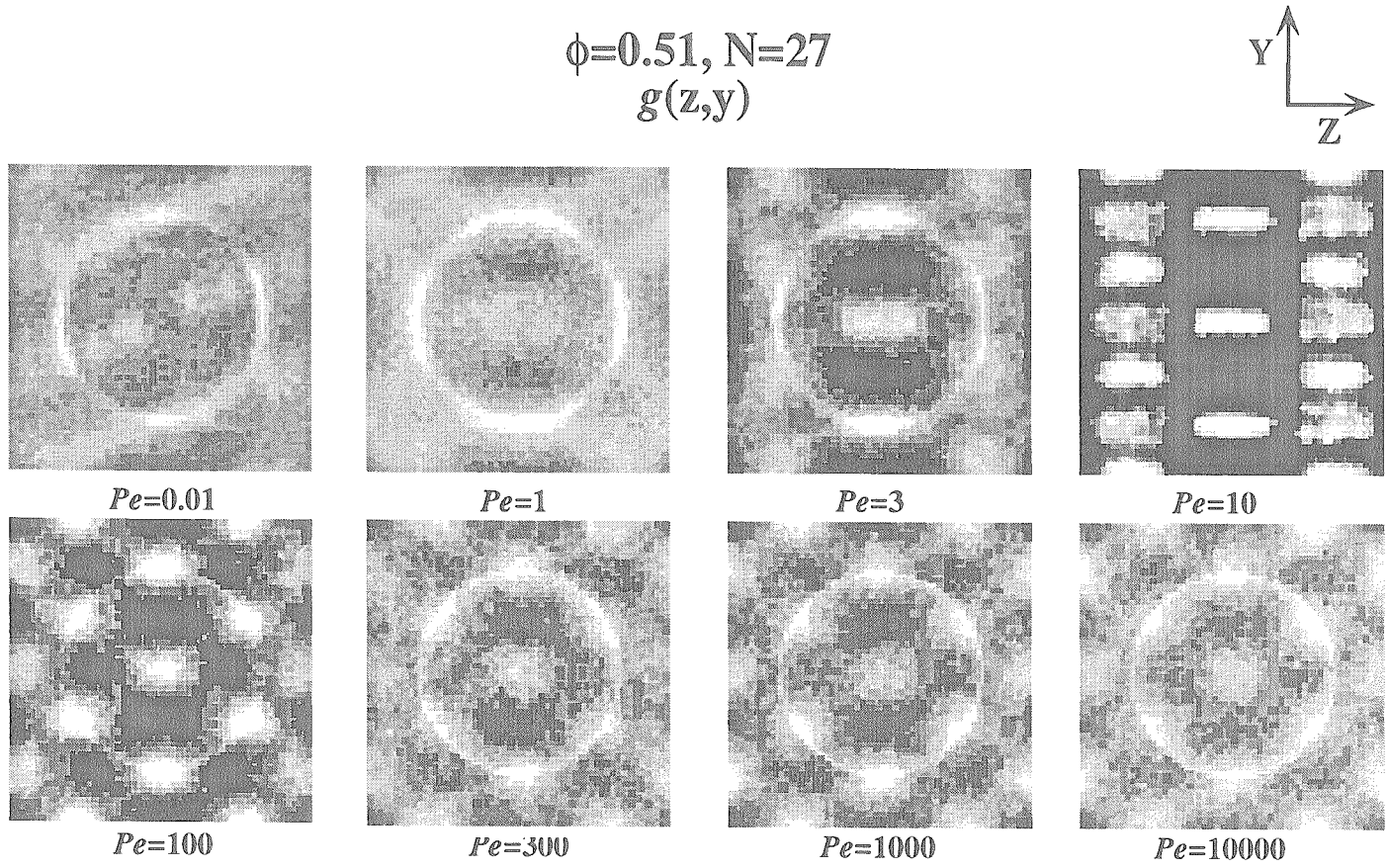

Figure 8.18.b: The probability density function $g(z,y)$ for dense hard spheres at a volume fraction ϕ=0.51 with 27 particles obtained by Stokesian dynamics for different Péclet numbers. Regions of light color represent high probability and regions of dark color represent low probability. The flow direction is perpendicular to the z-y plane with the vorticity direction the z-axis and the velocity gradient direction the y-axis. $g(z,y)$ shows a distinct "hexagonal" packing of strings of flowing particles for Pe=10 and 100. The hexagonal order begins to fluctuate at Pe=300 and is destroyed by high shear rates at Pe=10000.

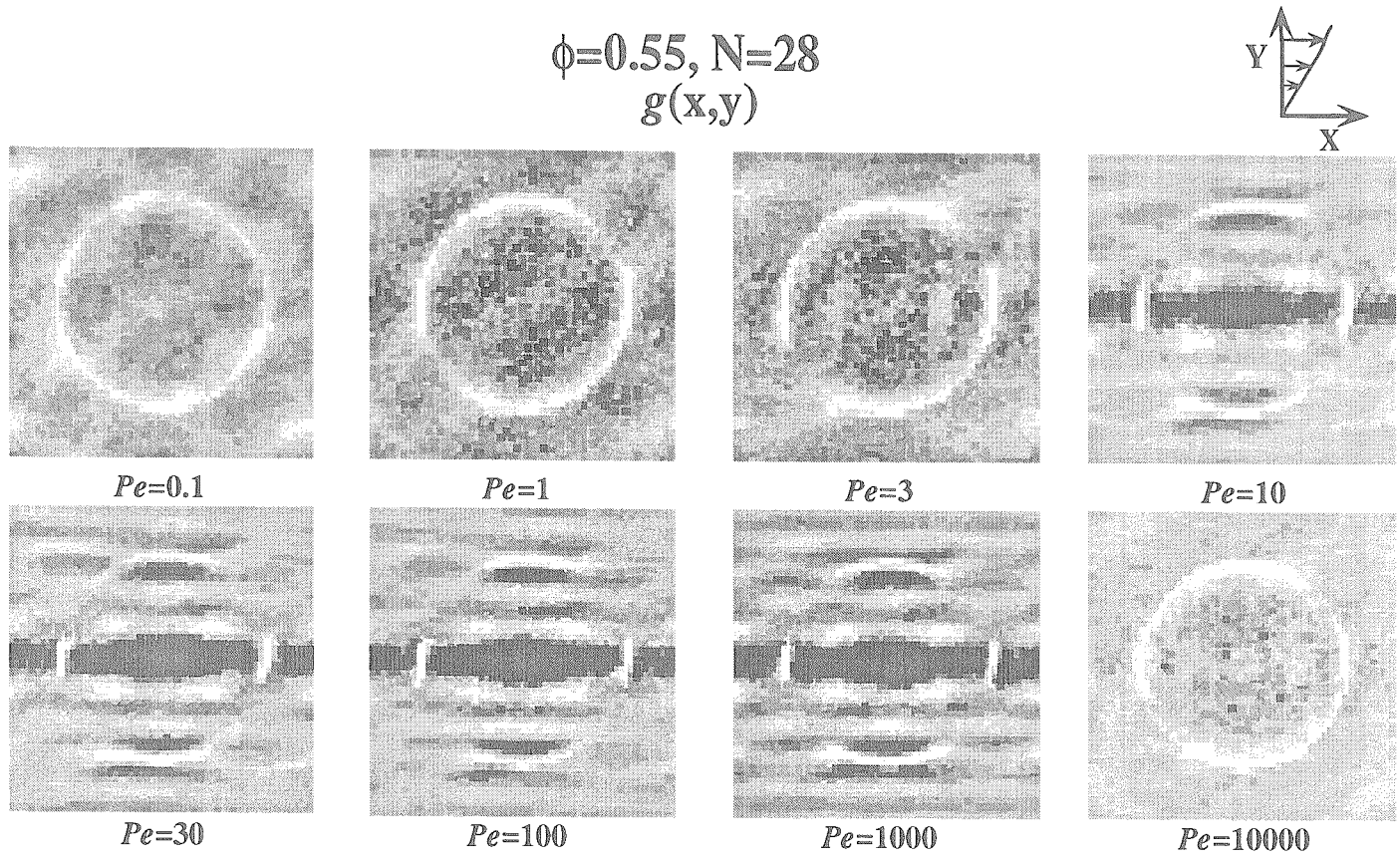

Figure 8.19.a: The probability density function $g(x,y)$ for very dense hard spheres at a volume fraction ϕ=0.55 with 28 particles obtained by Stokesian dynamics for different Péclet numbers. Regions of light color represent high probability and regions of dark color represent low probability. The flow direction is the horizontal x-axis and the velocity gradient direction is the vertical y-axis. Strings of flowing particles can be seen for *Pe* from 10 to 1000. The string order is by *Pe*=10000.

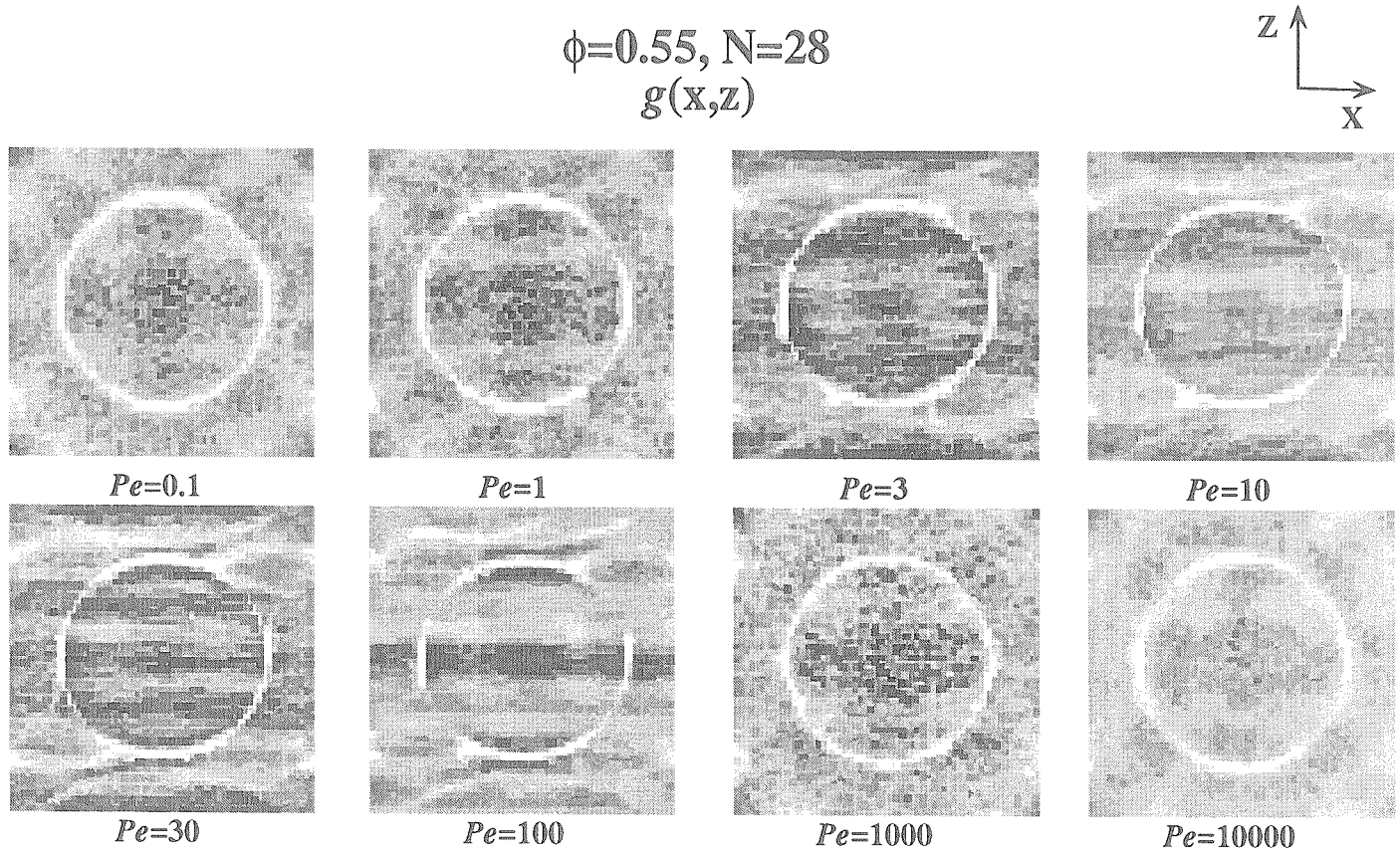

Figure 8.19.b: The probability density function $g(x,z)$ for very dense hard spheres at a volume fraction ϕ=0.55 with 28 particles obtained by Stokesian dynamics for different Péclet numbers. Regions of light color represent high probability and regions of dark color represent low probability. The flow direction is the horizontal x-axis and the vorticity direction is the vertical z-axis. $g(x,z)$ shows a "string" formation of flowing particles for *Pe* from 10 to 100. The string order is destroyed by *Pe*=10000.

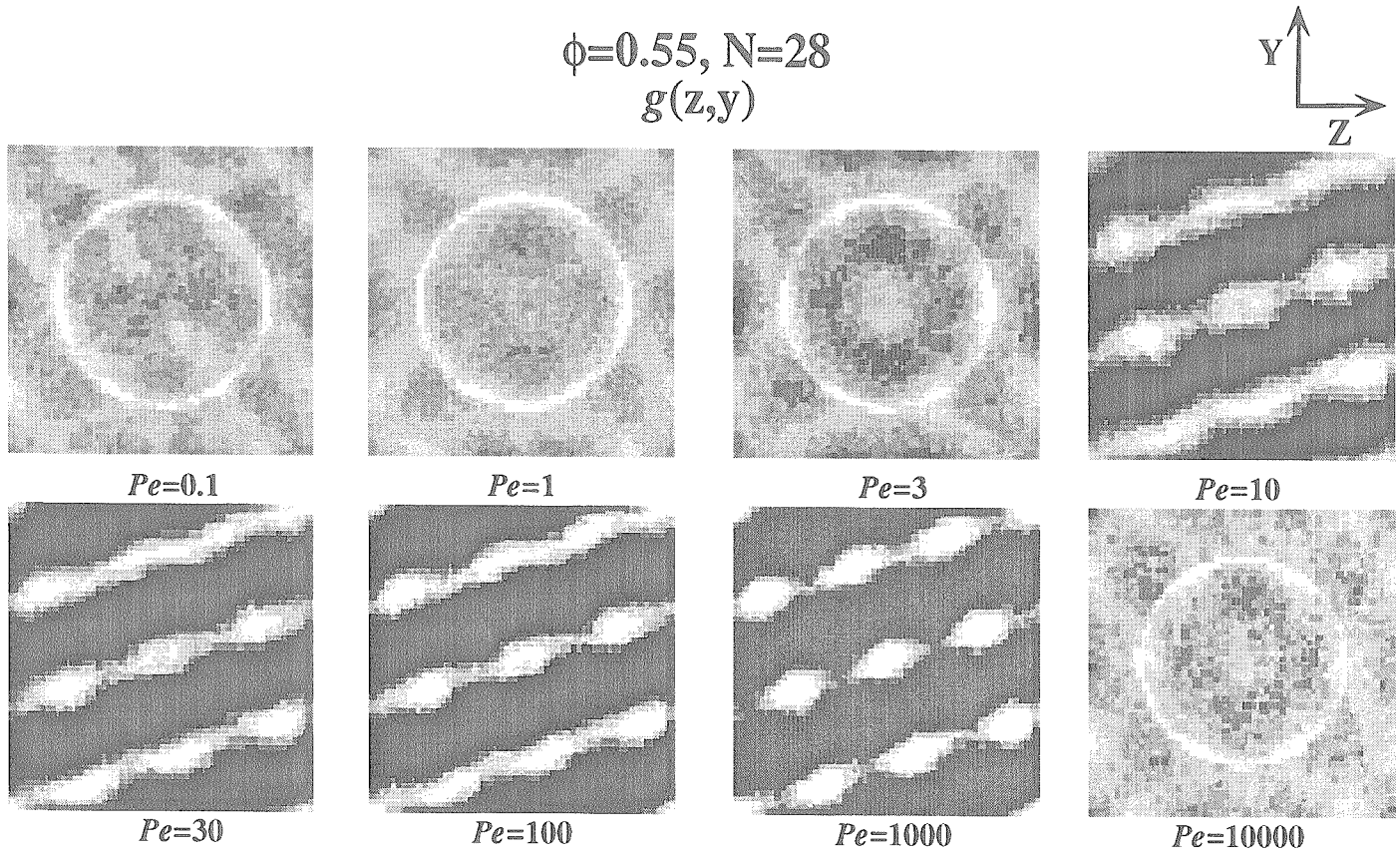

Figure 8.19.c: The probability density function $g(z,y)$ for very dense hard spheres at a volume fraction ϕ=0.55 with 28 particles obtained by Stokesian dynamics for different Péclet numbers. Regions of light color represent high probability and regions of dark color represent low probability. The flow direction is perpendicular to the z-y plane with the vorticity direction the z-axis and the velocity gradient direction the y-axis. Hexagonal ly packed strings of flowing particles can be seen for *Pe* in the range of 10 to 100. The hexagonal packing is stretched and inclined to accommodate 28 particles within the unit cell. At *Pe*=10000 the ordered structure is destroyed.

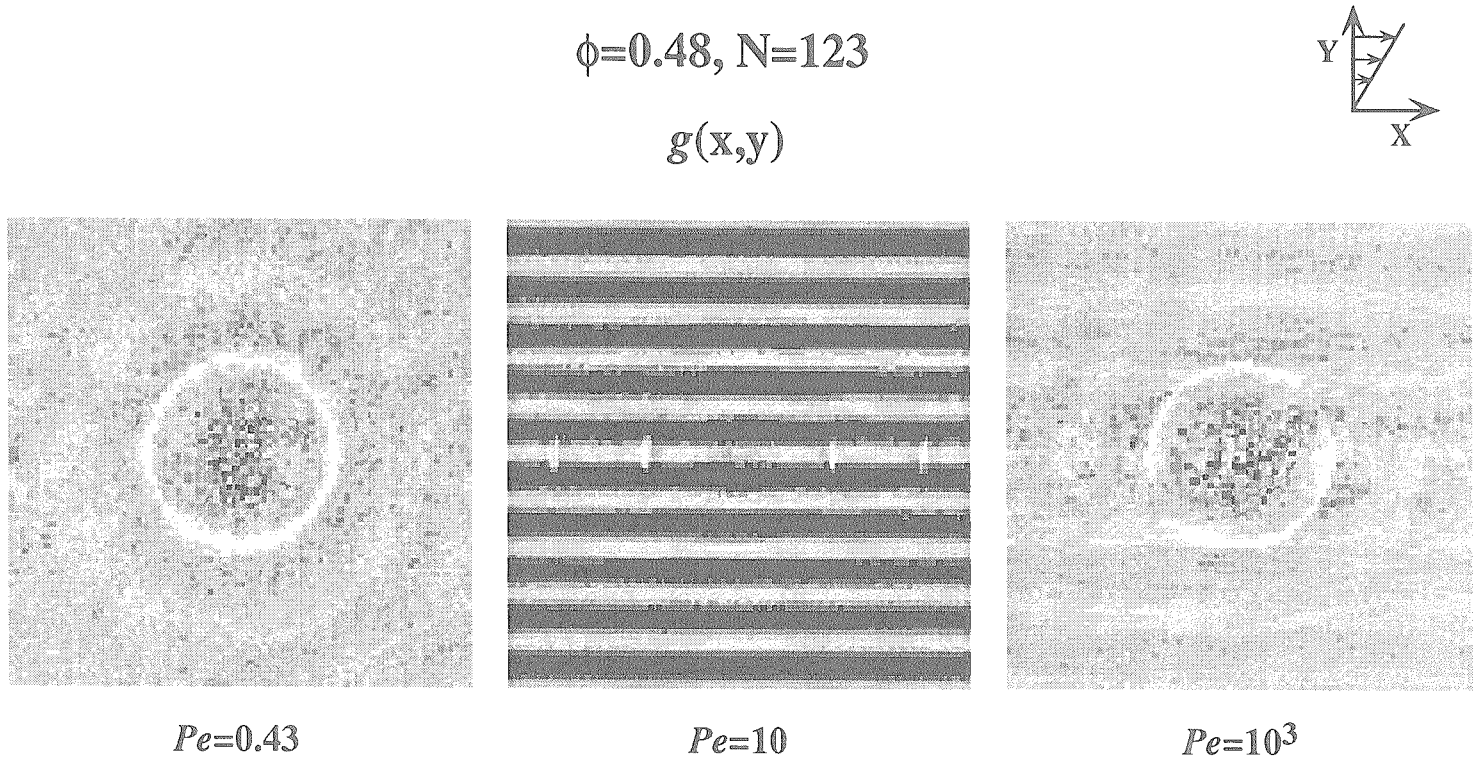

Figure 8.20.a: The probability density function $g(x,y)$ for hard spheres at a volume fraction ϕ=0.48 with 123 particles obtained by Stokesian dynamics for three different Péclet numbers: 0.43 (left figure), 10 (central figure) and 1000 (right figure). Regions of light color represent high probability and regions of dark color represent low probability. The flow direction is the horizontal x-axis and the velocity gradient direction is the vertical y-axis. At small shear rates (Pe=0.43), the equilibrium isotropic structure is slightly perturbed as shown by a slightly distorted symmetric ring. The formation of distinct strings of flowing particles in the flow direction can only be seen for Pe=10. At higher shear rates (Pe=1000), the string formation begins to fluctuate and is unclear. Note also the sharpening of the first nearest neighbor ring.

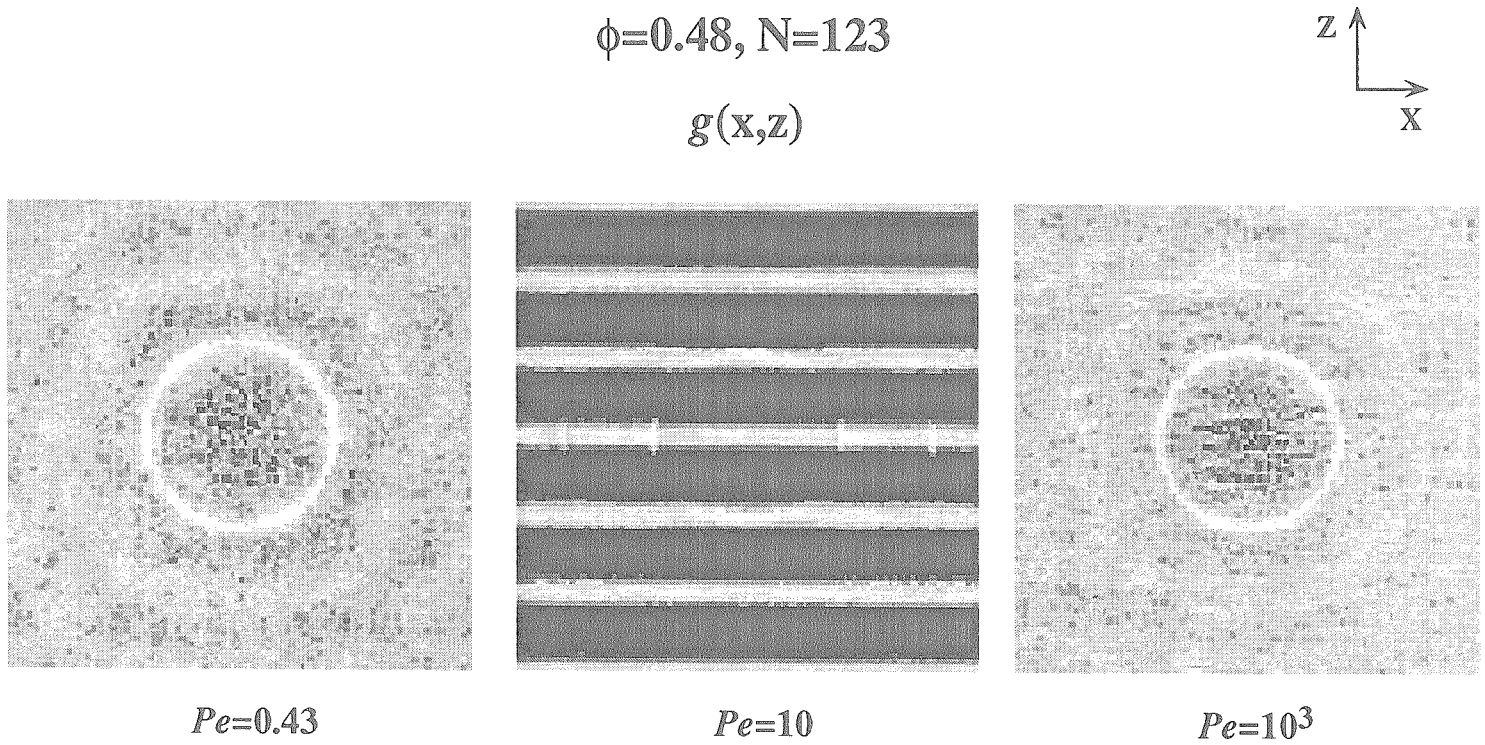

Figure 8.20.b: The probability density function $g(x,z)$ for hard spheres at a volume fraction ϕ=0.48 with 123 particles obtained by Stokesian dynamics for three different Péclet numbers: 0.43 (left figure), 10 (central figure) and 1000 (right figure). Regions of light color represent high probability and regions of dark color represent low probability. The horizontal x-axis is the flow direction and the vertical y-axis is the vorticity direction. Strings of flowing particles can only be seen for Pe=10 (central figure).

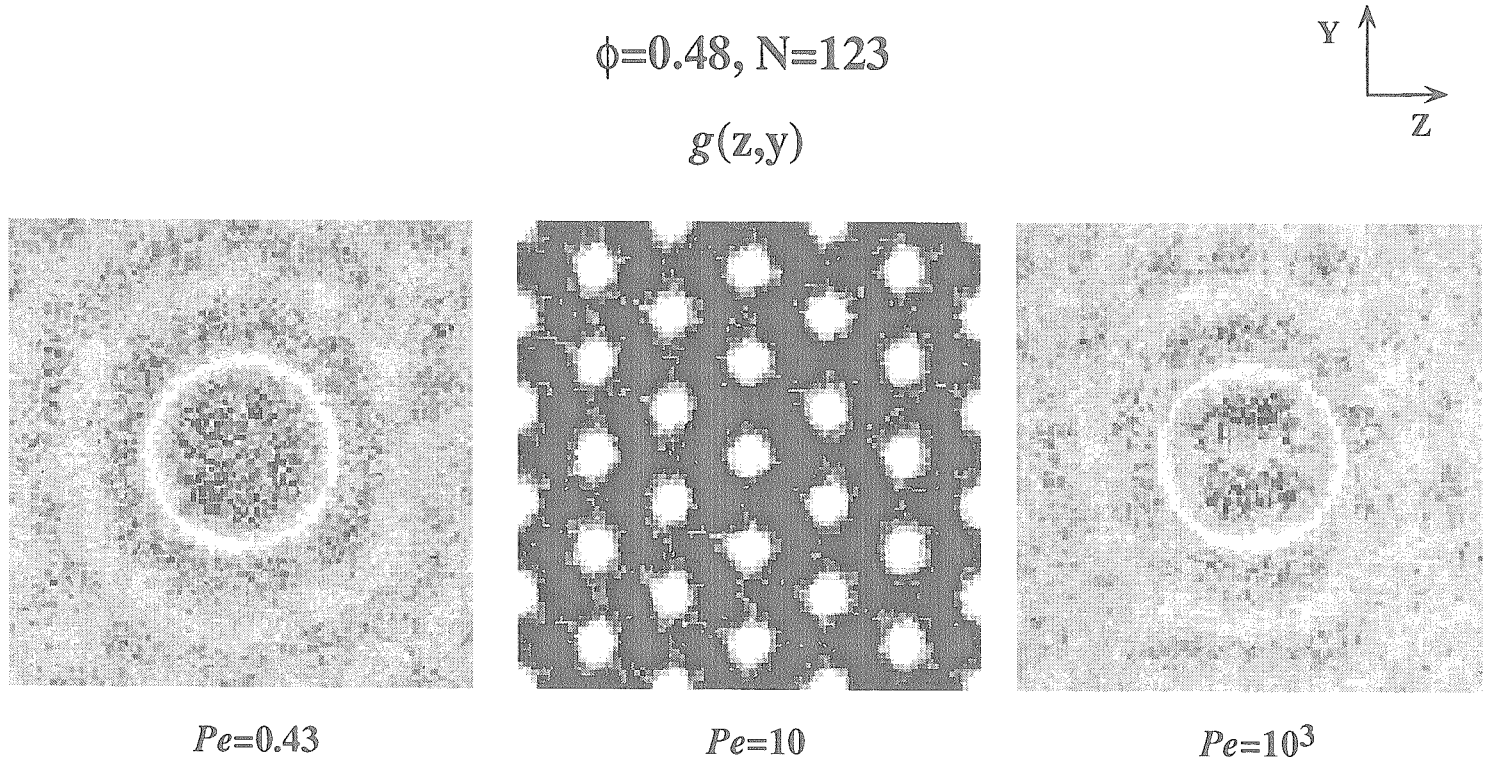

Figure 8.20.c: The probability density function $g(z,y)$ for hard spheres at a volume fraction ϕ=0.48 with 123 particles obtained by Stokesian dynamics for three different Péclet numbers: 0.43 (left figure), 10 (central figure) and 1000 (right figure). Regions of light color represent high probability and regions of dark color represent low probability. The flow direction is perpendicular to the z-y plane with the vorticity direction the horizontal z-axis and the velocity gradient direction the vertical y-axis. $g(z,y)$ shows a distinct "hexagonal" packing of strings of flowing particles at Pe=10. The hexagonal packing is destroyed by Pe=1000.

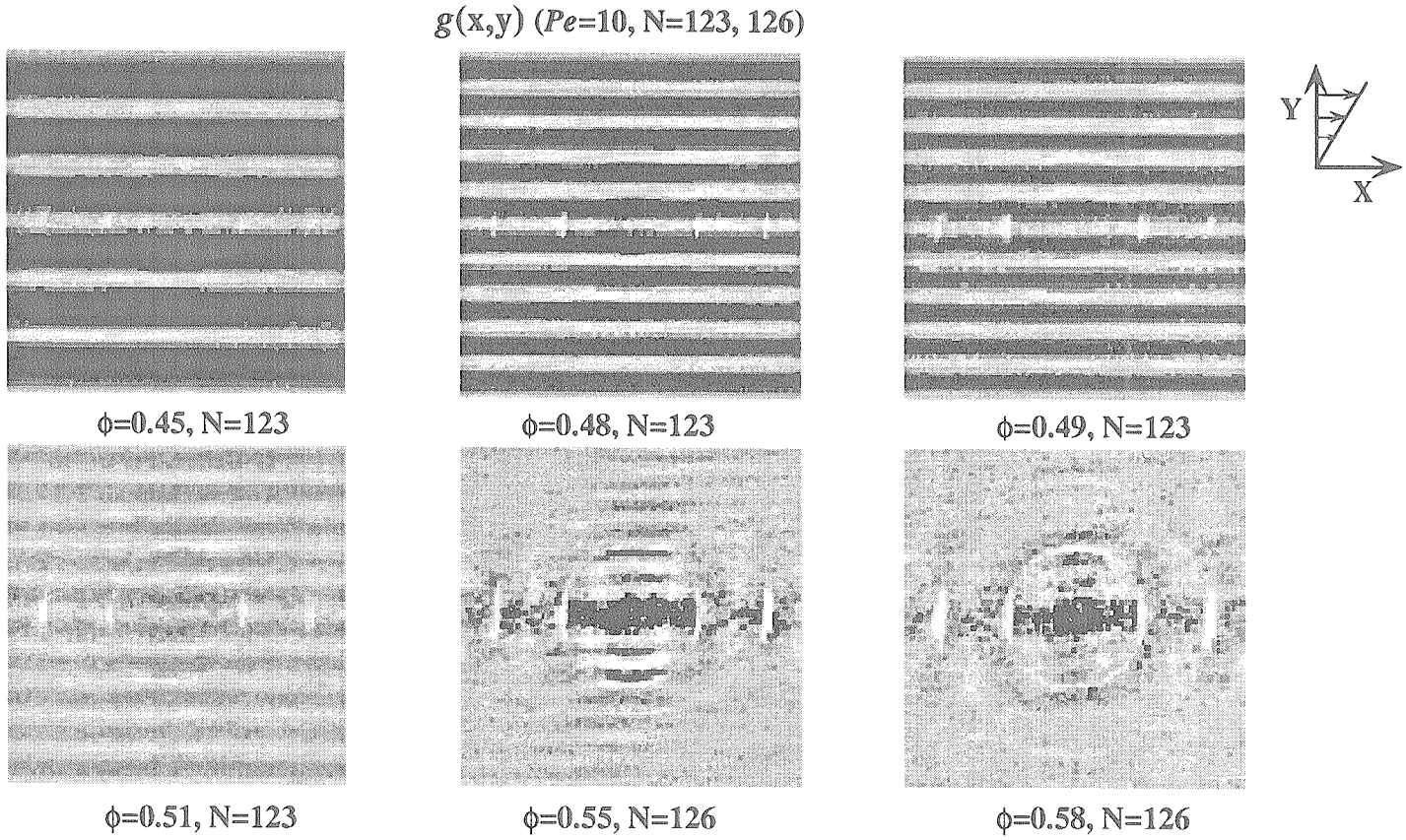

Figure 8.21.a: The probability density function $g(x,y)$ for hard spheres at Pe=10 for different volume fractions: from left to right, ϕ=0.45, 0.48, 0.49 (top row) and 0.51, 0.55 and 0.58 (bottom row). There are 123 or 126 particles in the unit cell. Regions of light color represent high probability and regions of dark color represent low probability. The flow direction is the horizontal x-axis and the velocity gradient direction is the vertical y-axis. Note the difference in the patterns of $g(x,y)$ which changes from five to nine strings as the volume fraction increases from 0.45 to the range of 0.48 to 0.51. $g(x,y)$ for ϕ=0.55 and 0.58 has not equilibrated after a dimensionless time of 40 and shows large fluctuations near the regions of string formation and the particles appear to be in the transition to order.

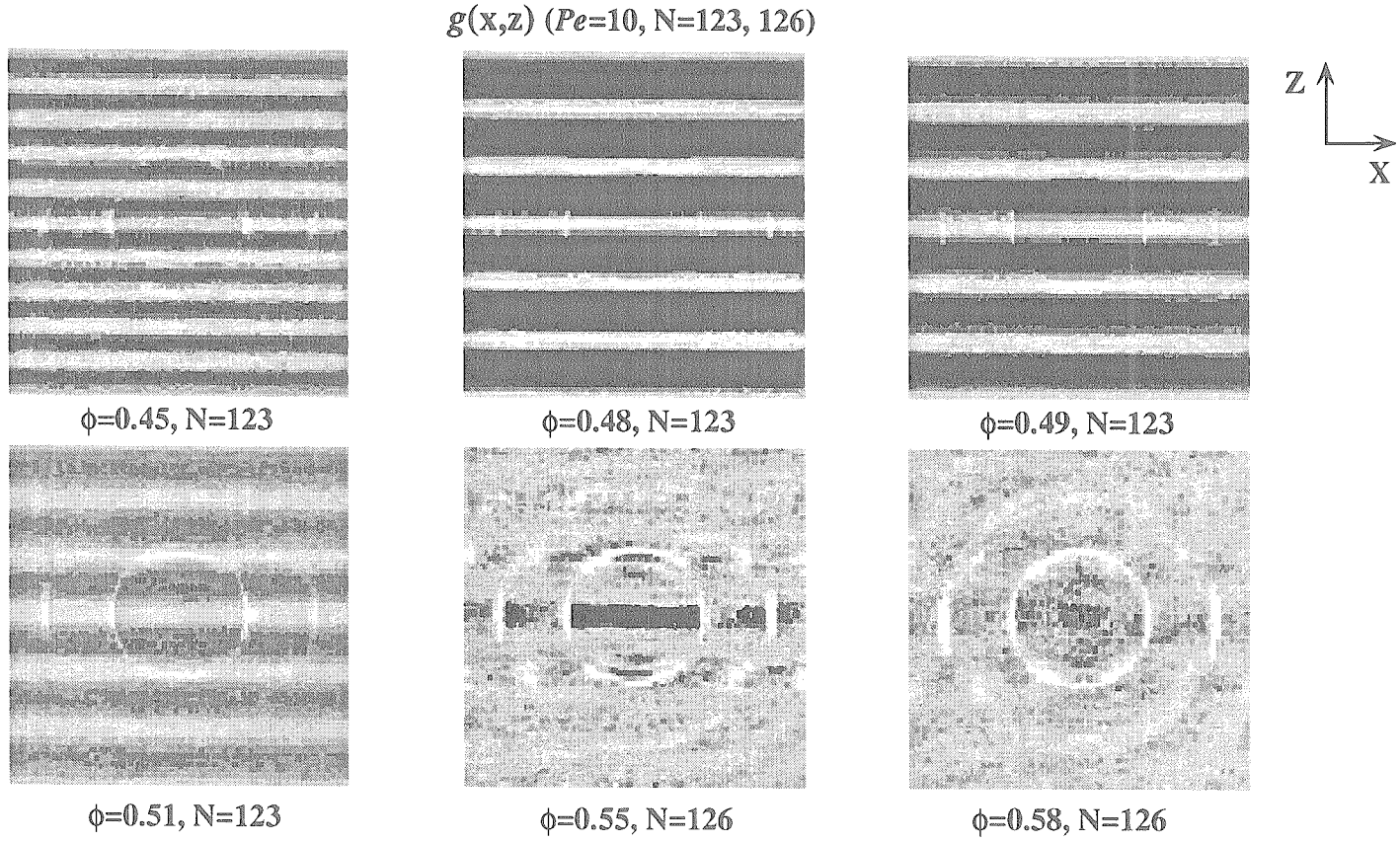

Figure 8.21.b: The probability density function $g(x,z)$ for hard spheres at Pe=10 and different volume fractions: from left to right, ϕ=0.45, 0.48, 0.49 (top row) and 0.51, 0.55 and 0.58 (bottom row). There are 123 or 126 particles in the unit cell. Regions of light color represent high probability and regions of dark color represent low probability. The flow direction is the horizontal x-axis and the vorticity direction is the vertical z-axis. Note the change of $g(x,z)$ as the volume fraction increases from 0.45 to the range of 0.48 to 0.51. $g(x,y)$ from Fig.8.21.a and $g(x,z)$ in this figure clearly demonstrate a switching of the packing pattern from y and z for ϕ=0.45 to z and y for ϕ from 0.48 to 0.51, respectively. The particles are still in the transition to order after a dimensionless time of 40 for ϕ=0.55 and 0.58.

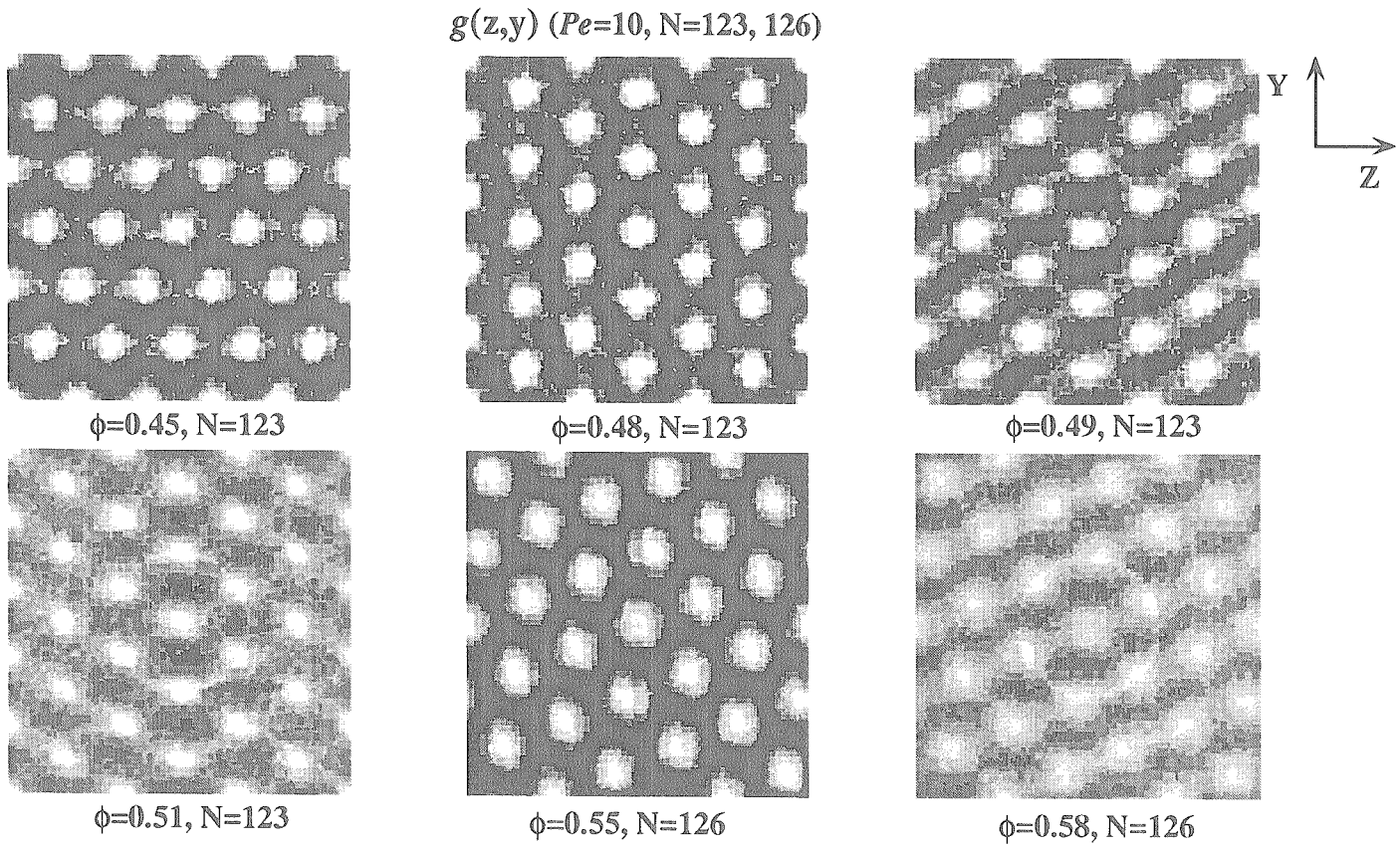

Figure 8.21.c: A comparison of $g(x,y)$ for hard spheres at Pe=10 with different volume fractions: from left to right, ϕ=0.45, 0.48, 0.49 (top row) and 0.51, 0.55 and 0.58 (bottom row). There are 123 or 126 particles in the unit cell. Regions of light color represent high probability and regions of dark color represent low probability. The flow direction is perpendicular to the z-y plane with the vorticity the z-axis and the velocity gradient the y-axis. At Pe=10, the shear and Brownian forces induce the flowing suspension to strongly order with hexagaonally packed strings of flowing particles. The symmetric hexagonal packing for ϕ=0.45 is rotated by an angle 90^0 and slightly stretched in the y-axis as ϕ increases to the range of 0.48 to 0.51. The new hexagonal packing is further inclined to accommodate 126 particles in the unit cell for ϕ=0.55 and 0.58.

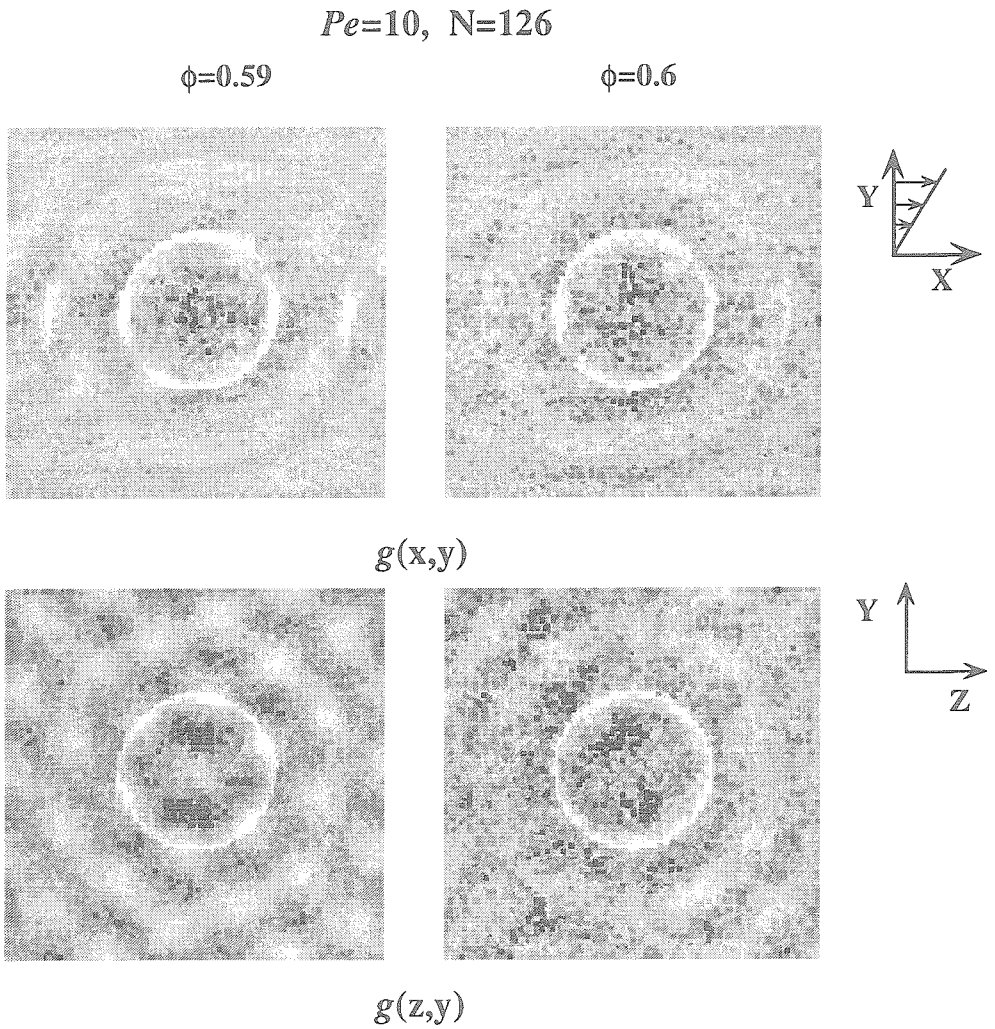

Figure 8.21.d: The probability density functions g(x,y) (top row) and g(z,y) (bottom row) obtained by Stokesian dynamics for hard spheres with Pe=10 and volume fractions ϕ=0.59 (left column) and 0.6 (right column). There are 126 particles in the unit cell and the initial particle configurations for the simulations are selected randomly. Regions of light color represent high probability and regions of dark color represent low probability. The flow direction is the horizontal x-axis (top figures) and perpendicular to the z-y plane (bottom figures). After 50 dimensionless time units, the microstructure has not equilibrated and large fluctuations are seen from the plot of g(x,y) and g(z,y). g(z,y) shows the onset signal of hexagonal packing of strings of flowing particles as the particles appear to be in the transition to order.

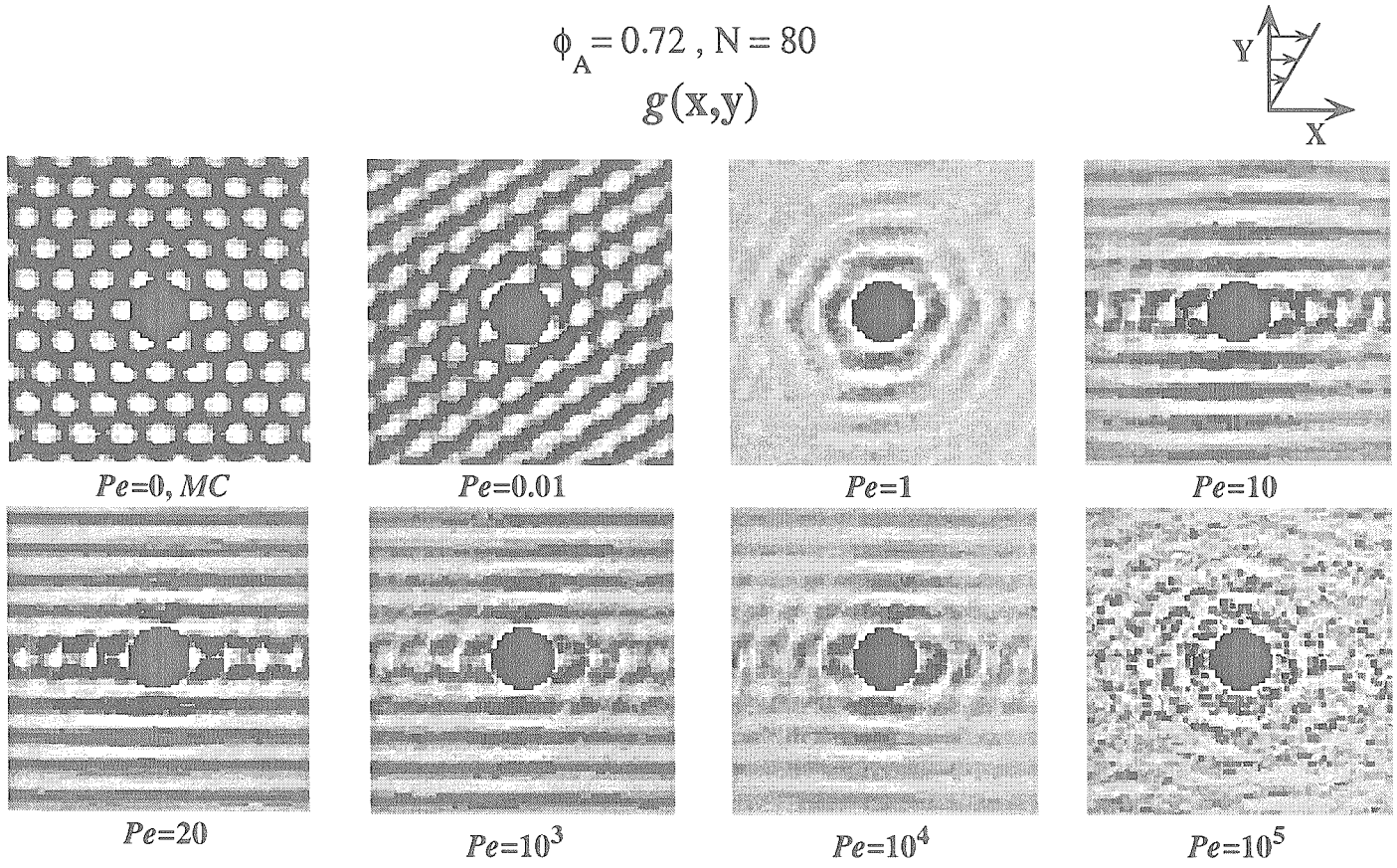

Figure 8.22.a: The probability density function $g(x,y)$ for a monolayer with 80 particles at an areal fraction $\phi_A = 0.72$ obtained by Stokesian dynamics for different Péclet numbers. Regions of light color represent high probability and regions of dark color represent low probability. The flow direction is the horizontal x-axis and the velocity gradient direction is the vertical y-axis. $g(x,y)$ shows a "string" formation of flowing particles for *Pe* from 10 to 10^4. The string-ordered microstructure is destroyed by very high shear rates at $Pe=10^5$. Note also the crystalline phase of the initial particle configuration obtained by a Monte-Carlo (*MC*) calculation for hard-disk fluid at the same areal fraction.

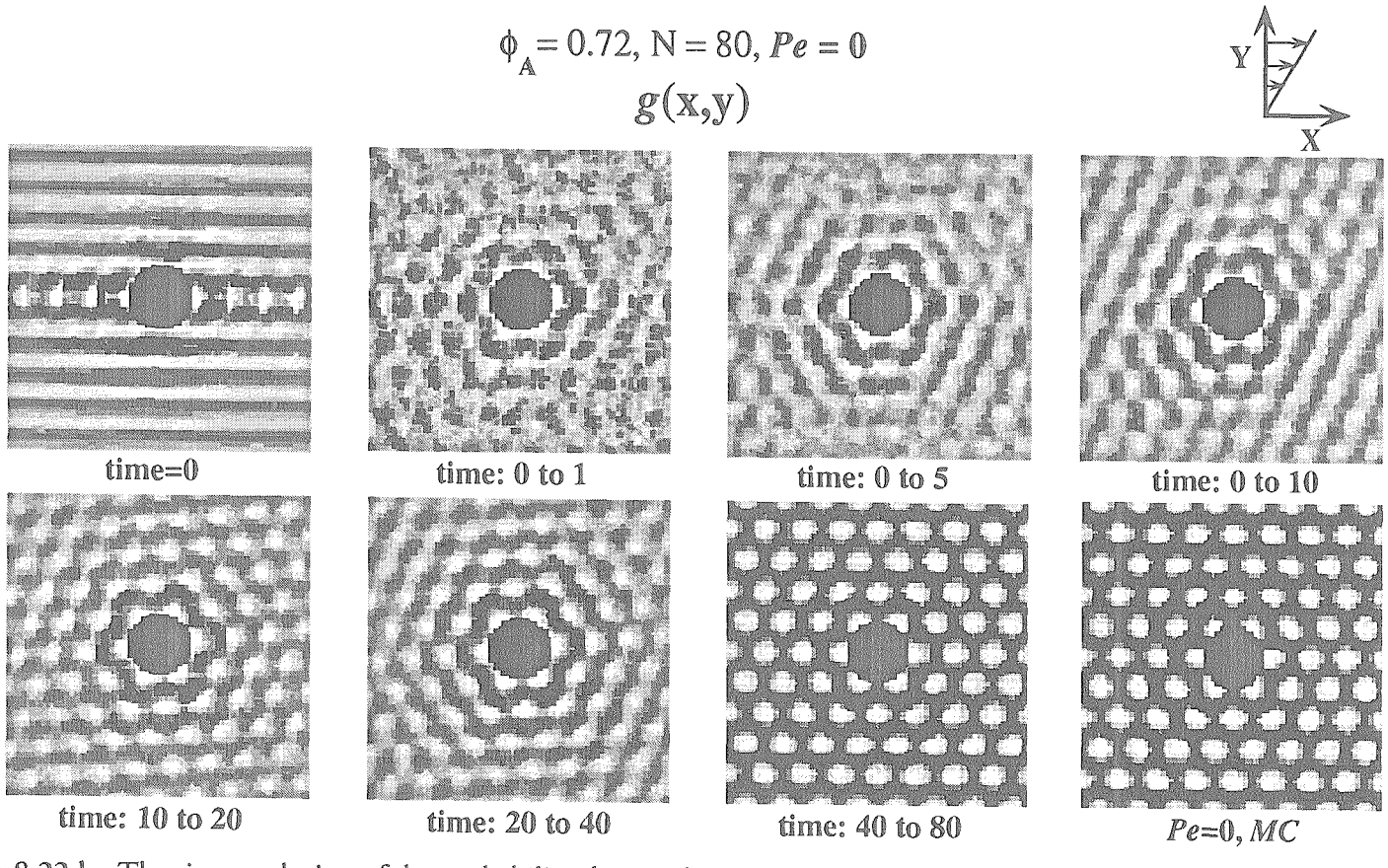

Figure 8.22.b: The time evolution of the probability density function g(x,y) obtained by Stokesian dynamics for a monolayer with 80 particles at an areal fraction ϕ_A= 0.72. Regions of light color represent high probability and regions of dark color represent low probability. The horizontal x-axis is the flow direction and the vertical y-axis is the velocity gradient direction. The relaxation of a shear-induced string-ordered microstructure at time=0 is shown at different times. The suspension recrystallizes after a dimensionless time of 80. Note an excellent comparison of the steady g(x,y) obtained by Stokesian dynamics for times of 40 to 80 and that of a Monte-Carlo sample (Pe=0, MC) at identical areal fraction.

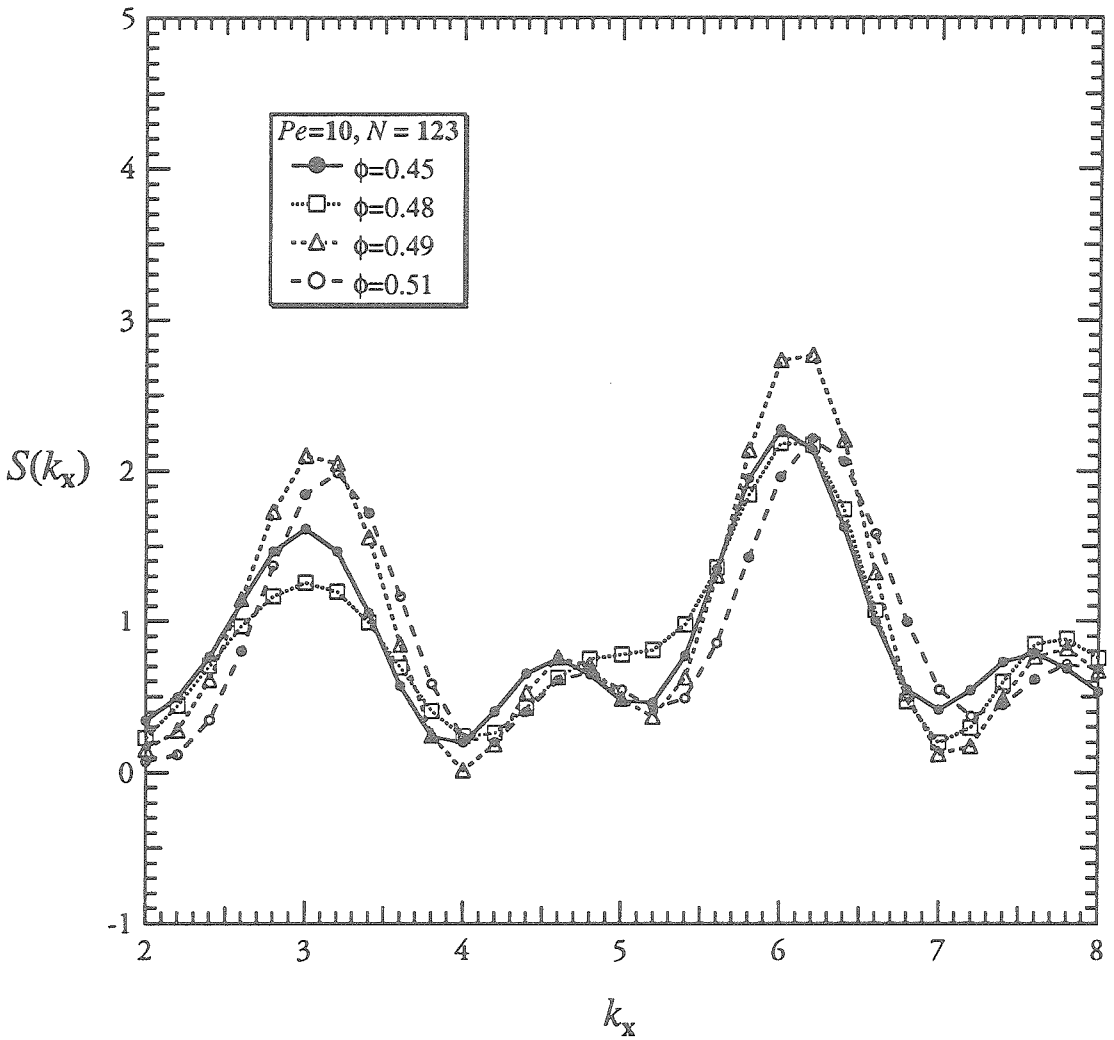

Figure 8.23.a: The line structure factor $S(k_x)$ obtained by Stokesian dynamics for hard-sphere suspensions with Pe=10 for different volume fractions: ϕ = (□) 0.48, (○) 0.49 and (△) 0.51. The line structure factor for a hard-sphere suspension at ϕ=0.45 (●) is also plotted in this figure as a reference for comparison. k_x is the dimensionless wave number in the flow direction, the x-axis. There are 123 particles in the unit cell. $S(k_x)$ shows little variation in this range of volume fraction and the scattering light intensity is small compared to that of $S(k_y)$ and $S(k_z)$ (cf. Fig.8.23.b-c).

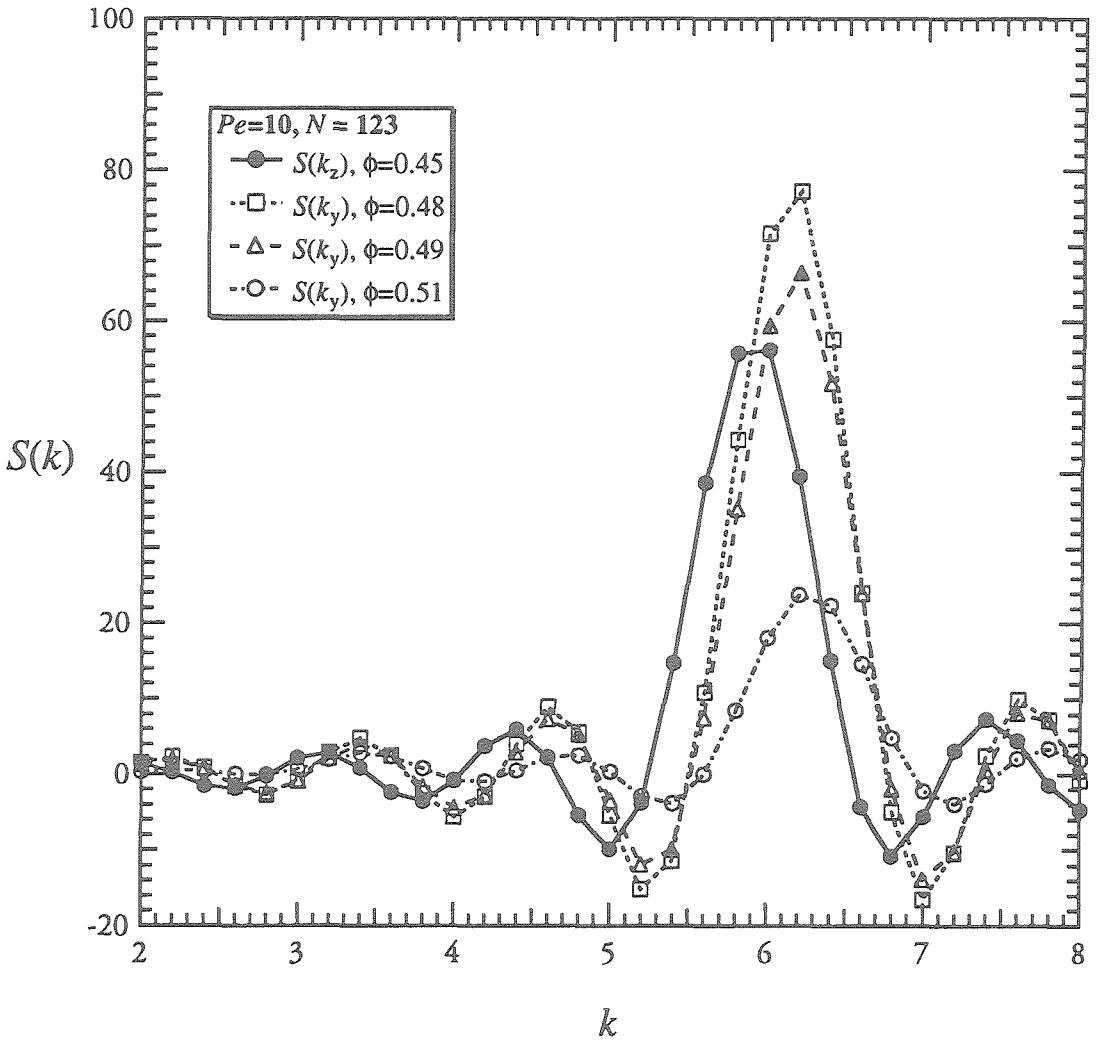

Figure 8.23.b: The line structure factor $S(k_y)$ obtained by Stokesian dynamics for hard-sphere suspensions with Pe=10 for different volume fractions ϕ = (□) 0.48, (○) 0.49 and (Δ) 0.51. k_y is the dimensionless wave number in the velocity gradient direction, the y-axis. There are 123 particles in the unit cell. $S(k_y)$ shows an intensity maxima peak at $k_y \approx 6.5$ for ϕ=0.48, 0.49 and 0.51. The line structure factor $S(k_z)$ for a hard-sphere suspension at ϕ=0.45 (●) is also plotted in this figure as a reference for comparison with $S(k_y)$ of ϕ=0.48, 0.49 and 0.51. The similarity of these curves shows a strong evidence of a change in microstructure from the y and z patterns of the particle order at ϕ=0.45 to the z and y patterns of hard spheres at volume fraction ϕ=0.48, 0.49 and 0.51, respectively.

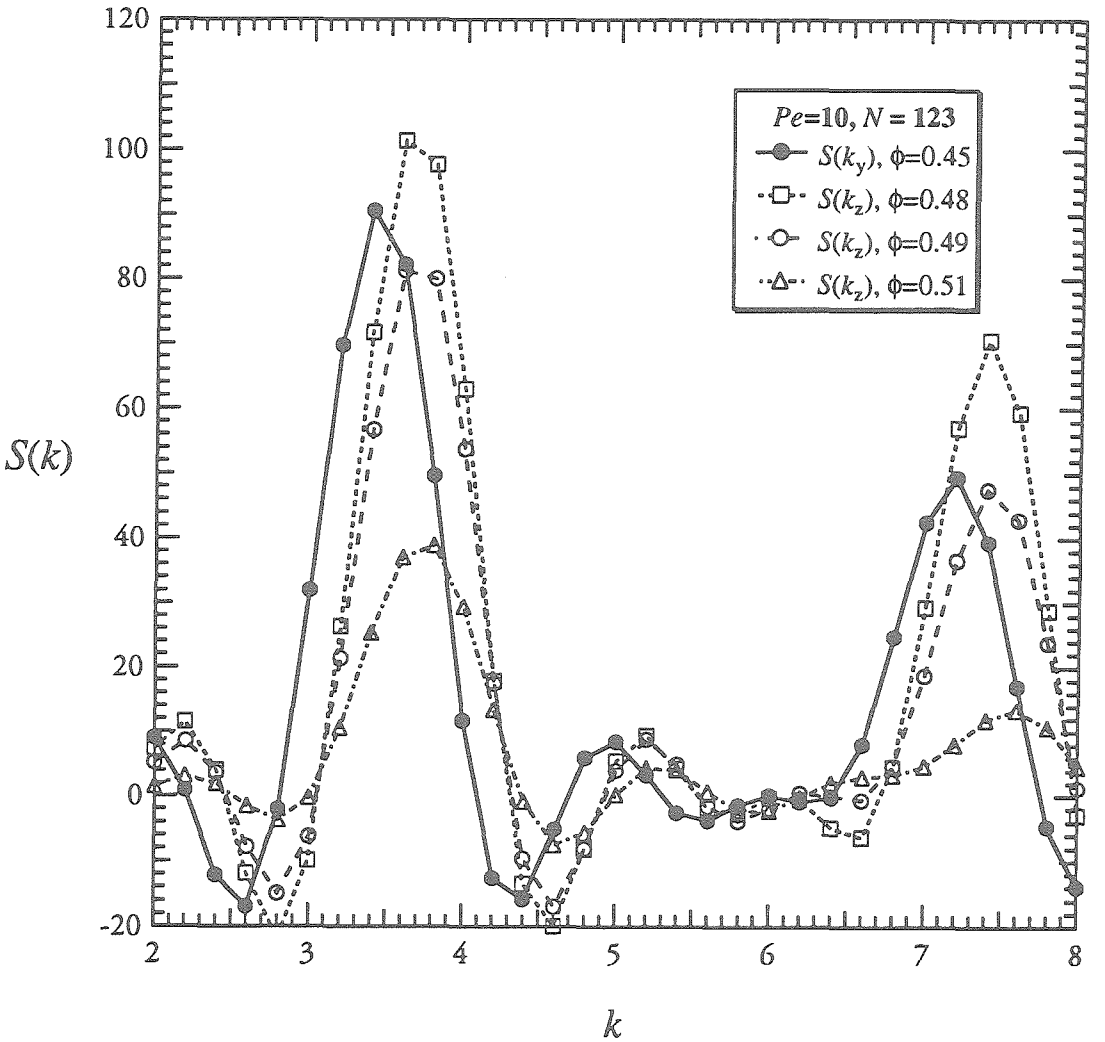

Figure 8.23.c: The line structure factor $S(k_z)$ obtained by Stokesian dynamics for hard-sphere suspensions with Pe=10 and different volume fractions ϕ = (□) 0.48, (○) 0.49 and (△) 0.51. k_z is the dimensionless wave number in the vorticity direction, the z-axis. There are 123 particles in the unit cell. $S(k_z)$ shows two intensity maxima peak at $k_z \approx 3.5$ and at $k_z \approx 7.5$ for ϕ=0.48, 0.49 and 0.51. The line structure factor $S(k_y)$ for a hard-sphere suspension at ϕ=0.45 (●) is also plotted in this figure as a reference for comparing with $S(k_z)$ of ϕ=0.48, 0.49 and 0.51. It is a clear evidence that the microstructure has switched from z and y packing patterns at ϕ=0.45 to y and z packing formations as ϕ increases from 0.45 to the range of 0.48 to 0.51.

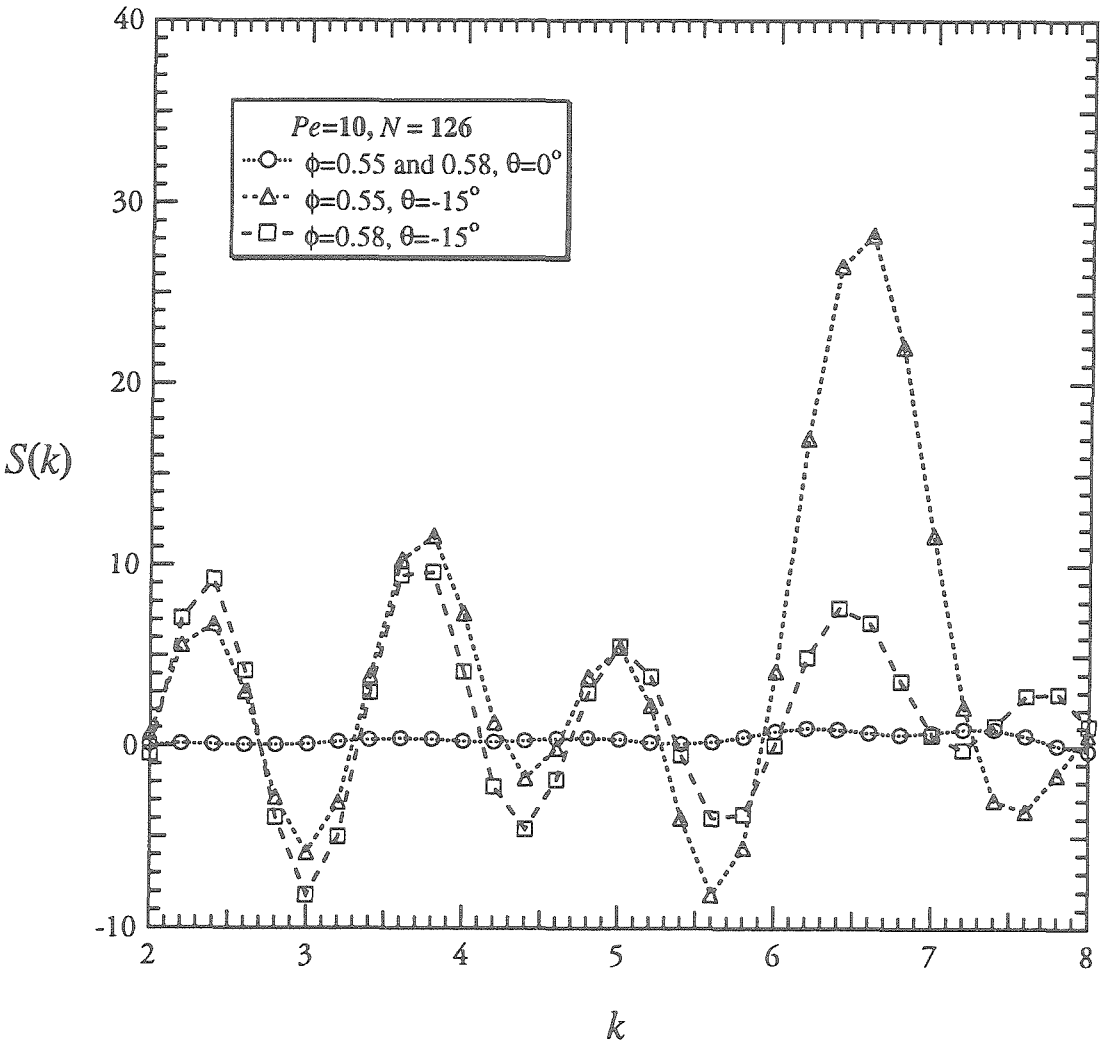

Figure 8.23.d: The line structure factor $S(k)$ obtained by Stokesian dynamics for hard-sphere suspensions with Pe=10 for volume fractions ϕ=0.55 and 0.58. k is the dimensionless wave number. There are 126 particles in the unit cell. The structure factor computed with an angle $\theta=0^0$ (○) (which is $S(k_y)$) shows minimum scattered intensity compared to the strong scattered intensity of the structure factor computed with an angle $\theta=-15^0$ for ϕ=0.55 (Δ) and 0.58 (□). This is confirmed by the plot of the probability density function $g(z,y)$ which also shows an inclined "hexgonal" packing of strings of flowing particles (cf. Fig.8.21.d).

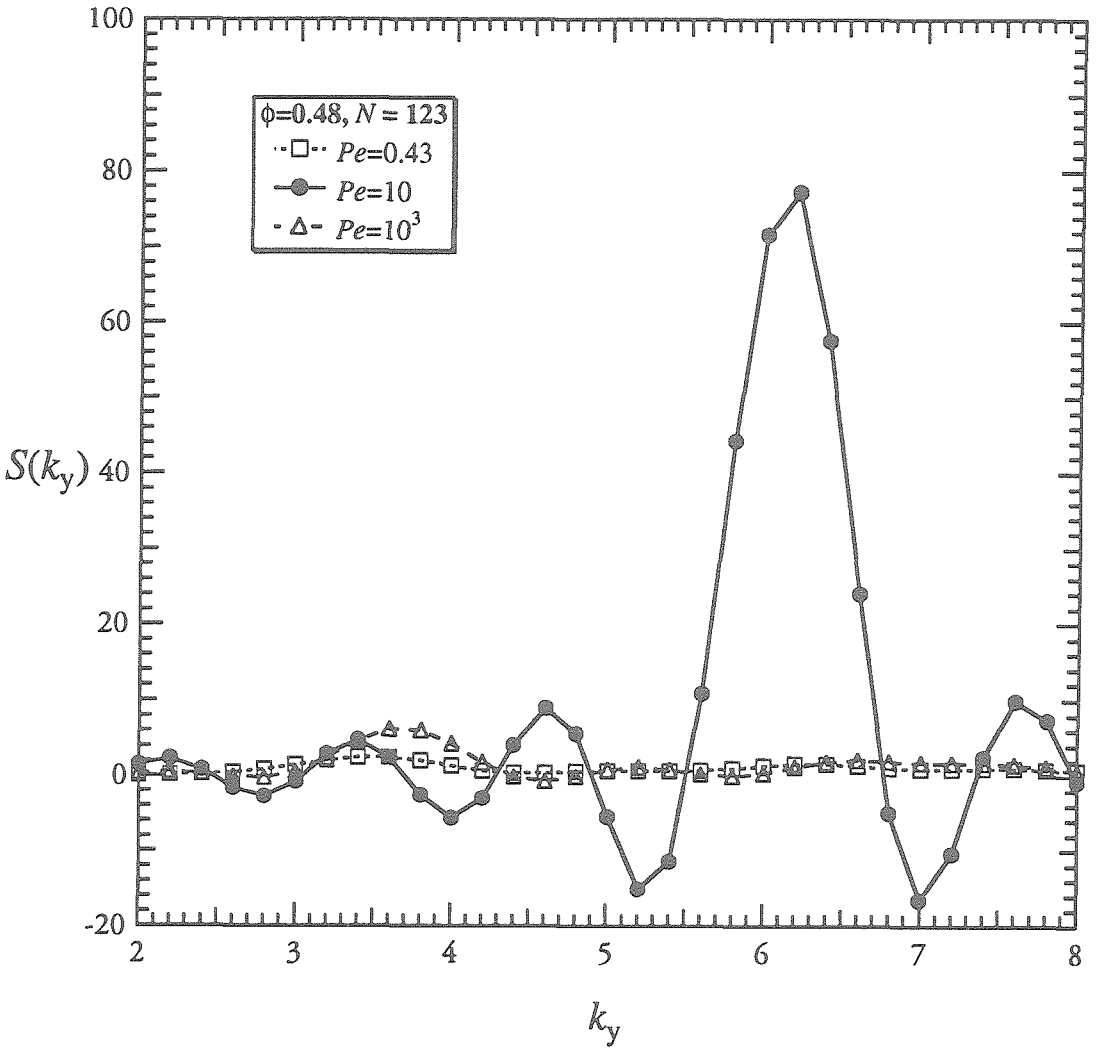

Figure 8.24.a: The line structure factor $S(k_y)$ for hard spheres at a volume fraction ϕ=0.48 with 123 particles obtained by Stokesian dynamics for three different Péclet numbers: Pe = 0.43 (□), 10 (●) and 1000 (Δ). k_y is the dimensionless wave number in the velocity gradient direction. $S(k_y)$ for Pe=10 displays strong scattered intensity pattern with an intense peak at k_y≈6.5 compared to small scattered intensity of $S(k_y)$ for Pe=0.43 and 1000.

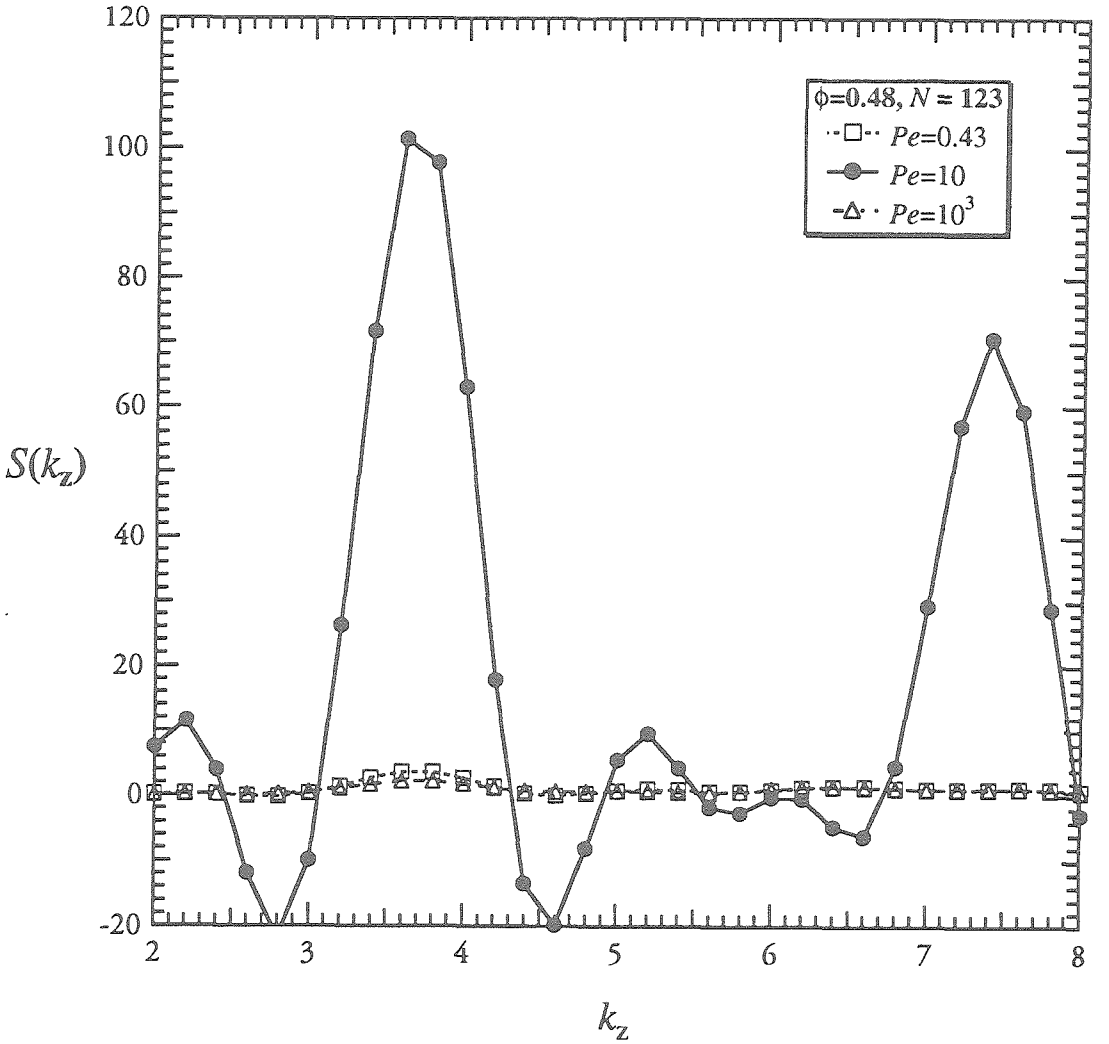

Figure 8.24.b: The line structure factor $S(k_z)$ for hard spheres at a volume fraction ϕ=0.48 with 123 particles obtained by Stokesian dynamics for three different Péclet numbers: Pe = 0.43 (□), 10 (●) and 1000 (Δ). k_z is the dimesionless wave number in the vorticity direction. $S(k_z)$ for Pe=10 displays strong scattered intensity pattern with two intense peaks at $k_z \approx 3.5$ and at ≈7.5 compared to insignificant scattered intensity of $S(k_z)$ for Pe=0.43 and 1000.

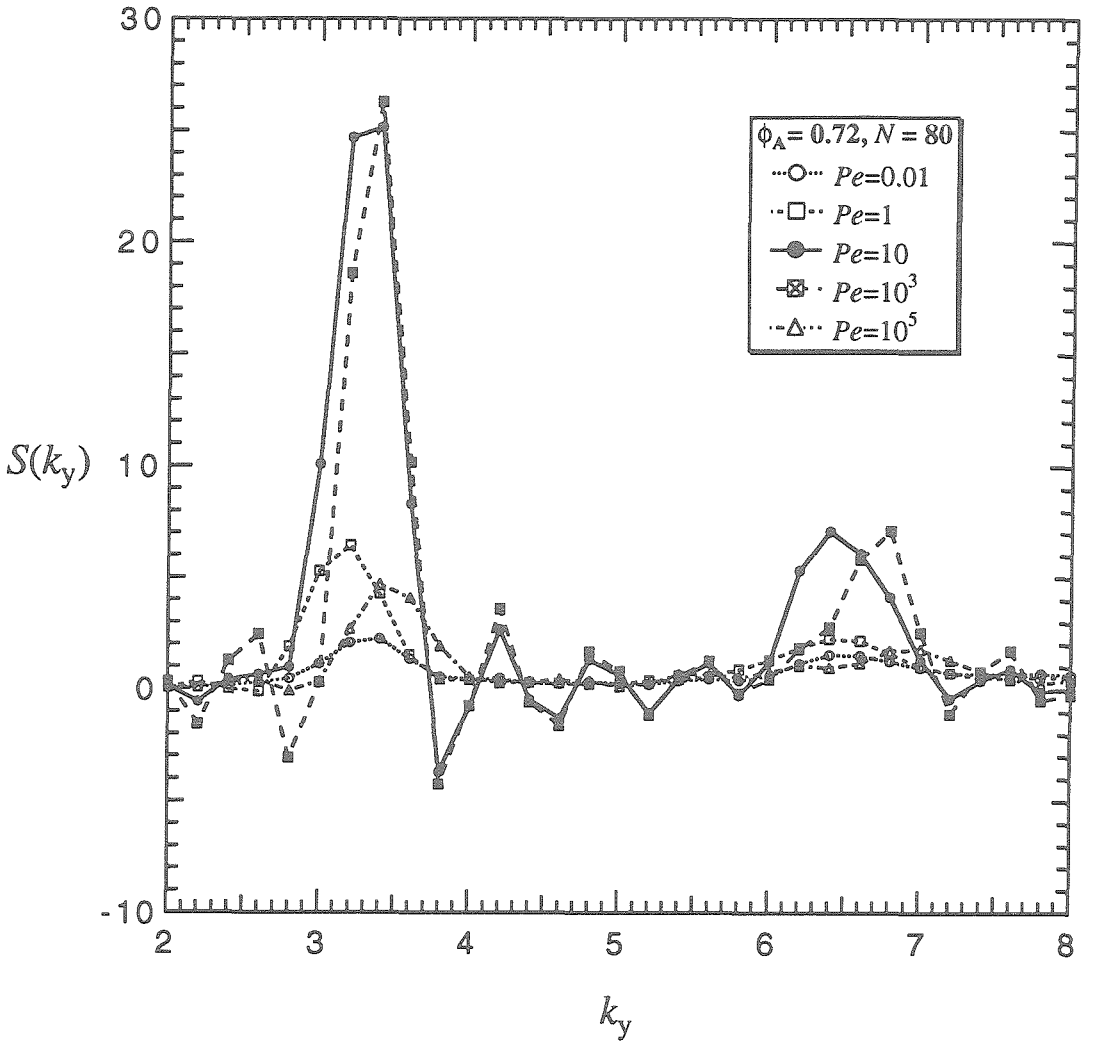

Figure 8.25: The line structure factor $S(k_y)$ of a monolayer with 80 particles at areal fraction ϕ_A= 0.72 obtained by Stokesian dynamics as a function of the Péclet number: Pe = 0.01 (○), 1 (□), 10 (●), 1000 (⊠) and 10^5 (Δ). k_y is the dimensionless wave number in the velocity gradient direction, the y-axis. $S(k_y)$ for Pe=10 and 1000 shows peaks with high scattering light intensity at k_y≈3.5 and at ≈6.5 reflecting the string formation of particles in the flow direction similar to the string formation of hard spheres at ϕ=0.45 (cf. Fig.6.21).

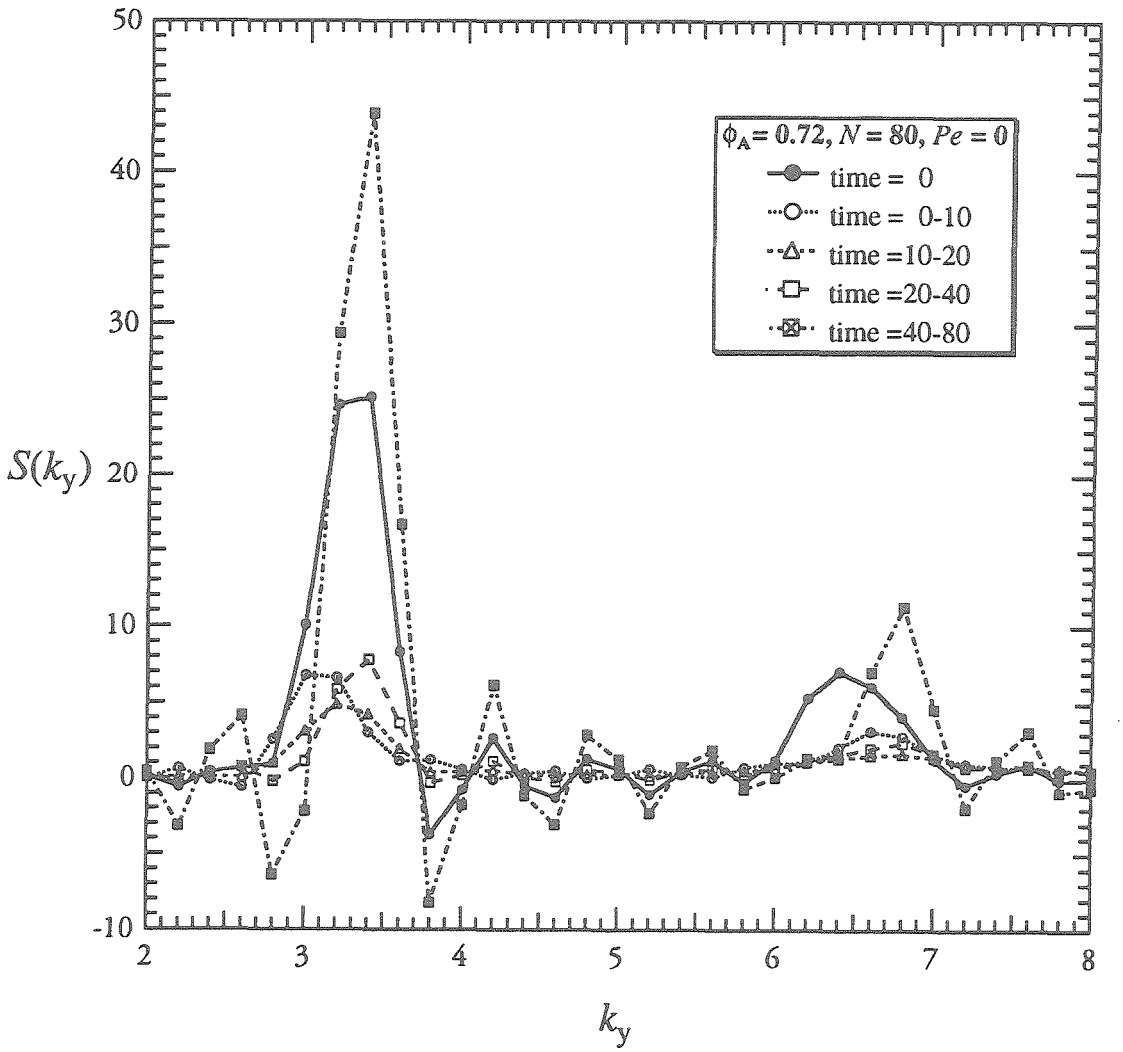

Figure 8.26: The time evolution of the line structure factor $S(k_y)$ of a monolayer with 80 particles at areal fraction ϕ_A= 0.72 obtained by Stokesian dynamics for different times: 0 (●, Pe=10), 0 to 10 (○), 10 to 20 (△), 20 to 40 (□) and 40 to 80 (⊠). k_y is the dimensionless wave number in the velocity gradient direction, the y-axis. $S(k_y)$ shows the relaxation of the string-ordered microstructure with time as the suspension returns to a rest state (Pe=0). The scattered intensity decreases with time and at equilibrium (after 80 dimensionless time units), strong scattered intensity of $S(k_y)$ reflects the crystalline phase transition of a hard-disk fluid at ϕ_A= 0.72.

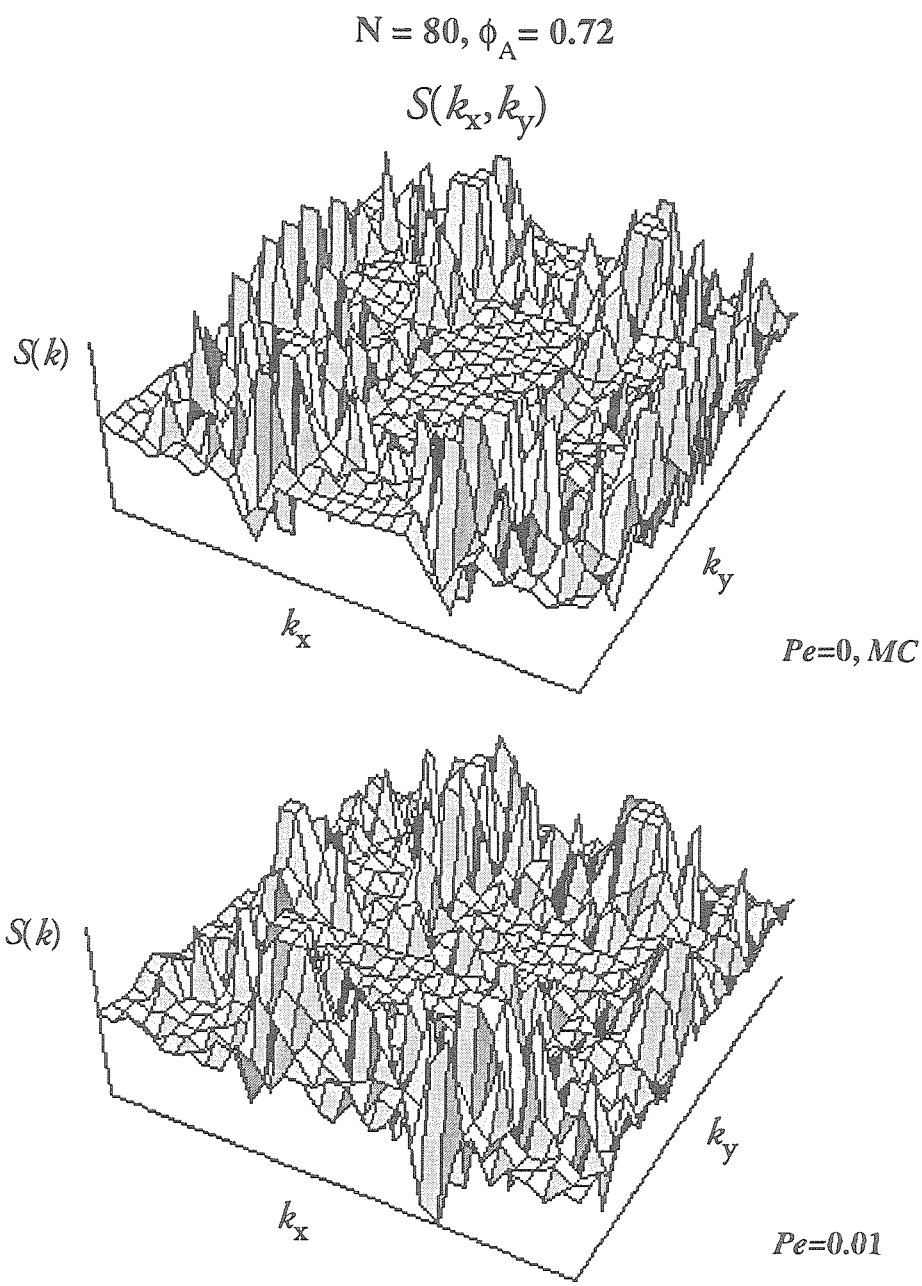

Figure 8.27.a: The structure factor $S(k_x,k_y)$ obtained by Stokesian dynamics for a monolayer with 80 particles at an areal fraction ϕ_A= 0.72 and Pe=0.01 (bottom). The range of the dimensionless wave numbers k_x and k_y is from +/-0.5 to +/-4.0. In comparison to $S(k_x,k_y)$ of the starting random configuration (top) obtained by a Monte-Carlo (MC) calculation, $S(k_x,k_y)$ for Pe=0.01 shows a small variation for a slightly perturbed isotropic hard-sphere distribution.

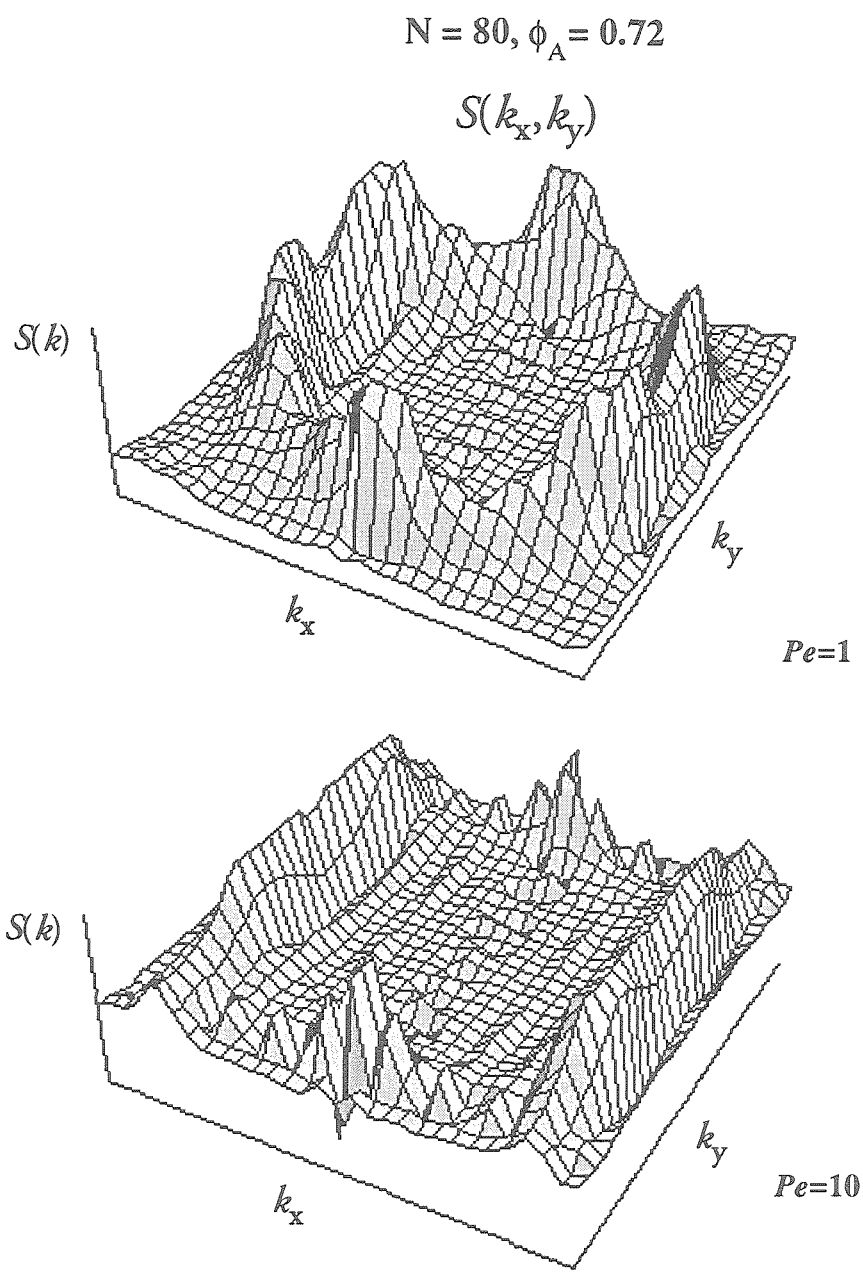

Figure 8.27.b: The structure factor $S(k_x,k_y)$ obtained by Stokesian dynamics for a monolayer with 80 particles at ϕ_A= 0.72 and *Pe*=1 (top) and 10 (bottom). The range of the dimensionless wave numbers k_x and k_y is from +/-0.5 to +/-4.0. As the Péclet number increases, $S(k_x,k_y)$ shows a pattern of scattering light intensity which forms two vertical bands along the wave numbers $k_x \approx$ +/- 3.5 and signals the onset of strings of flowing particles. This can clearly be seen for *Pe*=10.

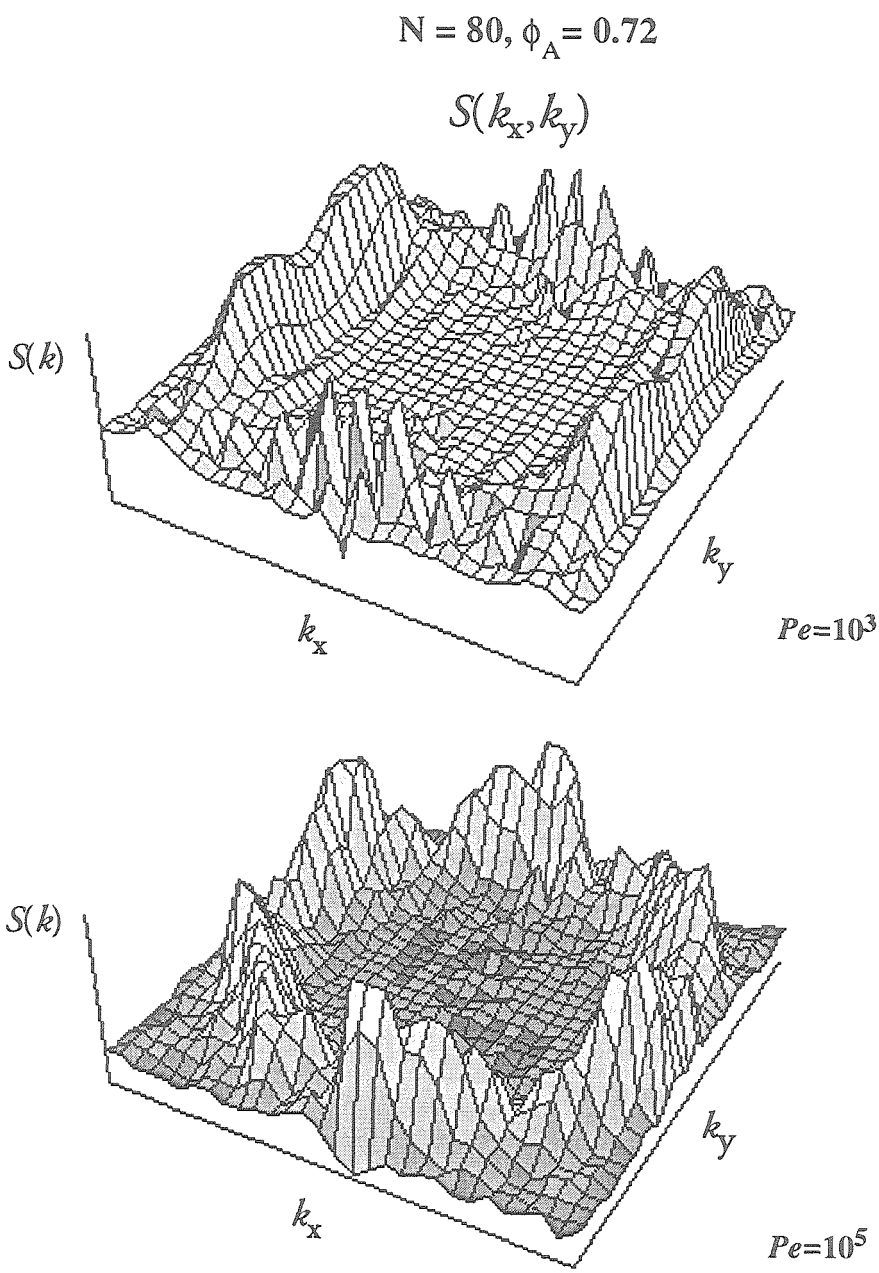

Figure 8.27.c: The structure factor $S(k_x,k_y)$ obtained by Stokesian dynamics for a monolayer with 80 particles at ϕ_A= 0.72 and Pe=10^3 (top) and 10^5 (bottom). The range of the dimensionless wave numbers k_x and k_y is from +/-0.5 to +/-4.0. The vertical-banded pattern of the scattering light intensity from $S(k_x,k_y)$ can still be seen at Pe=10^3. At a much higher shear rates (Pe=10^5), the pattern is destroyed.

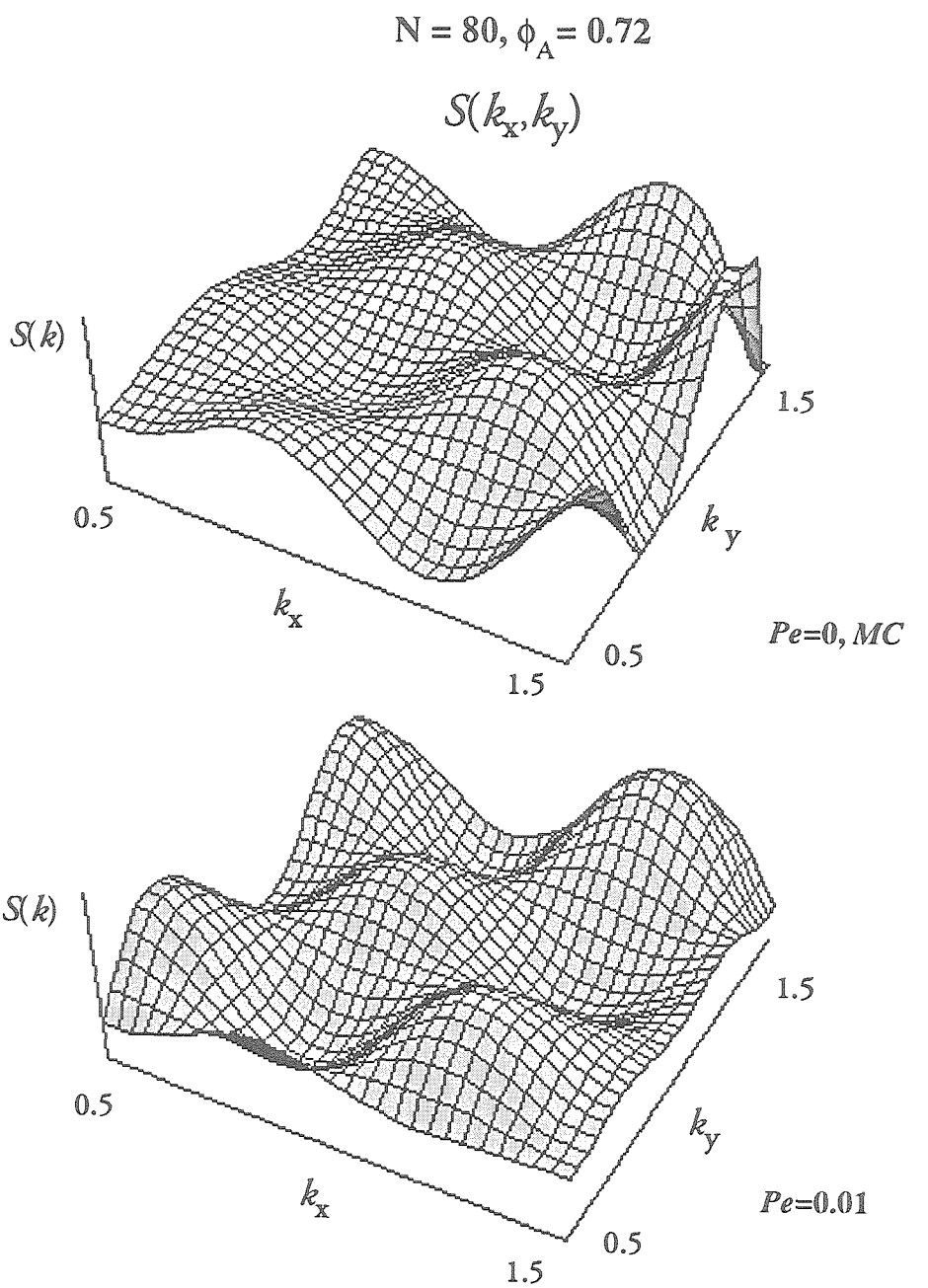

Figure 8.28.a: The structure factor $S(k_x,k_y)$ obtained by Stokesian dynamics for a monlayer with 80 particles at an areal fraction ϕ_A= 0.72 and *Pe*=0.01 (bottom). $S(k_x,k_y)$ is computed with a smaller range of k_x and k_y from 0.5 to 1.5. In comparison to $S(k_x,k_y)$ of the starting random configuration obtained by a Monte-Carlo (*MC*) calculation (top), $S(k_x,k_y)$ computed with small wave numbers for *Pe*=0.01 shows a noticeable variation for a slightly deformed hard-sphere structure.

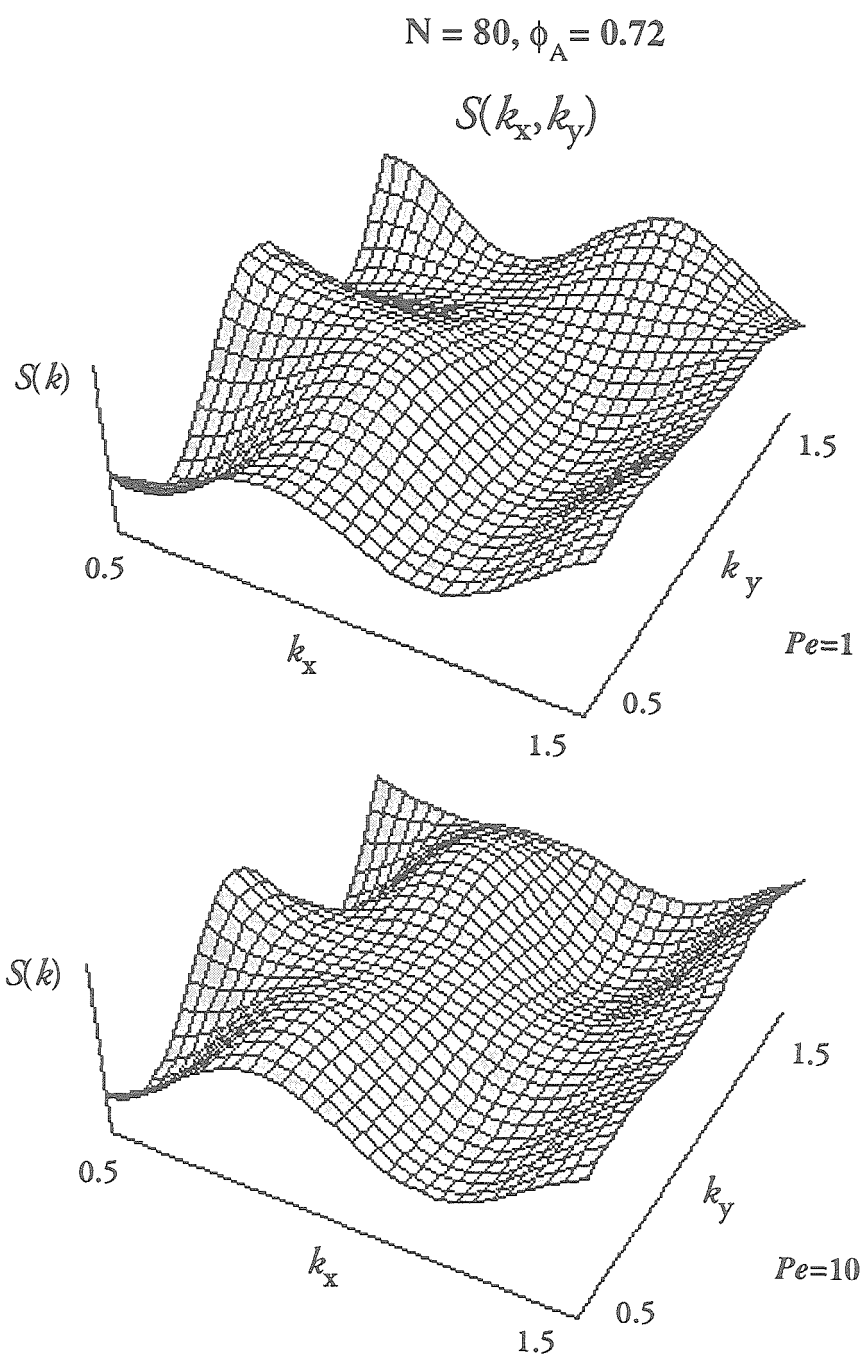

Figure 8.28.b: The structure factor $S(k_x,k_y)$ obtained by Stokesian dynamics for a monolayer with 80 particles at ϕ_A= 0.72 and Pe=1 (top) and 10 (bottom). As Pe increases, $S(k_x,k_y)$ computed with small wave numbers shows a pattern of scattering light intensity which forms two vertical bands along the lines with wave numbers $k_x \approx 0.75$ and $k_x \approx 1.5$. The string order of flowing particles is seen to be long ranged as shown for Pe=10.

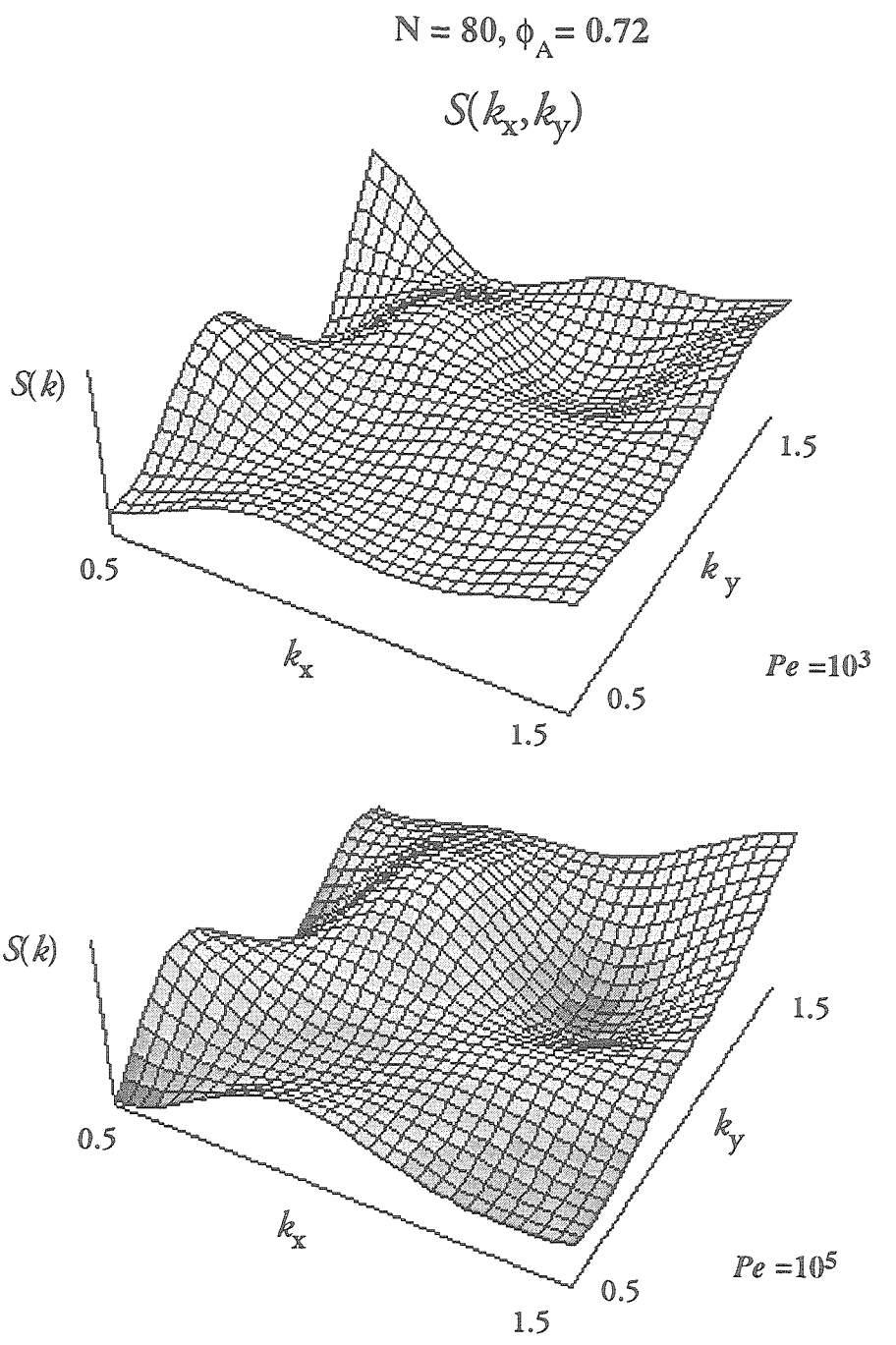

Figure 8.28.c: The structure factor $S(k_x,k_y)$ obtained by Stokesian dynamics for a monolayer with 80 particles at an areal fraction ϕ_A= 0.72 and Pe=10^3 (top) and 10^5 (bottom). While the short range order of the microstructure is seen at Pe=10^3 (cf. Fig.8.27.c), there is no long range order of the flowing particles at high shear rates as the vertical bands of $S(k_x,k_y)$ computed with small wave numbers for Pe=10 is destroyed by Pe=10^3 and 10^5.

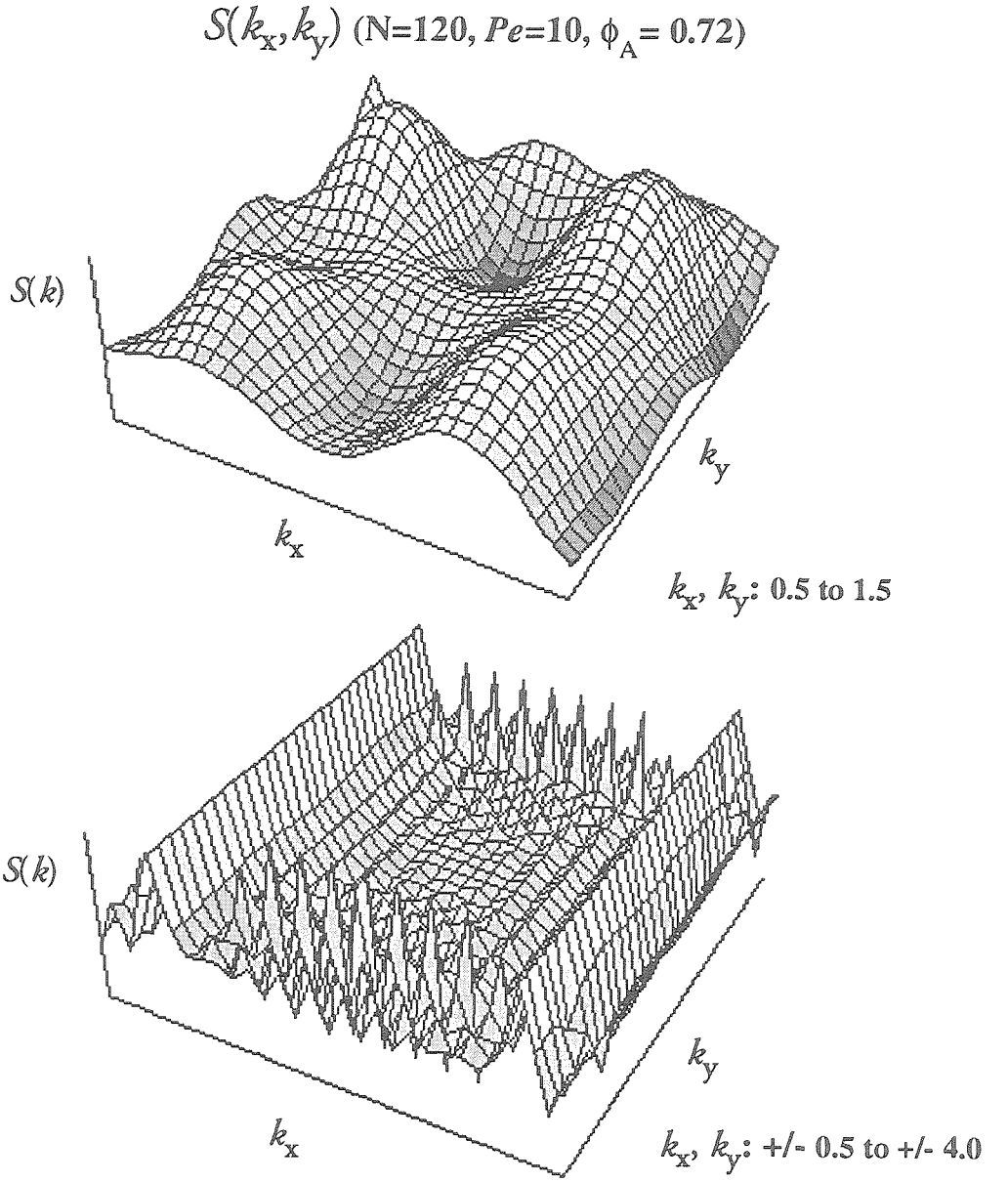

Figure 8.29: The structure factor $S(k_x,k_y)$ obtained by Stokesian dynamics for a monolayer with 120 particles at an areal fraction ϕ_A= 0.72 and Pe=10 for two different ranges of the dimensionless wave numbers k_x and k_y: from 0.5 to 1.5 (top) and from +/-0.5 to +/-4.0 (bottom). $S(k_x,k_y)$ computed with small wave numbers (top) and with large wave numbers comparable to the particle size (bottom) shows the long and short range order of the string formation of flowing particles, respectively. Vertical bands of intensity maxima are seen for $S(k_x,k_y)$ with both ranges of the wave number. Note that in a monolayer of 120 particles, each particle has up to six different layers of neighboring particles.

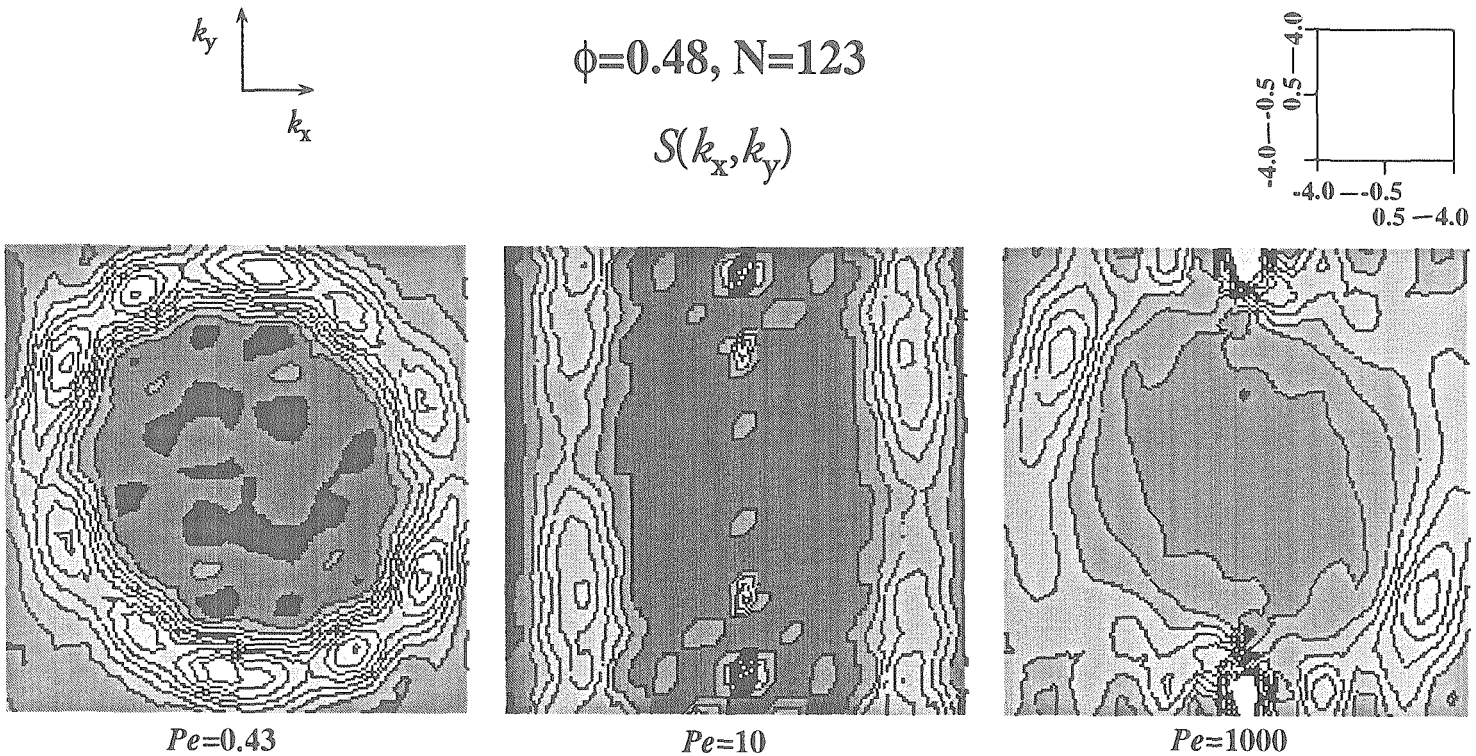

Figure 8.30.a: The structure factor $S(k_x,k_y)$ obtained by Stokesian dynamics for hard spheres at ϕ=0.48 with 123 particles and three different Péclet numbers: 0.43 (left), 10 (central) and 1000 (right). Regions of light color represent high scattering light intensity and regions of dark color represent low scattering light intensity. The upper right figure displays the range of the dimensionless wave numbers k_x and k_y. $S(k_x,k_y)$ shows a small distortion of the Debye-Scherrer ring for a Brownian dominated suspension (Pe=0.43) and two vertical bands of high scattering light intensity for an ordered suspension (Pe=10). At high shear rates (Pe=1000), the bands of intensity maxima are destroyed. Note also the absence of circular regions of intensity maxima for $S(k_x,k_y)$ at Pe=10 compared to that of hard spheres for ϕ=0.45 (cf. Fig.6.24).

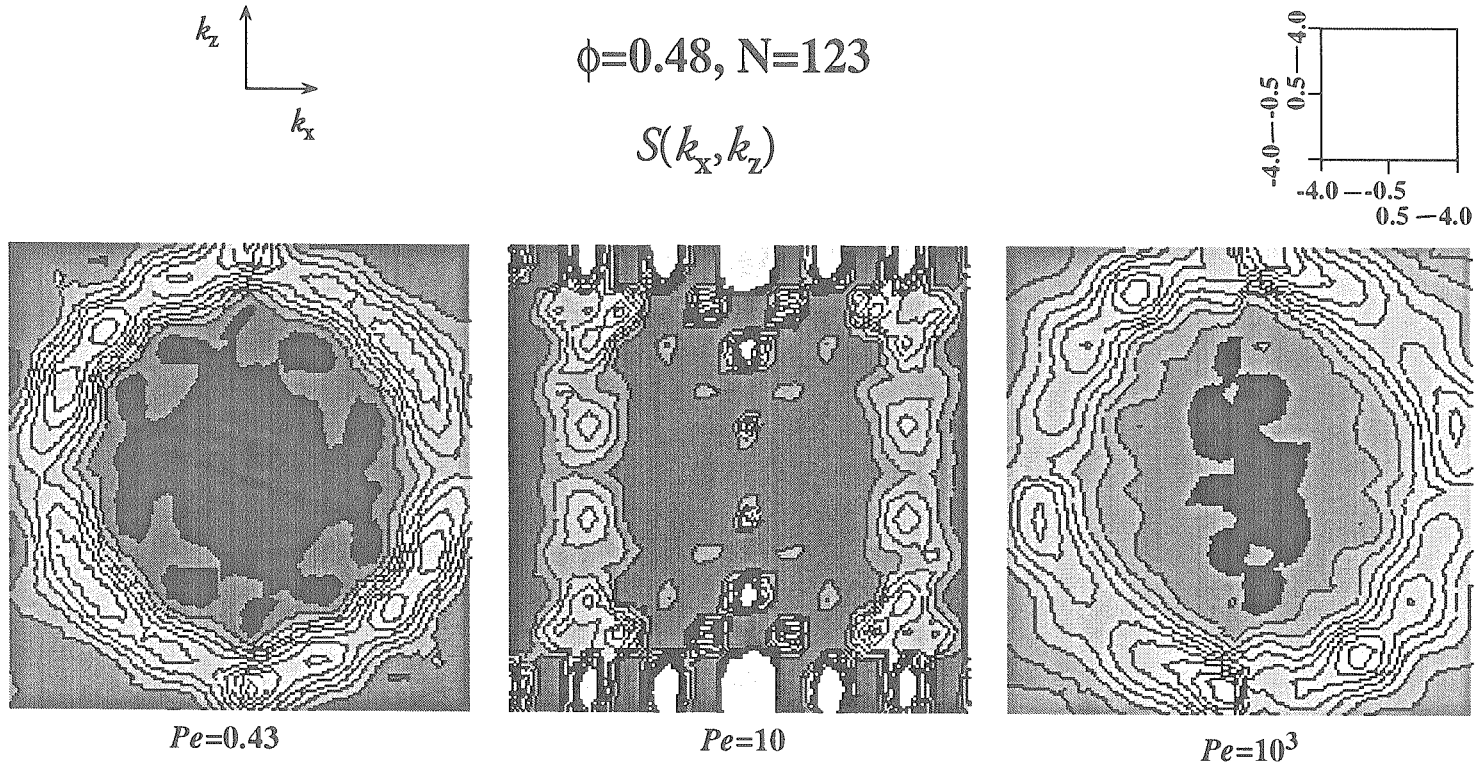

Figure 8.30.b: The structure factor $S(k_x,k_z)$ for hard spheres at ϕ=0.48 with 123 particles and different Péclet numbers: 0.43 (left), 10 (central) and 1000 (right). Regions of light color represent high scattering light intensity and regions of dark color represent low scattering light intensity. $S(k_x,k_z)$ shows a small distortion of the Debye-Scherrer ring for a slightly deformed suspension (Pe=0.43) and two vertical bands and circular regions of intensity maxima for a strongly ordered suspension (Pe=10). At high shear rates (Pe=1000), the intensity maxima patterns are destroyed. The similarity at Pe=10 of $S(k_x,k_y)$ of hard spheres for ϕ=0.45 (cf. Fig.6.24) and $S(k_x,k_z)$ for ϕ=0.48 here shows a clear evidence of a switching in the packing pattern of the particles from y and z to z and y as the volume fraction increases from 0.45 to 0.48, respectively.

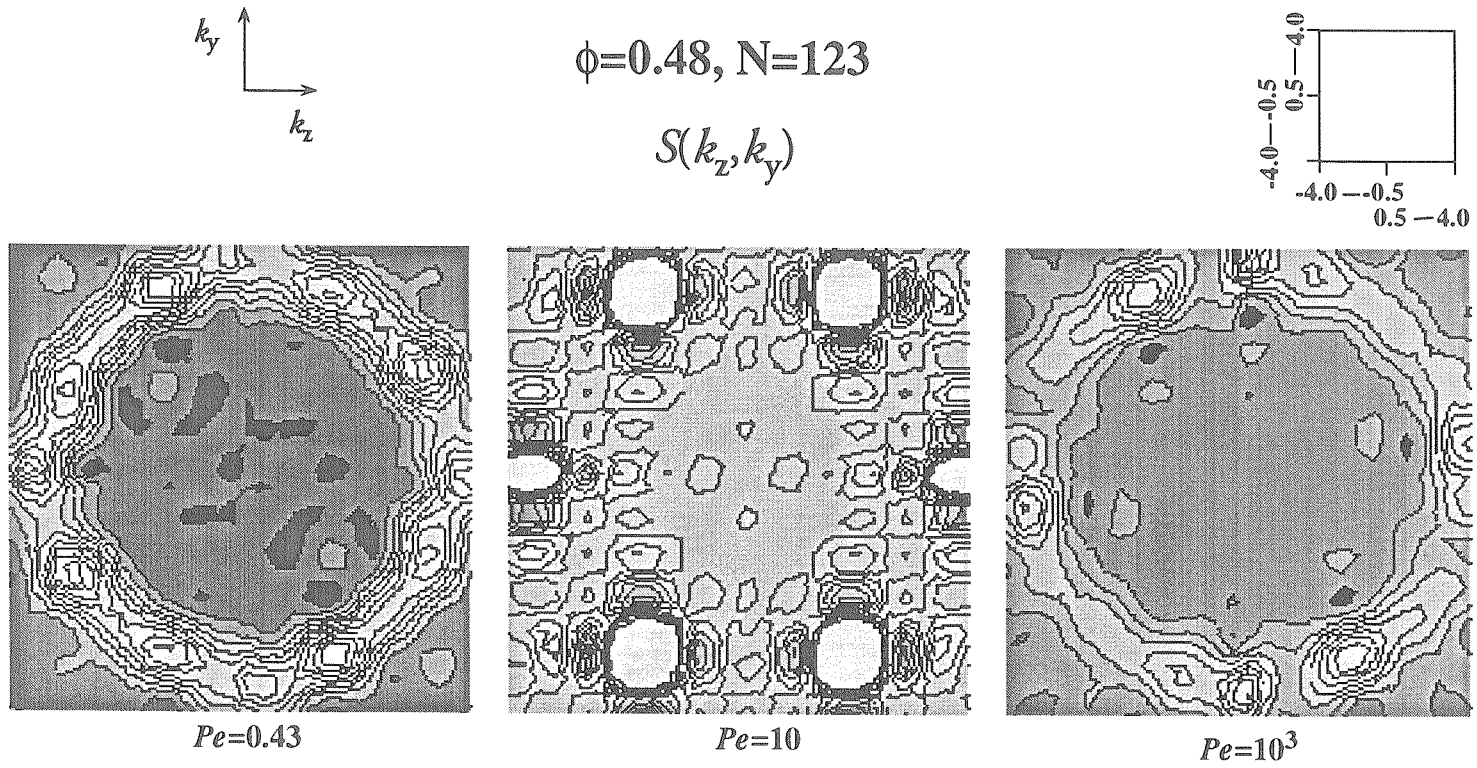

Figure 8.30.c: The structure factor $S(k_z,k_y)$ for hard spheres at ϕ=0.48 with 123 particles and three different Péclet numbers: 0.43 (left), 10 (central) and 1000 (right). Regions of light color represent high scattering light intensity and regions of dark color represent low scattering light intensity. $S(k_z,k_y)$ shows a distinct halo ring of six intensity maxima for strongly ordered suspension at Pe=10. The long range order of the flowing particles can also be seen from several smaller, less intense halo rings. At high shear rate (Pe=1000), the halo ring patterns are destroyed. In comparison to $S(k_z,k_y)$ of hard spheres for ϕ=0.45 and Pe=10 (cf. Fig.6.25), the new halo ring obtained for ϕ=0.48 shown here is seen as a result of a 90-degree rotation of the halo ring for ϕ=0.45.

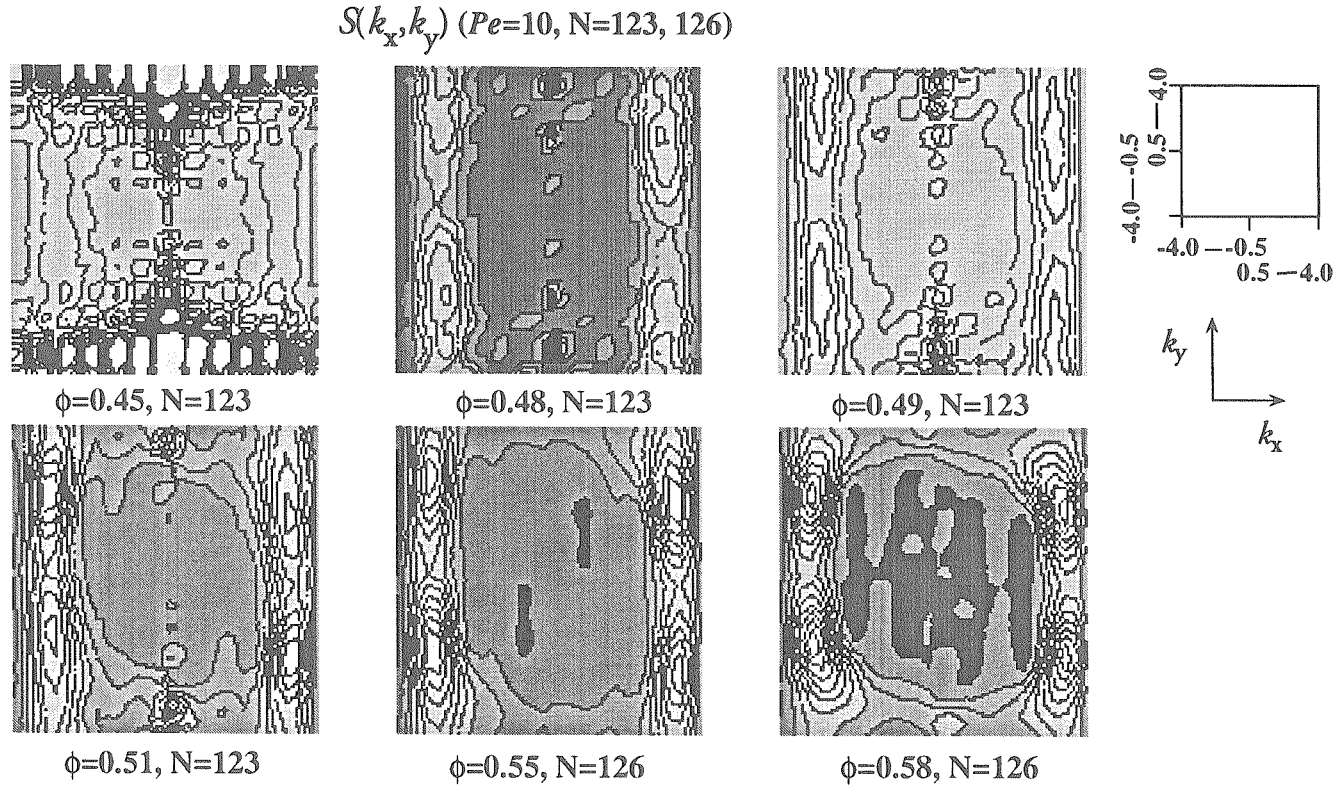

Figure 8.31.a: A comparison of the structure factor $S(k_x,k_y)$ for hard spheres at Pe=10 with different volume fractions: from left to right, ϕ=0.45, 0.48 and 0.49 (top row) and 0.51, 0.55 and 0.58 (bottom row). There are 123 or 126 particles in the unit cell. Regions of light color represent high scattering light intensity and regions of dark color represent low scattering light intensity. $S(k_x,k_y)$ displays two vertical bands of high intensity for string-ordered microstructure at Pe=10 for this range of volume fraction. Note also as the volume fraction increases, the intensity of the vertical bands increases as shown by the brightness of $S(k_x,k_y)$ in this region. The circular regions of intensity maxima along the horizontal lines with wave numbers $k_x \approx +/-3.5$ can only be seen for ϕ=0.45.

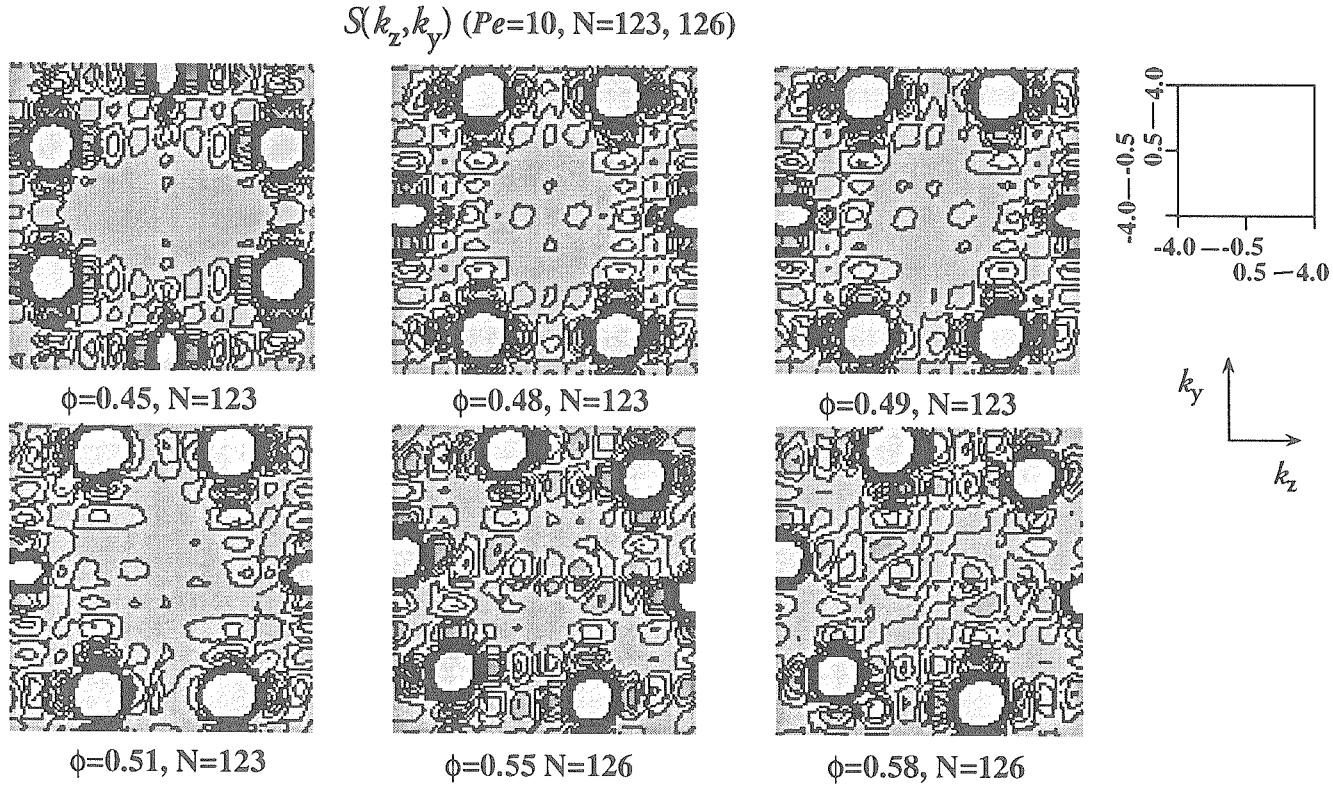

Figure 8.31.b: A comparison of $S(k_z,k_y)$ for hard spheres at Pe=10 with different volume fractions: from left to right, ϕ=0.45, 0.48 and 0.49 (top row) and 0.51, 0.55 and 0.58 (bottom row). There are 123 or 126 particles in the unit cell. Regions of light color represent high scattering light intensity and regions of dark color represent low scattering light intensity. $S(k_z,k_y)$ displays a distinct halo ring with six intensity maxima. The long range order of the flowing particles can be seen with smaller and less intense halo rings. Note also as the volume fraction increases from 0.45 to the range of 0.48 to 0.51, the halo ring rotates by an angle of 90 degrees. At ϕ=0.55 and 0.58, the halo ring further inclines by a small angle relative to the k_z-axis.

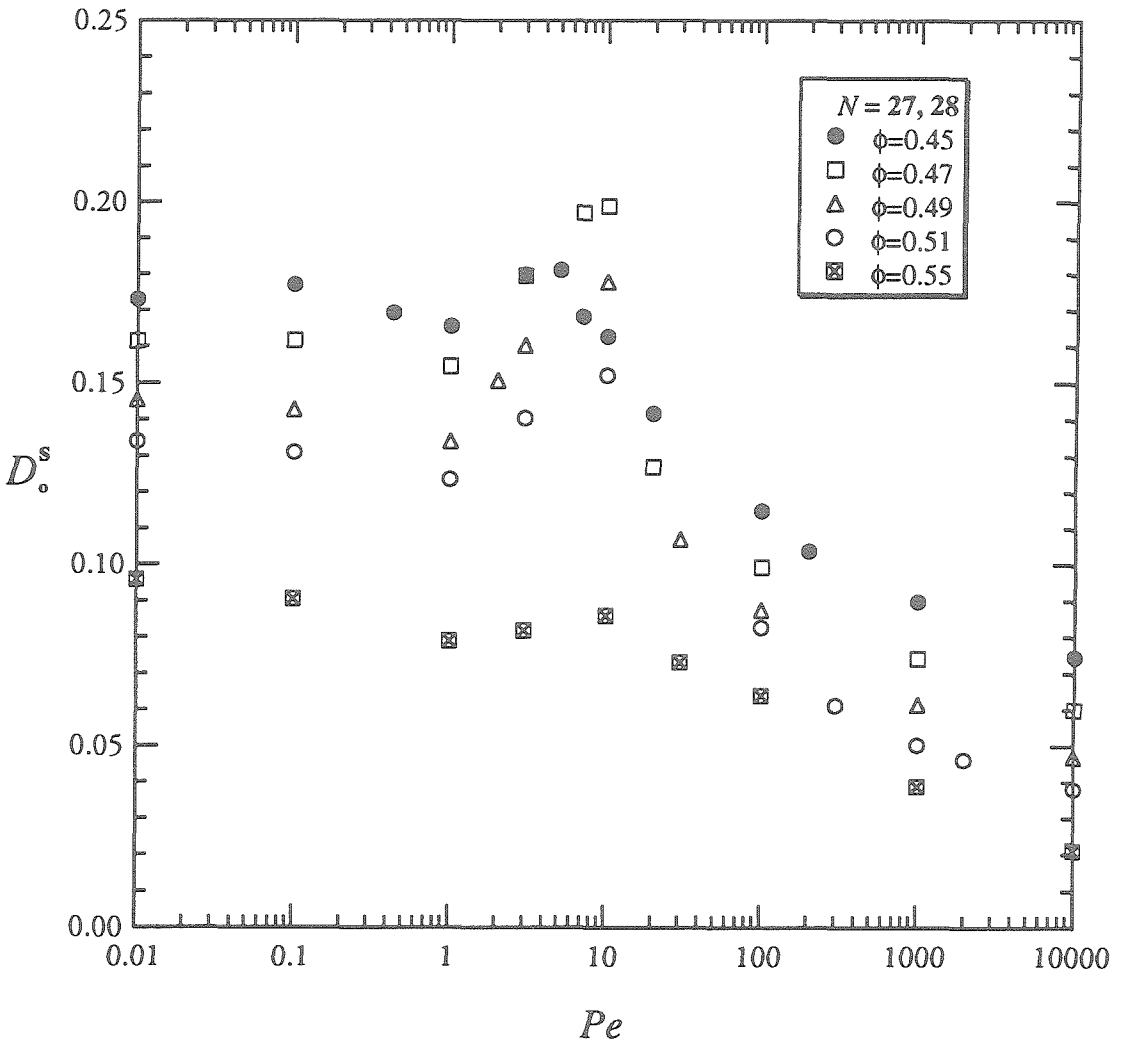

Figure 8.32.a: The short-time translation self-diffusion coefficient D_o^s normalized by the infinite dilution diffusion coefficient D_o obtained by Stokesian dynamics as a function of the Péclet number for hard spheres at volume fractions ϕ = 0.47 (□), 0.49 (△), 0.51 (○) and 0.55 (⊠). There are 27 or 28 particles in the unit cell. The self-diffusion coefficient of a hard-sphere suspension at ϕ=0.45 (●) is plotted as a reference for comparison. The short-time translational self-diffusion coefficient remains relatively constant for Pe<1, increases noticeably at Pe≈10, and decreases with increasing Pe. Note the maximum of the self-diffusion coefficients for ϕ=0.47 and 0.49 are larger than that of ϕ=0.45.

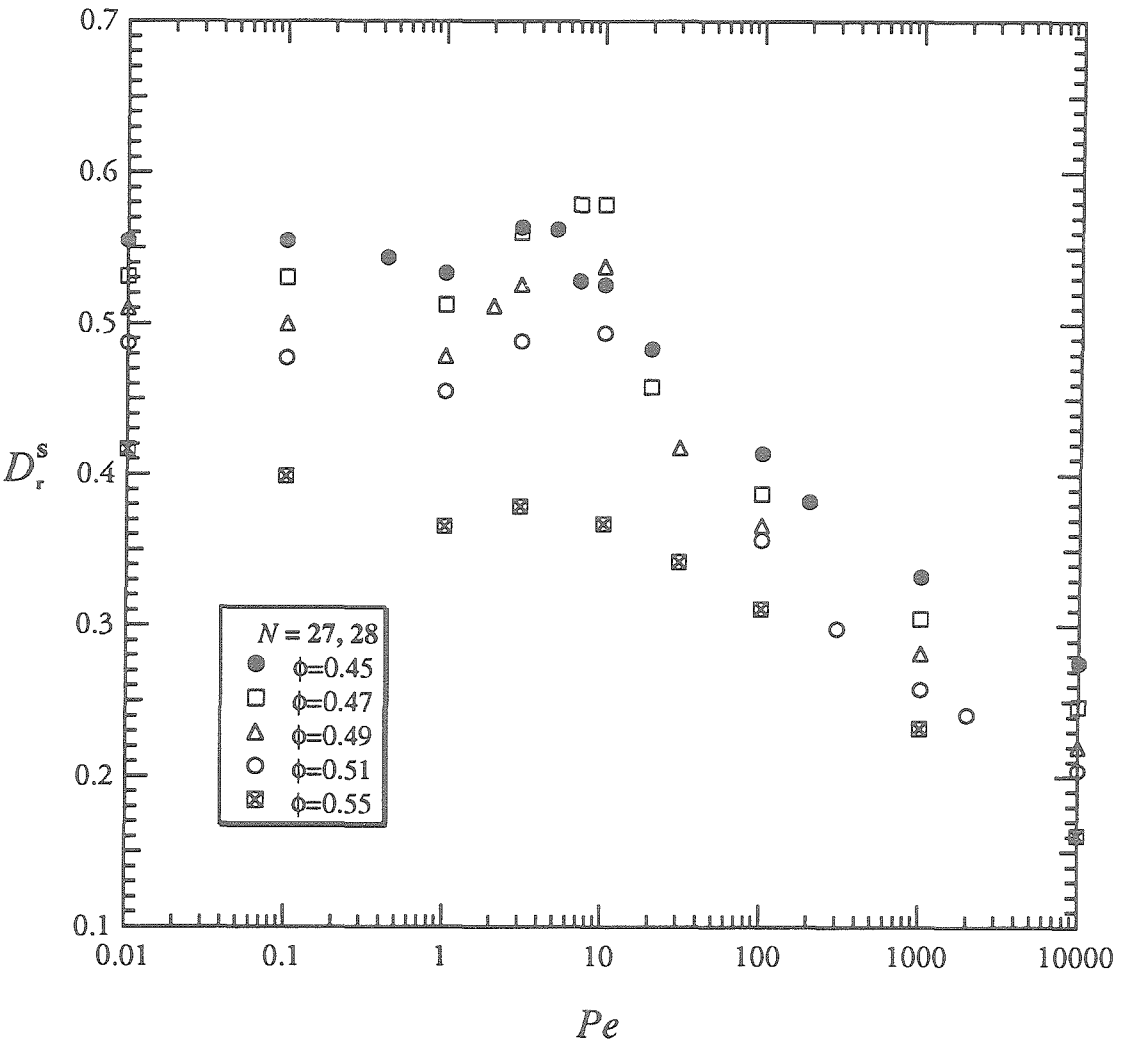

Figure 8.32.b: The short-time rotational self-diffusion coefficient D_r^s normalized by the infinite dilution diffusion coefficient D_o obtained by Stokesian dynamics as a function of the Péclet number for hard spheres at volume fraction ϕ=0.47 (□), 0.49 (△), 0.51 (○) and 0.55 (⊠). There are 27 or 28 particles in the unit cell. The short-time rotational self-diffusion coefficient remains relatively constant for Pe<1, increases for Pe≈10, and decreases with increasing Pe. Note the maximum of the self-diffusion coefficients for ϕ=0.47 and 0.49 are larger than that of ϕ=0.45 (●).

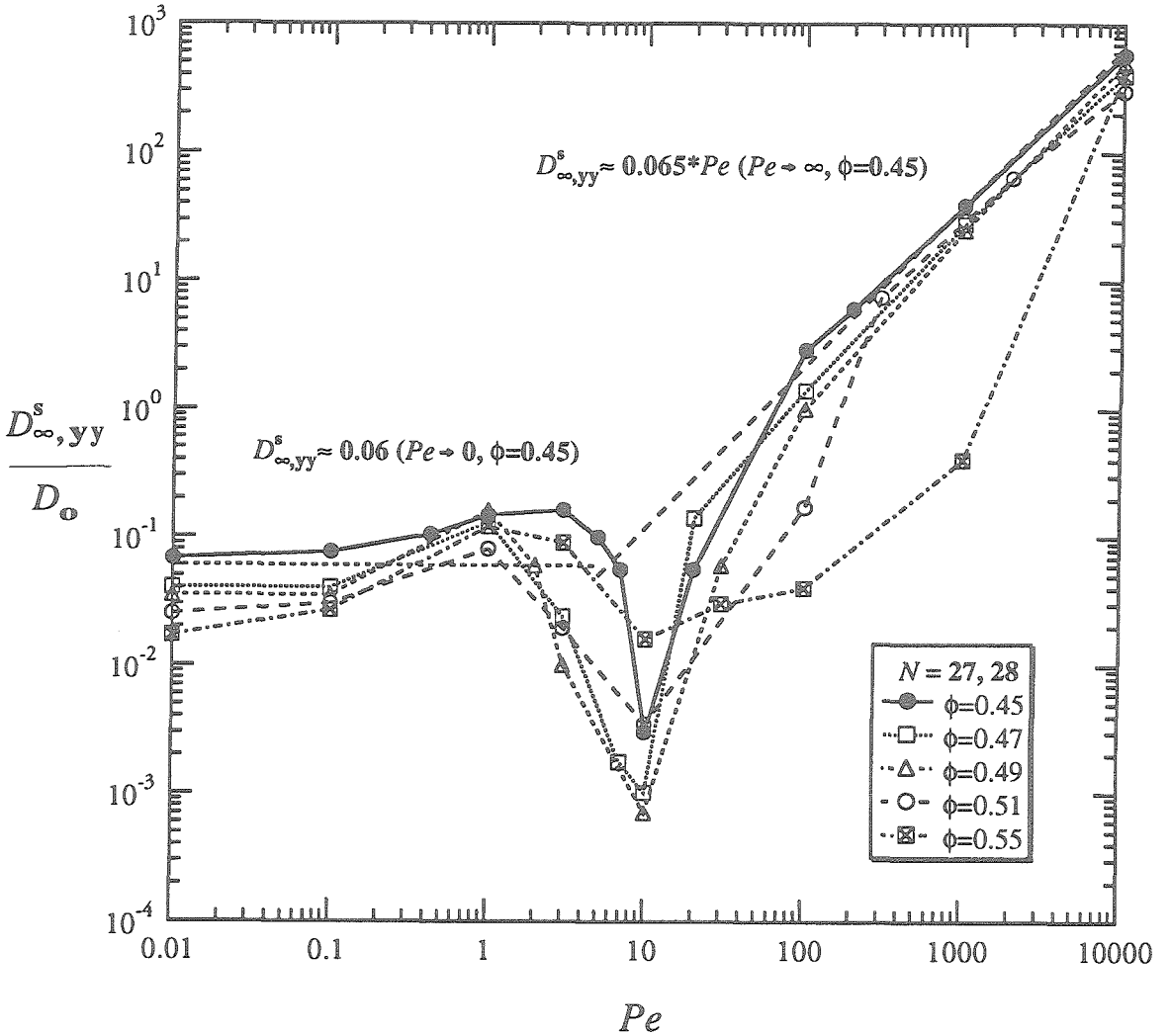

Figure 8.33.a: The long-time self-diffusion coefficient $D^s_{\infty,yy}$ normalized by the infinite dilution diffusivity D_o is plotted as a function of the Péclet number for hard spheres at volume fractions ϕ = 0.45 (●), 0.47 (□), 0.49 (△), 0.51 (○) and 0.55 (⊠). The limiting asymptotes are: $D^s_{\infty,yy} \approx O(D_o)$ as $Pe \to 0$ and $D^s_{\infty,yy} \approx 0.065\ Pe$ as $Pe \to \infty$. Note that as $Pe \to \infty$, the dimensional long-time self-diffusion coefficient scales as $\dot{\gamma}a^2$. The transition from the strong Brownian regime to the hydrodynamic domination limit occurs for $Pe \approx 10$. The two limits of $D^s_{\infty,yy}$ at $Pe \to 0$ and at $Pe \to \infty$ are shown in the figure for hard spheres at ϕ=0.45.

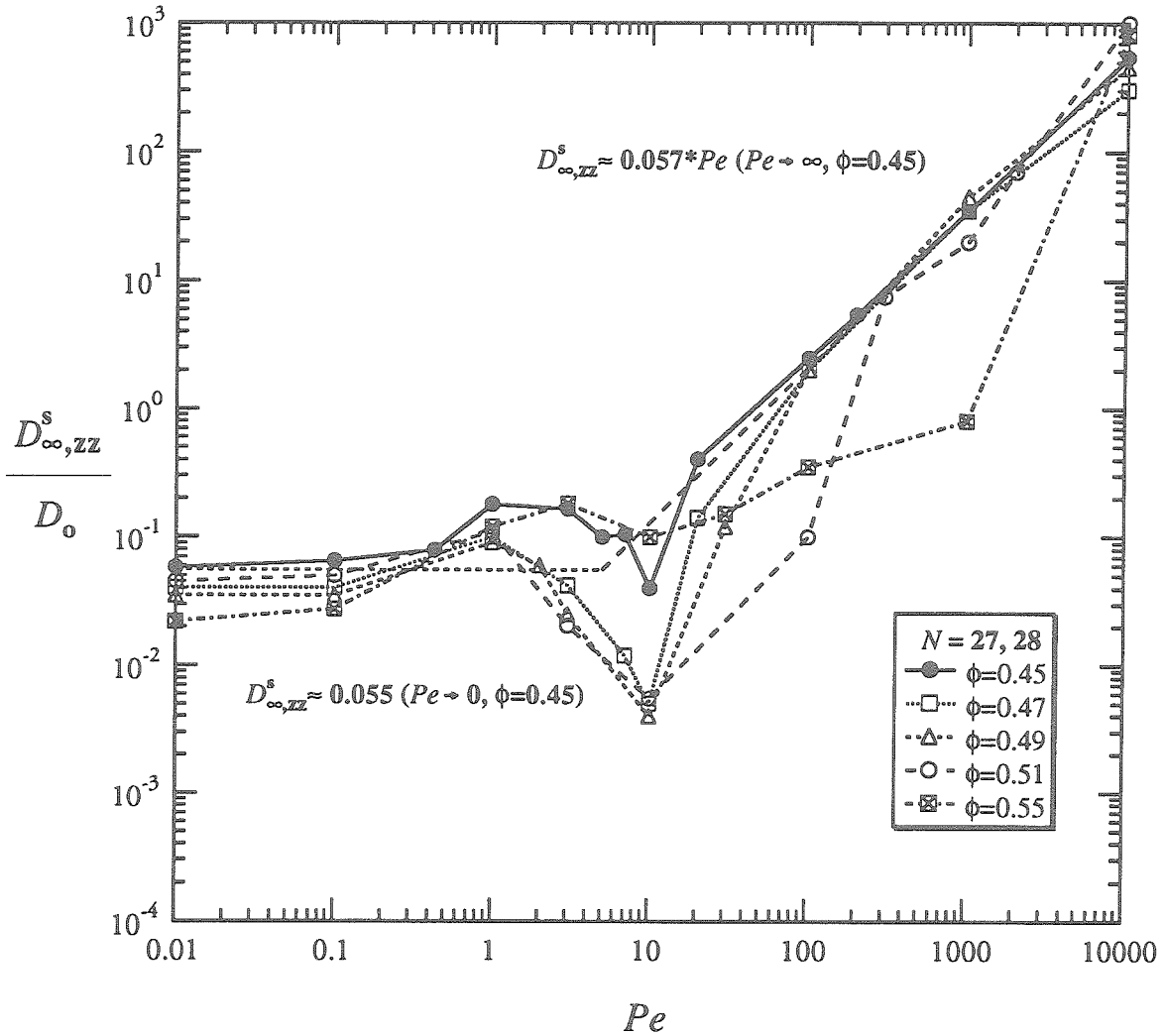

Figure 8.33.b: The long-time self-diffusion coefficient $D^s_{\infty,zz}$ normalized by the infinite dilution diffusivity D_o is plotted as a function of the Péclet number for hard spheres at volume fractions ϕ = 0.45 (●), 0.47 (□), 0.49 (△), 0.51 (○) and 0.55 (⊠). The limiting asymptotes are: $D^s_{\infty,zz} \approx O(D_o)$ as $Pe \to 0$ and $D^s_{\infty,zz} \approx 0.057\ Pe$ as $Pe \to \infty$. Note that as $Pe \to \infty$, the dimensional long-time self-diffusion coefficient scales as $\dot{\gamma}a^2$. The transition from the strong Brownian regime to the hydrodynamic domination limit occurs for $Pe \approx 10$. The two limits of $D^s_{\infty,zz}$ at $Pe \to 0$ and at $Pe \to \infty$ are shown in the figure for hard spheres at ϕ=0.45.

Chapter IX

MACROSCOPIC PROPERTIES OF HARD-SPHERE SUSPENSIONS

The two dimensionless parameters: the volume fraction and the Péclet number, play an essential role in suspension mechanics. Suspension macroscopic properties and the evolution of the microstructure are modeled as a function of only these two variables. In a colloidal suspension, the volume fraction sets the relative separation of the flowing particles, thus it dictates the strength of the many-body hydrodynamic interactions among the suspended particles. The resistance tensors $\mathbf{R}_{FU}$, $\mathbf{R}_{FE}$ and $\mathbf{R}_{SE}$ are purely geometric quantities and for spherical particles, they depend only on the separating distance between the particles, which in turn is a function of the volume fraction. The Péclet number, which can be viewed as the ratio of the diffusive relaxation time, $a^2/D_o^s(\phi)$, to the flow time, $\dot{\gamma}^{-1}$, determines the strength of the flow and the degree of the shearing deformation.

In the last three chapters, chapters VI to VIII, we presented our study and results for the rheology, the shear-induced microstructure and the short- and long-time self-diffusivities of hard-sphere suspensions with volume fraction ranging from 0.316 to 0.6. The flow of particles in a linear shear flow with different shear rates was, for the first time, shown in detail to illustrate the dynamical processes of the shearing deformation of the microstructure. More importantly, we have a detailed understanding of the relation of suspension macroscopic properties to the microstructure. In these studies, the shear rates were varied by changing the Péclet number from the limit of strong Brownian ($Pe = 0.01$) to the hydrodynamic dominated regime ($Pe \geq 10^4$) at a fixed volume fraction.

Our results showed behavior of dense hard-sphere suspensions in the three distinct limits: low ($Pe < 1$), intermediate ($Pe \approx 10$) and high Péclet numbers ($Pe > 10^2$).

For a slightly perturbed equilibrium structure in the low Péclet number limit ($Pe < 1$), the Brownian forces were strong and the time, which is scaled with a diffusive time, was large allowing the strong Brownian forces to restore the deformed structure to the isotropic structure of a rest state. The microstructure is close to that at equilibrium. The Brownian contribution to the stress, Brownian viscosity η_r^B, decreased as the imposed shear rate increased and is the cause of the shear thinning. Similar to the region of low Péclet number, the region of high Péclet number ($Pe > 10^2$) can be considered as a perturbation to the pure hydrodynamic limit ($Pe \rightarrow \infty$). In this region, we witnessed the formation of large clusters or chains of particles spanning the unit cell and disrupting the flow. The large increase in the hydrodynamic contribution to the stress, hydrodynamic viscosity η_r^H, is the main cause of the shear thickening as the Brownian contribution has essentially decayed and vanished for $Pe > 10^2$.

The region with $Pe \approx 10$ was special and attracted most of our attention. The flowing suspension was strongly ordered with distinct "hexagonal" packing of strings of flowing particles. In this region, the steady shear viscosity was minimum. For suspensions at ϕ=0.45, the mechanism which causes the shear thinning behavior was due only to the decrease of Brownian viscosity since hydrodynamic viscosity remains constant in this region. As the volume fraction increases into the range of 0.47 to 0.51, a small reduction in hydrodynamic viscosity combined with a decrease of Brownian viscosity gave a smaller shear viscosity than the small shear viscosity of suspension at ϕ=0.45. An examination of the microstructure for these denser suspensions showed that particles were further apart in the packing than in the hexagonal packing at ϕ=0.45. This is the brief summary of suspension behavior with varying Péclet numbers at fixed volume fraction.

For this chapter, we focus on the changes of the suspension macroscopic properties with varying volume fraction at fixed shear rates, i.e., at constant Péclet number. The simulation results, which were discussed at length in the last three chapters, are recompiled and shown as a function of the volume fraction. Data for the figures in this chapter are taken from Tables in chapters VI to VIII. Summarized results are presented in the first section, followed by the comparison of the experiments in the second section, then the relation of the rheology and the deformation of the suspension in the third section. Finally, in the last section the suspension temperature is computed according to $\langle \mathbf{U}'\mathbf{U}' \rangle$, with $\mathbf{U}$ the particle velocities and the prime denoting the fluctuation, i.e., $\mathbf{U}' \equiv \mathbf{U}\text{-}\mathbf{U}^{\infty}$ and $\mathbf{U}^{\infty}$ is the velocity due to the bulk shear flow.

IX.1 The Scaling of Suspension Macroscopic Properties with ϕ and Pe

As shown in Fig.9.1, the steady shear viscosity is plotted on a logarithmic scale versus the volume fraction for hard-sphere suspensions with different Péclet numbers: $Pe = 0.01$ (◇), 0.1 (△), 1 (○), 10 (●), 10^2 (□), 10^4 (▲) and for Pe in the range of 10^5 to ∞ (⊠). The steady shear viscosity curves show a shear thickening behavior with increasing volume fraction, which has generally been observed in experiments. The special curve for Pe=10 shows a strong shear thinning region when the volume fraction increases from 0.45 to the range of 0.47 to 0.51 which was discussed in chapter VIII. Another shear thickening behavior can also be seen by comparing the two shear viscosity curves for the perturbed Brownian suspension at Pe=0.01 and for the perturbed hydrodynamic suspension at $Pe > 10^4$. The shear viscosity for large Péclet number is higher than the shear viscosity for small Péclet number for all volume fractions, thus the suspension

must shear thicken and Stokesian dynamics displays the trend remarkably well. The shear thickening behavior in which the viscosity increases with increasing shear rates is commonly known as "dilatancy."

In Figure 9.2, we plot both the Péclet number and the relative viscosity for the onset region where the Brownian contribution to the stress is identical to the hydrodynamic contribution versus the volume fraction. The left vertical scale is for the special Péclet number, Pe^* (●) and the right vertical scale is for both the Brownian and hydrodynamic viscosity (□). Recall that the onset region can be viewed as a rheological signature for the start of the plateau region where the shear viscosity is minimum. Furthermore, the existence of the onset region, where the Brownian and hydrodynamic forces are properly balanced, is followed by a strongly ordered flowing suspension. For suspensions with a volume fraction below 0.419, the onset region does not exist and the change in the steady shear viscosity with Pe is small. The suspension cannot be sheared to order. The figure shows the onset region, which shifts to a larger Péclet number with increasing ϕ, for suspensions with a volume fraction $\phi \geq 0.419$.

Figure 9.3 shows the shearing deformation of the suspension which is represented by the angularly averaged pair-distribution function evaluated at particle center-center spacing $r = 2$ (for touching particles), $g(2)$, as a function of the volume fraction. The plot symbols for different Péclet numbers are: $Pe = 0.01$ (◇), 1 (○), 10 (●), 10^2 (□) and 10^4 (▲). Except the special curve for Pe=10, $g(2)$ increases monotonically with increasing volume fraction. For the curve with Pe=10, a significant reduction of nearly 100 fold occurs as the volume fraction ϕ increases from 0.45 to the range of 0.47 to 0.51. The

small values of $g(2)$ for these denser suspensions imply that during the course of dynamic simulation, the particles are seldom in contact and there is a large separation between particles. This is consistent with the steady shear viscosity curve in Fig.9.1 which shows a smaller minimum viscosity for suspensions with ϕ in the range of 0.47 to 0.51 than the small minimum viscosity for ϕ=0.45 at Pe=10. Figure 9.3 also displays an increase of $g(2)$ with increasing Péclet number at fixed volume fraction. In the limit of strong hydrodynamics ($Pe > 10^2$), the particles are closely spaced and form large elongated clusters resulting in a large value of $g(2)$ compared to small $g(2)$ for randomly dispersed particles in a slightly deformed suspension. As the volume fractions increases, $g(2)$ also increases and for the hard-sphere suspension, it is known that the radial-distribution function at contact diverges at the close packing (Russel *et al.* (1989), Brady (1993)) as:

$$g(2) \sim (1 - \phi/\phi_{mp})^{-1} \qquad \text{as } \phi \longrightarrow \phi_{mp} \ . \tag{9.1}$$

Here $\phi_{mp} \approx 0.63$ is the random close packing for the hard spheres. A plot of $g(2)$ as a function of the dimensionless group $(1 - \phi/\phi_{mp})^{-1}$ is shown in Figure 9.4 for the limit of vanishing shear rate with Pe=0.01 (◊). The figure captures this correct scaling with a slope of 1.08 and agrees well with 1.2 from Brady's theoretical prediction (1993).

Figures 9.5 and 9.6 show the relation of the short-time translational and rotational self-diffusion coefficients with the volume fraction, respectively. The curves with different Péclet numbers are: Pe = 0 (■) for the undeformed suspension, 0.01 (◊), 1 (○), 10 (●), 10^3 (△), 10^4 (▲) and ∞ (⊠) for pure hydrodynamic. Results for D_o^s and D_r^s are obtained from the simulations with 27 or 28 particles. Except for the special curve with

Pe=10, both D_o^s and D_r^s decrease with increasing volume fraction at constant Péclet number. Recall that the short-time self-diffusivities measure the instantaneous mobility of the flowing particles. In a dense suspension, the particles are less mobile due to a reduction in the fluid space separating the particles. The two figures also show a decrease of D_o^s and D_r^s with increasing Péclet number at constant ϕ. A reduction in the instantaneous mobility of the suspended particles as the Péclet number increases is due to the formation of clusters of particles which hinder the movement of individual particles even on the short-time scale. For the region with ϕ in the range of 0.47 and 0.51, the curve with Pe=10 shows an increase in the short-time self-diffusion coefficients which indicates the large separating distance among the flowing particles and results in the enhanced mobility for the flowing particles. Experiment by Pusey and van Megen (1983) and stokesian dynamics simulation by Phillips *et al.* (1988), Ladd (1990) and this work show that the short-time self diffusivity vanishes in the limit of close random packing as seen in these two figures.

The scaling of the reduced shear viscosity with a new dimensionless group Pe/D_o^s, where the diffusion coefficient of a particle at infinite dilution, D_o, employed in the definition of the Péclet number: $Pe \equiv \dot{\gamma}a^2/D_o = 6\pi\eta a^3\dot{\gamma}/kT$, is replaced by the short-time self-diffusion coefficient D_o^s. Figures 9.7 and 9.8 are plotted with D_o^s computed at the Péclet number and ϕ where the steady shear viscosity and $g(2)$ are obtained. The low ($Pe \leq 10$) and high shear limit ($Pe \geq 10$) steady shear viscosity are plotted in Figures 9.7 and 9.8, respectively. For the low shear limit, the reduced viscosity $\eta^\dagger$ is defined as:

$$\eta^\dagger \equiv \frac{\eta(Pe) - \eta(Pe = 10)}{\eta(Pe = 0.01) - \eta(Pe = 10)} \quad , \tag{9.2}$$

and for the high shear limit, the reduced viscosity η^* is defined as:

$$\eta^* \equiv \frac{\eta(Pe) - \eta(Pe = 10)}{\eta(Pe \geq 10^4) - \eta(Pe = 10)} \quad . \tag{9.3}$$

The reduced viscosities show a good scaling with the new dimensionless group Pe/D_o^e for volume fraction ranging from 0.316 to 0.55 and they are superimposed onto a universal curve as shown in these figures. Recall that for $Pe < 1$, D_o^e is essentially constant and the correlation of the reduced viscosity with Pe/D_o^e in the low shear limit is excellent as shown in Figure 9.7. In the high shear limit (Fig.9.8), the correlation displays some variations with more scattering of the reduced viscosities with D_o^e obtained in the limit of $Pe \rightarrow 0$.

In the following section, we present comparison of the simulation results for the rheology with experiments.

IX.2 Comparisons of Simulation Results with Experiments

As shown in Figure 9.9, the simulation results for the steady shear viscosity (●) in the low shear limit ($Pe = 0.01$) compare very well with the experiments of van der Werff and de Kruif (1989) for Pe=0.01 (△) and with the experiments of Kreiger (1972) in the limit of vanishing shear rates (□). The dashed curve is the scaling $(1 - \phi/\phi_{mp})^{-a}$ where the exponent equals 2 and ϕ_{mp}= 0.63 is the maximum packing for the random hard-sphere model. The agreement of our results with experiments and with the scaling in the low shear limit is excellent for the entire range of volume fraction in our study. The theoretical prediction of the steady shear viscosity in the low shear limit by Brady

(1993), which is based on the evolution equation for the pair-distribution function and the scaling derived from the viscoelastic response of Brownian contribution to the particle stress, displays truly remarkable results as shown by the solid curve in this figure. The zero shear-rate viscosity is given by Brady as:

$$\eta_r = 1 + \eta_r^H + \frac{12}{5}\phi^2 \frac{g(2;\phi)}{D_o^s(\phi)} \quad . \tag{9.4}$$

The viscosity computed from a random hard-sphere distribution, the high frequency hydrodynamic viscosity $\eta_\infty'(\phi)$, by Phillips *et al.* (1988) (♦) is also plotted in the figure for comparison. $\eta_\infty'(\phi)$ displays a good fit with the scaling $(1 - \phi/\phi_{mp})^{-a}$ where the exponent is found at 1.35 using ϕ_{mp}= 0.63.

In Figure 9.10, we plot the simulation results for the steady shear viscosity at finite shear rates for Pe=1 (●) and 10^2 (■) as a function of the volume fraction and compare them to the experiments of van der Werff and de Kruif at Pe=1 (○) and the experiments of Kreiger (1972) at a reduced shear rate $\tau_r \approx 300$ (□). For this intermediate shear rate limit, our simulation results compare equally well for the experimental results at Pe=1 and Pe=100, while the empirical scaling $(1 - \phi/\phi_{mp})^{-2}$ (dotted curve) with ϕ_{mp}= 0.63 shows significant variation with our results and with experiments. With the exponent reduced from 2 to 1.65, the empirical scaling shows a relative good fit for the shear viscosity with intermediate shear rates.

Figure 9.11 illustrates the relation of the steady shear viscosity and the volume fraction in the high shear limit ($Pe > 10^4$). Stokesian dynamics results (●) agrees well with the experiments of non-Brownian spheres from Rutgers (1962) (□) (the average

curve labeled as curve #1) and Gadala-Maria (1979) (○), while the experiments of Pätzold (1980) (△) which seems to fit very well with the scaling $(1 - \phi/\phi_{mp})^{-2}$ with $\phi_{mp} \approx 0.63$ shows small difference with our results.

We now turn to a slightly different comparison of the simulation results for the long-time self-diffusion coefficient computed in the velocity gradient direction, $D^s_{\infty,yy}$, in the limit of $Pe \to \infty$. The hydrodynamically induced diffusive motion comes from the deterministic chaos displayed by the highly nonlinear evolution equations for the particle positions (Eq. (2.7) with $Pe \to \infty$). It also emphasizes the important many-body hydrodynamic interactions in dense suspensions which induce diffusive displacements for the flowing particles. Figure 9.12 shows the comparison of $D^s_{\infty,yy}$ normalized by the infinite dilution diffusivity D_o of simulation results (●) with the experiments of Eckstein *et al.* (1977) (■), Leighton and Acrivos (1987) (○), (□) and (△) for various sizes of spheres and shear rates and the most recent experiments from Phan and Leighton (1992) (▲). The two sets of experiments agree only at low volume fraction ($\phi < 0.2$), but at higher ϕ, while the results from Eckstein *et al.* show an asymptotic value $D^s_{\infty,yy} \approx 0.03$ for $\phi > 0.2$, Leighton and Acrivos obtain increasing $D^s_{\infty,yy}$ with large ϕ. The solid curve is according to the correlation of experimental data of Leighton and Acrivos which captures $D^s_{\infty,yy}$ in the limit of dilution ($\phi < 0.2$). The most recent experiment from Phan and Leighton shows the long-time self-diffusivity saturated at a value of 0.09 for $\phi > 0.3$. Our results for the normalized $D^s_{\infty,yy}$ fluctuate between 0.05 to 0.06 for ϕ from 0.4 to 0.6 and lie between the results of these two groups and agree reasonably well with the new experiments.

IX.3 The Relation of Rheology with $g(2)/D_o^s$

The aim in the section is to determine the relation of the suspension rheology to the deformation of the suspension. The shearing deformation of a flowing suspension can be represented by the angularly averaged pair-distribution function evaluated at particle center-center spacing r=2, $g(2)$, and by the short-time self-diffusion coefficient, D_o^s, which measures the local mobility of the suspended particles in a suspension. Both $g(2)$ and D_o^s are function of ϕ and Pe and they offer value information of the microstructural deformation of the suspension in a shear flow.

Recent theoretical model for predicting the shear viscosity in the low shear limit developed by Brady (1993) has provided insight to the relation of the macroscopic properties to the shearing deformation of the suspension. The behaviors of dense hard-sphere suspensions in the limits of low and high Péclet numbers can clearly be seen when we plot the steady shear viscosity as a function of $g(2)/D_o^s$ in Figures 9.13 and 9.14, respectively. For the low shear limit with Pe=0.01 ($\Diamond$) and ($\triangle$) 0.1, the steady shear viscosities of these two small Péclet numbers show good fit for $g(2)/D_o^s$ less than 20, but as $g(2)/D_o^s$ increases the two viscosity curves display noticeable difference as shown in Fig.9.13. At Pe=0.1, the imposed shear begins to perturb the microstructural deformation and the diffusive Brownian motion contribution to macroscopic stress weakens as the volume fraction increases (large $g(2)/D_o^s$). As a result, we observe a shear thinning effect as the viscosity curve for Pe=0.1 falls below the curve for Pe=0.01. In the limit of high shear rates with Pe=10^3 ($\blacktriangle$) and 10^4 ($\boxtimes$), the dominant hydrodynamic forces contribute essentially all particle stress and the presence of the weak Brownian force can simply

contribute to the microscopic deformation of the flowing suspension. The steady shear viscosities display excellent scaling with this new dimensionless group which collapses the steady shear viscosity for all volume fractions onto an universal curve as shown in Figure 9.14.

IX.4 Suspension Temperature and The Time Auto-Correlation Functions

IX.4.1 Suspension Temperature

In this section, we present the suspension temperature which is computed according to $\langle \mathbf{U}'\mathbf{U}' \rangle$, with $\mathbf{U}$ the particle velocities and the prime denoting the fluctuation, i.e., $\mathbf{U}' \equiv \mathbf{U}\text{-}\mathbf{U}^{\infty}$. Care must be exercised here since the fluctuation in particle velocities, $\mathbf{U}'$, includes only the deterministic contribution from the hydrodynamic and one of the two contributions from the Brownian motion, the configurational divergence term $\nabla \cdot \mathbf{R}_{FU}^{-1}$. Missing in the computing of $\langle \mathbf{U}'\mathbf{U}' \rangle$ is the random step of the Brownian contribution. We present the simulation results for suspension temperature which is computed from the particle velocity fluctuation and from the particle displacements with the convective contribution from the applied shear removed.

The steady mean square of the translational and rotational velocity fluctuation are plotted with the Péclet number and shown in Figures 9.15.a-b and 9.16.a-b. $\langle \mathbf{U}'\mathbf{U}' \rangle$ is computed by averaging $\langle \mathbf{U}'\mathbf{U}' \rangle$ for the velocity gradient and the vorticity direction, the y and the z-axis, while $\langle \Omega'\Omega' \rangle$, with Ω the rotational fluctuation velocity, is averaged for the x and the y-axis. Figures 9.15.a-b for ϕ from 0.316 to 0.419 display two different behaviors of the mean square of the particle velocity fluctuation: for $Pe < 1$, both $\langle \mathbf{U}'\mathbf{U}' \rangle$ and

$\langle \Omega' \Omega' \rangle$ are small and constant, and for $Pe > 1$, $\langle U' U' \rangle$ and $\langle \Omega' \Omega' \rangle$ increase and approach an asymptotic limit for the pure hydrodynamic suspension ($Pe \rightarrow \infty$). Summarized results for the terms $\langle U' U' \rangle$ and $\langle \Omega' \Omega' \rangle$ as a function of the volume fraction ϕ is shown in Table 9.1 for $Pe > 10^4$. For more dense suspensions, $\langle U' U' \rangle$ and $\langle \Omega' \Omega' \rangle$ display a striking behavior for the region of $Pe=10$ as shown in Fig.9.16.a-b for suspensions with ϕ in the range of 0.45 to 0.55. In the region of minimum viscosity with $Pe=10$, $\langle U' U' \rangle$ and $\langle \Omega' \Omega' \rangle$ decrease significantly for $\phi=0.45$ to 0.51 and less pronounced for $\phi=0.55$. This behavior can be explained by referring to the shear-induced microstructure of the flowing suspension in this special region. The suspended particles which are strongly ordered flow as strings with the bulk flow and they are least diffusive. The fluctuation in the particle velocities must be small and minimum compared to other Péclet number regions as we see in these two figures. In the limit of high Péclet numbers, large value of suspension temperatures are due to the frequent forming and breaking clusters of particles which result in large fluctuations of the particle velocities.

For the region of low Péclet numbers ($Pe < 1$), the strong Brownian motion should give large fluctuations of the particle velocities due to rapid changes in the positions of highly diffusive particles. This set of figures do not show this trend because the computing of $\langle U' U' \rangle$ and $\langle \Omega' \Omega' \rangle$ from the particle velocities does not include the contribution of the random step of the Brownian contribution to particle displacements as we have already mentioned. The large suspension temperature in the strong Brownian limit can clearly be seen from the plots of suspension temperature computed from the particle displacements by the terms $\langle (\Delta X'/\Delta t)(\Delta X'/\Delta t) \rangle$ and $\langle (\Delta \theta'/\Delta t)(\Delta \theta'/\Delta t) \rangle$, with X and θ the particle displacement and the particle rotational angle, respectively. The prime

denotes the fluctuation. Figures 9.17.a-b for ϕ=0.316 to 0.419 and Figures 9.18.a-b for ϕ=0.45 to 0.55 show large suspension temperature in the region of low Péclet numbers ($Pe < 1$). In the limit of high Péclet numbers the two methods of computing the mean square of the particle velocity fluctuation that give the same results as the Brownian contribution have vanished. The interesting point is that for the special region at Pe=10, Figures 9.18.a-b do not show a noticeable reduction for $\langle(\Delta X^{'}/\Delta t)(\Delta X^{'}/\Delta t)\rangle$ and $\langle(\Delta\theta^{'}/\Delta t)(\Delta\theta^{'}/\Delta t)\rangle$ compared to a large decrease of $\langle \mathbf{U}^{'}\mathbf{U}^{'}\rangle$ and $\langle \mathbf{\Omega}^{'}\mathbf{\Omega}^{'}\rangle$ shown in Figures 9.16.a-b. The small contribution from the random step of Brownian motion tries to randomize the strings of flowing particles, but the time which is scaled with the shear rate is much shorter than the diffusive time and the random step can only slightly perturb the strings of flowing particles and is not able to break the packing order. A reduction in $\langle \mathbf{U}^{'}\mathbf{U}^{'}\rangle$ and $\langle \mathbf{\Omega}^{'}\mathbf{\Omega}^{'}\rangle$ is due only to the vanishing of the fluctuation from the deterministic shear in this strong shear thinning region. This is clearly seen by differentiating the two sets of figures: Figures 9.16.a-b which do not include the contribution of the random step and Figures 9.18.a-b which includes all the contributions to the fluctuation of particle velocities.

IX.4.2 The Time Auto-Correlation Function of Velocity Fluctuation

The amplitude and the persistence in time of the particle velocity fluctuation in a suspension determines the hydrodynamic dispersion coefficient, the long-time self-diffusivities. The long-time self-diffusion can be computed from the displacements of the

particles according to (2.27) which is repeated here for our reference

$$D_{\infty}^{s} \equiv \lim_{t\to\infty} \frac{1}{2N} \frac{d}{dt} \langle (\mathbf{X} - \langle \mathbf{X} \rangle)^2 \rangle \quad . \tag{9.5}$$

Equivalently, D_{∞}^{s} can be computed from the time auto-correlation function of the velocity fluctuation as the following:

$$D_{\infty}^{s} = \int_0^{\infty} \langle \mathbf{U}'\mathbf{U}' \rangle \, dt \quad . \tag{9.6}$$

The normalized time auto-correlation for the velocity fluctuation are defined as:

$$C(t) \equiv \frac{\langle \mathbf{U}'(0)\mathbf{U}'(t) \rangle}{\langle \mathbf{U}'(0)\mathbf{U}'(0) \rangle} \quad . \tag{9.7}$$

The time auto-correlation functions play an important role in the field of nonequilibrium statistical mechanics and have been extensively used to compute transport coefficients. To compute the time integration constant for (9.6), simulations with long run times were carried out for suspensions at ϕ=0.316, 0.45 and 0.51 and with three different Péclet numbers: 0.1, 1 and 10^5. From an average run time of 400, the time auto-correlation functions were sampled for a large number of time intervals to improve the statistic of its results. An average of 200 to 400 samples were taken from these long runs for the computing of C(t). The normalized time auto-correlation function for the velocity fluctuation in the velocity gradient and the vorticity direction, the y and the z-axis, are plotted with time in Figures 9.19.a-b for ϕ=0.316, in Figures 9.20.a-b for ϕ=0.45 and in in Figures 9.21.a-b for ϕ=0.51, respectively. In these sets of figures, the dotted curve is

for Pe=0.1, the solid curve is for Pe=1 and the dash curve is for Pe=10^5. The small line through zero is drawn in these figures to guide the eyes. These figures display a decay of C(t) as a single exponent in time, i.e., $C(t) = e^{-t/\tau}$, with a relaxation time constant τ varying from 1 to 4 dimensionless time units. The relaxation time constant τ decreases with increasing ϕ. Numerical integrations for these auto-correlation curves are carried out to determine the time integration constant and the results are displayed in Table 9.2 for both the translational and rotational velocity fluctuation . Results from Table 9.1 for the normalization constant $\langle \mathbf{U}'\mathbf{U}' \rangle$ and $\langle \mathbf{\Omega}'\mathbf{\Omega}' \rangle$ are plotted in Fig.9.22 for Pe>10^4. In the limit of hydrodynamic domination, the long-time self-diffusion coefficient $D^s_{\infty,yy}$ and $D^s_{\infty,zz}$ computed by (9.5) and (9.6) give similar results and indicate the correctness of the two methods.

IX.5 Conclusions

In this chapter, we detailed the relation of suspension macroscopic properties and the particle volume fraction for complete dense hard-sphere suspensions in our study. The results emphasize the distinct behavior of dense colloidal suspensions in the three limits of low, intermediate and high Péclet number. The reduced shear viscosity defined in (9.1) and (9.2) shows a scaling with the new dimensionless group $Pe/(1/D^s_o)$with Pe=10 taken as a cut point for the two limits of low and high Péclet numbers, respectively. The simulation results provide, for the first time, a complete set of results for the rheology, the shear-induced microstructure, the short- and long-time self-diffusivities and the suspension temperature. These have not yet been reported or achieved by experiment and/or theory. Our results provide the essential physical understanding of suspension

mechanics and supply the foundation where new theories as well as simulations can be tested against ours.

Finally before we end this chapter, the results of the steady shear viscosity as a function of the volume fraction and the Péclet number, i.e., $\eta_r = \eta_r\ (Pe,\phi)$ are illustrated in Fig.9.23. The horizontal logarithmic scale is for the Péclet number varying from 0.01 to 10^4 and the vertical scale is for the volume fraction ϕ ranging from 0.316 to 0.55. Fig.9.23 is a contour plot of the steady shear viscosity and the legend of the high and low logarithmic scale of the shear viscosity is shown in the right-hand side of the figure. Contour regions of light color represent high viscosity and dark low. The interpretation of this figure is simple. We can march along the horizontal direction which specifies a constant volume fraction, for example the line with ϕ=0.45, and examine the change of the shear viscosity with the change in the Péclet number. Starting from Pe=0.01, the steady shear viscosity enters the region of darker color for Pe=0.1 and 1 as the suspension shear thins. Continuing to the region of $Pe \approx 10$, the steady shear viscosity is minimum as shown by very dark color, and as the Péclet number increases, we enter the shaded regions with light color indicating the suspension shear thickens as the steady shear viscosity increases. We can also march along the vertical line which specifies a constant shear rate, i.e., constant Péclet number, and examine the change of the steady shear viscosity as with the changing volume fraction. For example by traveling along the vertical line at Pe=1 starting from the top for ϕ=0.316 to the bottom for ϕ=0.55, the steady shear viscosity is seen to increase as the volume fraction increases at Pe=1. The final method is to follow a contour line with the same color and determine the operating conditions at a particular volume fraction and a particular shear rate which

are necessary to maintain a steady shear viscosity. The figure shows the complete details of the shear viscosity which is highly sought and extremely valuable to scientists and to engineers as it provides the completion of the process characterization and optimum operating conditions.

Table 9.1: Results of the suspension temperature in the limit of large Péclet number ($Pe>10^4$). Column (1) is the volume fraction. Columns (2) is the y and z averaged mean square of the particle translational velocity fluctuation. The y-axis is the velocity gradient direction and the z-axis is the vorticity direction. Similarly, column (3) is the mean square of the particle rotational velocity fluctuation which is avraged for the x- and y-direction.

ϕ	$\langle \mathbf{U}'\mathbf{U}' \rangle$	$\langle \mathbf{\Omega}'\mathbf{\Omega}' \rangle$
0.05	0.009	0.002
0.15	0.043	0.008
0.27	0.100	0.025
0.316	0.149	0.031
0.37	0.204	0.051
0.4	0.238	0.060
0.419	0.305	0.084
0.45	0.364	0.096
0.47	0.397	0.097
0.49	0.428	0.103
0.51	0.483	0.107
0.55	0.555	0.129

Table 9.2: Results of the time integration constant for the auto-correlation function of the velocity fluctuation. Columns (1) and (2) are the volume fraction and Péclet number. Columes (3) and (4) are the time integration constants for the auto-correlation function of the particle translational velocity fluctuation in the y- and z-direction. Columns (5) and (6) are the time integration constants for the auto-correlation function of the particle rotational velocity fluctuation in the x- and y-direction.

ϕ	Pe	$\mathcal{T}_{U'_yU'_y}$	$\mathcal{T}_{U'_zU'_z}$	$\mathcal{T}_{\Omega'_x\Omega'_x}$	$\mathcal{T}_{\Omega'_y\Omega'_y}$
0.316	0.1	0.397	0.262	0.289	0.283
0.316	1.0	0.238	0.216	0.206	0.245
0.316	10^5	0.126	0.145	0.643	0.895
0.45	0.1	0.321	0.265	0.277	0.255
0.45	1.0	0.176	0.202	0.190	0.194
0.45	10^5	0.144	0.181	0.443	0.457
0.51	0.1	0.395	0.334	0.285	0.307
0.51	1.0	0.131	0.153	0.161	0.161
0.51	10^5	0.083	0.098	0.100	0.183

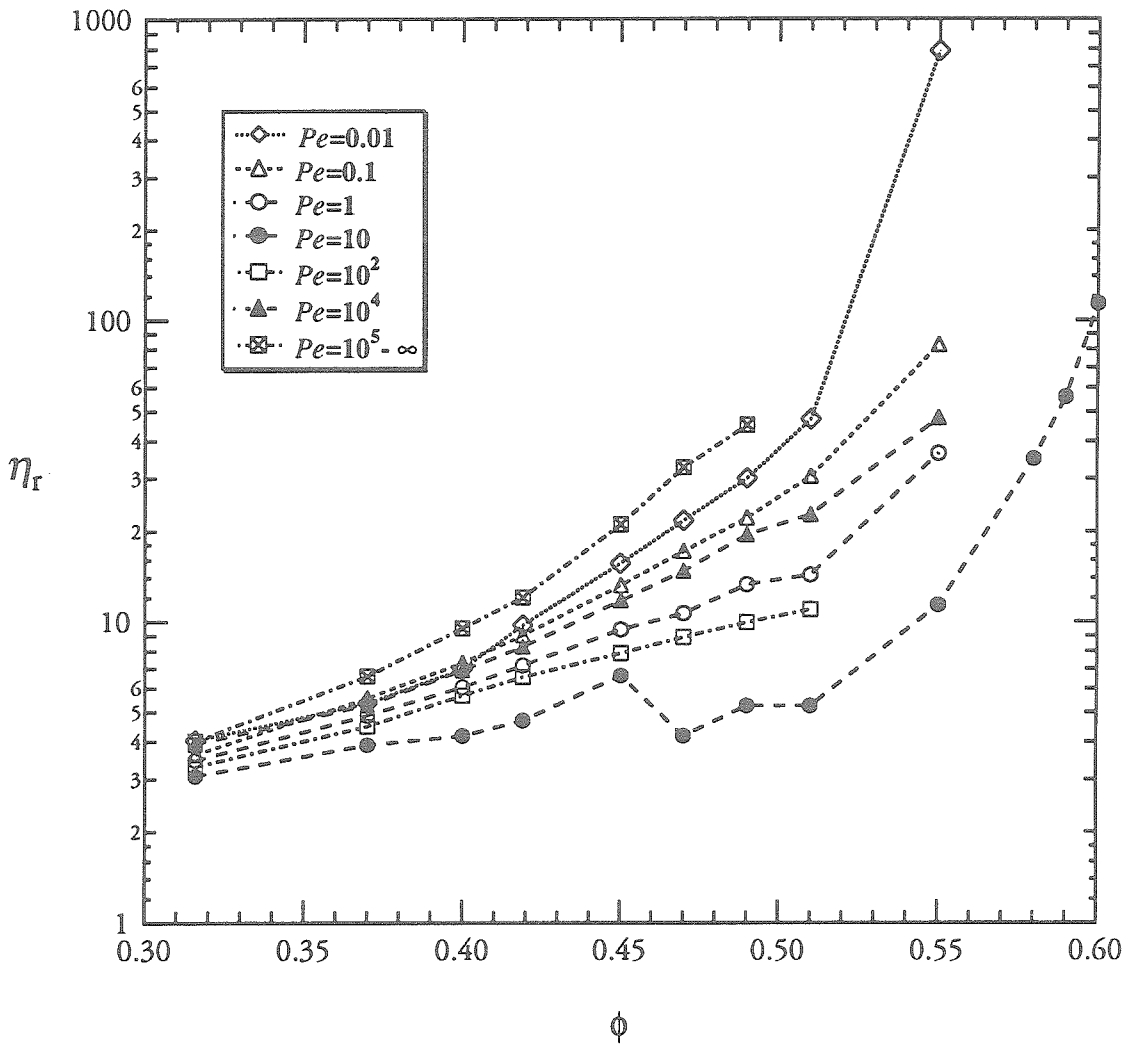

Figure 9.1: The steady shear viscosity obtained by Stokesian dynamics as a function of the volume fraction for hard-sphere suspensions with different Péclet numbers: Pe = 0.01 (◇), 0.1 (△), 1 (○), 10 (●), 100 (□), 10000 (▲) and 10^5 - ∞ (⊠). The viscosity curves show a shear thickening behavior with increasing volume fraction ϕ. The special curve for the shear viscosity at Pe=10 shows a region of strong shear thinning as the volume fraction increases from 0.45 to the range of 0.47 to 0.51.

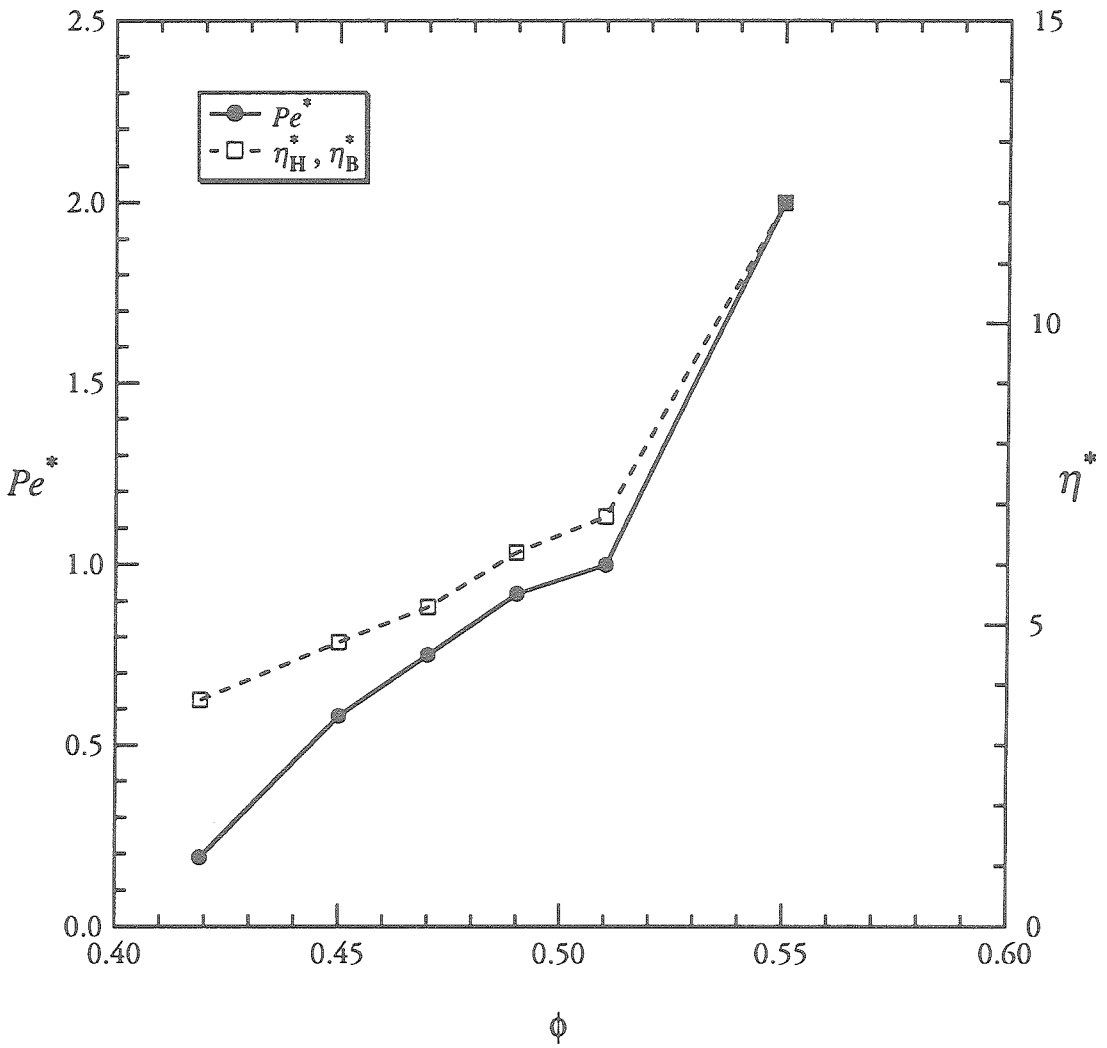

Figure 9.2: A plot of the Péclet number (●) and the steady shear viscosity (□) for the onset region, where the Brownian and hydrodynamic contributions to the stress are identical, as a function of the volume fraction for hard-sphere suspensions. The left vertical scale is for the Péclet number Pe^* and the right vertical scale is for the steady Brownian and hydrodynamic viscosities computed at Pe^*.

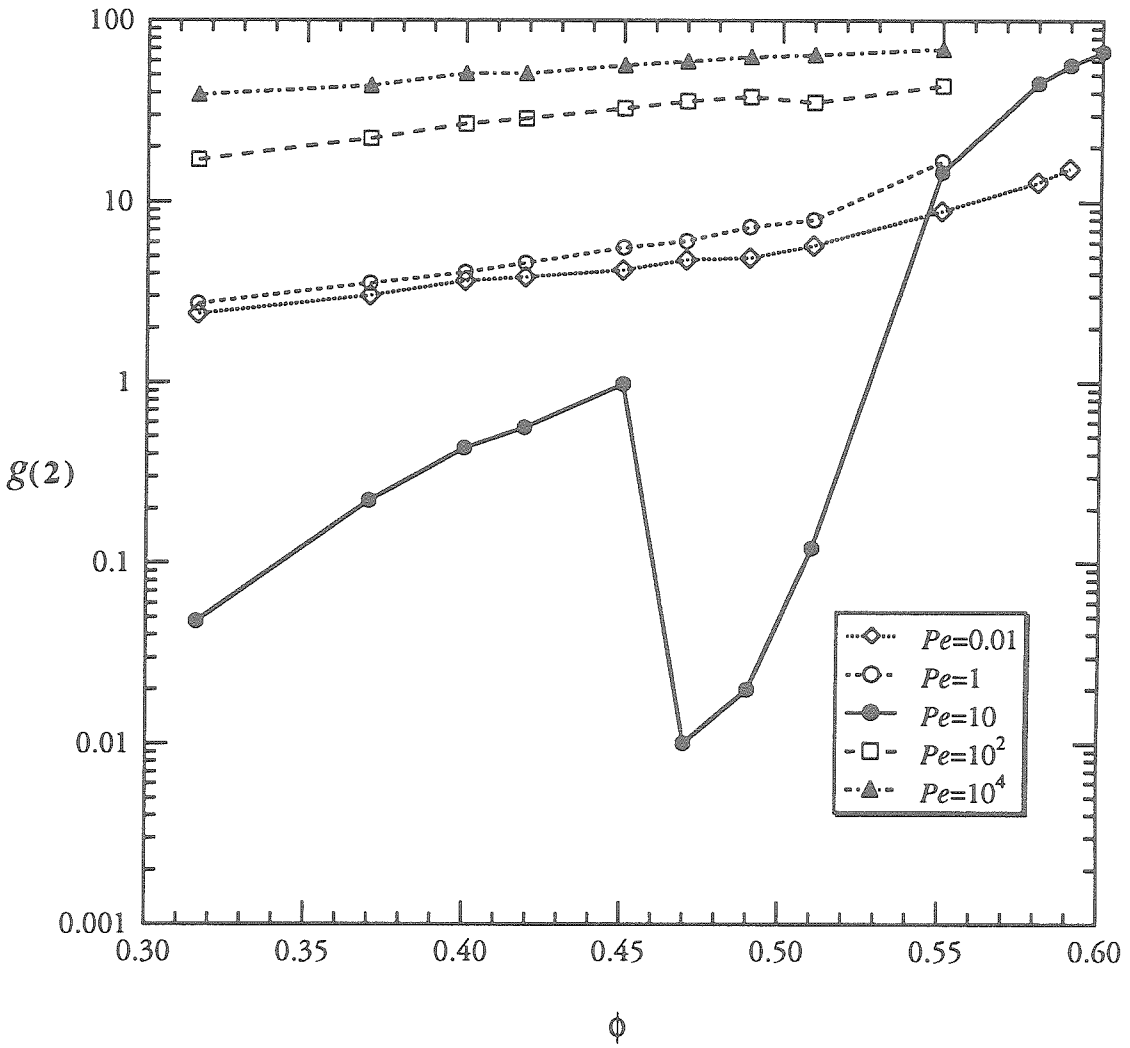

Figure 9.3: The angularly averaged pair-distribution function evaluated at particle center-center radial spacing r=2 (when the particles come in contact), $g(2)$, obtained by Stokesian dynamics as a function of the volume fraction for hard-sphere colloidal suspensions with different Péclet numbers: Pe = 0.01 (◇), 1 (○), 10 (●), 100 (<??>G) and 10000 (▲). The special cuvre for $g(2)$ with Pe=10 shows a significant decrease as the volume fraction ϕ increases from 0.45 to the range of 0.47 to 0.51. $g(2)$ with other Péclet numbers increases with increasing ϕ.

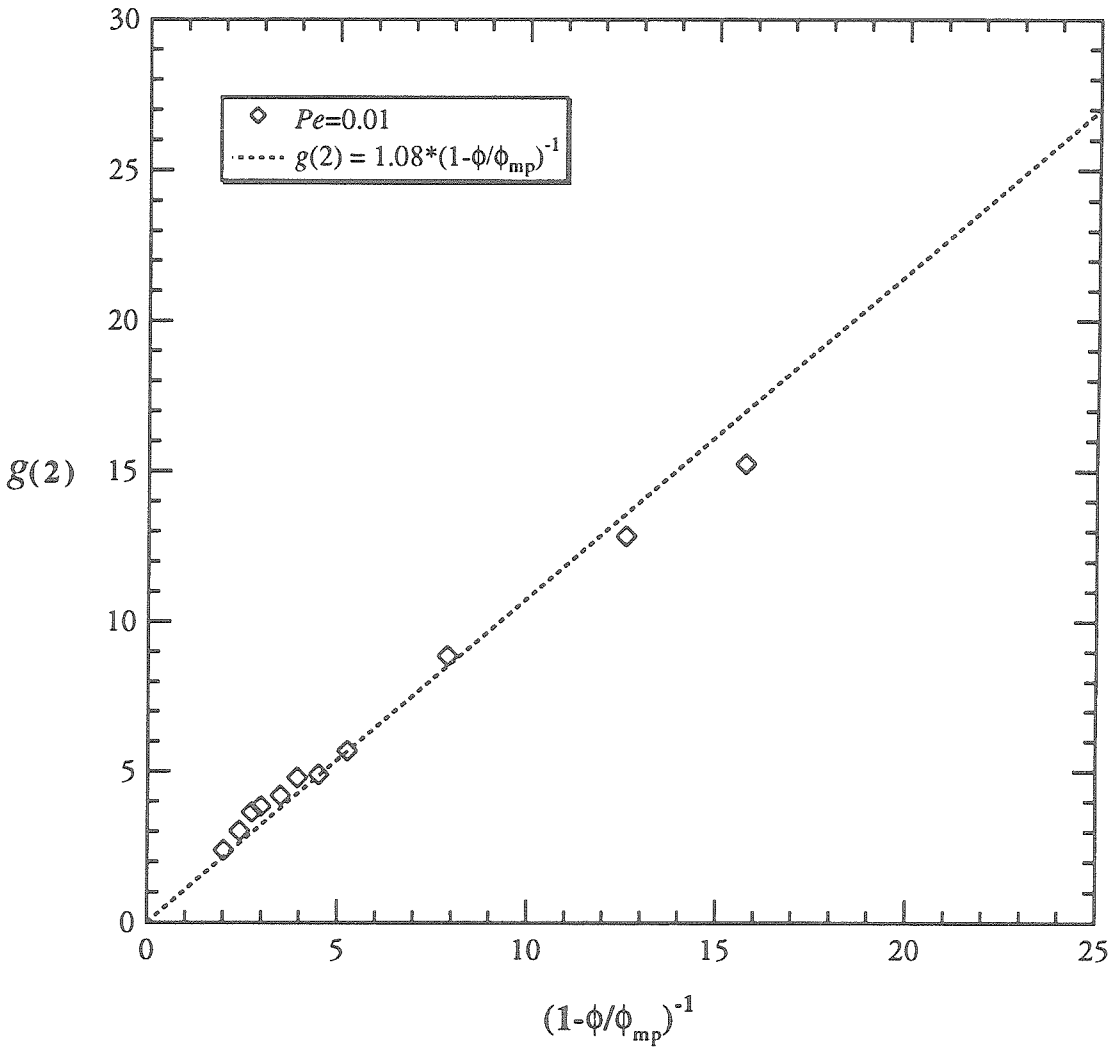

Figure 9.4: The angularly averaged pair-distribution function evaluated at particle center-center radial spacing r=2 (when the particles come in contact), $g(2)$, obtained by Stokesian dynamics as a function of the dimensionless group $(1-\phi/\phi_{mp})^{-1}$ with ϕ_{mp}= 0.63 the maximum packing of the random hard spheres. The curves are for Pe = 0.01 (◇) and best-fitted line with $g(2) = 1.08*(1-\phi/\phi_{mp})^{-1}$.

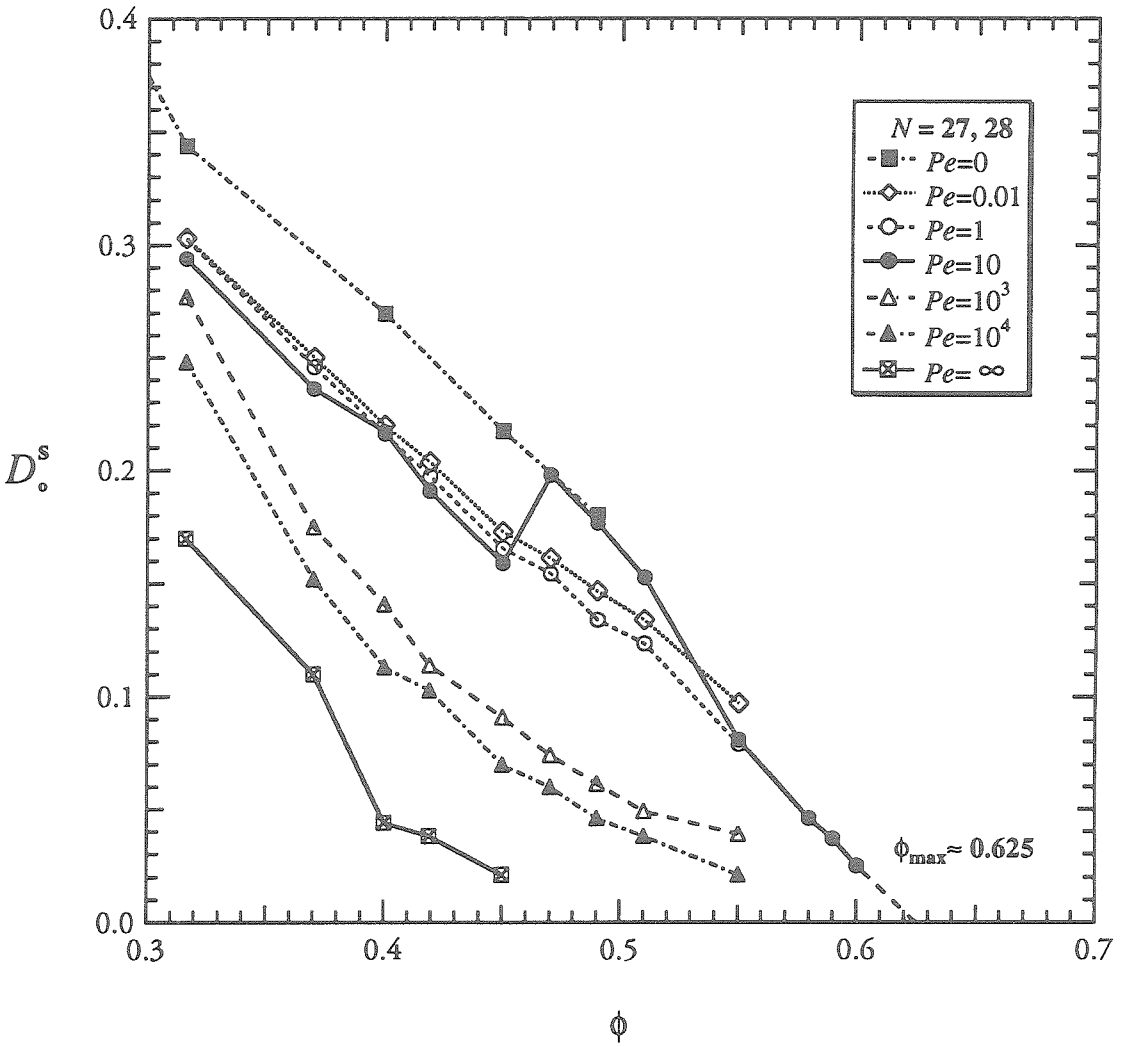

Figure 9.5: The short-time translational self-diffusion coefficients obtained by Stokesian dynamics as a function of the volume fraction for hard-sphere suspensions with different Péclet numbers: Pe = 0 (■), 0.01 (◇), 1 (○), 10 (●), 1000 (△), 10000 (▲) and ∞ (⊠). The short-time translational self-diffusion coefficient for Pe=10 displays an interesting behavior: D_o^s increases for the volume fraction ϕ in the range of 0.47 to 0.51 and is larger than that of a hard-sphere suspension at ϕ=0.45. D_o^s for other Péclet numbers decreases monotonically with increasing ϕ. The short-time translational self-diffusion coefficients are computed from simulations with 27 or 28 particles. Dotted line shows the extrapolation of zero self-diffusivities at $\phi_{max} \approx 0.625$ for Pe=10.

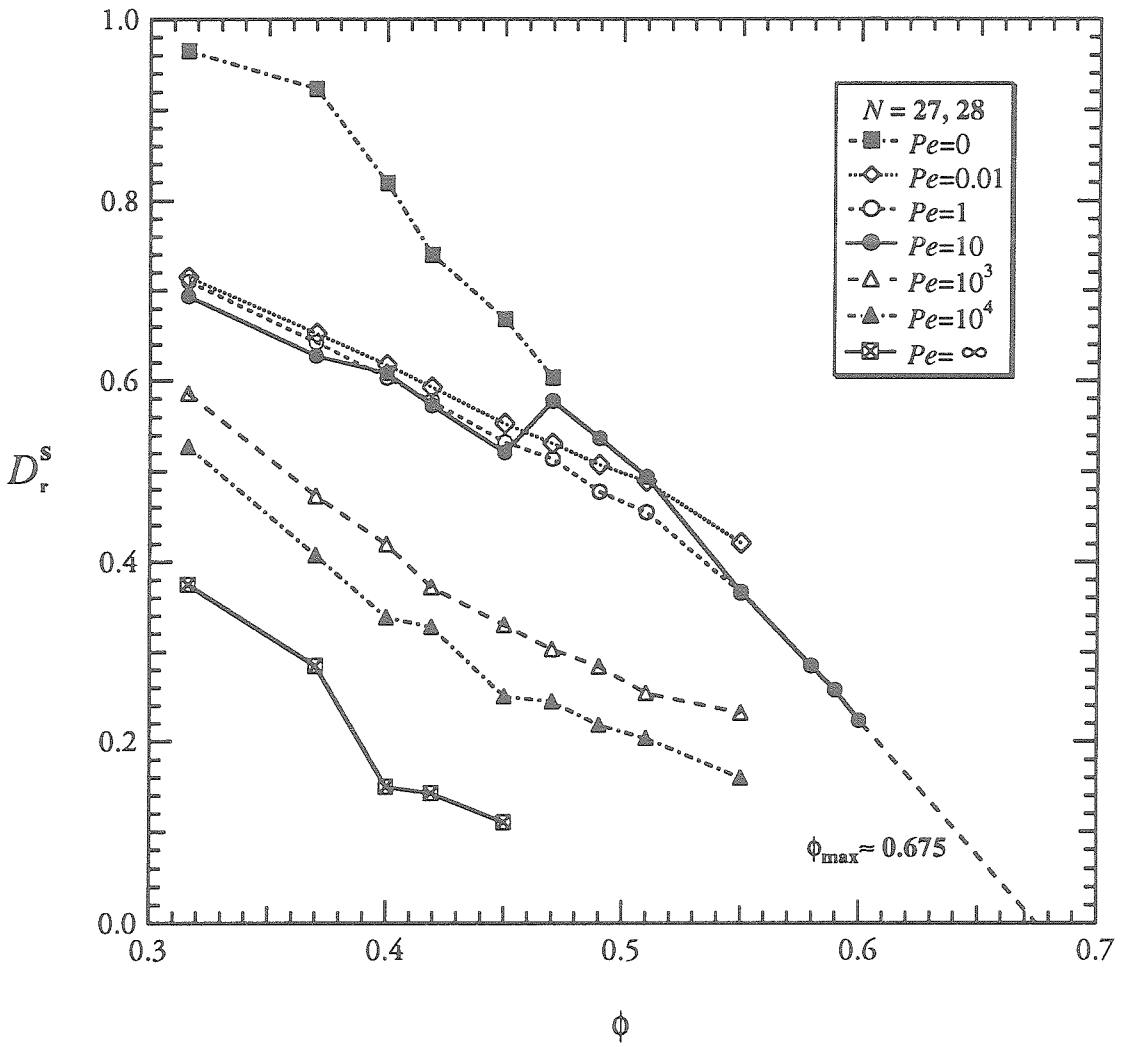

Figure 9.6: The short-time rotational self-diffusion coefficients obtained by Stokesian dynamics as a function of the volume fraction for hard-sphere suspensions with different Péclet numbers: Pe = 0 (■), 0.01 (◇), 1 (○), 10 (●), 1000 (△), 10000 (▲) and ∞ (⊠). The short-time rotational self-diffusion coefficient for Pe=10 increases for the volume fraction ϕ in the range of 0.47 to 0.51 and is larger than that of a hard-sphere suspension at ϕ=0.45. D_r^s for other Péclet numbers decreases monotonically with increasing ϕ. Results are obtained from simulations with 27 or 28 particles. The limit of zero self-diffusivities at $\phi_{max} \approx 0.675$ is shown by dotted line for Pe=10.

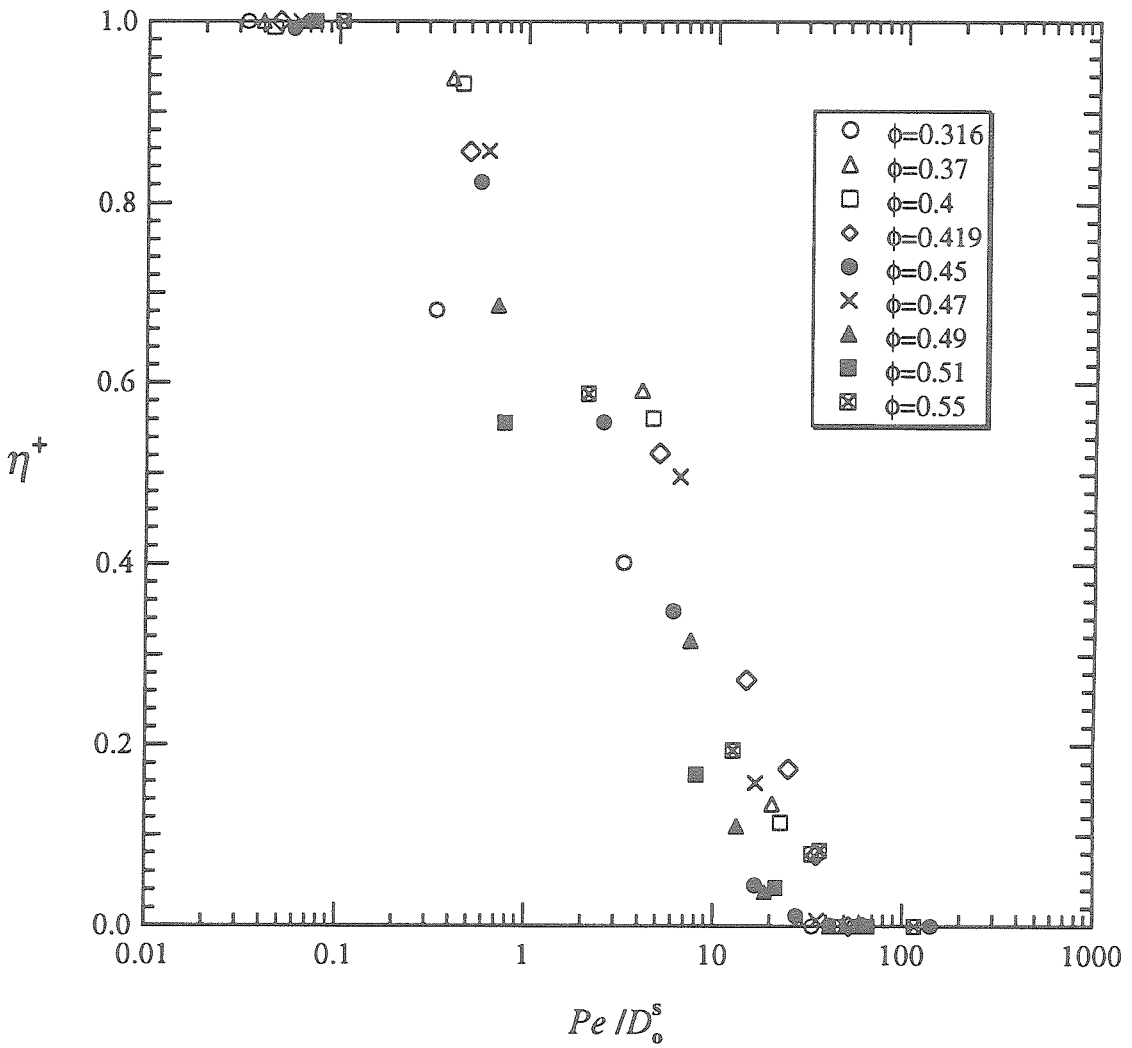

Figure 9.7: The reduced viscosity η^+ for the low shear limit obtained by Stokesian dynamics as a function of the new dimensionless group $Pe\,/\,D_o^s$ with the short-time self-diffusion coefficient D_o^s obtained at the same Péclet number. The range of the volume fraction ϕ is from 0.316 to 0.55. The reduced viscosity η^+ is defined as $(\eta(Pe)-\eta(Pe{=}10))\,/\,(\eta(Pe{=}0.01)-\eta(Pe{=}10))$.

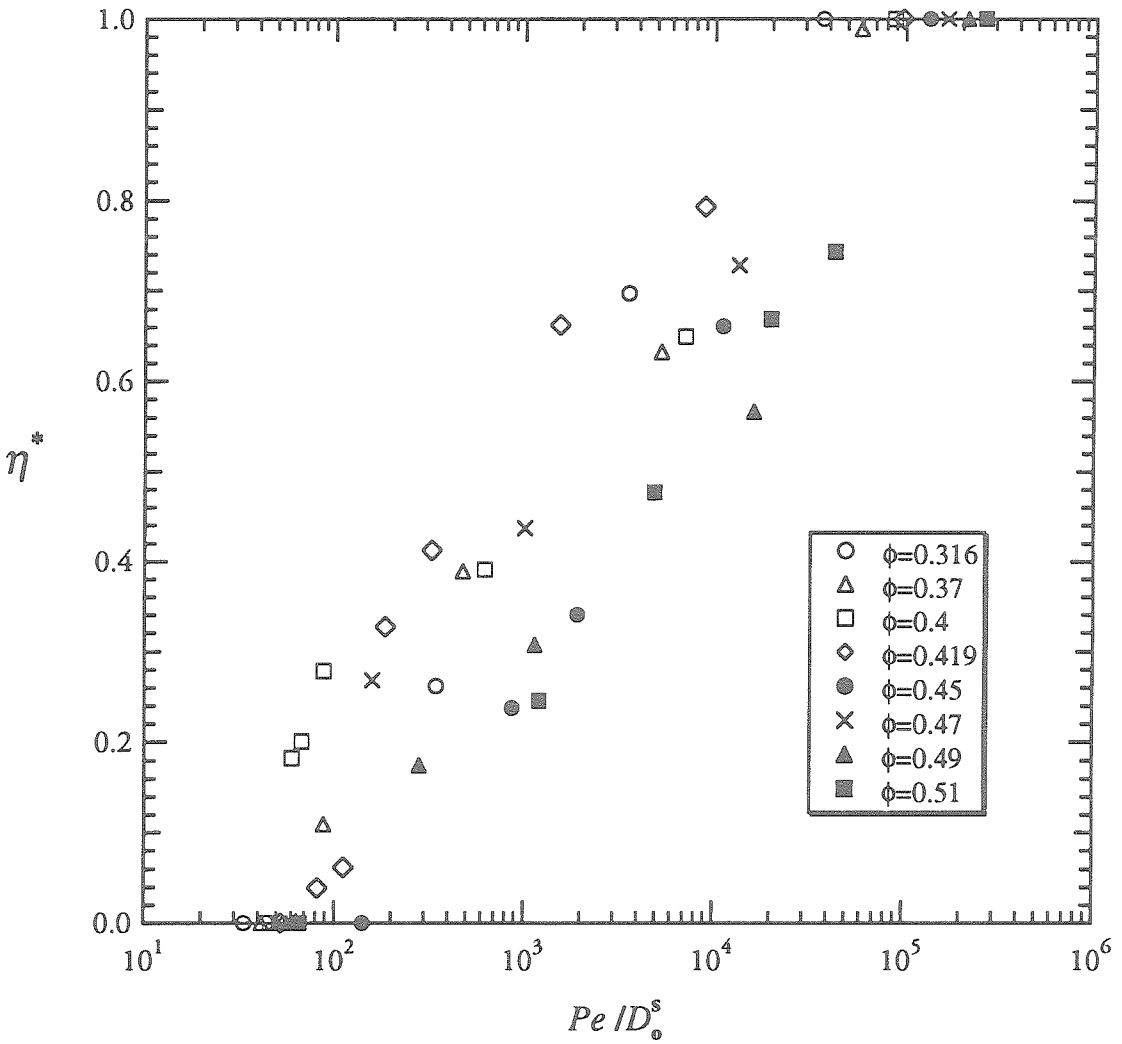

Figure 9.8: The reduced viscosity η^* in the high shear limit obtained by Stokesian dynamics as a function of the new dimensionless group $Pe\,/\,D_o^s$ with the short-time self-diffusion coefficient D_o^s computed at the same Péclet number. The range of the volume fraction ϕ is from 0.316 to 0.51. The reduced viscosity η^* is defined as $(\eta(Pe)-\eta(Pe=10))\,/\,(\eta(Pe=\infty)-\eta(Pe=10))$.

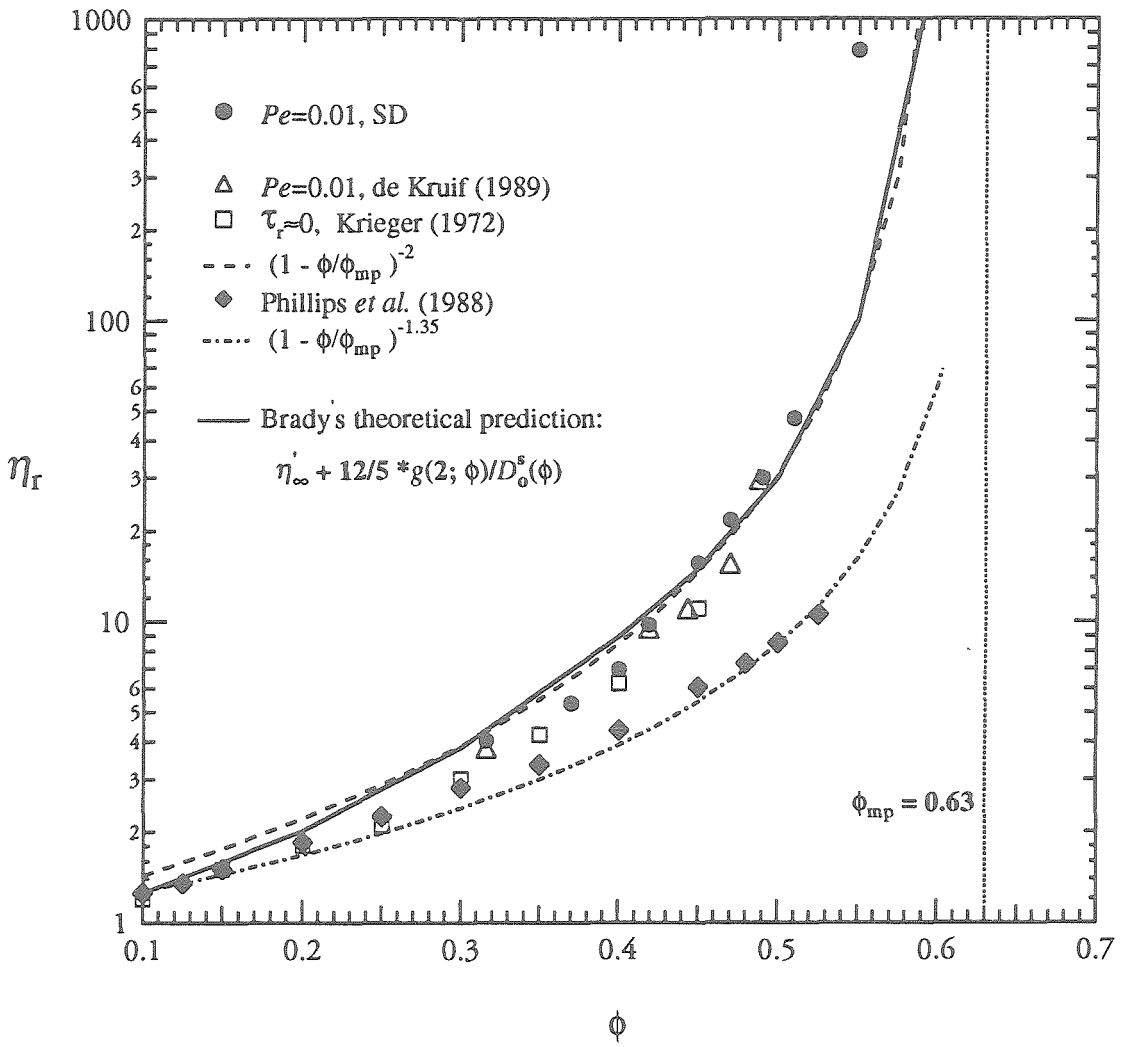

Figure 9.9: Comparison of the simulation results for the steady shear viscosity in the low shear limit (●) (at Pe=0.01) as a function of the particle volume fraction ϕ with the experiments of van der Werff and de Kruif (1989) at the same Péclet number Pe=0.01 (Δ) and the experiments of Krieger (1972) in the limit of vanishing shear rate (□). The dashed curve is according to the scaling $(1-\phi/\phi_{mp})^{-2}$ with the maximum packing for the random hard-sphere model ϕ_{mp}= 0.63. The viscosity of random hard spheres computed by Phillips *et al.* (1988) (◆) is also plotted in the figure, which shows a good fit with the scaling $(1-\phi/\phi_{mp})^{-1.35}$ (dotted-dash curve) with ϕ_{mp}= 0.63. Brady's (1993) theoretical prediction for the shear viscosity in the low shear limit is excellent as shown by the solid curve for the entire range of ϕ.

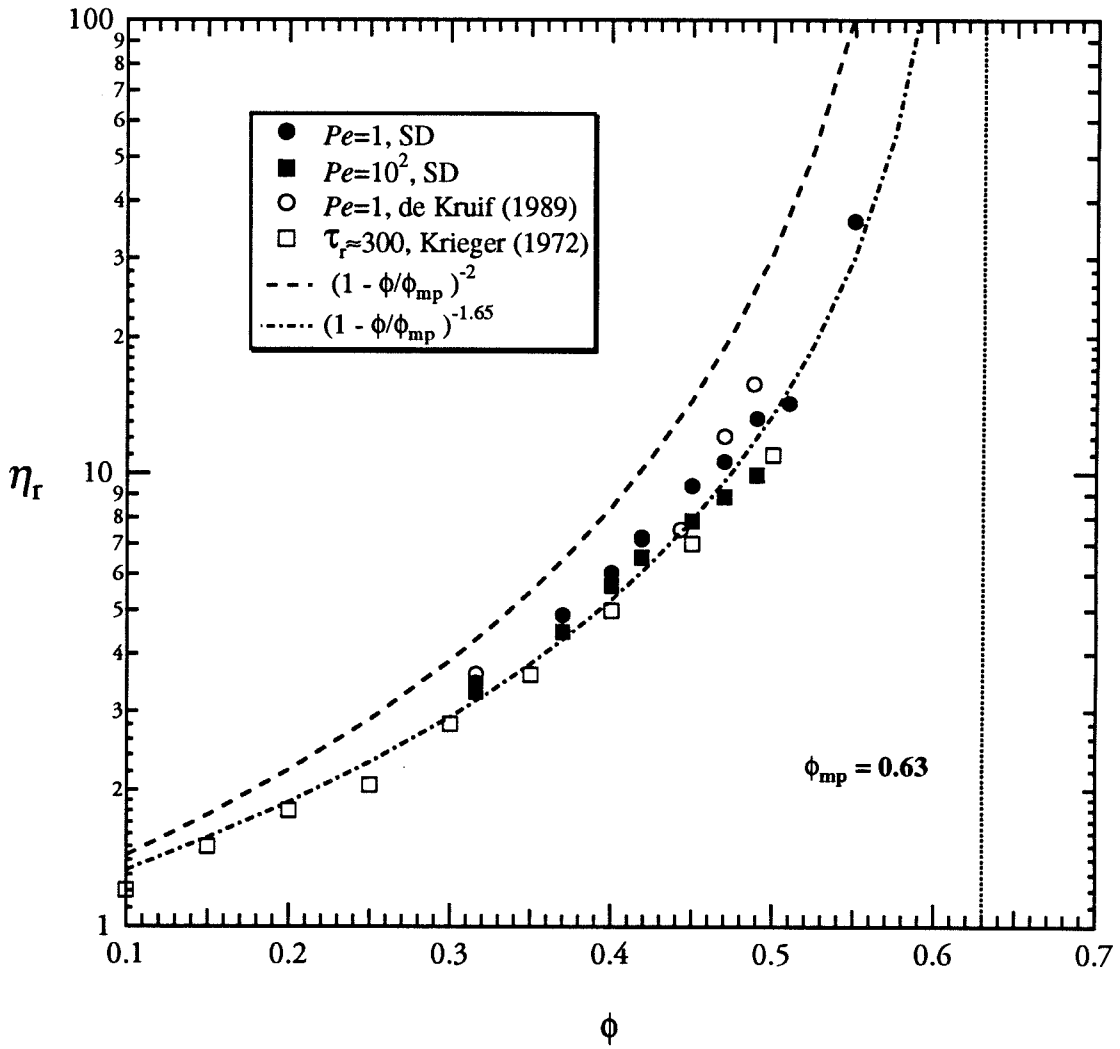

Figure 9.10: Comparison of the simulation results for the steady shear viscosity in the intermediate shear limit: Pe = 1 (●) and 100 (■) as a function of the particle volume fraction ϕ with the experiments of van der Werff and de Kruif (1989) for Pe=1 (○) and the experiments of Krieger (1972) with a reduced shear rate of 300 (□). The dashed curve is according to the scaling $(1-\phi/\phi_{mp})^{-2}$ with ϕ_{mp}= 0.63 the maxium packing of the random hard spheres. The dotted-dash curve is fitted with the scaling $(1-\phi/\phi_{mp})^{-1.65}$.

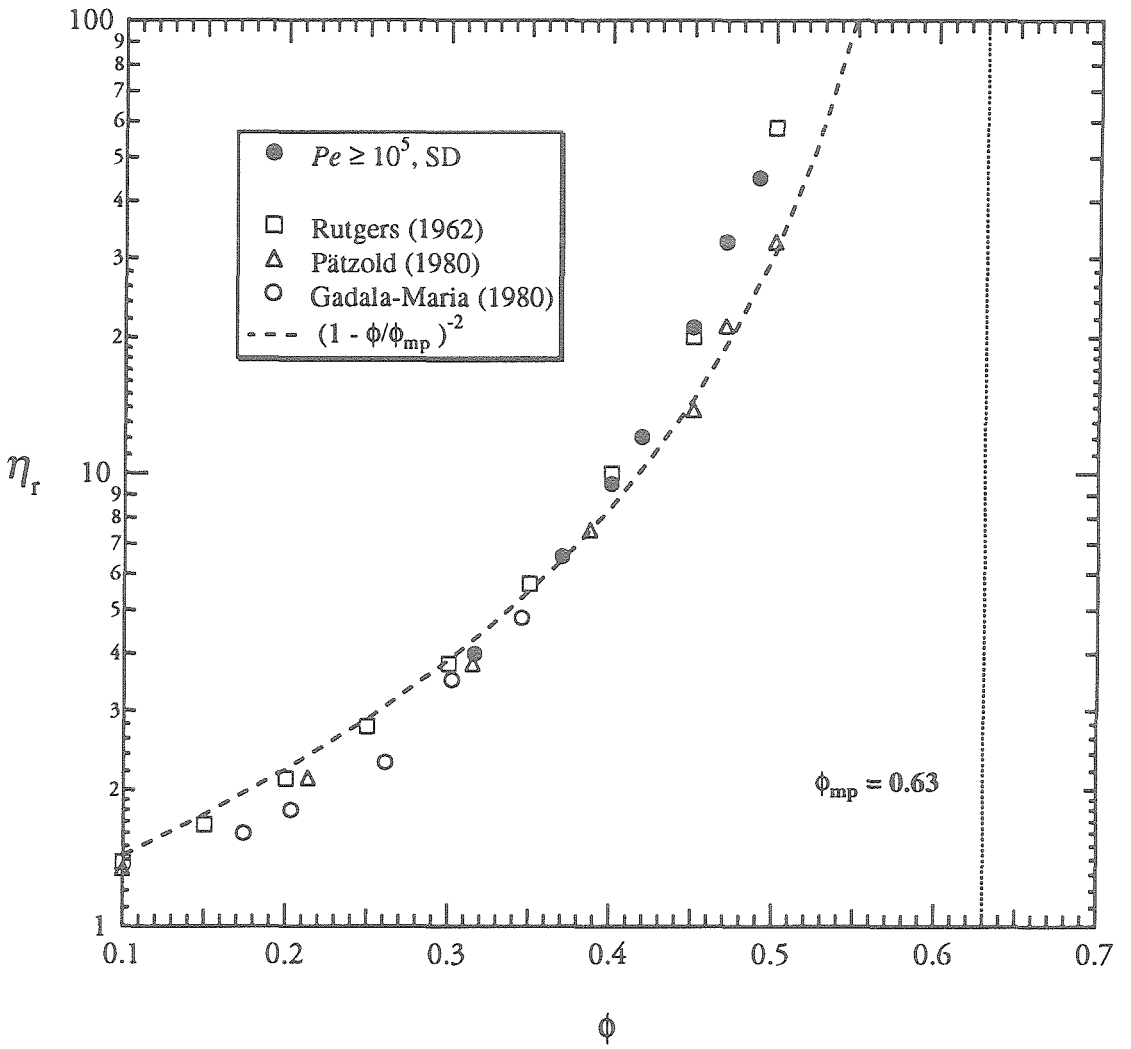

Figure 9.11: Comparison of the simulation results for the steady shear viscosity in the high shear limit (●) ($Pe \geq 10^5$) as a function of the volume fraction ϕ with the experiments of Rutgers (curve #1, 1962) (□), Pätzold (1980) (Δ) and Gadala-Maria (1980) (○) for non-Brownian suspensions ($Pe \to \infty$). The dashed curve is according to the scaling $(1-\phi/\phi_{mp})^{-2}$ with $\phi_{mp} = 0.63$ the maxium packing of the random hard spheres.

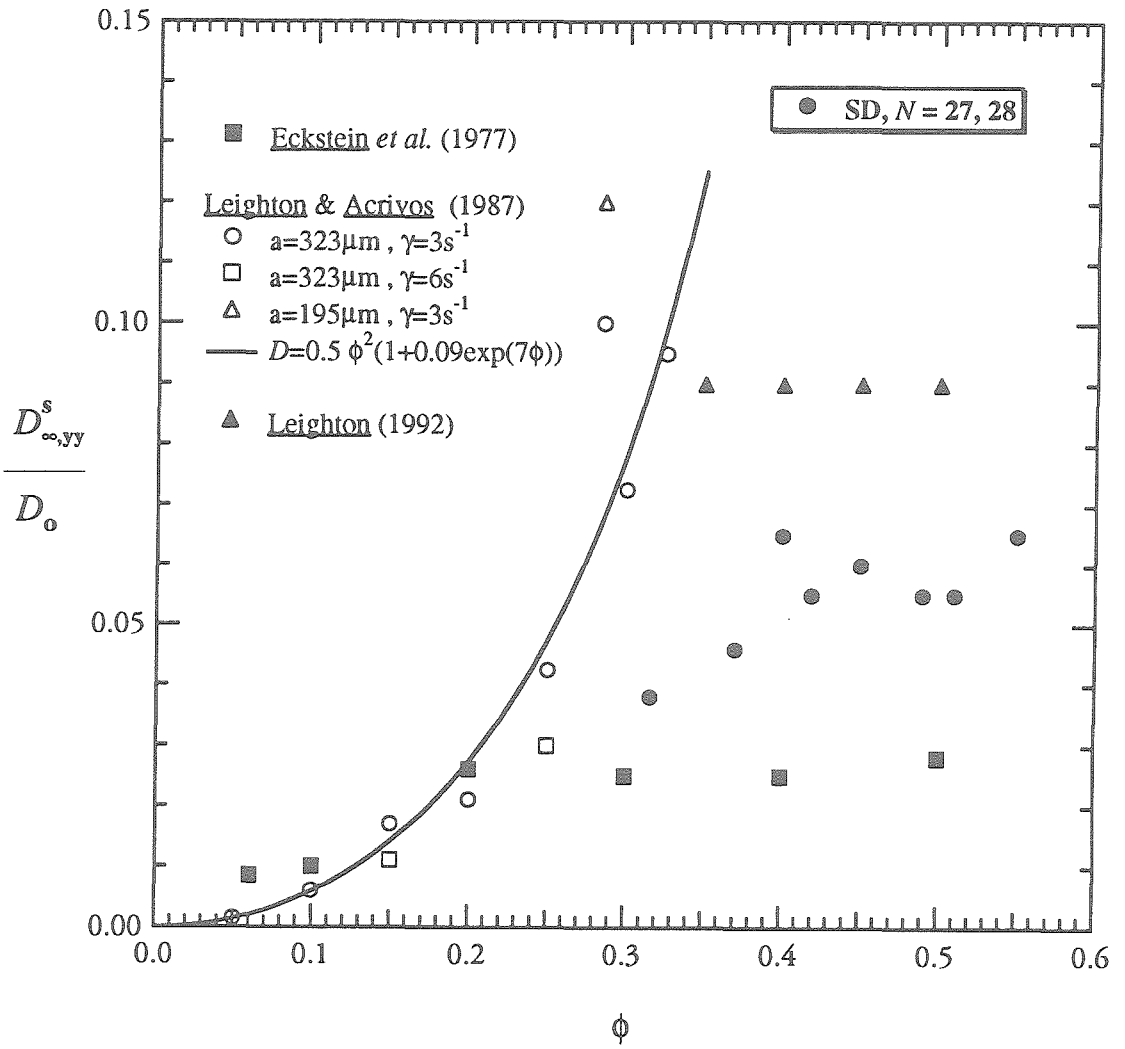

Figure 9.12: Comparison for the long-time self-diffusion coefficient in the velocity gradient direction, $D^s_{\infty,yy}$, normalized by the infinite dilution diffusivity D_o in the limit of $Pe \to \infty$: (●) simulation results with 27 or 28 particles, the experiments of Eckstein *et al.* (1977) (■), Leighton and Acrivos (1987) (○, □ and Δ for various sizes of spheres and shear rates) and the most recent experiments of Phan and Leighton (1992) (▲).

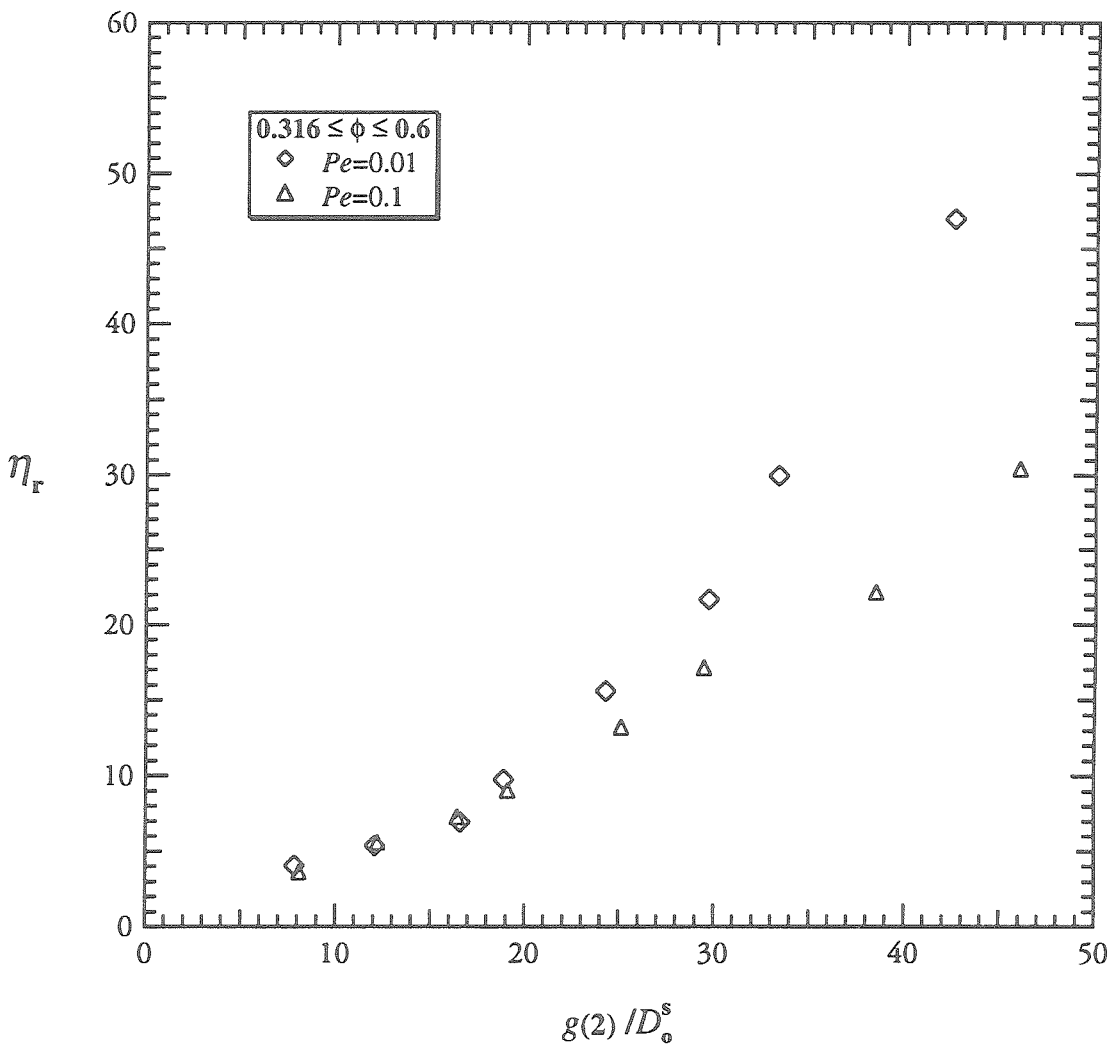

Figure 9.13: The steady shear viscosity in the low shear limit with three small Péclet numbers: Pe = 0.01 (◇) and 0.1 (△) obtained by Stokesian dynamics for hard-sphere suspensions as a function of the dimensionless group $g(2)/D_o^s$. $g(2)$ is the angularly averaged pair-distribution function evaluated at particle center-center spacing r=2 (when the particles come in contact) and D_o^s is the short-time self-diffusion coefficient evaluated at the same Péclet number where the shear viscosity and $g(2)$ are obtained. The range of the volume fraction ϕ is from 0.316 to 0.6.

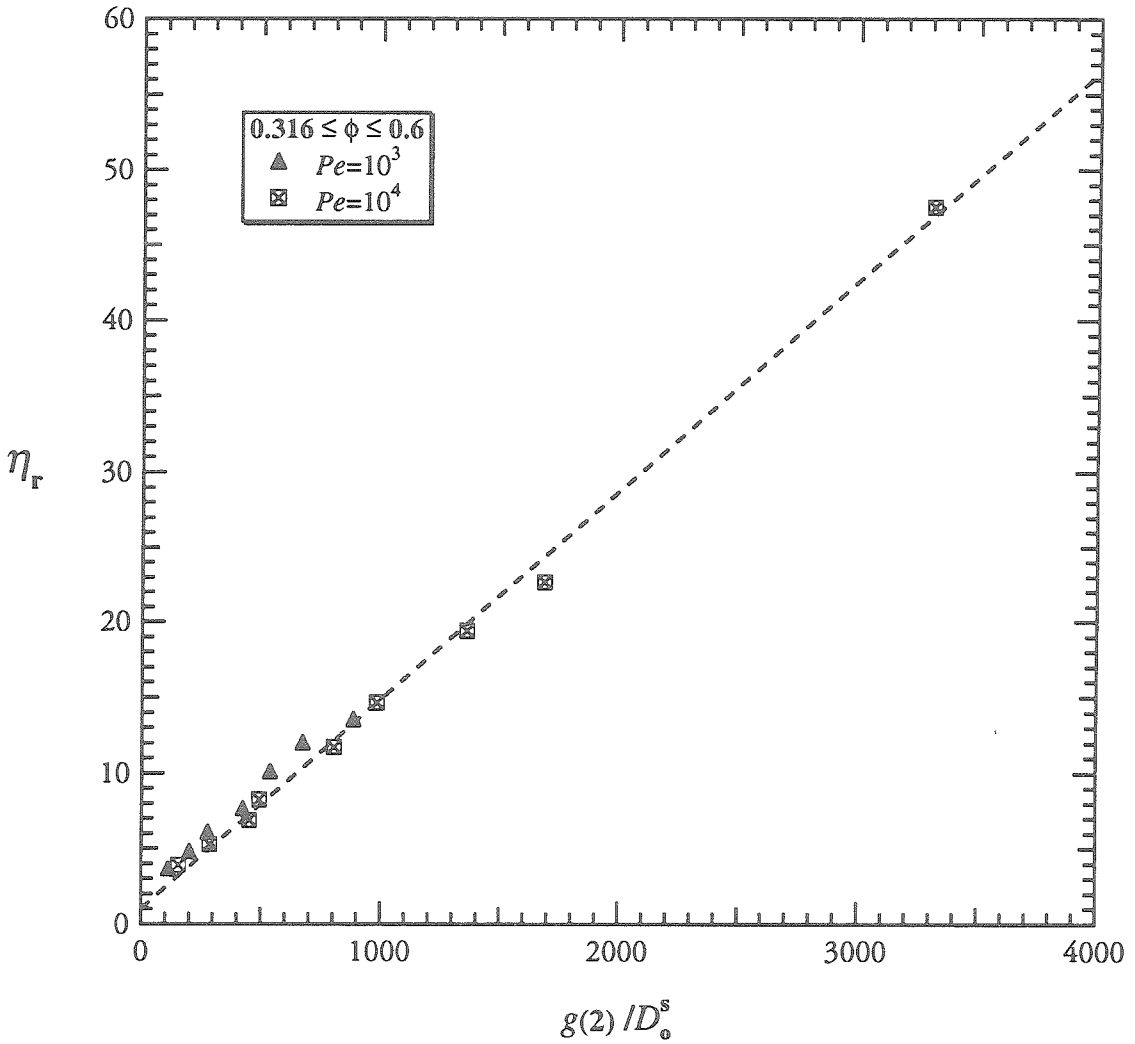

Figure 9.14: The steady shear viscosity in the high shear limit with two large Péclet numbers: Pe = 1000 (▲) and 10000 (⊠) obtained by Stokesian dynamics for hard-sphere suspensions as a function of the dimensionless group $g(2)/D_o^s$. $g(2)$ is the angularly averaged pair-distribution function evaluated at particle center-center spacing r=2 (when the particles come in contact) and D_o^s is the short-time self-diffusion coefficient evaluated at the same Péclet number where the shear viscosity and $g(2)$ are obtained. The range of the volume fraction ϕ is from 0.316 to 0.6. The dotted line is is according to $\eta = m * g(2)/D_o^s + b$ with the slope m≈0.014 and intercept b=1.

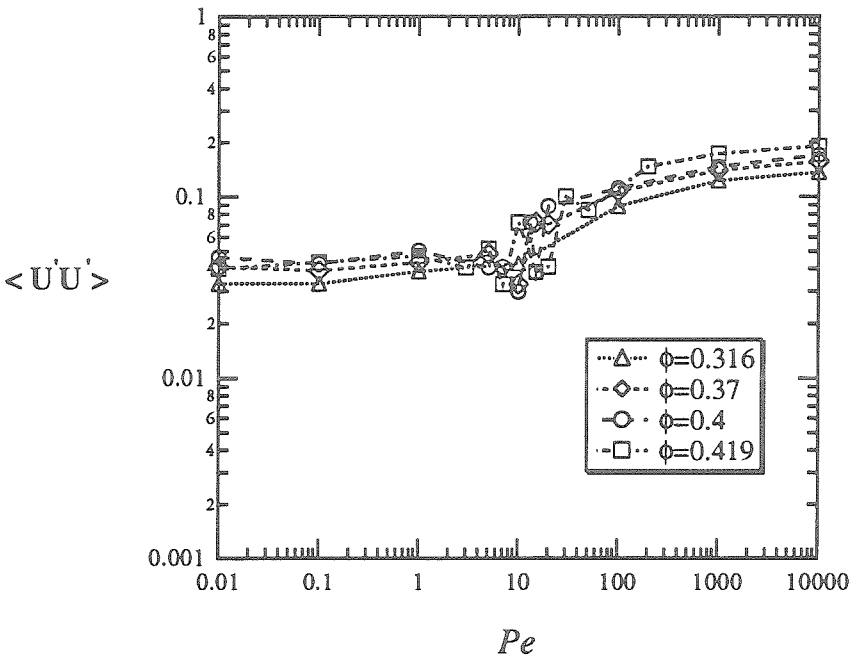

Figure 9.15.a

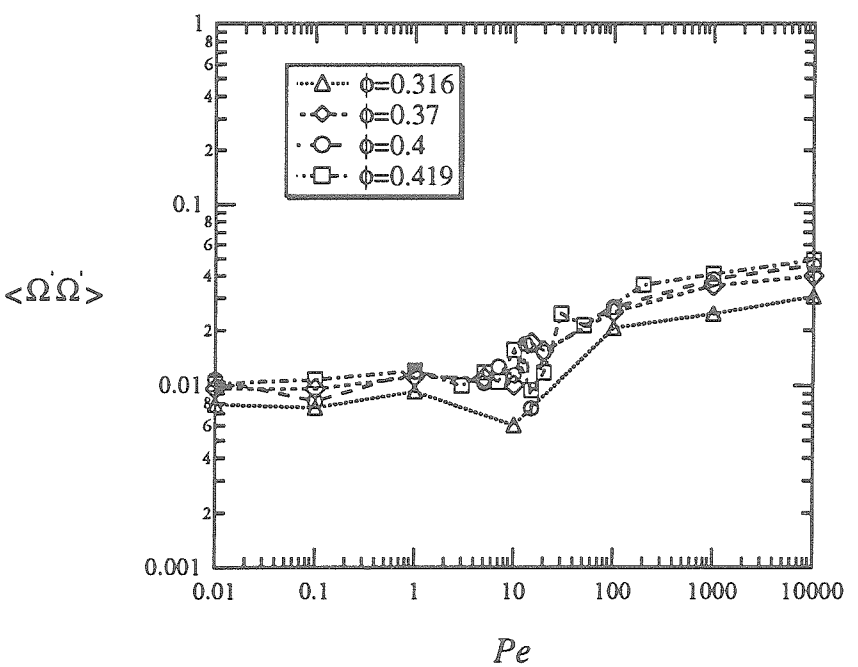

Figure 9.15.b

Figure 9.15.a-b: The steady mean square of the translation and rotational velocity fluctuations obtained by Stokesian dynamics as a function of the Péclet number for hard spheres at different volume fractions: ϕ = 0.316 (Δ), 0.37 (◇), 0.4 (○) and 0.419 (□). The prime denotes the fluctuation.

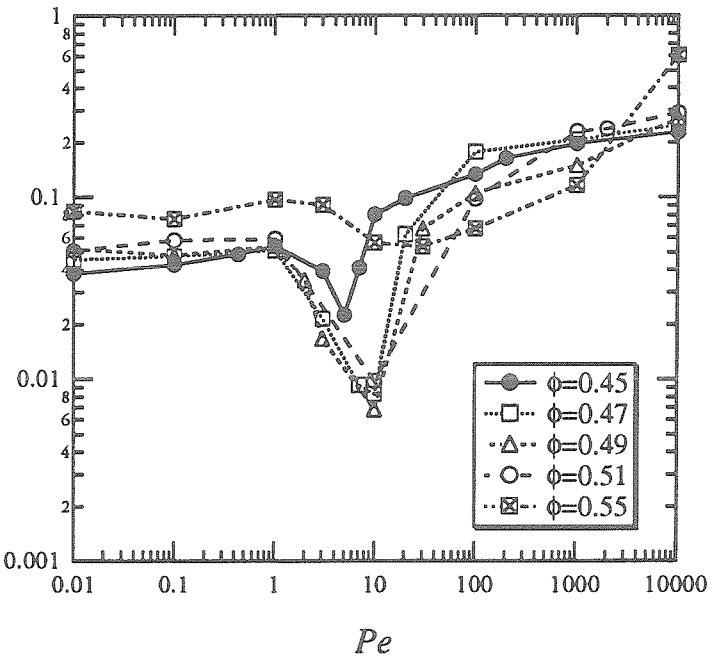

Figure 9.16.a

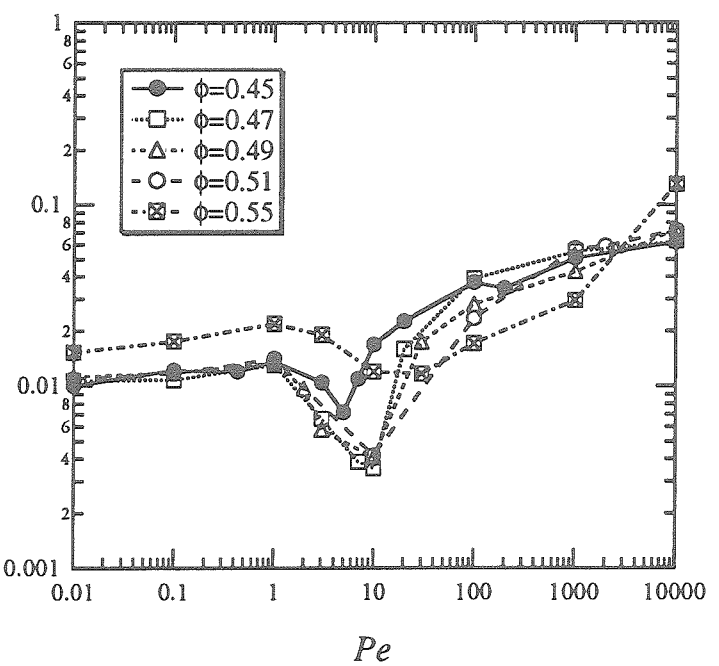

Figure 9.16.b

Figure 9.16.a-b: The steady mean square of the translation and rotational velocity fluctuations obtained by Stokesian dynamics as a function of the Péclet number for hard spheres at different volume fractions: ϕ = 0.45 (●), 0.47 (□), 0.49 (△), 0.51 (○) and 0.55 (⊠). The prime denotes the fluctuation.

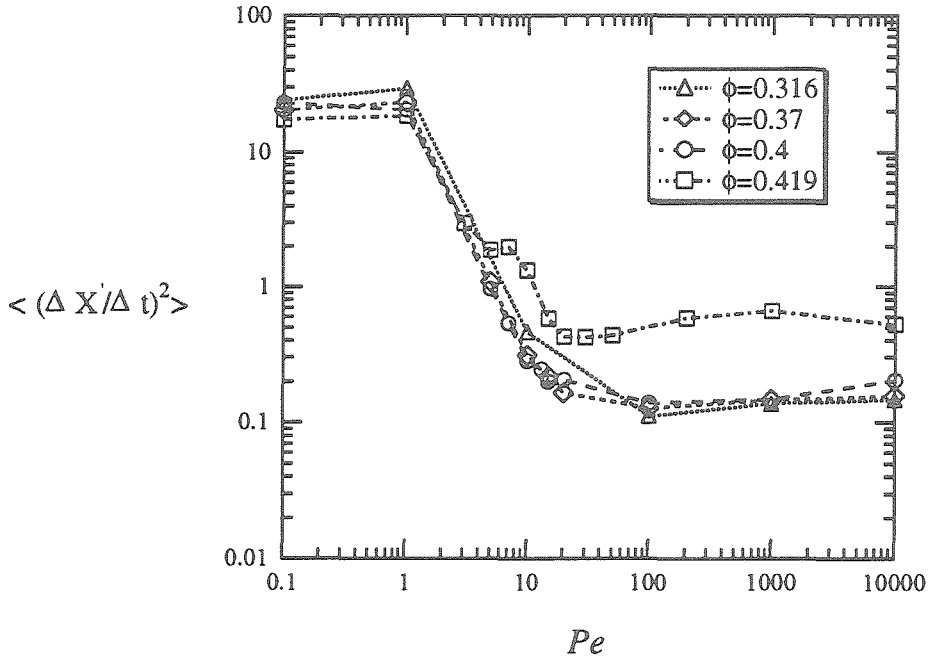

Figure 9.17.a

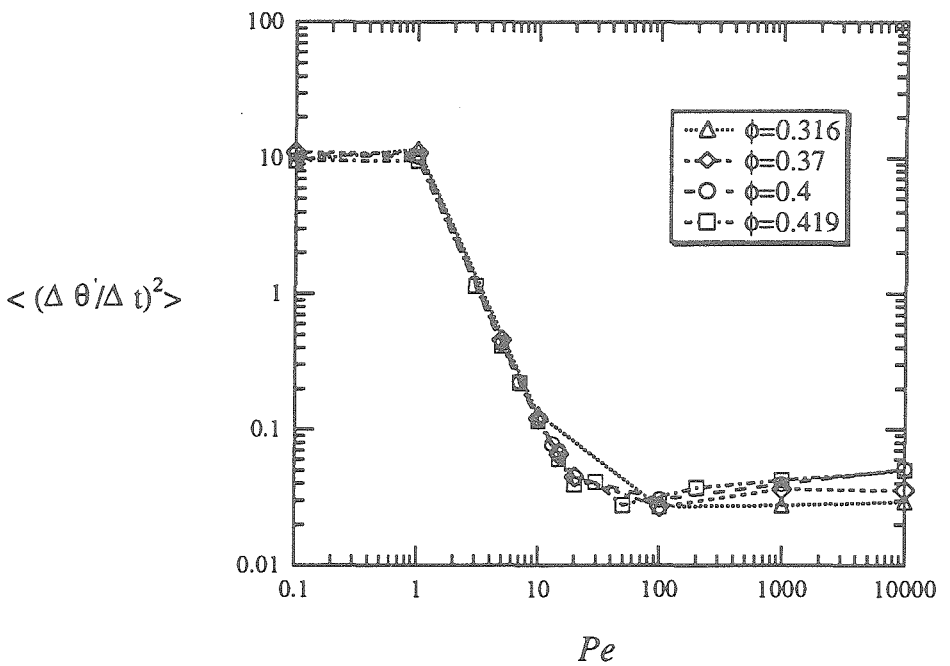

Figure 9.17.b

Figure 9.17.a-b: The steady mean square of the translation and rotational velocity fluctuations computed from the displacements of the particles as a function of the Péclet number for hard spheres at different volume fractions: ϕ = 0.316 (Δ), 0.37 (◇), 0.4 (○) and 0.419 (□). The prime denotes the fluctuation.

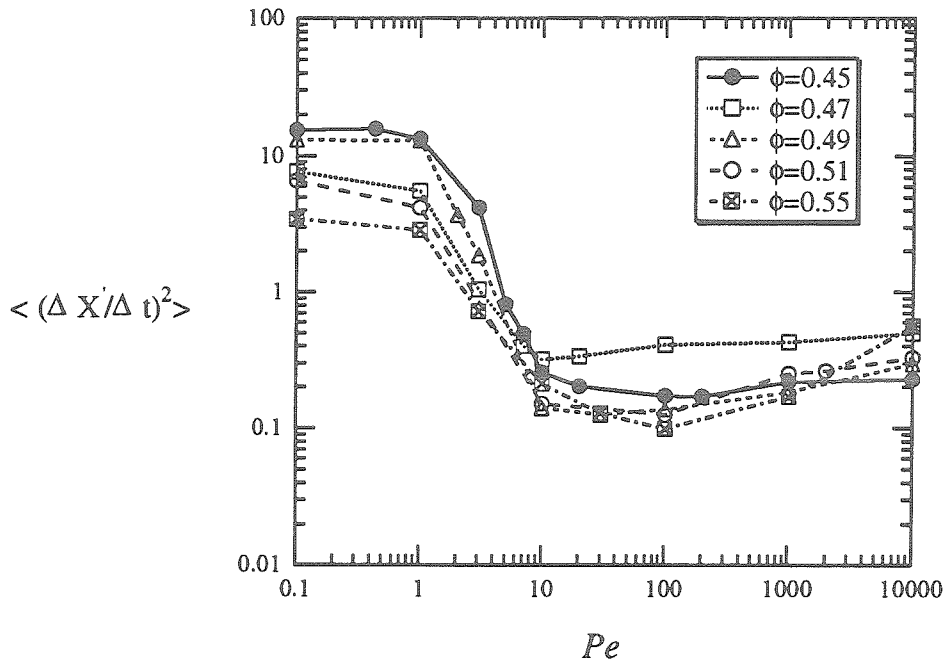

Figure 9.18.a

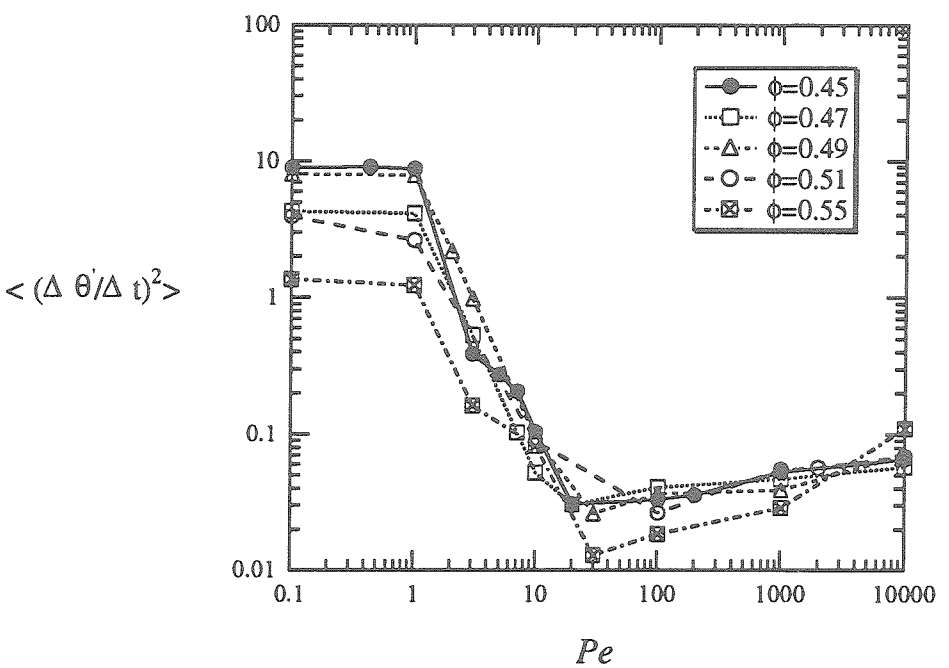

Figure 9.18.b

Figure 9.18.a-b: The steady mean square of the translation and rotational velocity fluctuations computed from the displacements of the particles as a function of the Péclet number for hard spheres at different volume fractions: ϕ = 0.45 (●), 0.47 (□), 0.49 (Δ), 0.51 (○) and 0.55 ⊠). The prime denotes the fluctuation.

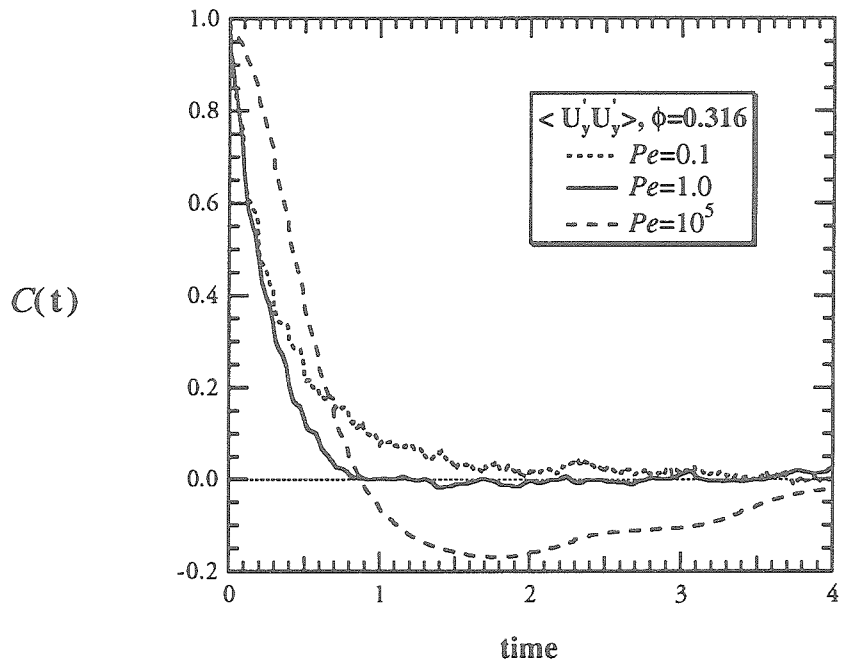

Figure 9.19.a

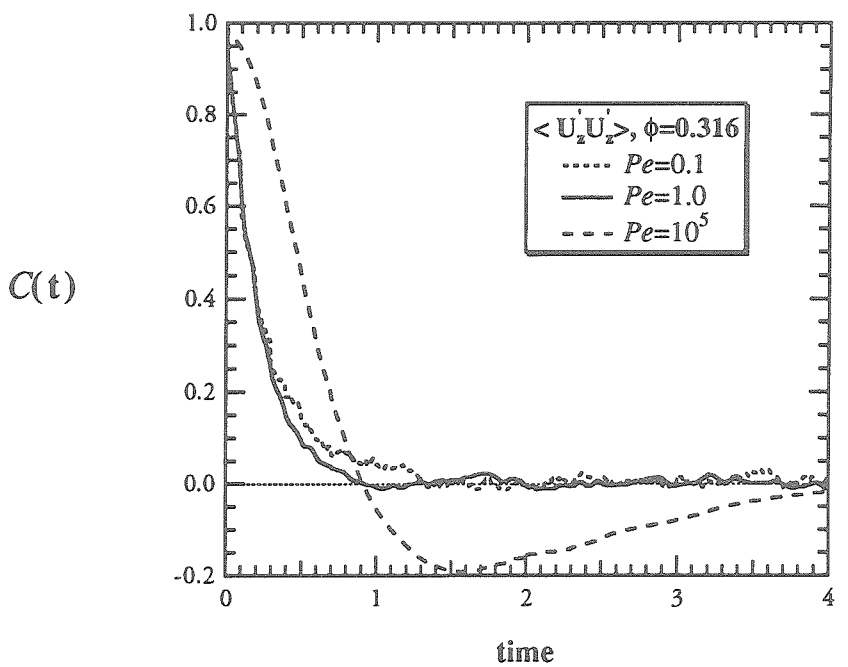

Figure 9.19.b

Figure 9.19.a-b: The time auto-correlation function of the velocity fluctuation in the velocity gradient direction, the y-axis, and the vorticity direction, the z-axis, for hard spheres at a volume fraction ϕ=0.316 and three different Péclet numbers: Pe = 0.1 (dotted curve), 1 (solid curve) and 10^5 (dashed curve).

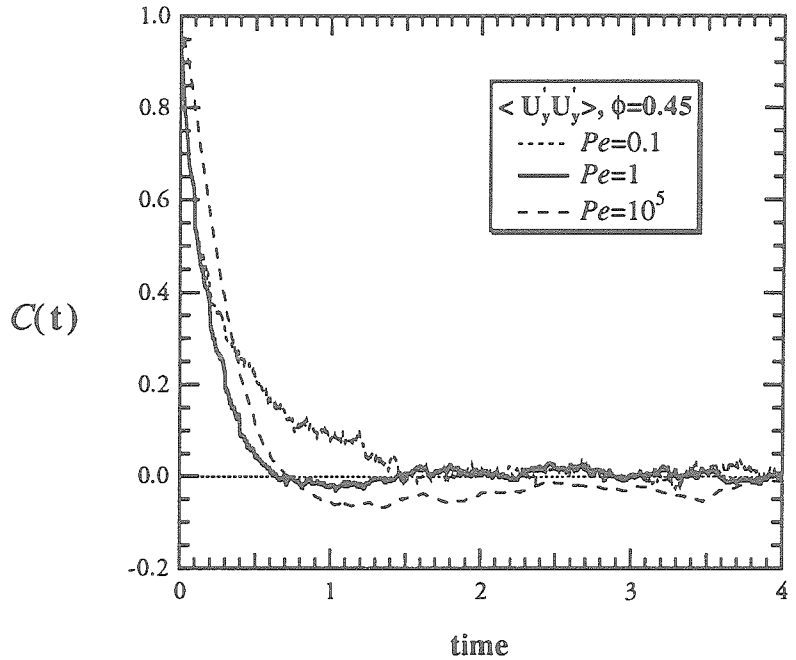

Figure 9.20.a

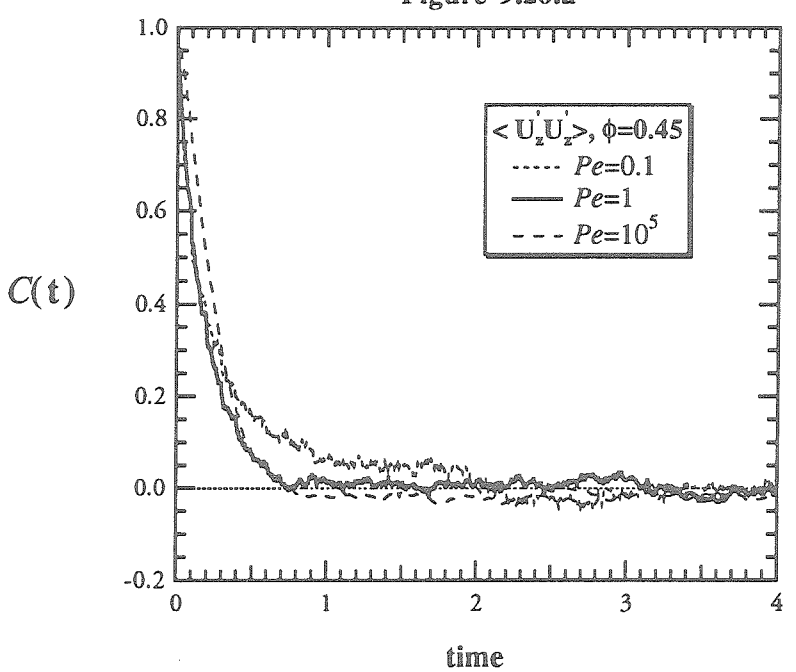

Figure 9.20.b

Figure 9.20.a-b: The time auto-correlation function of the velocity fluctuation in the velocity gradient direction, the y-axis, and the vorticity direction, the z-axis, for hard spheres at a volume fraction ϕ=0.45 and three different Péclet numbers: Pe = 0.1 (dotted curve), 1 (solid curve) and 10^5 (dashed curve).

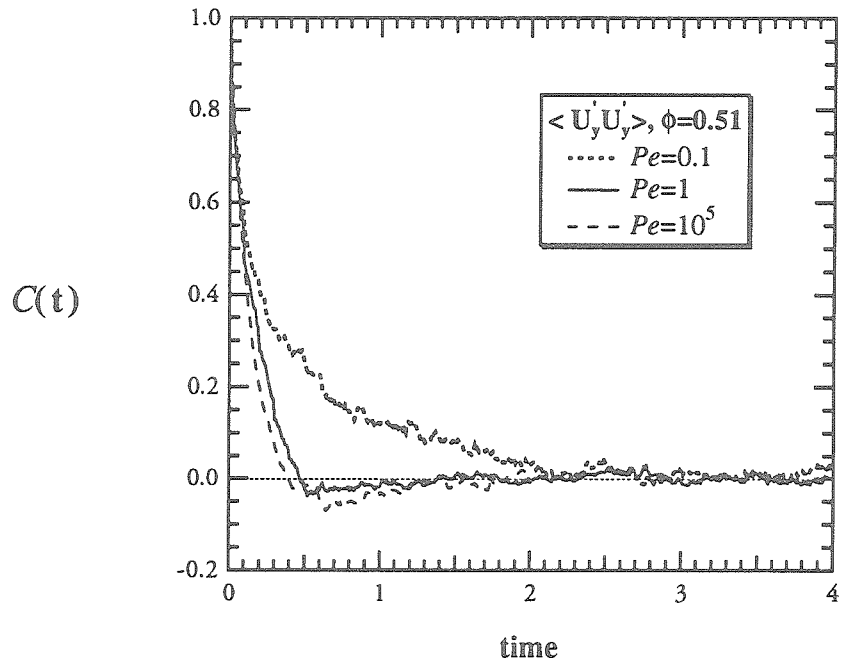

Figure 9.21.a

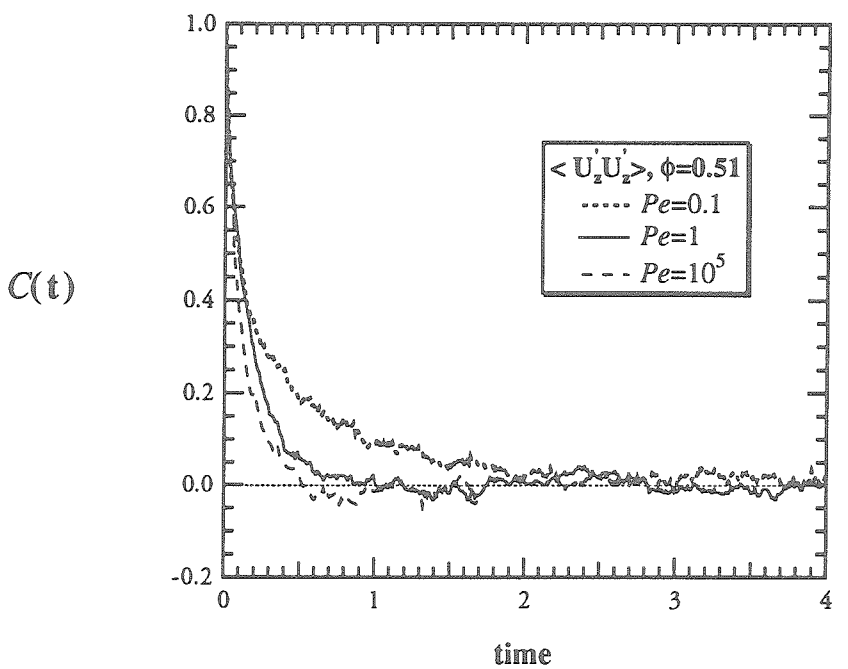

Figure 9.21.b

Figure 9.21.a-b: The time auto-correlation function of the velocity fluctuation in the velocity gradient direction, the y-axis, and the vorticity direction, the z-axis, for hard spheres at a volume fraction ϕ=0.51 with three different Péclet numbers: Pe = 0.1 (dotted curve), 1 (solid curve) and 10^5 (dashed curve).

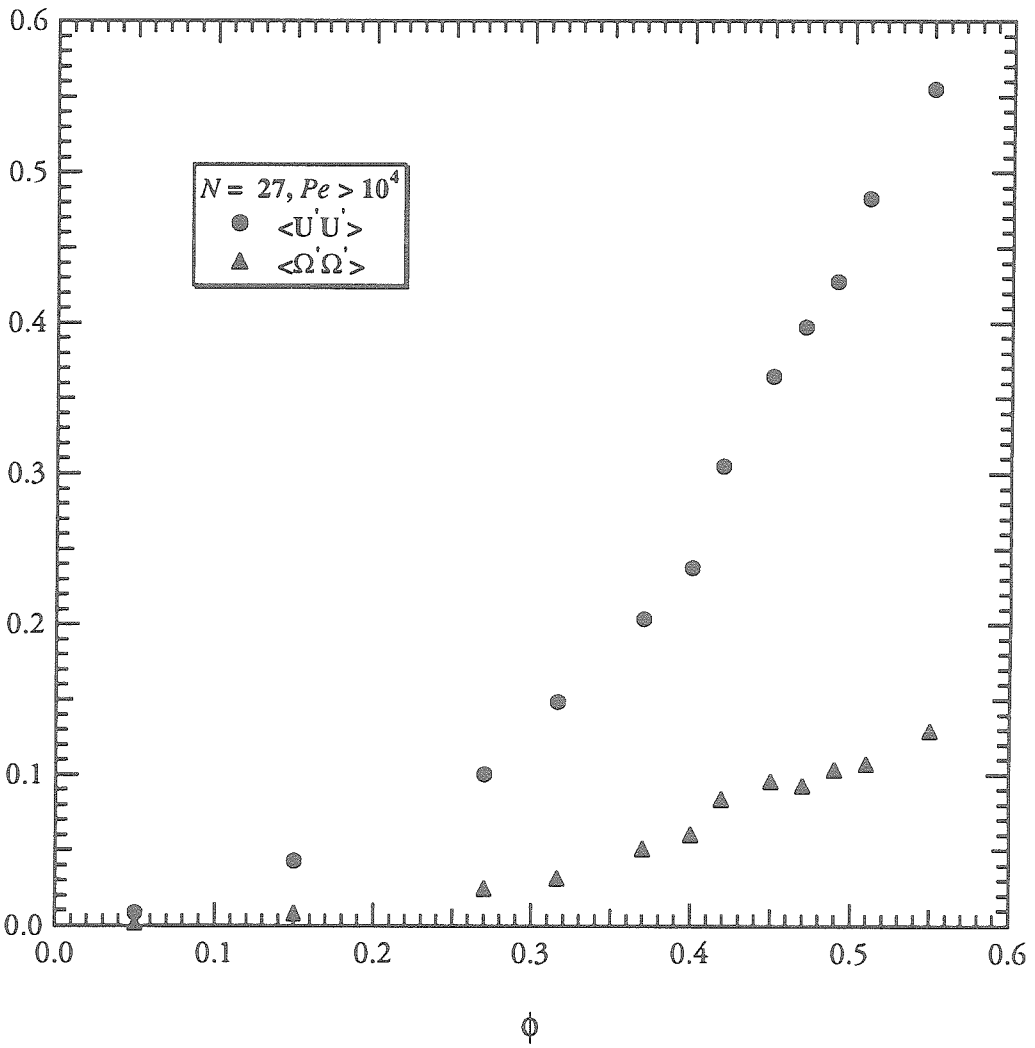

Figure 9.22: The mean square of the particle translational (●) and rotational (▲) velocity fluctuations obtained by Stokesian dynamics as a function of volume fraction for the high Péclet number limit ($Pe > 10^4$).

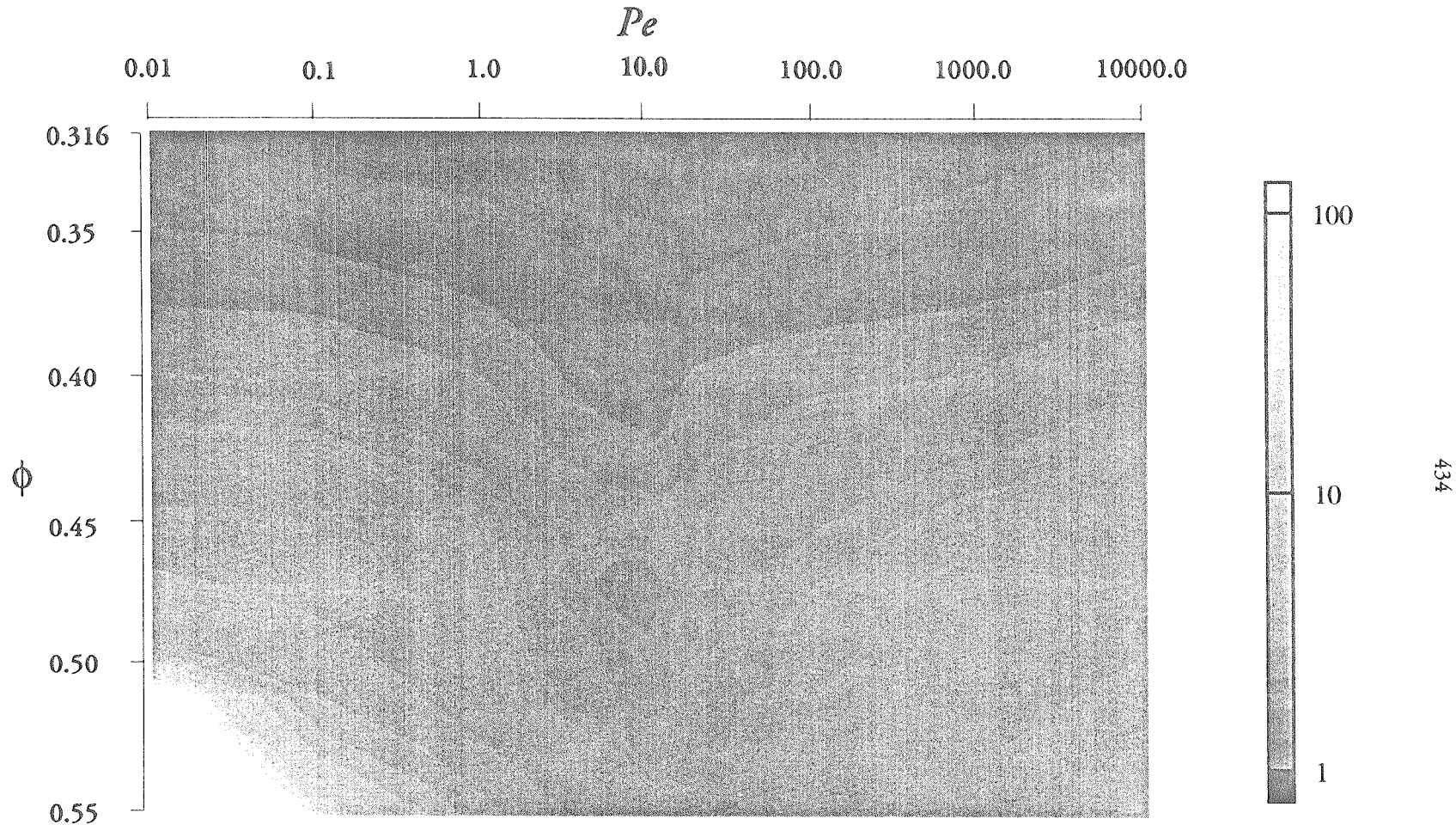

Figure 9.23: The steady shear viscosity as a function of the volume fraction, ϕ, and the Péclet number, *Pe*, obtained by Stokesian dynamics for hard-sphere suspensions. The Péclet number is shown in the horizontal logarithmic scale and the volume fraction is shown in the vertical scale. Contour regions of light and dark colors represent high and low shear viscosity, respectively. The legend color with high and low logarithmic scale is shown in the right hand side of this figure.

Chapter X

SEDIMENTATION OF COLLOIDAL PARTICLES IN CONCENTRATED SUSPENSIONS

In this chapter, we present a brief study for the sedimentation of colloidal particles in dense suspensions. While the sedimentation of particles have been examined only in the limit of pure hydrodynamics or infinite dilution by theories (Batchelor (1972, 1982), Batchelor and Wen (1982), Koch and Brady (1985, 1987), Koch and Shaqfeh (1989, 1991)), experiments (Mirza and Richardson (1979), Acrivos and Herbolzheimer (1979), Herbolzheimer and Acrivos (1981)), and also by simulations (Ansell and Dickinson (1986), Lester (1987), Ladd (1988, 1990, 1992)), the sedimentation of colloidal particles at finite Péclet numbers has not been investigated. Here, the Péclet number is defined as the ratio of the gravitational and Brownian forces. Our objective is to determine the sedimentation velocity and the related microstructure of colloidal particles settling under gravity. The simulation method is presented first, followed by simulation results for the mean sedimentation velocity, the radial pair-distribution function, and the short-time self-diffusivity, and finally the sediment microstructure.

X.1 The Simulation Method

One of the advantages offered by the Stokesian dynamics simulation method is that it can be modified with relative ease for variety of applications. To simulate the sedimentation of Brownian particles, the evolution equation (2.7) or (2.9) can be simplified by setting the deterministic convective terms identically zero, i.e., $\mathbf{U}^{\infty} \equiv 0$ and $\mathbf{E}^{\infty} \equiv 0$, and assigning a gravitational force for all N particles, $\mathbf{F}^{P} = \mathbf{F}_{g}$. The evolution equation (2.9) becomes:

$$\Delta \mathbf{x} = (\mathbf{R}_{FU}^{-1} \cdot \mathbf{F}_{g})\, \Delta t + \frac{1}{Pe} (\nabla \cdot \mathbf{R}_{FU}^{-1}\, \Delta t + \mathbf{X}(\Delta t)) \ . \tag{10.1}$$

Here, the new Péclet number, $Pe \equiv |\mathbf{F}_y|a/kT = 4\pi a^4 \Delta\rho g/kT$, measures the relative importance of the gravitational and Brownian forces. In (10.1), a is the characteristic particle size, $\Delta\rho equiv\rho_s$-ρ_f is the density difference between the solid particle and the suspending fluid, g is the gravitational constant, k is the Boltzmann's constant, and T is the absolute temperature. The evolution equation (10.1) is applicable for $Pe > 1$ which is the regime for this study. For $Pe < 1$, we scale the time with the diffusive time a^2/D_o and the equivalent form of (10.1) in the limit of Brownian domination is:

$$\Delta\mathbf{x} = Pe\,(\mathbf{R}_{FU}^{-1} \cdot \mathbf{F}_y)\,\Delta t + (\nabla \cdot \mathbf{R}_{FU}^{-1}\,\Delta t + \mathbf{X}(\Delta t)) \ . \qquad (10.2)$$

As seen in (10.1) or (10.2), there are two main contributions to the particle displacements: a deterministic contribution from the gravtitational force $\mathbf{F}_y$: $[\mathbf{R}_{FU}^{-1} \cdot \mathbf{F}_y]\ \Delta t$ and the two familiar contributions from the Brownian forces: the deterministic displacement from the configurational-space divergence of the N-particle diffusivity $\nabla \cdot \mathbf{R}_{FU}^{-1}\ \Delta t$, and the random step $\mathbf{X}(\Delta t)$ whose properties are such that the fluctuation-dissipation theorem is satisfied and given by (2.8.a) and (2.8.b). Note that the Péclet number scales with a^4 compared to a^3 for sheared suspensions.

The dynamic simulations are carried out with three different Péclet numbers: 10, 10^3 and ∞. Particle volume fractions vary from 0.27 to 0.49. The number of particles in all runs is N=27 and the run times range from 200 to 400 dimensionless time units with a time step Δt from 10^{-3} to 10^{-2}. The sedimentation velocity is plotted with time to verify that the equilibration has been reached before we compute its time-averaged mean. Periodic boundary conditions are applied to model unbounded suspensions. The

y-axis is the direction of gravity. The Reynolds number which is scaled with the mean sedimentation velocity $|\mathbf{U}|$ is assumed to be small, i.e., $Re = \rho|\mathbf{U}|a/\eta \ll 1$, so that Stokes' flow is applicable.

X.2 Simulation Results

Figures 10.1.a and 10.1.b are the plots of the sedimentation velocity, $\langle \mathbf{U}_y \rangle$, and the angularly averaged pair-distribution function evaluated at particle center-center-spacing r=2, $g(2)$, with different particle volume fractions, respectively. The symbol $\langle\rangle$ implies that the sedimentation velocity is first averaged for all N particles and then averaged for over the last 150 time units. The symbols for three Péclet numbers are: $Pe = (\bullet)$ 10, $(\triangle)$ 10^3 and $(\circ)$ ∞. Figure 10.1.a shows a large decrease in the sedimentation velocity with increasing volume fraction for all three Péclet numbers. At the same volume fraction, $\langle \mathbf{U}_y \rangle$ increases with increasing Péclet number. At high ϕ value, ϕ=0.49, the differences in $\langle \mathbf{U}_y \rangle$ are small for three Péclet numbers as the curves for $\langle \mathbf{U}_y \rangle$ converge to the same value of ≈ 0.04. In the limit of $Pe \rightarrow \infty$, simulation results $(\circ)$ compare well with the empirical scaling $\langle \mathbf{U}_y \rangle = (1 - \phi)^{4.6}$ (dotted curve) for $\phi \geq 0.3$ from Mirza and Richardson (1979). For ϕ in the range of 0.4 to 0.419, the two curves are indistinguishable. A comparison of our results $(\circ)$ with simulation results of Ladd (1990) $(\square)$ (reported in column (3) of Table IV for the sedimentation velocities adjusted for the limit of $N \rightarrow \infty$) displays noticeable difference, especially in the region of low ϕ values. This is expected since Ladd's results were computed from the isotropic dispersions of hard spheres (no dynamics were performed) compared to ours which have no restrictions on the microstructure. The figure shows a resemblance of our Pe=10^3 curve and Ladd's results for $Pe \rightarrow \infty$.

To explain the small values of $\langle U_y \rangle$ for $Pe = 10$, we can refer to the sediment microstructure. Figure 10.1.b shows a plot of the angularly averaged pair-distribution function $g(2)$ for the same three Péclet numbers above with different volume fractions. $g(2)$ for $Pe = 10$ (●) is identically zero for this range of volume fraction, a clear indication of well separated settling particles compared to a large mean value of 50 for $g(2)$ at $Pe \rightarrow \infty$ (○). The results of our study for sheared suspensions have shown that the instantaneous mobility of particles measured by the short-time self-diffusivity is large if the particles do not touch. This is exactly what we see from the plot of the short-time translational and rotational self-diffusion coefficient D_o^s and D_r^s in Figures 10.2.a and 10.2.b, respectively. D_o^s and D_r^s for Pe=10 (●) are large compared to that of Pe=10^3 (△) and ∞ (○). The extrapolation to the limit of zero self-diffusivities for Pe=10 (dotted lines) show the maximum packing $\phi^{max} \approx 0.7$ where D_o^s=D_r^s=0. In the next section, we present the sediment microstructure in the form of the probability density.

X.3 The Sediment Microstructure

The probability density $g(x, z)$ is plotted for $Pe = 10$ with different volume fractions ranging from 0.27 (upper left) to 0.49 (bottom right). There are 27 particles in the unit cell. Region of light color represent high and regions of dark color represent low probability. The direction of sedimentation is the y-axis normal to the x−z plane. $g(x, z)$ shows a hexagonal packing of strings of settling particles only for ϕ=0.419. This is different than the sheared suspensions which show strongly ordered structure for a much wider range of ϕ from 0.419 to as high as 0.6. It is *important* to note that even though we do not find ordered sediment structures at $Pe = 10$ for different volume fractions

than 0.419, the sedimentation velocities are consistently small as shown in Fig.10.a. As long as the settling particles are well separated from each other, the reduction in the sedimentation velocity is obtained irrespective of the hexagonal formation. The hexagonal packing is destroyed as Pe increases from 10 to 10^3 as shown in Fig.10.4.

We also study the suspension of bi-dense settling colloidal particles by randomly assigning 13 out of 27 particles a gravitational force $\mathbf{F}_{2_y}$ slightly larger than $\mathbf{F}_{1_y} \equiv$ -1 of the other 14 particles. The Péclet number is scaled with the smaller $\mathbf{F}_{1_y}$. Figure 10.5 displays the plot of $g(x, z)$ for ϕ=0.419 at Pe=10 with $\mathbf{F}_{2_y}$=-1 (left) (the uniformly dense suspension from Fig.10.3), $\mathbf{F}_{2_y}$=-1.25 (central) and $\mathbf{F}_{2_y}$=-2 (right). The figure clearly shows that as $\mathbf{F}_{2_y}$ increases in magnitude, the ordered formation with hexagonal packing is weakened (central) and destroyed (right).

X.4 Conclusions

In this work, we examined the dynamical process of sedimentation of Brownian particles and demonstrated the versatility of the Stokesian dynamics simulation which can be employed to model a variety of different physical problems. Our results indicate an important relation of the sedimentation velocity and the microstructure. A large reduction in the sedimentation velocity at $Pe = 10$ relates to the sediment microstructure in which the settling particles are well separated from each other and do not form large aggregates or clusters. For ϕ=0.419, the microstructure forms an hexagonal packing of strings of settling particles along the direction of the gravity. Correspondingly for closely spaced particles, the sedimentation velocity increases. We identified and provided some explanations for the mechanisms which cause the change in the macroscopic properties

of settling Brownian particles. It is suggested that this investigation should be continued since there are interesting questions that need to be answered. The occurrence of strongly ordered sediment structure only for Pe=10 and ϕ=0.419 and the large reduction in sedimentation velocities need to be investigated in detail.

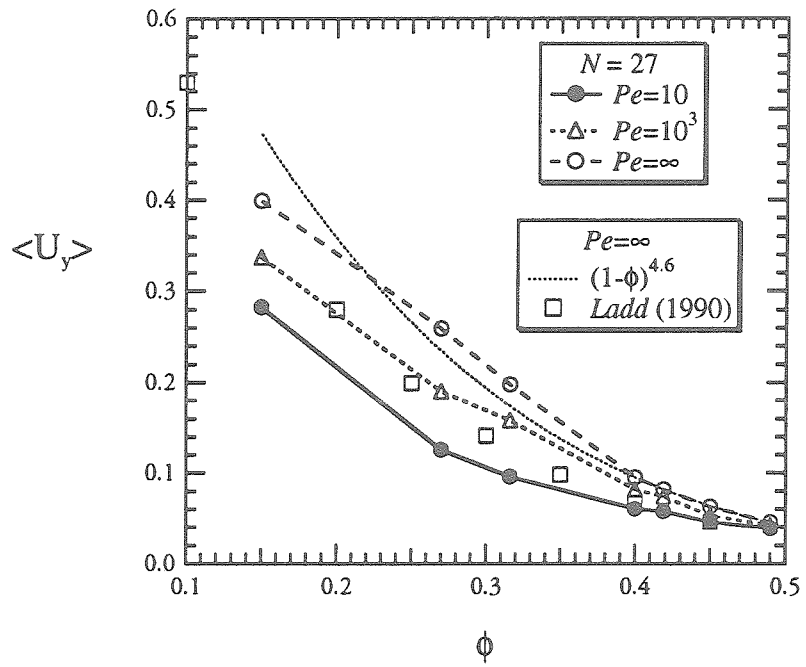

Figure 10.1.a

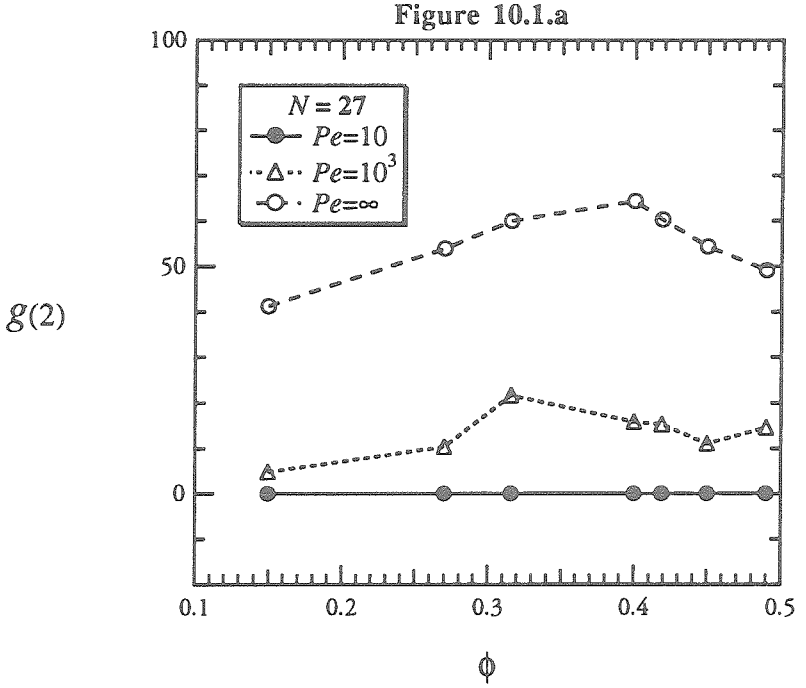

Figure 10.1.b

Figure 10.1.a-b: The sedimentation velocity (Fig.10.1.a) and the angularly averaged pair-distribution function (Fig.10.1.b) evaluated at particle center-center spacing r=2, $g(2)$, obtained by Stokesian dynamics as a function of volume fraction for three different Péclet numbers: Pe = (●) 10, (Δ) 1000 and (○) ∞. The Péclet number is defined as the ratio of the gravitational and Brownian forces. In Fig.10.1.a, the dotted curve is according to the scaling $(1-\phi)^{4.6}$ of *Richardson* (1979) and (□) symbols are simulation results taken from Table IV of *Ladd* (1990); both results are applicable for the limit of $Pe \to \infty$.

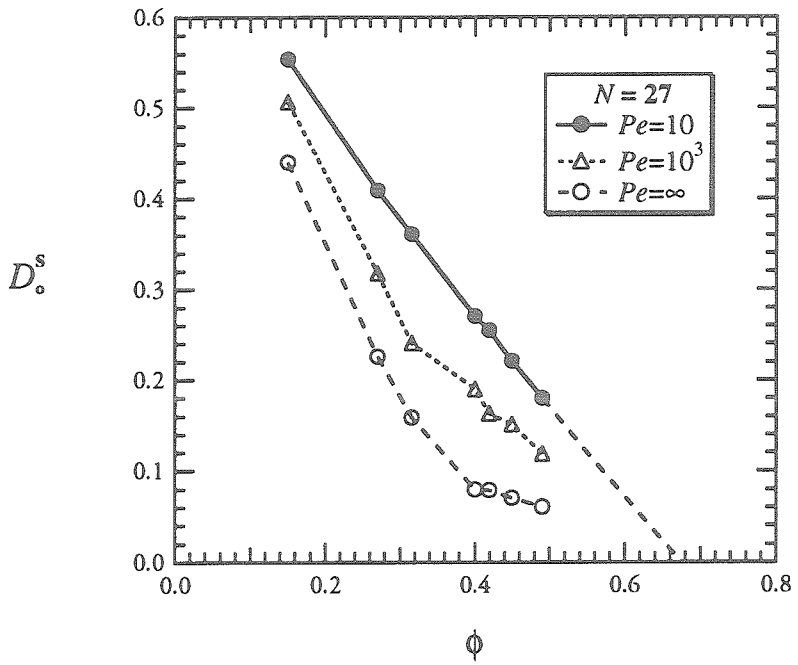

Figure 10.2.a

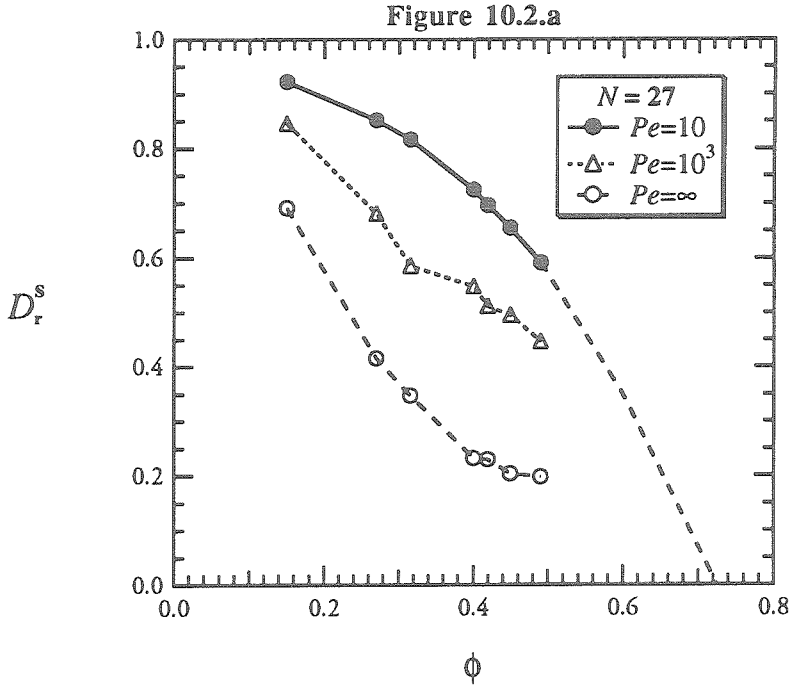

Figure 10.2.b

Figure 10.2.a-b: The translational (Fig.10.2.a) and rotational (Fig.10.2.b) short-time self-diffusion coefficients obtained by Stokesian dynamics as a function of volume fraction for suspensions of settling colloidal particles with Pe = (●) 10, (Δ) 1000 and (□) ∞. There are 27 particles in the unit cell. Both the diffusion coefficients are normalized by the diffusion coefficient at infinite dilution. The Péclet number is defined as the ratio of the gravitational and Brownian forces. Dotted lines are extrapolated to the limit of zero self-diffusivities for Pe=10.

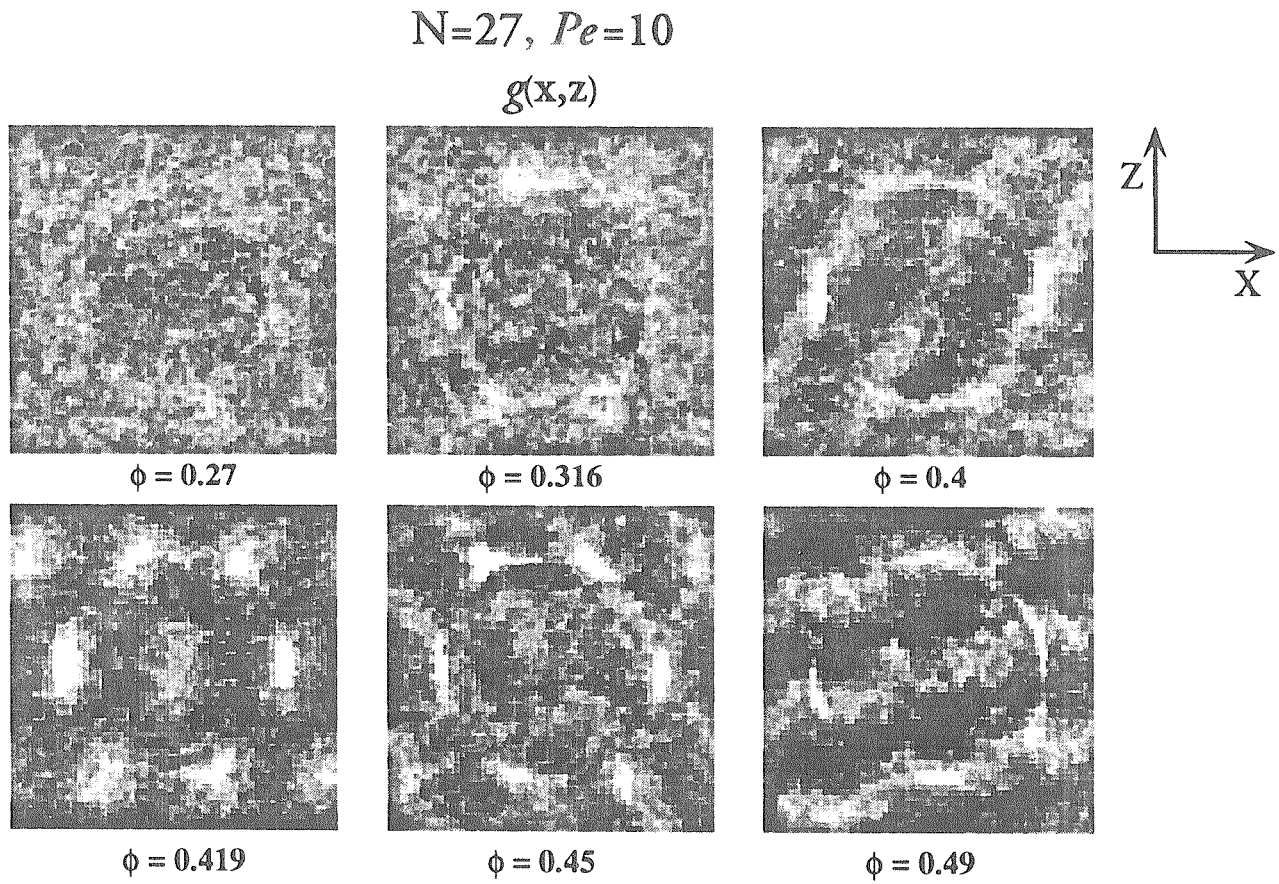

Figure 10.3: The probability density $g(x,z)$ obtained by Stokesian dynamics for suspensions of settling colloidal particles at Pe =10 and different volume fractions: from left to right, ϕ=0.27, 0.316, 0.4 (top row) and 0.419, 0.45 and 0.49 (bottom row). There are 27 particles in the unit cell. Regions of light color represent high probability and region of dark color represent low probability. The Péclet number is defined as the ratio of the gravitational and Brownian forces. $g(x,z)$ shows hexagonally packed strings of settling particles in the direction of gravity, the y-axis, normal to the x-z plane for ϕ=0.419 (bottom left most figure).

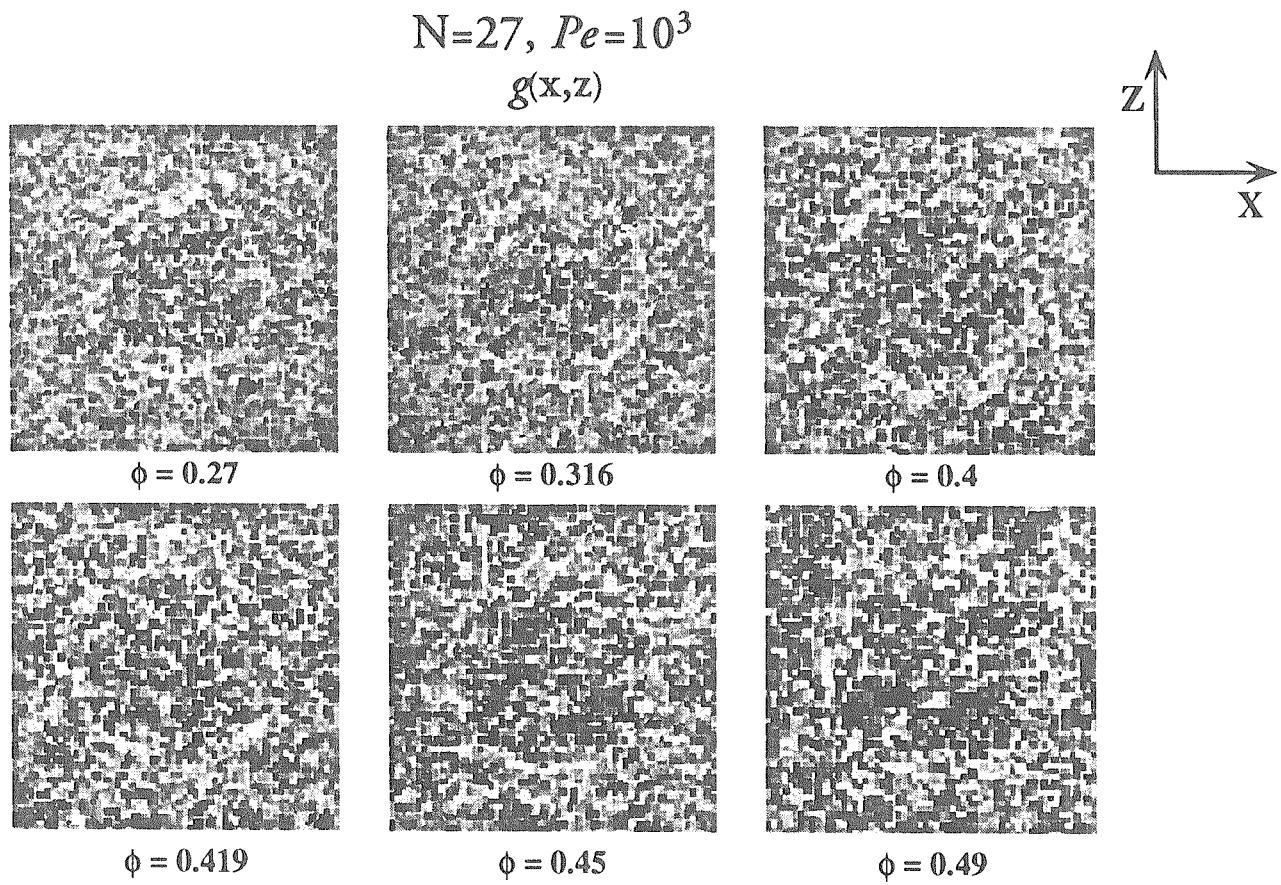

Figure 10.4: The probability density $g(x,z)$ obtained by Stokesian dynamics for suspensions of settling colloidal particles at Pe=1000 and different volume fractions: from left to right, ϕ=0.27, 0.316, 0.4 (top row) and 0.419, 0.45 and 0.49 (bottom row). There are 27 particles in the unit cell. Regions of light color represent high probability and regions of dark color represent low probability. The Péclet number is defined as the ratio of the gravitational and Brownian forces. The hexagonally packed strings of settling particles which are seen for ϕ=0.419 and Pe=10 (cf. Fig.10.3) is destroyed by Pe=1000.

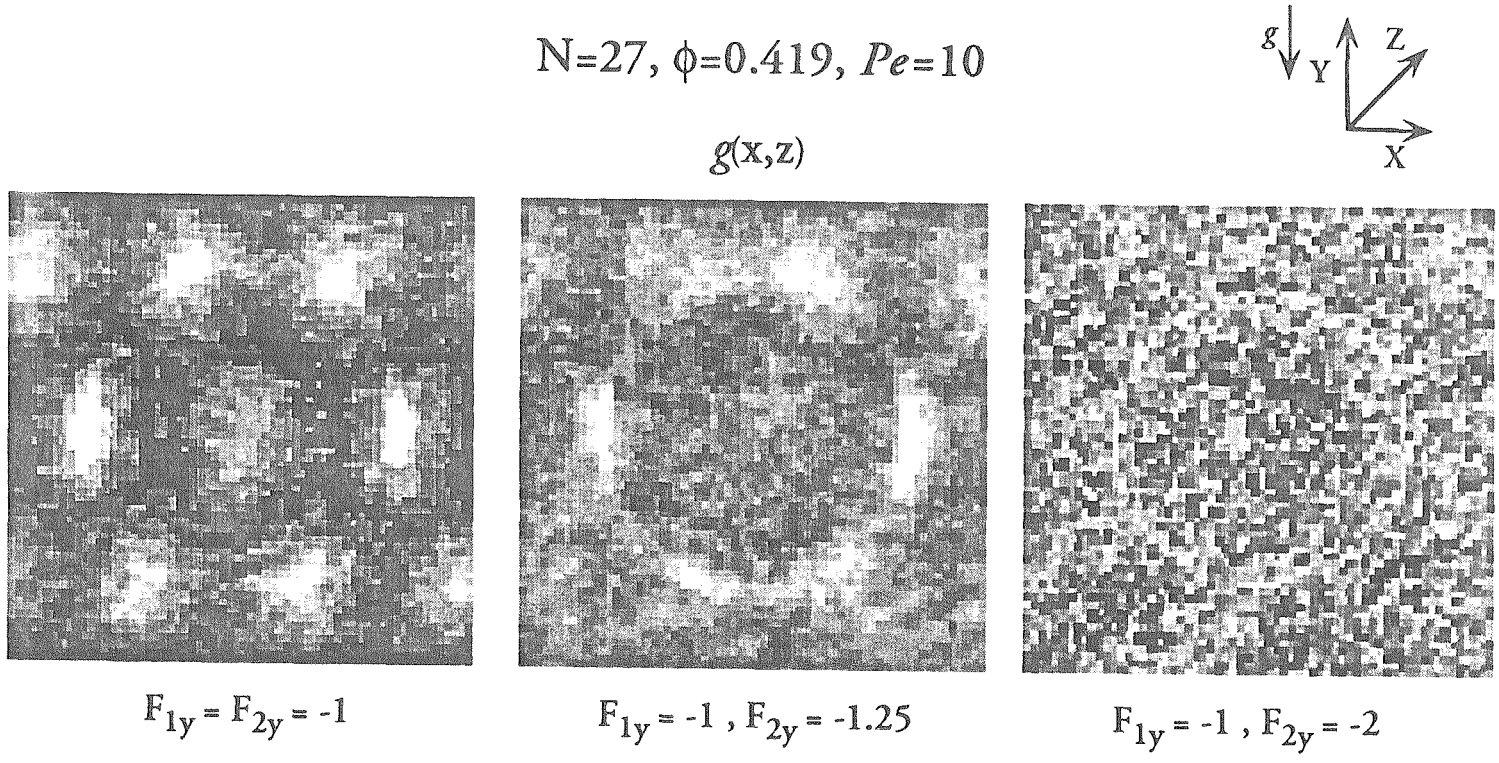

Figure 10.5: The probability density $g(x,z)$ for obtained by Stokesian dynamics for suspensions of settling colloidal particles at a volume fraction ϕ=0.419 and *Pe*=10. There are 27 particles in the unit cell with 14 particles of force F_{1y} and 13 particles of force F_{2y}. Regions of light color represent high probability and regions of dark color represent low probability. The Péclet number is defined as the ratio of the gravitational and Brownian forces. The hexagonal packing of strings of particles settling along the direction of gravity, the y-axis, normal to the x-z plane can only be seen for suspensions of settling particles with uniform density (left most figure).

Chapter XI

CONCLUDING REMARKS

In this work, we have applied the Stokesian dynamics simulation method to study the behavior of concentrated colloidal suspensions in shear flow. The main objectives have been the prediction of suspension macroscopic properties and their relation to the microstructure. The simulation method gives an accurate treatment of many-body hydrodynamic interactions from which the Brownian forces are computed. Suspension macroscopic properties and the shear-induced microstructure were modeled as a function of the only two parameters: the volume fraction, ϕ, and the Péclet number, Pe. The volume fraction sets the relative separation between particles, thus it sets the strength of the hydrodynamic forces. The Péclet number, which measures the relative importance of the imposed shear and Brownian forces, specifies the degree of the shearing deformation of the suspension.

Simulation results for the shear viscosity and the self-diffusivity agreed very well with experimental results and revealed three "distinct" behaviors in the limits of low, intermediate and high Péclet numbers. For a slightly perturbed equilibrium structure in the limit of small Péclet numbers ($Pe < 1$), strong Brownian forces coupled with the relatively large diffusive time scale act to restore the perturbed structure to an equilibrium state. The decrease of Brownian contribution to the stress with increasing shear rates in the strong Brownian limit was the cause of shear thinning. Both the short- and long-time self-diffusivities are close to that of isotropic hard-sphere distribution. The microstructure was slightly deformed, but particles were still relatively well dispersed; no ordered structure was found in the shear thinning region.

Similar to the region of low Péclet numbers, the region of high Péclet numbers

($Pe > 10^3$) represents a perturbation to the pure hydrodynamic suspension by the presence of weak Brownian forces. In this region, particles were closely spaced and formed large, elongated clusters disrupting the shear flow. The large increase in hydrodynamic contribution to the stress accounts for the shear thickening. The reduction of the short-time self-diffusivity with increasing Pe indicated a significant decrease of the instantaneous mobility of suspended particles owing to the formation of particle clusters. The long-time self-diffusivity increased linearly with Pe in the limit of pure hydrodynamics ($Pe \to \infty$) and compared favorably with tracer diffusion experiments. Even though the direct contribution from Brownian forces has vanished, its presence was capable of disturbing and inducing an anisotropic structure in the region of large Péclet number.

In the special plateau region with $Pe \approx 10$, a proper balance of hydrodynamic and Brownian forces induced a strongly ordered microstructure. The flowing suspension no longer shear thinned and the shear viscosity was a minimum. Our results show a most revealing microstructure with hexagonally packed particles flowing as strings with the shear flow. In the hexagonal packing, the particles were not only relatively well separated but also evenly spaced. The hexagonal packing has a perfect six-fold symmetry, allowing the particles to flow with ease relative to one another following the imposed shear flow. The orientation of the hexagon was found to depend on the number of particles in the simulation. While the short-time self-diffusivity is maximum due to enhanced local mobility of suspended particles, the long-time self-diffusivity was minimum as a result of the string formation from which the particles could not escape. The most important finding was that the shear thinning, which has essentially terminated in the

plateau region, *does not* directly relate to the shear-induced ordered microstructure in the minimum viscosity region. The string formation of hexagonally packed particles was determined by the Brownian forces which act as short-ranged spring-like repulsive forces to counter the shearing deformation and prevent particles from touching each other.

Our simulation results provide complete detail of suspension macroscopic properties and, for the first time, the dynamics of shearing deformation of the suspension microstructure. The flow of particles in a suspension has been probed and this information helps our understanding of sheared suspensions. We have also provided a complete process characterization by mapping the relation of the steady shear viscosity to the volume fraction and the Péclet number (cf. Fig.9.23) for dense hard sphere suspensions. Such information is valuable to the processing industries where an optimum operating condition suitable to a particular process can now be selected. By controlling the Péclet number and volume fraction, colloidal suspensions can be processed to homogeneous order and this provides an opportunity for fine material processing.

Stokesian dynamics has been brought to an efficient and fast computing level allowing the completion of this study. A run with 27 particles and 50,000 time steps in three dimensions with Brownian motion, which represents one (ϕ, Pe) point in the simulation results discussed in this thesis, requires 5.5 hours on an IBM RiSC/6000 model 530. The time requirement increases by a factor of 10 for N=64 and by 80 for N=123 (slightly less than the N^3 scaling). A similar 50,000 time-step simulation but without Brownian motion ($Pe \rightarrow \infty$) requires only 1.5 hours for N=27, a nearly four-fold reduction. With the present power of workstations, simulations in three dimensions with less than 100

particles can be routinely performed, making the method accessible. Thus, the range of problems of both a fundamental and practical nature that can be addressed through Stokesian dynamics is quite extensive.

Appendix A

PROGRAMMING AND OPTIMIZING BROWNIAN MOTION AND BROWNIAN STRESS

In this section, we present the optimization for the mathematical operations for Brownian motion, $\nabla \cdot \mathbf{R}_{FU}^{-1}$, and Brownian stress, $\nabla \cdot (\mathbf{R}_{SU} \cdot \mathbf{R}_{FU}^{-1})$. $\nabla \cdot \mathbf{R}_{FU}^{-1}$ is the deterministic contribution of Brownian forces to particle displacements shown in the evolution equation (2.5), and $\nabla \cdot (\mathbf{R}_{SU} \cdot \mathbf{R}_{FU}^{-1})$ is the direct contribution of Brownian forces to the bulk stress $\langle \sum \rangle$ shown in equation (2.20.c). These two terms, as written, are computationally intensive and not yet in a form suitable for dynamic simulation. Efficient computer algorithms were developed and implemented to speed up these numerically intensive operations and to minimize CPU memory requirement.

A.1 Programming and Optimizing Brownian Motion

Introduce two column vectors A_i and B_i of dimensions $(6N)$, where N denotes the number of particles, as the following:

$$\nabla \cdot \mathbf{R}_{FU}^{-1} \equiv A_i + B_i \quad . \tag{A.1}$$

Using the following mathematical identity:

$$\nabla \cdot \mathbf{R}_{FU}^{-1} = - \mathbf{R}_{FU}^{-1} \cdot (\nabla \mathbf{R}_{FU}) : \mathbf{R}_{FU}^{-1} \quad , \tag{A.2}$$

and with the grand resistance tensor $\mathcal{R}$ constructed according to (2.13), (A.2) is identical to:

$$\nabla \cdot \mathbf{R}_{FU}^{-1} = - \mathbf{R}_{FU}^{-1} \cdot \nabla (\mathcal{M}^{*-1} + \mathbf{R}_{FU}^{lub}) : \mathbf{R}_{FU}^{-1} \quad , \tag{A.3}$$

where $\mathbf{R}_{FU}^{lub}$ is the near-field lubrication resistance tensor of dimension $(6N \times 6N)$ added

to the invert of grand mobility tensor, $\mathcal{M}^{*-1}$, to form the grand resistance tensor $\mathcal{R}$. Applying the mathematical identity in (A.2) for $\mathcal{M}^{*-1}$, (A.3) further reduces to:

$$\nabla\cdot\mathbf{R}_{FU}^{-1} = \mathbf{R}_{FU}^{-1}\cdot\left(\mathcal{M}^{*-1}\cdot\left[\nabla\mathcal{M}^{*}\right]:\mathcal{M}^{*-1} - \nabla\mathbf{R}_{FU}^{lub}\right):\mathbf{R}_{FU}^{-1} \quad . \tag{A.4}$$

Since the resistance tensor $\mathbf{R}_{FU}^{lub}$ is constructed pairwise, $\nabla\mathbf{R}_{FU}^{lub} \equiv \partial\mathbf{R}_{FU_{jk}}^{lub}/\partial x_l$ can be analytically computed in a similar pairwise fashion. Each spherical particle has three translational partial derivatives $\partial/\partial x_l$, where l = 1,2,3. The three rotational partial derivatives $\partial/\partial\theta_l$ are identically zero for spheres. There are six degree of freedom (3 translational and 3 rotational) in $\mathbf{R}_{FU}$ and $\mathbf{R}_{FU}^{-1}$, so the dimensions of $\nabla\mathbf{R}_{FU}^{lub}$ for each pair of particles are (6×6×3).

For Brownian motion, the upper portion of the tensors $\mathcal{M}^{*}$ and $\mathcal{M}^{*-1}$ are used. They relate the translation/rotational velocity to the force/torque on the particles and their dimensions are $(6N\times 11N)$. Similar to the operation of $\nabla\mathbf{R}_{FU}^{lub}$, we can analytically compute $\nabla\mathcal{M}^{*}\equiv\partial\mathcal{M}_{mp}^{*}/\partial x_l$, where l = 1,2,3 and the sizes of $\nabla\mathcal{M}^{*}$ for each pair of particles are $(11N\times 11N\times 3)$. Define a matrix Q of dimension $(6N\times 11N)$ and two column vectors: $\hat{T}_m$ of size $(11N)$ and P_j of size $(6N)$, as follows:

$$Q_{lp} \equiv \mathbf{R}_{FU_{lj}}^{-1}\,\mathcal{M}_{jp}^{*-1} \quad , \tag{A.5}$$

$$\hat{T}_m \equiv \frac{\partial\mathcal{M}_{mp}^{*}}{\partial x_l}\,Q_{lp} \quad , \tag{A.6}$$

$$P_j \equiv \frac{\partial\mathbf{R}_{FU_{jk}}^{lub}}{\partial x_l}\,\mathbf{R}_{FU_{lk}}^{-1} \quad . \tag{A.7}$$

In (A.5), l,j = 1,6N and p = 1,11N. Equation (A.5) requires (6N×6N×11N) operations for the matrix-matrix multiplication. To save significant computer memory, we compute $\nabla\mathcal{M}^*$ in pairwise fashion and then multiply to matrix Q_{lp} to obtain the vector $\hat{T}_m$ as shown in (A.6) with m,p = 1,11N and l = 1,2,3 for each pair of particles. Equation (A.6) requires (11N×11N×3N) operations. Similarly, P_j defined in (A.7) requires (6N×6N×3N) operations with j,k = 1,6N and l = 1,2,3 for each pair of particles. Hence the dynamic simulation with Brownian motion problem demands $O(\mathcal{N}^3)$ computations with $\mathcal{N}$ ranging from 6N to 11N. Without this optimization technique, a direct calculation for (A.4) requires $O(\mathcal{N}^5)$ calculations which are prohibitively costly and possibly beyond the computing power of workstations. Also since both $\mathcal{M}^{*-1}$ and $\mathbf{R}_{FU}^{-1}$ are symmetric, the following identity holds:

$$Q \equiv \mathbf{R}_{FU}^{-1}\,\mathcal{M}^{*-1} = \mathcal{M}^{*-1}\mathbf{R}_{FU}^{-1} \quad . \tag{A.8}$$

(A.4) can be expressed as:

$$\nabla\cdot\mathbf{R}_{FU}^{-1} = (\mathbf{R}_{FU}^{-1}:\mathcal{M}^{*-1})\cdot(\nabla\mathcal{M}^*) : (\mathcal{M}^{*-1}:\mathbf{R}_{FU}^{-1}) - \mathbf{R}_{FU}^{-1}\cdot(\nabla\mathbf{R}_{FU}^{lub} : \mathbf{R}_{FU}^{-1}) \quad , \tag{A.9}$$

and with the introduction of matrix Q and two column vectors $\hat{T}_m$ and P_j, (A.9) simplifies to:

$$\nabla\cdot\mathbf{R}_{FU}^{-1} \equiv A_i + B_i = Q_{im}\cdot\hat{T}_m - \mathbf{R}_{FU_{ij}}^{-1}\cdot P_j \quad . \tag{A.10}$$

The final results for A_i and B_i are:

$$A_i = Q_{im}\cdot\hat{T}_m \quad , \tag{A.11}$$

$$B_i = - \mathbf{R}^{-1}_{FU_{ij}} \cdot P_j \quad . \tag{A.12}$$

Both A_i and B_i require only $\mathbf{O}(\mathcal{N}^2)$ operations for matrix-vector multiplication in the final steps of Brownian motion. Some of these calculations are saved and used for the calculation of Brownian stress $\mathbf{S}^B$.

We need to add one more part, the random step $\mathbf{X}(\Delta t)$ defined in (2.8.a) and (2.8.b), to complete Brownian motion. Results for $\mathbf{X}(\Delta t)$ have been derived by Bossis and Brady (1987, 1989) and we shall use them for our simulations. Their results for the random step $\mathbf{X}$ are:

$$\mathbf{X} = \sqrt{\Delta t}\, \mathbf{A}^{-1} \cdot \mathbf{Y} \quad , \tag{A.13}$$

where $\mathbf{A}^{-1}$ is given by the LU-decomposition of $\mathbf{R}_{FU}$, i.e.,

$$\mathbf{R}^{-1}_{FU} = \mathbf{A}^{-1} \cdot (\mathbf{A}^{-1})^{\dagger} \tag{A.14}$$

The symbol † indicates a transpose operation and $\mathbf{A}^{-1}$ is the lower inverse of $\mathbf{R}_{FU}$. $\mathbf{Y}$ is a random vector of dimensions $(6N)$ with a mean of zero and a corvariance $\langle \mathbf{YY} \rangle = 2\mathbf{I}$.

A.2 Programming and Optimizing Brownian Stress

For the Brownian contribution to particle stress, we have:

$$\nabla \cdot (\mathbf{R}_{SU} \cdot \mathbf{R}^{-1}_{FU}) = \nabla \mathbf{R}_{SU} : \mathbf{R}^{-1}_{FU} + \mathbf{R}_{SU} \cdot (\nabla \cdot \mathbf{R}^{-1}_{FU}) \quad . \tag{A.15}$$

Using A_i and B_i from (A.11) and (A.12), (A.15) can be expressed as:

$$\nabla\cdot(\mathbf{R}_{SU}\cdot\mathbf{R}_{FU}^{-1}) = \nabla\mathbf{R}_{SU}\colon \mathbf{R}_{FU}^{-1} + \mathbf{R}_{SU}\cdot (A_i + B_i) \quad . \tag{A.16}$$

Following the same derivation for the operation of $\nabla\mathbf{R}_{FU}$, $\nabla\mathbf{R}_{SU}$ can be written as:

$$\nabla\mathbf{R}_{SU} = \nabla\mathcal{R} = \nabla\mathcal{M}^{*-1} + \nabla\mathbf{R}_{SU}^{lub} \quad , \tag{A.18}$$

and applying (A.2) for $\mathcal{M}^*$, (A.17) simplifies to:

$$\nabla\mathbf{R}_{SU} = -\,\mathcal{M}^{*-1}\cdot(\nabla\mathcal{M}^*) : \mathcal{M}^{*-1} + \nabla\mathbf{R}_{SU}^{lub} \quad . \tag{A.18}$$

For the Brownian stress we use the lower portion of $\mathcal{M}^*$ and $\mathcal{M}^{*-1}$ of dimensions $(5N\times 11N)$. They are the couplings of the rate of strain $\mathbf{E}^{\infty}$ and the particle stress S. $\nabla\cdot(\mathbf{R}_{SU}\cdot\mathbf{R}_{FU}^{-1})$ is equal to:

$$\nabla\cdot(\mathbf{R}_{SU}\cdot\mathbf{R}_{FU}^{-1}) = -\,\mathcal{M}^{*-1}\cdot(\nabla\mathcal{M}^*):\mathcal{M}^{*-1}\colon \mathbf{R}_{FU}^{-1} + \nabla\mathbf{R}_{SU}^{lub}\colon \mathbf{R}_{FU}^{-1} + \mathbf{R}_{SU}\cdot(A_i+B_i), \tag{A.19}$$

$$\nabla\cdot(\mathbf{R}_{SU}\cdot\mathbf{R}_{FU}^{-1}) = -\,\mathcal{M}^{*-1}\cdot\hat{T}_m + \nabla\mathbf{R}_{SU}^{lub} : \mathbf{R}_{FU}^{-1} + \mathbf{R}_{SU}\cdot(A_i+B_i), \tag{A.20}$$

with $\hat{T}_m$ defined in (A.6). Introduce the column vectors $\hat{A}_j$, $\hat{B}_j$, $\hat{C}_j$, and $\hat{D}_j$ of dimensions $(5N)$ as follows:

$$\hat{A}_j \equiv -\,\mathcal{M}_{jm}^{*-1}\colon \hat{T}_m \quad , \tag{A.21}$$

$$\hat{B}_j \equiv \frac{\partial \mathbf{R}_{SU_{jk}}^{lub}}{\partial x_l}\ \mathbf{R}_{FU_{kl}}^{-1} \quad , \tag{A.22}$$

$$\hat{C}_j \equiv \mathbf{R}_{SU_{ji}}\cdot A_i \quad , \tag{A.23}$$

$$\hat{D}_j \equiv \mathbf{R}_{SU_{ji}} \cdot B_i \quad . \tag{A.24}$$

Hence, the final form of the Brownian stress $\nabla\cdot(\mathbf{R}_{SU}\cdot\mathbf{R}_{FU}^{-1})$ is:

$$\nabla\cdot(\mathbf{R}_{SU}\cdot\mathbf{R}_{FU}^{-1}) = \hat{A}_j + \hat{B}_j + \hat{C}_j + \hat{D}_j \quad . \tag{A.25}$$

In (A.21) $m = 1{,}11N$, in (A.22) $k = 1{,}6N$ and $l = 1{,}2{,}3$ for each pair of particles; in (A.23) and (A.24) $i = 1{,}6N$ and $j = 1{,}5N$ for all. The calculation of $\hat{B}_j$ in (A.22) is similar to that of the column vector P_j in (A.7). $\hat{B}_j$ requires $(5N\times6N\times3N)$ multiplications. $\hat{A}_j$, $\hat{C}_j$ and $\hat{D}_j$ are a matrix-vector multiplication and is $\mathbf{O}(\mathcal{N}^2)$ computations.

Particle translational/rotational velocities $\mathbf{U}$ are computed at each time step by solving:

$$\mathbf{R}_{FU}\ (\mathbf{U} - \mathbf{U}^{\infty}) = [\mathbf{R}_{FE}\colon \mathbf{E}^{\infty} + \mathbf{F}^{P}] \quad . \tag{A.26}$$

We can solve for $\mathbf{U}$ by either using a direct solve method by inverting $\mathbf{R}_{FU}$ or by an indirect solve method operating on both $\mathbf{R}_{FU}$ and the right-hand side of (A.26). It is $\mathbf{O}(\mathbf{C}\mathcal{N}^3)$ operations with $\mathcal{N}=6N$ and the coefficient $\mathbf{C} = \frac{1}{2}$ or $\frac{4}{3}$ depending on the method employed. Iterative methods can be used with significant time saving but the solution is approximated within some predetermined tolerances and more importantly, $\mathbf{R}_{FU}^{-1}$ cannot be obtained as part of the solution. By inverting $\mathbf{R}_{FU}$, the full Brownian contribution can be computed and it is of our interest to include Brownian motion in the Stokesian dynamics simulation method to improve the computer model for colloidal dispersions.

Appendix B

THE SIMULATION PROCESS OF STOKESIAN DYNAMICS METHOD

Figure 3.1 illustrates a flowchart of the Stokesian dynamics simulation method and in chapter III, we presented the general process of a dynamic simulation. In this section, we emphasize on the execution of a Stokesian dynamic computer program and explain step-by-step the procedure to run an efficient dynamic simulation, especially when the Brownian motion and Brownian stress are of importance ($Pe \neq 0$). Referring to the flowchart of Stokesian dynamics, the following section will guide the users from the start to the completion of a simulation:

Step 1: An initial sample of N particles is selected. It can be from a random selection using the Monte-Carlo method, or a periodic lattice or any particular configuration obtained, for example, from another simulation for the purpose of testing the influence of initial particle configurations on suspension macroscopic properties. Stokesian dynamics simulation method is capable of simulating a specific or any particle configuration, static or dynamic.

Step 2: The grand mobility tensor $\mathcal{M}^*$ is computed. The Ewald summation with periodic boundary condition is used to form $\mathcal{M}^*$ for an unbounded suspension. $\mathcal{M}^*$ is then inverted using the Cholesky inversion method for a symmetric and positive definite matrix. It is important to note here that to save the computing time we do not need to form and invert $\mathcal{M}^*$ at every time step since the change of $\mathcal{M}^*$ is small provided that particles do not move a length comparable to their characteristic size a. In the simulation, we form and invert $\mathcal{M}^*$ once every dimensionless time of $t \approx 0.1$ and during this time particles in a simple shear flow move a distance less than its own size. Comparisons for simulations with $\mathcal{M}^*$ and $\mathcal{M}^{-1}$ computed at every time step and with $\mathcal{M}^*$

and $\mathcal{M}^{-1}$ formed once every $t \approx 0.1$ show very small and negligible differences in macroscopic properties of relatively dense suspensions. The near-field lubrication is computed at every time step and then added to $\mathcal{M}^{-1}$ to form the grand resistance tensor $\mathcal{R}$.

Step 3: From the partition of $\mathcal{R}$, $\mathbf{R}_{FU}$ is obtained and inverted using the same Cholesky method. During the inversion of $\mathbf{R}_{FU}$, we save $\mathbf{A}^{-1} = \sqrt{\mathbf{R}_{FU}^{-1}}$ for the random step $\mathbf{X}(\Delta t)$.

Step 4: Using $\mathbf{R}_{FU}^{-1}$, particle velocities $\mathbf{U}$ are computed according (A.26). If there is the interparticle/external force $\mathbf{F}^{P}$ then it is straightforward to compute it from the specified input form.

Step 5: The Brownian motion $\nabla \cdot \mathbf{R}_{FU}^{-1}$ defined in (2.9) is computed. In appendix A, we explained and optimized $\nabla \cdot \mathbf{R}_{FU}^{-1}$ in section A.1. We need to compute the matrix Q defined in (A.5), $\hat{T}_m$ in (A.6) and P_j in (A.7) to complete A_i and B_i according to (A.11) and (A.12), respectively. While Q, P_j and B_i are computed at every time step, $\hat{T}_m$ and A_i are computed and renewed at the same frequency of $\mathcal{M}^*$ for the reason that the changes of $\mathcal{M}^*$ are small for $t \approx 0.1$; therefore, the change of $\nabla \mathcal{M}^*$ is also small.

Step 6: New particle trajectories are computed from particle velocities $\mathbf{U}$ and from Brownian motion. The 4^{th} order Adam-Bashforth integrating scheme is employed to update new particle positions from the deterministic contribution $\mathbf{U}$ of step 4. To complete particle displacements, the two contributions from Brownian motion: $\nabla \cdot \mathbf{R}_{FU}^{-1}\ \Delta t$ from step 5 and $\mathbf{X}(\Delta t)$ from step 3 are added to particle placements. $\mathbf{A}^{-1}$ is saved from step 3 and now used with the random vector $\mathbf{Y}$ according to (A.13). We generate 12 random numbers from 0.0 to 1.0 for each of the $6N$ entries of $\mathbf{Y}$ to improve the sampling statistics

at each time step. $\mathbf{Y}$ is chosen to satisfy $\langle \mathbf{Y} \rangle = 0$ and $\langle \mathbf{YY} \rangle = 2\mathbf{I}$. The 1^{st} order Euler integration scheme is used for both Brownian motion terms.

Step 7: $\mathbf{S}^H$ and $\mathbf{S}^P$ are computed according to equation (2.20.a) and (2.20.b), respectively. $\mathbf{S}^H$ is the hydrodynamic contribution to particle stress and $\mathbf{S}^P$ is the added stress resulting from the interparticle/external force acting on the particle.

Step 8: Brownian stress $\mathbf{S}^B$ defined in (2.20.c) is computed using (A.25). We need to compute $\hat{A}_j$, $\hat{B}_j$, $\hat{C}_j$ and $\hat{D}_j$ which are defined in (A.21), (A.22), (A.23), and (A.24), respectively. Similar to the procedure to obtain A_i from step 5, $\hat{A}_j$ and $\hat{C}_j$ are computed at the same frequency of $\mathcal{M}^*$, while $\hat{B}_j$ and $\hat{D}_j$ are computed at every time step. Together with the computing for $\mathbf{S}^H$ and $\mathbf{S}^P$ in step 7, we have the complete set of bulk stress $\langle \Sigma \rangle$ to determine the suspension rheology.

Step 9: The final step of the simulation process is designated for computing the number-averaged mean and statistics of suspension bulk properties: shear viscosity from $\langle \Sigma \rangle$, short-time self-diffusion coefficients defined in (2.25) with $\mathbf{R}_{FU}^{-1}$ is saved from step 3. Output results for final analysis are saved at the desired frequency.

The dynamic simulation returns to step 2 until the final time t_{final} is reached and the execution is terminated. As we present here, Stokesian dynamics requires $\mathbf{O}(\mathcal{N}^3)$ operations mainly from the inversion of $\mathcal{M}^*$ and $\mathbf{R}_{FU}$. We do not invert $\mathcal{M}^*$ of dimensions $(11N \times 11N)$ at every time step, so it is a tremendous saving in computer time. $\mathbf{R}_{FU}$ with smaller dimension $(6N \times 6N)$ needs to be inverted at every time step. Once $\mathbf{R}_{FU}^{-1}$ is obtained, we have the full benefit of determining Brownian contribution to particle motion

and to particle stress in addition to just solving for $\mathbf{U}$ from (A.26). It is important to note that there is no need to assemble the operation $\nabla \mathbf{R}_{FU}^{lub}$, $\nabla \mathcal{M}$, and $\nabla \mathbf{R}_{SU}^{lub}$ into matrices. These operations are analytically computed in pairwise fashion, multiplied to the proper right-hand side matrix and then summed for all pairs of particles. This technique saves significant amount of computer memory and enables simulations to be run on workstations. Had we formed all of these matrices, then their sizes would be $(11N \times 11N \times 3)$ for $\nabla \mathcal{M}$, $(6N \times 6N \times 3)$ for $\nabla \mathbf{R}_{FU}^{lub}$ and $(5N \times 6N \times 3)$ for $\nabla \mathbf{R}_{SU}^{lub}$. For simulations with 123 particles, the matrix with sizes $(11N \times 11N \times 3)$ will require $\approx$ 20 Megabytes to store in double precisions and is a big block of CPU memory for a workstation.

Appendix C

OPTIMIZATION AND TIMING

FOR

STOKESIAN DYNAMICS SIMULATION

In this appendix section, we present the optimizing techniques which speed up Stokesian dynamics simulation and report the timing for specific computational tasks as well as the overall stokesian dynamics program. Details of mathematical operations for Brownian motion and Brownian stress and the simulation process are given in appendices A and B, respectively. Our important goal is to develop and implement efficient and fast algorithms which allow computer simulations of O(100) particles in a workstation computer like the IBM RiSC/6000 computers which have a high speed but small size cache ranging from 64 to 128 KiloBytes.

The three major computational tasks of stokesian dynamics simulation are the formation of the grand mobility matrix $\mathcal{M}^*$ and its inverse $\mathcal{M}^{*-1}$, the computing of $\mathbf{R}_{FU}^{-1}$ which is required for the calculation of the particle velocities and Brownian motion, and the computing of Brownian motion $\nabla\cdot\mathbf{R}_{FU}^{-1}$ and Brownian stress $\nabla\cdot(\mathbf{R}_{SU}\cdot\mathbf{R}_{FU}^{-1})$. The first two tasks require explicit matrix inversions and the last one requires matrix-matrix and matrix-vector multiply. The number of numerical operations of these three tasks are of $\mathbf{O}((11N)^3)$ for $\mathcal{M}^{*-1}$ and $\mathbf{O}((6N)^3)$ for $\mathbf{R}_{FU}^{-1}$, $\nabla\cdot\mathbf{R}_{FU}^{-1}$ and $\nabla\cdot(\mathbf{R}_{SU}\cdot\mathbf{R}_{FU}^{-1})$. Here, N is the number of particles in the simulation.

The first optimizing technique is implemented to speed up the formation of the mobility inverse $\mathcal{M}^{*-1}$ which satisfies the following mathematical identity:

$$\mathcal{M}\ \mathcal{M}^{*-1} = \mathbf{I}\ . \tag{C.1}$$

I is the unit matrix with the same dimensions as $\mathcal{M}^*$ and $\mathcal{M}^{*-1}$ which are $(11N\times 11N)$. Since $\mathcal{M}^*$ is symmetric and positive definite, its inverse, $\mathcal{M}^{*-1}$, is also symmetric and

positive definite. Following the same decomposition of $\mathcal{M}^*$ as shown in (2.12), we write the mobility inverse $\mathcal{M}^{*-1}$ as:

$$\mathcal{M}^{*-1} = \begin{pmatrix} \mathbf{A} & \mathbf{B} \\ \mathbf{C} & \mathbf{D} \end{pmatrix} . \tag{C.2}$$

Equation (C.1) becomes:

$$\begin{pmatrix} \mathbf{M}_{UF} & \mathbf{M}_{US} \\ \mathbf{M}_{EF} & \mathbf{M}_{ES} \end{pmatrix} \begin{pmatrix} \mathbf{A} & \mathbf{B} \\ \mathbf{C} & \mathbf{D} \end{pmatrix} = \begin{pmatrix} \mathbf{I}_1 & 0 \\ 0 & \mathbf{I}_2 \end{pmatrix} . \tag{C.3}$$

In (C.3) $\mathbf{I}_1$ and $\mathbf{I}_2$ are square unit submatrices. $\mathbf{A}$ and $\mathbf{I}_1$ have the same dimensions ($6N \times 6N$) as $\mathbf{M}_{UF}$. $\mathbf{D}$ and $\mathbf{I}_2$ have the same dimensions ($5N \times 5N$) as $\mathbf{M}_{ES}$. Similarly, dimensions of $\mathbf{B}$ and $\mathbf{C}$ are the same as $\mathbf{M}_{US}$ and $\mathbf{M}_{EF}$ which are ($6N \times 5N$) and ($5N \times 6N$), respectively. The submatrix operations of (C.3) give:

$$\begin{cases} \mathbf{M}_{UF}\,\mathbf{A} + \mathbf{M}_{US}\,\mathbf{C} = \mathbf{I}_1 \\ \mathbf{M}_{UF}\,\mathbf{B} + \mathbf{M}_{US}\,\mathbf{D} = 0 \\ \mathbf{M}_{EF}\,\mathbf{A} + \mathbf{M}_{ES}\,\mathbf{C} = 0 \\ \mathbf{M}_{EF}\,\mathbf{B} + \mathbf{M}_{ES}\,\mathbf{D} = \mathbf{I}_2 \end{cases} \tag{C.4}$$

By solving the linear system of equations (C.4), we obtain the results of submatrices $\mathbf{A}$, $\mathbf{B}$, $\mathbf{C}$ and $\mathbf{D}$ as follows:

$$\begin{cases} \mathbf{A} = (\mathbf{M}_{UF} - \mathbf{M}_{US}\mathbf{M}_{ES}^{-1}\mathbf{M}_{EF})^{-1} \\ \mathbf{B} = -\mathbf{M}_{UF}^{-1}\mathbf{M}_{US}(\mathbf{M}_{ES} - \mathbf{M}_{EF}\mathbf{M}_{UF}^{-1}\mathbf{M}_{US})^{-1} \\ \mathbf{C} = -\mathbf{M}_{ES}^{-1}\mathbf{M}_{EF}(\mathbf{M}_{UF} - \mathbf{M}_{US}\mathbf{M}_{ES}^{-1}\mathbf{M}_{EF})^{-1} \\ \mathbf{D} = (\mathbf{M}_{ES} - \mathbf{M}_{EF}\mathbf{M}_{UF}^{-1}\mathbf{M}_{US})^{-1} \end{cases} \tag{C.5}$$

(C.5) requires two explicit matrix inversion operations to invert $\mathbf{M}_{UF}$ and to invert the matrix group ($\mathbf{M}_{ES}$- $\mathbf{M}_{EF}\mathbf{M}_{UF}^{-1}\mathbf{M}_{US}$) and seven matrix-matrix multiplies. Press *et al.* (1988) derives the eleven-step process for the inversion of a general matrix. This technique is similar to Strassen's method (1969) for accelerating matrix-matrix multiply and reducing the number of operations from $\mathbf{O}(N^3)$ to $\mathbf{O}(N^{2.8})$.

By using the symmetric condition of $\mathcal{M}^*$ and $\mathcal{M}^{*-1}$, we can further reduce the total of number of matrix-matrix operations from seven to four and the process of inverting $\mathcal{M}^*$ is given by the following six-step process:

Step 1: Compute $\mathbf{Z}_1 \equiv \mathbf{M}_{UF}^{-1}$;

Step 2: Compute $\mathbf{Z}_2 \equiv \mathbf{M}_{US}^T\mathbf{M}_{UF}^{-1} = \mathbf{M}_{US}^T\mathbf{Z}_1$;

Step 3: Compute $\mathbf{Z}_3 \equiv \mathbf{M}_{US}^T(\mathbf{M}_{US}^T\mathbf{M}_{UF}^{-1})^T = \mathbf{M}_{US}^T\mathbf{Z}_2^T$ (first $\mathbf{Z}_2$ is transposed and then multiplied);

Step 4: Compute $(\mathbf{M}_{ES}$ - $\mathbf{M}_{US}^T(\mathbf{M}_{US}^T\mathbf{M}_{UF}^{-1})^T)^{-1} = (\mathbf{M}_{ES}$ - $\mathbf{Z}_3)^{-1} \Longrightarrow \mathbf{D}$;

Step 5: Compute $(\mathbf{M}_{US}^T\mathbf{M}_{UF}^{-1})^T$ - $(\mathbf{M}_{ES}$-$\mathbf{M}_{US}^T(\mathbf{M}_{US}^T\mathbf{M}_{UF}^{-1})^T)^{-1} = \mathbf{Z}_2^T$- $\mathbf{D} \Longrightarrow \mathbf{C} = \mathbf{B}^T$;

Step 6: Compute $\mathbf{M}_{UF}^{-1}$- $(\mathbf{M}_{US}^T\mathbf{M}_{UF}^{-1})^T\mathbf{C} = \mathbf{M}_{UF}^{-1}$- $\mathbf{Z}_2^T\mathbf{C} \Longrightarrow \mathbf{A}$.

Note that there is no need to compute C and hence to invert (M_{UF}- $M_{US}M_{ES}^{-1}M_{EF}$) since C=B^T given by the symmetric condition of $\mathcal{M}^{*-1}$. In addition, M_{UF}, M_{ES}, their inverses M_{UF}^{-1} and M_{ES}^{-1}, A and D are all symmetric and positive definite.

As shown in Figure C.1, the two main computing kernels for the mobility inverse $\mathcal{M}^{*-1}$ are the Cholesky method of inverting a positive definite and symmetric matrix and BLAS3 (Basic Linear Algebra Subprograms) DGEMM for fast matrix-matrix multiply. It is the implementation of BLAS3 DGEMM kernel which we shall show to significantly speed up the numerically intensive task of inverting $\mathcal{M}^*$. The BLAS kernels exploit the technique of loop blocking and rolling to effectively fill the high speed cache with data. This technique optimizes the cycles which the computer replaces the unused with the new data from the memory for next computational tasks. It also allows more computational cycles per filled cache.

To illustrate this speed up, we plot the performance measured in MFLOPS (Millions of Floating Point Operations per Second) in double precision of the IBM RiSC/6000 model 560 computer with 128KBytes cache size as a function of the matrix size in Figure C.2 for the matrix-matrix multiplication. The solid curve is the rated 40 MFLOPS for this model. While the multiplication of the transpose of matrix AA with matrix BB gives a relatively good performance at 38 MFLOPS (■) which is very closed to the peak speed, a simply naive matrix AA and BB multiplying yields very poor and unacceptable performance at 2 MFLOPS as the matrix size increases to larger than 400 as shown by the (●) curve. This is a significant twenty-fold speed down due to poor system scalibility because of large missed cache per time cycle. With the optimizing technique of loop

blocking and rolling as coded in BLAS3, we eliminate the poor system scalibility and not only double the performance from the rated 40 MFLOPS to 80 MFLOPS, but more importantly the speed up is independent of matrix size as shown by two top curves ((○) and (□).) Note that for Stokesian dynamics simulation with 27 particles in three dimensions, the size of $\mathcal{M}^*$ and $\mathcal{M}^{*-1}$ is (297,297) and it is where the poor scalibility begins to show and the performance significantly decreases. For relatively less powerful computer and smaller cache size of 64 KBytes like the RiSC/6000 model 520 and 530, the degradation starts with smaller matrix dimensions of (100×100).

The second optimizing technique is to modify the Cholesky method to avoid the naive AA*BB operation by replacing it with AA^T* BB. The Cholesky method includes three computational phases: the $L(L)^T$ decomposition, the inversion of $(L)^T$ to obtain the square-root of full inverse and the multiplication of the square-root of the full inverse with its transpose to obtain the full inverse. In the last two phases, the main computing kernel is the matrix-matrix multiply of the upper half $(L)^T$ to the lower half L and our optimizing technique shows great improvement in speed up the matrix inversion process. Furthermore by decomposing the grand mobility matrix to submatrices, we need to invert only two smaller matrices shown in step 1 and step 4 and exploit the fast matrix-matrix multiply from the other four steps to speed up the inverting process. This technique proves to work well for all workstation computers like Sun, Stardent, IRIS and with the supercomputer Cray Y-MP as well, which for simulations with 123 particles, we obtained the average speed of near 210 MFLOPS per a single CPU. This is a near ten-fold speed up compared to earlier version of stokesian dynamics programs.

The fast matrix-matrix multiplication is also implemented in the computing of Brownian motion and Brownian stress. Figure C.3 shows the details of this task. The formation of the vector $\hat{T}_m$ in (A.6) requires the matrix Q_{lp} which is defined in (A.5) as:

$$Q_{lp} \equiv \mathbf{R}^{-1}_{FU_{lj}} \mathcal{M}^{*-1}_{jp} \quad , \tag{C.6}$$

for which the fast matrix-matrix multiply is applied to speed up the result.

The timing in seconds of these three computational tasks is reported in Table C.1 for the IBM RiSC/6000 model 560 computer. The simulation is with 126 particles and the time results are averaged for 100 sample runs. Column 1 shows the specific task and subtasks, columns 2 and 3 are the CPU and total time in seconds. With our six-step optimizing technique, the formation of the mobility inverse of dimensions (1386×1386) consumes 50 seconds and gives a performance speed of 71 MFLOPS (The Cholesky inversion of a symmetric matrix requires $\frac{4}{3}P^3$ number of operations where $P = 11{\times}N$ is the size of the matrix.) In forming Brownian motion and Brownian stress, the most time consuming task is to compute Q_{lp} shown in (C.6). The number of operations for this task is $2{\times}6N{\times}6N{\times}11N$ (one add and one multiply per cycle), and for N=126 it consumes 19 seconds and delivers a performance of 83 MFLOPS (labeled as the subroutine BIGSTEP in Table C.1). The last task is the inversion of $\mathbf{R}_{FU}$ of dimension $(6N{\times}6N)$. Because of the need of saving the square-root of $\mathbf{R}^{-1}_{FU}$ required for the computing of the random step for Brownian motion in (A.14), it is impossible to recursively decompose $\mathbf{R}_{FU}$ and we can only perform the Cholesky inversion which gives a performance of nearly 45 MFLOPS (computed from 13 seconds consumption to invert a matrix size of (756×756).)

Table C.2 gives the timing results in minutes of the overall stokesian dynamics simulation for three sample sizes with N=27, 81 and 126. The timing is for 1000 time steps for which we form $\mathcal{M}^*$, $\mathcal{M}^{*-1}$ and $\nabla\cdot\mathcal{M}^*$ one for every 100 time steps and is averaged for 100 sample runs. Column 1 gives the main specific tasks which are the computing and saving of the separation of each pair of particles (CALDIST), forming and inverting of mobility matrix (FORMOBI), adding the near-field lubrication resistance to form the grand resistance matrix (ADDLUB3D), computing $\mathbf{R}_{FU}^{-1}$ and particle velocities (CALVELO), forming Brownian motion and Brownian stress (BRWNIAN), computing particle rheology (CALSTRS), and integrating new particle trajectories (TRAJECT). Under the columns of sample sizes, we report the timing in minutes and the percentage of total time for each computational task. The table clearly shows that the inversion of $\mathbf{R}_{FU}$, which must be executed at every time step, plays an essential role in stokesian dynamics simulation. Its percentage of total simulation time ranges from 70% for N=27 to 86% for N=126. A 10^5 time-step simulation (100 shear time units) with 27 particles requires approximately 250 minutes or 4.2 hours on the IBM RiSC/6000 model 560 computer. With the less powerful RiSC/6000 model 530 computer rated at 20 MFLOPS, the similar 10^5 time-step simulation requires about 11 hours. With the present power of workstations, simulations in three dimensions with less than 100 particles can be routinely performed, making the Stokesian dynamics method accessible to scientists, researchers and engineers.

Table C.1: Details of the timing for the three main computational tasks of **stokesian**: forming and inverting the grand mobility matrix $\mathcal{M}^*$, forming Brownian motion $\nabla \cdot \mathbf{R}_{FU}^{-1}$ and Browian stress $\nabla \cdot (\mathbf{R}_{SU} \cdot \mathbf{R}_{FU}^{-1})$, and forming $\mathbf{R}_{FU}^{-1}$ and computing particle velocity U. The runs are with 126 particles on the IBM RiSC/6000 model 560 computer and the timing in seconds is averaged for 100 runs.

COMPUTATIONAL TASKS (NUMPART=126)	Time in Seconds	Total Time in Seconds
1. Form and invert moblity matrix		67.80
1.a Form mobility matrix $\mathcal{M}^*(N11 \times N11)$	17.80	
1.b Compute mobility inverse $\mathcal{M}^{*-1}$	50.00	
CHOLESKY matrix inversion		
1.b.1 $N6 \times N6$	13.10	
1.b.2 $N5 \times N5$	7.18	
BLAS3 DGEMM matrix-matrix multiply		
1.b.3 $N5 \times N6 \times N6$	7.90	
1.b.4 $N5 \times N5 \times N6$	7.00	
1.b.5 $N6 \times N5 \times N5$	6.92	
1.b.6 $N6 \times N6 \times N5$	7.90	
2. Compute Brownian motion $\nabla \cdot \mathbf{R}_{FU}^{-1}$ and Brownian stress $\nabla \cdot (\mathbf{R}_{SU} \cdot \mathbf{R}_{FU}^{-1})$		20.10
2.a Subroutine BRWNIAN	1.07	
2.b Subroutine BIGSTEP	19.03	
3. Compute $\mathbf{R}_{FU}^{-1}$ and particle velocities U		13.20
3.a Compute $\mathbf{R}_{FU}^{-1}$	13.10	
3.b Compute U	0.10	

Table C.2: Timing for the main computational tasks of stokesian dynamics program. The final time of these tasks is averaged with 100 sample runs. Each run has 1000 time steps of DT=0.001.$\mathcal{M}^*$, $\mathcal{M}^{*-1}$ and $\nabla\cdot\mathcal{M}^*$ are formed one for every 100 time steps. CPU timing in minutes is taken for the IBM RiSC/6000 computer model 560 computer. The columns show these runs with three different numbers of particles: N=27, 81 and 126. A production run with N=27 and 10^5 time steps of DT=0.001 (shear time of 100 units) as reported in this thesis requires approximately 250 minutes or 4.2 hours on the IBM RiSC/6000 model 560 computer.

	NUMPART = 27		NUMPART = 81		NUMPART = 126	
Subroutine	**Time (min.)**	**% Total Time**	**Time (min.)**	**% Total Time**	**Time (min.)**	**% Total Time**
CALDIST	0.02	0.76	0.21	0.29	0.51	0.20
FORMOBI	0.21	7.95	3.51	4.91	11.54	4.53
ADLUB3D	0.19	7.20	3.78	5.29	11.81	4.64
CALVELO	1.86	70.44	60.02	84.03	220.21	86.50
BRWNIAN	0.33	12.50	3.63	5.08	9.92	3.90
CALSTRS	0.03	1.14	0.26	0.36	0.58	0.23
TRAJECT	0.01	0.01	0.02	0.03	0.01	0.00
**********	*****	****	*****	****	*****	****
Total Time	2.64	100.00	71.43	100.00	254.58	100.00

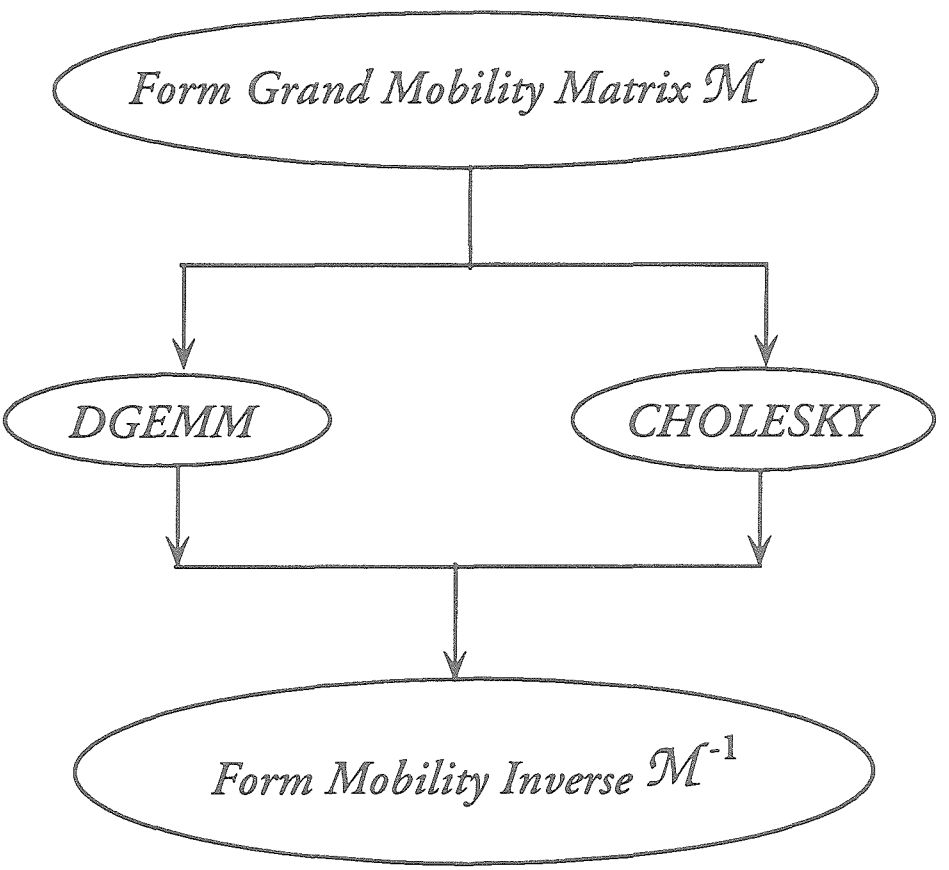

Figure C.1: Flow chart of subroutine "*FORMOBI*" which forms the grand mobility matrix $\mathcal{M}$ and its inverse $\mathcal{M}^{-1}$. The two subroutines "*CHOLESKY*" for inverting a symmetric and positive definite matrix and BLAS3 (Basic Linear Algebra Subprograms) "*DGEMM*" subprogram for fast matrix-matrix multiply are used to invert $\mathcal{M}$.

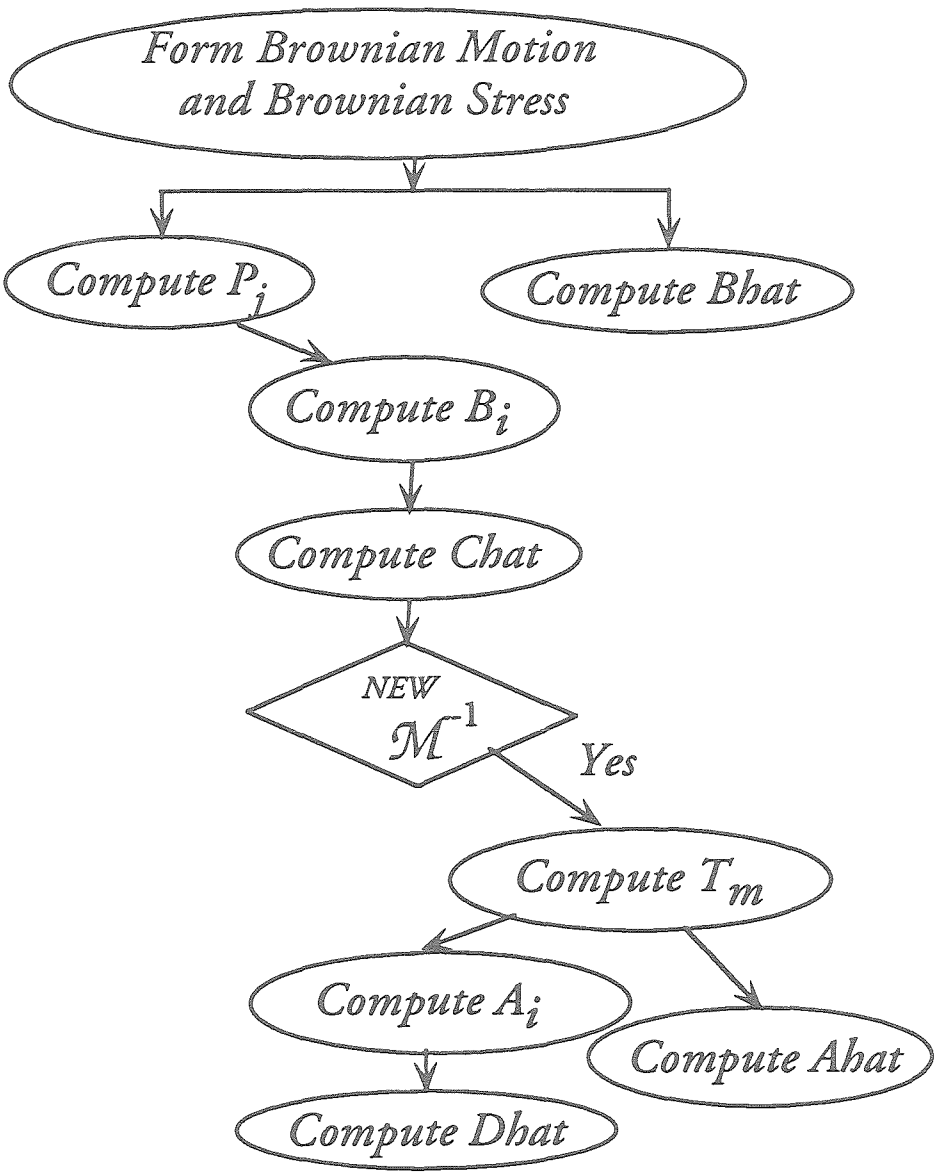

Figure C.3: Details of the computational tasks for Brownian motion $\nabla . R^{-1}_{FU} = A_i + B_i$ and Brownian stress $S^B = Ahat + Bhat + Chat + Dhat$.

REFERENCES

Ackerson B. J., Clark N. A., "Shear-Induced Melting," *Phys. Rev. Lett.*, **46**, 123, 1981.

Ackerson B. J., van der Werff, de Kruif C. G., "Hard-Sphere Dispersions: Small-Wave-Vector Structure Factor Measurements in a Linear Shear Flow," *Phys. Rev. A.*, **37**, 4819, 1988.

Ackerson B. J., Pusey P. N., "Shear-Induced Order in Suspensions of Hard Spheres," *Phys. Rev. Lett.*, **61**, 1033, 1988.

Ackerson B. J., de Kruif C. G., Wagner N. J., Russel W. B., "Comparison of Small Shear Flow Rate-Small Wave Vector Static Structure Factor Data With Theory," *J. Chem. Phys.*, **90**, 3250, 1989.

Ackerson B. J., "Shear-Induced Order and Shear Processing of Model Hard Sphere Suspensions," *J. Rheol.*, **34**, 553, 1990.

Acrivos A., Herbolzheimer E., "Sedimentation in Settling Tanks with Inclined Walls. the Boycott Effect," *J. Fluid Mech.*, **92**, 435, 1979.

Adler P. M., Brenner H., "Spatially Periodic Suspensions of Convex Particles in Linear Shear Flows. I. Description and Kinematics," *Int. J. Multiphase Flow*, **11**, 361, 1985.

Adler P. M., Zuzovsky M., Brenner H., "Spatially Periodic Suspensions of Convex Particles in Linear Shear Flows. II. Rheology," *Int. J. Multiphase Flow*, **11**, 387, 1985.
Allen M. P., Tildesley D. J., in "Computer Simulation of Liquids," page 58, Oxford University Press, 1990.

Adler B. J., Wainwright T. E., "Phase Transition in Elastic Disks," *Phys. Rev.*, **127**, 359, 1962.

Ansell G. C., Dickinson E., "Sediment Formation of Brownian Dynamics Simulation; Effect of Colloidal and Hydrodynamic Interactions on the Sediment Structure," *J. Chem. Phys.*, **85**, 1986.

Barnes H. A., "Shear-Thickening (Dilatancy) in Suspensions of Nonaggregating Solid Particles Dispersed in Newtonian Liquids," *J. Rheol.*, **33**, 329, 1989.

Batchelor G. K., "The Stress System in a Suspension of Force-Free Particles," *J. Fluid Mech.*, **41**, 545, 1970.

Batchelor G. K., "Sedimentation in a Dilute Dispersion of Spheres," *J. Fluid Mech.*, **52**, 245, 1972.

Batchelor G. K., "The Effect of Brownian Motion on the Bulk Stress in a Suspension of Spherical Particles," *J. Fluid Mech.*, **83**, 97, 1977.

Batchelor G. K., "Sedimentation in a Dilute Polydisperse System of Interacting Spheres. Part 1. General Theory," *J. Fluid Mech.*, **119**, 379, 1982.

Batchelor G. K., Wen C. S., "Sedimentation in a Dilute Polydisperse System of Interacting Spheres. Part 2. Numerical Results," *J. Fluid Mech.*, **124**, 495, 1982.

Bauer J. E., "Hydrodynamic Interactions in Polymer Dynamics," Ph. D. Thesis, *Dept. of Chem. Eng.*, California Institute of Technology, 1992.

Beenakker C. W. J., Mazur P., "Diffusion of Spheres in a Concentrated Suspension: Resummation of Many-Body Hydrodynamics Interactions ," *Phys. Lett.*, **A98**, 22, 1983.

Beenakker C. W. J., Mazur P., "Diffusion of Spheres in a Concentrated Suspension. II.," *Physica*, **126A**, 349, 1984.

Berne B. J., Pecora R., in "*Dynamic Light Scattering*," Wiley, New York, 1976.

Boersma W. H., Laven J., Stein H. N., "Shear Thickening (Dilatancy) in Concentrated Dispersions," *A.I.Ch.E. J.*, **36**, 321, 1990.

Bonnecaze R. T., Brady J. F., "Dynamic Simulation of an Electrorheological Fluid," *J. Chem. Phys.*, **96**, 2183, 1992.

Bossis G., Brady J. F., "Dynamic Simulation of Sheared Suspensions. I. General Method," *J. Chem. Phys.*, **80**, 5141, 1984.

Bossis G., Brady J. F., "Self Diffusion of Brownian Particles in Concentrated Suspensions," *J. Chem. Phys.*, **87**, 5437, 1987.

Bossis G., Brady J. F., "The Rheology of Brownian Suspensions," *J. Chem. Phys.*, **91**, 1866, 1989.

Brady J. F., Bossis G., "The Rheology of Concentrated Suspensions of Spheres in a Simple Shear Flow by Numerical Simulation," *J. Chem. Phys.*, **155**, 105, 1985.

Brady J. F., Bossis G., "Stokesian Dynamics," *Ann. Rev. Fluid Mech.*, **20**, 111, 1988.

Brady J. F., Phillips R. J., Lester J. C., Bossis G., "Dynamic Simulation of Hydrodynamically Interacting Suspensions," *J. Fluid Mech.*, **185**, 257, 1988.

Brady J. F. , "Modeling Particulate Flows by Stokesian Dynamics Simulation," in "*Particulate Two-Phase Flow*," Editors: Rocco M. C., Massuyama T., vol. **118**, the American Society of Mechanical Engineers, Butterworths 1991.

Brady J. F., "The Shear Thinning Behavior of Colloidal Dispersions," *unpublished work*

Brady J. F., "The Rheological Behavior of Concentrated Colloidal Dispersions," to appear in *J. Chem. Phys.*, 1993.

Chae D. G., Ree F. H., Ree T., "Radial Distribution Functions and Equation of State of the Hard-Disk Fluid," *J. Chem. Phys.*, **50**, 1581, 1969.

Choi G. N., Kreiger I. M., "Rheological Studies on Sterically Stabilizied Model Dispersion of Uniform Colloidal Spheres. II. Steady Shear Viscosity," *J. Coll. Interface Sci.*, **113**, 101, 1986.

Chwang A. T., Wu T. Y., "Hydromechanics of Low-Reynolds-Number Flow. Part 2. Singularity Method for Stokes Flows," *J. Fluid Mech.*, **67**, 787, 1974.

Cichocki B., Felderhof B. U., "Long-Time Self-Diffusion Coefficient and Zero Frequency Viscosity of Dilute Suspensions of Spherical Brownian Particles," *J. Chem. Phys.*, **89**, 3705, 1988.

Cook R., Wilemski G., "Packing Constraints and Number Dependence in Simulations of Sheared Colloidal Suspensions," *J. Phys. Chem.*, **96**, 4023, 1992.

Dhont J. K. G., *Physica A*, "Steady State Viscosity Coefficients of Charged Colloidal Systems," **146**, 541, 1987.

Dhont J. K. G., "On the Distortion of the Static Structure Factor of Colloidal Fluids in Shear Flow," *J. Chem. Phys.*, **204**, 421, 1989.

Durlofsky L., Brady J. F., Bossis G., "Dynamic Simulation of Hydrodynamically Interacting Particles," *J. Fluid Mech.*, **180**, 21, 1987.

Eckstein E. C., Bailey D. G., Shapiro A. H., "Self-Diffusion of Particles in Shear Flow of a Suspension," *J. Fluid Mech.*, **79**, 191, 1977.

Erickson U., Engsrtöm G., Rigdahl M., "Viscosity of Some Clay-Based Coatings Colors at High Shear Rates," *Rheo. Acta*, **29**, 1990.

Ermak D. L., McCammon J. A., "Brownian Dynamics with Hydrodynamic Interactions," *J. Chem. Phys.*, **69**, 1352, 1978.

Erpenbeck J. J., "Nonequilibrium Molecular Dynamics Calculations of the Shear Viscosity of Hard Spheres," *Physica*, **118A**, 144, 1983.

Erpenbeck J. J., "Shear Viscosity of the Hard-Sphere Fluid Via Nonequilibrium Molecular Dynamics," *Phys. Rev. Lett.*, **52**, 1333, 1984.

Felderhof B. U., "Brownian Motion and the Creeping Flow on the Smoluchowski Time Scale," *Physica A*, **147**, 202, 1989.

Ferrini F., Ercolani D., de Cindio B., Nicolais L., Randano S., "Shear Viscosity of Settling Suspensions," *Rheo. Acta*, **29**, 289, 1990.

Jeffrey D. J., Acrivos A., "The Rheological Properties of Suspensions of Rigid Particles," *A.I.Ch.E. J.*, **22**, 417, 1976.

Johnson S. J., de Kruif C. G., May R. P., "Structure Factor Distortion for Hard-Sphere Dispersions Subjected to Weak Shear Flow: Small-Angle Neutron Scattering in the Flow-Vorticity Plane," *J. Chem. Phys.*, **89**, 5909, 1988.

Gadala-Maria F. A., "The Rheology of Concentrated Suspensions," Ph. D. Thesis, *Dept. of Chem. Eng.*, Standford University, 1979.

Graham A. L., Bird R. B., "Particle Clusters in Concentrated Suspensions. 1. Experimental Observations of Particle Clusters," *Ind. Eng. Chem. Fundma.*, **23**, 406, 1984.

Graham A. L., Bird R. B., "Particle Clusters in Concentrated Suspensions. 2. Information Theory and Particle Clusters," *Ind. Eng. Chem. Fundma.*, **23**, 411, 1984.

Graham A. L., Bird R. B., "Particle Clusters in Concentrated Suspensions. 3. Prediction of Suspension Viscosity," *Ind. Eng. Chem. Fundma.*, **23**, 420, 1984.

Hasimoto H., "On the Periodic Fundamental Solution of Stokes Equations and Their Applications to Viscous Flow Past a Cubic Array of Spheres," *J. Fluid Mech.*, 317, 1958.

Herbolzheimer E., Acrivos A., "Enhanced Sedimentation in Narrow Titled Channels," *J. Fluid Mech.*, **108**, 485, 1981.

Heyes D. M., "Rheology of Molecular Liquids and Concentrated Suspensions by Microscopic Dynamic Simulations," *J. nonNewt. Fluid Mech.*, **27**, 47, 1988.

Hoffman R. L., "Discontinuous and Dilatant Viscosity Behavior in Concentrated Suspensions. I. Observation of a Flow Instability," *Trans. Soc. Rheo.*, **16**, 152, 1972.

Hoffman R. L., "Discontinuous and Dilatant Viscosity Behavior in Concentrated Suspensions. II. Theory and Experimental Tests," *J. Coll. Interface Sci.*, **46**, 491, 1974.

Hoffman R. L.,"Discontinuous and Dilatant Viscosity Behavior in Concentrated Suspensions. III. Necessary Conditions for Their Occurrence in Viscometric Flows," *Adv. Coll. Interface Sci.*, **17**, 161, 1982.

Hoover W. G., Ree F. H., "Melting Transition and Communal Entropy for Hard Spheres," *J. Chem. Phys.*, **49**, 3609, 1968.

Kalos M. H., Whitlock P. A., in "Monte Carlo Methods. Volume I: Basics," John Wiley, Wiley-Interscience publication, 1986.

Koch D. L., Brady J. F., "Dispersion of Fixed Beds," *J. Fluid Mech.*, **154**, 399, 1985.

Koch D. L., Brady J. F., "A Non-Local Description of Advection-Diffusion with Application to Dispersion in Porous Media," *J. Fluid Mech.*, **180**, 387, 1987.

Koch D. L., Shaqfeh E. S. G., "The Instability of a Dispersion of Sedimenting Spheroids," *J. Fluid Mech.*, **209**, 521, 1989.

Kock D. L., Shaqfeh E. S. G., "Screening in Sedimenting Suspensions," *J. Fluid Mech.*, **224**, 275,1991.

Kops-Werkhoven M. M., Pathmamanoharan C., Vrij A., Fijnaut H. M., "Concentration Dependence of the Self-Diffusion Coefficient of Hard, Spherical Particles Measured With Photon Correlation Spectroscopy," *J. Chem. Phys.*, **77**, 5913, 1982.

Kops-Werkhoven M. M., Fijnaut H. M., "Dynamic Light Scattering and Sedimentation Experiments on Silica Dispersions at Finite Concentrations," *J. Chem. Phys.*, **74**, 1618, 1981.

Kose A, Hachisu S., "Kirkwood-Adler Transition in Monodispersed Latexes I. Nonaqueous System," *J. Coll. Interface Sci.*, **46**, 460, 1974.

Krieger I. M., "Rheology of Monodispersed Latices," *Adv. Coll. Interface Sci.*, **3**, 111, 1972.

Ladd A. J. C., "Hydrodynamic Interactions in a Suspension of Spherical Particles," *J. Chem. Phys.*, **88**, 5051, 1988.

Ladd A. J. C., "Hydrodynamic Transport Coefficients of Random Dispersions of Hard Spheres," *J. Chem. Phys.*, **93**, 3484, 1990.

Ladd A. J. C., "Dynamical Simulations of Sedimenting Spheres," submitted to *Phys. of Fluids A*, 1992.

Laun H. M., "Rheological Properties of Polymer Dispersions with respect to Shear-Induced Particle Structures," *Prog. Trends Rheol. II*, Supplement to *Rheological Acta*, 287, 1988.

Laun H. M., Bung R., Hess S., Loose W., Hess O., Hahn K., Hädicke E., Hignmann R., Schmidt F., Lindner P., "Rheological and Small Angle Neutron Scattering Investigation of Shear-Induced Particle Structures of Concentrated Polymer Dispersions Submitted to Plane Poiseuille and Couette Flow," *J. Rheol.*, **36**, 743, 1992.

Leighton D., Acrivos A., "Measurement of Shear-Induced Self-Diffusion in Concentrated Suspensions of Spheres," *J. Fluid Mech.*, **177**, 109, 1987.

Lester J. C., "Hydrodynamic Dispersion in Concentrated Sedimenting Suspensions," Ph.D. Thesis, *Dept. of Chem. Eng.*, California Institute of Technology, 1988.

McQuarrie D. A., chapter 13, "Statistical Mechanics," Harper&Row, 1976.

Mirza S., Richardson J. F., "Sedimentation of Suspensions of Particles of Two or More Sizes," *Chem. Eng. Sci.*, **34**, 447, 1979.

Nunan K. C., Keller J. B., "Effective Viscosity of a Periodic Suspension," *J. Fluid Mech.*, **142**, 269, 1984.

O'Brien R. W., "A Method for the Calculation of the Effective Transport Properties of Suspensions of Interacting Particles," *J. Fluid Mech.*, **91**, 17, 1979.

Pätzold R., "Die Abhängigkeit des FlieBverhaltens Konzentrierter Kugelsuspensionen von der Strömungsform: Ein Vergleich der Viskosität in Scher-und Dehnströmungen," *Rheo. Acta*, **19**, 322, 1980.

Phan S. E., Leighton D. T., "Measurement of the Shear-Induced Tracer Diffusivity in Concentrated Suspensions," in preparation for submitting to *J. Fluid Mech.*, 1992.

Phillips R. J., Brady J. F., Bossis G., "Hydrodynamic Transport Properties of Hard-Sphere Dispersions: I. Suspensions of Freely Mobile Particles," *Phys. Fluids*, **31**, 3462, 1988.

Phillips R. J., Brady J. F., Bossis G., "Hydrodynamic Transport Properties of Hard-Sphere Dispersions: II. Porous Media," *Phys. Fluids*, **31**, 3473, 1988.

Phung T. N., Brady J. F., "Microstructured Fluids: Structure, Diffusion, and Rheology of Colloidal Dispersions," submitted for Proc. First Tohwa Symposium: "Slow dynamics in condense matter," AIP Conference Proceeding #256, p.391 (1992).

Press W. H., Teukolsky S. A., Vetterling W. T., Flannery B. P., chapter 2, "Solution of Linear Algebraic Equations," in "Numerical Recipes in C: The Art of Scientific Computing," Cambridge University Press, 1988.

Pusey P. N., van Megen W., "Physics of Complex and Supermolecular Fluids," Eds. Safran S. A., Clark N. A., Wiley, New York, 1987.

Pusey P. N., van Megen W., "Phase Behavior of Concentrated Suspensions of Nearly Hard Colloidal Spheres," *Nature*, **320**, 340, 1986.

Pusey P. N., chapter 10, "Colloidal Suspensions," in "Liquid, Freezing, and Glass Transition," edited by Hansen J. P., Levesque D, and Zinn-Justin, Elsevier Science Publisher, B.VI., 1991.

Qiu X., Ou-Yang H. D., Pine D. J., Cahikin P. M., "Self-Diffusion of Interacting Colloids Far From Equilibrium," *Phys. Rev. Lett.*, **61**, 28, 1988.

Rallison J. M., Hinch E. J., "The Effect of Particle Interactions on Dynamic Light Scattering From a Dilute Suspension," *J. Fluid Mech.*, **167**, 131, 1986.

Rigors A. A., Wilemski G., "Brownian Dynamics Simulations of an Order-Disorder Transition in Sheared Sterically Stabilized Colloidal Suspensions," *J. Phys. Chem.*, **96**,3981, 1992.

Robbins M. O., Kremer K., Grest G. S., "Phase Diagram and Dynamics of Yukawa Systems," *J. Chem. Phys.*, **88**, 3286, 1988.

Ronis D., "Deybe-Scherrer Light-Scattering Patterns for Dilution Colloidal Suspensions Undergoing Shear Flow," *Phys. Rev. Lett.*, **52**, 473, 1984.

Ronis D., "Theory of Fluctuation in Colloidal Suspensions Undergoing Steady Shear Flow," *Phys. Rev. A.*, **29**, 1453, 1984.

Ronis D., "Configurational Viscosity of Dilute Colloidal Suspensions," *Phys. Rev. A.*, **34**, 1422, 1986.

Rotne J, Prager S., "Variational Treatment of Hydrodynamic Interaction in Polymers," *J. Chem. Phys.*, **50**, 4831, 1969.

Russel W. B., Gast A. P., "Nonequilibrium Statistical Mechanics of Concentrated Colloidal Dispersions: Hard Spheres in Weak Flows," *J. Chem. Phys.*, **84**, 1815, 1986.

Russel W. B., Saville D. A., Scholwater W. R., in "Colloidal Dispersion," Cambridge Monographs on Mechanics and Applied Mathematics, 1989.

Rutgers Ir. R., "Relative Viscosity of Suspensions of Rigid Spheres in Newtonian Liquids," *Rheo. Acta*, **2**, 202, 1962.

Schwarzl J. F., Hess S., "Shear-Flow-Induced Distortion of the Structure of a Fluid: Application of a Simple Kinetic Equation," *Phys. Rev. A.*, **33**, 4277, 1986.

Snook I., van Megen W., Tough R. J. A., "Diffusion in Concentrated Hard Sphere Dispersions: Effective Two Particle Mobility Tensors," *J. Chem. Phys.*, **78**, 5825, 1983.

Stoer J., Bulirsch R., "Introduction to Numerical Analysis", Springer-Verlag, New York, 1980, 169-172.

Strassen Volker, "Gaussian Elimination is not Optimal," *Numerische Mathematik*, **13**, 354, 1969.

Tomita M., van de Ven I. G. M., "The Structure of Sheared Ordered Lattices," *J. Coll. Interface Sci.*, **99**, 374, 1984.

van der Werff J. C., de Kruif C. G., "Hard-Sphere Colloidal Dispersions: the Scaling of Rheological Properties with Particle Size, Volume Fraction and Shear Rate," *J. Rheol.*, **33**, 421, 1989.

van der Werff J. C., "The Rheology of Hard-Sphere Dispersions," Ph. D. thesis, Van't Hoff Laboratory, University of Utrecht, Padualaan 8, 3584 CH Utrecht, the Netherlands, 1990.

van de Ven T., in "Colloidal Hydrodynamics," Academic Press, 1989.

van Megen W. , Underwood S. M., Snook I., "Tracer Diffusion in Concentrated Colloidal Dispersions," *J. Chem. Phys.*, **85**, 4065, 1986.

van Veluwen A., Lekkerkerker H. N. W., de Kruif C. G., Vrij A., "Influence of Polydispersity on Dynamic Light Scattering Measurements on Concentrated Suspensions," *J. Chem. Phys.*, **89**, 2810, 1988.

Wagner N. J., Russel W. B., "Nonequilibrium Statistical Mechanics of Concentrated Colloidal Dispersions: Hard Spheres in Weak Flows With Many-Body Thermodynamic Interactions," *Physica*, **155**, 475, 1989.

Weider T., Stottut U., Loose W., Hess S., "Order in Fluids: Shear Induced Anisotropy in Dense Fluids of Spherical Particles and in Gases of Rotating Molecules," *Physica A*, **174**, 1, 1991.

Wilemski G., "Nonequilibrium Brownian Dynamics Simulations of Shear Thinning in Concentrated Colloidal Suspensions," *J. Stat. Phys.*, **62**, 1239, 1991.

Woodcock L. V., "Glass Transition in the Hard-Sphere Model and Kauzman's Paradox," *Ann. New York Acad. Sci.*, **371**, 274, 1981.

Xue W., Grest G., "Shear-Induced Alignment of Colloidal Particles in the Presence of a Shear Flow," *Phys. Rev. Lett.*, **64**, 419, 1990.

Zick A. A., Homsy G. M., "Stokes Flow Through Periodic Arrays of Spheres," *J. Fluid Mech.*, **115**, 13, 1981.

Zuzovsky M., Adler P. M., Brenner H., "Spatially Periodic Suspensions of Convex Particles in Linear Shear Flows. III. Dilute Arrays of Spheres Suspended in Newtonian Fluids," *Phys. Fluids*, **26**, 1714, 1983.